Springer Proceedings in Physics 259

Gongtian Shen
Junjiao Zhang
Zhanwen Wu *Editors*

Advances in Acoustic Emission Technology

Proceedings of the World Conference on Acoustic Emission—2019

Springer

Springer Proceedings in Physics

Volume 259

Indexed by Scopus

The series Springer Proceedings in Physics, founded in 1984, is devoted to timely reports of state-of-the-art developments in physics and related sciences. Typically based on material presented at conferences, workshops and similar scientific meetings, volumes published in this series will constitute a comprehensive up-to-date source of reference on a field or subfield of relevance in contemporary physics. Proposals must include the following:

- name, place and date of the scientific meeting
- a link to the committees (local organization, international advisors etc.)
- scientific description of the meeting
- list of invited/plenary speakers
- an estimate of the planned proceedings book parameters (number of pages/articles, requested number of bulk copies, submission deadline).

Please contact:

For Americas and Europe: Dr. Zachary Evenson; zachary.evenson@springer.com
For Asia, Australia and New Zealand: Dr. Loyola DSilva; loyola.dsilva@springer.com

More information about this series at http://www.springer.com/series/361

Gongtian Shen · Junjiao Zhang · Zhanwen Wu
Editors

Advances in Acoustic Emission Technology

Proceedings of the World Conference on Acoustic Emission—2019

Springer

Editors
Gongtian Shen
China Special Equipment Inspection
and Research Institute
Hepingjie, Chaoyang, Beijing, China

Junjiao Zhang
China Special Equipment Inspection
and Research Institute
Hepingjie, Chaoyang, Beijing, China

Zhanwen Wu
China Special Equipment Inspection
and Research Institute
Hepingjie, Chaoyang, Beijing, China

ISSN 0930-8989 ISSN 1867-4941 (electronic)
Springer Proceedings in Physics
ISBN 978-981-15-9836-4 ISBN 978-981-15-9837-1 (eBook)
https://doi.org/10.1007/978-981-15-9837-1

© The Editor(s) (if applicable) and The Author(s), under exclusive license to Springer Nature Singapore Pte Ltd. 2021
This work is subject to copyright. All rights are solely and exclusively licensed by the Publisher, whether the whole or part of the material is concerned, specifically the rights of translation, reprinting, reuse of illustrations, recitation, broadcasting, reproduction on microfilms or in any other physical way, and transmission or information storage and retrieval, electronic adaptation, computer software, or by similar or dissimilar methodology now known or hereafter developed.
The use of general descriptive names, registered names, trademarks, service marks, etc. in this publication does not imply, even in the absence of a specific statement, that such names are exempt from the relevant protective laws and regulations and therefore free for general use.
The publisher, the authors and the editors are safe to assume that the advice and information in this book are believed to be true and accurate at the date of publication. Neither the publisher nor the authors or the editors give a warranty, expressed or implied, with respect to the material contained herein or for any errors or omissions that may have been made. The publisher remains neutral with regard to jurisdictional claims in published maps and institutional affiliations.

This Springer imprint is published by the registered company Springer Nature Singapore Pte Ltd.
The registered company address is: 152 Beach Road, #21-01/04 Gateway East, Singapore 189721, Singapore

Committees

Organization Committee

Chair

Gongtian Shen, China Special Equipment Inspection and Research Institute

Co-chairs

Gary Qi, University of Memphis
Wei Li, Northeast Petroleum University

Members

Allen Green, Acoustic Emission Technology Consulting
Jingyuan Ji, Chinese Society for Non-destructive Testing
Shifeng Liu, QingCheng AE Institute
Zhen Huo, Wuhan Boiler and Pressure Vessel Inspection Institute
Weihe Guan, Hefei General Machinery Research Institute
Zhejun Liu, Aerospace Research Institute of Materials and Processing Technology
Guanghai Li, China Special Equipment Inspection and Research Institute
Jun Jiang, Nanjing Boiler and Pressure Vessel Inspection Institute
Yanting Xu, Zhejiang Provincial Special Equipment Inspection and Research Institute
Yibiao Dong, QingCheng AE Institute
Zhanwen Wu, China Special Equipment Inspection and Research Institute

Paper and Program Committee

Chair

Gongtian Shen, China Special Equipment Inspection and Research Institute

Co-chair

Gary Qi, University of Memphis

Members

Allen Green, Acoustic Emission Technology Consulting
Oswaldo Santos Filho, Technology Center, Eletronorte
Karen M Holford, Cardiff University
Andy Chit Tan, Universiti Tunku Abdul Rahman
Gerald Lackner, TÜV Austria Services GmbH
Tomoki Shiotani, Kyoto University
Oleg Viktorovich Bashkov, Komsomolsk-on-Amur State Technical University
Shifeng Liu, QingCheng AE Institute
Guanghai Li, China Special Equipment Inspection and Research Institute
Cherdpong Jomdecha, King Mongkut's University of Technology

Secretary Committee

Chair

Guanghai Li, China Special Equipment Inspection and Research Institute

Members

Zhanwen Wu, China Special Equipment Inspection and Research Institute
Jingyuan Ji, Chinese Society for Non-destructive Testing
Junjiao Zhang, China Special Equipment Inspection and Research Institute
Yaqing Zhu, Chinese Society for Non-destructive Testing
Yingyun Wang, Chinese Society for Non-destructive Testing

Advisory Committee

Gary Qi, University of Memphis, USA
Allen Green, Acoustic Technology Group, USA
Gongtian Shen, China Special Equipment Inspection and Research Institute, China
Manabu Enoki, University of Tokyo, Japan
Karen M Holford, Cardiff University, UK
Oswaldo Goncalves dos Santos Filho, Eletronorte Technology Center, Brazil
Tomoki Shiotani, Kyoto University, Japan
Peter Tscheliesnig, AT—Consult e.U., Austria
Gerald Lackner, TÜV AUSTRIA SERVICES GMBH, Austria
Andy Chit Tan, Universiti Tunku Abdul Rahman, Malaysia
Oleg Bashkov, Komsomolsk-on-Amur State Technical University, Russia

Cherdpong Jomdecha, King Mongkut's university of technology Thonburi, Thailand
Hartmut Vallen, Vallen System, Germany
Jason Dong, MISTRAS Group, Inc., USA
Elizarov Sergey, "INTERUNIS-IT" LLC, Russia
Janez Grum, University of Ljubljana, Slovenia
Rhys Pullin, Cardiff University, UK
Rongsheng Geng, Beijing Aeronautical Technology Research Center, China
Shifeng Liu, QingCheng AE Institute, China
Bangxian Li, China Special Equipment Inspection and Research Institute, China
Guanghai Li, China Special Equipment Inspection and Research Institute, China
Zhen Huo, Wuhan Boiler and Pressure Vessel Inspection Institute, China
Guang Dai, Northeast Petroleum University, China
Wei Li, Northeast Petroleum University, China
Weihe Guan, Hefei General Machinery Research Institute, China
Zhejun Liu, Aerospace Research Institute of Materials and Processing Technology, China
Jun Jiang, Nanjing Boiler and Pressure Vessel Inspection Institute, China
Yanting Xu, Zhejiang Provincial Special Equipment Inspection and Research Institute, China
Yibiao Dong, QingCheng AE Institute, China
Didem Ozevin, University of Illinois, USA
Alain Proust, Mistras France, France
Martin Browne, University of Southampton, UK
Steven F. Wayne, The University of Memphis, USA
Alan A. Barhorst, Texas Tech University, USA
Vaclav Svoboda, PREDITEST, Czech
Jonathan Awerbuch, Drexel University, USA
Vladimir Genis, Drexel University, USA
Boris Muravin, Margan Physical Dianostics Ltd., Israel
Oh-Yang Kwon, Inha University, Korea
Michael C Forde, University of Edinburgh, UK
Els Verstrynge, Ku Leuven (University of Leuven), Belgium
Guiyun Tian, University of Newcastle, UK
Reuben, Robert, Heriot-Watt University, UK
Antolino Gallego Molina, University of Granada, Spain
David E. Kosnik, CTL Group, USA
Victor Shemyakin, Diapac, Russia
Pedro Feres Filho, Physical Acoustics South America, Brazil
Mochen Ge, Missouri University of Science and Technology, USA
Rickard Nordstrom, Richard Nordstrom Consulting, USA
Gordon Schneider, Acoustic Technology Group, Inc., USA
Jan Plowiec, Warsaw University of Technology, Poland
Gabor Por, University of Dunaujvaros, Hungary
Athanasios (Nassos) Anastasopoulos, Mistras Greece, Greece

Hermann Shubert, Mistras Germany, Germany
Manuel Lohr, Mistras Germany, Germany
Hossain Saboonchi, Mistras USA, USA
Obdulia Ley, Mistras USA, USA

Preface

This volume includes the papers selected from the World Conference on Acoustic Emission—2019 (WCAE-2019) that was held during November 5–8 in Guangzhou, China. WCAE was the formal conference of the International Society on Acoustic Emission (ISAE). WCAE-2019 was jointly organized by Chinese Society for Non-destructive Testing (ChSNDT) and China Special Equipment Inspection and Research Institute (CSEI). This was the fifth of such event of ISAE followed by its inaugural one in 2011 in Beijing, second in 2013 in Shanghai, China, third in 2015 in Hawaii, USA, and fourth in 2017 in Xi'an, China. WCAE is aimed at providing a platform to scientists and practitioners in both academia and industry in the field of acoustic emission and exchanging research and application information, with particular emphasis on scientific and technical development and cooperation worldwide.

The WCAE-2019 consisted of five invited keynote lectures, ten oral, and one poster sessions. It covered all the major areas of acoustic emission applications, including Instrumentation, signal processing and analysis, material characteristics, structure, condition Monitoring and diagnosis, and miscellaneous.

WCAE-2019 received 73 submissions, which were documented in the extended abstracts of WCAE-2019. Fifty-eight full papers were submitted for the consideration of achieved formal proceedings. After peer reviews, 50 were included in this volume.

We are grateful to all the members of the committees who contributed their efforts to review the manuscripts. We would also like to express our sincere gratitude to Chinese Society for Non-destructive Testing (ChSNDT) and China Special Equipment Inspection and Research Institute (CSEI) for their enormous supports. Last but not least, we thank the contributions of all the delegates who participated in WCAE-2019.

Beijing, China

Gongtian Shen
Junjiao Zhang
Zhanwen Wu

Contents

Part I Keynote Lecture

1 Localization and Discrimination of Microseismic/AE Sources in Mining: From Data to Information 3
Longjun Dong

Part II Instrumentation

2 Internet of Things Acoustic Emission: Systems and Applications 19
Jiehui Xie, Shuang Wang, Wei Liu, Huilan Yang, Lidong Zhang, and Shifeng Liu

3 About an Initial Draft of a Standard Concerning Sensitivity Verification of Acoustic Emission Sensors 33
Hartmut Vallen

4 Comparative Analysis of the International Status of Acoustic Emission Equipment Performance Testing 41
Junjiao Zhang, Gongtian Shen, Yilin Yuan, Yongna Shen, and Zhanwen Wu

Part III Signal Processing and Analysis

5 An Improved Beam Method for Acoustic Emission Source Localization in Thin Plates 53
Zihao Zhao, Ran Zhao, Xianlei Ye, Jianwen Wang, Tian He, and Qiang Pan

6 Correlation Analysis of Acoustic Emission Signals at Different Distances Form Hypervelocity Simulation Damage Source 63
Liu Wugang, Hou Chuantao, Wang Long, and Ren Fang

7 An Acoustic Emission Source Localization Method Based Ant Colony Without Premeasured Velocity 71
Qingchun Hu and Longjun Dong

8 Acoustic Emission and Dual-Tree Complex Wavelet Transform with Soft Threshold De-Noising to Enhance Pipeline Leak Detection and Location 79
L. L. Ting, J. Y. Tey, A. C. Tan, Y. J. King, and F. A. Rahman

9 Burst Analysis for Multi-Level Leakage Detection in Water-Filled Pipeline Based on Acoustic Emission Signal 93
Bach Phi Duong, Jaeyoung Kim, Inkyu Jeong, and Jong-Myon Kim

10 Prediction of Residual Life of Oil and Gas Pipeline Corrosion Based on Deep Learning 105
Wang Xinying, Zhang Huiran, Zhang Ruicheng, Zhao Bin, Huang Xuan, and Zhang Ying

11 Improving Bearing Diagnostic Performance by Using New Discriminatory Fault-Feature Evaluation 115
Viet Tra and Jong-Myon Kim

12 Application of Kurtosis Analysis in Fault Detection of Rolling Bearing 127
Yang Yu, Yangyang Guo, and Ping Yang

13 Fatigue Evolution of Ball Bearing with Improved Acoustic Emission Index 135
Zhihai Wang, Xiaoqin Liu, and Xing Wu

14 Study on the Propagation Law of Lamb Wave in High Stiffened Panels 149
Yantao Liu, Guoliang Xu, Gang Sun, and Zhe Wang

15 Research on AE Source Location and Identification Method of Tank Bottom Corrosion 159
Feng Qiu, Guang Dai, Mingjun Li, Dingrong Qu, and Yongliang Yu

16 Research on Extraction Method of Fatigue State Magneto Acoustic Emission Characteristic Parameters Based on CEEMD 171
Sha Wu, Gongtian Shen, Zenghua Liu, Yongna Shen, and Zhinong Li

Part IV Material Characteristics

17 Cluster Analysis of Acoustic Emission Signals on Tensile Damage Process of C/SiC Using an Improved K-Means Algorithm 185
Yongzhen Zhang, Xiaoyan Tong, and Leijiang Yao

18 Investigation of Flexural Progressive Damage of Three-Dimensional Braided Composites by Acoustic Emission and Micro-CT 199
Wei Zhou, Peng-Fei Zhang, Ran Liu, Ya-Ping Liu, Zhi-Yuan Wei, and Sa Yang

19 Fatigue Crack Growth of TC4 Titanium Alloy Using Acoustic Emission Technique 213
Wenjun Zhang, Gongtian Shen, and Yongna Shen

20 Experiment Research on Tensile Process of Glass Fiber Reinforced Plastics Basing on AE 223
Hui Luo, Wenchao Han, Yilin Yuan, Bo Ke, and Baodi Zhao

21 High-Temperature Creep Damage Evolution of C/SiC Based on Acoustic Emission 235
Guodong Bai, Xiaoyan Tong, and Leijiang Yao

22 Acoustic Emission Monitoring of Pitting Corrosion on Zirconium Metal 255
Cheng Ye, Zhongzheng Zhang, Jun Jiang, Yongliang Yu, and Yu Xue

23 Acoustic Emission in Coatings—A Review 269
Yachen Zhang, Jia Meng, Liang Wang, and Lixin Song

24 Experiment Research on Tensile Process of Type IV Gas Cylinder Liner-HDPE Based on Acoustic Emission 281
Yilin Yuan, Gongtian Shen, Junjiao Zhang, Bo Zhao, Yongna Shen, and Ke Bo

Part V Structure

25 Detection and Evaluation of Vascular Network Based Self-healing Concrete Using Acoustic Emission 299
Y. Wang, R. Pullin, M. Pearson, R. Davies, and K. Holford

26 Damage Evaluation Inside the Concrete Dam by Tomography and AE Analysis 313
Y. Yang, H. Asaue, T. Shiotani, and K. Hashimoto

27 Evaluation of Fatigue Damage in RC Slabs Considering Water Infiltration by Means of 3D AE and Elastic Wave Tomography 325
H. Asaue, T. Shiotani, S. Fukumoto, and T. Maeshima

28 Research on Acoustic Emission Technology for Tank Floor Under Interference of Nitrogen Sealing System 335
He Yan, Gongtian Shen, Liang Du, Wenjing Zhao, and Shu Xing

29 Difference Analysis of Acoustic Emission Testing Methods on Storage Tank Floor 347
Huatian Xu, Yewei Kang, Zhenghong Guo, Wei Yang, Jinggang Cao, and Linjie Duan

30 Waveguide Methods for AE Online Testing of Several Cryogenic Vertical Double-Wall Tanks 355
Yanting Xu, Yadong Wang, and Jianyong Zheng

31 Research on Immersion-Type Acoustic Emission Detection and Location Method for Large Tank Bottom 363
Junwei Gao, Ying Zhang, Shi Liu, and Zidong Zhu

32 Study on a Method of Corrosion Acoustic Emission Location for the Tank Floor 377
Zhihai Hu, Keqin Ding, Huazhong Wei, and Jiwang Zhang

33 Experiment Research on Acoustic Emission of Impact-Damaged Fully-Wrapped Composite Gas Cylinder with Non-metallic Liner 383
Ke Bo, Sanjiang Liu, Liang Cheng, Yilin Yuan, and Hui Luo

34 Application and Research of Acoustic Emission in Using Hoop-Wrapped Composite Cylinders 393
Yaping Liu, Ruipeng Zhang, Wei Zhao, and Kai Zhao

35 Acoustic Emission Testing of Energy Field Objects 403
V. V. Bardakov, S. V. Elizarov, V. A. Barat, D. A. Terentyev, V. G. Kharebov, and K. A. Medvedev

36 AE Detection of Leakage Location in an Ethylene Oxide Reactor 413
Yanting Xu, Yadong Wang, Gangyi Cai, and Jiele Xu

37 A Method of Vacuum Leak Detecting Based on Acoustic Emission Characteristics Analysis 419
Qi Lei, Sun Lichen, Liu Gaotong, Rui Xiaobo, Liu Tao, and Wang Lina

38 Acoustic Emission Testing for the Large Vacuum System and Analysis of Signal Source Data 429
Yue Kaibai, Ma Xuerong, Lu Jun, Zuo Jifeng, Yao Li, and Chen Xiaohui

39 Study on AE Detection Signal of Composite Barrel Under Axial Compression Failure Load 441
Xiaolin Li, Wei Yin, Hao Chen, Gang Sun, and Lixia Wang

40 Localization of Acoustic Emission Sources in the Steel Bifurcated Pipe of Hydropower Station 449
Weiping Wu, Zhejun Liu, Shulin Cao, Donfeng Li, and Zhen Huo

41 Study of Acoustic Emission Response to Vortex Shedding of a Bluff Body 465
Fatematuz Zohora, David Holmes, Pietro Borghesani, Michael Cholette, and YuanTong Gu

42 Damage Localization of Debris Cloud Hypervelocity Impact Based on Acoustic Emission 475
Kai Zhang, Runqiang Chi, and Baojun Pang

43 The Influence of Rod Waveguide on Acoustic Emission Signal of Different Frequencies 487
Xianglong Zeng, Qiong Deng, Bo Wang, Zhilun Deng, Xudong Wang, and Chengyu Zhang

44 Acoustic Emission Characteristics of Defects in Crawler Crane Truss Beam 503
Zhanwen Wu, Gongtian Shen, Daihua Sun, Yongna Shen, and Junjiao Zhang

Part VI Condition Monitoring and Diagnosis

45 Identification of Acoustic Emission Signals for Bearings Fault Based on Neural Network of Cuckoo Search Algorithm 517
Ping Yang, Yun Li, and Yang Yu

46 Bearing Fault Diagnosis Using Grad-CAM and Acoustic Emission Signals 527
Jaeyoung Kim and Jong-Myon Kim

47 Bearing Fault Transfer Diagnosis Based on Acoustic Emission Signal Under Variable Working Conditions 535
Jiwang Zhang, Keqin Ding, Hongzhu Wang, and Guang Chen

48 The AE Monitoring in Load Testing in Helicopter Tail Beam with Prefabricated Defects 543
Zhengjie Shao, Siyi Liu, Wei Wu, Xi Chen, and Guanhua Wu

Part VII Miscellaneous

49 A Comparison of Acoustic Emission in Cadaveric Specimens and Artificial Sawbones During Surgical Screw Implants 549
S. Grigg, B. J. Wright, and R. Pullin

50 Acoustic Emissions of Cathode Carbon Block from Aluminum Electrolytic Cell Under Deformation 561
Yu Luo, Shengxiang Li, Chao Li, Xiling Liu, and Xibing Li

Contributors

H. Asaue Department of Urban Management, Kyoto University, Kyoto, Japan; Graduate School of Engineering, Kyoto University, Kyoto, Japan

Guodong Bai National Key Laboratory of Science and Technology on UAV, Northwestern Polytechnical University, Xi'an, China

V. A. Barat INTERUNIS-IT LLC, Moscow, Russia

V. V. Bardakov INTERUNIS-IT LLC, Moscow, Russia

Zhao Bin School of Environmental and Safety Engineering, Changzhou University, Changzhou, China

Ke Bo China Special Equipment Inspection and Research Institute, Beijing, China

Pietro Borghesani School of Mechanical and Manufacturing Engineering, University of New South Wales, Sydney, NSW, Australia

Gangyi Cai Zhejiang Academy of Special Equipment Science, Hangzhou, China

Jinggang Cao PetroChina Pipeline R&D Center, Langfang, China

Shulin Cao National Center of Quality Inspection and Testing for Hydraulic Metal Structure Ministry of Water Resources, Zhengzhou, China

Guang Chen China Special Equipment Inspection and Research Institute, Beijing, China

Hao Chen Beijing Institute of Structure and Environment Engineering, Beijing, China

Xi Chen Key Laboratory of Nondestructive Testing (Nanchang Hangkong University) Ministry of Education, Jiangxi, China

Liang Cheng China Special Equipment Inspection and Research Institute, Beijing, China

Runqiang Chi Harbin Institute of Technology, Harbin, China

Michael Cholette School of Mechanical, Medical and Process Engineering, Queensland University of Technology, Brisbane, QLD, Australia

Hou Chuantao Beijing Institute of Structure and Environment Engineering, Beijing, China

Guang Dai Northeast Petroleum University, Daqing, China

R. Davies Cardiff School of Engineering, Cardiff University, Cardiff, UK

Qiong Deng School of Aeronautics, Northwestern Polytechnical University, Xi'an, China

Zhilun Deng School of Aeronautics, Northwestern Polytechnical University, Xi'an, China

Keqin Ding China Special Equipment Inspection and Research Institute, Beijing, China

Longjun Dong School of Resources and Safety Engineering, Central South University, Changsha, China

Liang Du China Special Equipment Inspection and Research Institute, Beijing, China

Linjie Duan PetroChina Pipeline R&D Center, Langfang, China

Bach Phi Duong School of Electrical Engineering, University of Ulsan, Ulsan, South Korea

S. V. Elizarov INTERUNIS-IT LLC, Moscow, Russia

Ren Fang Beijing Institute of Structure and Environment Engineering, Beijing, China

S. Fukumoto IHI Inspection and Instrumentation Co., Ltd., Yokohama, Kanagawa, Japan

Junwei Gao College of Mechanical Science and Engineering, Northeast Petroleum University, Daqing, Heilongjiang, China

Liu Gaotong Institute of Spacecraft Environment Engineering, Beijing, China

S. Grigg Cardiff School of Engineering, Cardiff University, Cardiff, UK

YuanTong Gu School of Mechanical, Medical and Process Engineering, Queensland University of Technology, Brisbane, QLD, Australia

Yangyang Guo Shenyang University of Technology, Shenyang, China

Zhenghong Guo PetroChina Pipeline R&D Center, Langfang, China

Wenchao Han China Special Equipment Inspection and Research Institute, Beijing, China

K. Hashimoto Department of Civil and Earth Resources Engineering, Kyoto University, Kyoto, Japan

Tian He School of Transportation Science and Engineering, Beihang University, Beijing, China

K. Holford Cardiff School of Engineering, Cardiff University, Cardiff, UK

David Holmes School of Mechanical, Medical and Process Engineering, Queensland University of Technology, Brisbane, QLD, Australia

Qingchun Hu School of Resources and Safety Engineering, Central South University, Changsha, China

Zhihai Hu School of Mechanical and Electrical Engineering, Wuhan Institute of Technology, Hubei, Wuhan, China;
China Special Equipment Inspection and Research Institute, Beijing, China

Zhang Huiran School of Environmental and Safety Engineering, Changzhou University, Changzhou, China

Zhen Huo Wuhan Boiler and Pressure Vessel Inspection Institute, Wuhan, China

Inkyu Jeong School of Electrical Engineering, University of Ulsan, Ulsan, South Korea

Jun Jiang Nanjing Boiler and Pressure Vessel Supervision and Inspection Institute, Nanjing, China

Zuo Jifeng China Aerodynamics Research and Development Center, Mianyang, China

Lu Jun China Aerodynamics Research and Development Center, Mianyang, China

Yue Kaibai China Aerodynamics Research and Development Center, Mianyang, China

Yewei Kang PetroChina Pipeline R&D Center, Langfang, China

Bo Ke China Special Equipment Inspection and Research Institute, Beijing, China

V. G. Kharebov LLC Research and Development Centre EGIDA, Moscow, Russia

Jaeyoung Kim Department of Electrical, Electronics and Computer Engineering, University of Ulsan, Ulsan, South Korea;
School of Electrical Engineering, University of Ulsan, Ulsan, South Korea

Jong-Myon Kim School of IT Convergence, University of Ulsan, Ulsan, South Korea;
Department of Electrical, Electronics and Computer Engineering, University of Ulsan, Ulsan, South Korea;
School of Electrical Engineering, University of Ulsan, Ulsan, South Korea

Y. J. King Lee Kong Chian Faculty of Engineering and Science, Universiti Tunku Abdul Rahman, Selangor, Malaysia

Qi Lei Institute of Spacecraft Environment Engineering, Beijing, China

Chao Li Aluminum Branch Company, Chongqing Qineng Electrictity and Aluminum Co., LTD, Chongqing, China

Donfeng Li National Center of Quality Inspection and Testing for Hydraulic Metal Structure Ministry of Water Resources, Zhengzhou, China

Mingjun Li SINOPEC Qingdao Research Institute of Safety Engineering, Qingdao, China

Shengxiang Li School of Resources and Safety Engineering, Central South University, Changsha, China

Xiaolin Li Beijing Institute of Structure and Environment Engineering, Beijing, China

Xibing Li School of Resources and Safety Engineering, Central South University, Changsha, China

Yao Li China Aerodynamics Research and Development Center, Mianyang, China

Yun Li Shenyang University of Technology, Shenyang, China

Zhinong Li College of Mechanical Engineering and Applied Electronics Technology, Beijing University of Technology, Beijing, China

Sun Lichen Institute of Spacecraft Environment Engineering, Beijing, China

Wang Lina Institute of Spacecraft Environment Engineering, Beijing, China

Ran Liu China Special Equipment Inspection and Research Institute, Beijing, China

Sanjiang Liu China Special Equipment Inspection and Research Institute, Beijing, China

Shi Liu Shenyang Longchang Pipeline Testing Center, Shenyang, Liaoning, China

Shifeng Liu Qing Cheng AE Institute Co., LTD, Guangzhou, China

Siyi Liu Aviation Industry Helicopter Design Institute(602), Jingdezhen, China

Wei Liu Qing Cheng AE Institute Co., LTD, Guangzhou, China

Xiaoqin Liu Faculty of Mechanical and Electrical Engineering, Kunming University of Science and Technology, Kunming, China

Xiling Liu School of Resources and Safety Engineering, Central South University, Changsha, China

Ya-Ping Liu Hebei Province Special Equipment Supervision and Inspection Institute Baoding Branch, Baoding, China

Yantao Liu Beijing Institute of Structure and Environment Engineering, Beijing, China

Yaping Liu Hebei Special Equipment Supervision and Inspection Institute Branch of Baoding, Baoding, China

Zenghua Liu College of Mechanical Engineering and Applied Electronics Technology, Beijing University of Technology, Beijing, China

Zhejun Liu Aerospace Research Institute of Materials & Processing Technology, Beijing, China

Wang Long Beijing Institute of Structure and Environment Engineering, Beijing, China

Hui Luo China Special Equipment Inspection and Research Institute, Beijing, China

Yu Luo School of Resources and Safety Engineering, Central South University, Changsha, China

T. Maeshima College of Engineering, Nihon University, Koriyama, Fukushima, Japan

K. A. Medvedev LLC Research and Development Centre EGIDA, Moscow, Russia

Jia Meng Key Laboratory of Inorganic Coating Materials CAS, Shanghai Institute of Ceramics, Chinese Academy of Sciences, Shanghai, China

Qiang Pan School of Transportation Science and Engineering, Beihang University, Beijing, China

Baojun Pang Harbin Institute of Technology, Harbin, China

M. Pearson Cardiff School of Engineering, Cardiff University, Cardiff, UK

R. Pullin Cardiff School of Engineering, Cardiff University, Cardiff, UK

Feng Qiu SINOPEC Qingdao Research Institute of Safety Engineering, Qingdao, China

Dingrong Qu SINOPEC Qingdao Research Institute of Safety Engineering, Qingdao, China

F. A. Rahman Lee Kong Chian Faculty of Engineering and Science, Universiti Tunku Abdul Rahman, Selangor, Malaysia

Zhang Ruicheng School of Environmental and Safety Engineering, Changzhou University, Changzhou, China

Zhengjie Shao Key Laboratory of Nondestructive Testing (Nanchang Hangkong University) Ministry of Education, Jiangxi, China

Gongtian Shen College of Mechanical Engineering and Applied Electronics Technology, Beijing University of Technology, Beijing, China;
China Special Equipment Inspection and Research Institute, Beijing, China

Yongna Shen China Special Equipment Inspection and Research Institute, Beijing, China

T. Shiotani Department of Civil and Earth Resources Engineering, Kyoto University, Kyoto, Japan;
Graduate School of Engineering, Kyoto University, Kyoto, Japan

Lixin Song Key Laboratory of Inorganic Coating Materials CAS, Shanghai Institute of Ceramics, Chinese Academy of Sciences, Shanghai, China

Daihua Sun Beijing Special Equipment Inspection & Testing Center, Beijing, China

Gang Sun Beijing Institute of Structure and Environment Engineering, Beijing, China

A. C. Tan Lee Kong Chian Faculty of Engineering and Science, Universiti Tunku Abdul Rahman, Selangor, Malaysia

Liu Tao Institute of Spacecraft Environment Engineering, Beijing, China

D. A. Terentyev INTERUNIS-IT LLC, Moscow, Russia

J. Y. Tey Lee Kong Chian Faculty of Engineering and Science, Universiti Tunku Abdul Rahman, Selangor, Malaysia

L. L. Ting Lee Kong Chian Faculty of Engineering and Science, Universiti Tunku Abdul Rahman, Selangor, Malaysia

Xiaoyan Tong National Key Laboratory of Science and Technology on UAV, Northwestern Polytechnical University, Xi'an, China

Viet Tra School of IT Convergence, University of Ulsan, Ulsan, South Korea

Hartmut Vallen Vallen Systeme GmbH, Icking, Bavaria, Germany

Bo Wang School of Aeronautics, Northwestern Polytechnical University, Xi'an, China

Hongzhu Wang China Special Equipment Inspection and Research Institute, Beijing, China

Jianwen Wang School of Transportation Science and Engineering, Beihang University, Beijing, China

Liang Wang Integrated Computational Materials Research Centre, Shanghai Institute of Ceramics, Chinese Academy of Sciences, Shanghai, China

Lixia Wang Beijing Institute of Structure and Environment Engineering, Beijing, China

Shuang Wang Qing Cheng AE Institute Co., LTD, Guangzhou, China

Xudong Wang Beijing Softland Times Scientific & Technology Co. LTD, Beijing, China

Y. Wang Cardiff School of Engineering, Cardiff University, Cardiff, UK

Yadong Wang Zhejiang Academy of Special Equipment Science, Hangzhou, China;
Key Laboratory of Special Equipment Safety Testing Technology of Zhejiang Province, Hangzhou, China

Zhe Wang Beijing Institute of Structure and Environment Engineering, Beijing, China

Zhihai Wang Faculty of Mechanical and Electrical Engineering, Kunming University of Science and Technology, Kunming, China

Huazhong Wei School of Mechanical and Electrical Engineering, Wuhan Institute of Technology, Hubei, Wuhan, China

Zhi-Yuan Wei School of Quality and Technical Supervision, Hebei University, Baoding, China

B. J. Wright Vestre Viken, Ringerike Sykehus, Hønefoss, Norway

Guanhua Wu Key Laboratory of Nondestructive Testing (Nanchang Hangkong University) Ministry of Education, Jiangxi, China

Sha Wu College of Mechanical Engineering and Applied Electronics Technology, Beijing University of Technology, Beijing, China

Wei Wu Key Laboratory of Nondestructive Testing (Nanchang Hangkong University) Ministry of Education, Jiangxi, China

Weiping Wu National Center of Quality Inspection and Testing for Hydraulic Metal Structure Ministry of Water Resources, Zhengzhou, China

Xing Wu Faculty of Mechanical and Electrical Engineering, Kunming University of Science and Technology, Kunming, China

Zhanwen Wu China Special Equipment Inspection and Research Institute, Beijing, China

Liu Wugang Beijing Institute of Structure and Environment Engineering, Beijing, China

Rui Xiaobo Institute of Spacecraft Environment Engineering, Beijing, China

Chen Xiaohui China Aerodynamics Research and Development Center, Mianyang, China

Jiehui Xie Qing Cheng AE Institute Co., LTD, Guangzhou, China

Shu Xing China Special Equipment Inspection and Research Institute, Beijing, China

Wang Xinying School of Environmental and Safety Engineering, Changzhou University, Changzhou, China

Guoliang Xu Beijing Institute of Structure and Environment Engineering, Beijing, China

Huatian Xu PetroChina Pipeline R&D Center, Langfang, China

Jiele Xu Zhejiang Academy of Special Equipment Science, Hangzhou, China

Yanting Xu Zhejiang Academy of Special Equipment Science, Hangzhou, China; Key Laboratory of Special Equipment Safety Testing Technology of Zhejiang Province, Hangzhou, China

Huang Xuan School of Environmental and Safety Engineering, Changzhou University, Changzhou, China

Yu Xue Nanjing Boiler and Pressure Vessel Supervision and Inspection Institute, Nanjing, China

Ma Xuerong China Aerodynamics Research and Development Center, Mianyang, China

He Yan China Special Equipment Inspection and Research Institute, Beijing, China

Huilan Yang Qing Cheng AE Institute Co., LTD, Guangzhou, China

Ping Yang Shenyang University of Technology, Shenyang, China

Sa Yang School of Quality and Technical Supervision, Hebei University, Baoding, China

Wei Yang China Petroleum Pipeline Engineering Corporation, Langfang, China

Y. Yang Department of Civil and Earth Resources Engineering, Kyoto University, Kyoto, Japan

Leijiang Yao National Key Laboratory of Science and Technology on UAV, Northwestern Polytechnical University, Xi'an, China

Cheng Ye Nanjing Boiler and Pressure Vessel Supervision and Inspection Institute, Nanjing, China

Xianlei Ye Aerospace Technology Research Institute, China Aerospace Science and Industry Corp, Beijing, China

Wei Yin Beijing Institute of Structure and Environment Engineering, Beijing, China

Zhang Ying School of Environmental and Safety Engineering, Changzhou University, Changzhou, China

Yang Yu Shenyang University of Technology, Shenyang, China

Yongliang Yu SINOPEC Qingdao Research Institute of Safety Engineering, Qingdao, China;
Nanjing Boiler and Pressure Vessel Inspection and Research Institute, Nanjing, China

Yilin Yuan China Special Equipment Inspection and Research Institute, Beijing, China

Xianglong Zeng School of Aeronautics, Northwestern Polytechnical University, Xi'an, China

Chengyu Zhang School of Materials Science and Engineering, Northwestern Polytechnical University, Xi'an, China

Jiwang Zhang China Special Equipment Inspection and Research Institute, Beijing, China

Junjiao Zhang China Special Equipment Inspection and Research Institute, Beijing, China

Kai Zhang Changshu Institute of Technology, Changshu, China;
Dalian University of Technology Changshu Research Institute Co., Ltd, Changshu, China

Lidong Zhang Qing Cheng AE Institute Co., LTD, Guangzhou, China

Peng-Fei Zhang School of Quality and Technical Supervision, Hebei University, Baoding, China

Ruipeng Zhang China Construction Installation Group Beijing Company, Beijing, China

Wenjun Zhang China Special Equipment Inspection and Research Institute, Beijing, China

Yachen Zhang Key Laboratory of Inorganic Coating Materials CAS, Shanghai Institute of Ceramics, Chinese Academy of Sciences, Shanghai, China;
School of Physical Science and Technology (SPST), ShanghaiTech University, Shanghai, China

Ying Zhang College of Environmental and Safety Engineering, Changzhou University, Changzhou, Jiangsu, China

Yongzhen Zhang National Key Laboratory of Science and Technology on UAV, Northwestern Polytechnical University, Xi'an, China

Zhongzheng Zhang Nanjing Boiler and Pressure Vessel Supervision and Inspection Institute, Nanjing, China

Baodi Zhao China Special Equipment Inspection and Research Institute, Beijing, China

Bo Zhao China Special Equipment Inspection and Research Institute, Beijing, China

Kai Zhao Hebei Special Equipment Supervision and Inspection Institute Branch of Baoding, Baoding, China

Ran Zhao School of Transportation Science and Engineering, Beihang University, Beijing, China

Wei Zhao Hebei Special Equipment Supervision and Inspection Institute Branch of Baoding, Baoding, China

Wenjing Zhao China Special Equipment Inspection and Research Institute, Beijing, China

Zihao Zhao School of Transportation Science and Engineering, Beihang University, Beijing, China

Jianyong Zheng Zhejiang Academy of Special Equipment Science, Hangzhou, China

Wei Zhou School of Quality and Technical Supervision, Hebei University, Baoding, China

Zidong Zhu Shenyang Longchang Pipeline Testing Center, Shenyang, Liaoning, China

Fatematuz Zohora School of Mechanical, Medical and Process Engineering, Queensland University of Technology, Brisbane, QLD, Australia

Part I
Keynote Lecture

Chapter 1
Localization and Discrimination of Microseismic/AE Sources in Mining: From Data to Information

Longjun Dong

Abstract With the development of the mining industry, the mining depth is increasing rapidly. Due to the effects of deep high geo-stress, destructive disasters like rockburst are likely to happen in deep mines, which will cause huge casualties and economic losses. Microseismic/Acoustic Emission (MS/AE) monitoring is a widely used and effective method for rock stress monitoring in deep mining. MS/AE monitoring technology mainly includes source localization, source type discrimination, source mechanism inversion, and disaster early warning and control. In this paper, a series of source localization methods that can eliminate the negative impact of premeasured P-wave velocity, straight wave path, and abnormal arrivals on the locating accuracy were introduced. Four source classification methods are presented for solving the difficulty that the discrimination of microseismic events and blasts is heavily dependent on manual classification. On the basis of the above research, the full waveform inversion methods are used to investigate the different microseismic source mechanisms in a more quantitative way. Based on the Spatio-temporal characteristics of seismic sequences before large magnitude events in mines, the precursors of large magnitude seismicities in mines are analyzed. As a result, some rock support suggestions are put forward considering the source mechanism.

1.1 Introduction

Mining is a global industry with a long development history, which has a close connection with everyone. It can provide abundant raw materials to different industries. With the development of the economy, resource extraction is occurring at greater depths. Geotechnical risks are increasing significantly, particularly the rockmass instability relates to geo-stress. Therefore, the management of geo-stress in deep mining is very important for geological disaster prevention and control, which will directly affect productivity, cost, and safety of the mine.

L. Dong (✉)
School of Resources and Safety Engineering, Central South University, Changsha 410083, China
e-mail: lj.dong@csu.edu.cn

© The Author(s), under exclusive license to Springer Nature Singapore Pte Ltd. 2021

G. Shen et al. (eds.), *Advances in Acoustic Emission Technology*, Springer Proceedings in Physics 259, https://doi.org/10.1007/978-981-15-9837-1_1

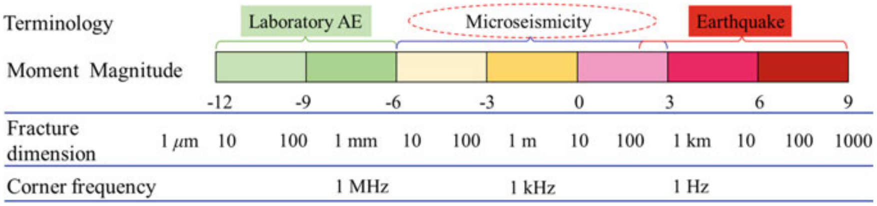

Fig. 1.1 Key aspects and parameters associated with rock fracture at different scales (Revised from [2])

Currently, Microseismic/Acoustic Emission (MS/AE) monitoring is an effective method for geo-stress monitoring in deep mining [1]. According to the fracture scale of the monitoring, the technology would be defined as AE technology, MS technology, and seismic monitoring technology (as shown in Fig. 1.1), though the essence of the three technologies are almost the same [2]. It has been widely used in the safety monitoring of ground pressure in many deep mines and high-stress mines [3–6]. For instance, MS monitoring systems have been established in several mines of Canada, South Africa, and other countries [7, 8]. The MS monitoring system is an important foundation for deep geo-stress monitoring and disaster control, which is one of the most vital parts of intelligent mining.

In this paper, a set of studies about MS monitoring would be introduced, including localization methods of MS/AE sources, source mechanism inversion and discrimination, and ground motion prediction, and hazard control.

1.2 Localization Methods of MS/AE Sources

Presently, the localization methods for MS sources applied in actual engineering have 3 main disadvantages: (1) P-wave velocity is premeasured as a fixed value; (2) Abnormal arrival time cannot be eliminated; (3) The wave path from the source to the sensor is assumed as a straight line. A set of localization methods were proposed to solve these problems [9–13], as shown in Fig. 1.2.

1.2.1 Iterative Localization Method Without Pre-Measured Velocity

As for most MS/AE source localization methods, it is necessary to give a practical pre-measured wave velocity of the structure. It is well known that the wave velocity is influenced by the materials, size, surface conditions of the transmission media, and other factors [14, 15]. The input wave velocity is a fixed value, which is different from the real wave velocity of the measured object [16]. Because the average wave

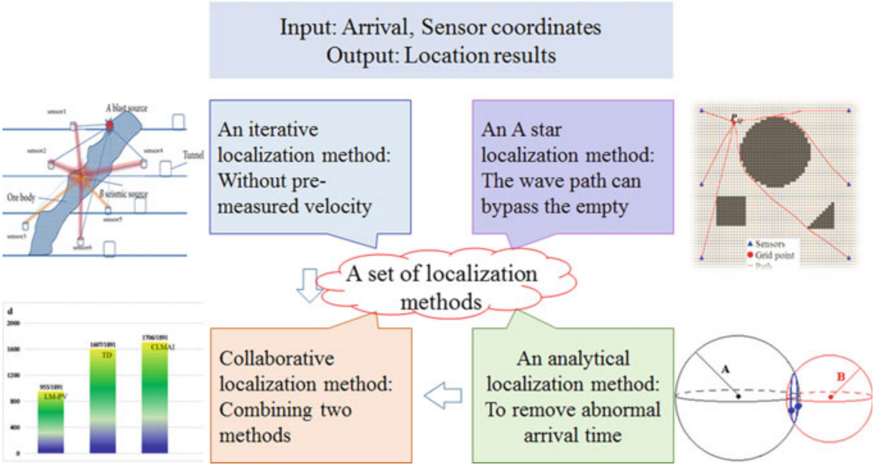
Input: Arrival, Sensor coordinates
Output: Location results
An iterative localization method: Without pre-measured velocity
An A star localization method: The wave path can bypass the empty
A set of localization methods
Collaborative localization method: Combining two methods
An analytical localization method: To remove abnormal arrival time
A blast source
Tunnel
Ore body
B seismic source
Sensors
Grid point
Path
LM-PV
TD
CLMAI
A
B

Fig. 1.2 A set of localization methods

velocity is different from that of the various regions, the premeasured P-wave velocity significantly affects the locating accuracy.

To eliminate the temporal and spatial error caused by the premeasured P-wave velocity, the MS/AE source locating method without premeasured velocity was proposed to improve the locating accuracy (Velocity- free, VF). The basic equations of these methods can be expressed as

$$\sqrt{(x_k - x_0)^2 + (y_k - y_0)^2 + (z_k - z_0)^2} = C(t_k - t_0) \tag{1.1}$$

where t_0 is the origin time of the MS/AE event; (x_k, y_k, z_k) are the coordinates of the k -th sensor; (x_0, y_0, z_0) are the coordinates of MS source location; and the average equivalent wave velocity C is an unknown parameter, which is different from the traditional localization methods.

1.2.2 Analytical Localization Method Without Pre-Measured Velocity

To solve the problems of the local optimal solution, iterative method, initial value, premeasured P-wave velocity, and square root calculations (no solution), the analytical localization methods for random sensor networks were researched to solve the unique global optimal solution [9].

The coordinates of the MS/AE source and the 6 sensors are assumed as P (x, y, z) and $S_i(x_i, y_i, z_i)$ $(i = 1, 2, 3, 4, 5, 6)$ respectively. t_0 is the origin time of the MS/AE source. v represents the average P-wave velocity. The governing equation for the coordinates of the MS/AE source is shown below:

$$(x_i - x)^2 + (y_i - y)^2 + (z_i - z)^2 = v^2(t_i - t_0)^2 \tag{1.2}$$

Taking difference of the equations with $i = 2$ and $i = 1$, $i = 3$ and $i = 1$, $i = 4$ and $i = 1$, $i = 5$ and $i = 1$, as well as $i = 6$ and $i = 1$, respectively.

$$2x(x_m - x_1) + 2y(y_m - y_1) + 2z(z_m - z_1) + 2v^2(t_m - t_1)t_0 + v^2\left(t_1^2 - t_m^2\right) = l_{m-1} \tag{1.3}$$

Substituting V, S for v^2, Vt_0, and changing the non-linear equation to linear equation. The five-variable linear equation can be rewritten as a matrix:

$$AT = B \tag{1.4}$$

The important parameters including the coordinates of the source (x, y, z), the average velocity of P-wave, and the trigger time t_0 can be obtained easily through the proposed analytical method. Furthermore, there is no need to measure the velocity before monitoring. The form of calculating formulas is explicit. A set of unique coordinates for MS/AE sources can be determined by every 6 sensors.

In fact, it is common that more than 6 sensors are used to improve the locating accuracy in practical engineering. Therefore, it is a vital problem to take full advantage of the remaining sensors. A comprehensive analytical localization method can be applied to determine the reasonable and reliable source coordinates. Firstly, the invalid sensors should be excluded. Secondly, all the analytical solutions were analyzed statistically. The coordinates of the MS/AE source are exactly the abscissa corresponding to the maximum value of the probability density function which fits the data best.

1.2.3 Collaborative Localization Method Without Pre-Measured Velocity

The collaborative localization method using analytical and iterative solutions (CLMAI) was proposed to elimate the influence of the abnormal arrivals and premeasured P-wave velocity on locating accuracy. The CLMAI includes two main processes: filtering the abnormal arrivals using the analytical solutions and locating the MS/AE sources using the iterative localization methods with clear arrivals [10].

1.2.4 Source Localization Method for Hole-Containing Structures

A new localization method based on the improved A* search algorithm without premeasured velocity (ALM) was proposed for source localization in complex structures. The main steps of ALM are listed as follows.

- Firstly, meshing the location region to the grid and using the grid node P_{ijk} with the digits 0 or 1 to represent the shape.
- Secondly, searching the fastest wave path between each sensor and each node by the improved A* search algorithm. The improved A* search algorithm was based on the A* search algorithm [17, 18] to establish more connection with more adjacent layer nodes to search the wave path more effectively.
- Thirdly, the coordinates of the kth sensor S_k are recorded as (x_k, y_k, z_k). The arrivals of the AE event is set as t_0^k. Calculating the actual time difference of the two different sensors S_l and S_m, denoted by Δt_0^{lm}.
- Finally, the D_{ijk} is introduced to describe the degree of deviation of the point P_{ijk} from the unknown AE source based on the principle of the least square method. Therefore, the XYZ coordinate corresponding to the minimum D_{xyz} value can be considered as the coordinate of the AE source.

Compared with the 2D localization method, the 3D localization method needs to link more nodes in the second step to reduce the location errors and ensure that the location accuracy meets the high requirements in the complex structure. The number of the linked nodes reaches 342 in the 3D localization method when the current node is connected to the adjacent 3 layers, while that in the 2D localization method is only 48. Since the ALM can bypass the empty area, the localization accuracy of the ALM is much higher than the commonly used methods.

1.3 Source Discrimination and Mechanism Inversion

1.3.1 Discrimination of Microseismic Events and Blasts

Presently, the discrimination for microseismic events and blasts mainly relies on manual identification, which results in a huge amount of work, high labor costs, and delayed identification. At the same time, there will also be an error in determining the source location due to the difference of individual experience, which seriously restricts the real-time prevention and control of large magnitude microseismic events. Aiming at solving the problem, a set of classification methods are proposed, as shown in Fig. 1.3.

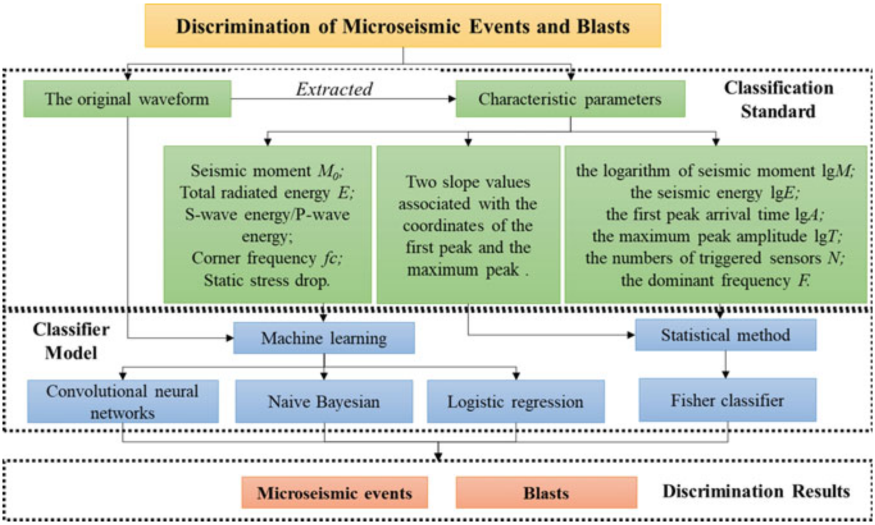
Discrimination of Microseismic Events and Blasts
The original waveform
Extracted
Characteristic parameters
Classification Standard
Seismic moment M_0; Total radiated energy E; S-wave energy/P-wave energy; Corner frequency fc; Static stress drop.
Two slope values associated with the coordinates of the first peak and the maximum peak .
the logarithm of seismic moment lg$M$; the seismic energy lg$E$; the first peak arrival time lg$A$; the maximum peak amplitude lg$T$; the numbers of triggered sensors N; the dominant frequency F.
Classifier Model
Machine learning
Statistical method
Convolutional neural networks
Naive Bayesian
Logistic regression
Fisher classifier
Microseismic events
Blasts
Discrimination Results

Fig. 1.3 A set of classification methods for microseismic events and blasts

1.3.1.1 A Statistical Method to Identify Microseismic Events and Blasts [19]

The parameters including the seismic moment, the seismic energy, the P and S wave energy ratios, the event occurrence time, the static stress drop, the sensor triggers, and the corner frequency were analyzed based on the database of microseismic events and blasts. The probability density distributions of the first peak arrival time, the first peak amplitude, the maximum peak arrival time, and the maximum peak amplitude were compared and analysed. In addition, the frequency distributions of two kinds of signals are collected and analyzed using Fast Fourier Transform (FFT). Finally, the logarithm of seismic moment, the seismic energy, the event occurrence time, the first peak arrival time, the maximum peak amplitude, the numbers of triggered sensors, and the dominant frequency were selected as the characteristic parameters according to the probability density distribution of each parameter, the performance of classification, and the difficulty of acquisition.

1.3.1.2 Classification of Mine Microseismic Events and Blasts Using Starting-Up Features [20]

The microseismic and blast signals databases are established based on the manual classification to find discriminating features for microseismic events and blasts. Criteria including the repetition of waveforms, tail decreasing, dominant frequency, and occurrence time of day were taken into account when setting up the database. The signals are extracted from the databases and set into a unified coordinate system. It is noticed that the starting-up angles of the two types tend to be concentrated into two different intervals. The inaccuracy of the P-wave arrival's picking led to the difficulty of calculating the staring-up angle directly. The slope value of the starting-up trend line obtained by linear regression was selected to substitute the angle. Two slope values associated with the coordinates of the first peak and the maximum peak were extracted as the characteristic parameters. The discrimination model was established based on the Fisher discriminant analysis and the accuracy of classification reached 97.1%.

1.3.1.3 Discrimination of Mine Seismic Events and Blasts Using Machine Learning [21]

Five typical parameters of blasts, the probability density functions of blast time, and probability density functions of origin time difference for neighbouring blasts were extracted as discriminant indicators. The discrimination models were established based on the Fisher classifier, naïve Bayesian classifier, and logistic regression, which were performed on three databases from Australia and Canada. The proposed discrimination models have explicit and simple functions, which are convenient for workers in mines or researchers. Back-test, applied results, cross-validated results, and analysis of ROC curves in different mines have demonstrated that established discrimination models have a reasonably good performance.

1.3.1.4 Discrimination of Mining Microseismic Events and Blasts Using Convolutional Neural Networks and Original Waveform

The source parameters used in the statistical methods are extracted from the original waveforms according to criteria or experience, which may lead to a partial loss of information or mixed subjective factors affecting the real expression. The waveform can provide the most complete source information as the original information. It is usually argued that the P-wave caused by blasts is simple than the P-wave produced by the rock microfracture, and the energy of blasts mainly concentrated in the first half of the timeline, sometimes there will be obvious in the wave window of several same waveforms in the blasts. Compared with blasting waveform, the microseismic waveform has obvious S-wave and the energy of the microseismic events distributes in all time periods. Therefore, a wave classification model is established based on the difference between microseismic events and blasts in waveform using the Convolution Neural Network (CNN). It not only decreases the influence from individual differences in experience, but also removes the errors induced by source and waveform parameters. Results proved that the established discriminant method improved the efficiency and accuracy of microseismic data processing for monitoring rock instability and seismicity.

1.3.2 Source Mechanism Inversion [22]

The discrimination of seismic source mechanisms is a crucial and fundamental issue to analyze and control seismic hazard in mining environments. Different types of mechanisms have been observed and modelled in the past, including cavity collapses, rock falls, pillar bursts, explosions, tensional ruptures, and fault-slips [23–25]. By fitting the amplitude spectrum in the frequency domain and the displacement waveform in the time domain, the point source moment tensor is obtained. A probabilistic method is used to calculate the likelihood of a given candidate event to a certain source, so as to identify the type of the induced seismicity in a more quantitative way. The displacement field (u_k) caused by a seismic source can be expressed as the convolution of the moment tensor and the Green's functions (which is used to account for wave propagation from source to receiver), mathematically presented as following [26]:

$$u_k = M_{ij} * \frac{\partial G_{ki}}{\partial x_j} = M_{ij} * G_{kij} i, j, k = 1, 2, 3 \tag{1.5}$$

where M_{ij} are the moment tensor elements of the force couples acting in the direction of x_i axis with arm in line with the x_j axis; G_{ki} is the Green's function; and the symbol '*' denotes convolution. In 3D space, displacements in the far field are a sum of the displacements caused by each of the force couples M_{ij}.

Theoretically, the mining explosions are associated with abrupt volume changes. In terms of the moment tensor, it can be represented by three orthogonal linear force dipoles, which constitute a pure ISO source [25]. A cavity collapse reproduces the effects of rockfalls caused by gravity or more energetic rockbursts, where the source mode produces a moment tensor consisting of a negative ISO component and a CLVD with vertical symmetry [25]. For a tensile failure of the roof rock, horizontal dipoles could be used to describe the source radiation patterns. A fault slip can be represented by a pure DC. In fact, the proposed mechanism may occur simultaneously, which leads to a superposition of the ISO, DC, and CLVD components. The elemental failure models in the mining environment, their diagonalized moment tensors, beachballs, and their corresponding positions in the source type diagram are shown in Fig. 1.4.

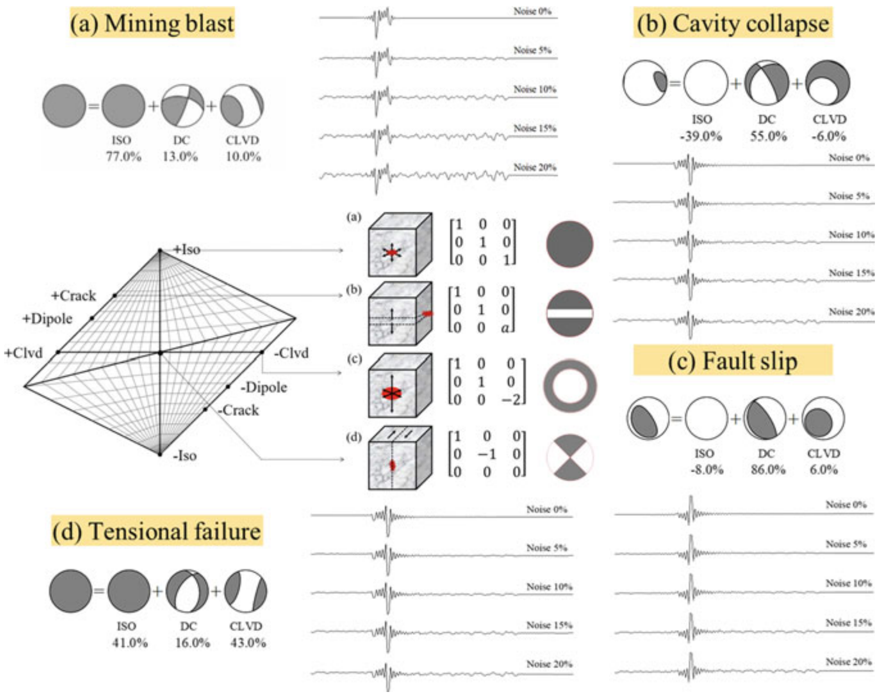
(a) Mining blast
ISO 77.0%
DC 13.0%
CLVD 10.0%
(b) Cavity collapse
ISO -39.0%
DC 55.0%
CLVD -6.0%
(c) Fault slip
ISO -8.0%
DC 86.0%
CLVD 6.0%
(d) Tensional failure
ISO 41.0%
DC 16.0%
CLVD 43.0%
Noise 0%
Noise 5%
Noise 10%
Noise 15%
Noise 20%
+Iso
+Crack
+Dipole
+Clvd
-Clvd
-Dipole
-Crack
-Iso
(a)
(b)
(c)
(d)

Fig. 1.4 Schematic diagram of possible failure models, their moment tensors, beachballs, and corresponding positions in the Hudson plot [22]

1.4 Pre-alarming of Microsiesmic Events with Large Magnitude and Disaster Control

1.4.1 Statistical analysis of Precursors for Induced Seismicity in Mines [27]

In order to monitor the sequence evolution, the seismic sequence is analyzed with the aim of detecting changes in statistical parameters describing the seismic event occurred before the main shocks. The acquisition and processing of the multiple monitoring data is shown in Fig. 1.5.

(1) The Gutenberg-Richter magnitude-frequency relationship is used to calculate the Minimum Magnitude of Completeness (Mmin), *a*, and *b* in an area [30]:

$$logN = a - bM_W \tag{1.6}$$

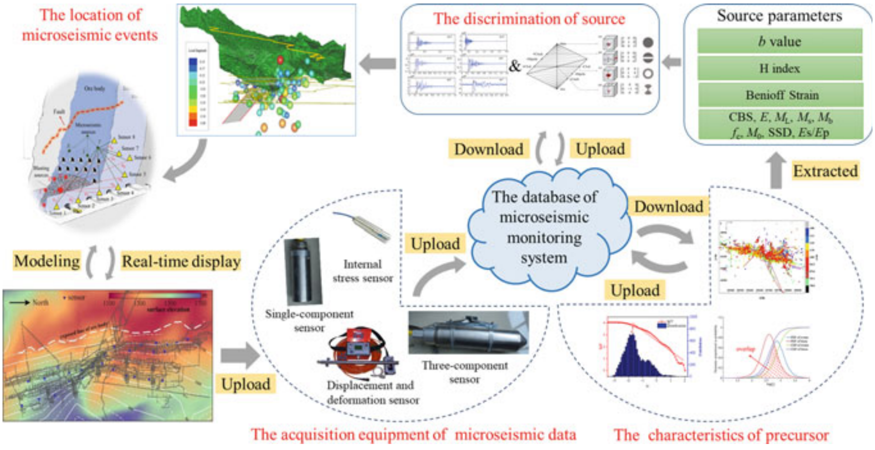
The location of microseismic events
The discrimination of source
Source parameters
b value
H index
Benioff Strain
CBS, E, ML, Ms, Mb
fc, M0, SSD, Es/Ep
Download
Upload
Extracted
The database of microseismic monitoring system
Download
Upload
Upload
Modeling
Real-time display
Internal stress sensor
Single-component sensor
Three-component sensor
Displacement and deformation sensor
Upload
The acquisition equipment of microseismic data
The characteristics of precursor

Fig. 1.5 Diagram of real-time acquisition and processing of the multiple monitoring data (Revised from [9, 10, 22, 28, 29]).

where M_W is the moment magnitude. N is the cumulative number of a seismic event in the magnitude range $(M \pm \Delta M)$. a and b are empirical constants. The b value is an important parameter to measure the regional seismicity level and to describe the proportional relationship for numbers of large magnitude events and small magnitude events in the area.

(2) The Hurst exponent can be calculated by rescaled range analysis (R/S analysis) [31, 32]. For a time series of the moment magnitude for microseismic events, $\mathrm{M} = \mathrm{M}_1, \mathrm{M}_2, \ldots, \mathrm{M}_n$, R/S analysis method is described as follows:

$$M_A = \frac{1}{t}\sum_{i=1}^{t} M_i \tag{1.7}$$

$$Y_i = M_i - M_A, i = 1, 2, \ldots, t \tag{1.8}$$

$$Z_i = \sum_{i=1}^{t} Y_i, i = 1, 2, \ldots, t \tag{1.9}$$

$$R_m = max(Z_1, Z_2, \ldots, Z_t) - min(Z_1, Z_2, \ldots, Z_t) \tag{1.10}$$

$$S_m = \sqrt{\frac{1}{t}\sum_{i=1}^{t}(M_i - M_A)^2, i = 1, 2, \ldots, t} \tag{1.11}$$

$$\left(\frac{R}{\mathrm{S}}\right)=\frac{R_m}{S_m}, m=1,2,\ldots,M \tag{1.12}$$

$$\left(\frac{R}{S}\right)_t=c*t^H \tag{1.13}$$

where M_A is the average value, Y_i is the average adjusted series, Z_i is the cumulative deviate series, R_m is the range series, Sm is the standard deviation series, (*R/S*) is the rescaled range series (*R/S*), c is a constant, and H is called the Hurst exponent.

In general, H exponent is between 0.5 and 1 for some physical phenomena. It is widely accepted that there is a kind of persistence when $H > 0.5$, which means the latter events are correlated with the former events positively. Similarly, the latter events correlating with the former events negatively are called antipersistence when $H < 0.5$. As for seismic events with long range correlation and the latter events would be affected by the former events. It is regular and random for the occurrence of seismic events, the degree that H exponent deviates from 0.5 can measure the proportion of random factors and certain factors in the seismic time distribution.

(3) Some seismologists [33, 34] have observed the seismic activation prior of a lot of major earthquakes and quantified as accelerated releases of the cumulative (square root sum) of seismic energy in the time series. The power exponent m in the above formula is approximately equal to 0.3 when using the Benioff strain [35]. The calculating method of Benioff strain is shown as

$$B_i=\sum\sqrt{E_i}=\sum\sqrt{10^{1.695M_i+10.18}} \tag{1.14}$$

where M_i is the moment magnitude of the seismic event *i*. Bufe and Varnes [33] concluded that the cumulative Benioff strain is more accurate than the cumulative seismic moment in the aspect of forecasting large magnitude seismic events. Through the analysis of 27 major seismic activities, it is found that the microseismic activity parameters before 25 major seismic activities have the following significant precursory characteristics: 1. The H exponent within the vicinity of a forthcoming large event is greater than 0.5, which means that they have correlation and the latter events would be affected by the former events; 2. The duration of precursory features is about 3 ~ 4 weeks; 3. The *b* value shows a trend of “increase–decrease” in windows with 3 or 4 weeks as the precursory features; and 4. The cumulative Benioff strain increases continuously.

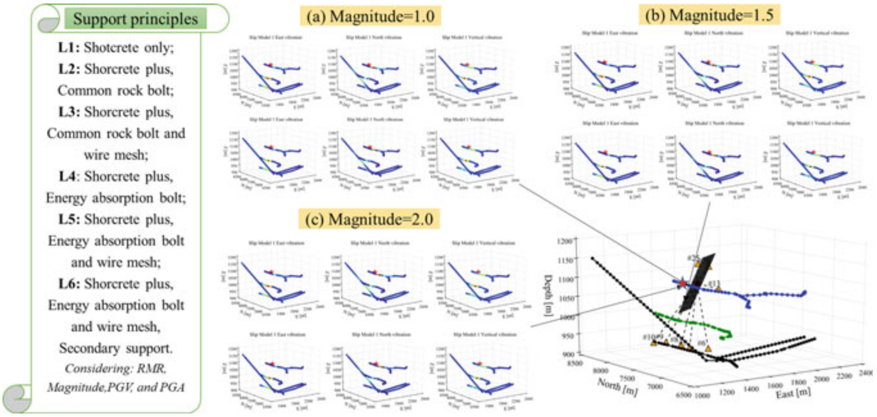

Fig. 1.6 The theoretical calculated PGVs and PGAs along the tunnels induced by the three imaginary radiation patterns with moment magnitude 1.0, 1.5, and 2.0 [28]

1.4.2 Suggestions on Support of Rockmass Considering Rockmass Quality and Dynamic Load [36]

The radiation pattern of seismic waveforms at the source is affected by the source mechanism. The complicated refraction and reflection processes between seismic waveforms and geological discontinuities should be considered in the propagation. Therefore, the dynamic load requirement of surrounding rock under the influence of earthquakes should be taken into account when supporting the rock mass, which is ignored in the actual support process of the rock mass. The vibration distribution of the exposed surface of the roadway caused by the fault at different slip angles is analyzed. Also, the Peak Ground Velocities (PGVs) at the surrounding rock of the roadway in three-dimensional space are calculated (Fig. 1.6). Even on the same fault (the strike and trend of the fault remain unchanged) and the same magnitude, the vibration at the surrounding rock will be greatly different when the slip angle of the fault is different, which indicates that PGV does not uniformly decay with the distance from the source to the rock mass.

1.5 Conclusion

Presently, the commonly used source localization methods have 3 main disadvantages: (1) P-wave velocity is premeasured as a fixed value; (2) Abnormal arrival time cannot be eliminated; (3) The wave path between the source to the sensor is assumed as a straight line. A set of localization methods were proposed to solve these problems. As the difficulties like premeasured P-wave velocity and local optimal solution have been solved through the iterative methods and analytical localization method, the abnormal arrivals can be filtered through the collaborative localization method using analytical and iterative solutions (CLMAI). The localization method based on the improved A* search algorithm without premeasured velocity (ALM) was proposed for localization in the complex hole-containing structure. Four discrimination methods were proposed for classifying microseismic events and blasts, which solved the situation of relying on artificial identification. Meanwhile, the full waveform inversion methods were used to investigate the different microseismic source mechanisms in a more quantitative way. Suggestions on the support of rockmass considering PGA and PGV calculated by full waveform inversion were proposed. The seismic sequence for detecting changes in statistical parameters before the main shocks is also analyzed. Finally, three parameters related to the precursor of large magnitude events were summarized, which can provide theoretical support for disaster early warning.

References

1. X. Feng, J. Liu, B. Chen, Y. Xiao, G. Feng, F. Zhang, Monitoring, warning, and control of rockburst in deep metal mines. Engineering **3**(4), 538–545 (2017)
2. X. Lei, S. Ma, Laboratory acoustic emission study for earthquake generation process. Earthq. Sci. **27**(6), 627–646 (2014)
3. A.M. Milev, S.M. Spottiswoode, A.J. Rorke, G.J. Finnie, Seismic monitoring of a simulated rockburst on a wall of an underground tunnel. J. South. Afr. Inst. Min. Metall **101**(5), 253–260 (2001)
4. H. Wang, M. Ge, Acoustic emission/microseismic source location analysis for a limestone mine exhibiting high horizontal stresses. J. Rock Mech. Min. Sci. **45**(5), 720–728 (2008)
5. A. Hirata, Y. Kameoka, T. Hirano, Safety management based on detection of possible rock bursts by AE monitoring during tunnel excavation. Rock Mech. Rock. Eng. **40**(6), 563–576 (2007)
6. L. Li, J. Tan, D.A. Wood, Z. Zhao, D. Becker, Q. Lyu, B. Shu, H. Chen, A review of the current status of induced seismicity monitoring for hydraulic fracturing in unconventional tight oil and gas reservoirs. Fuel **242**, 195–210 (2019)
7. M. Ge, Efficient mine microseismic monitoring. Int. J. Coal Geol. **64**(1–2), 44–56 (2005)
8. R.J. Durrheim, Mitigating the risk of rockbursts in the deep hard rock mines of South Africa: 100 years of research. Extracting the Science: a century of mining research, in *Society for Mining, Metallurgy, and Exploration, Inc*, ed. by J. Brune, pp. 156–171 (2010)
9. L.J. Dong, W.W. Shu, X.B. Li, G.J. Han, W. Zou, Three dimensional comprehensive analytical solutions for locating sources of sensor networks in unknown velocity mining system. IEEE Access **5**, 11337–11351 (2017)
10. L. Dong, W. Zou, X. Li, et al., Collaborative localization method using analytical and iterative solutions for microseismic/acoustic emission sources in the rockmass structure for underground mining. Eng. Fracture Mech. S0013794417312997 (2019)
11. L. Dong, X. Li, A microseismic/acoustic emission source location method using arrival times of PS waves for unknown velocity system. Int J Distrib Sens Netwo **9**(10), 307489 (2013)
12. Q. Hu, L. Dong, Acoustic emission source location and experimental verification for two-dimensional irregular complex structure. IEEE Sens J 20 (5):2679–2691
13. L. Dong, H. Qingchun, X. Tong, Y. Liu, Velocity-free MS/AE source location method for three-dimensional hole-containing structures. Eng **6**(7), 827–834 (2020)
14. Y. Potvin, Strategies and tactics to control seismic risks in mines. J. Southern African Inst. Mining Metallurgy **109**(3), 177 (2009)

15. J.C. Chen, R.E. Hudson, K. Yao, Maximum-likelihood source localization and unknown sensor location estimation for wideband signals in the near-field. IEEE Trans. Signal Process **50**(8), 1843–1854 (2002)
16. M. Ge, H.R. Hardy, H. Wang, J. Wang, Development of a simple mechanical impact system as a non-explosive seismic source. Geotech. Geol. Eng. **29**(1), 137–142 (2011)
17. P.E. Hart, N.J. Nilsson, B. Raphael, A formal basis for the heuristic determination of minimum cost paths, IEEE Trans. Sys. Sci. Cybern. **4**(2), 100–107 (1968)
18. P.E. Hart, N.J. Nilsson, B. Raphael, Correction to a formal basis for the heuristic determination of minimum cost paths. ACM SIGART Bulletin **37**, 28–29 (1972)
19. L. J. Dong, D. Y. Sun, X. B. Li, J. Ma, G. H. Chen, C. X. Zhang, A statistical method to identify blasts and microseismic events and its engineering application. Chinese J. Rock Mech. Eng. **35**(7), 1423–1433 (2016)
20. G.Y. Zhao, J. Ma, L.J. Dong, X.B. Li, G.H. Chen, C.X. Zhang, Classification of mine blasts and microseismic events using starting-up features in seismograms. Trans. Nonferrous Metals Soc China **25**(10), 3410–3420 (2015)
21. L.J. Dong, J. Wesseloo, Y. Potvin, X.B. Li, Discrimination of mine seismic events and blasts using the fisher classifier, Naive Bayesian Classifier and Logistic Regression. Rock Mech. Rock Eng. **49**(1), 183–211 (2016)
22. J. Ma, L.J. Dong, G.Y. Zhao, X.B. Li, Discrimination of seismic sources in an underground mine using full waveform inversion. Int. J. Rock Mech. Min. Sci. **106**, 213–222 (2018)
23. H. S. Hasegawa, R. J. Wetmiller, D. J. Gendzwill, Induced seismicity in mines in Canada—an overview. Pure Appl Geophys **129**(3), 423–453 (1989)
24. S.R. Ford, D.S. Dreger, W.R. Walter, Source characterization of the 6 August 2007 Crandall Canyon Mine seismic event in central Utah. Seismol. Res. Lett. **79**(5), 637–644 (2008)
25. S. Cesca, A. Rohr, T. Dahm, Discrimination of induced seismicity by full moment tensor inversion and decomposition. J. Seismology**17**(1), 147–163 2013.
26. M.U. Jost, R.B. Herrmann, A student's guide to and review of moment tensors. Seismol. Res. Lett. **60**(2), 37–57 (1989)
27. L. J. Dong, D. Y. Sun, W. W. Shu, X. B. Li, L. Y. Zhang, Statistical precursor of induced seismicity using temporal and spatial characteristics of seismic sequence in mines, in *World Conference on Acoustic Emission* (2017), pp. 409–420
28. J. Ma, L.J. Dong, G.Y. Zhao, X.B. Li, Qualitative method and case study for ground vibration of tunnels induced by fault-slip in underground mine. Rock Mech. Rock Eng. **52**(6), 1887–1901 (2018)
29. Z. Wang, X. Li, X. Shang, L. Dong, D. Liu, Y. Zhou, VFOM-based source location and local magnitude calibration for micro-seismic events in mine. Chin J Geotech Eng **39**(8), 1408–1415 (2017)
30. L.J. Dong, D.Y. Sun, X.B. Li, J. Ma, L.Y. Zhang, X.J. Tong, Interval non-probabilistic reliability of surrounding jointed rockmass considering microseismic loads in mining tunnels. Tunn. Undergr. Space Technol. **81**, 326–335 (2018)
31. H.E. Hurst, Long-term storage of reservoirs: an experimental study. J Royal Stat. Soc. Series a (General) **129**(4), 591–593 (1966)
32. M. Gilmore, C.X. Yu, T.L. Rhodes, W.A. Peebles, Investigation of rescaled range analysis, the Hurst exponent, and long-time correlations in plasma turbulence. Phys. Plasmas **9**(4), 1312–1317 (2002)
33. C.G. Bufe, D.J. Varnes, Predictive modeling of the seismic cycle of the Greater San Francisco Bay Region. J. Geophys. Res. Solid Earth **98**(B6), 9871–9883 (1993)
34. D.J. Brehm, L.W. Braile, Intermediate-term earthquake prediction using the modified time-to failure method in Southern California. Bull. Seismol. Soc. Am. **89**(1), 275–293 (1999)
35. Y. Benzion, V. Lyakhovsky, Accelerated seismic release and related aspects of seismicity patterns on earthquake faults. Earthquake Processes: Physical Modelling, Numerical Simulation and Data Analysis Part II. Birkhäuser, Basel **159**(10), 2385–2412 (2002)
36. L.J. Dong, J.H. Wang, J. Ma, Response and support suggestions of surrounding rock of underground cavern under different microseismic source mechanism. Hazard Control in Tunnelling and Underground Engineering **1**(3), 68–76 (2019)

Part II
Instrumentation

Chapter 2
Internet of Things Acoustic Emission: Systems and Applications

Jiehui Xie, Shuang Wang, Wei Liu, Huilan Yang, Lidong Zhang, and Shifeng Liu

Abstract Internet of Things Acoustic Emission (IOT AE) was developed and introduced in hardware, software and network structure. IOT AE transmits the data and analysis results to the network server through the Internet/intranet. The analysis results can go to the end user's smart phones and PCs as alarm info. Users don't need the acoustic emission technicians to operate IOT AE. So IOT AE can be used as remote long-term unattended monitoring and automatic alarm system. Compared with traditional acoustic emission instrument which needs to process the data manually to get the detection and monitoring results, IOT AE control the data acquisition and data analysis by embedded software automatically. Besides the long-term cycle of self-learning correction of artificial intelligence based on big data on the server makes the system have the ability of self-learning, self-improvement and continuous improvement of performance. This paper introduces the IOT AE systems developed and discusses the application of IOT AE technology of monitoring and alarming for valve leakage, wire rope breakage and tool wear, etc.

2.1 IOT AE System Introduction

2.1.1 Architecture of IOT AE Monitoring and Alarm System

IOT AE system consist of AE sensor, AE data acquisition and data analysis module (AE module), internet/intranet communication module, server/smart phone/PC. Firstly, the AE sensor installed on the monitoring object (valve pipeline, bridge steel cable broken wire, CNC machine tool, etc.) collects signals, and converts the tiny mechanical vibration signals into voltage signals. Then the AE module processes the voltage signal and outputs the results (alarm info, AE waveform and AE hit parameters). The outputs of the AE module are transmitted to the server/smart phone/PC by internet/intranet communication module.

J. Xie (✉) · S. Wang · W. Liu · H. Yang · L. Zhang · S. Liu
Qing Cheng AE Institute Co., LTD, Guangzhou 510670, China
e-mail: xjh@ae-ndt.com

© The Author(s), under exclusive license to Springer Nature Singapore Pte Ltd. 2021

G. Shen et al. (eds.), *Advances in Acoustic Emission Technology*, Springer Proceedings in Physics 259, https://doi.org/10.1007/978-981-15-9837-1_2

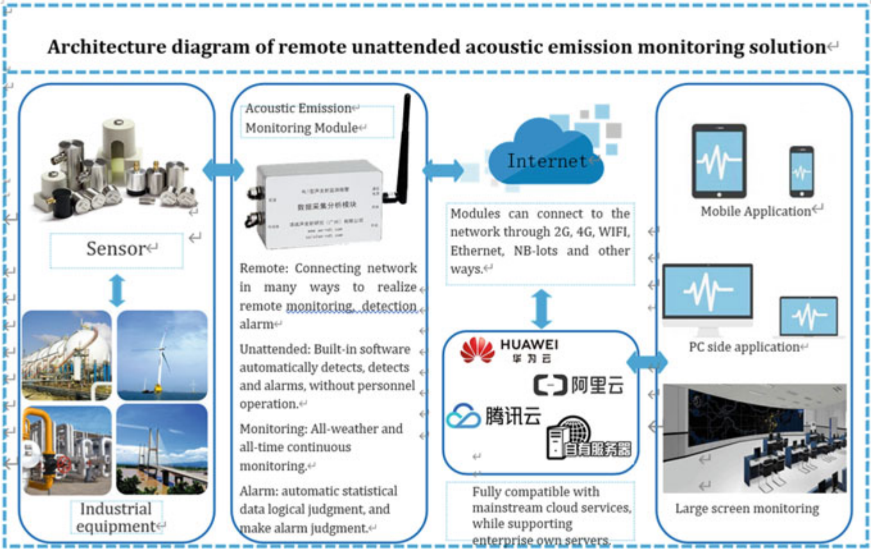
Architecture diagram of remote unattended acoustic emission monitoring solution
Sensor
Industrial equipment
Acoustic Emission Monitoring Module
Remote: Connecting network in many ways to realize remote monitoring, detection alarm
Unattended: Built-in software automatically detects, detects and alarms, without personnel operation.
Monitoring: All-weather and all-time continuous monitoring.
Alarm: automatic statistical data logical judgment, and make alarm judgment.
Internet
Modules can connect to the network through 2G, 4G, WIFI, Ethernet, NB-Iots and other ways.
HUAWEI 华为云
阿里云
腾讯云
自有服务器
Fully compatible with mainstream cloud services, while supporting enterprise own servers.
Mobile Application
PC side application
Large screen monitoring

Fig. 2.1 Architecture of IOT AE monitoring and alarm system

The system architecture is shown in Fig. 2.1

There are many available internet/intranet communication ways such as GPRS, 4G, 5G, NB-IoT, Lora, ZigBee, WiFi, RJ45 Cable, etc. for various applications.

Servers can be Internet cloud servers such as Alibaba cloud Internet of things servers, local LAN servers such as petrochemical plant for valve monitoring and alarm system which only needs to display alarm results in the control room of the plant. Servers can also be local servers + Internet servers and other networking structures according to applications.

2.2 IOT AE Systems Developed/developing

2.2.1 RL1 IOT AE System

RL1 IOT AE is designed and developed/developing for continuous AE signals such as leakage signals. Table 2.1 is the specification and Fig. 2.2 is the system functional block diagram.

Figure 2.3 shows the AE module, its battery and NB-IOT(Narrow band interenet of Things) chip are in the box, sensor is out off the box.

Table 2.1 RL1 and RAE1 specifications

IOT AE acquisition system			
RL1 specifications		RAE1 specifications	
Sampling accuracy	16 bit	Sampling accuracy	16 bit
Sampling frequency	10–200 KHz	Maximum sampling rate	2 MHz
Input bandwidth	100 Hz–70 kHz	Input bandwidth	1 KHz–2.2 MHz
Sampling points	100 k, 200 k		
Filter	20 K–100 KHz	Filter	Digital filter, high pass filter(KHz): 1 < Fl < 400, low pass filter(KHz): 20 < Fh < 2000
Sampling form	Timing sampling, manual button sampling	Sampling form	Continuous sampling
Characteristic parameter	Timing generation time parameter, including RMS, ASL, power, battery voltage	Characteristic parameter	Alarm, MaxAmp, MaxEnergy, MaxRing
Preamplifier voltage	5 V	Preamplifier voltage	5 V
Sensor	Can be built-in or external	Sensor	Can be built-in or external
IOT module	Can be built-in or external	IOT module	Can be built-in or external
Appearance size	52 mm diameter and unequal height metal cylinder structure	Appearance size	52 mm diameter and unequal height metal cylinder structure

2.2.2 RAE1 IOT AE System

RAE1 IOT AE is designed and developed/developing for burst AE signals such as cracking signals. Table 2.1 is the specification and Fig. 2.4 is the system functional block diagram.

New RL1/RAE1 IOT AE systems are in developing and can be the integrate structure or separate structures as shown in Fig. 2.5 for various applications.

Figure 2.5 shows the integrate and separate RL1/RAE1: Above right: integrate of sensor/battery/AE module/4G module; Above left: DC power and sensor are out of metal cylinder with AE module and 4G module; Above center: 4G module out of cylinder; Below left: DC power out of the cylinder; Below right: Different cylinders holding different parts inside.

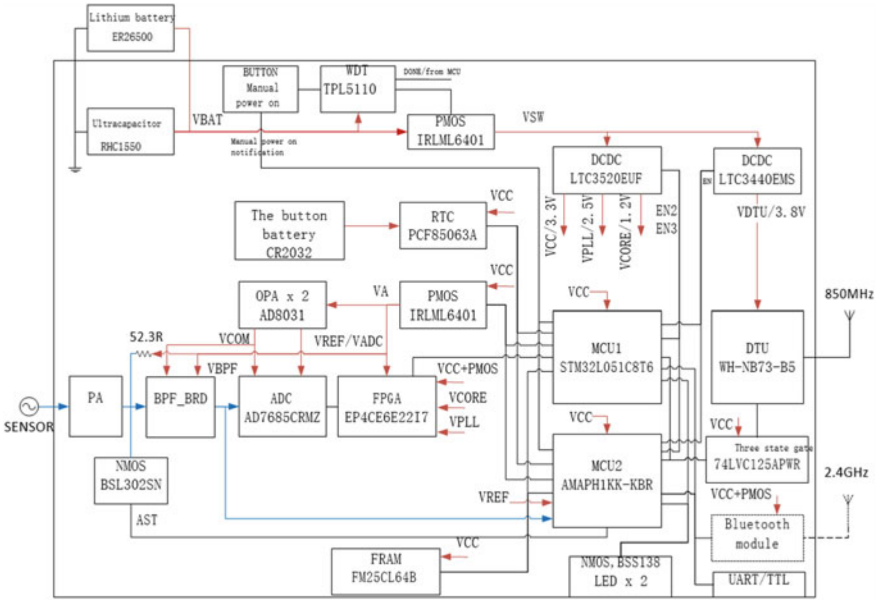
Lithium battery
ER26500
Ultracapacitor
RHC1550
VBAT
BUTTON
Manual
power on
WDT
TPL5110
DONE/from MCU
PMOS
IRLML6401
VSW
Manual power on notification
DCDC
LTC3520EUF
DCDC
LTC3440EMS
EN
VCC/3.3V
VPLL/2.5V
VCORE/1.2V
EN2
EN3
VDTU/3.8V
The button
battery
CR2032
RTC
PCF85063A
VCC
VCC
OPA x 2
AD8031
VA
PMOS
IRLML6401
VCC
850MHz
52.3R
VCOM
VREF/VADC
VBPF
VCC+PMOS
MCU1
STM32L051C8T6
DTU
WH-NB73-B5
SENSOR
PA
BPF_BRD
ADC
AD7685CRMZ
FPGA
EP4CE6E22I7
VCORE
VPLL
VCC
VCC
Three state gate
74LVC125APWR
2.4GHz
NMOS
BSL302SN
AST
MCU2
AMAPH1KK-KBR
VREF
VCC+PMOS
Bluetooth
module
VCC
FRAM
FM25CL64B
NMOS, BSS138
LED x 2
UART/TTL

Fig. 2.2 RL1 functional block diagram

2.3 Testing of RAE1 and RL1 IOT AE System

2.3.1 Testing Layout and Procedures

The water tap and water pipeline are used for generating water leakages. The sensors are placed on the water tap to monitor the water leakages of the tap. The water leakages are generated by operate the tap at the positions of close, open a little, open large, corresponding to no leakage, small leakage and large leakages. Figure 2.6 shows the testing layout and the RAE1 and RL1.

2.3.2 The RL1 Testing Data

The setting of RL1 in this experiment: 16 bit sampling accuracy; 200 kHz sampling rate; filter 20–100 khz; manual sampling once every 5 min; ls35 sensor, resonance frequency 15–70 khz, central resonance frequency 35 kHz. The operation process of faucet controlling water flow is shown in Table 2.3.

Access the server through the laptop, and the historical data is shown in Table 2.2. It can be clearly distinguished from the historical RMS data of the five stages.

Figure 2.7 shows that alarm data can be notified to users through WeChat official account, e-mail, text message, etc.

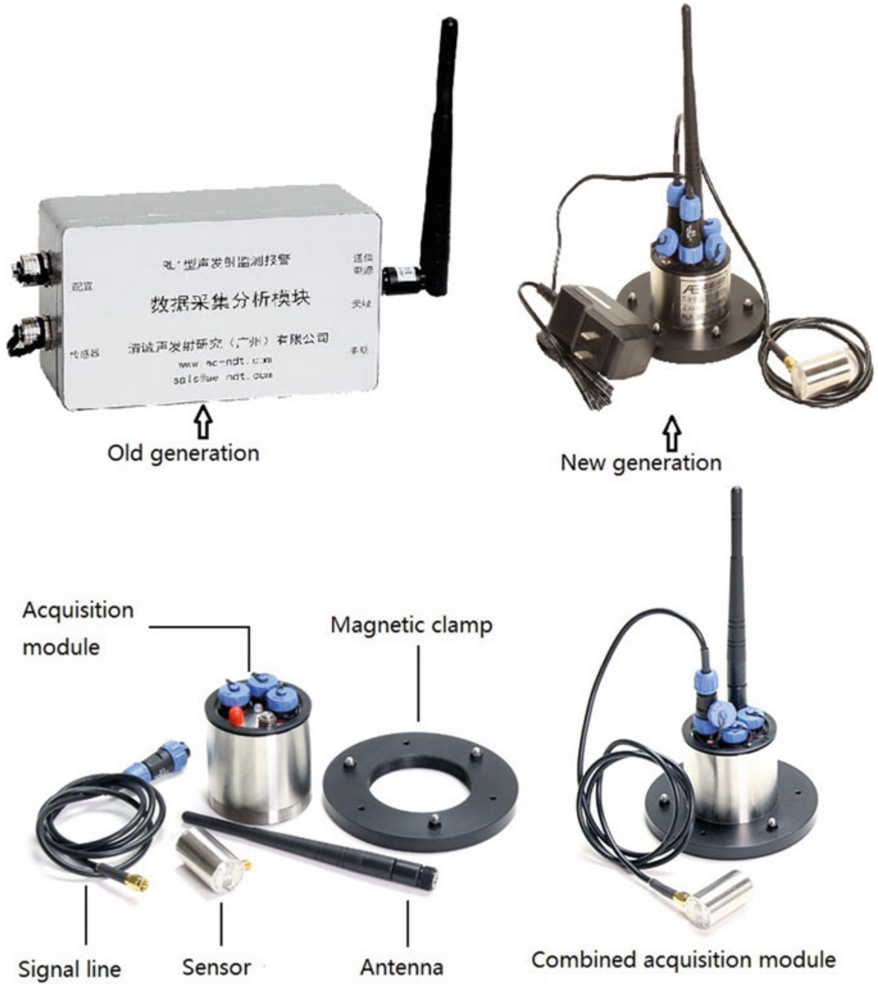
数据采集分析模块
Old generation
New generation
Acquisition module
Magnetic clamp
Signal line
Sensor
Antenna
Combined acquisition module

Fig. 2.3 RL1 IOT AE photo

Figures 2.8 and 2.9 show the history data from server of RL1 AE IOT system. RMS and ASL have useful references. When the water out, no water out and different effluent, the differences are obvious, as shown in the figure.

Table 2.3 records the experimental process and the statistical results of RMS and ASL.

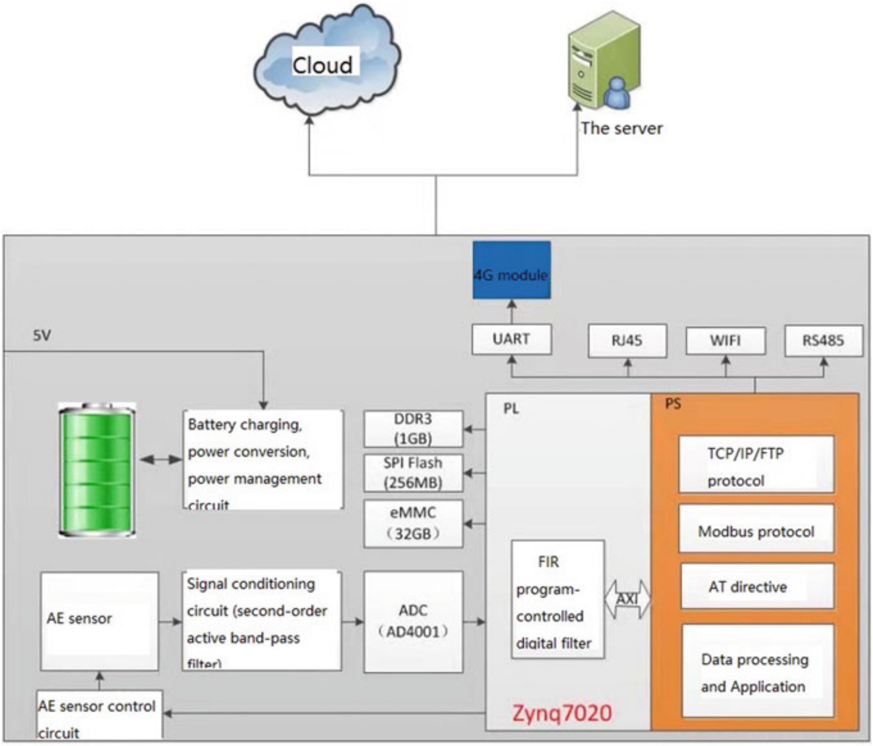
Cloud
The server
4G module
5V
UART
RJ45
WIFI
RS485
PL
PS
Battery charging, power conversion, power management circuit
DDR3 (1GB)
SPI Flash (256MB)
eMMC （32GB）
TCP/IP/FTP protocol
Modbus protocol
AT directive
AE sensor
Signal conditioning circuit (second-order active band-pass filter)
ADC （AD4001）
FIR program-controlled digital filter
AXI
Data processing and Application
AE sensor control circuit
Zynq7020

Fig. 2.4 RAE1 functional block diagram

2.3.3 *The RAE1 Testing Data*

The setting of RAE1 in this experiment: Digital filter 20–100khz; Hit threshold 60 dB; HDT = 5us, PDT = 3us, HLT = 5us; ls35 sensor, resonance frequency 15–70khz, central resonance frequency 35 kHz. The operation process of faucet controlling water flow is shown in Table 2.4.

Figure 2.10 shows the history data from server of RL1 AE IOT system. RMS and ASL have useful references, and the difference between water out and no water out is obvious, as shown in the figure. Figure 2.11 shows the leakage alarm display on the smart phone for RAE1.

2.3.4 *Discussion*

It is very clear that both RAE1 and RL1 IOT AE systems can correct monitoring and alarms the leakages of the water tap. It can be concluded that valve leakages can be

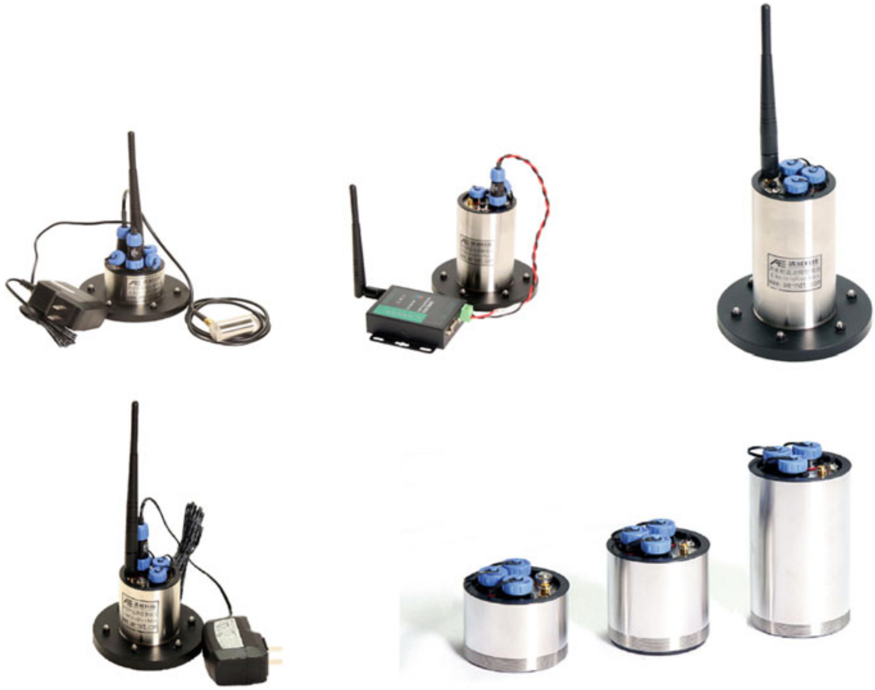

Fig. 2.5 Integrate and separate RL1/RAE1

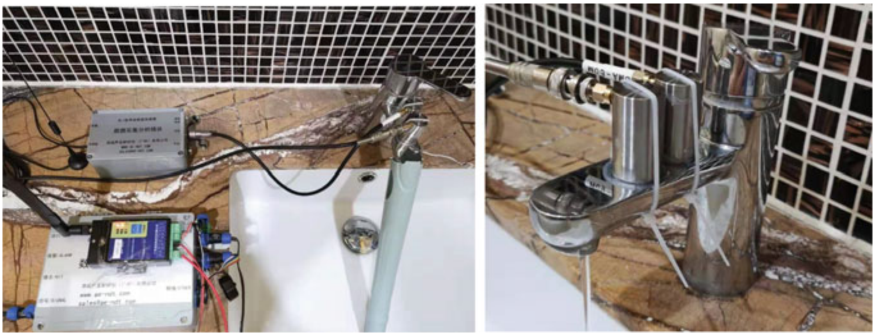

Fig. 2.6 Layout of testing on tap and RAE1/RL1

success monitored and alarm report by RL1 and RAE1 IOT AE systems if just use the valves instead of tap for the same testing.

Table 2.2 Data of RL1 for tap water leakages

Equipment number	Instrument name	Data point ID	Time	Characteristic parameter	Numerical value	Characteristic parameter	Numerical value
356,566,078,314,267	RL1-099	29,907	2019–11-02 07:14:23	RMS	20.0	ASL	23.7
356,566,078,314,267	RL1-099	29,907	2019–11-02 07:14:59	RMS	21.8	ASL	24.7
356,566,078,314,267	RL1-099	29,907	2019–11-02 07:23:35	RMS	21.2	ASL	24.7
356,566,078,314,267	RL1-099	29,907	2019–11-02 07:30:11	RMS	19.4	ASL	23.7
356,566,078,314,267	RL1-099	29,907	2019–11-02 07:38:51	RMS	18.2	ASL	22.5
356,566,078,314,267	RL1-099	29,907	2019–11-02 07:40:31	RMS	2008.5	ASL	64.1
356,566,078,314,267	RL1-099	29,907	2019–11-02 07:46:18	RMS	1791.6	ASL	63.1
356,566,078,314,267	RL1-099	29,907	2019–11-02 07:52:11	RMS	1764.6	ASL	63.0
356,566,078,314,267	RL1-099	29,907	2019–11-02 07:57:23	RMS	2194.5	ASL	64.8
356,566,078,314,267	RL1-099	29,907	2019–11-02 08:03:36	RMS	1488.3	ASL	61.5
356,566,078,314,267	RL1-099	29,907	2019–11-02 08:08:43	RMS	1918.8	ASL	63.7
356,566,078,314,267	RL1-099	29,907	2019–11-02 08:16:03	RMS	1596.9	ASL	62.1
356,566,078,314,267	RL1-099	29,907	2019–11-02 08:19:47	RMS	1855.5	ASL	63.4
356,566,078,314,267	RL1-099	29,907	2019–11-02 08:22:05	RMS	17.3	ASL	21.2
356,566,078,314,267	RL1-099	29,907	2019–11-02 08:28:06	RMS	17.8	ASL	22.5
356,566,078,314,267	RL1-099	29,907	2019–11-02 08:34:39	RMS	17.1	ASL	21.2
356,566,078,314,267	RL1-099	29,907	2019–11-02 08:35:58	RMS	8734.8	ASL	76.8
356,566,078,314,267	RL1-099	29,907	2019–11-02 08:37:24	RMS	9026.6	ASL	77.1
356,566,078,314,267	RL1-099	29,907	2019–11-02 08:43:44	RMS	10,345.4	ASL	78.3
356,566,078,314,267	RL1-099	29,907	2019–11-02 08:49:17	RMS	10,229.3	ASL	78.2
356,566,078,314,267	RL1-099	29,907	2019–11-02 08:54:56	RMS	9178.0	ASL	77.3

(continued)

Table 2.2 (continued)

Equipment number	Instrument name	Data point ID	Time	Characteristic parameter	Numerical value	Characteristic parameter	Numerical value
356,566,078,314,267	RL1-099	29,907	2019–11-02 09:01:36	RMS	10,299.0	ASL	78.3
356,566,078,314,267	RL1-099	29,907	2019–11-02 09:06:47	RMS	10,191.2	ASL	78.2
356,566,078,314,267	RL1-099	29,907	2019–11-02 09:08:23	RMS	15.3	ASL	19.6
356,566,078,314,267	RL1-099	29,907	2019–11-02 09:13:58	RMS	13.0	ASL	17.7
356,566,078,314,267	RL1-099	29,907	2019–11-02 09:17:58	RMS	10.8	ASL	15.2
356,566,078,314,267	RL1-099	29,907	2019–11-02 09:24:48	RMS	11.0	ASL	17.7
356,566,078,314,267		29,907	2019–11-2 09:34:36	RMS	11.5	ASL	17.7

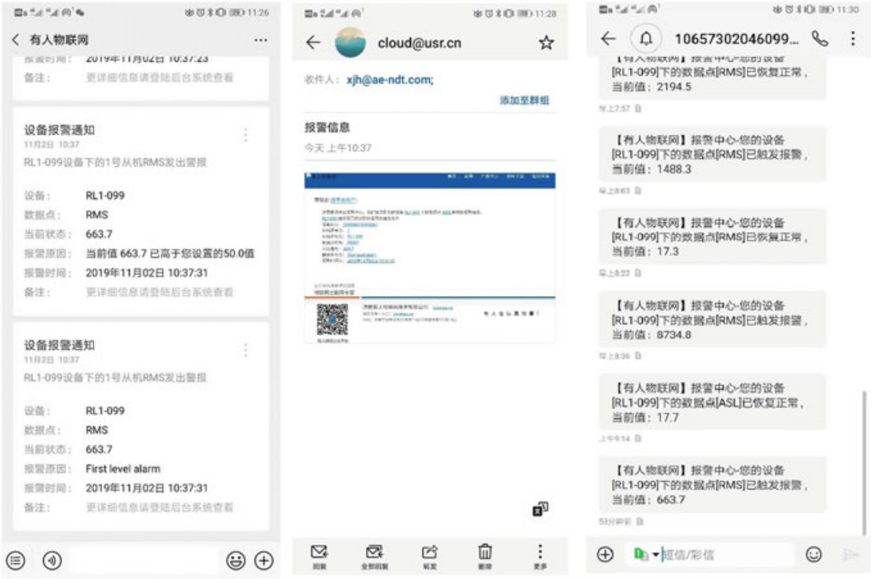

有人物联网

报警时间： 2019年11月02日 10:37:23
备注： 更详细信息请登陆后台系统查看

设备报警通知
11月2日 10:37
RL1-099设备下的1号从机RMS发出警报

设备： RL1-099
数据点： RMS
当前状态： 663.7
报警原因： 当前值 663.7 已高于您设置的50.0值
报警时间： 2019年11月02日 10:37:31
备注： 更详细信息请登陆后台系统查看

设备报警通知
11月2日 10:37
RL1-099设备下的1号从机RMS发出警报

设备： RL1-099
数据点： RMS
当前状态： 663.7
报警原因： First level alarm
报警时间： 2019年11月02日 10:37:31
备注： 更详细信息请登陆后台系统查看

cloud@usr.cn
收件人： xjh@ae-ndt.com;
添加至群组

报警信息
今天 上午10:37

10657302046099...

【有人物联网】报警中心-您的设备[RL1-099]下的数据点[RMS]已恢复正常，当前值：2194.5

【有人物联网】报警中心-您的设备[RL1-099]下的数据点[RMS]已触发报警，当前值：1488.3

【有人物联网】报警中心-您的设备[RL1-099]下的数据点[RMS]已恢复正常，当前值：17.3

【有人物联网】报警中心-您的设备[RL1-099]下的数据点[RMS]已触发报警，当前值：8734.8

【有人物联网】报警中心-您的设备[RL1-099]下的数据点[ASL]已恢复正常，当前值：17.7

【有人物联网】报警中心-您的设备[RL1-099]下的数据点[RMS]已触发报警，当前值：663.7

Fig. 2.7 Smart phone displays of RL1 for tap water leakage monitoring and alarm

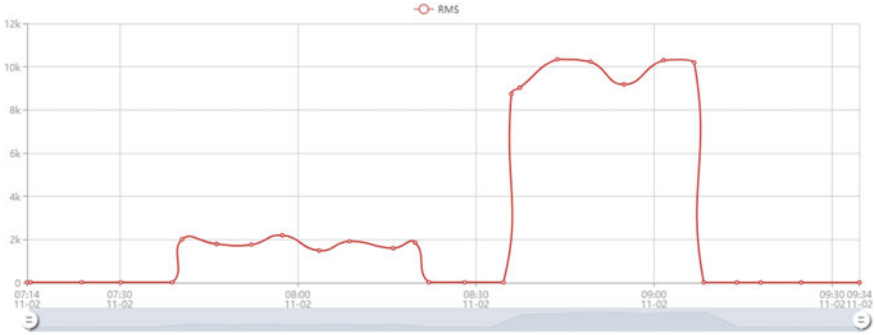

Fig. 2.8 RMS to time, the displays of monitoring data on the laptop by visiting the servers to get the data

2.4 Conclusions

From above jobs it can be concluded that IOT AE systems are technically available now and IOT AE are useful for remote unattended monitoring and alarm report.

In future the long-term cycle of self-learning correction of artificial intelligence based on big data on the server makes the system have the ability of self-learning, self-improvement and continuous improvement of performance.

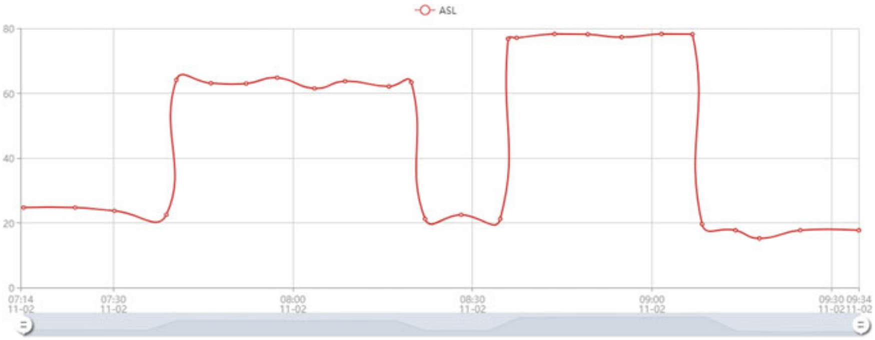

Fig. 2.9 ASL to time, the displays of monitoring data on the laptop by visiting the servers to get the data

Table 2.3 Results of the testing of RL1 IOT AE for tap water leakages

				RL1	
Experimental process			Water leakage	RMS	ASL
07:14–07:39	25 min	Tap off	0 ml/s	18.2–21.3	22.5–24.7
07:40–08:19	40 min	Tap small angle on	11 ml/s	1488.3–2194.5	61.5–64.8
08:20–08:34	14 min	Tap off	0 ml/s	17.1–17.8	21.2–22.5
08:35–09:07	32 min	Tap large angle on	30 ml/s	8734.8–10,345.4	76.8–78.3
09:08–09:35	27 min	Tap off	0 ml/s	10.8–15.3	15.2–19.6

Table 2.4 Results of the testing of RAE1 IOT AE for tap water leakages.

Time	Experimental content	MaxAmp	Conclusion
21:14–9:29	Tap off	45−55 dB	(1) Background noise 45–55 db; (2) Accurate acquisition of lead breaking signal;
21:30–22:00	Tap small angle on (12.5 ml/s) + Lead breaks at 21:40	45–70 dB	
22:00–22:12	Tap off	45–60 dB	
22:12–22:21	Tap large angle on (70 ml/s) + Lead breaks at 22:20	45–78 dB	
22:21–22:26	Tap off	0–55 dB	

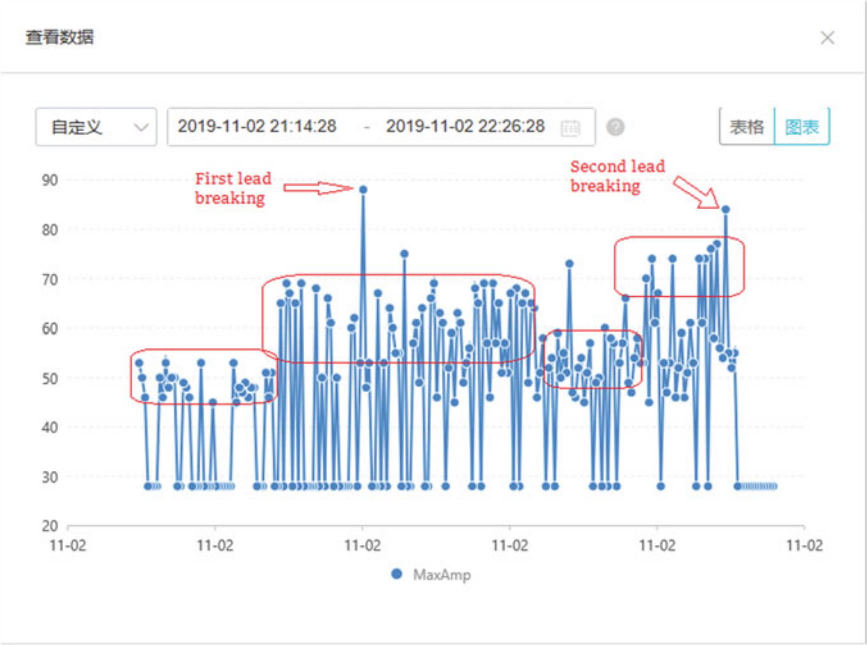
查看数据
×
自定义
2019-11-02 21:14:28 - 2019-11-02 22:26:28
表格
图表
90
80
70
60
50
40
30
20
11-02
11-02
11-02
11-02
11-02
11-02
MaxAmp
First lead breaking
Second lead breaking

Fig. 2.10 Check historical data through laptop access server

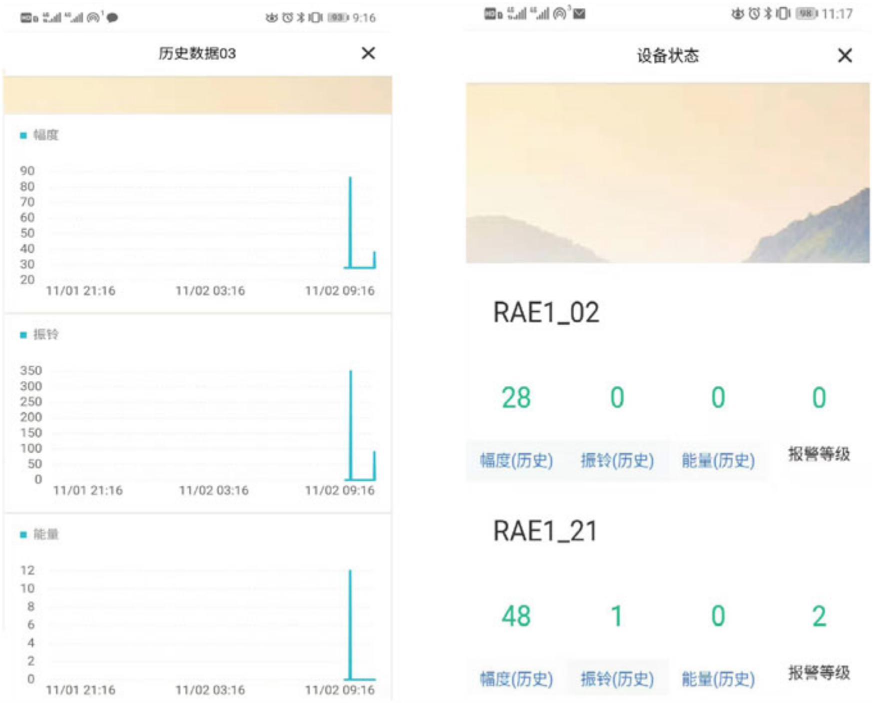
9:16
历史数据03
✕
■ 幅度
90
80
70
60
50
40
30
20
11/01 21:16
11/02 03:16
11/02 09:16
■ 振铃
350
300
250
200
150
100
50
0
11/01 21:16
11/02 03:16
11/02 09:16
■ 能量
12
10
8
6
4
2
0
11/01 21:16
11/02 03:16
11/02 09:16
11:17
设备状态
✕

RAE1_02

28	0	0	0
幅度(历史)	振铃(历史)	能量(历史)	报警等级

RAE1_21

48	1	0	2
幅度(历史)	振铃(历史)	能量(历史)	报警等级

Fig. 2.11 Smart phone displays of RAE1 for tap water leakage monitoring and alarm

Chapter 3
About an Initial Draft of a Standard Concerning Sensitivity Verification of Acoustic Emission Sensors

Hartmut Vallen

Abstract This paper summarizes an initial draft for a new standard submitted to ISO TC 135 SC 9 (acoustic emission). The draft comprises 30 pages. Only the basics can be treated in this compressed format.

3.1 Introduction

This paper briefly describes an initial draft of a standard, submitted to ISO, Technical Committee (TC) 135, Subcommittee (SC) 9, acoustic emission (AE), as a new work item proposal (NWIP). The scope of the NWIP is reproduced in next chapter.

In the introduction the draft lists the three existing ISO standards for acoustic emission (AE) sensor calibration: ISO 12713:1998 [1], ISO 12714:1999 [2], ISO/TR 13115:2011 [3] and explains why another standard is urgently needed: The two of 1998 and 1999 are obviously outdated, the third is not a normative document and controversial discussed. It also must be stated that the National Institute of Standards and Technology (NIST, USA), the only neutral offerer of primary AE sensor calibration in the western world, has discontinued such offer to external clients some years ago. Within ISO TC135 SC9 a revision of ISO 12714 has been started but stopped in 2017 due to the non-availability of new primary calibrated reference sensors. Some long existing AE organizations may still operate a working verification setup according to ISO 12714, but younger or new organizations interested in performing AE applications do have serious problems due to the absence of a practicable sensor sensitivity verification standard: Many standards for AE applications specify the needed sensor sensitivity, hence each AE sensor manufacturer, but also each AE service provider must ensure that the sensors sold and used meet those requirements. Since no international up-to-date standard for determining the sensor sensitivity exists, such a verification is rather difficult and the creation of such a standard is an urgent matter.

H. Vallen (✉)
Vallen Systeme GmbH, Icking, Bavaria 82057, Germany
e-mail: hartmut@vallen.de

© The Author(s), under exclusive license to Springer Nature Singapore Pte Ltd. 2021

G. Shen et al. (eds.), *Advances in Acoustic Emission Technology*, Springer Proceedings in Physics 259, https://doi.org/10.1007/978-981-15-9837-1_3

The chapter "Introduction" of the initial draft lists some advantages of the proposed face-to-face (F2F) method, e.g. the avoidance of a heavy transfer block, a simpler handling, the absence of indirect paths between source and sensor, the good reproducibility. It also presents the disadvantage of the F2F method: The obtained sensitivity spectra are only valid for plane waves arriving in normal direction. Cancellation effects, that happen with e.g. Rayleigh waves, depending on the dimension of the sensitive face of the sensor, do not occur with the F2F method and hence, are not considered.

3.2 Scope

Reproduced from Chap. 1 of the initial draft: "This document specifies (a) a method of determining the receiving sensitivity spectrum of a piezoelectric acoustic emission sensor in absolute units of volt output per units of particle motion input. Units of motion can be millimeter per second velocity or nanometer displacement, over a frequency range used for acoustic emission testing, from about 20 kHz to 1 MHz, whereby the sensor is stimulated by a particle velocity pulse in normal direction to the sensor's face from a directly coupled piezoelectric transmitter; and (b) a method of determining a transmitter's transmitting sensitivity spectrum in absolute units of millimeter per second output per unit of volt input, by measuring both, the particle velocity pulse over the transmitter's active face and the transmitter's input voltage spectrum, by using measurement channels of common frequency characteristics as offered by a hireable scanning laser vibrometer.

This document does not include the effects on a sensor's response, when the length of the wave passing across the sensor's sensitive face is shorter than about 5 times of the dimension of the sensor's sensitive face."

3.3 Other Chapters

Three mandatory chapters (Chaps. 2–4) concern: Normative references, Terms and definitions, Symbols and abbreviations.

Chapter 5 describes the face-to-face setup (F2F), which is used to determine the SUT's receiving sensitivity, and the laser vibrometer setup (LVM), which is used to determine the transmitter's transmitting sensitivity.

Chapter 6 defines all requirements on the hardware described in Chap. 5.

Chapter 7 "Determination of the receiving sensitivity" contains subchapters "7.1 Scaling of FFT results", "7.2 Interpolation of time series data of 8–25 ns sampling interval", "7.3 DC offset compensation", "7.4 Recommended stimulation signal", "7.5 Windowing of SUT responses", "7.6 Relevant spectra for sensor sensitivity determination", "7.7 Formulae for obtaining sensitivities and F2F velocity", "7.8 Examples of velocity sensitivity spectra" (of a wideband, a narrowband and a multi-resonant SUT), 7.9 “Examples of displacement sensitivity spectra”, “7.10 Reproducibility of sensitivity spectra”.

Chapter 8 “Determination of transmitting sensitivity spectra” contains, among others, the subchapters “8.2 Measuring the stimulation signal by the LVM’s reference input”, “8.3 Increasing the sampling rate of LVM by interpolation”, “8.4 Averaging the particle velocity measured by LVM setup”, “8.5 Windowing of the averaged velocity signals”, “8.6 Pre-trigger considerations”, “8.7 Relevant spectra for transmitting sensitivity determination”.

Chapter 9 deals with “Criteria for sorting out unsuitable transmitter units”.

Chapter 10 deals with “Reports”.

Informal “Annex B” shows how the sensitivity spectra obtained from F2F setup can be adapted to the acoustic impedance of the test object material.

3.4 Basics of the Proposed Face to Face Setup

Figure 3.1 shows the block diagram for the face-to-face (F2F) setup with text describing the blocks.

The sensor’s receiving sensitivity spectrum Rv shall be expressed in absolute units of volts of sensor output per millimeter per second particle velocity input. The sensor output spectrum is obtained by the FFT of the measured sensor output US. The particle velocity input spectrum is obtained by multiplying the transmitting sensitivity spectrum of the transmitter by the spectrum of the measured transmitter

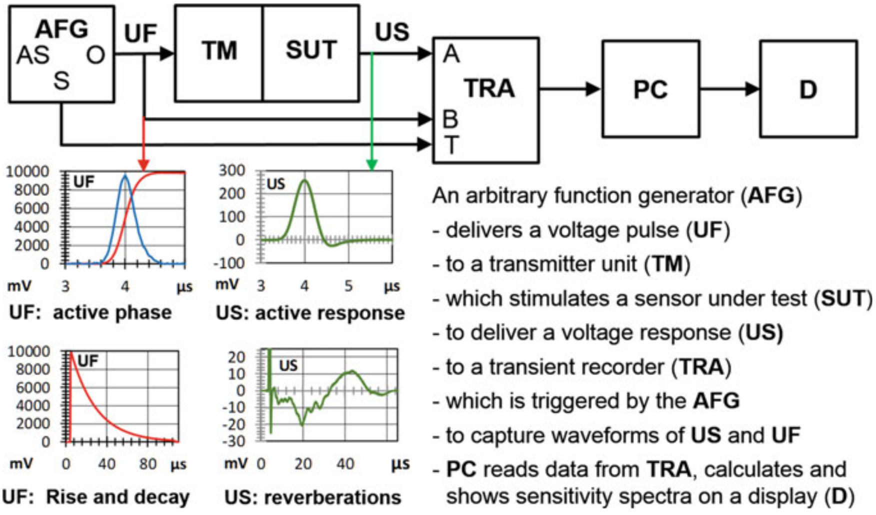
AFG
AS
O
S
UF
TM
SUT
US
A
TRA
B
T
PC
D
10000
8000
6000
4000
2000
0
UF
mV
3
4
µs
UF: active phase
300
200
100
0
-100
US
mV
3
4
5
µs
US: active response
10000
8000
6000
4000
2000
0
UF
mV
0
40
80
µs
UF: Rise and decay
20
10
0
-10
-20
-30
US
mV
0
20
40
µs
US: reverberations

An arbitrary function generator (**AFG**)
- delivers a voltage pulse (**UF**)
- to a transmitter unit (**TM**)
- which stimulates a sensor under test (**SUT**)
- to deliver a voltage response (**US**)
- to a transient recorder (**TRA**)
- which is triggered by the **AFG**
- to capture waveforms of **US** and **UF**
- **PC** reads data from **TRA**, calculates and shows sensitivity spectra on a display (**D**)

Fig. 3.1 Block diagram of the F2F-setup

voltage UF. The transmitting sensitivity is obtained by using the laser vibrometer setup described hereafter.

3.5 Basics of the LVM Setup

LVM stands for Laser Vibrometer. The LVM-setup is used for determining the transmitting sensitivity spectrum of a transmitter. The setup is similar to the F2F setup. Instead of a SUT and a transient recorder the LVM measures the motion pulse generated by the transmitter. Figure 3.2 shows the block diagram of the LVM setup.

Since the LVM is less sensitive than a SUT the transmitter (TM) needs a stronger excitation pulse in order to cause a sufficient signal-to-noise ratio of the LVM output. A high voltage amplifier (x50) has been used which delivered the transmitter voltage UL, a pulse amplitude of almost 100 V (peak). Since this is too high a voltage for the reference channel of the LVM, a high impedance voltage divider (39:1) has been used to feed UL/39 into the reference channel. The synch output of the AFG triggers the LVM to measure both, the motion pulse VL and the reference channel. 200 measurements per position have been averaged for an optimal signal-to-noise ratio.

Since the SUT converts the average motion over its sensitive face, the transmitter's motion has been measured at 145 positions arranged in 9 concentric rings of 16 positions each and the central position. In this way 9 velocity signals, averaged over 9 different diameters have been derived, so that for each SUT a velocity signal averaged over a diameter near to that of the SUT's sensitive face can be selected for sensitivity determination.

The motion pulse is measured at the free face of the transmitter. The sensor's receiving sensitivity shall be scaled to the motion at the free surface of the test object (according to E 1106). The acoustic impedance of the test object has influence on the sensitivity and must be considered. Annex B of the initial draft deals with the consideration of the acoustic impedance of the material the sensor shall be mounted to.

The reference channel output UR and the velocitv output VF are processed by FFT with a resolution of 1.22 kHz.

Fig. 3.2 Block diagram of the LVM-setup

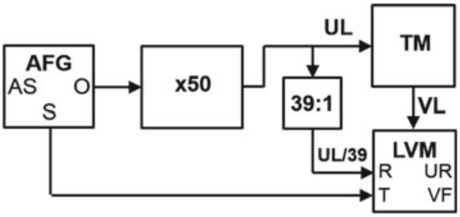

3.6 Calculating the Transmitting and Receiving Sensitivities

Figure 3.3 shows the spectra derived by FFT from the symbols seen in the F2F and the LVM setup:

in blue: **UR**, the voltage at TMA (the transmitter A), measured by the LVM reference channel, then transformed by FFT and converted to dB.

in green: **UF**, the voltage at TMA, measured by TRA in F2F setup, then transformed by FFT and converted to dB.

in red: **VF**, the particle velocity, measured by LVM, then transformed by FFT and converted to dB.

in black: **VT**, the particle velocity in F2F setup at free TMA, obtained by Formula 3.2.

Formula (3.1) is to obtain **Tv**, the transmitting sensitivity of the transmitter in dB(mm/sV), (3.2) is to obtain **VT**, the particle velocity in F2F setup, (3.3) is to obtain **Rv**, the receiving sensitivity of the SUT in dB (Vs/mm), and (3.4) is to obtain **Rd**, the receiving sensitivity in dB (V/nm).

$$\mathbf{Tv}\text{ in dB (mm/sV)} = \mathbf{VF}\text{ in dB(mm/s)} - \mathbf{UR}\text{ in dB(V)} \tag{3.1}$$

$$\mathbf{VT}\text{ in dB (mm/s)} = \mathbf{VF}\text{ in dB(mm/s)} - \mathbf{UR}\text{ in dB(V)} + \mathbf{UF}\text{ in dB(V)} \tag{3.2}$$

$$\mathbf{Rv}\text{ in dB(Vs/mm)} = \mathbf{US}\text{ in dB(V)} - \mathbf{VT}\text{ in dB (mm/s)} \tag{3.3}$$

$$\mathbf{Rd}\text{ in dB(V/nm)} = \mathbf{Rv}\text{ in dB(Vs/mm)} + (\text{dB}(2\pi\text{f}) - 120) \tag{3.4}$$

whereby “dB (unit)” shall read “0 dB refer to 1 unit”.

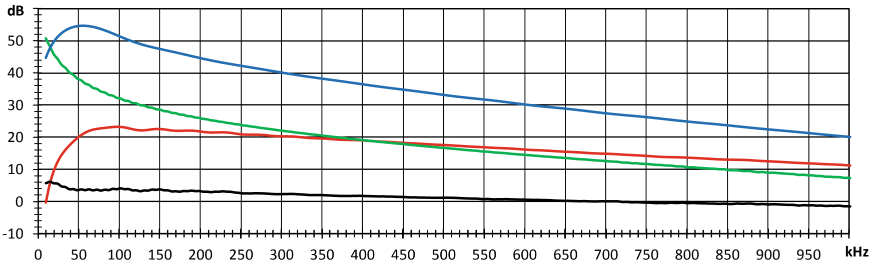

Fig. 3.3 The relevant spectra to obtain VT, the particle velocity spectrum in the F2F setup, vs. frequency in kHz

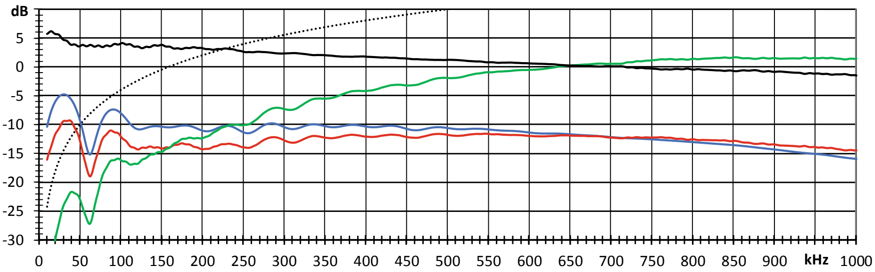

Fig. 3.4 The relevant spectra for obtaining the receiving sensitivities Rv and Rd versus frequency in kHz

The flatness of the black VT curve in Fig. 3.3 shows that particle velocity is almost constant over frequency, this is optimal for a large dynamic range of spectral results.

Figure 3.4 shows relevant spectra for the receiving sensitivity determination.

in black: **VT**, the calculated particle velocity spectrum in F2F setup at free TMA.

in blue: **US,** the SUT output voltage, measured by TRA, then transformed by FFT and converted to dB.

in red: **Rv,** the calculated velocity receiving sensitivity.

in green: **Rd,** the calculated displacement receiving sensitivity.

dotted: dB(2 π f) – 120, whereby dB(x) refers to 20 × lg (x).

The conversion of a linear displacement spectrum in meters to a velocity spectrum in meters per second can be done by multiplication by 2πf (see [10] Subclause 7.5.5). If displacement refers to nm and velocity shall refer to mm/s, a unit-conversion factor of $1/10^6$ applies. Hence, a spectrum in dB(nm) (means 0 dB refer to 1 nm) can be differentiated by adding (dB(2πf)−120), whereby the mentioned unit-conversion is done by subtracting 120 dB. Vice versa, a velocity spectrum in dB(mm/s) can be converted to a displacement spectrum in dB(nm) by subtracting (dB (2πf)−120).

Figure 3.5 shows examples of displacement receiving sensitivities (Rd) of three types of SUT:

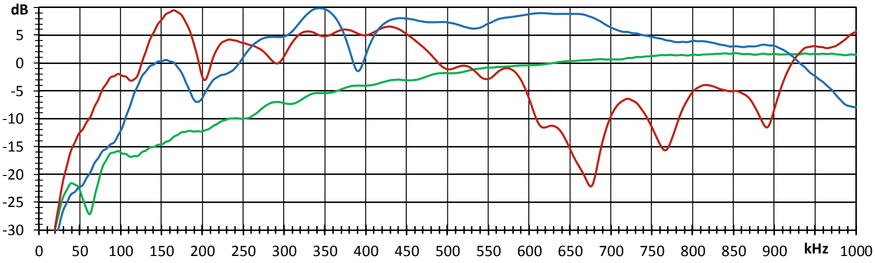

Fig. 3.5 The displacement receiving sensitivity Rd of 3 types of SUT versus frequency

in blue: **V103** Olympus 1 MHz UT probe, often used as wideband AE sensor.

in red: **VS150M** Vallen 150 kHz resonant sensor.

in blue: **VS900M** Vallen multi-resonant sensor.

3.7 Conclusion

The initial draft comprises 31 pages and deals with many details. Only few can be treated in such short manuscript. Some complexity was introduced while solving bottlenecks of the used LVM-setup:

- LVM sampling rate of velocity signal is only 2.56 MS/s and needs interpolation to 10 or 40 MS/s.
- LVM-internal high-pass of velocity signal causes −3 dB loss already at about 60 kHz. This can be compensated (see VT in Fig. 3.3) but this adds complexity.
- Velocity measurement buries some low-frequency displacement info below noise.

Meanwhile another laser vibrometer product has been evaluated which eliminates these bottlenecks. In addition, Prof. Kanji Ono published recently a new paper [8] titled "Progress in Sensitivity Verification of AE Sensors" that includes recommendations for consideration in a new standard.

We feel obliged to consider such advice before submitting a first ISO working draft (WD). The availability of a 1st official WD is now planned for the end of January 2020.

Acknowledgements We are thankful for the many suggestions and representations received from Professor Kanji Ono and the lot of experience he distributed in recent publications concerning AE sensor verification, especially in [4–9].

References

1. ISO 12713:1998(E), Non-destructive testing—Acoustic emission inspection—Primary calibration of transducers, International Organization for Standardization, Geneva, Switzerland
2. ISO 12714:1999, Non-destructive testing—Acoustic emission inspection—Secondary calibration of acoustic emission sensors, International Organization for Standardization, Geneva, Switzerland,
3. ISO/TR 13115:2011, Non-destructive testing—Methods for absolute calibration of acoustic emission transducers by the reciprocity technique, International Organization for Standardization, Geneva, Switzerland
4. K. Ono, Calibration methods of acoustic emission sensors. Materials **9**, 508 (2016). https://doi.org/10.3390/ma9070508
5. K. Ono, Critical examination of ultrasonic transducer characteristics and calibration methods. RNDE (2017). https://doi.org/10.1080/09349847.2017.1375585

6. K. Ono, Frequency dependence of receiving sensitivity of ultrasonic transducers and acoustic emission sensors, MDPI, https://www.mdpi.com/1424-8220/18/11/3861 (2018)
7. K. Ono, Receiving Sensitivities of Acoustic Emission Sensors: A data compilation. https://www.aewg.org/jae/JAE-Vol_36-2019-4A.pdf, pp. 1–8
8. K. Ono, Progress in Sensitivity Verification of AE Sensors. https://www.aewg.org/jae/JAE-Vol_36-2019-4B.pdf, pp. s37-s45
9. K. Ono, Rayleigh wave calibration of acoustic emission sensors and ultrasonic transducers. Not yet published
10. ASTM E1106–12 Standard method for primary calibration of acoustic emission sensors, in *ASTM International*, West Conshohocken, PA, USA

Chapter 4
Comparative Analysis of the International Status of Acoustic Emission Equipment Performance Testing

Junjiao Zhang, Gongtian Shen, Yilin Yuan, Yongna Shen, and Zhanwen Wu

Abstract The good performance of acoustic emission equipment is an important guarantee for the reliability of test results. With the continuous improvement of the research and development technology of acoustic emission instruments and sensors, the performance testing methods and standards are also constantly improving. The international status of acoustic emission instruments and sensors performance testing was introduced. In terms of testing standards, a detailed comparison was carried out. The commonalities and differences of test methods in various countries were put forward to provide references for testers and users of acoustic emission equipment.

4.1 Introduction

Acoustic emission (AE) is a dynamic inspection method that detects the energy emitted by the object itself. It has the advantages of online inspection, insensitive to the geometry of the object, and able to detect defects in the whole structure. AE technology is suitable for on-line monitoring and early or near-damage prediction of industrial processes. The beginning of AE technology is marked by Kaiser's research work in Germany in the early 1950. After more than 60 years of development, AE technology has been widely used in petrochemical, electric power, aerospace, transportation, machinery manufacturing, construction and other industries. AE equipment is the carrier for the implementation of AE detection. AE instruments and sensors are the core equipment for testing and detection. Their performance directly affects the ability of AE detection and the accuracy of the testing results. In order to ensure the effectiveness and reliability of AE testing, the performance testing of AE instruments and sensors is particularly important.

J. Zhang · G. Shen (✉) · Y. Yuan · Y. Shen · Z. Wu
China Special Equipment Inspection and Research Institute, Beijing 100029, China
e-mail: shengongtian@csei.org.cn

Y. Shen
e-mail: shengongtian@csei.org.cn

© The Author(s), under exclusive license to Springer Nature Singapore Pte Ltd. 2021

G. Shen et al. (eds.), *Advances in Acoustic Emission Technology*, Springer Proceedings
in Physics 259, https://doi.org/10.1007/978-981-15-9837-1_4

With the development of AE technology and the advent of AE equipment, related institutions in the world have successively developed and issued standards for AE instruments and sensors performance testing. At present, the International Organization for Standardization (ISO), the American Society for Testing and Materials (ASTM), the European Committee for Standardization (CEN), and the Standardization Administration of China (SAC) have all issued standards for AE equipment performance test. Based on these standards, performance testing and calibration testing of AE instruments and sensors of in-use are performed.

This paper summarized the development process of AE instruments in the world, and the performance testing standards and current status of AE instruments and sensors were introduced and compared. The testing purposes and contents of different standards are sorted out and analyzed to provide a reference for testers to select standards and methods according to actual needs. It also helps users understand the performance differences of AE equipment from different countries.

4.2 The Development of AE Equipment

The development of AE instruments experienced three stages including analog, semi-digital, and fully digital [1]. In 1965, Dunegan Corporation of the United States launched the first commercial AE instrument in the world. In the late 1970, the Shenyang Institute of Electronics in China developed a single-channel acoustic emission instrument. In the early 1980, the American PAC introduced modern micro-processing computer technology into the AE system and designed a second-generation source-location instrument with a smaller size and weight. China Changchun Testing Machine Research Institute developed a 32-channel AE location and analysis system controlled by a microprocessor computer. In the 1990, the American PAC and the German Vallen Systeme developed the third-generation digital multi-channel AE detection and analysis system with a higher degree of computerization and a smaller volume and weight. China Boiler and Pressure Vessel Inspection and Research Center has developed a multi-channel AE detection and analysis system with PC-AT bus for hardware and WINDOWS interface for software. Since the beginning of the twenty-first century, the research and development of AE instrument have adopted more advanced technologies and developed more comprehensive functions in data transmission, analysis and processing. The development of AE sensors is also proceeding simultaneously with the development of instruments. At present, sensors have a variety of specifications in terms of type, frequency band and size, which can meet different actual detection requirements.

AE instruments and sensors currently on the market mainly come from PAC (USA), Vallen Systeme (Germany), Beijing Soundwel Technology Co., Ltd (China) and INTERUNIS-IT (Russia). Each manufacturer produces different types of instruments and sensors, which have their own performance characteristics.

4.3 Comparative Analysis of Performance Test of AE Instruments

4.3.1 Testing Status and Standards

In the production process of AE instruments in various countries, the performance parameters need to be tested and verified, and a quality certificate and test report will be issued after the results meeting the technical requirements. After the instrument put into use, the manufacturer or measuring agency conducts a calibration test once a year to verify whether its performance parameters meet the AE testing requirements.

With the advent of AE instruments and the continuous improvement of product research and development technology, countries around the world have successively developed and issued standards for AE instrument performance testing, including American ASTM standards, European EN standards and Chinese standards, as shown in Table 4.1.

The United States developed the first AE instrument standard ASTM E750 in 1980, and the latest edition was revised in 2015. This standard is recommended for use in testing and measuring operating characteristics of acoustic emission electronic components or units. European CEN developed a series of standards for the characteristics of AE equipment in the early twenty-first century. EN13477.1 describes the main components that constitute an AE monitoring system and EN13477.2 specifies methods for routine verification of the performance of an AE equipment comprising one or more sensing channels. China first developed the AE instrument standard JB/T 8283 in 1987, and the latest version was revised in 1999. This standard specifies the performance test method of AE instruments. Then the product standard

Table 4.1 AE instrument standards

Standard issuer	Standard name
USA	ASTM E750-15 standard practice for characterizing acoustic emission instrumentation
Europe	EN 13477–1:2001 non-destructive testing—acoustic emission—equipment characterisation—part 1: equipment description EN 13477–2:2010 non-destructive testing—acoustic emission—equipment characterisation—part 2: verification of operating characteristics
China	JB/T 8283–1999 methods for testing the operating characteristics of acoustic emission instrumentation JB/T 5754–2011 non-destructive testing instruments-specifications for one-channel acoustic emission testing instrument JB/T 11603.1–2013 non-destructive testing instruments-acoustic emission-equipment characterization-part 1: equipment description JB/T 11603.2–2013 non-destructive testing instruments-acoustic emission-equipment characterization-part 2: verification of operating characteristic JJF 1505–2015 calibration specification for acoustic emission instrumentation

JB/T 5754 was developed, which specifies the technical conditions, testing methods, testing rules, signs and packaging of single-channel AE instruments. In addition, the calibration standard JJF 1505 for the AE instruments has been developed in 2015 [2–9].

4.3.2 Comparison and Analysis

The standards for performance test of AE instruments in different countries are compared in terms of test parameters and test devices, as shown in Table 4.2.

It is found that all the standards use the signal generator, Oscilloscope, Variable attenuator, RMS voltmeter and some other devices to build the testing systems for the performance test of AE instruments. In terms of test parameters, bandwidth, threshold, and the measured AE burst signal parameters are all present in American, European and Chinese standards, which means that these parameters are very important for the AE instrument performance. In addition, the American standards also propose test methods for gain, dynamic range, dead time, counter accuracy, and waveform accuracy. The European standards pay attention to the external parameter, AE signal acquisition rate of the system, and the delta-t measurement. The Chinese

Table 4.2 Comparison of AE instrument test standards

Standard	Test parameters	Test devices
ASTM E750	Frequency Response and Bandwidth, Threshold Level, Computer-Measured Parameters, Gain, Dynamic Range, Dead Time, Counter Accuracy, Waveform Accuracy	Variable Sine Wave Generator or Oscillator, True RMS Voltmeter, Oscilloscope, Variable Attenuator, Tone Burst Generator, Electronic AE Simulator
EN 13477 JB/T 11603	Bandwidth, detection threshold, the measured AE burst signal parameters, the external parameter, AE signal acquisition rate of the system, the Delta-t measurement	Sweep function/variable pulse signal generator, Random noise generator, Dual channel storage oscilloscope, Variable attenuator, Multimeter, RMS voltmeter, DC Power supply
JB/T 8283	Bandwidth, Gain, Dynamic Range, Noise, Overload recovery time, Input impedance Output impedance, Threshold voltage	Signal generator, Variable attenuator, Oscilloscope, RMS voltmeter, Pulse modulation signal generator
JB/T 5754	Bandwidth, detection threshold, the measured AE burst signal parameters, the external parameter, Temperature resistance	Sweep function/variable pulse signal generator, Random noise generator, Dual channel storage oscilloscope, Variable attenuator, Multimeter, RMS voltmeter, DC Power supply, High and low temperature test chamber
JJF 1505	Frequency range, Noise, Dynamic range, Crosstalk between channels, Waveform parameters	Function signal generator, Oscilloscope, Variable attenuator, Digital AC voltmeter, Reference preamplifier

standards combine the parameters from the American and European standards, and also proposes other parameters based on the different functions of the standards. For example, noise, overload recovery time, input impedance and output impedance are proposed in the instrument performance test standard, temperature resistance is proposed in the product standard, and crosstalk between channels is proposed in the calibration standard.

4.4 Comparative Analysis of Performance Test of AE Sensors

4.4.1 Testing Status and Standards

Each newly produced AE sensor is accompanied by a sensitivity test report with spectrum curves. After it is put into use, the AE sensor is generally calibrated once a year. The performance of the sensor will gradually decrease with the increase in use. The sensor may be damaged when the environment is harsh or the operation is improper. When the detection sensitivity of the sensor decreases significantly, the performance test should be carried out in time to verify whether it meets the detection needs.

The performance test standards for AE sensors mainly include American ASTM standards, European EN standards, ISO standards and Chinese standards, as shown in Table 4.3.

The AE sensor test standards appeared later than the instrument test standards. The United States first developed and issued ASTM E976 in 1984 and the latest version was revised in 2015. This standard provides simple procedures for testing or comparing the performance of AE sensors. These procedures allow the user to check for degradation of a sensor or to select sets of sensors with nearly identical performances, but not capable of providing an absolute calibration. Then ASTM also developed and issued the other 4 standards. ASTM E650M proposes the AE sensor mounting method, requirements and response verification after sensor mounting. ASTM E2075M proposes to use an acrylic rod to verify the sensitivity of the AE sensor by breaking the lead. ASTM E1106 and ASTM E1781M are important standards for the calibration of AE sensors. They provide primary and secondary calibration methods for sensors. The first editions of the two standards were issued in 1986 and 1996 respectively. The European EN has only one technical report EN ISO/TR 13115 which was jointly developed by CEN and ISO. This report describes the methods for the calibration of AE transducers by the reciprocity technique. In addition to the above technical report jointly developed with CEN, ISO has also issued two standards ISO 12713 and ISO 12714. ISO 12713 is similar to ASTM E1106. It specifies a method for the absolute calibration of AE transducers. The calibration yields the frequency response of a transducer to waves of the type normally encountered in AE work. This standard is applicable to secondary standard transducers and

Table 4.3 AE sensor standards

Standard issuer	Standard name
USA	ASTM E650M-17 Standard Guide for Mounting Piezoelectric Acoustic Emission Sensors ASTM E976-15 Standard Guide for Determining the Reproducibility of Acoustic Emission Sensor Response ASTM E1106-12 Standard Test Method for Primary Calibration of Acoustic Emission Sensors ASTM E1781M-19 Standard Practice for Secondary Calibration of Acoustic Emission Sensors ASTM E2075M-15 Standard Practice for Verifying the Consistency of AE-Sensor Response Using an Acrylic Rod
ISO	ISO 12,713:1998 Acoustic emission inspection—Primary calibration of transducers ISO 12,714:1999 Acoustic emission inspection—Secondary calibration of acoustic emission sensors EN ISO/TR 13,115:2011 Non-destructive testing—Methods for absolute calibration of acoustic emission transducers by the reciprocity technique
China	GB/T 19800–2005 Non-destructive testing—Acoustic emission inspection—Primary calibration of transducers GB/T 19801–2005 Non-destructive testing—Acoustic emission inspection—Secondary calibration of acoustic emission sensors JJF 1337–2012 Calibration Specification for Acoustic Emission Sensors (Comparative Method)

to AE application transducers. ISO 12714 is similar to ASTM E1781. It specifies a method for the secondary calibration of AE sensors as receivers of elastic waves at the surface of a solid medium. This standard is applicable to laboratory tertiary standard sensors and AE application sensors. There are 3 AE sensor test standards in China. Among them, GB/T 19800 and GB/T 19801 have transformed from ISO 12713 and ISO 12714 respectively. JJF 1337 refers to GB/T 19801, which specifies the calibration conditions and methods of AE sensors that receive surface waves and longitudinal waves of the solid medium, and is suitable for secondary calibration of AE sensors [10–20].

4.4.2 Comparison and Analysis

Comparing the AE sensor standards in different countries, it is found that the number of ASTM standards is the largest, but most of them test the consistency of amplitude response. Only the primary calibration and secondary calibration standards provide the test methods for the frequency response of AE sensors. These two standards are also the core basis for the AE sensor calibration in the world.

The primary calibration specifies a method for the absolute calibration of AE sensors. A glass capillary tubing with an outside diameter of 0.2 mm is broke by force of the loading screw, which produces an impact on a large steel transfer block. The sensor under test is calibrated by a standard transducer. The frequency spectrum of the sensor under test is obtained by data processing. The primary calibration devices are shown in Fig. 4.1. The secondary calibration method is a little simpler than the primary calibration, but it still needs to use the glass capillary tube breaking source, a primary calibrated reference sensor and a steel block to calibrate the sensor under test. The diagram of the test device is shown in Fig. 4.2.

Because the above calibration methods require the use of a huge steel block and fine glass capillary tube, also the test methods are complicated, most sensor users do

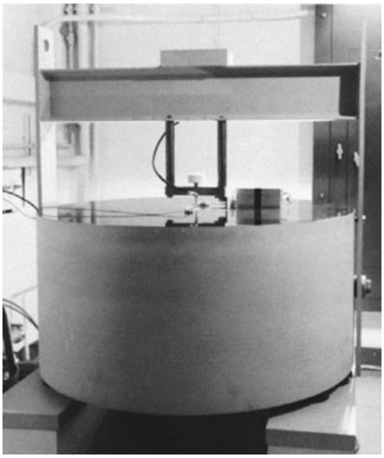

Fig. 4.1 Apparatus for the primary calibration of AE sensors

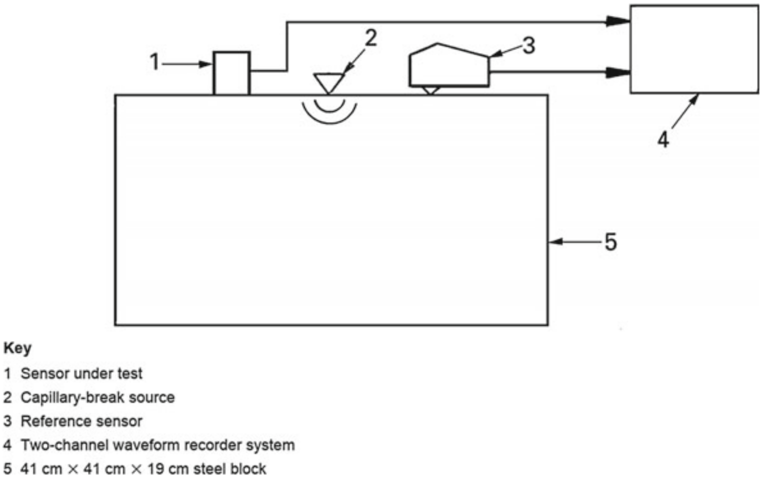
1
2
3
4
5
Key
1 Sensor under test
2 Capillary-break source
3 Reference sensor
4 Two-channel waveform recorder system
5 41 cm × 41 cm × 19 cm steel block

Fig. 4.2 Apparatus schematic of the secondary calibration of AE sensors

not have the test conditions and capabilities. Only a few institutions in different countries have the ability of the AE sensor calibration. And, the primary calibrated sensor is a necessary condition for secondary calibration. In China, the National Institute of Metrology uses a laser vibrometer instead of the standard transducer to perform primary calibration of the AE sensors. In western countries, since the National Institute of Standards and Technology (NIST, USA), the only neutral supplier of calibration services stopped offering primary calibration service to external customers, no such primary calibrated sensor can be provided to other organizations for the secondary calibration services of AE sensors. The AE sensor manufactures, such as PAC and Vallen, use face-to-face method to get the sensor's frequency response. It was also suggested as a secondly calibration method [21]. Based on the research of this method, Mr. Hartmut Vallen proposed an ISO standard draft and the project has been established in ISO/TC135/SC9. The standard ISO/WD 24543 "Non-destructive testing—Acoustic emission testing—Verification of the receiving sensitivity spectra of piezoelectric acoustic emission sensors" now is in the working draft stage [22].

4.5 Conclusions

After more than 50 years of development of AE equipment, the performance of the AE instruments and sensors has gradually improved. More and more types of AE instruments and sensors have been developed, and the corresponding performance testing methods and standards have also been continuously improved. A comprehensive understanding of the performance testing of AE instruments and sensors was obtained by comparing and analyzing the performance testing status and standards, and the following conclusions were obtained.

(1) For the performance test of AE instruments, the United States developed standards is the earliest. The standards developed in Europe are systematized, and the number of standards developed in China is the largest. Most of the test devices used by each standard are the same, and there are certain commonalities and differences in the test parameters. In addition to the bandwidth and some other parameters that are of common concern, there are also some specific parameters that each standard focuses on.

(2) For the performance test of AE sensors, the United States, ISO and China all use the standards of primary calibration and secondary calibration as the test basis. In view of the inconvenience of the test devices and the lack of test suppliers, ISO is developing a new standard and hoping to provide an alternative to AE sensor calibration.

Acknowledgements This work is financially supported by the Science and Technology Plan Project of State Administration for Market Regulation (No. 2020MK175), also the Internal Research Project of China Special Equipment Inspection and Research Institute (No. 2020QingNian02).

References

1. G. Shen, *Acoustic Emission Detection Technology and Application* (Science Press, Beijing, 2015)
2. ASTM E750–15 Standard Practice for Characterizing Acoustic Emission Instrumentation
3. EN 13477–1:2001 Non-destructive testing—Acoustic emission—Equipment characterisation—Part 1: Equipment description
4. EN 13477–2:2010 Non-destructive testing—Acoustic emission—Equipment characterisation—Part 2: Verification of operating characteristics
5. JB/T 8283–1999 Methods for testing the operating characteristics of acoustic emission instrumentation
6. JB/T 5754–2011 Non-destructive testing instruments-Specifications for one-channel acoustic emission testing instrument
7. JB/T 11603.1–2013 Non-destructive testing instruments-Acoustic emission-Equipment characterization-Part 1: Equipment description
8. JB/T 11603.2–2013 Non-destructive testing instruments-Acoustic emission-Equipment characterization-Part 2: Verification of operating characteristic
9. JJF 1505–2015 Calibration Specification for Acoustic Emission Instrumentation
10. ASTM E650M-17 Standard Guide for Mounting Piezoelectric Acoustic Emission Sensors
11. ASTM E976–15 Standard Guide for Determining the Reproducibility of Acoustic Emission Sensor Response
12. ASTM E1106–12 Standard Test Method for Primary Calibration of Acoustic Emission Sensors
13. ASTM E1781M-19 Standard Practice for Secondary Calibration of Acoustic Emission Sensors
14. ASTM E2075M-15 Standard Practice for Verifying the Consistency of AE-Sensor Response Using an Acrylic Rod
15. ISO 12713:1998 Acoustic emission inspection—Primary calibration of transducers
16. ISO 12714:1999 Acoustic emission inspection—Secondary calibration of acoustic emission sensors
17. EN ISO/TR 13115:2011 Non-destructive testing—Methods for absolute calibration of acoustic emission transducers by the reciprocity technique
18. GB/T 19800–2005 Non-destructive testing—Acoustic emission inspection—Primary calibration of transducers
19. GB/T 19801–2005 Non-destructive testing—Acoustic emission inspection—Secondary calibration of acoustic emission sensors
20. JJF 1337–2012 Calibration Specification for Acoustic Emission Sensors (Comparative Method)
21. L.B. He, M. Wang, J. Kang and P. Yang, Discussion on elastic wave sources for AE Sensor calibration at low frequency, in *Proceedings of the World Conference on Acoustic Emission-2017 Advances in Acoustic Emission Technology*, pp. 3–8 (2019)
22. ISO/WD 24543 Non-destructive testing—Acoustic emission testing—Verification of the receiving sensitivity spectra of piezoelectric acoustic emission sensors

Part III
Signal Processing and Analysis

Chapter 5
An Improved Beam Method for Acoustic Emission Source Localization in Thin Plates

Zihao Zhao, Ran Zhao, Xianlei Ye, Jianwen Wang, Tian He, and Qiang Pan

Abstract Using beamforming method to localize the AE source has been developed for years. However, if there is no accurate wave speed, the localizing results of beamforming may have a great deviation. After analyzing the beamforming localization characteristics, by comparing the two arrays of localizing effect, an improved beamforming method based on X array is proposed to reduce the localization error caused by the uncertainty of array direction and speed. The pencil-lead-broken experiment on a thin plate is conducted to verify the presented method, the result shows that this method can effectively localize the AE source under the condition of unknown accurate localizing speed.

5.1 Introduction

Acoustic emission technology has been widely applied in the field of nondestructive testing. This method can directly detect the energy released by the artifacts without providing energy to the inspected object. Therefore, acoustic emission testing has been widely applied in metalworking [1], welding monitoring [2], civil engineering [3].

Acoustic emission source location is one of the important applications of acoustic emission technology. Beamforming method is a common source localizing method. Time difference of arrival (TDOA) is a conventional AE localization method, and it has become the most popular tool to estimate AE source location to date [4]. Recently

---

Z. Zhao · R. Zhao · J. Wang · T. He (✉) · Q. Pan
School of Transportation Science and Engineering, Beihang University, Beijing 100191, China
e-mail: hetian@buaa.edu.cn

Z. Zhao
e-mail: fant0709@buaa.edu.cn

X. Ye
Aerospace Technology Research Institute, China Aerospace Science and Industry Corp, Beijing 100174, China

© The Author(s), under exclusive license to Springer Nature Singapore Pte Ltd. 2021

G. Shen et al. (eds.), *Advances in Acoustic Emission Technology*, Springer Proceedings in Physics 259, https://doi.org/10.1007/978-981-15-9837-1_5

some new localization methods are introduced to AET. Among them, AE Beamforming method is a superior localization method. Compared with TDOA method, beamforming has some particular advantages, such as the simplified sensor arrangement, negligible channel attenuation, and localization of multiple sources. But its localizing accuracy is affected by many variables such as wave velocity, array position and artifacts structure, and its location in the vertical array direction is relatively sensitive, while the localizing parallel to the array direction is relatively stable [5]. So, Beamforming still needs to be improved.

Based on the localization characteristics of beamforming, this paper proposes a improved localizing method by introduced X arrays, and verifies the localizing effect of the presented method.

5.2 The Establishment of the Improved Beamforming Based on X Array

Beamforming uses arrays composed of a group of sensors distributed in a fixed position in space to measure the sound field. The acoustic emission sensor in the arrays plays a role in collecting waveforms. Due to the large number of sensors in use, the placement of sensors has a great impact on the accuracy of the localizing results. This experiment adopts simulation method to study the influence of array placement on the localizing results.

5.2.1 Linear Array

A linear array is the most direct and simplest array, the basic form of all arrays. Placing multiple sensors on the same line creates a linear array. The position of sensor and sound source are shown in Fig. 5.1.

As can be seen from Fig. 5.1, the projection of the sound source point on the linear array falls within the array segment. To study the localizing range of linear array, the location of the point source of simulation experiments should be changed for many times. Considering the large model and time consuming of calculation, so we fix the source location and rotate the sensors for 10° clockwise each time, the center is the midpoint of the array, then we get 10 arrays, the result is shown in Fig. 5.2. Calculating time is reduced and efficiency is improved. By calculating the 10 groups of data, the localizing results are shown in the Fig. 5.3.

The deviation distance is the linear distance between the location point and the acoustic source point, and the calculation formula is as follows:

$$s = \sqrt{(X - x_0)^2 - (Y - y_0)^2} \tag{5.1}$$

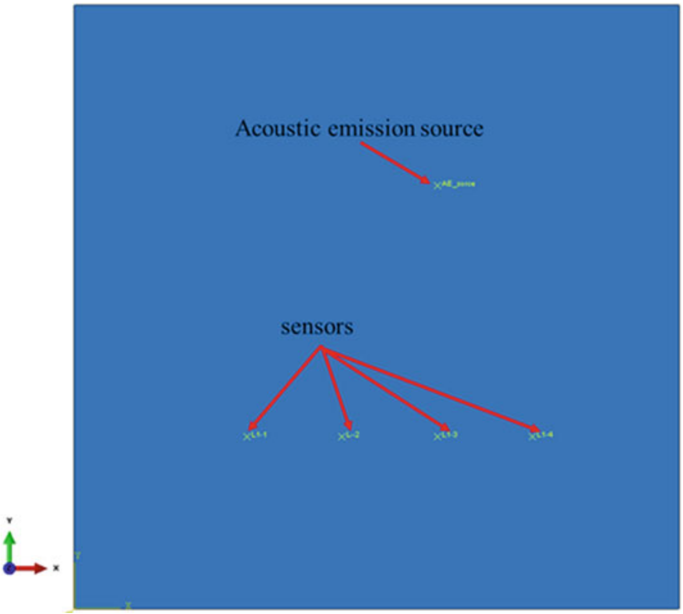
Acoustic emission source
AE_sorce
sensors
L1-1
L-2
L1-3
L1-4
Y
X
Y
X

Fig. 5.1 Schematic diagram of sound source and sensor position

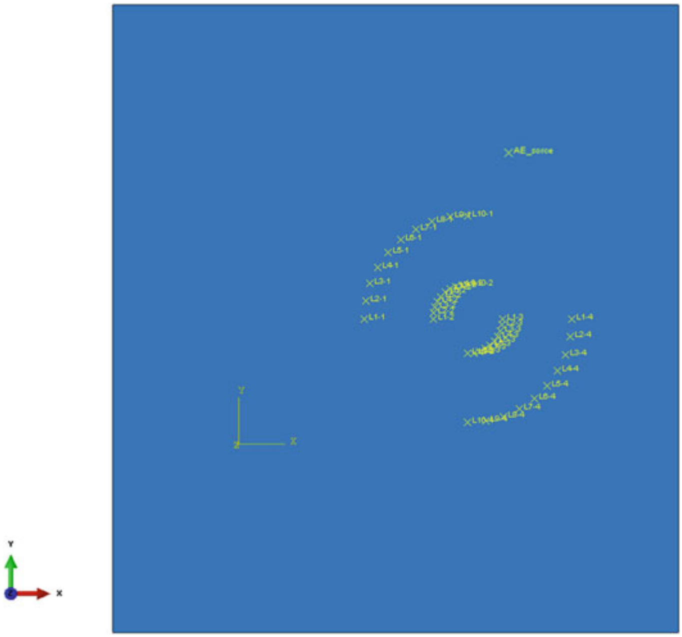
AE_sorce
L10-1
L7-1
L6-1
L5-1
L4-1
L3-1
L2-1
L1-1
L10-2
L1-2
L1-3
L1-4
L2-4
L3-4
L4-4
L5-4
L6-4
L7-4
L10-4
Y
X
Z
Y
X

Fig. 5.2 Schematic diagram of sound source and sensors rotation position

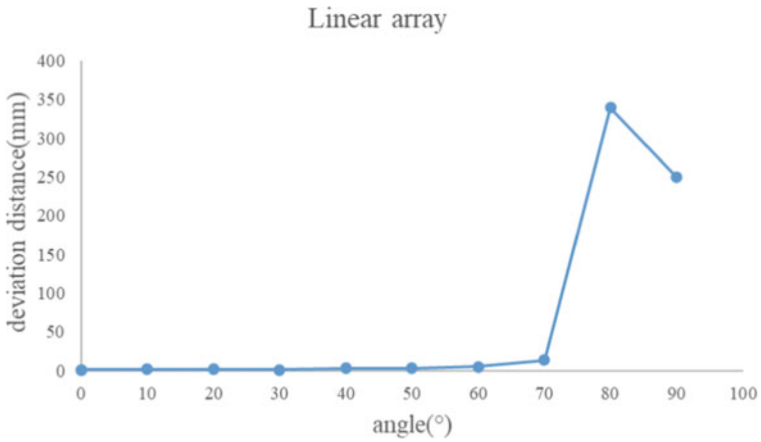

Fig. 5.3 Localizing effect of linear array

where, X and Y are the horizontal and vertical coordinates of the anchor point, x_0 and y_0 are the horizontal and vertical coordinates of the sound source point respectively, s is the deviation distance.

It can be seen that the linear array is more accurate in localizing within a certain range, and there will be a large error in the other range, so a single linear array is not enough to localize structural damage.

5.2.2 X Array

X array is formed by the intersection of two linear arrays, as shown in Fig. 5.4. The intersection point of two linear arrays is a sensor of the array segment. As can be seen from the picture, X array also has a high localizing accuracy in the array. However, the angle between the two arrays has a great influence on the localizing result. Therefore, we fix the source and array 1 and rotate array 2. The results are as shown in Fig. 5.5.

It can be seen from Fig. 5.5 that when the angle is near 30°, the X array has a best localizing effect, and the X array has a larger localizing range than the linear array. Therefore, we assume that the angle of X type array is 30° in subsequent experiments.

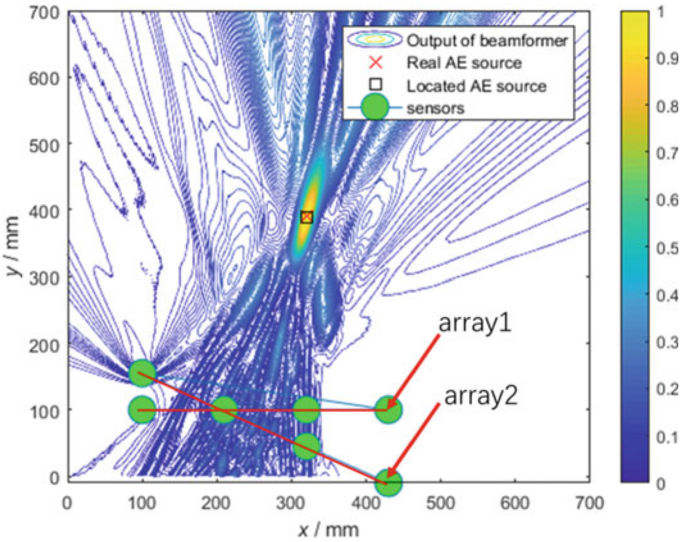

Fig. 5.4 Schematic diagram of X array

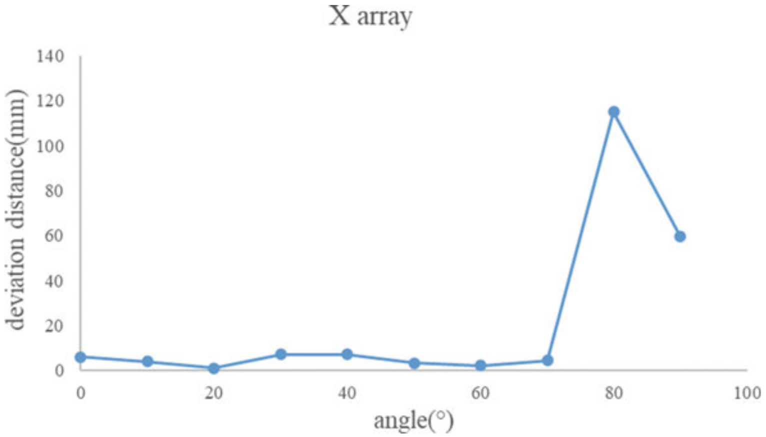

Fig. 5.5 Localizing effect of X array

5.3 Localization of Beamforming with Inaccurate Wave Velocity

5.3.1 The Proposal of Vertical Line Method

It can be seen from the above experiments, beamforming has a good localizing effect, but it requires a high accuracy of localization speed and good sensor positions, if

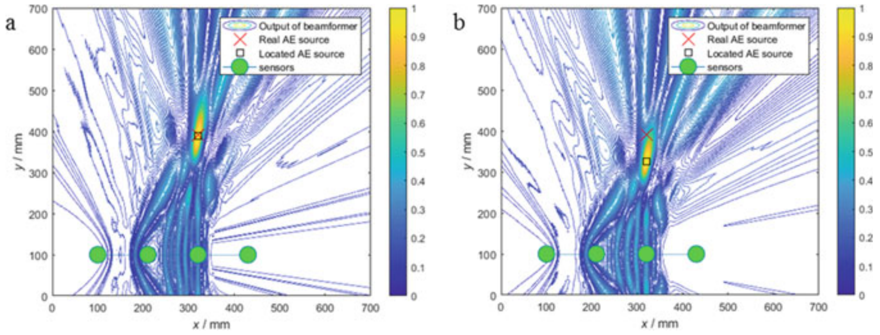

Fig. 5.6 Comparison of localizing results at different speeds

there is no accurate localizing speed, localizing results will appear large deviation distance (Fig. 5.6a is the localizing result of accurate localizing speed, and Fig. 5.6b is the abnormal localizing speed). So, if we make a straight line through located and real AE source, it is almost perpendicular to the array line.

5.3.2 *Application of Vertical Line Method in Finite Element Simulation*

From the above introduction, it can be seen that there must be two arrays in order to use the vertical line method, so we use the X array to introduce the method. Suppose there is an X array as shown in Fig. 5.4. In the picture, 7 sensors constitute two linear arrays. The flow of vertical line method is as follows:

(1) in the case of unknown accurate wave velocity, two linear arrays are used for localizing respectively with conventional beamforming method, so that two sets of coordinates can be obtained;
(2) making the corresponding array perpendicular through these two points respectively and get two straight lines;
(3) calculating the intersection point coordinates of two straight lines, which is the AE source point obtained by vertical line method.

Taking the localizing speed of 4300 m/s as an example (the accurate speed is 5300 m/s), the result using vertical line method is shown below (Fig. 5.7).

The calculation results are shown in the Fig. 5.8:

It can be seen that in the case of inaccurate localizing speed, vertical line method can significantly reduce localizing error and improve localizing accuracy.

Fig. 5.7 Schematic diagram of vertical line method

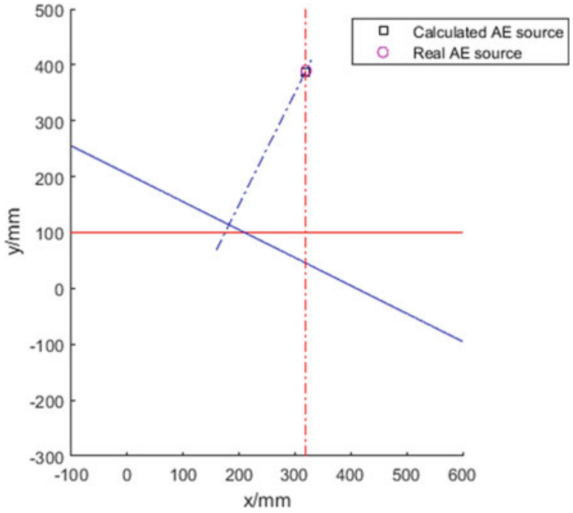

5.3.3 Application of Vertical Line Method in Pencil-Lead-Broken Experiment

The size of the steel plate used in the experiment is 700 mm*700 mm*5 mm. The position of sensors and pencil-lead-break are shown in the Fig. 5.9. A rectangular coordinate system is established with a point in the lower right corner as the origin, and the acoustic emission sampling frequency is 3 MHz.

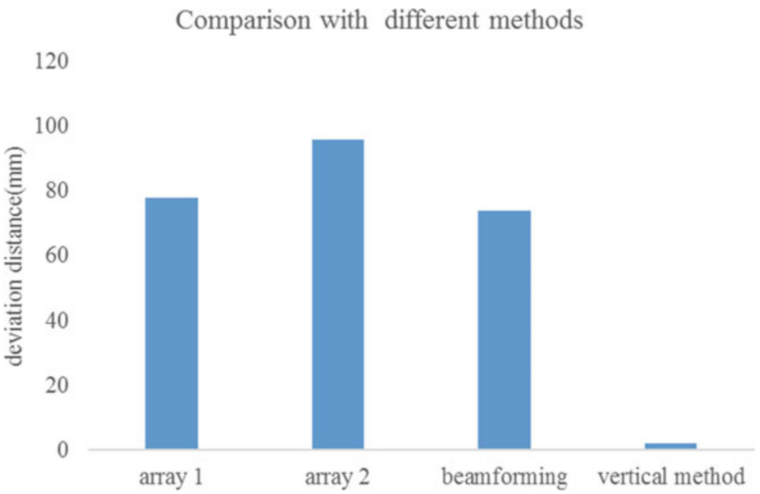

Fig. 5.8 Comparison of localizing results with different methods

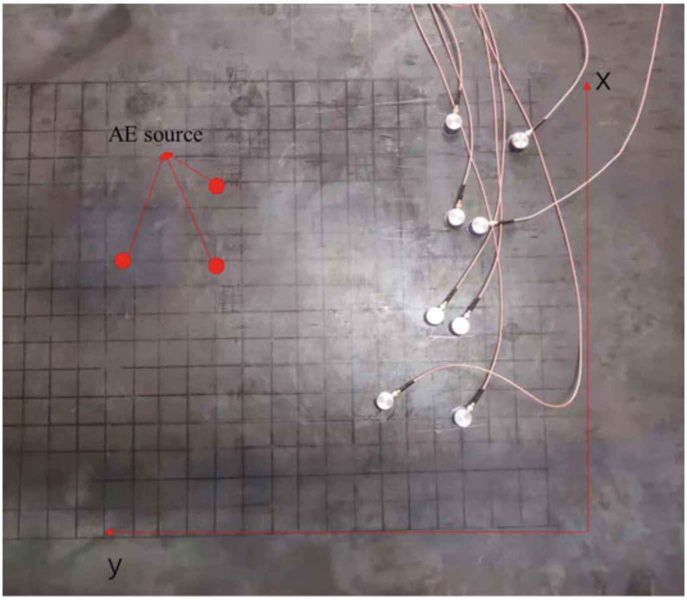

Fig. 5.9 The pencil-lead-broken experiment

Many acoustic emission signals generated by structural damage belong to burst acoustic emission signals. Burst acoustic emission signals are usually simulated by pencil-lead-broken experiment [6]. Lead breaking signal is the most commonly used simulated acoustic emission source in acoustic emission detection technology and is widely representative.

Considering the broken lead experiment easily affected by various factors, such as the length of the broken lead, direction, the installation of sensors and so on, the results differ greatly from simulation, but it still can see clearly in the Table 5.1 that on the premise of localizing speed is not accurate, vertical line method's deviation distance is lower than the beamforming's. Other experiments results are similar.

Table 5.1 Comparison of localizing results with different arrays and methods

Array	Localizing method	X	Y	Deviation distance
1,2	Beamforming	269	302	76.42
2	Beamforming	381	371	70.83
1	Beamforming	348	409	99.05
1,2	Vertical line method	348	261	49.10

5.4 Conclusion

This paper makes a further improvement on the beamforming method. A new array form and AE source location method is proposed. In order to verify this method for the source localization, lead breaking experiment is simulated in finite element analysis and verified on steel plate. Some conclusions are drawn based on analysis of the localization results as follows:

(1) compared with linear array, X array has a larger localizing range and respectively improves the localizing accuracy;
(2) as a supplement to beamforming, in the case of inaccurate localizing speed, the vertical line method can greatly reduce the localizing error and help the damage localizing of thin plate structure.

References

1. S.Y. Liang, D.A. Dornfeld, Tool wear detection using time series analysis of acoustic emission. J. Eng. Indus. **111**(3), 199–205 (1989)
2. C. Chen, R. Kovacevic, D. Jandgric, Wavelet transform analysis of acoustic emission in monitoring friction stir welding of 6061 aluminum. Int. J. Mach. Tools Manuf. **43**(13), 1383–1390 (2003)
3. G.C. Mclaskey, S.D. Glaser, C.U. Grosse, Beamforming array techniques for acoustic emission monitoring of large concrete structures. J. Sound Vib. **329**(12), 2384–2394 (2010)
4. T. Kundu, Acoustic source localization. Ultrasonics **54**(1), 25–38 (2014)
5. D. Xiao, T. He, Q. Pan et al., A novel acoustic emission beamforming method with two uniform linear arrays on plate-like structures. Ultrasonics **54**(2), 737–745 (2014)
6. T. He, D.H. Xiao, X.D. Liu, Y.C. Shan, Research of acoustic emission source location based on near-field beamforming. J. Vibr. Eng. **25**(02), 199–205 (2012)

Chapter 6
Correlation Analysis of Acoustic Emission Signals at Different Distances Form Hypervelocity Simulation Damage Source

Liu Wugang, Hou Chuantao, Wang Long, and Ren Fang

Abstract Acoustic Emission (AE) technology is widely used in many industrial applications because it can provide the key information from the analysis of damage signals produced in the materials and the structures. The results from the analysis can be taken out, such as the source localization, damage modes and severity level of the material. The characteristics of AE signals can be varied with the different distances to the damage sources and with the effects of amplitude-frequency response of AE sensors, the structure types and the frequency dispersion. The material damage evaluation based on the analysis of AE signals can be unreliable. In this paper, AE signals were generated by hypervelocity impact simulation tests due to these signals without the effects of AE sensors, degree of coupling and acquisition system, and can be used to analysis structural effects on the characteristics of those signals. The correlations among the signals from different propagation distances were computed with algorithm of probability statistics. The results of correlation coefficient variations were presented. The conclusions can be used to analyses the precision of damage localization and evaluate the reasonability of failure modes in the materials and the structures.

6.1 Introduction

Correlation analysis method for signal processing is widely used in Acoustic Emission application. Similarities among the AE signals obtained can be performed with correlation analysis method which is crucial to detect and extract the characteristics of AE signals and can be used to localize AE sources [1–6]. The effective signals can be extracted from the powerful stochastic noises with correlation analysis method under enough large time delay in various engineering ranges such as communication, radar detection and fault diagnosis applications [3–5]. Acoustic emission features and

---

L. Wugang (✉) · H. Chuantao · W. Long · R. Fang
Beijing Institute of Structure and Environment Engineering, Beijing 100076, China
e-mail: liuwug@139.com

© The Author(s), under exclusive license to Springer Nature Singapore Pte Ltd. 2021

G. Shen et al. (eds.), *Advances in Acoustic Emission Technology*, Springer Proceedings in Physics 259, https://doi.org/10.1007/978-981-15-9837-1_6

correlations of sandstone fractures with Pearson product-moment correlation coefficient method were studied and showed that large rupture and small crack were independent of each other in [5]. When the impulse method was applied to power cable fault location, with the problem of the inaccuracy of fault time detection, the authors proposed a signal correlation technique based on wavelet transform and obtained the accurate arrival time of the pulses in Refs. [6–9] utilized the simulated acoustic emission signals to located the damage source and found that it was feasible to adopt the cross-correlation method to locate the AE source. Zhongwei et al. [10] proposed a generalized cross-correlation method based on weighted functions with a theoretical analysis of cross-correlation. From the articles above mentioned, correlation analysis method has been widely studied and used in theoretical and practical realms.

It is crucial to obtain the effective AE signals for the post analysis such as failure localization, damage evaluation and identification for damage modes when AE is used to detect the in-situ safety of materials and structures. Figure 6.1 shows two main types of analysis methods currently widely used. The key technique in acoustic emission (AE) localization is to determine the time difference estimation from different sensors with different propagation distances to the AE source. There is an important hypothesis broadly accepted by researchers for all post-process and analysis currently. All signals involved must come from the same damage source and have common features. However, the characteristics of AE signals can be mainly changed in waveforms and frequency components with the long propagation distance in structures. It is important for researchers to evaluate the precision effect on the source localization and damage mode identification based on AE signals. In this paper, the authors explore the similarity features of AE signals from different propagation distances based on cross-correlation method.

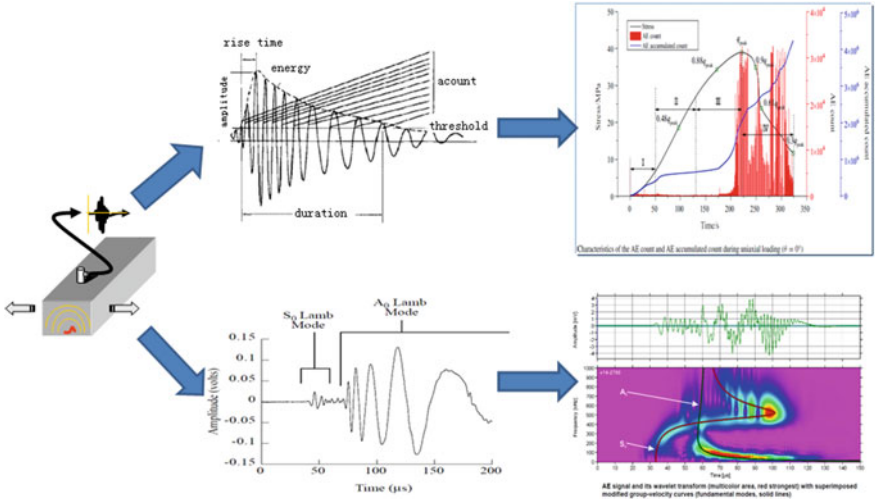
rise time
energy
amplitude
acount
threshold
duration
Stress/MPa
Time/s
AE count
AE accumulated count
Characteristics of the AE count and AE accumulated count during uniaxial loading
S0 Lamb Mode
A0 Lamb Mode
Amplitude (volts)
0.15
0.1
0.05
0
-0.05
-0.1
-0.15
0
50
100
150
200
Time (μs)
A0
S0
AE signal and its wavelet transform (multicolor area, red strongest) with superimposed modified group-velocity curves (fundamental modes, solid lines)

Fig. 6.1 AE signal analysis methods

6.2 Principle of Cross-Correlation

The dependence of instantaneous value at different time points is described by the correlation function. Presumption that x(t) is a sample of stationary stochastic process. In practical application, x(t) is the signal which the sensors received from signal source. In this article, x(t1) and $x(t_1 + \tau)$ represent the signals at different propagation distances to the same damage source.

Cross-correlation of x(t) at $t = t_1$ and $t = t_1 + \tau$ is computed by the average value of multiplication for different x(t) in the range of T. Correlation function $R_x(\tau)$ of x(t) can be obtained by the limitation algorithm.

$$R_x(\tau) = \lim_{T\to\infty} \frac{1}{T} \int_0^T x(t)x(t + \tau)dt \tag{6.1}$$

In order to simplify the dependence between x(t) at $t = t_1$ and $t = t_1 + \tau$ and to avoid the signal amplitude effects, with the correlation function normalized by introducing the dimensionless groups, correlation coefficients are obtained. Where μ_x is the mean of x(t) and σ_x^2 is the variance of x(t). From Formula (6.2), there exists a linear relation between $\rho_x(\tau)$ and $R_x(\tau)$, and so $\rho_x(\tau)$ is used to describe the AEsignal correlation.

$$\rho_x(\tau) = \frac{\lim\limits_{T\to\infty} \int_0^T [x(t) - \mu_x][x(t + \tau) - \mu_x]dt}{\sigma_x^2} = \frac{R_x(\tau) - \mu_x^2}{\sigma_x^2} \tag{6.2}$$

6.3 Acoustic Emission Signals

To overcome the complexity of practical signals, hypervelocity impact simulation is utilized to give the effective and simplified AE signals which have the broad frequency components with less noise and evident amplitude features at different propagation distances. AE signals were obtained at the gauges placed at different distances to the impact damage source, as shown in Fig. 6.2. Ref. [9] gives the details of the model and algorithm for the hypervelocity impact simulation.

Stress wave emission is produced in the impact failure point when the hypervelocity projectiles impact the Aluminum plate. AE signals can be sampled with the normal velocity at 44 different gauges. Table 6.1 lists the representations of different gauges from the impact damage source.

Fig. 6.2 Numerical model of hypervelocity impact and gauges

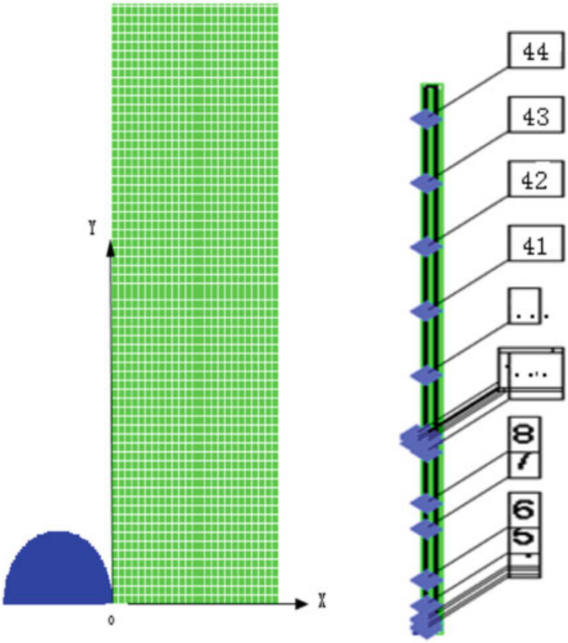

Table 6.1 Representation of different gauges from the impact damage source (unit: mm)

Gauges	Distance	Gauges	Distance	Gauges	Distance	Gauges	Distance
1	10	12	65	23	140	34	250
2	15	13	70	24	150	35	260
3	20	14	75	25	160	36	270
4	25	15	80	26	170	37	280
5	30	16	85	27	180	38	290
6	35	17	90	28	190	39	300
7	40	18	95	29	200	40	320
8	45	19	100	30	210	41	340
9	50	20	110	31	220	42	360
10	55	21	120	32	230	43	380
11	60	22	130	33	240	44	400

6.4 Cross-Correlation at Different Propagation Distances

Figure 6.3 shows the cross-correlation coefficients at different propagation distances to the impact source. The climax of each curve presents the self-correlation coefficient, and the others mean the cross correlation between the signal at the climax and at the other gauges. We can see that there exists a steep drop in small extent from the

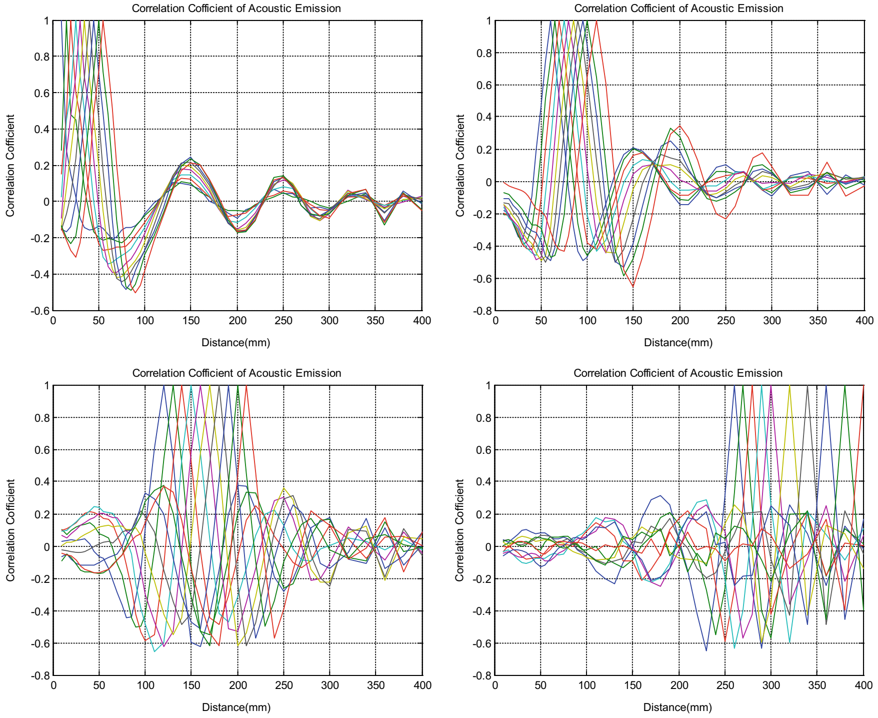

Fig. 6.3 Correlation coefficients for measuring points

curve climax, which means the little similarity between the others of these signals. The correlation coefficients give the fluctuation trend and attenuate with the increase of propagation distances.

6.5 Relation Between Correlation Coefficient and Signal Wave Feature

Relations between correlation coefficients and signal wave features are analyzed in order to find out the reasons for the correlation coefficient fluctuations. Table 6.2 lists the correlation coefficients between the signal at 50 mm from impact damage point and at other gauges. Form Table 6.2, the coefficient 0.7158 means some linear

Table 6.2 Correlation coefficients for AE signals at 50 mm position and other gauges

Distance (mm)	50	55	60	65	140	150	160	170
Coefficients	1	0.7158	0.4772	0.1895	0.1909	0.2369	0.2016	0.1161

relationship between the signals at 55 mm and at 50 mm, while a little linear relationships describe the coefficient 0.4772 at 50 mm and at 60 mm and 0.1895 at 50 mm and at 65 mm. And then, the other coefficients fluctuate with the increase of propagation distance. The signals corresponding to the coefficients in Table 6.2 are shown in Fig. 6.4. The four signal waves have very similar forms at 50, 55, 60 and 65 mm, while corresponding correlation coefficients have great differences. The signal wave

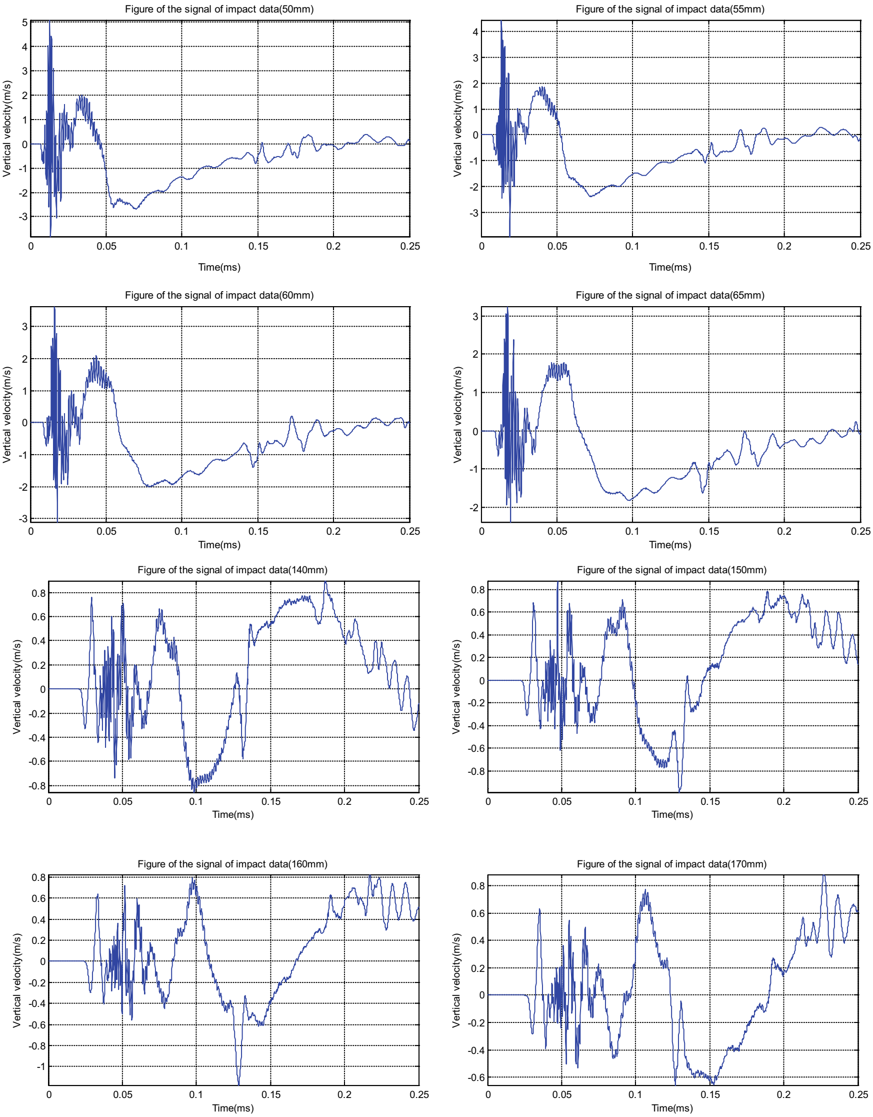

Fig. 6.4 Acoustic emission signals at different gauges from impact point

at 50 mm has some little similarity with those at 140, 150, 160 and 170 mm, so the relevant coefficients have lower values than those at 55, 60 mm and 65 mm. Based on discussion above, there is no evident relationship between the correlation coefficients and the AE signal wave features.

6.6 Relation Between Correlation Coefficients and AE Signal Frequency Components

Amplitude-frequency characteristics of the AE signals discussed in Sect. 6.4 were obtained with FFT transform, as shown in Fig. 6.5. As described in Fig. 6.5a, the whole range of frequency components is divided into two evident parts, 0~580 kHz and 580~1200 kHz. The two parts of AE signal frequencies are respectively presented in Fig. 6.5b, c. The amplitudes of the lower frequency parts have consistent features, while the amplitudes of the higher frequency parts have strong fluctuation and attenuation features with the increase of propagation distances.

Correlation coefficients from frequency components of obtained signals are listed in Fig. 6.5, divided into three parts. From Fig. 6.5a, coefficients form 15~35 mm attenuate slowly in the range of 100 mm and fluctuate besides this range. Coefficients form Fig. 6.6a, b are different form Fig. 6.6a, attenuating and fluctuating sharply in little rang form the gauge point. The signals have more similarities in the vicinity

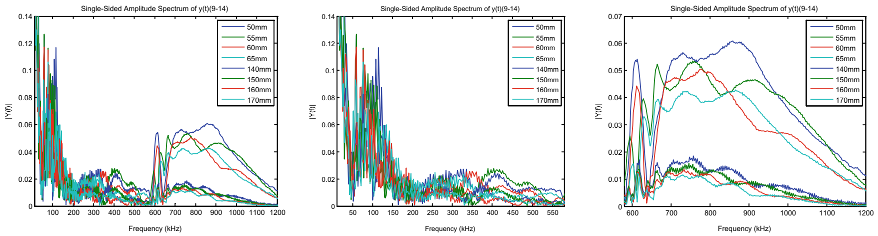

(a)0~1200kHz (b)0~580kHz (c)580kHz~1200kHz

Fig. 6.5 Frequency distribution of AE signals

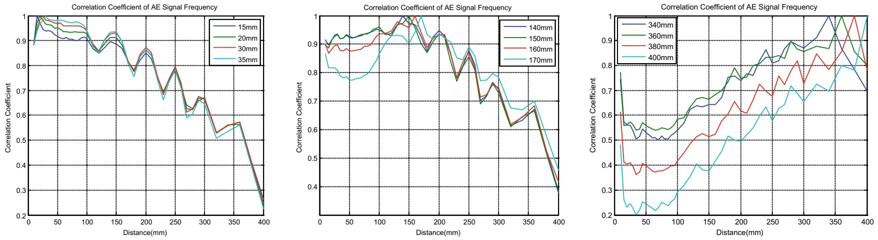

(a) coefficients from 15mm~35mm (b) coefficients from 110mm~170mm (c) coefficients from 340mm~400mm

Fig. 6.6 Correlation coefficients for frequency components

of the impact damage point, and the different dispersion abilities of the AE signal frequency components have changed with the increase of propagation distances. The signal wave form and its frequency components have more common features near the impact source than those far from it. By comparison to the analysis of the AE signal waves, the correlation coefficients for frequency components have more abilities to represent the resemblances of AE signals.

6.7 Conclusions

In this paper, we examine the cross-correlations among the AE signals obtained from a hypervelocity impact simulation. The correlation coefficients for the impact signals were computed and the results show great differences of the coefficients from different propagation distances. The correlation coefficients represent the fluctuation trend and attenuate irregularly with the increase of propagation distance. There is no evident relationship between correlation coefficients and AE signal wave features, but the correlation coefficients for frequency components have more abilities to represent the resemblances of AE signals.

Reference

1. Y.H. Chen, S.F. Liu, R.S. Geng, et al., Spectral and correlation analysis of acoustic emission signals. Nondestruct Test **24**(9), 395–399 (2002)
2. Z. Tan, C. Min, X. Zhan, et al., The application research of acoustic emission technique on high-temperature strength-thermal coupling experiment for composite structure. Struct. Environ. Eng. **42**(5), 59–64 (2015)
3. S. Ying, Signal analysis and the use in engineering test. J. Chongqing Petroleum College **4**(5), 22–24 (2002)
4. W.J.Z. Jianli, The application of wavelet transform and autocorrelation analysis to fault location on power cable. Electr. Eng. **2**, 46–49 (2009)
5. B. Chen, Y. Zhang, J. Li, Study on acoustic emission features and correlations of sandstone fracture. Mining Res. Develop. **34**(3), 74–77 (2014)
6. T. Shi, J. Gao, The choice of the modeling mechanism based on source signal distribution characteristics and correlation. China Rural Water Hydropower **29**(119), 69–72 (2005)
7. W. Han, J. Wu, Application of wavelet transform based signal correlation technique in fault location of power cable. Power Syst. Technol. **29**(119), 69–72 (2005)
8. Z.M.L.L.L. Xiujuan, The research on locating method of acoustic emission source in metal plate based on correlation analysis. J. China Three Gorges University (Natural Sciences) **31**(5), 60–62 (2009)
9. W. Liu, B.J. Pang, Z.Y. Han, et al., Damage identification of single aluminum plate produced by hypervelocity impact based acoustic emission. J. Astronautics **32**(3), 671–675 (2011)
10. Z. Jin, M.S. Jiang, Q.M. Sui, et al., Acoustic emission localization technique based on generalized cross-correlation time difference estimation algorithm. Chinese J. Sens. Actuat. **26**(11), 1513–1518 (2013)

Chapter 7
An Acoustic Emission Source Localization Method Based Ant Colony Without Premeasured Velocity

Qingchun Hu and Longjun Dong

Abstract Source localization in Acoustic Emission (AE) is the core element of AE monitoring technology. However, conventional source location algorithms are generally based on assumptions, which are limiting in the AE monitoring for complex structures with geometric irregularities (such as lugs and caves). In this study, an Ant Colony Localization Method (ACLM) without premeasured velocity was proposed for AE accurate source location. The results of the lead-breaking test show that the location accuracy of ACLM is higher than that of conventional location methods in the complex structure.

7.1 Introduction

Acoustic emission (AE) monitoring technology has been paid attention to and developed rapidly in various fields in recent years [1–3]. Because it can be used in nondestructive testing for materials and structures as an effective method. AE source localization is the core element of AE monitoring technology [4]. There are many conventional source location methods applied in various projects, such as Geiger's, Inglada's, the USBM, the location method based on simplex stepping, and the location methods of time difference without pre-measuring velocity (TD) [5–9]. However, these methods [5–9] are based on two main assumptions: (1) the wave path between the source and the AE sensor is assumed to be a straight path; (2) the velocity of the elastic wave is set as a fixed value without considering the error between pre-measured wave velocity and actual wave velocity.

The two assumptions were ineligible in the process of continuous AE monitoring for complex heterogeneous structures with geometric irregularities (such as lugs and caves). Because the P -wave velocity changes with time, temperature, and pressure, especially during the cracking process. Moreover, the wave path is usually not a straight line in the complex heterogeneous structure. Therefore, it is necessary to

---

Q. Hu · L. Dong (✉)
School of Resources and Safety Engineering, Central South University, Changsha 410083, China
e-mail: lj.dong@csu.edu.cn

© The Author(s), under exclusive license to Springer Nature Singapore Pte Ltd. 2021

G. Shen et al. (eds.), *Advances in Acoustic Emission Technology*, Springer Proceedings in Physics 259, https://doi.org/10.1007/978-981-15-9837-1_7

propose an AE source location method to improve the location accuracy in the real complex structure, which is different from the conventional methods.

In this study, an Ant Colony Localization Method (ACLM) without premeasured velocity was proposed, which is based on the ant colony algorithm [10] and the grid method. The accuracy and applicability of the ACLM are verified by the lead-breaking test.

7.2 Ant Colony Localization Method (ACLM)

The ACLM uses the ant colony algorithm to search the fastest wave path from the source to the sensor and determines the AE source according to the relationship between the fastest wave path and the arrivals, which also does not need to premeasure the velocity of the complex structure. It can be divided into six parts, which are detailed below.

7.2.1 Determine Region of Localization

The ACLM is proposed as a source location method for complex structures. It is suggested to determine the region of interest before localization. Though it is possible for ACLM to locate the source in the complete structure, it would be time-consuming and would not improve the accuracy of source location. Therefore, the first step of ACLM prefers to determine the important region of the structure, including the region where failure or fracture can be predicted.

7.2.2 Construct Grid and Represent Region

The geometry and specific position of the complex region are determined in the location region. Moreover, the size of the unit square grid is determined according to the sharp of the complex structure and the accuracy requirement of the source location. Up to a point, the higher the resolution of the grid, the better the location result of this method. However, the location accuracy would not be obviously improved when the grid is sufficiently densely divided. A matrix M with the same size as the grid node is established, and the matrix index position (i, j) corresponding to the grid node is marked with the digits 0 or 1 to represent the location region. The grid nodes P_{ij} form a set GN that serves as the starting point to search for the fastest waveform path among subsequent nodes. Assuming that the propagation velocity of the P wave in the surrounding non-empty region is a fixed unknown value and is represented by C. Because the wave velocity changes with time, temperature, and pressure in the dynamic monitoring, there's no need to measure the P -wave velocity in the test. For the unknown source P_0, set its position coordinate to (x_0, y_0), and the initial time of excitation to t_0.

7.2.3 *Search for the Fastest Waveform Path*

Every grid node P_{xy} in the set GN is used as the potential source excitation position. Then the theoretical shortest path L_{xy}^k can be obtained by tracing the shortest path from the node P_{xy} to the kth sensor. If the grid node P_{xy} is in the empty region, the L_{xy}^k is considered to ∞. ACLM uses the ant colony algorithm to trace the shortest path L_{xy}^k.

7.2.3.1 Ant Colony Algorithm [10]

An ant colony has the ability to select the shortest pathway from a set of alternative pathways between their nest and the food source. Ants find the shortest path based on the simple communication mechanism, which is guided by a pheromone trail that is left from ants on the ground. The level of pheromone will dissipate over time. Therefore, the shorter path will end up with a higher level of pheromone as it required less travel time. The role of this trail is to guide the other ants towards the target point.

7.2.4 *Calculate the Theoretical Travel Time*

Interpolation can be used to increase the density of the grid in complex areas. The shortest path between the sensor and the point that is not in the grid can be interpolated from the nodes in the surrounding region. It is a useful way to reduce the calculation of the algorithm, though this may introduce small errors into the location results because of the distance error between interpolation and the shortest path.

For the source generated by the point P_{xy}, the theoretical travel time t_{ij}^k corresponds to the shortest propagation path L_{xy}^k between the source and the kth sensor divided by the velocity C. The time difference between two different sensors l and m corresponds to the difference of travel time $\triangle\ t_{xy}^{lm}$.

7.2.5 *Collect Data of Arrivals*

m sensors are installed at different positions of the structure to capture the arrivals of the AE event. Each sensor is located on the grid node so the position of the sensor is known. For the two-dimensional model, there are four unknowns (P -wave velocity, coordinates of AE source (x_0, y_0), initial time of excitation t_0), so sensor number m should be an integer greater than or equal to 4. For the kth sensor S_k receiving the signal, the coordinates are recorded as (x_k, y_k), and the first arrival time of the received P wave signal is t_0^k. Calculate the actual time difference of the two different sensors S_l and S_m, denoted by $\triangle\ t_0^{lm}$.

7.2.6 *Source Location*

According to the square of the difference between $\triangle\ t_0^{lm}$ and $\triangle\ t_{xy}^{lm}$, D is introduced to describe the deviation degree of the point P_{xyz} from the unknown MS/AE source P_0, which is expressed as:

$$D_{xyz} = \sum \left(\triangle\ t_{xy}^{lm} - \triangle\ t_0^{lm}\right)^2 \tag{1}$$

Among them, when the sources fall into the empty area, $D_{xyz} = INF$.

Each grid point will get the corresponding D_{xy} value. The deviation degree of the point P_{xyz} from the unknown source P_0 increases with the growth of the value of D_{xy}. Therefore, the coordinate corresponding to the minimum D_{xy} value can be considered as the coordinate of the AE source location.

7.3 Results and Discussion

Lead-breaking tests were carried out to evaluate the performance of the proposed ACLM method. There was a cavity on the square flagstone of 50 cm*50 cm, as shown in Fig. 7.1d. 100 grid cells and 100 grid central nodes were obtained by dividing the two-dimensional plane into 10*10 grid cells Fig. 7.1a. The cubes in the empty area mean that the path cannot pass, which are marked with the digit 1, as shown in Fig. 7.1b. Other cubes that the path can pass are marked with the digit 0. The matrix M is constructed with the digit 1 and 0. Four sensors were arranged on the grid nodes for the localization of ACLM. The coordinates of the four sensors were $S_1(2.5, 47.5)$, $S_2(47.5, 2.5)$, $S_3(47.5, 47.5)$, $S_4(47.5, 2.5)$. The coordinates of the four sensors S_1, S_2, S_3, and S_4 were translated to obtain the corresponding position of the center nodes of the 4 cells. The spatial distribution of sensors and AE sources was shown Fig. 7.1d. The paths L_S searched between each potential source are shown in Fig. 7.1.(c), following by the calculation of the path distances. Then, interpolation was used to get more distances between the sensors and the point in the flagstone but not the grid central node.

To facilitate the calculation, the model coordinates were transformed so that the index of the node matrix M is in one-to-one correspondence with the coordinate positions. The data acquisition chooses the model with a 40 dB threshold and a 5 MHz

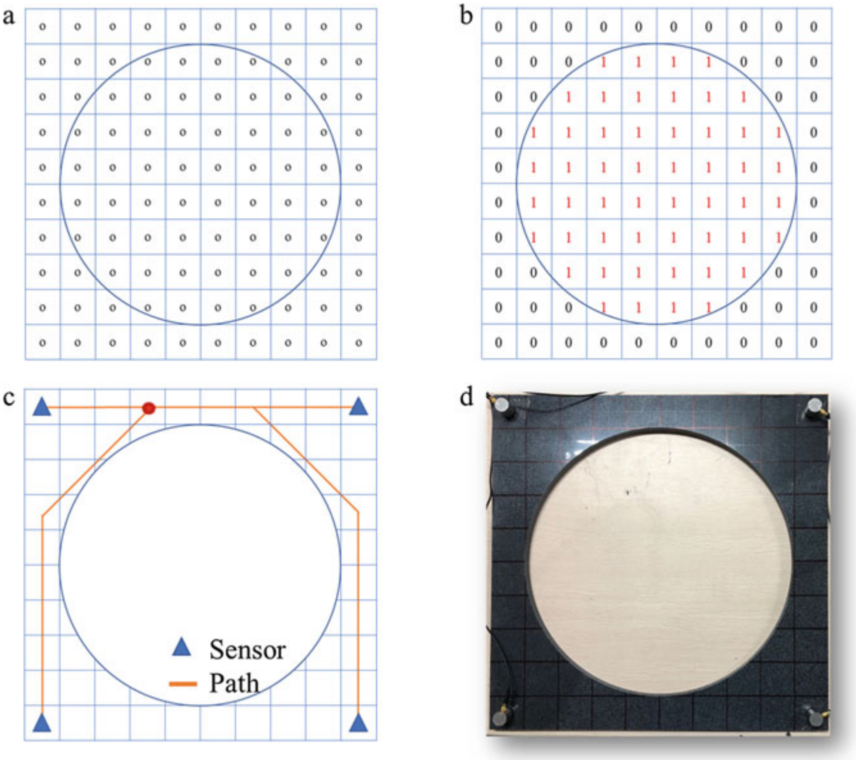

Fig. 7.1 The process of localization with the ACLM. **a** The grid that constructed for path searching; **b** The matrix M with the digits 0 or 1; **c** The paths searched by the ant colony algorithm from a node to 4 sensors; and **d** The shape of the specimen

sampling rate. According to the symmetry of the arrangement of the test piece and the sensor, the lead-breaking tests were carried out at a quarter of the plane (Fig. 7.2), and each position was performed twice. The arrivals of the P wave generated by MS/AE event are recorded by the sensors. Then, according to the arrivals recorded by the sensors, the deviation value D_{xyz} of each potential source is calculated. The coordinates (x, y, z) of the source location on the specimen corresponding to the minimum D_{xyz} is determined and is converted to the position coordinates. The location results of ACLM are shown in Table 7.1. Meanwhile, the results of TD are performed and shown in Table 7.1.

The localization results between ACLM and TD with the actual lead-breaking points and the error records are shown in Table 7.1. Though the TD has reduced the error introduced by the pre-measured velocity in the heterogeneous flagstone, it still assumed the wave path between the source and the AE sensor is a straight path, which is quite different from reality. As seen from the table, the maximum location error of the TD is 6.1 cm, which is much larger than the location error of the ACLM.

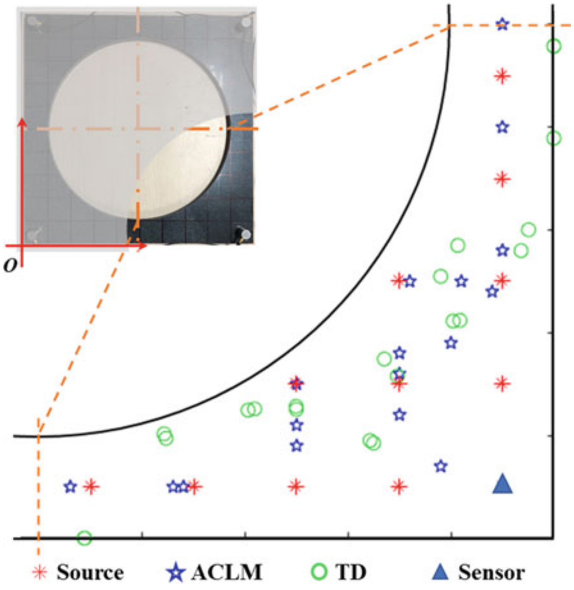

Fig. 7.2 Location results of AE sources using two methods on the flagstone

For the convenience of observation, Fig. 7.2 shows the visualization of the location results and location errors of the two methods. It can be clearly seen that the distances between the actual lead-breaking points and the results obtained by TD are much larger than that between the actual lead-breaking points and the results obtained by ACLM. According to the location error of each lead-breaking test in the table, the average location error of the ACLM is 1.9 cm, while the average location error of the TD is 2.8 cm. The average location accuracy of the ACLM is nearly 32% greater than the TD. Therefore, it can be concluded that the location accuracy of the ACLM is greatly improved comparing to the TD.

AE transfer function is very complex with many variables, and the location accuracy is affected by many factors, such as the size of the sensor, homogeneity of material, and the location method. If it is required to obtain more accurate location results of AE source in this experiment, the fastest wave path between the source and the sensor should be searched more accurate. As shown in Fig. 7.1c, the path searched by the traditional ant colony algorithm has a serrated shape, which is not coincident with the fact. It is feasible to improve the ant colony search algorithm or smooth the search path. Moreover, it is also effective to improve the location accuracy by picking-up more precise arrivals and using more suitable sensors with smaller diameter.

Table 7.1 Location results and errors of ACLM and TD (Unit: cm)

The coordinates of AE source	ACLM					TD				
	X	*Y*	△ *X*	△ *Y*	*D*	*X*	*Y*	△ *X*	△ *Y*	*D*
(27.5, 2.5)	26.5	2.5	−1	0	1.0	27.2	0.0	−0.3	−2.5	2.5
	26.5	2.5	−1	0	1.0	27.2	0.0	−0.3	−2.5	2.5
(32.5, 2.5)	32	2.5	−0.5	0	0.5	31.2	4.9	−1.3	2.4	2.7
	31.5	2.5	−1	0	1.0	31.1	5.1	−1.4	2.6	3.0
(37.5, 2.5)	37.5	4.5	0	2	2.0	35.1	6.2	−2.4	3.7	4.4
	37.5	5.5	0	3	3.0	35.5	6.3	−2.0	3.8	4.3
(42.5, 2.5)	42.5	6	0	3.5	3.5	41.1	4.8	−1.4	2.3	2.7
	44.5	3.5	2	1	2.2	41.2	4.6	−1.3	2.1	2.5
(37.5, 7.5)	37.5	7.5	0	0	0.0	37.5	6.3	0.0	−1.2	1.2
	37.5	7.5	0	0	0.0	37.5	6.4	0.0	−1.1	1.1
(42.5, 7.5)	42.5	8	0	0.5	0.5	42.4	7.9	−0.1	0.4	0.4
	42.5	9	0	1.5	1.5	41.8	8.7	−0.7	1.2	1.4
(47.5, 7.5)	45	9.5	−2.5	2	3.2	45.1	10.6	−2.4	3.1	3.9
	45	9.5	−2.5	2	3.2	45.4	10.6	−2.1	3.1	3.7
(42.5, 12.5)	47	12	4.5	−0.5	4.5	48.4	14.0	5.9	1.5	6.1
	43	12.5	0.5	0	0.5	44.5	12.7	2.0	0.2	2.0
(47.5, 12.5)	47.5	14	0	1.5	1.5	48.8	15.0	1.3	2.5	2.8
	45.5	12.5	−2	0	2.0	45.3	14.2	−2.2	1.7	2.8
(47.5, 17.5)	47.5	20	0	2.5	2.5	50.0	19.5	2.5	2.0	3.2
	47.5	20	0	2.5	2.5	50.0	19.5	2.5	2.0	3.2
(47.5, 22.5)	47.5	25	0	2.5	2.5	50.0	23.9	2.5	1.4	2.9
	47.5	25	0	2.5	2.5	50.0	24.0	2.5	1.5	2.9
Average error			−0.2	1.2	1.9			0.1	1.4	2.8

7.4 Conclusions

In this paper, an ant colony Localization Method (ACLM) without premeasured velocity was proposed. It can bypass the empty area and also does not need to premeasure the velocity of the structure. Therefore, this method can be applied to the structure with complex geometry during the monitoring process, which can reduce the location error caused by the changing wave velocity.

To evaluate the effectiveness of the ACLM, the lead-breaking test was carried out on the square flagstone with cavity. The location results show that the average location error obtained by the ACLM is 1.9 cm, and its average location accuracy is 32% higher than the TD. It can be concluded that the ACLM can effectively adapt to complex structures. This method is also applicable to three-dimension complex structures for source location.

References

1. J. Ma, L. Dong, G. Zhao, X. Li, Discrimination of seismic sources in an underground mine using full waveform inversion. Int. J. Rock. Mech. Min. **106**, 213–222 (2018)
2. L. Dong, J. Wesseloo, Y. Potvin, X. Li, Discrimination of mine seismic events and blasts using the Fisher Classifier, Naive Bayesian Classifier and Logistic Regression. Rock Mech. Rock Eng. **49**(1), 183–211 (2016)
3. B. Park, H. Sohn, S.E. Olson, M.P. DeSimio, K.S. Brown, M.M. Derriso, Impact localization in complex structures using laser-based time reversal. Struct. Health Monit. **11**(5), 577–588 (2012)
4. L. Dong, W. Zou, X. Li, W. Shu, Z. Wang, Collaborative localization method using analytical and iterative solutions for microseismic/acoustic emission sources in the rockmass structure for underground mining. Eng. Fract. Mech. S0013794417312997 (2018)
5. L. Geiger, Probability methods for the determination of earthquakes epicenters from the arrival time only. Bull. St. Louis Univ. **8**, 60–71 (1912)
6. V. Inglada, Die berechnung der herdkoordinated eines nahbebens aus den dintrittszeiten der in einingen benachbarten stationen aufgezeichneten P-oder P-wellen. Gerlands Beitr. Geophys. **19**, 73–98 (1928)
7. F. Leighton, W. Blake, Rock noise source location techniques, USBM RI 7432 (1970)
8. A. Prugger, D. Gendzwill, Microearthquake location: a non-linear approach that makes use of a simplex stepping procedure. Bull. Seismol. Soc. Amer. **78**(2), 799–815 (1988)
9. L. Dong, X. Li, L. Tang, F. Gong, ‘Mathematical functions and parameters for microseismic source location without pre-measuring speed. Chin. J. Rock Mech. Eng. **30**(10), 2057–2067 (2011)
10. M. Dorigo, E. Bonabeau, G. Theraulaz, Ant algorithms and stigmergy. Future Gener. Comput. Syst. **16**(8), 851–871 (2000)

Chapter 8
Acoustic Emission and Dual-Tree Complex Wavelet Transform with Soft Threshold De-Noising to Enhance Pipeline Leak Detection and Location

L. L. Ting, J. Y. Tey, A. C. Tan, Y. J. King, and F. A. Rahman

Abstract Water leakage control is a subject of growing interest among researchers and pipeline owners. Various water leak detection methods have been developed and acoustic leak detection technique has manifested as a decent approach. However, the demerit of this method is that the collected signal always interferes with noises. This reduces the accuracy of leak detection and triggers a false alarm. Traditional noise reduction methods such as digital filtering and wavelet de-noising are not efficient to eliminate noise from interested signals. To overcome this drawback, an improved de-noising method derived from Dual-Tree Complex Wavelet Transform (DTCWT) and a soft threshold proposed in this paper to reduce the noise and consequently minimize false trip rate. The signal is decomposed by DTCWT to separate the raw signal into different frequency bandwidths. Then, soft threshold method is employed to suppress noise by rescaling the signals which are lower than the prescribed threshold to zero. Experimental results demonstrate that the proposed de-noising method performs well than ordinary wavelet de-noising. The accuracy of leak localisation can be increased by twice. The method accentuates the cross-correlation peak related to the time delay for leak localization and thereupon increases the accuracy of leak locating. The proposed method outperforms other methods in term of detectable range of leak source as it can detect leak up to 24 m whereas the conventional way only can detect up to 14.5 m.

8.1 Introduction

Water is an important and irreplaceable natural resource. Unfortunately, an abundant amount of water lost when they are transporting from treatment plants to consumers. The water lost is classified as non-revenue water (NRW). A statistics provided by the National Water Services Commission [1] stated that 35.3% of supplied water in Malaysia consists of NRW which is equals to 5929 million litres per day. The loss

---

L. L. Ting · J. Y. Tey · A. C. Tan (✉) · Y. J. King · F. A. Rahman
Lee Kong Chian Faculty of Engineering and Science, Universiti Tunku Abdul Rahman, Selangor, Malaysia
e-mail: tanacc@utar.edu.my

© The Author(s), under exclusive license to Springer Nature Singapore Pte Ltd. 2021

G. Shen et al. (eds.), *Advances in Acoustic Emission Technology*, Springer Proceedings in Physics 259, https://doi.org/10.1007/978-981-15-9837-1_8

of NRW are due to leakages, pipe bursts, public usage, metering errors and theft, but it has been identified as mainly due to to leakages [2].

Leaks result in serious consequences such as loss of money and natural resources. They also create public health risk because contaminants may pass into the pipe when there is a pressure drop in the pipe [2]. The critical aftermath caused by leakages is the unnecessary water wastage. This may put up to water demand along with population growth and urbanization [3]. For this reason, water leakage control has been a growing concern in many countries with an aim to promote water conservation.

Detection of water leaks using acoustic method is a popular way because it can provide a faster and real-time response [4] in spite of the occurrence of false alarm or missed detection is high [5]. According to the ASTM E1316 Standard, Acoustic Emission (AE) is a phenomenon by which emission of transient waves due to the rapid release of energy in a material. When there are discontinuities in the material, it will create sound and the sound can be captured by the sensors. Thereafter, the leak source can be located by means of determining the time difference between the sound waves reach sensors.

Essentially, the signals must be pre-processed first in order to filter noise out. Noise is unwanted signals that inevitably exist in the signals. In the work conducted by Liu [4], the leakage signal is prominent after filtering. Therefore, noise reduction is a crucial step in acoustic leak detection method. Digital filtering is generally used to eliminate noise from an interested signal if the noise bandwidth is known. Commonly defined filter types are low pass, high pass, band pass and band stop. Hunaidi [2] and Srirangarajan et al. [6] applied low pass and band pass filtering in their leak detection practices to band-limit the signals. However, design of filter requires prior information of both signal and noise so it is only applicable when desired signal has different frequency with the noise [4].

On the other hand, wavelet de-noising is a noise reduction method through wavelet analysis. It decomposes a signal into wavelet coefficients and applies a threshold on the decomposed coefficients in order to eliminate noisy parts. Meng et al. [7] and Wan et al. [8] employed wavelet de-noising to de-noise their collected signal. Their results depict that wavelet de-noised signals are effective to increase leak positioning accuracy by detecting a leak with error of 5%. Nevertheless, there are few indispensable challenges associated with wavelet de-noising which are the decomposition level [9], threshold method [8] and the threshold value [10].

Several methods had been introduced to extract the feature of non-stationary leakage signals such as Discrete Wavelet Transform (DWT) [9], Wavelet Packet Decomposition (WPD) [11, 12], Empirical Mode Decomposition (EMD) [13, 14] and Dual-Tree Complex Wavelet Transform. DTCWT is introduced in this work because it is a propitious method to restrain acoustic noise without eliminating useful signal characteristics [15]. The demerits of DWT and WPD are lack of shift-invariance, poor directional selectivity and frequency aliasing. Diversely, EMD suffers from major difficulty such as mode mixing because it is difficult to decompose a signal that has multiple overlapping modes [16].

The concept of leak localization is illustrated in Fig. 8.1. The waves due to leak will travel in both upstream and downstream of the pipe. Consequently, the waves

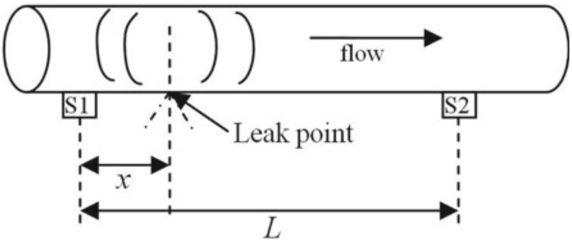
flow
S1
S2
Leak point
x
L

Fig. 8.1 Localization of leak source

will be propagated to both sensor 1 (S1) and sensor 2 (S2) with time lag in their arrival times. Cross-correlation is typically used to determine the time lag between two signals. Thereafter, the leak can be pinpointed in conjunction with wave speed by using Eq. (8.1).

$$x = 0.5(L + vt) \tag{8.1}$$

where x is leak location relative to the sensor 1; L is the distance apart between the two sensors; v is wave speed and t is the time lag.

The signal will be first pre-processed by applying low pass filtering. Then, Wavelet Transform applied to decompose the signal for de-noising and signal feature extraction. Lastly, cross correlation is applied to the de-noised signals to locate the leak. The goals of this paper are to reduce acoustic noise and to improve the leak localization accuracy by employing DTCWT with a soft threshold.

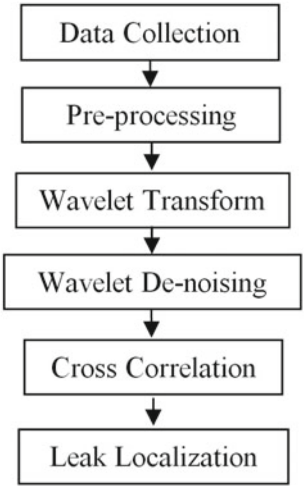
Data Collection
Pre-processing
Wavelet Transform
Wavelet De-noising
Cross Correlation
Leak Localization

Fig. 8.2 State-of-the-art leak detection procedure

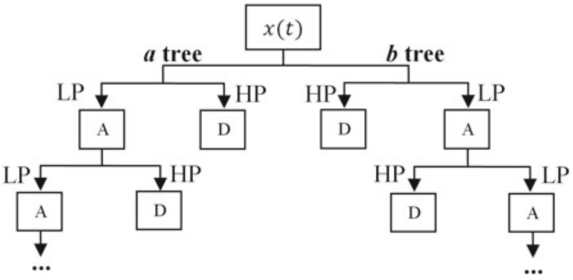

Fig. 8.3 Two levels of DTCWT decomposition

8.2 Methods

8.2.1 Dual Tree Complex Wavelet Transform

DTCWT is originated by Kingsbury [17] and improved by Selesnick et al. [18]. It is designed based on the Wavelet Transform. It performs decomposition and reconstruction process through two parallel sets of real wavelet transforms. Each of the real wavelet (*a* tree and *b* tree) has a set of high pass and low pass filter. The two transforms are aim at obtaining real and imaginary of the complex coefficients [15]. Figure 8.3 describes the process of decomposition via DTCWT where *x(t)* is the input signal, with high pass filter (*HP*) and low pass filter (*LP*). At the end of the decomposition, low pass filter gives coefficients in the low frequency known as approximation coefficients. On the other hand, the high pass filter results in coefficients that are present in high frequency or called as detail coefficients. The approximation coefficients will be decomposed further at the next level.

The merits of DTCWT over traditional Discrete Wavelet Transform (DWT) are its approximate shift-invariance, directional selectivity and frequency anti-aliasing properties. This indicates that DTCWT can measure spectral energy accurately and the frequency components are completely assigned to specified bands without creating spurious frequency [17, 18]. On the contrary, DWT will cause great variations in energy distribution when the input signal has minor shifts. Furthermore, the frequency components are not perfectly divided into specific bands or overlapped with others if using DWT or WPD.

8.2.2 Wavelet De-Noising

Wavelet de-noising was introduced by Donoho and Johnstone [19] to suppress noise through wavelet analysis. The signal will first be decomposed by DWT. The wavelet coefficients contain important signal information tend to present in large amplitude but appear in small amounts; while those of the noises are scattered evenly with low amplitudes. Therefore, the coefficients which are smaller than the threshold can be eliminated as noise. Lastly, remaining coefficients will be reconstructed.

The performance of wavelet de-noising is greatly affected by the selection of decomposition level, threshold method and the threshold value. De-noising with high level may result in loss of excessive information meanwhile de-noising effect is ineffective if the decomposition level is insufficient. Thus, Wan [8] formulated an equation to calculate the optimum level:

$$\frac{f_s}{2^{n+1}} \geq f_{\min} \tag{8.2}$$

where f_s is a sampling frequency, n is optimum decomposition level and f_{min} is minimum interested frequency.

There are two threshold methods proposed by Donoho and Johnstone [20] which are soft threshold and hard threshold. Hard threshold tends to make the wavelet coefficients discontinuous at the threshold value so oscillations may appear. Yet, the soft threshold makes the de-noised signal smooth and has better continuity [19, 21]. In this paper soft threshold is preferable.

The threshold value is the key point of de-noising performance. If the threshold is too small, some noises might still remain thus diminish the de-noising effect. On the contrary, if the threshold too high, important information will be lose. Therefore, threshold value is calculated by Eq. (8.2) [20]. Median is a robust estimator to estimate noise level because it is more resilient to the outliers in case the wavelet coefficients contain some small amount of signal that is buried in noise [19].

$$T = \frac{median(|W|)}{0.6745} \times \sqrt{2\log m} \tag{8.3}$$

where W is wavelet coefficients and m is the signal length.

8.2.3 Distribution

Distribution curve is used to find probability distribution function for a population which most likely to produce a distribution that exists in collected data. The most well-known distribution in statistics is the normal distribution. Figure 8.4 shows a normal distribution with mean, μ of 1 and standard deviation, σ of 0.2. To determine the likelihood of a range of value that will take place, a z-score probability can be used. Z formula below and z-table can determine the probability.

$$Z = \frac{|X - \mu|}{\sigma} \tag{8.4}$$

where Z is z-score.

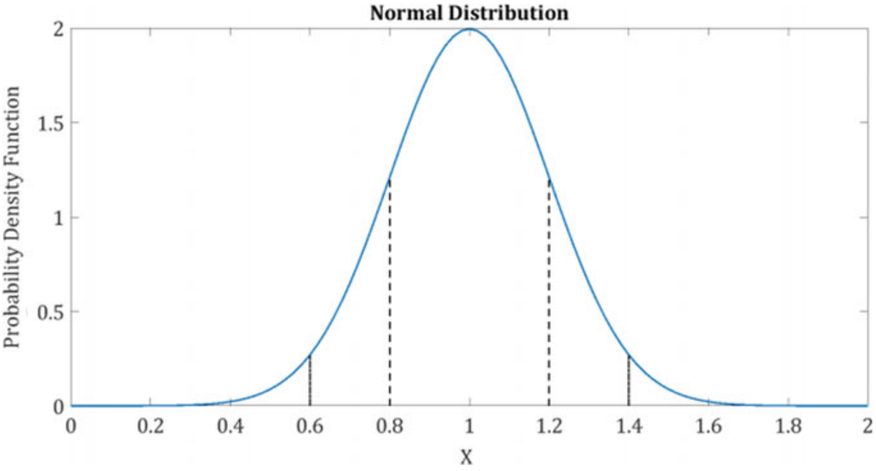

Fig. 8.4 Normal distribution curve with mean of 1

Hence, the obtained localization results were tested whether they are normally distributed. The portion of results falls within a certain number of σ from μ is calculated by using Eq. (8.4).

8.2.4 Integration of DTCWT and Soft Threshold

In physics, wave velocity is dispersive because it varies with transmitting medium, surrounding media, pipe properties and wave frequency [22]. Therefore, the superiority of employing multilevel DTCWT decomposition before localize leak is that the signal will be decomposed into several frequency bands in which their frequency range at each level can be calculated as follow:

$$\begin{aligned} f(d_n) &\in \left(\frac{f_s}{2^{n+1}}, \frac{f_s}{2^n}\right) \\ f(a_n) &\in \left(0, \frac{f_s}{2^{n+1}}\right) \end{aligned} \tag{8.5}$$

where d_n is detail coefficients, a_n is approximation coefficients and n is level.

In such a case, the dispersion phenomenon is taken into account because the velocity of a wave is evaluated based on its frequency. Figure 8.5 is a dispersion curve plotted using PCDISP software [23]. There are three elemental modes which are longitudinal, flexural and torsional modes. Since the sensors placed on the pipe in a radial direction, the sensors are sensitive to the waves which have significant radial displacement. Torsional wave only contributes circumferential mode, θ displacement

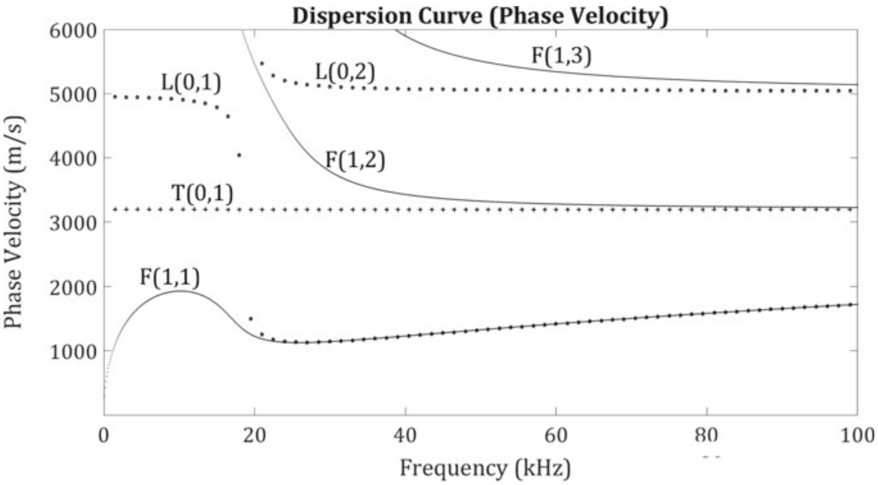

Fig. 8.5 Phase velocity dispersion curve for 3 inches pipe

[24] hence the sensors are cannot pick up the wave. Figure 8.6 shows the radial displacement of longitudinal and flexural modes. The figure shows that $L(0,1)$ and $F(1,1)$ modes are more dominant. $F(1,1)$ is preferable in our work because $L(0,1)$ is very dispersive especially between 0 and 20 kHz.

Figure 8.7 describes the procedures of the proposed method to reduce noise and pinpoint the leak source. Ordinary wavelet de-noising utilizes DWT to decompose signal before de-noise. The key question is whether that DWT has a problem with a lack of shift-invariance. The de-noised signals might encounter great perturbations

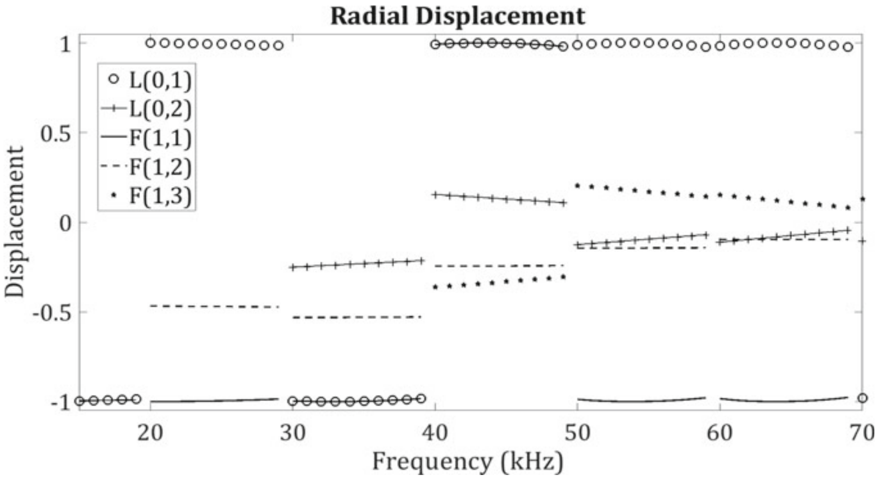

Fig. 8.6 Radial displacement of longitudinal and flexural modes

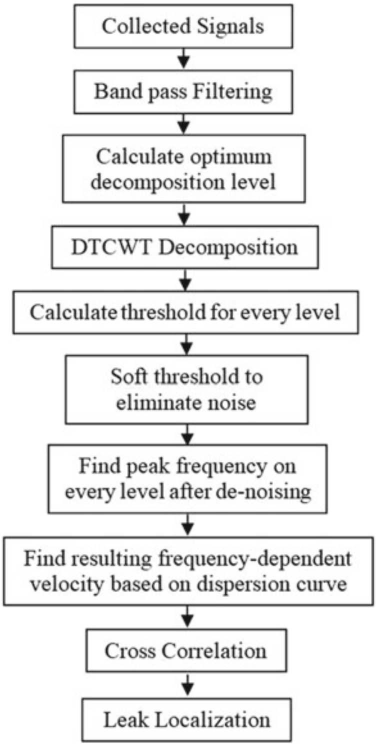
Collected Signals
Band pass Filtering
Calculate optimum decomposition level
DTCWT Decomposition
Calculate threshold for every level
Soft threshold to eliminate noise
Find peak frequency on every level after de-noising
Find resulting frequency-dependent velocity based on dispersion curve
Cross Correlation
Leak Localization

Fig. 8.7 Procedure of the proposed method to locate leak

when there is a modification on decomposed coefficients. Therefore, in this proposed scheme, shift-invariant DTCWT has introduced in pursuance to overcome the shortcomings of DWT. After DTCWT decomposition, a soft threshold will be applied to restrain noise. The decomposition level of DTCWT and a level-dependent threshold value can be calculated by using Eqs. (8.2) and (8.3), respectively.

8.3 Experimental Setup

An experiment was conducted on a 46 m long galvanized iron pipeline which its inner diameter and thickness are 80.4 mm and 4 mm, respectively. The leak hole is created by threading using a screw. A linear array of seven identical AE sensors were used in this experiment and Fig. 8.8 shows their mounting positions. Data was

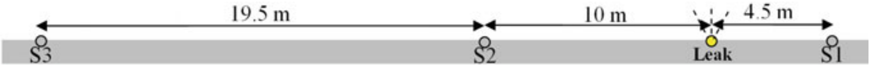
19.5 m
10 m
4.5 m
S3
S2
Leak
S1

Fig. 8.8 Schematic diagram of experimental setup

Table 8.1 Specification of sensors

Sensor model	SR 40 M
Dimension OD × H (mm)	22 × 36.8
Operating Frequency range (kHz)	15–70
Resonant frequency (kHz)	40
Peak sensitivity	>75 dB

collected by LabView acquisition system and amplified using pre-amplifiers with 40 dB gain value. 250 sets signals with 27.5 ms length were acquired at 1 MHz sampling frequency and the operating water pressure is 2 bar. The specifications of AE sensors stated in Table 8.1.

8.4 Results and Discussion

Five levels of DTCWT decomposition is sufficient in the work based on aforesaid [2] since the minimum interested frequency is 15 kHz. Signals which those are lower than 15 kHz are unreliable and had been filtered out because the minimum operating frequency of the sensor is 15 kHz. Figure 8.9 shows the decomposed wavelet coefficients before and after de-noised by the proposed method. The figure clearly shows that DTCWT itself is not sufficient to eliminate the noise but the proposed method can give a smooth signal. The de-noised signal has sharpened feature with more recognized peaks. Meanwhile, comparison between ordinary wavelet de-noising and the proposed method is shown in Fig. 8.10. It is shown that DTCWT performs better in

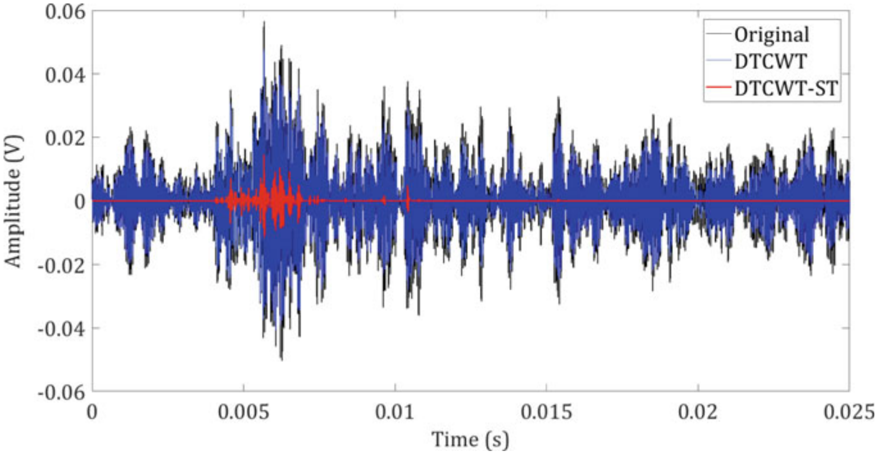

Fig. 8.9 Comparison of DTCWT and DTCWT-Soft threshold

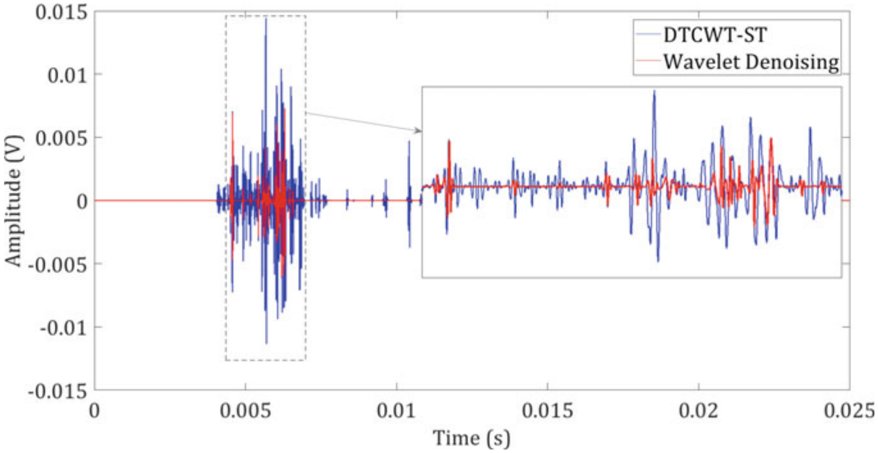

Fig. 8.10 Comparison of wavelet de-noising and DTCWT-soft threshold

de-noising compared with DWT because DTCWT tends to preserve signal characteristics. However, wavelet de-noising eliminates abundant information and makes the signals discontinuous.

To ascertain the reliability of the proposed method in leak detection, source localization results had been compared. Figure 8.11 shows it is difficult to identify a

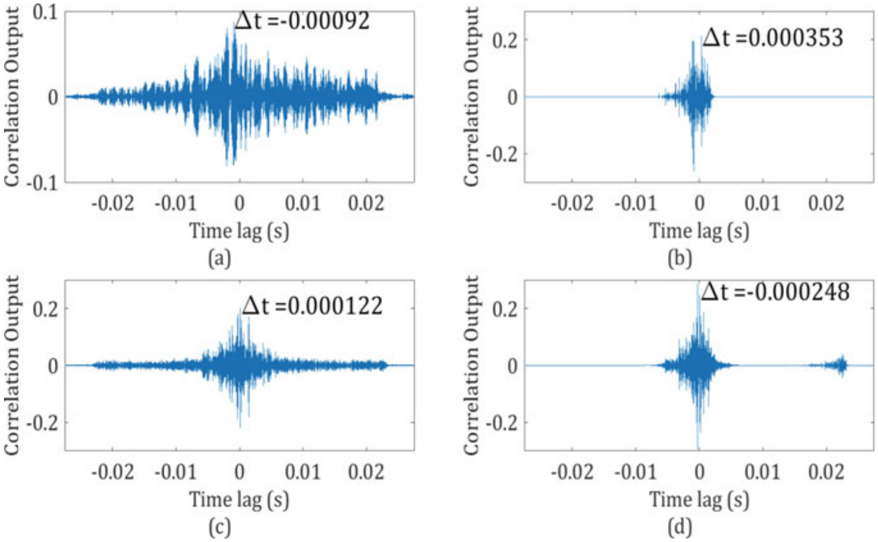

Fig. 8.11 Cross-correlation on **a** original signals **b** wavelet de-noised signals **c** DTCWT-decomposed signals **d** DTCWT-soft threshold signals

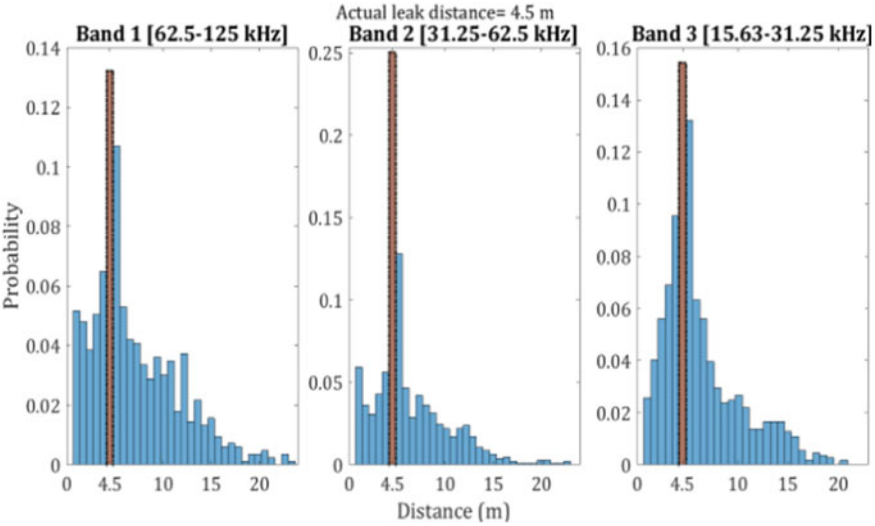

Fig. 8.12 Comparison of leak localization among levels

vulnerable peak from the cross-correlation function of original signals. Nonetheless, cross-correlation peaks are more identifiable after signals being decomposed; furthermore, a sharp and the pronounced peak can be determined after the signals were de-noised via DTCWT with the soft threshold.

In this work, leak location is evaluated based on the probabilistic approach and statistical method. Leak source is indicated by the highest probability. Figure 8.12 shows the leak localization using wavelet coefficients obtained at different frequency bands. The result given by Band 2 has the highest reliability because they can pinpoint the leak with highest occurrence rate. This is attributed due to the resonant frequency of the sensors is 40 kHz hence the sensors are more sensitive in this frequency region.

Figures 8.13 and 8.14 show the results of leak localization results using the proposed method, cross-correlation, wavelet de-noising and DTCWT-Correlation for 250 samples. Normal distribution curve is plotted and dotted lines indicate ± 0.5 σ from the mean.

The leak location is calculated by using Eq. (8.1) in combination with computed time delays and estimated velocity. For conventional cross-correlation method, the velocity is assumed as 1226 m/s because the resonant frequency of the sensor is 40 kHz and dispersion curve shows the velocity is 1226 m/s when frequency equals to 40 kHz. Meanwhile, the velocity is determined based on peak frequency when DTCWT is applied.

From Fig. 8.13, all methods are able to locate the leak accurately and the results are normally distributed. The reliability of DTCWT application can be validated because it provides higher accuracy compared to conventional cross-correlation and wavelet de-noising. Localization accuracy offered by DTCWT is double of ordinary wavelet de-noising. Conventional cross-correlation, wavelet de-noising and

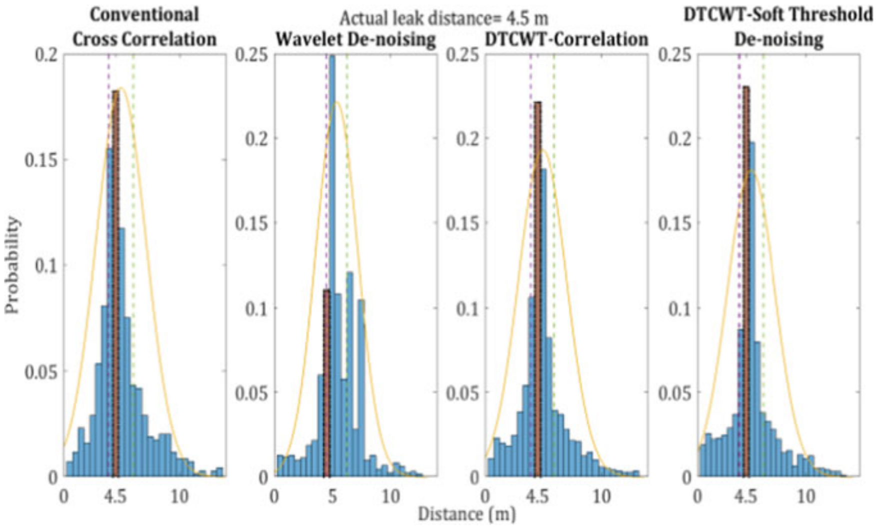

Fig. 8.13 Comparison of different localization methods for S1 and S2

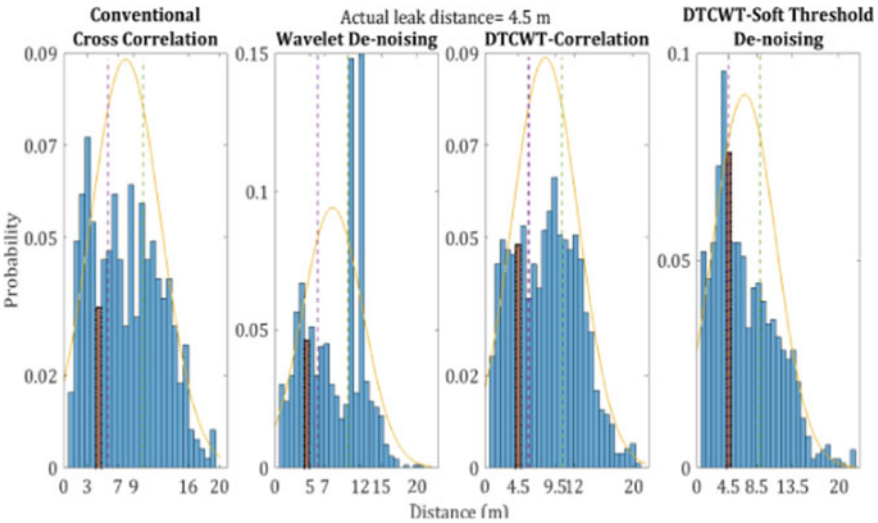

Fig. 8.14 Comparison of different localization methods for S1 and S3

DTCWT-Correlation perform well to locate the leak source in short distance (14.5 m) but they became problematic when the measuring range increases to 24 m (Fig. 8.14). According to their results, a susceptible leak occurs at 3 m, 12 m and 9.5 m, respectively which are deviated from actual leak location. As of propagating distance increases, the acoustic wave was attenuated and became more dispersive. So, the localization error increases.

As a result, conventional cross-correlation fails to locate a leak when the waves propagate in longer distance. The proposed method can still locate the leak and the results show normal distribution behaviour despite of low precision by comparison with shorter distance. In such a word, the proposed algorithm has outstanding performance in terms of distance range and positioning accuracy. Furthermore, it can reduce the occurrence of false detection.

8.5 Conclusion

In conclusion, this work presents DTCWT with Soft Threshold De-noising method. The signal is decomposed via DTCWT then soft threshold is applied to eliminate coefficients which smaller than the threshold. Thereafter, frequency-dependent velocity is evaluated based on peak frequency from every level and used to locate the water leak source, with time delay computed by cross-correlation. Experimental results have verified that the proposed method has outstanding de-noising performance than wavelet de-noising by enhancing the signal features. In addition, it is able to accentuate the cross-correlation peak. Thus, DTCWT-Soft Threshold De-noising is proven as an effective approach to reduce pipeline noise and locate leak accurately by providing highest true detection rate.

Acknowledgements This research was financially supported by the Malaysian Ministry of Higher Education (TRGS/1/2016/UTAR/01/2/3). The authors would like to acknowledge the support of Universiti Tunku Abdul Rahman for providing the facilities.

References

1. SPAN, *Water Services Industry Performance Report* (Cyberjaya, Selangor, 2017)
2. O. Hunaidi, W. Chu, A. Wang, W. Guan, Detecting Leaks in Plastic Pipes. J. American Water Works Association. **92**(2), 82–94 (2000)
3. C. van den Berg, *The Drivers of Non-Revenue Water: How Effective are Non-Revenue Water Reduction Programs?* World Bank Group (2014)
4. C. Liu, Y. Li, L. Fang, M. Xu, Experimental study on a de-noising system for gas and oil pipelines based on an acoustic leak detection and location method. Int. J. Press. Vessels Pip. **151**, 20–34 (2017)
5. J. Yang, Y. Wen, P. Li, X. Wang, Study on an Improved Acoustic Leak Detection Method for Water Distribution Systems. Urban Water Journal. **10**(2), 71–84 (2013)
6. S. Srirangarajan et al., Wavelet-based burst event detection and localization in water distribution systems. J. Signal Process. Syst. **72**(1), 1–16 (2012)
7. L. Meng, Y. Li, W. Wang, J. Fu, Experimental study on leak detection and location for gas pipeline based on acoustic method. J. Loss Prev. Process Ind. **25**(1), 90–102 (2012)
8. J. Wan, Y. Yu, Y. Wu, R. Feng, N. Yu, Hierarchical Leak Detection and Localization Method in Natural Gas Pipeline Monitoring Sensor Networks. Sensors. **12**(1), 189–214 (2012)

9. S. Rashid, S. Qaisar, H. Saeed, E. Felemban, A Method for Distributed Pipeline Burst and Leakage Detection in Wireless Sensor Networks Using Transform Analysis. Int. J. Distrib. Sens. Netw. **10**(7), 1–14 (2014)
10. H. Jin, L. Zhang, W. Liang, Q. Ding, Integrated leakage detection and localization model for gas pipelines based on the acoustic wave method. J. Loss Prev. Process Ind. **27**, 74–88 (2014)
11. C. Xu et al., An Acoustic Emission based Multi-level Approach to Buried Gas Pipeline Leakage Localization. J. Loss Prev. Process Ind. **44**, 397–404 (2016)
12. J. Zhao, F. Sun, H. Wang, Pipeline leak fault feature extraction based on wavelet packet analysis and application, in *International Conference on Electrical and Control Engineering* (Yichang, China, 2011)
13. X. Cui, Y. Yan, Y. Ma, L. Ma, X. Han, Localization of CO2 Leakage from Transportation Pipelines through Low Frequency Acoustic Emission Detection. Sens. Actuators, a **237**, 107–118 (2016)
14. J. Sun, R. Wang, H.-F. Duan, Multiple-fault Detection in Water Pipelines using Transient-based Time-Frequency Analysis. Journal of Hydroinformatics. **18**(6), 975–989 (2016)
15. X. Yu, W. Liang, L. Zhang, H. Jin, J. Qiu, Dual-Tree Complex Wavelet Transform and SVD based Acoustic Noise Reduction and Its Application in Leak Detection for Natural Gas Pipeline. Mechanical Systems and Signal Processing. **72–73**, 266–285 (2016)
16. N.E. Huang, Z. Wu, A Review on Hilbert-Huang Transform: Method and Its Applications to Geophysical Studies. Rev. Geophys. **46**(2), 1–23 (2008)
17. N. Kingsbury, Complex Wavelets for Shift Invariant Analysis and Filtering of Signals. Applied and Computational Harmonic Analysis. **10**(3), 234–253 (2001)
18. I.W. Selesnick, R.G. Baraniuk, N. G. Kingsbury, The Dual-tree Complex Wavelet Transform, in *IEEE Signal Processing Magazine*. IEEE, pp. 123–151 (2005)
19. D.L. Donoho, I.M. Johnstone, Adapting to Unknown Smoothness via Wavelet Shrinkage. Journal of the American Statistical Association. **90**(432), 1200–1224 (1995)
20. D.L. Donoho, I.M. Johnstone, Ideal Spatial Adaptation by Wavelet Shrinkage. Biometrika **81**(3), 425–455 (1994)
21. M.A. Golroudbari, Signal denoising based on wavelet transform using a multi-level threshold function, in *7th International Conference on Application of Information and Communication Technologies* (Baku, Azerbaijan, 2013)
22. G. Shen, X. Qin, R. He, C. Xiu, Theoretical analysis and experimental study of gas pipeline leak acoustic emission signal transmit speed. in *Proceedings of 30th European Conference on Acoustic Emission Testing & 7th International Conference on Acoustic Emission* University of Granada
23. F. Seco, et al., PCDISP: a tool for the simulation of wave propagation in cylindrical waveguides. in, *9th International Congress on Sound and Vibration*. (2002), pp. 1–7
24. J.L. Rose, *Ultrasonic Guided Waves in Solid Media. Vol* (Cambridge University Press, New York, 2014)

Chapter 9
Burst Analysis for Multi-Level Leakage Detection in Water-Filled Pipeline Based on Acoustic Emission Signal

Bach Phi Duong, Jaeyoung Kim, Inkyu Jeong, and Jong-Myon Kim

Abstract This paper establishes a methodology to exploit the characteristics of burst waveform in acoustic emission (AE) signals and combine with the signal analysis process to enhance the accuracy of multi-level leak detection in steel pipelines. The AE bursts are signal waveforms that contain the continual imbrication transients with variable strengths in the form of impulses and these impulses include the pivotal information of the leakage syndromes. Capturing and isolation of a burst waveform against the background signal strengthen the capability of a pipeline's fault diagnosis system. First, this research employs a method using the Enhanced Constant False Alarm Rate (ECFAR) to identify the bursts. Then, the information which is extracted from the burst waveform segment is used to recognize their various sizes of leakage in a laboratory simulated leak system. The training multi-class support vector machine in the one-against-all strategy is responsible for the leak categorization. The result of classification from the proposed method is compared with another algorithm utilizing the wavelet threshold-based burst detection algorithm, which demonstrates the ECFAR method gives an outperforms the wavelet threshold-based algorithm in classification with the accuracy of 93% for different sizes of leakage.

9.1 Introduction

Metropolitan piping systems are popularly used to supply water, gas, and petroleum for human lifestyle activities. The huge pipe systems, which are larger, longer, and more complex, have become important assets of the government when they are used in large-scale industrial factories for conducting different types of liquids, such as chemicals, petroleum, oil, and spread over a long-range distance. In the water supply system, approximately 20–30% of the water has been lost every year, some of the loss quantity can be even up to 50% [1]. A pipeline leak not only wastes resources but also increases risks of collapse or explosion and environmental pollution. Since leaks are unavoidable consequence over a long-time using, the condition monitoring

---

B. P. Duong · J. Kim · I. Jeong · J.-M. Kim (✉)
School of Electrical Engineering, University of Ulsan, Ulsan 680-749, South Korea

© The Author(s), under exclusive license to Springer Nature Singapore Pte Ltd. 2021

G. Shen et al. (eds.), *Advances in Acoustic Emission Technology*, Springer Proceedings in Physics 259, https://doi.org/10.1007/978-981-15-9837-1_9

of the pipelines and on-time maintenance have inspired the reconsideration over the recent years. Numerous diagnosis programs can early recognize some abnormal symptoms in the pipeline system, including hardware-based methods, fiber optic, visual inspection, cable sensor, and acoustic emission (AE) [2–4]. Apparently, the AE signal techniques have been auspicious since it exhibited effectively for offering high sensitivity concerning fault detection, quickly recognize small leaks, and supply the advances in data collection and analyzing speeds with the huge amount of gathered signals [5, 6]. Pipeline leakage mechanism creates the high-frequency signal in the elastic wave types which transmitted along the tube wall, reflected between the two surfaces of the pipeline [7]. When a solid wall of the pipe is excited by an abrupt displacement or an impact, it creates a dynamic vibration problem (generate dynamic stress). Escaping liquid in high-pressure pipes passes through a perforation, releases elastic energy in the form of stress waves caused by localized loss of energy, and these generated signals usually represent the abnormal AE events. Stress waves are transmitted through the pipe wall which can be collected by using an acoustic emission sensor installed on the pipe body [8, 9]. The analysis of the AE event from leakage obtained via the pipe body stimulation is a significant key for leakage fault diagnosis. However, the signal characteristics that are non-stationary could be treated as a broadband random noise modulated by a slow-changing random process and are ineliminable contamination with non-leak signals that make it difficult to distinguish AE signals. The AE event that makes an appearance from an abrupt change in flow generates transient bursts. By detecting a burst event, it is also essential to compute the time-differences-of-arrival (TDOA) between AE signals recorded by the sensors, which aids for AE source localization. Therefore, burst segmentation and exact analysis of the characteristics of this AE wave have acquired useful knowledge. In previous research, some researchers have been introduced to enhance leak detection in water-filled pipelines using the wavelet decomposition and denoising has to recognize the transient bursts [10]. However, the presented methods have their own limitation because most of the components decomposed wavelet transform are mostly related to the remains of attenuated leak signals. On the other hand, an important issue existing in the fault diagnosis algorithm is to distinguish the leakage signal without giving false alarms. Previously, object detection with a constant false alarm rate (CFAR) was employed in the radar system with the doppler effect [11]. However, the considering of burst inside the AE leak signal as objects, which are necessary to be identified and employ the detector with CFAR, has not been researched yet.

The main objective of this research is detection the burst events associated with leakage and isolation of the burst waveform by the Enhance Constant Faults Alarm Rate (ECFAR) methodology to identify the characteristics of this dispersive AE signal in leakage phenomenon. Then, the investigating characteristics of bursts are utilized to distinguish the different levels of leak signal using the multiclass support vector machines in the strategy of one-against-all (OAA-MCSVM).

The organization of this paper is illustrated as follows. The data acquisition system to record the leakage dataset in the type of acoustic emission, which is applied with the proposed algorithm for evaluation purposes and the testbed are introduced in Sect. 9.2. After that, Sect. 9.3 describes in detail burst event detection and isolation techniques using the ECFAR algorithm. The method is evaluated by the performance of the classification of multi-level leakage and the result is presented in Sect. 9.4. In the end, Sect. 9.5 provides conclusions and issues for future implementation.

9.2 Seed to Data Acquisition System and the Experimental Testbed Setup

As illustrated in Fig. 9.1, a particular testbed with a water-filled pipeline was meticulously designed to simulate leakage in a piping system. Two ductile iron pipe testing sections were made of stainless steel 304 with 2 m length, 3.38 mm wall thickness, and 34 mm outside diameter. At each end of the test-section, a blind-flange connection is welded to assemble the test-section to the other parts of the system. A water circulatory system is conducted to imitate the working condition of the pipeline and includes a centrifugal pump and a tank. A pump was employed to keep the water flow at a constant speed. The water is pumped from the tank flows pass into the pipeline system, test-section, and then back to the tank. Two pressure meters and two regulators are located on either end of the test-section to indicate and adjust the pressure of the inflow and outflow of water, respectively. Two flow transmitters are also placed in the pipeline testing system to measure the flow rate. The leak is simulated by an orifice (or drill hole) with a solenoid valve. In this research, the four levels of the leak are 0.3 mm, and 0.5 mm, 1 mm, 2 mm is generated by four orifices with diameters respectively, as shown in Fig. 9.1. AE sensors were mounted on two sides of the leak's position. The high-sensitive sensors are mounted near leak location, could primarily measure leak signals while other signals might be virtually removed due to their quick attenuation in close propagation range.

For sensing signals, the data acquisition devices used in the test include a data acquisition card PCI-2 with a peripheral component interconnect bus. This card is

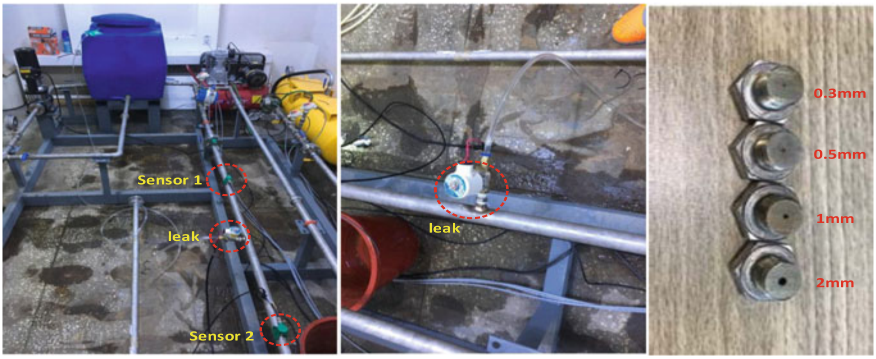

Fig. 9.1 AE signal acquisition from a water pipeline testbed with four sizes of leak includes 2 mm, 1 mm, 0.5 mm, 0.3 mm

Table 9.1 The data acquisition devices for collecting the acoustic emission signal

Device names	Detailed parameters of the acquisition devices	
PCI 2- DAQ card	– Input: 2 channels – Dynamic range: >85 dB – ADC 18-bit 40 MHz	
WDI-AST sensor	– Resonant frequency: 650 kHz – Directionality o f ± 1.5 dB – Range of working: 200–900 kHz – Peak sensitivity: – 25 dB [V/μbar]	

connected with two piezoelectric WDI-AST wideband sensors to acquire the AE signal generated by disorderly flow near the leak's position. A detailed characterization of the devices is presented in Table 9.1. Two AE sensors are installed on the top of the pipe wall by adhesive types. By customizing the regulators at each end of the test-section, the inner pressure at the inflow water is stabilized at 1.77 bar. The experiment process was operated at a fixed temperature of approximately 30 °C. To supply the appropriate signal/noise ratio (SNR) for further processing, the recorded signals are then filtered and amplified using a signal conditioning unit. The vibration signal was also collected in this experiment. To record the vibration signal, accelerometer-type sensors were attached to the pipe near the leak position. The normal or leak state of the testing pipeline is related to a closed or open position of a valve assembled on the orifices (or drill holes). The process of experiment starting with operating the pump to circulate the water inside the pipe. First, the leak is deactivated with the closed valve. The normal state of the signal is recorded over 10. This normal state is used as the baseline for comparison with the leak state. Later, the leak is activated by opening the valve. The abnormal signal is recorded after a while until the leakage flow to be stable. This process is iterated for different sizes of leakage orifices.

9.3 The Burst Detection and Pipeline Fault Diagnosis Using the ECFAR

A collected AE signal in an actual fluid pipeline consists of many AE bursts. They can be inspired by abnormal points—crack, bending-segments, collisions, blockage, or leaks in the pipe body. Since the elastic energy of the AE bursts is low, they are easily distorted by the wave attenuation and the noise presence. To remove that affective from the random noise component, the envelope analysis is employed to increase the energy of the leak signal. Thus, the AE burst is searched from the envelope of the signal. The process starts with an AE burst detecting using a Hilbert-Huang transform and the envelope detector. The Hilbert-Huang transform is responsible for converting a sequence of real value signal into a complex signal (analytic form). Then, the envelope detector calculates the modulus from the complex signal to get the envelope signal. Hence, the bursts are then detected from the output of the envelope detector. Burst events, which are the result of an instant change in fluid pressure such as turbulent, produce consecutively transient peaks that are overlapping together. Depend on the number of transient peaks, the burst events have various lengths. Transients in the acoustic emission signals from leakage are often hard to isolate using the conventional threshold approaches. These transients have a different frequency, strength, shape, and duration, etc. In consequence, since the complexity inside the acquired signal increases, the advanced analyzing methods are enforced to separate these impulses instead of a fixed threshold. The acoustic emission signal which is collected from the leak case with include the bursts inside is shown in Fig. 9.2

In this research, the authors defined the transient bursts like the outstanding objects, which is necessary to recognize, against the normal level of background signal. In order to robust to the noise level, the proposed ECFAR method is used to calculate an adaptive threshold due to the estimated level of noise. In an actual acquirement, the existence of noise with unquantified power is the cause of many false alarms if the detecting threshold was chosen at low value. Conversely, if the threshold value is set too high, fewer bursts will be detected, and the information is lost. The process of burst analyzing uses statistical analysis, which guarantees a burst event to be detected with a constant false alarm rate. The detection threshold holds the value, which must be exceeded to be identified as an object that exists in this sample. The authors assume the noise model to be the zero-mean complex-valued Gaussian random variable that has an independently and identically distribution. To determine an adaptive threshold for the noise model, the noise power has to be computed. For detecting the object in a signal, there are two hypotheses that are defined for this analysis: (1) the sample signal only contains the background (H_0); and (2) the sample signal contains an object with a background (H_1). If the hypothesis (H_0) appropriate, the detection algorithm affirms that the object is not present

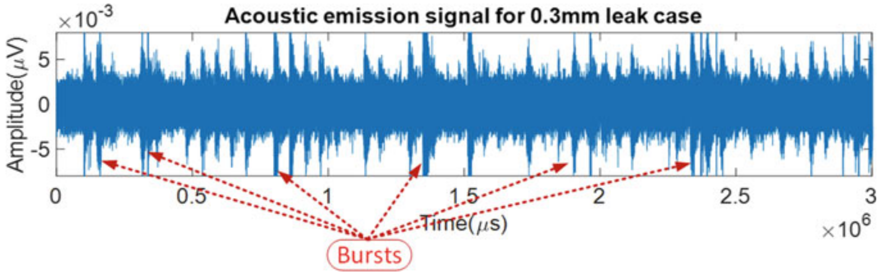

Fig. 9.2 The AE signal collected from the 0.3 mm leak case with the burst inside

in this sample. If the hypothesis (H_1) is more appropriate, the detection algorithm affirms that the object is present. Assume the process is applied to a one-dimension signal ($1 \times m$) sample. This signal is segmented by windowing to n segments. Each segment is associated with a test cell (C_T) and contains N samples. ECFAR calculates the detection threshold depends on the power in the cells which surround the test cell. The immediate cells next to the test cell are called neighbor cells. These neighbor cells are excluded from the average calculation to detect if the object is presented. Because of the fact that bursts, or impulses, are not located at one cell but rather spreads across some range cells, the reference segment is not directly placed nearby the test cell. An adaptive threshold (T) is estimated depending on values from the surrounding cells of this test cell and a multiplier coefficient (α). This multiplier coefficient is a constant that is determined to associate with the false alarm probability (P_{fa}) to attenuate or amplify the detection threshold. Hence, the ECFAR algorithm maintains a constant false alarm rate but it makes varying in the detection threshold. This indicates that contextual information around the test cell is considered in the estimation of the threshold. This turns ECFAR into an adaptive method to make the detections based on contextual information. Then, the comparison unit compares the current test cell value with the detection threshold T. If the test cell value exceeds the threshold, the algorithm affirms that the object is present. This process is recursively employed in the next cell.

For an estimated (P_{fa}), the required value should be satisfied with the theorem of detection with:

$$P_{fa} = \int\limits_{(s:\lambda(s)>\varsigma)} p(s|H_0)ds \tag{1}$$

where the $\lambda(s) = \frac{p(s|H_1)}{p(s|H_0)}$ is the likelihood ratio, and $p(\cdot)$ is the probability density function (pdf).

The desirable detection threshold is estimated as a parameter $\alpha > 0$ multiple of the estimated noise power in each window $NP = \frac{1}{N}\sum\limits_{i=1}^{N} s_i^2$ as

$$T = \alpha \times NP \tag{2}$$

This adaptive threshold permits to consider a false alarm rate, even when the noise power varies. The threshold computed by Eq. (9.2) is a random variable. α is the constant in each cell and depending on the segment size N and the given false-alarm P_{fa}

$$\alpha = N\left(P_{fa}^{-1/N} - 1\right) \tag{3}$$

In this research, the authors suggested a pre-processing methodology in which the integrated signal from the output of the envelop analysis, which has a lower level of noise and raises the energy of the salient transient bursts. The integrated signal has a reaction similar to the power variation of the signal. As a consequence, the algorithm is sensitive to the immediate variation in the sample signal created by the burst or the impulse (Fig. 9.3).

After the bursts are detected and isolated, the characteristics relate to a different type of source is extracted to distinguish the various levels of the leak. Otherwise, the AE burst signals supply intrinsic information about a mechanical characteristic such as crack, blockage, or leak. To enhance the reliability of the pipeline fault classification method to classify between classes, a variety of AE features are utilized together with representative statistical features. In addition, the AE burst features such as the measured area under the rectified signal envelope energy, duration, hit counts, and peak amplitude, of the burst waveform signal, are calculated. Moreover, traditional statistical features such as kurtosis, skewness, entropy, and root mean square of the signal are also calculated from the signal in time-domain. The extracted features establish a multi-dimensional matrix data structure which is called a multi-dimension feature pool. Then, to categorize the features into separated classes, the one-against-all multi-classes support vector machine is trained with the dataset as the classifier [12]. A number of feature samples representing the leak of various sizes refer to the normal state signal in the pipeline monitoring system is used to train OAA-SVM. Owing to the fact that an individual SVM only solves for the two-classes issue, we set up an SVM set composed by several SVMs to distinguish different states of the pipeline. According to the application requirements to analyze

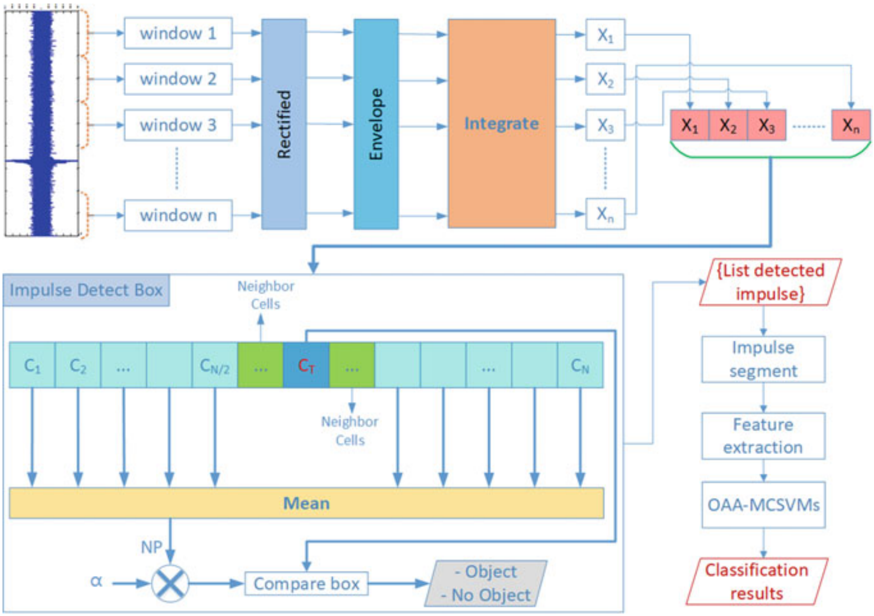
window 1
window 2
window 3
window n
Rectified
Envelope
Integrate
X_1
X_2
X_3
X_n
X_1 X_2 X_3 .... X_n
Impulse Detect Box
Neighbor Cells
C_1 C_2 … $C_{N/2}$ … C_T … … C_N
Neighbor Cells
Mean
NP
α
Compare box
- Object
- No Object
{List detected impulse}
Impulse segment
Feature extraction
OAA-MCSVMs
Classification results

Fig. 9.3 The Enhance Constant False Alarm Rate algorithm for burst detection

for leak detection in different leak sizes, the pipeline has five types of recognition states 0.3 mm, 0.5 mm, 1 mm, 2 mm, and normal. As a result, we need to conduct five SVMs to respect to the five kinds of states. For the i^{th} SVM, the recognition output value of i^{th} pipeline state should be $(+1)$ while the output values of other states should be all (-1). The classification principle of SVM for distinguishing multi-classes is based on the kernel method and the structural risk minimization principle.

$$f(z) = \operatorname{sgn}\left(\sum_{i=1}^{n} \lambda_i y_i \psi(z_i, z) + b\right) \tag{4}$$

where z_i and z describe training and measured feature samples, respectively; $y = \{-1, +1\}$ is the target label. λ represents the Lagrange coefficient, which satisfies the condition that $0 \le \lambda_i \le C$, $\sum_{i=1}^{n} \lambda_i y_i = 0$ with $i = 1, 2, ..., n$. The parameter C is the penalty factor, b represents the threshold value for classification. $\psi(z_i, z)$ is the kernel function. Depending on whether specific engineering problems of leakage features in the pipeline, the Gaussian radial basis kernel (RBF) $\psi(z_i, z) = \exp\left(-\gamma \|z_i - z\|^2\right)$ is considered as the kernel function. To solve the issue of parameter selection, the hyperparameters (C, γ) of the SVMs, which can directly affect classification accuracy, can be obtained by using the grid search method to obtain the maximum accuracy.

9.4 Pipeline Fault Experimental Analyzed Results

Applying the proposed method to the collected dataset from the experimental testbed, which is introduced in Sect. 9.2. Considering different leak sizes, including 0.3 mm orifice, 0.5 mm orifice, 1 mm orifice, 2 mm orifice, each type of fault signal is put into the burst detector to detect and segment to the list of burst segment signals. Hence, for each burst segment, the features are extracted and input to the OAA-MCSVMs. The classification result for five classes, four sizes of the leak and the normal state, is illustrated in Fig. 9.4a with the confusion matrix describes the result of the OAA-MCSVMs classifier of the ECFAR. As depicted in Fig. 9.4a, the average accuracy of the MCSVMs with the proposed method is equal to 93%. For illustration, the research also compares the result of the ECFAR burst detection with the wavelet-based threshold burst detection. The wavelet-based threshold is another methodology used for burst detection as described in [8]. Observing that wavelet spectrums of noise signals and leak signals have different performance characteristics in each scale, signals are decomposed into both wavelet coefficients and the scaling values through the wavelet decomposition technique. The complete decomposition hierarchy is provided based on this technique. Consequently, because of uniform frequency secondary groups, the wavelet decomposition is extremely adaptable. The first some decomposition levels, extremes of the details are both due to noise and signal characteristics. When the scale increases, noise extremes decay while the noise-free signal can be obtained. The noise in each level is evaluated based on the standard deviation of the detail coefficients and is computed as the threshold. After the burst detection stage, the same procedure of signal characteristics calculation and classification with OAA-MCSVMs is applied for the burst segment signals. The results of the different leak size classes distinguishing by using the OAA-MCSVMs and the wavelet-based threshold are described in Fig. 9.4b. The classification results indirectly illustrate that the ECFAR renders outperforming in comparison to the wavelet-based threshold.

In addition, most of the misclassification for leak signals happens between the 2 mm drill hole class and normal class for both two methods of burst detection, which is caused by the water leakage in high-flow rate thereby generating significantly reducing the pressure inside the pipeline. This pressure dropping induces the reduce the stress of turbulence flow at the leakage position that decreases the amplitude in the collected AE signal near the leakage point. In consequence, the leakage signal level is closer to the background signal. This appearance case can be inspected by exploring the wavelet scalograms, which are yielded from the signals of different fault states refer to the normal state of the pipeline system, as shown in Fig. 9.5.

According to Fig. 9.5, the number of salient transient peaks, which is distinct to the background signal, from the 2 mm drill hole class has a substantial decrease compared with the signal of the 1 mm drill hole class. However, if we compare the result with the normal signal, the density of the burst in the 2 mm drill hole was still higher concentrated.

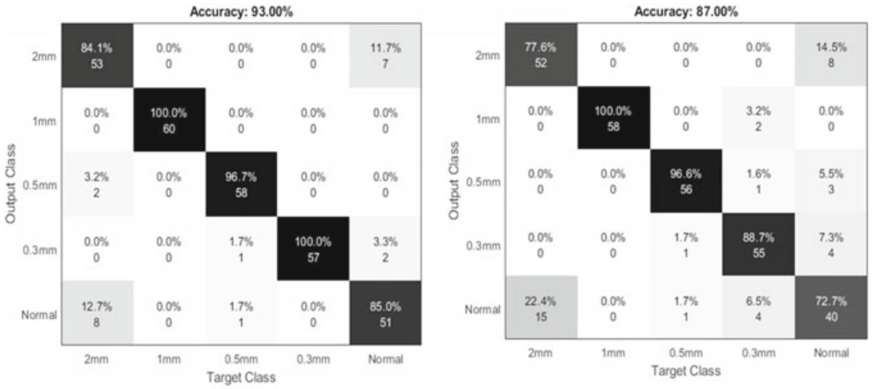

Accuracy: 93.00%

	2mm	1mm	0.5mm	0.3mm	Normal
2mm	84.1% 53	0.0% 0	0.0% 0	0.0% 0	11.7% 7
1mm	0.0% 0	100.0% 60	0.0% 0	0.0% 0	0.0% 0
0.5mm	3.2% 2	0.0% 0	96.7% 58	0.0% 0	0.0% 0
0.3mm	0.0% 0	0.0% 0	1.7% 1	100.0% 57	3.3% 2
Normal	12.7% 8	0.0% 0	1.7% 1	0.0% 0	85.0% 51

(a)

Accuracy: 87.00%

	2mm	1mm	0.5mm	0.3mm	Normal
2mm	77.6% 52	0.0% 0	0.0% 0	0.0% 0	14.5% 8
1mm	0.0% 0	100.0% 58	0.0% 0	3.2% 2	0.0% 0
0.5mm	0.0% 0	0.0% 0	96.6% 56	1.6% 1	5.5% 3
0.3mm	0.0% 0	0.0% 0	1.7% 1	88.7% 55	7.3% 4
Normal	22.4% 15	0.0% 0	1.7% 1	6.5% 4	72.7% 40

(b)

Fig. 9.4 Result of confusion matrices respect to the two methods of impulse detection **a** ECFAR **b** wavelet threshold-based

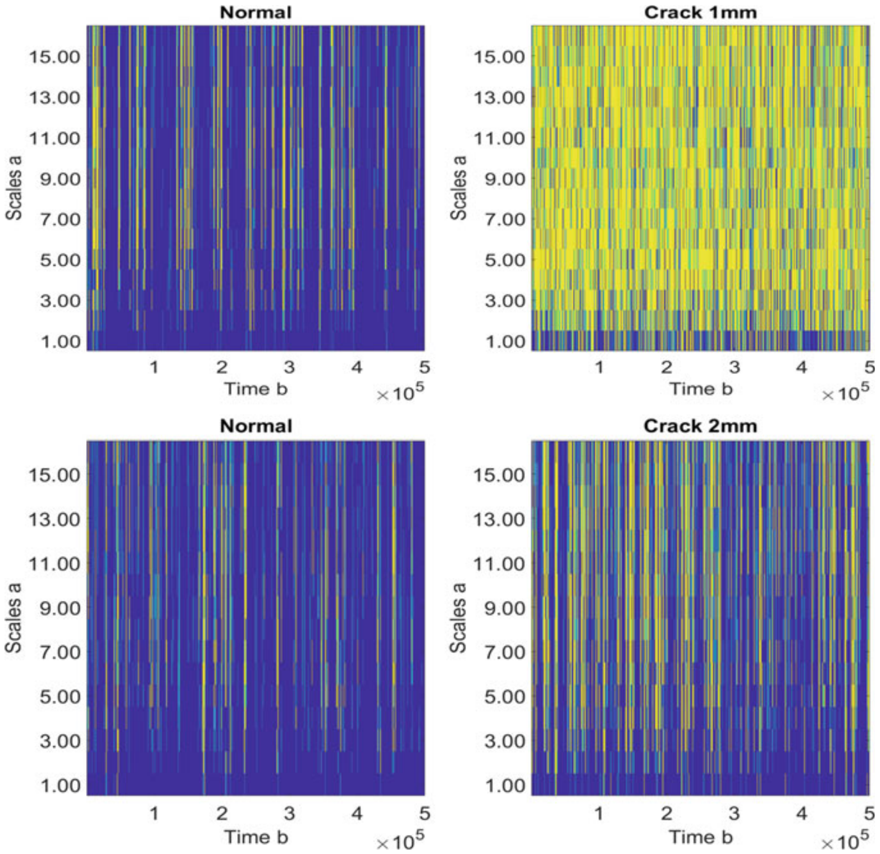

Fig. 9.5 Wavelet visualization analysis of normal signal and leakage signal of 2 mm hole and 1 mm hole

9.5 Conclusion

Owing to the fact that burst waveform in an AE signal contains vital characteristics regarding leakage phenomenon in a water-filled pipeline system, this research proposed a reliable methodology for detecting and isolating the transient salient burst signal distinct to the background signal with the ECFAR algorithm. This algorithm can effectively recognize and the burst waveform and robust to the variable length of burst waveform. The effectiveness of the ECFAR detector algorithm is indirectly assessed through classification accuracy of multiple sizes of the leak using the obtained characteristic features from the isolated burst signal. The experimental results illustrate that the ECFAR detector yields high-quality results in comparison to the wavelet-based threshold burst detection method, with classification obtain to 93% average accuracy. Unfortunately, the authors have not employed the methodology to locate the leak point, which will be performed in future research.

Acknowledgements This research was supported by Basic Science Research Program through the National Research Foundation of Korea(NRF) funded by the Ministry of Education(2019R1D1A3A03103840)

References

1. R. Frauendorfer, R. Liemberger, *The Issues and Challenges of Reducing Non-Revenue Water*. Asian Development Bank (2010)
2. Z. Liu, Y. Kleiner, State of the art review of inspection technologies for condition assessment of water pipes. Measurement **46**(1), 1–15 (2013)
3. K.B. Adedeji, Y. Hamam, B.T. Abe, A.M. Abu-Mahfouz, Towards achieving a reliable leakage detection and localization algorithm for application in water piping networks: An overview. IEEE Access **5**, 20272–20285 (2017)
4. T.K. Chan, C.S. Chin, X. Zhong, Review of current technologies and proposed intelligent methodologies for water distributed network leakage detection. IEEE Access **6**, 78846–78867 (2018). https://doi.org/10.1109/ACCESS.2018.2885444
5. A. Martini, M. Troncossi, A. Rivola, Leak detection in water-filled small-diameter polyethylene pipes by means of acoustic emission measurements. Appl. Sci. **7**(1), 2 (2017)
6. T.B. Quy, J.-M. Kim, Leak localization in industrial-fluid pipelines based on acoustic emission burst monitoring. Measurement **151**, 107150 (2020). https://doi.org/10.1016/j.measurement.2019.107150
7. A. Mostafapour, S. Davoudi, Analysis of leakage in high pressure pipe using acoustic emission method. Appl. Acoust. **74**(3), 335–342 (2013)
8. M.J. Thomas, N.M. Jay, J.W. Daniel, Acoustic emission leak detection on a metal pipeline buried in sandy soil. J. Pipeline Syst. Eng. Practice **4**(3), 149–155 (2013)
9. Y. A. Khulief, A. E. Khalifa, R. Ben-Mansour, and M. A. Habib, Acoustic detection of leaks in water pipelines using measurements inside pipe. J. Pipeline Syst. Eng. Practice **3**(2), (2012)
10. S. Srirangarajan, M. Allen, A. Preis, M. Iqbal, H.B. Lim, A.J. Whittle, Wavelet-based burst event detection and localization in water distribution systems. J. Sign. Process Syst. **72**(1), 1–16 (2013)
11. G.G. Acosta, S.A. Villar, Accumulated CA–CFAR process in 2-D for online object detection from sidescan sonar data. IEEE J. Oceanic Eng. **40**(3), 558–569 (2015)
12. M. M. Manjurul Islam, J.-M. Kim, Reliable multiple combined fault diagnosis of bearings using heterogeneous feature models and multiclass support vector Machines. Reliability Eng. Syst. Saf. **184**, 55–66 (2019)

Chapter 10
Prediction of Residual Life of Oil and Gas Pipeline Corrosion Based on Deep Learning

Wang Xinying, Zhang Huiran, Zhang Ruicheng, Zhao Bin, Huang Xuan, and Zhang Ying

Abstract Corrosion of buried oil and gas pipelines will lead to perforation, leakage and even ruptures of oil and gas pipelines, causing huge property losses. In order to reduce gas oil leakage accidents caused by pipeline corrosion, a deep learning method for predicting residual life oil and gas corroded pipeline is proposed. For this, the author simulated pipeline corrosion in the laboratory, using acoustic emission detection method to detect the corrosion state of the pipeline, and with the deep learning model, studied the corrosion rate changes of the pipeline. Finally, the corrosion rate of the pipeline was predicted to further obtain the remaining life of the pipeline. The final result proved that the method can accurately predict the remaining life of corroded pipeline.

10.1 Introduction

Generally, China mainly uses pipelines to transport natural gas. Because of the noise generated during transportation, there is little waste and almost no pollution. However, since gas pipelines are distributed underground, it is difficult to be noticed when gas pipelines are corroded or even perforated. It is easy to cause a large leakage accident and cause great consequences. Therefore, it is particularly important to find the corrosion status of the pipeline in time to predict the remaining life of the pipeline [1]. At present, there are many prediction methods for the residual life of pipeline corrosion, such as the residual life prediction model based on the finite element analysis method to predict the residual strength of the pipeline and predict the remaining life of the pipeline, relying on a large number of corrosion detection data. Reliability probabilistic residual life prediction model for secondary corrosion detection data and pipeline life prediction model based on artificial neural network theory that requires measurement of various corrosion factors and corrosion results. In recent years, the deep learning boom has emerged. The deep learning network structure is a network with a high level of nonlinear computing [2]. The obvious difference

---

W. Xinying (✉) · Z. Huiran · Z. Ruicheng · Z. Bin · H. Xuan · Z. Ying
School of Environmental and Safety Engineering, Changzhou University, Changzhou 213164, China

© The Author(s), under exclusive license to Springer Nature Singapore Pte Ltd. 2021

G. Shen et al. (eds.), *Advances in Acoustic Emission Technology*, Springer Proceedings in Physics 259, https://doi.org/10.1007/978-981-15-9837-1_10

compared with the shallow structure neural network is that the hidden layer of the network structure is more “deep” and can better characterize the complexity [3]. High-dimensional functions, optimized information sharing, and stronger representation. It can make up for the shortcomings of neural network applications and achieve better results. Deep learning provides a new method for predicting the remaining life of oil pipelines.

The deep learning network is applied to the field of pipeline residual life prediction, because deep learning has the advantage of approximating arbitrary continuous functions with arbitrary precision. The principle of the method is to use the acoustic emission detector to analyze certain parameters of the pipeline, such as energy and amplitude, when the pipeline is corroded. As a training sample, the DBN of the deep confidence network is trained, the weight is adjusted, and the model is established [4]. Then, the corresponding oil pipeline parameters are input into the trained DBN network model in real time, and the deep reliability network DBN judges whether the oil pipeline is corroded, and predicts the remaining life under the existing environmental stability conditions. This method improves the reliability of the remaining life prediction.

10.2 Basic Theory

10.2.1 Basic Ideas

Deep learning simulates the process of human brain analysis problems, and combines and learns low-level data to form more abstract high-level feature representations (attributes, categories, etc.) to improve the accuracy of subsequent recognition and classification.

Suppose system S has n layers, $S_1,\ldots,S_n$, whose input is 1 and output is 0. If output 0 is equal to input 1, that is, input 1 does not change after passing through this system, which means input 1 passes through each layer of S_i. There is no loss of information, or the lost information is redundant. The basic idea of deep learning is to stack multiple layers and use the output of the previous layer as the input of the next layer. In this way, the hierarchical representation of the input information is realized. It can be seen that this layered unsupervised feature learning is an important basis for deep learning. It maps the feature representation of the sample in the original space into a new feature space through layer-by-layer feature transformation, with a large number of simple Features build complex representations that eliminate the impact of changes in input data that are independent of learning tasks on learning performance [5], and retain information useful for learning tasks.

Deep learning can be understood as the extension and development of neural networks. It is a new field in machine learning research. The motivation is to establish a neural network that simulates human brain for analysis and learning. It interprets data according to the mechanism of human brain and forms a low-level feature.

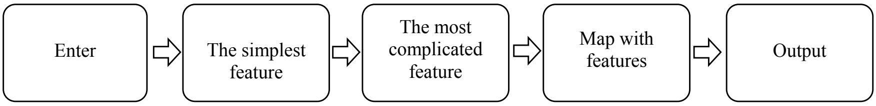

Fig. 10.1 Deep learning system training flow chart

More abstract high-level representations of attribute categories or features to discover distributed feature representations of data, as shown in Fig. 10.1. The dashed box indicates the information learned from the raw data.

10.2.2 Restricted Boltzmann Machine

Restricting the Boltzmann machine is a generative random neural network proposed by Smolensky in 1986. It comes from an improvement to the Boltzmann machine. Although BM has strong unsupervised learning ability, but the training time is long, and the distribution represented by BM cannot be accurately calculated, it is difficult to obtain a random sample obeying the distribution represented by BM. Therefore RBM was introduced to solve this problem [6].

In RBM, neurons are random, and only the two states are inactivated and activated, generally represented by binary 0 and 1, and the values are determined according to the probability and statistics rule. Like BM, RBM has a visible layer and a hidden layer, as shown in Fig. 10.1. But the difference is that there is no connection in the layer. This structure makes the activation condition of each hidden layer unit independent when RBM is given the visible layer unit state [7]; otherwise, when the hidden layer unit state is given, the activation condition of the visible layer unit is also independent.

The constrained Boltzmann machine is a bipartite graph model consisting of a visual layer v and a hidden layer h. All nodes are random binary variable nodes (0 or 1), and the full probability distribution satisfies the Blotzmann distribution $P(v', h)$. There is no connection between them. Whether in the visible or hidden layer, the nodes are independent, so in the case of known visual layers v:

$$P(h \mid v) = \prod_{i=1}^{n} P(h_i \mid v) \tag{1}$$

Similarly, under the premise that the hidden layer h is known, the visible layer can be obtained according to $P(v', h)$, and the $P\big(v', h\big)$ represents the visible layer unit estimated according to the hidden layer [8]. By adjusting the parameters, if the v obtained from the hidden layer is the same as the original visible layer v, the hidden layer can be considered as the characteristic representation of the input data of the visible layer, and Fig. 10.2 shows the training process of the RBM.

As shown in Fig. 10.3, if the number of layers of the hidden layer is increased, we can get the depth Boltzmann machine DBM, if the Bayesian belief network is used

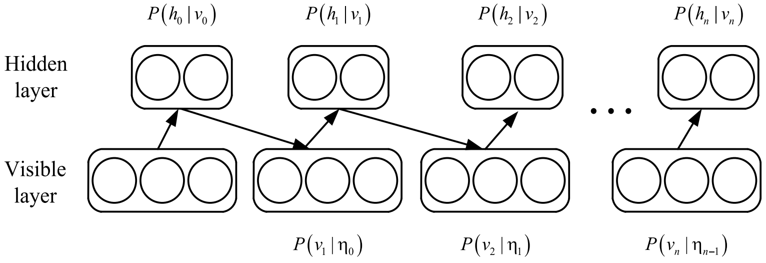
$P(h_0 | v_0)$
$P(h_1 | v_1)$
$P(h_2 | v_2)$
$P(h_n | v_n)$
Hidden layer
Visible layer
$P(v_1 | \eta_0)$
$P(v_2 | \eta_1)$
$P(v_n | \eta_{n-1})$

Fig. 10.2 RBM training process

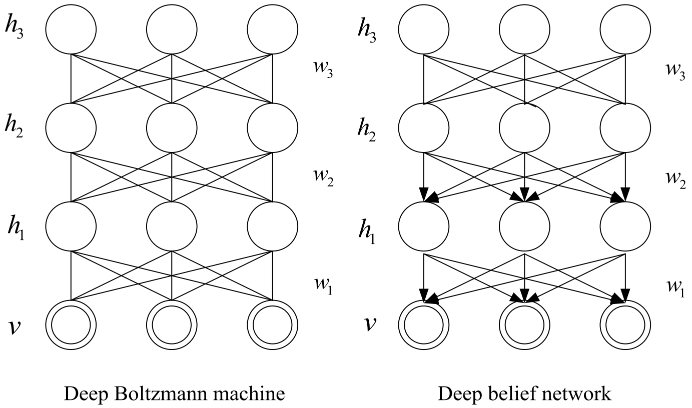
h_3
h_2
h_1
v
w_3
w_2
w_1
Deep Boltzmann machine
Deep belief network

Fig. 10.3 Typical deep network

in the part close to the visible layer, and the part farthest from the visible layer. Still using RBM, you can get a deep confidence network.

10.2.3 *Deep Reliability Network*

The deep confidence network is a Bayesian probability generation model consisting of multiple layers of random hidden variables. The upper two layers have undirected symmetric connections, and the lower layers get directed connections from the upper layer. As shown in Fig. 10.3, the basic structural unit of the DBM is an RBM, and the number of visible layer nodes of each RBM unit is equal to the number of hidden layer nodes of the previous RBM unit.

In the deep confidence network framework, the top two layers constitute the associative memory, and the connections between the other layers are determined by the top-down generated weights. In the training process, the value of the visible layer unit is first mapped to the hidden layer unit, and then the visible layer unit is reconstructed by the hidden layer unit, and the new visible layer unit is mapped to the hidden layer unit again to obtain a new hidden layer [6]. The unit, this step of reversing and retreating is called Gibbs sampling. Since the difference in probability distribution between the visual layer input and the hidden layer activation unit is the main basis for weight update, the contrast divergence algorithm is used to pre-train to obtain the weight of the generated model, and the training time is significantly reduced, requiring only a small amount. It can converge in a few steps.

For the top two layers, the output of the lower layer provides relevant reference clues to the top layer. The top layer links the output to its memory content based on these clues, and finally completes the discriminant classification task. The performance of the network after this processing is better than that of the BP algorithm alone, because the DBN BP algorithm only needs to perform a local search on the weight parameter space, and the training and convergence time is less.

RBM is like a brick of architecture. It is easy to learn the weight of connection, which makes DBN have flexible expansion performance. CDBN is one of the convolutional deep confidence networks [8]. CD-BN takes into account the two-dimensional structure information of the image, and uses the spatial domain relationship of the neighboring pixels to achieve the transformation invariance of the generated model by convolving the RBM model, and can easily transform the high-dimensional image.

10.3 Deep Life Prediction of Deep Pipeline Network Pipeline

In this paper, the deep confidence network prediction method is used to realize the remaining life prediction of pipelines. The feasibility is as follows:

(1) When using the acoustic emission detection method, the corroded gas pipeline has a special elastic wave [9]. When the detection background is constant and the detection position is fixed, the non-defective material has a uniform elastic wave frequency, and the defective frequency is only partially grayscale. Differences, these characteristics apply to the strong feature extraction capabilities of DBN.
(2) DBN combines elastic wave frequency processing and feature extraction into one, which greatly shortens the defect detection time and can better meet the online product detection. It also provides a theoretical basis for parallelization.
(3) DBN can quickly complete the weight training so that it can meet the production needs when the product background, location and model change.
(4) DBN combined with traditional identification network (usually adding a recognition layer at the top layer), not only can achieve signal processing, feature extraction [10], but also pattern recognition, providing data for further predicting pipeline corrosion rate and further predicting pipeline remaining life Processing route.

10.4 DBN-Based Pipeline Corrosion Residual Life Prediction Model

Establish a deep confidence prediction model for the residual life of corrosion pipelines on Matlab platform. Select sensitivity count, RMS voltage, rise time, amplitude, absolute energy, ring count, duration, peak count, and experimental corrosion time and/constructs a deep confidence pipeline residual life prediction model.

Under laboratory conditions, the acoustic emission technology and DBN algorithm are used to predict the corrosion rate of the gas pipeline. The specific steps are as follows:

(1) Acoustic emission detection data and recording time at different times during the pipeline corrosion process are collected and divided into test sets and training sets.
(2) Establish a DBN-based pipeline residual life prediction model.
(3) Input the training sample into the established DBN-based pipeline residual life prediction model, input data to the first RBM, and train the output data as the input data of the next layer, and then cycle until All RBM learning is done.
(4) According to the tagged data and classification error in the training sample, the parameters are fine-tuned from the top layer to the lowest layer in the DBN model until the training of the entire DBN model is completed.
(5) Input the test sample into the trained DBN classification model for classification performance test.
(6) The output pipe corrosion rate prediction result, combined with the time and the pipe specification thickness to obtain the remaining life.

10.5 Implementation of Deep Confidence Model in Pipeline Corrosion Prediction

Acquire acoustic emission signal data of a pipeline under different corrosion conditions [11]. The test pipe size is X720 mm, X10 mm, and the initial wall thickness of the oil and gas pipeline is 8.0 mm. The section of the pipe is partially immersed in a low-concentration acidic solvent to accelerate the simulated corrosion, and the acoustic emission detection is performed after a certain time.

Time domain analysis was carried out on the corrosion acoustic emission signal of the oil and gas pipeline. According to the results of time domain analysis, the frequency domain analysis results of acoustic emission signals with other uncorroded areas show that under different corrosion states, the acoustic emission signal frequency of the corrosion state is very different, so it can be based on the frequency information of the acoustic emission signal. Judging the corrosion state of the oil and gas pipeline, the corrosion of the oil and gas pipeline can be successfully detected [12], and the specific corrosion state and speed of the oil and gas pipeline can be determined according to the analysis result of the acoustic emission signal. The corrosion

Table 10.1 Corrosion actual monitoring data

Time (week)	Corrosion rate/mm·a^{-1}
1	0.7283
2	0.6842
3	0.6151
4	0.5476
5	0.4098
6	0.4123
7	0.4014

rate values measured in one of the oil and gas pipelines in recent years are selected as examples. The deep learning model is established to predict the development of corrosion rate (Table 10.1).

As the input sample of the deep learning network, the test data is written by MatLab software, and the appropriate RBM is selected for training to establish a deep confidence network prediction model. The measured value is then simulated as the input value of the network. The predicted result is shown in Table 10.2.

Compared with the measured value, the calculated C value is 0.0736, and the small error probability P is 1.0. It can be seen that the depth learning network prediction accuracy meets the requirements (Fig. 10.4).

In order to verify the reliability of the method, the method proposed in this paper is compared with the prediction performance of the pipeline corrosion rate prediction model based on BP network. Seamless steel pipes with nominal diameters of DN6, DN15, and DN20 are selected for the acoustic corrosion monitoring experiments of pipeline, And input into the DBN-based pipeline corrosion prediction model, and select weeks 3 to 8 as the verification time. Compare the prediction results of the DBN-based pipeline corrosion rate prediction model with the BP network-based pipeline corrosion rate prediction results, and use the average relative To evaluate the error, the calculation formula is as follows:

$$e_{mde} = \frac{1}{n}\sum_{i=1}^{n}\left|\frac{y_i - \widehat{y_i}}{y_i}\right| \times 100\% \tag{2}$$

Table 10.2 Deep learning network prediction model prediction result

Time (week)	Corrosion rate/mm·a^{-1}
1	0.71898
2	0.69373
3	0.62729
4	0.53237
5	0.41784
6	0.41179
7	0.40127

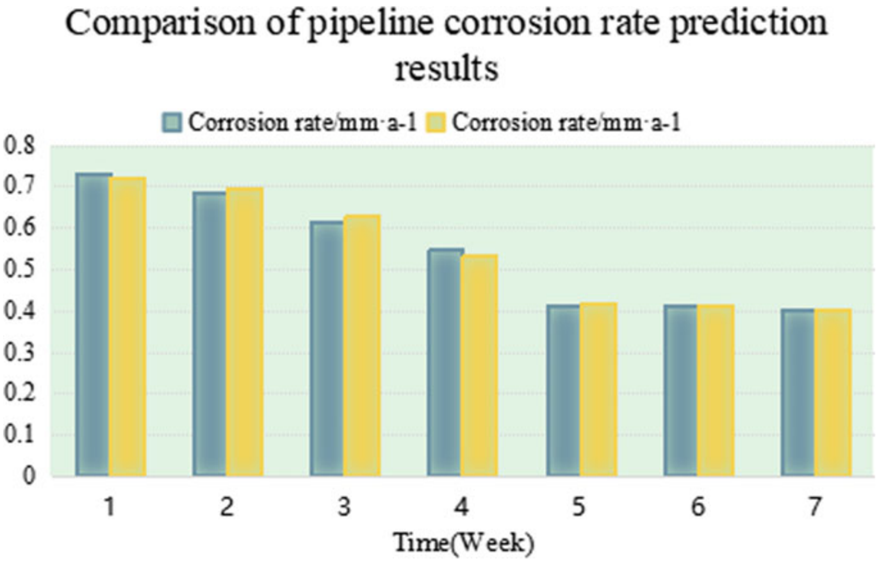

Fig. 10.4 Comparison of pipeline corrosion rate prediction results

The average relative errors obtained are shown in Table 10.3.

According to the above table, under the basic conditions of a large amount of experimental data, compared with the BP network-based pipeline corrosion rate prediction model, the average relative error of the prediction results of the DBN pipeline corrosion rate prediction model is smaller, indicating that the method proposed in this paper is more in line with the actual situation. It is scientific (Fig. 10.5).

According to the predicted corrosion rate of the pipeline, combined with the thickness of the pipe wall, the remaining life of the pipeline can be known. The area of the shadow in the figure is calculated by calculus, that is, the corrosion depth of the pipeline. When the corrosion depth is equal to the initial thickness of the pipe wall, the pipe will be pierced. Time is the remaining life of the pipeline, providing advice on the routine maintenance of the gas pipeline.

Table 10.3 Average relative errors of the two algorithms

Algorithm model	Monitoring pipeline corrosion rate(mm·a^{-1})
BP	0.054
DBN	0.023

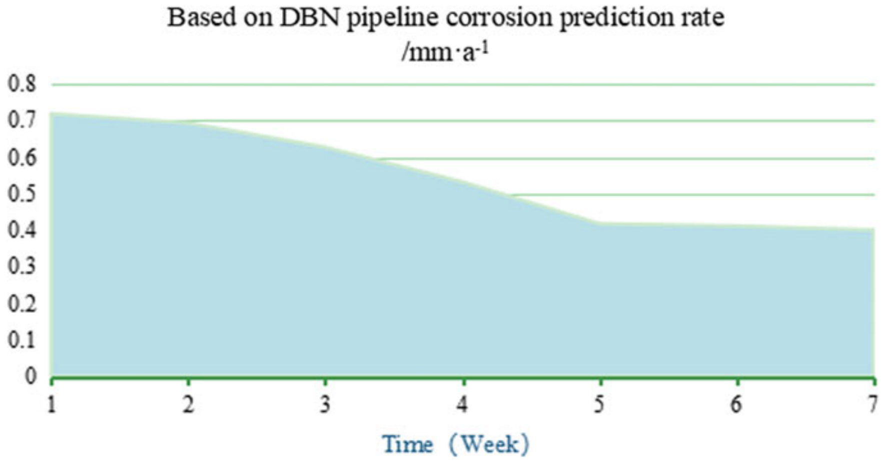

Fig. 10.5 Deep learning network prediction model prediction result

10.6 Conclusion

The artificial intelligence detection method based on deep learning is an important aspect of the future development of pipeline detection [13]. The article first introduces the basic ideas of deep learning and the system structure, including the basic model of the network, the network formation method and model structure, and the training method. The feasibility of applying the pipeline corrosion detection in deep learning system is discussed and further applied. Combined with the test, the corrosion life prediction method of gas pipeline based on deep confidence network proposed in this paper can effectively predict the corrosion rate of the pipeline with a minimum error probability of 1.0. Combined with the corrosion time and the design of the wall thickness, the remaining life of the pipeline is finally obtained. At present, there are many kinds of techniques for pipeline corrosion detection. Relevant scholars have studied and improved them, but they all have certain limitations. According to the corrosion characteristics and types of pipelines, appropriate detection methods should be selected to accurately predict pipeline life. Prevent accidents caused by corrosion and leakage of gas pipelines.

References

1. Chindaprasirt, Mechanical properties, microstructure and drying shrinkage of hybrid fly ash-basalt fiber geopolymer paste. Construct Build. Mater **186**(62–70) (2018)
2. A.P. Bhardwaj, T.C. Guedes Soares, M. S. Azad, W. Punurai, P. Asavadorndeja, Reliability assessment of thick high strength pipelines with corrosion defects. Int. J. Pressure Vessels Piping **177**(103982)
3. V. Niesen, M. Gould, Detecting pipeline leaks. Mech. Eng. **139**(11), 34–39 (2017)

4. Q. Wang, W. Zhou, A new burst pressure model for thin-walled pipe elbows containing metal-loss corrosion defects. Eng. Struct. **200**(109720) (2019)
5. M. Elleuch, N. Tagougui, M. Kherallah, Optimization of DBN using regularization methods applied for recognizing arabic handwritten script. Procedia Comput. Sci. **108**(6), 2292–2297 (2017)
6. G. Lipeng, L. Yong, Research on gear fault diagnosis based on the combination of isometric mapping and DBN. J. Mech. Strength **41**(05), 1029–1034 (2019)
7. L. Chunliu, Z. Zheng, Application of improved depth confidence network in urban water consumption prediction. Software Guide **11**, 1–6 (2019)
8. M. Elleuch, N. Tagougui, M. Kherallah, Optimization of DBN using regularization methods applied for recognizing Arabic handwritten script. Procedia Comput. Sci. **108**, 2292–2297 (2018)
9. W. Fang, W. Yuangen, L. Lin, Feasibility study on Dr detection of urban gas pipeline. Pipeline Technique Equipment **05**, 58–62 (2019)
10. A. R. Triki, M. B. Blaschko, Y. M. Jung, S. Song, H. J. Han, Intraoperative margin assessment of human breast tissue in optical coherence tomography images using deep neural networks. Computerized Med Imaging Graph **69**, 21–32 (2018)
11. W. Jianye, W. Huijie, Z. Guangrao, Damaged corrosion on the buried steel gas pipeline corrosion leakage detection and corrective. Total Corrosion Control **33**(04), 102–106 (2019)
12. W. Xinying, J. Zhiwei, Research on multi-information fusion urban gas pipeline leakage diagnosis technology. China Saf. Sci. J. **24**(6), 165–171 (2014)
13. F. N. Varela, M. Y. Tan, M. Forsyth, A novel approach for monitoring pipeline corrosion under disbonded coatings, in *2014 10th International Pipeline Conference* (2014)

Chapter 11

Improving Bearing Diagnostic Performance by Using New Discriminatory Fault-Feature Evaluation

Viet Tra and Jong-Myon Kim

Abstract Locating different defect types in bearings using the information of the characteristic frequencies in the envelope power spectrum of analyzed acoustic emission (AE) signals has been widely utilized. However, this approach only shows effectiveness as the rotational speed of bearing elements is constant. In contrast, if the bearing speed frequently alters during operation, the value of these characteristic frequencies is not stable, therefore, it is useless for diagnostic purposes. In order to resolve this issue, this study proposes an approach that (a) adopts heterogeneous feature modes to extract as many statistical features as possible in transformed domains (i.e., the time domain, the frequency domain, and the wavelet domain); (b) explores the most discriminatory features using new feature selection scheme. The scheme is the combination of the genetic algorithm (GA)-based feature analysis and the k-nearest neighbors (k-NN); (c) the defect types of a typical bearing are categorized by the k-NN-based classifier. The performance of the proposed method is validated by two datasets of AE samples measured from our bearing testbed.

11.1 Introduction

It is common knowledge that bearings are important components in induction motors. However, they are the primary roots of collapse in such motors. Without early detection of incipient defects occurring on the surface of bearing elements, more chances are the equipment is broken down. This leads to the interruption of productions and exorbitant repair costs. Therefore, operators need to have timely maintenance of such bearing elements.

Among common bearing diagnostic methodologies, vibration signal-based approaches have long been used for the applications of bearing diagnosis, using informative information lying in the moderate frequency band of the characterizing vibration signal. However, in recent time acoustic emission (AE) signal-based analyses have gradually placed a vital role in the field of bearing fault diagnosis. The

---

V. Tra (✉) · J.-M. Kim
School of IT Convergence, University of Ulsan, Ulsan 680-749, South Korea
e-mail: traviet.vt@gmail.com

© The Author(s), under exclusive license to Springer Nature Singapore Pte Ltd. 2021

G. Shen et al. (eds.), *Advances in Acoustic Emission Technology*, Springer Proceedings in Physics 259, https://doi.org/10.1007/978-981-15-9837-1_11

reason is that characterizing AE signals are highly sensitive to the low-energy acoustic emissions released by developing cracks in bearings [1, 2]. For this reason, this study designed a bearing fault diagnostic model with the input of AE signals.

The envelope power spectrum-based analysis is the notable approach that uses the information of characteristic frequencies located in the envelope spectrum of the signal. The location of these frequencies is closely related to the defective condition of a bearing. However, these characteristic frequencies are not only dependent on the crack types of the bearing but also are heavily affected by the rotational speed of elements in a bearing. In other words, this approach is not effective when being applied in the context of variable speed. One ideal alternative, which is not affected by change of operating speed, is the data-driven approach. The fundamental of this approach is trying to extract as many feature signatures as possible in transformed domains. These features serve as input to a classification model to determine defective status as well as the fault type of the bearing. However, it seems to be impossible to assure that all extracted features are valuable for diagnostic purposes. Some features may be relevant and redundant which are likely to deteriorate the classification performance. Therefore, the feature evaluation step is necessary to select the most useful fault-signatures in a given plentiful candidate pool. Through this step, the dimension of the feature vector is reduced while the characterizing information regarding the device's status is still retained.

Two representative feature-selection methods based on the foundation of component analyses are principal component analysis (PCA) [3] and linear discriminant analysis (LDA) [4]. The PCA method compresses and transforms the original fault-features into principal components that can reflect the symptom of a bearing [5]. However, due to the lack of means to calculate inter-category separability estimation, this approach still faces the problem of conserving the most discriminative features. In contrast, LDA, with the ability to utilize the information of between-category and within-category scatter matrices, has shown a great performance in evaluating and selecting discriminative features among original potential fault-signatures. However, this approach still exits shortcomings. The penalty graph that represents inter-category separability is sometimes not able to reflect neighborhood relationships between various categories. As a result, the quality of the selected feature-set can suffer which deteriorates the model's classification performance. These limitations have prompted us to propose a new genetic algorithm (GA)-based feature analysis methodology that incorporates well with the k-nearest neighbors (k-NN) classifier. Experimental outcomes have shown the outstanding ability of the proposed scheme in picking up the most discriminatory fault-features in a given original candidate pool, regardless of the distribution of initial fault-signatures. In terms of a classification module, this study uses the k-nearest neighbors (k-NN) classifier, a nonparametric method that operates well with a limited training set. Besides, it is also remarkable with greater classification speed, compared to other state-of-the-art classification algorithms [6].

Following this section, we describe the proposed methodology of bearing fault diagnostic model in Sect. 11.2. Section 11.3 illustrates solid experiments to prove the model's effectiveness. Conclusions are finally shortened in Sect. 11.4.

11.2 The Proposed Diagnostic Methodology for Bearings in Induction Motors

The pictorial diagram in Fig. 11.1 demonstrates modules and the flowchart of the proposed bearing diagnostic system. Overall, the diagnostic system begins with extracting potential features from input measured signals in the transformed domains and ends with detecting and categorizing bearing-fault types. To begin with, the statistical calculations of signals in the time domain, the frequency domain, and the wavelet domain are used to extract fault features from characterizing signals. Once fault-signatures are extracted, they are analyzed and validated to find the most discriminative traits among them. This step is carried out by the new feature-selection scheme based on the combination of the GA algorithm and the k-NN. The whole model ends with the determination of the status and the fault type of the bearing, using the k-NN classifier.

11.2.1 *Hybrid Feature Mode*

Determining the most potential features in a larger number of characteristics without prior knowledge is a harsh task of most researchers. Therefore, this study tried to use different feature modes to extract as many statistical features as possible. This procedure helps to avoid missing crucial information characterizing the symptom of a bearing. Such feature paradigms are then combined in parallel to create a heterogeneous feature pool. In this study, a total of 38 fault-signatures, which are statistical values of signals in the time domain, the frequency domain, and the wavelet domain, are extracted. To be specific, 16 features are extracted in the time domain which are peak value (PV), root mean square (RMS), kurtosis value (KV), crest factor (CF), clearance factor (CRF), impulse factor (IF), shape factor (SF), entropy value (EV), skewness value (SV), square mean root (SMR), 5th normalized moment, 6th normalized moment, mean value (MV), peak-to-peak (PPV), margin factor (MF), kurtosis factor (KF); six features that represent the typical characteristics of bearings

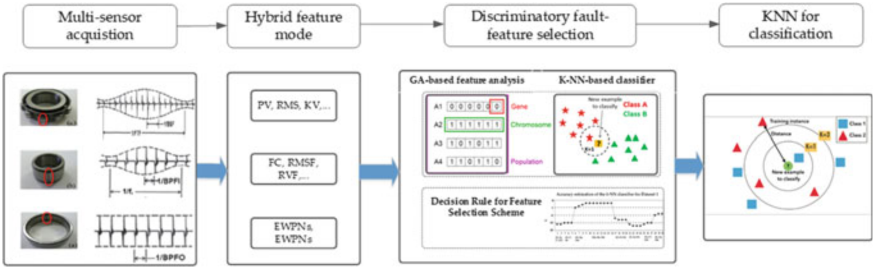
Multi-sensor acquistion
Hybrid feature mode
Discriminatory fault-feature selection
KNN for classification
1/BPFI
1/BPFO
PV, RMS, KV,...
FC, RMSF, RVF,...
EWPNs, EWPNs
GA-based feature analysis
K-NN-based classifier
Gene
Chromosome
Population
Class A
Class B
Decision Rule for Feature Selection Scheme
Class 1
Class 2

Fig. 11.1 The flowchart of the proposed bearing fault diagnostic model

in the frequency domain, including frequency center (FC), RMS frequency (RMSF), root variance frequency (RVF), kurtosis frequency (KF), entropy frequency (EF), sum square frequency (SSF) [2]; and 16 features which are the relative energy in a wavelet packet node (REWPN) and the entropy in a wavelet packet node (EWPN) [7]. However, because the number of features in a pool is quite large and redundant, it is essential to have a proper feature selection technique so that we can withdraw redundant features but still retain informative features.

11.2.2 GA-Based Fault Feature Selection

The genetic algorithm (GA), which is the hypothesis of Darwinian about natural selection and genetic nature in biological systems, has been a notable algorithm in generating optimal solutions for search problems. Determining the most optimal features among numerous options is a representation of search problems, in which a set of potential features (i.e., a feature vector) is considered as an individual in a population. In order to apply the genetic algorithm in our feature-selection scheme, each candidate fault-feature in the feature-pool is treated as a gene in a chromosome. The value of a gene is 1 if the corresponding feature is considered to be useful and to need to be conserved. In contrast, if a specific feature is determined redundant, the corresponding gene is assigned a value of 0. In order to search exhaustively potential solutions, a series of iterative generational computations are implemented. For each iteration, new offspring is randomly generated by the process of crossover or mutation to create the successive population. Since the genetic algorithm utilizes an objective function or fitness function to evaluate the quality of candidate solutions, so it is crucial to design a fitness function that matches well to the problem. In this study, the Gaussian radial basis function (RBF), which is able to measure the similarity of two input samples, is used as a kernel of the GA-based feature-selection scheme.

$$k(x, z) = \exp(-\gamma \|x - z\|), \tag{11.1}$$

where $\gamma = 1\big/2\sigma^2$ and σ is an adjustable parameter. This parameter is selected via experimental tests and is carefully tuned into the scheme. From (11.1), it makes sense that the *within-category RBF* value and *between-category RBF* value of two input samples x and z belonging to the same category are expected as (11.2) and (11.3), respectively

$$k(x, z) \approx 1, \forall x, z \in C_i, \forall i = 1, 2, \ldots, L, \tag{11.2}$$

$$k(x, z) \approx 0, \forall x \in C_i, \forall z \in C_j, \forall i, j = 1, 2, \ldots, L, i \neq j, \tag{11.3}$$

where C_i is a set of samples in the category i, $i = 1, 2, \ldots, L$, and L is the number of categories. Figures 11.2 and 11.3 illustrate the *within-category RBF* values and

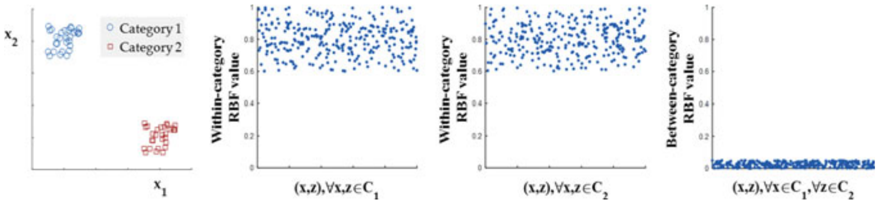

Fig. 11.2 Within-category RBF values (intracategory compactness) and between-category RBF values (intercategory separability) of two separable categories

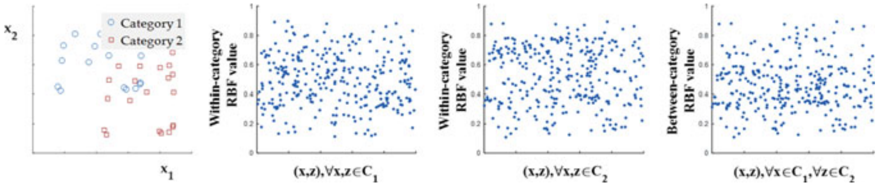

Fig. 11.3 Within-category RBF values (intracategory compactness) and between-category RBF values (intercategory separability) of two indistinguishable categories

between-category RBF values of samples that belong to two separable categories and two indistinguishable categories in terms of a visualization perspective. From Fig. 11.2, it is noticeable that when the clusters representing samples in two categories are highly separable, the *within-category RBF* values for each category are high, while the *between-category RBF* values are close to 0. By contrast, when two categories are not clearly separable, both the *within-category RBF* values and the *between-category RBF* values are widely distributed in the range from 0.2 to 1 (Fig. 11.3).

From the two above properties, we designed a new fitness function that covers well the problem in this study. Two entities, which are $RBF_{within}(F_{mat})$, and $RBF_{between}(F_{mat})$, are defined. The first one, $RBF_{within}(F_{mat})$, is the mean of the *within-category RBF* values calculated from F_{mat}. F_{mat} is the $L \times M \times N$ matrix where L is the number of categories, M is a total number of training samples in each category, and N is a number of fault-features in every solution:

$$RBF_{within}(F_{mat}) = \frac{1}{L \times M} \sum_{i=1}^{L} \sum_{j=1}^{M} \sum_{k=1}^{M} k(F_{mat}(i, j, :), F_{mat}(i, k, :)) \tag{11.4}$$

The second criterion, $RBF_{between}(F_{mat})$, is the mean of *between-category RBF* values calculated from F_{mat}:

$$RBF_{between}(F_{mat}) = \frac{1}{L \times (L-1) \times M^2} \sum_{i=1}^{L} \sum_{\substack{j=1 \\ j \neq i}}^{L} \sum_{k=1}^{M} \sum_{l=1}^{M} k(F_{mat}(i, k, :), F_{mat}(j, l, :)). \tag{11.5}$$

It is common knowledge that the best solution is the feature-set that represents categories in the way that minimizes the intracategory compactness and maximizes the intercategory separability between them. From (11.4) and (11.5), it is clear that the two above conditions is proportional to the small value of $RBF_{between}(F_{mat})$, and the large value of $RBF_{within}(F_{mat})$. The fitness function is ultimately defined as follows:

$$Obj(F_{mat}) = 1 - RBF_{within}(F_{mat}) + RBF_{between}(F_{mat}). \tag{11.6}$$

11.2.3 Feature Evaluation Metric Using k-NN-Based Classifier

11.2.3.1 k-NN-Based Classifier

With the subtle architecture and the ability to generalize classification problems quickly with a limited dataset, the k-nearest neighbors (k-NN) algorithm has been widely used as a flexible and straightforward classifier. As a type of a non-parametric method, the k-NN uses a voting scheme to classify samples. More specifically, to determine what category a specific sample belongs to, the k-NN utilizes the information of voting papers of that sample's nearest neighbors. This means that there is no training phase in the k-NN algorithm and to solve a classification task, training samples are stored in memory and are used as reference points to determine the category of a new sample. Operating with such the mechanism, the input data needs to be pre-processed in a way that reduces the dimension of the input feature vector. Without this procedure, the k-NN classifier will certainly suffer from severe computational complexity. For this reason, it is extremely important to adopt a feature-selection scheme to select discriminatory features among potential ones and reduce the dimension of the input vector as well.

To design the k-NN classifier, researchers need to pick up and tune carefully two vital parameters (i.e., the parameter k that defines the number of neighbors of an objective and the type of distance metric). While the value of k can be chosen randomly or through a cross-validation process, the distance metric is chosen among popular ones. In this study, the Euclidian distance is used as the metric due to its effectiveness and simplicity.

11.2.3.2 Determining the Most Discriminative Fault Features Using GA-Based Feature Analysis and k-NN-Based Classifier

The quality of candidate feature-sets is assessed by using the GA-based feature-selection scheme as described in Sect. 2.2. In order to reduce the variability as well as increase the robustness of the optimal solution determined by the scheme, the study adopts k-fold cross-validation (k-cv) to the original dataset (i.e., k = 2). This means the dataset is divided into two parts or sub-datasets. One sub-dataset is used to determine the most discriminatory feature-set or the optimal solution and another sub-dataset is utilized to validate the fitness of the solution via calculating the classification accuracy of the k-NN classifier. This process is repeated until each sub-dataset is reserved as either the training dataset or the test dataset at least once. Correspondingly, k candidate feature-sets are yielded for each iteration.

To search for exhaustly possible solutions, we repeat the above procedure $N_{interations}$ times (i.e., $N_{interations} = 15$). It means after $N_{interations}$, the total of $N_{interations} \times k$(i.e., 30) optimal feature-sets are determined. In order to pick up the best among them, a decision rule is proposed in which the decision is made based on 2 criteria. The first one is the estimated diagnostic performance of a solution and the second is the occurring frequency of the candidates. The most optimal feature-set is the one that helps the k-NN classifier achieve the highest performance and improve the model's robustness. In this study, the estimated classification accuracy, or predicted classification accuracy (CA), is determined as follows:

$$CA = \frac{\sum_L N_{TP}}{N_{samples}} \times 100(\%) \qquad (11.7)$$

where L is the number of categories, N_{TP} is the number of samples in the test dataset belonging to the category i that are exactly classified to be the category i, and $N_{samples}$ is the total number of samples in the test dataset.

11.3 Experimental Results and Discussion

11.3.1 Training Dataset and Test Dataset Configuration

This study uses datasets made of acoustic emission (AE) signals that are obtained in the conditions of a free-defect (BFD) and incipient single defects at different bearing elements i.e., a crack on the outer raceway (BCO), crack on the inner raceway (BCI), and crack on the roller (BCR). Two datasets, according to two different rotating speeds (i.e., 300 revolutions per minute (r/min) and 500 (r/m)), are used to validate the effectiveness of the proposed method. The total number of samples in each dataset is $N_{Classes} \times N_{Signals}$ or 360 samples, where $N_{Classes}$ is the number of defect types ($N_{Classes} = 4$), and $N_{Signals}$ is the number of AE signal segments collected under

Table 11.1 Description of the datasets for two different crack sizes

Dataset with single and compound seeded bearing failures		Revolutions per minute (r/min)	Crack size		
			Length (mm)	Width (mm)	Depth (mm)
Dataset 1	Training set	300 RPM	3	0.35	0.30
	Test set	300 RPM		0.35	0.30
Dataset 2	Training set	500 RPM	3	0.35	0.30
	Test set	500 RPM		0.35	0.30

each bearing condition ($N_{Signals} = 90$). Each segmented signal is 5 s in length. The datasets are presented in detail as given in Table 11.1.

11.3.2 Most Optimal Fault-Feature Sets

To select the most optimal feature-set, we first adopt the GA-based feature-selection scheme to find potential feature-sets. By using the k-cv with k is 2 and run the scheme 15 times (i.e., $N_{interations} = 15$ and $\mathrm{k} = 2$ for k-cv), the total of 30 feature-sets are yielded. Following this, the decision rule is applied via two steps. First, the classification accuracies of the k-NN classifier, according to different feature-sets, are estimated using 11.7). Second, the occurring frequency of each feature-set in the 30 original solutions is considered to decide which feature-set will be chosen as the best solution. Figure 11.4 illustrates the predictive accuracies of the k-NN classifier, according to the 30 candidate solutions searched by the proposed feature-selection scheme.

Overall, it is clear that the k-NN classifier's performance is heavily dependent on the choice of an input feature-set. Also, the model's robustness is improved with some feature-sets and vice versa. More specifically, as using dataset 1 for validation, the k-NN classifier achieves the highest predicted accuracy values with the input feature-set of f_5, f_7, and f_{10}, at approximately 98%. This feature-set also helps the model to be robust as its classification performance is stable over different testing times. Whereas, the predictive capacity of the model tends to be deteriorated as using some other input-feature sets. The reason behind this result is that the ability to represent samples of different classes in the form of separate clusters depends on the choice of an input feature-set. In terms of dataset 2, the k-NN classifier's classification accuracies associated with different input feature-sets also shows a similar trend. The occurring frequency of the feature-set of f_2, f_{10}, and f_{13} is 4 and its according predicted accuracy is about 95%, relatively higher than most of the counterparts' figures. For the evidence described above, it is obvious that the optimal feature-set has a significant impact on the classifier's performance. Therefore, selecting the best solution among potential candidates must be the priority of the model's designers.

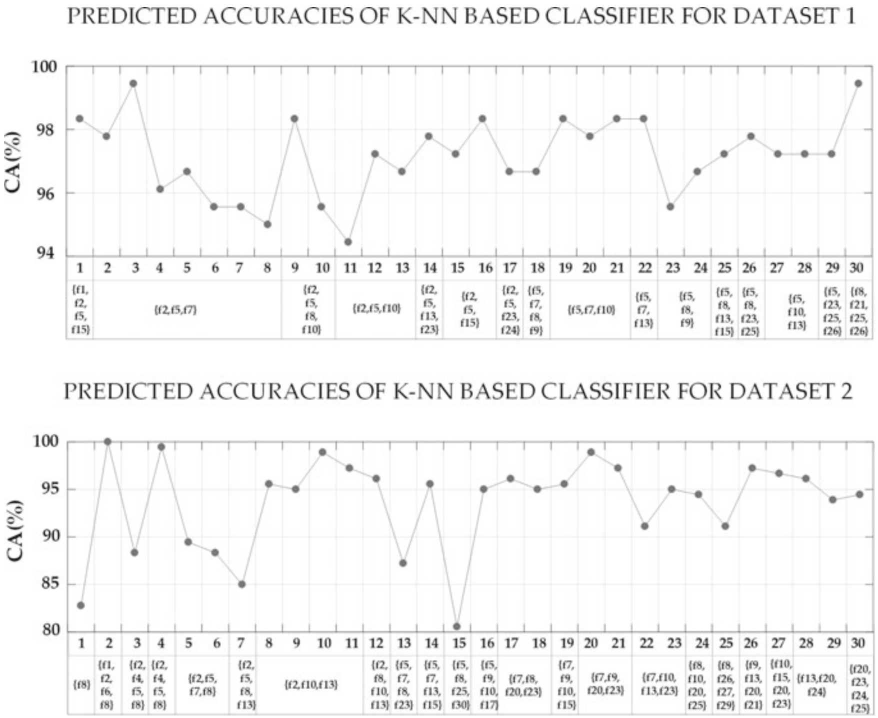

Fig. 11.4 Predicted classification accuracies of the k-NN-based classifier using 30 discriminatory feature subset candidates

Table 11.2 Summary of feature subsets determined by the proposed faul-signature analysis

Dataset	The most discriminatory feature subset
Dataset 1	$\{f_5, f_7, f_{10}\}$
Dataset 2	$\{f_2, f_{10}, f_{13}\}$

Based on the above analyses and the decision rule, the two most discriminatory feature sets, associate with two datasets, are determined as in Table 11.2.

11.3.3 *Efficacy of the New GA-Based Feature-Selection Scheme*

This section proves the outstanding quality of a new feature-evaluation scheme by comparing the predicted accuracy of the classifier utilizing the new-feature scheme and the figures of the classifier as applying two other state-of-the-art counterparts. These rival methods are principal component analysis (PCA) and independent component analysis (ICA). Such methods are a kind of the component analysis in which *n* optimal fault-features are determined according to *n* highest eigenvalues of a covariance matrix defined by the original feature space.

Table 11.3 shows the average classification accuracy of the k-NN classifier as its input is feature-sets selected by different feature-analysis schemes. To increase the reliability of the experimental results, we utilize k-cv scheme with $k = 3$ which means the initial dataset is divided into three folds. For each iteration, one of the three folds is reserved as the test dataset and the other two folds are exploited as the training dataset. The corresponding predicted classification accuracy is determined by using (11.7). Repeating the process until each fold is reserved as either the training dataset or the test dataset at least once. The average classification performance (ACA) of the model is determined by averaging three predicted accuracies according to three iterations in the process.

From Table 11.3, it is obvious that for both the datasets, the average classification accuracy of the classifier associated with our new feature-selection scheme is higher than the figures for two rivals. More specifically, in terms of dataset 1, the feature-set yielded by the proposed feature-selection scheme helps the k-NN classifier achieve the highest accuracy percentage, at 98.33%, much higher the figure of 77.7% for PCA, and the figure of 80.49% for ICA. The results are also similar in terms of dataset 2. While the figure for the proposed model is 97.22%, the accuracy percentages of those utilizing PCA and ICA are lower, at about 82%.

The reason behind this result is that although component analysis-based methods have shown their effectiveness in many areas, there is no rule to determine the ideal number of principal components. The wrong decision would deteriorate the quality of a feature-set. Also, due to the inability of measuring inter-category separability, the feature-sets yielded by two unsupervised approaches PCA and ICA are unable to represent samples in different categories separately. As a result, the models using these feature-sets have lower classification accuracy than those using the feature-set produced by supervised methods such as the proposed GA-based feature-selection scheme.

Table 11.3 Average classification accuracies of proposed model and other rival models

Datasets	Methodologies	ACA (%)
Dataset 1	PCA	77.7
	ICA	80.4
	Proposed method	98.3
Dataset 2	PCA	81.3
	ICA	82.4
	Proposed method	97.2

11.4 Conclusions

This study proposed the new feature-selection scheme that combines the GA-based feature analysis and the k-NN classifier. This scheme is integrated into the model for diagnosing bearing faults under variable operating conditions. The new feature-selection scheme proved its outstanding performance via experimental results. More specifically, the proposed scheme's output, which is the optimal feature-set, helps the classifier model achieve the classification accuracies of 98.33% and 97.22% in terms of dataset 1 and dataset 2, respectively. much higher than the figures of the two state-of-the-art rivals.

Acknowledgements This work was supported by the Korea Institute of Energy Technology Evaluation and Planning (KETEP) and the Ministry of Trade, Industry & Energy (MOTIE) of the Republic of Korea (Nos. 20162220100050, 20161120100350, 20172510102130). It was also funded in part by The Leading Human Resource Training Program of Regional Neo industry through the National Research Foundation of Korea (NRF) funded by the Ministry of Science, ICT and future Planning (NRF-2016H1D5A1910564), and in part by the Basic Science Research Program through the National Research Foundation of Korea (NRF) funded by the Ministry of Education (2016R1D1A3B03931927).

References

1. V. Tra, J. Kim, S.A. Khan, J.-M. Kim, Bearing fault diagnosis under variable speed using convolutional neural networks and the stochastic diagonal levenberg-marquardt algorithm. Sensors **17**(12), 2834 (2017)
2. V. Tra, J. Kim, S.A. Khan, J.-M. Kim, Incipient fault diagnosis in bearings under variable speed conditions using multiresolution analysis and a weighted committee machine, J. Acoust. Soc. Am. **142**(1), EL35–EL41 (2017)
3. M. Zhao, X. Jin, Z. Zhang, B. Li, Fault diagnosis of rolling element bearings via discriminative subspace learning: visualization and classification. Expert Syst. Appl. **41**(7), 3391–3401 (2014)
4. X. Jin, M. Zhao, T.W. Chow, M. Pecht, Motor bearing fault diagnosis using trace ratio linear discriminant analysis. IEEE Trans. Industr. Electron. **61**(5), 2441–2451 (2013)
5. V.H. Nguyen, J.-C. Golinval, Fault detection based on kernel principal component analysis. Eng. Struct. **32**(11), 3683–3691 (2010)
6. X. Wu et al., Top 10 algorithms in data mining. Knowl. Inf. Syst. **14**(1), 1–37 (2008)
7. R. Yan, R.X. Gao, X. Chen, Wavelets for fault diagnosis of rotary machines: a review with applications. Sig. Process. **96**, 1–15 (2014)

Chapter 12
Application of Kurtosis Analysis in Fault Detection of Rolling Bearing

Yang Yu, Yangyang Guo, and Ping Yang

Abstract As the joint of rotating machinery, rolling bearing plays an important role in the development of national industry. Its performance and working condition will directly affect the performance of the whole mechanical equipment. According to statistics, 30% of the faults in rotating machinery are caused by bearings. Therefore, the study of the fault mechanism of rolling bearings has practical significance for reducing the maintenance cost of equipment and ensuring the long-term safe and stable operation of equipment. In this paper, the traditional kurtosis analysis is improved, and equal time difference kurtosis analysis is created according to the practical application. Equal time difference kurtosis analysis is to calculate the kurtosis value of the data in a fixed time interval, which is easy to highlight the periodic characteristics of the signal, and is conducive to the identification and analysis of the acoustic emission signal. It can be seen from the analysis results that the method of equal time difference kurtosis analysis can make a good qualitative analysis on the damage degree of rolling bearing.

12.1 Introduction

In all kinds of mechanical operation, rolling bearing plays a very important role. The quality of rolling bearing is the key to ensure the safe operation of machinery. According to relevant statistics, about 30% of mechanical failures are caused by the damage of rolling bearings, and the high failure rate of rolling bearings has always been the focus of researchers [1]. There are many reasons for the fault of rolling bearing after running for a certain period of time, including unreasonable design, poor installation process, bad working environment, drastic load change, etc. [2]. These defects aggravate the deterioration of mechanical operation, resulting in the change of rolling bearing operation state, which will directly threaten the safety and normal service life of machinery. In high-speed operation, the abnormal change of rolling bearing will be intensified, and then a major accident will occur,

---

Y. Yu · Y. Guo (✉) · P. Yang
Shenyang University of Technology, Shenyang 110870, China
e-mail: 1316817411@qq.com

© The Author(s), under exclusive license to Springer Nature Singapore Pte Ltd. 2021

G. Shen et al. (eds.), *Advances in Acoustic Emission Technology*, Springer Proceedings in Physics 259, https://doi.org/10.1007/978-981-15-9837-1_12

resulting in incalculable loss. The importance of rolling bearing makes detection and maintenance become a long-term work. Because the service life of rolling bearing varies greatly under different working conditions, the maintenance period cannot be completely determined according to the service life [3–5]. Therefore, the traditional timing maintenance method is very unscientific, which not only wastes resources, but also can not guarantee the absolute safety of rotating machinery in operation.

Based on this situation, the method of equal time difference kurtosis analysis is proposed to diagnose the early fault of rolling bearing [6]. Through fault diagnosis to prevent the occurrence of faults, so as to avoid mechanical accidents due to the damage of rolling bearings, to ensure the safety of the running machinery.

12.2 Kurtosis Analysis Method

Let x(t) be a random acoustic emission signal, and have $x_1 = x\,(t)$, $x_2 = x\,(t + \tau_1) \ldots x_k = x\,(t + \tau_{k-1})$ (τ is the delay amount), the k-order moment m_k of random acoustic emission signal x(t) is defined as:

$$m_k(\tau_1 \ldots \tau_{k-1}) = E\big[x(t)x(t + \tau_1) \ldots x(t + \tau_{k-1})\big] \tag{12.1}$$

The higher-order cumulants of AE signals can be expressed by higher-order moments. For zero mean signals, the fourth-order cumulants are:

$$\begin{aligned} c_4(\tau_1, \tau_2, \tau_3) &= m_4(\tau_1, \tau_2, \tau_3) - m_2(\tau_1)m_2(\tau_3 - \tau_2) \\ &- m_2(\tau_2)m_2(\tau_3 - \tau_1) - m_2(\tau_3)m_2(\tau_2 - \tau_1) \end{aligned} \tag{12.2}$$

When $\tau1 = \tau2 = \tau3 = 0$, from (12.2):

$$c_4(0, 0, 0) = m_4(0, 0, 0) - 3m_2^2(0) = E[x_4(t)] - 3\{E[x_2(t)]\}^2 \tag{12.3}$$

where, c4 (0, 0, 0) is the kurtosis of the acoustic emission signal, and the kurtosis of the zero mean random acoustic emission signal is defined as follows:

$$K = \frac{E[(x)4]}{\{E[(x)2]\}2} = \frac{1}{N}\sum_{i=1}^{N}\left(\frac{xi - \bar{X}}{\sigma x}\right)^4 \tag{12.4}$$

where formula (12.4): $\bar{X} = \frac{1}{N}\sum_{i=1}^{N} xi$,σ_x is the standard deviation, n is the signal length.

According to formula (12.4), the fourth-order cumulants of AE signal is kurtosis, because the high-order cumulants of Gaussian process is always 0, so kurtosis takes a low value for Gaussian signal. In fault diagnosis, the acoustic emission signal amplitude of normal rolling bearing presents normal distribution. When the rolling bearing fails, the amplitude of AE signal will deviate from the normal distribution, and kurtosis K reflects the deviation. The more serious the fault is, the greater the deviation degree is and the greater the kurtosis value is.

12.2.1 Equal Time Difference Kurtosis Analysis Method

In this paper, the traditional kurtosis analysis is improved. According to the actual needs, the equal time difference kurtosis analysis method is created, that is, the kurtosis analysis of the rolling bearing acoustic emission data collected in each fixed time interval. Kurtosis is an derived function to describe the spike of waveform, a numerical statistic reflecting the distribution characteristics of random variables, and a normalized fourth-order center distance, which is defined as:

$$\beta = \int_{-\infty}^{+\infty} x^4 P x d x \tag{12.5}$$

where x is the amplitude of the signal and P(x) is the probability density function of the signal.

When the signal data is the discrete-time data X_1, X_2, … ,X_N of N sampling points, kurtosis is defined as [7]:

$$\beta = \frac{1}{N} \sum_{i=1}^{N} X_i^4 \tag{12.6}$$

In the acoustic emission characteristic parameters, the effective voltage value is RMS [8, 9], which is defined as:

$$X_{RMS} = \sqrt{\sum_{i=1}^{N-1} \frac{1}{N} X_i^2} \tag{12.7}$$

Therefore, kurtosis coefficient K can be expressed as:

$$\mathrm{K} = \frac{\beta}{X_{RMS}^4} \tag{12.8}$$

Kurtosis processing can enlarge the energy of acoustic emission signal and suppress the energy of noise signal, which will highlight the acoustic emission signal well. When there is no acoustic emission signal, that is, when the material is intact, there is only noise signal [10]. At this time, the acoustic emission signal amplitude of rolling bearing presents normal distribution. The schematic diagram of kurtosis coefficient is shown in Fig. 12.1.

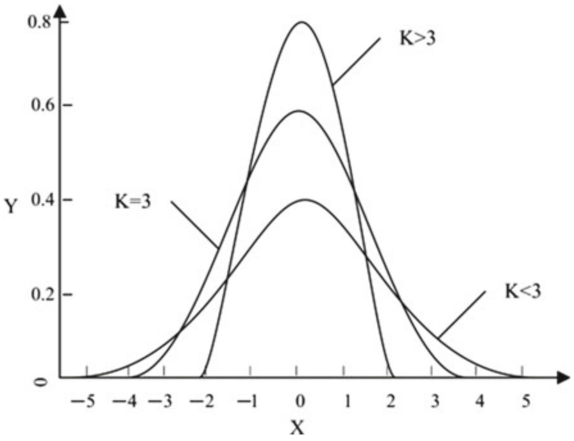

Fig. 12.1 Schematic diagram of kurtosis coefficient

When the rolling bearing operates without fault, the amplitude distribution of the collected acoustic emission signal is close to the normal distribution, and the kurtosis index value $K \approx 3$. With the occurrence and development of the fault, the probability density of the large amplitude in the acoustic emission signal increases, and the amplitude distribution of the rolling bearing acoustic emission signal deviates from the normal distribution, and the normal curve deviates or disperses, and the kurtosis value also increases. The larger the absolute value of kurtosis index is, the more serious the fault is. When $k > 4$, it means that the rolling bearing may have been damaged. When $k > 8$, it means that there is a big fault. At this time, we should replace the fault bearing in time to ensure the normal and safe operation of the machine.

12.3 Result

With the increasing amount of acoustic emission data collected, the kurtosis calculation contains more and more data. If the amount of data is too large, it may contain a lot of noise signals, so it is likely to hide some important information and lose the significance of kurtosis calculation. If the amount of data is too small, it will make the amount of information very small, and cannot highlight the acoustic emission signal of the rolling bearing, as well as the effect of noise suppression. Therefore, the selection of data volume should be appropriate. Therefore, in this paper, the rolling bearing with damage is taken as the experimental object, the equal time difference kurtosis analysis method is used to analyze the acoustic emission signal of the rolling bearing, and the kurtosis curves of different time differences are drawn for comparison.

Figure 12.2 shows that when the time interval is 2 s, there are many prominent kurtosis values greater than 3, which indicates that there are many noise interference signals. Figure 12.3 shows that when the time interval is 4 s, it has a preliminary

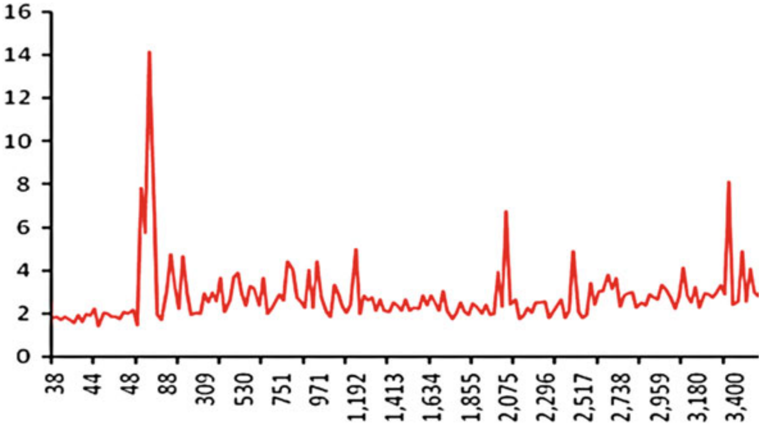

Fig. 12.2 Kurtosis analysis chart with time difference of 2 s

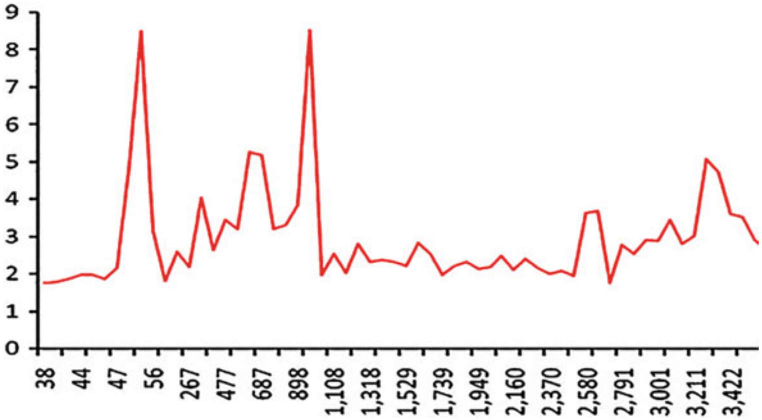

Fig. 12.3 Kurtosis analysis chart with time difference of 4 s

suppression effect on the interference signal and can clearly see the outstanding useful signal. It can be seen from Fig. 12.4 that the interference signal is further suppressed, which greatly highlights the useful signal. From Fig. 12.5, it can be clearly seen that all signals except useful ones have been greatly suppressed.

12.4 Conclusion

In this paper, the traditional kurtosis analysis method is improved, and the equal time difference kurtosis analysis method is established according to the practical application. Equal time difference kurtosis analysis is to calculate the kurtosis value of

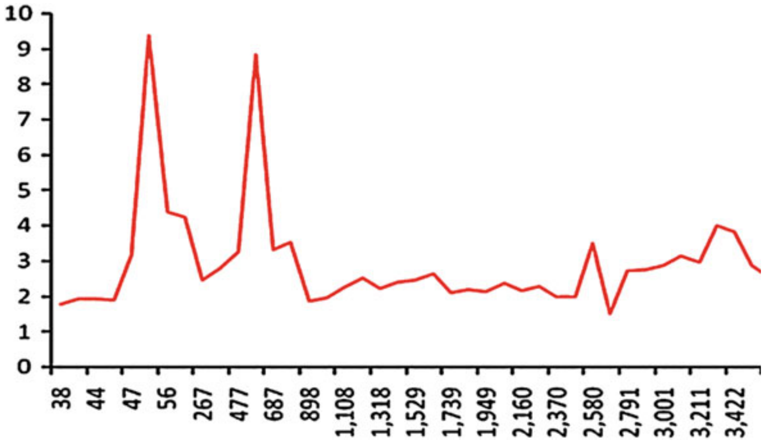

Fig. 12.4 Kurtosis analysis chart with time difference of 6 s

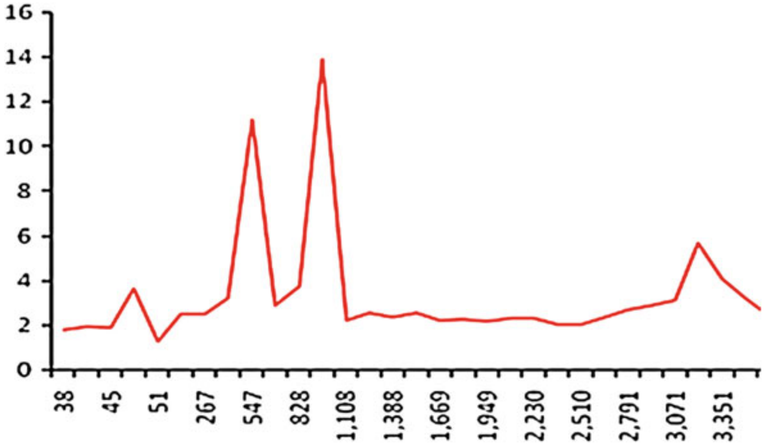

Fig. 12.5 Kurtosis analysis chart with time difference of 8 s

the data in a fixed time interval, which is easy to highlight the periodic characteristics of the signal, and is conducive to the identification and analysis of the acoustic emission signal. It can be seen from the results that the equal time difference kurtosis analysis method can well carry out qualitative analysis on the damage degree of rolling bearing.

References

1. B.L. Zhong, R. Huang, *Mechanical Fault Diagnosis* (Mechanical Industry Press, Beijing, 2002), pp. 25–43
2. T. Huang, H. Zhang, Research on fault diagnosis of rolling bearing by acoustic emission technology. J. Pet. Chem. Univ. **9**(1), 49–52 (1996)
3. Y. Jiao, J. Hou, G.H. Li, C. Chen, Acoustic emission signal processing technology and its application in rolling bearing detection. J. Hebei Univ. Sci. Technol. **34**(4), 1–2 (2013)
4. T. Kaewkongka, Y.H.J. Au, Application of acoustic emission to condition monitoring of rolling element bearing. Meas. Control **34**, 245–247 (2001)
5. H.B. Zhao, Research status and development direction of acoustic emission detection technology. Electron. World **21**(3), 193–194 (2014)
6. H.B Zhao, P. Wu, C.L. Xia, Study on the application of sectional kurtosis value to the diagnosis of acoustic emission of rolling bearing fault. Dev. Innov. Mech. Electr. Products **28**(6), 58–60 (2015)
7. B.B. James, M.R. Gary, Evaluation of the dispersional analysis method for fractal time series. Ann. Biomed. Eng. **4**, 50–54 (1995)
8. G.T. Shen, R.S. Geng, S.F. Liu, Parameter analysis method of acoustic emission signal. Nondestruct. Test. **24**(2), 72–77 (2002)
9. J. Yang, *Acoustic Emission Signal Processing and Analysis Technology*. (Jilin University, 2002)
10. A Choudhury, N. Tandon, Application acoustic emission technique for the detection of defects in rolling element bearing. Tribol. Int. **33**, 39–45 (2000)

Chapter 13
Fatigue Evolution of Ball Bearing with Improved Acoustic Emission Index

Zhihai Wang, Xiaoqin Liu, and Xing Wu

Abstract To obtain fatigue evolution information of ball bearing accurately, deficiency of the conventional acoustic emission (AE) monitoring indexes are analyzed. New acoustic emission monitoring index based on floating threshold and averaging method is proposed. Firstly, calculating the standard deviation of the original collected acoustic emission data. After that, to obtain floating threshold of each segment AE data with threshold shrinkage method. Then, trend analysis of seven improved acoustic emission indexes is carried out based on accelerated fatigue test data. Compared with the trend of conventional acoustic emission indexes and statistical indexes, the results show that: the improved AE index is more sensitive to the fatigue of ball bearing. Fatigue evolution information of the ball bearing can be given better. In the end, general evolution law of ball bearing is summarized with the test observation.

13.1 Introduction

Rolling bearing is one of the important components of rotating machinery. In the event of a rotating machinery failure, rolling bearing faults can account for up to 30% [1]. The fatigue damage information can be obtained from the state detection process data of rolling bearing in real time. It can effectively avoid the economic losses and even casualties caused by unexpected incidents. When an object is subjected to plastic deformation or fracture, it will release energy in the form of elastic stress waves which can be named acoustic emission. Fatigue damage information of ball bearing can be obtained earlier by AE technique than by vibration method [2, 3]. Basic fatigue information is obtained by the trend analysis with the conventional acoustic emission characteristics. The acoustic emission signal test of deep groove ball bearing was carried out by Al-Ghamd, etc. [4]. It is considered that the RMS and the maximum amplitude are good indexes. Achmad, etc. [5] did the research on time domain indexes

---

Z. Wang (✉) · X. Liu · X. Wu
Faculty of Mechanical and Electrical Engineering, Kunming University of Science and Technology, Kunming 650500, China
e-mail: 252481138@qq.com

© The Author(s), under exclusive license to Springer Nature Singapore Pte Ltd. 2021

G. Shen et al. (eds.), *Advances in Acoustic Emission Technology*, Springer Proceedings in Physics 259, https://doi.org/10.1007/978-981-15-9837-1_13

and spectrum envelope with acoustic emission signal. Yoshiok and Fujiwara [6]'s study points out that AE event rate can be used to predict the faults earlier than RMS of the vibration signal. Elforjani and Mba [7–9] carried out an accelerated fatigue test with SKF-51210 ball bearing. RMS and absolute energy information of event are considered to be the good performance degradation indexes. Then, Warren, etc. [10] analyzed the rolling contact fatigue process of hyperfine polished surface. It is pointed out that amplitude and RMS are more sensitive. The study of rolling contact [11] shows that there is a close relationship between the AE event count and the initial damage size of rolling surface. Filip, etc. [12] did trend analysis with event count, duration, rise time and amplitude. It is concluded that the ball bearing has two stages before the appearance of slight pitting. Abdullah, etc. [13] investigated RMS, amplitude and kurtosis. The relationship between acoustic emission duration and damage size was studied. There still some other scholars keep on doing the research with AE indexes to detect damages inside materials [14–16]. From the papers above, it can be fully demonstrated that acoustic emission technology is an effective means to detect the internal damage of materials from the studies above. The damage degree of ball bearing can be expressed by acoustic emission index.

Conventional AE indexes are specified from each AE event. The threshold voltage of acoustic emission events is usually determined manually. That is easy to introduce subjective errors. If AE data is large, and the fatigue life of ball bearing is long. It will discount computing efficiency greatly. It is not good for a real-time monitoring test. Moreover, the conventional acoustic emission index is difficult to correspond with statistical index in time. It is hard to make a comprehensive judgment of fatigue damage of ball bearings. To solve the problems above, a method of ball bearing fatigue monitoring with improved acoustic emission new index is proposed. Then, AE data from a self-made accelerated fatigue test rig for ball bearings are studied. Compared with the monitoring with conventional acoustic emission indexes and statistical indexes. A more comprehensive analysis and damage sensitive indexes of ball bearing are obtained. The effectiveness of the proposed algorithm is verified.

13.2 Fatigue Monitoring with Acoustic Emission Technology

13.2.1 Acoustic Emission Detection and Acoustic Emission Source of Ball Bearing

The phenomenon of transient elastic waves produced by the rapid energy release from local sources in materials is called acoustic emission [17]. Materials produce acoustic emission signals due to plastic deformation or crack propagation. The simplified waveform parameter method is usually used in acoustic emission analysis. The waveform parameters of conventional acoustic emission signal include: event count, ring count, rise time, duration, etc. The method extracts the structure parameters from

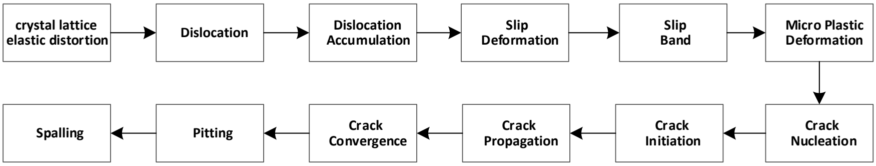

Fig. 13.1 Metal fatigue stages

AE events to describe AE event state. It has been used since the 1950s. It is a widely used classical acoustic emission signal analysis method and a certain engineering application effectiveness has been obtained.

Usually, ball bearing fatigue failure occurs below rolling contact surface. It is easy to produce local stress concentration around weak points such as non-metallic inclusions in bearing steel, which leads to crack initiation and propagation. A crack extends to surface may further cause fatigue pitting on raceway surface or rolling body surface. The fatigue evolution of ball bearing is the same as rolling contact fatigue of metal. Metal fatigue stages are shown in Fig. 13.1.

All the stages before micro-plastic deformation belong to the very early stage of its fatigue life. It does not affect the actual production. Therefore, the study of the crack initiation stage and its subsequent evolution stage will be more needed in practice. AE source is different at different stages. Therefore, different evolution stages information of ball bearing can be obtained by AE index.

13.2.2 Improved AE Index

Conventional acoustic emission indexes can describe the fatigue damage of ball bearings. However, since each index value is from each specific AE event. In different evolution stage, the appearance of emergencies or the change of working conditions may lead to signal to noise ratio changes of AE signals. It may lead to 'over-treatment' or 'weak-treatment' problems with conventional fixed threshold voltage. The validity of AE index will be weakened. Simultaneously, conventional AE index and other statistical index can not correspond well in time. It is easy to make the boundaries of each evolution stage fuzzily. It is also inconvenient to share information and compare differences among parameters.

Hence, an improved AE parameter method combines with a floating threshold voltage and average algorithm is proposed. The method is described as follows:

(1) First of all, according to empirical Equation, estimating standard deviation of noise component σ in AE signals. The empirical Equation is shown as follows:

$$\sigma = \frac{median(\{x|x = |x_i|,\ i = 1, 2, \ldots, N\})}{0.6745} \tag{13.1}$$

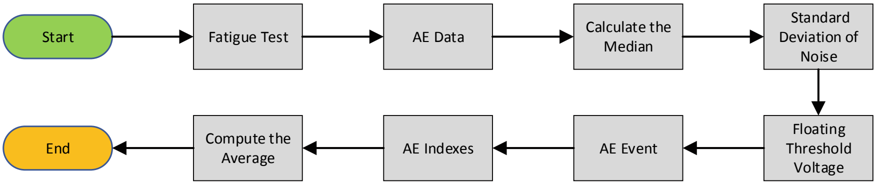

Fig. 13.2 Flow chart of improved acoustic emission index algorithm

In (13.1), x_i is the No. i data value of analysed sample x. N is the length of the analysed data. Symbol 'median' represents the median of a sample.

(2) Then, the noise threshold of each AE sample is estimated adaptively with shrinkage method theory by L. Donohod [18], and use it as the floating threshold voltage to replace the conventional fixed threshold voltage. Its mathematical expression is:

$$T = \gamma \times \sigma \times \sqrt{2\lg(N)/N} \tag{13.2}$$

In this Equation, γ is a threshold constant. It can be set according to the actual noise level. σ is the estimation of noise standard deviation of data. N is the length of data. T is the floating threshold voltage. It can adjust the voltage value adaptively according to different sample conditions.

(3) In the end, each AE index is averaged. AE index obtained by floating threshold voltage is averaged according to each sample with statistical indexes time process accurately, and its data display can be reduced.

The flow chart of the improved AE index algorithm is shown as follows (Fig. 13.2):

Improved AE index can better describe comprehensive performance and characteristics of AE events with these steps above. It can provide a better fatigue damage process information of ball bearing.

13.3 Test and Analysis

13.3.1 Ball Bearing Fatigue Test Rig

To verify effectiveness of the proposed algorithm, AE data is obtained from a self-designed accelerated fatigue test rig for ball bearings. The test bearing is a SKF-51115 thrust ball bearing. Hydraulic loading is used to stabilize the loading force. A GCr15 circular plate which has the same thickness as fixed bearing race with equivalent heat treatment is used to accelerate the bearing fatigue process.

Apart from AE sensor (PAC), an acceleration sensor (PCB), an eddy current sensor (XELI) and a K-type thermocouple (SWT) are used to make sure ball bearings state can be detected better. The operating temperature, vibration and speed are measured

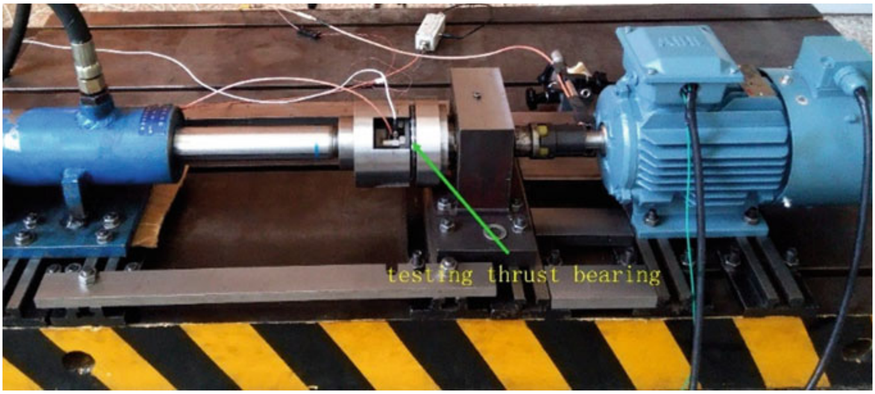

Fig. 13.3 Ball bearing fatigue test rig

Table 13.1 Test conditions

Item	Value
Environment temperature	around 23 °C
Operating temperature	around 37 °C
Test load	20 kN (P/C = 33%)
Test speed	600 rpm
Sampling frequency (AE\vibration\temperature)	1,000,000\25,600\1 Hz
Data save interval	5 min
Data length	10 s

respectively. The corresponding acquisition cards are: PCI-9846H, NI-9234, NI-9219. The driving part is composed of ABB motor (QABP90L2A) and its frequency converter (ACS550-01-05A4-4). The fatigue test rig is shown in Fig. 13.3. Test conditions are listed in Table 13.1.

13.3.2 Fatigue Monitoring of Ball Bearings with Improved AE Index

In this paper, event count, average amplitude, total ring count, mean duration, average ring count, mean rise time and average ring count maximum, these 7 improved AE indexes are used to monitor the running state of ball bearing. Figure 13.4 is the mixing trend diagram of ball bearings with improved AE indexes for a total of 19 h and 20 min fatigue life-cycle.

From Fig. 13.4, the trend of 7 improved AE indexes has the similar tendency. Four distinct evolution stages can be distinguished (dash dot line). The whole area

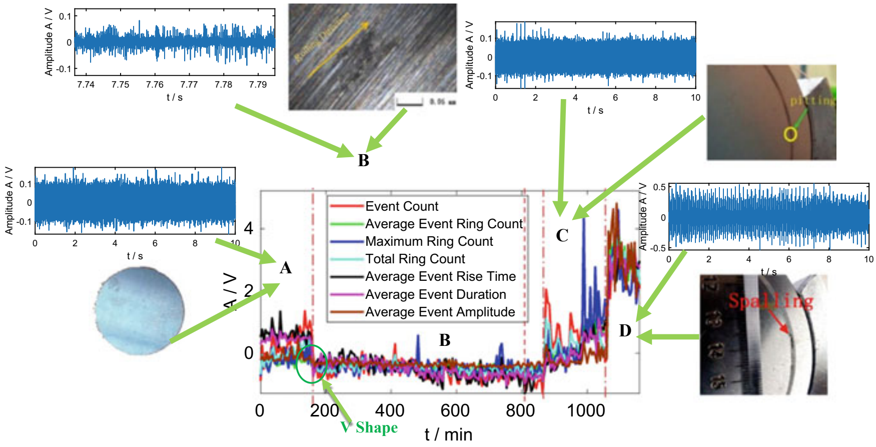

Fig. 13.4 Trends of improved AE index and stage observations

is divided into A area (between [0,160.7]), B area (between [160.7,863.7]), C area (between [863.7,1055]) and D area (between [1055,1160]).

A area stage is a process with small shocks. A quick saltation appears at the end of the stage (V shape) before it goes into B area. Event count has the most volatility in A area. Ring count maximum and total ring count have the 2nd and 3rd volatility respectively. Other indexes are relatively steady. At this stage, AE signal has no obvious impact and the background noise is large. The reason for this may be the micro-plastic deformation that leads to a large number of AE events. No obvious damage is found in disassembly observation of ball bearing at this stage. To define this phase as a running initial stage.

The trend of each index remains relatively stable in B area with a long period of relative stability. However, individual AE event during this period is emerged. Slight damage on race surface of ball bearing in this stage is observed with color industrial camera as shown in Fig. 13.4. By measurement and calculation, the size of the slight damage is around 0.05 mm (50 micron). The damage length direction is almost in line with the rolling direction (see the arrow in Fig. 13.4). Therefore, it is likely to be the period of subsurface crack initiation that leads to the slight damage at the beginning of the stage. In B area, the stability performance of improved AE index may be due to the stabilization of the microplastic deformation process. Newlyformed surface damage is compacted rapidly (work hardening) and that restrains the damage expansion. There's a new stress concentration which is occurred around the damage. This will become the main damage source in the subsequent evolutionary stage in a very high probability. This stage is defined as slight damage stage.

In C area, steady ascent appears around 863 min. AE amplitude gradually increased at this stage. There are many shocks in AE signal. It has a certain random characteristic. It is observed that a slight pitting occurs at the same location as the slight damage by shutdown observation of the test rig. The size of the pitting is about

0.3 mm. Hence, this stage can be defined as primary pitting stage. The cause of this stage may be due to the damage accumulation leads to the gradual surface damage expansion until the pitting is occurred. Trend amplitude increases gradually from macro signal performance.

In D Area, amplitude in each index trend shows a sharp increase. And a high level amplitude is maintained until the end. There are obvious and regular shock components in AE signal at this stage. The impact is also significantly increased. In this process, AE signal is released from material with high strain energy. At this time, disassembly observation is carried out. The size of pitting has already reached about 2.5 mm. The dramatic growth in AE signal is the rapid cracks growing on the race surface. Therefore, this stage is defined as the spalling stage.

Among these improved AE indexesaveragege rise time and average duration have a better consistency. And these two parameters can earlier excavation of the material surface damage (dashed line) compare to other improved AE indexes. As early as around 808.5 min, average duration and average rise time can detect damage on the surface about 55 min earlier than the other indexes. AE event, average ring count and total ring count have a good consistency. They have slight difference in trend in B area. Compared with other parameters, it is more stable and less volatile.

13.3.3 Comparison and Verification

In order to observe the effect of the improved AE index. Conventional AE index such as ring count, rise time, duration and amplitude parameter are brought in for comparison. First, typical signals from each stage above are observed. The threshold voltage is set manually to 0.0459 V (Consider the 20 dB preamplifier, the threshold after conversion is 73.2363 dB), the analysis results of trend with fixed thresholds are shown as follows:

From the figures below, conventional AE index with floating threshold is obviously better than the trend of manual selected fixed threshold. However, the distinction between each evolution stage is still not obvious. And its data is large and fluctuate. It still not well matches with other statistical indexes in time. The fatigue process accurate judgment of ball bearing is affected. By comparison, it can be known that the data size with improved AE index is the same as the data size of the other statistic index. It can be better matched with other statistical indexes in time and a better ball bearing fatigue process information can be given. It is convenient for the subsequent comprehensive judgment (Figs. 13.5, 13.6, 13.7 and 13.8).

In the end, trend analysis with 20 statistical indexes (Table 13.2) is also carried out. Compared with the improved AE index, the standardized results can be divided into three categories. See Figs. 13.9 and 13.10.

In Fig. 13.9, it can be seen that the trend of variance, RMS, Mean Square Frequency, etc. These 11 statistic indexes are similar to each other. They are close to the trend with the improved AE index. RMS Frequency can point out the slight pitting moment better. However, it still has a certain lag with nearly 50 min compares

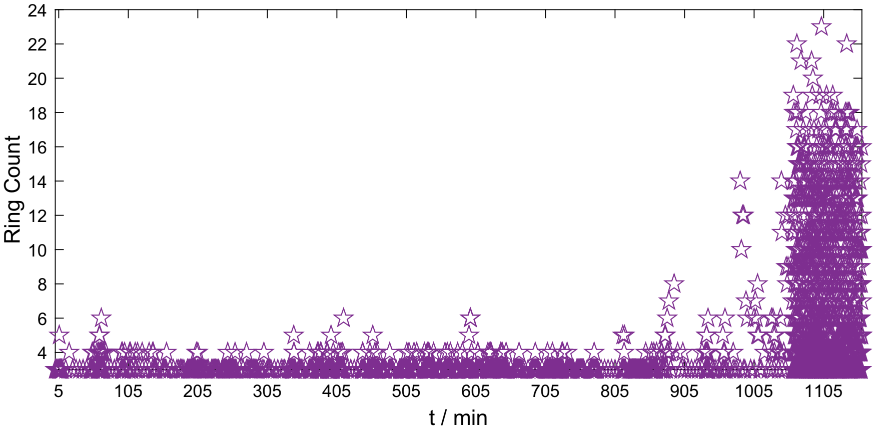

Fig. 13.5 Ring count

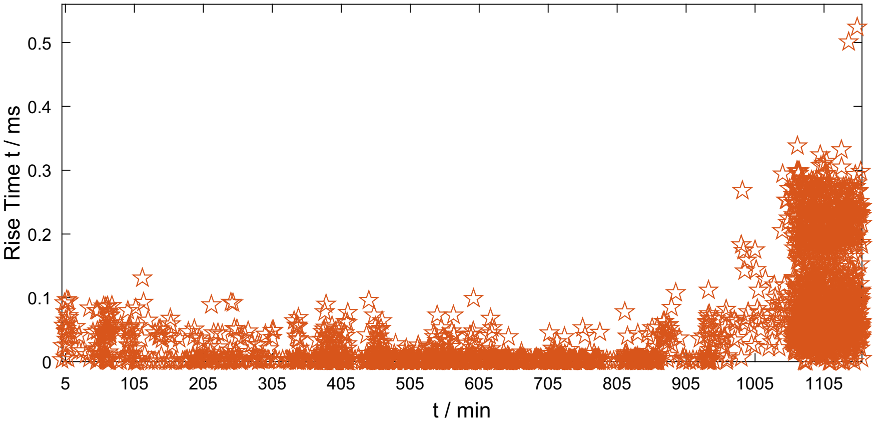

Fig. 13.6 Rise time

with the improved AE index. Peak-peak and peak are relatively stable in B area. But the judgement for slight damage and slight pitting is a little later than frequency domain peak.

In Fig. 13.10, the trend of these five indexes is opposite in B and C area compare with the same area in Fig. 13.9. These five indexes show an upward trend in initial operation stage. Kurtosis and waveform index are relatively stable at this stage. In a short period of time before entering the stage of minor injury, each index has an upward mutation process. Judgement in slight damage stage by pulse index margin index and peak index is relative delay. But it can be able to determine the appearance of slight pitting earlier than the indexes in group 1.

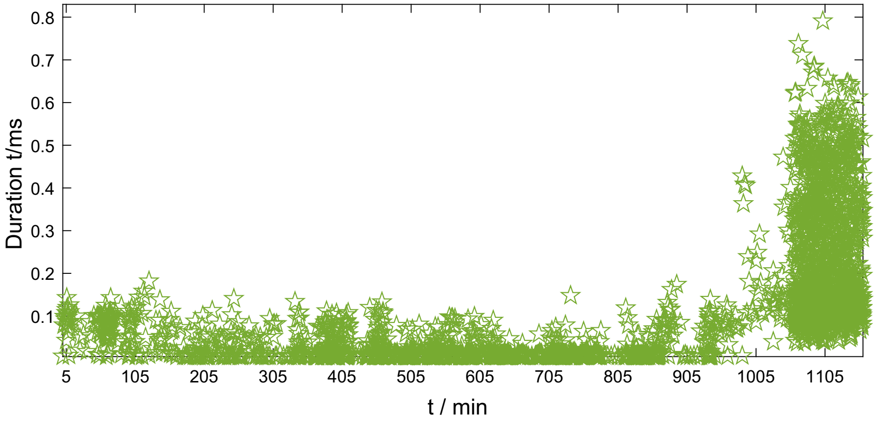

Fig. 13.7 Duration

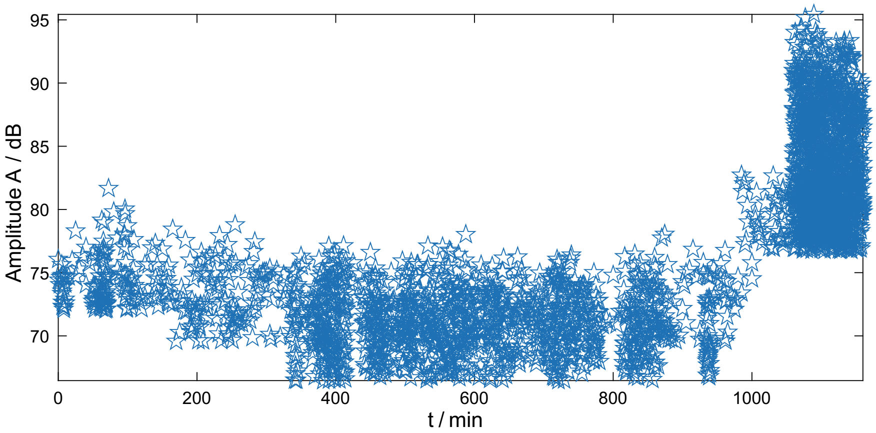

Fig. 13.8 Amplitude

The third category index shows a worse trend performance with obvious random character. Although the indexes in this group can also give some information about the fatigue evolution process. But their accuracy and stability are poor. Hence, this group will not be studied thereafter.

To sum up, average identification of each index group is summarized in Table 13.3.

From the table above, the black bold number is the least used time in each stage. The improved AE index group is more sensitive to these three stages. It can be seen that the improved AE indexes have a certain advantage to predict the evolution stage of ball bearing compare with the other indexes from the judging time of each stage in Table 13.3.

Table 13.2 Characteristic parameters

Parameter type	Parameter name
Time domain index	Variance, RMS, peak-peak, peak Square root amplitude, skewness Kurtosis, absolute average magnitude Centroid amplitude
Dimensionless index	Peak index, pulse index, margin index Waveform index, kurtosis index
Frequency domain index	Centroid frequency, mean square frequency RMS frequency, frequency domain peak Frequency domain variance Frequency domain mean amplitude Frequency domain peak frequency

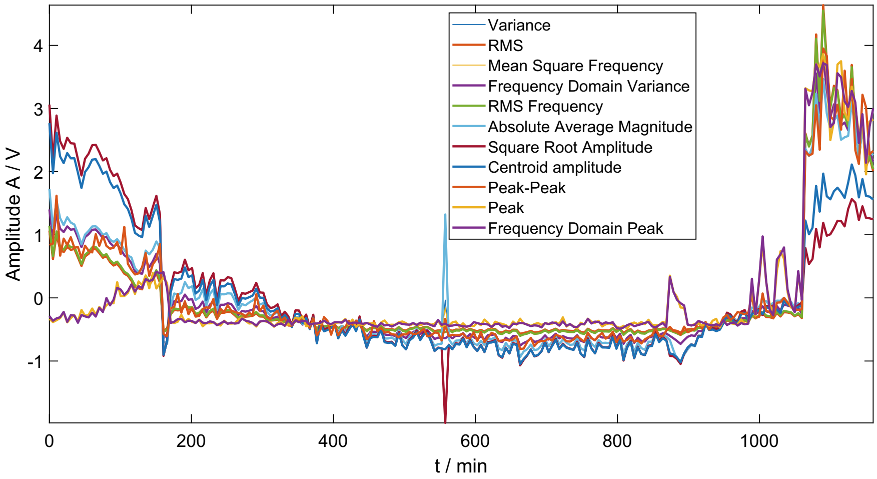

Fig. 13.9 Statistical index group 1

13.3.4 Fatigue Evolution Law of Ball Bearing

To sum up, the ball bearing fatigue evolution law with acoustic emission is summarized as follows which is based on the trend analysis with the improved AE Index.

The acoustic emission fatigue evolution of ball bearings can be divided into initial operation stage, slight damage stage, pitting stage and spalling stage.

(1) On initial stage, most of the indexes amplitude are at a high level. This may be due to the slight plastic deformation process at this stage. Usually, at the

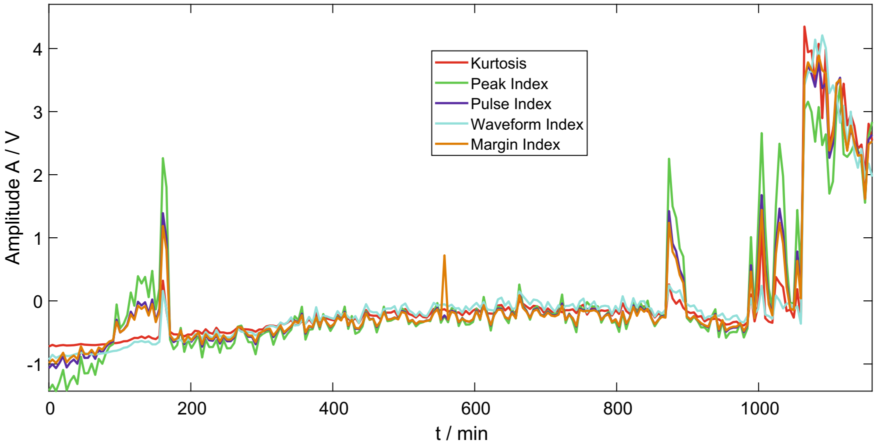

Fig. 13.10 Statistical index group 2

Table 13.3 Fatigue process recognition time

Recognition time (min)	Improved AE index group	Group 1	Group 2
Slight damage	145.6	160.7	165.7
Slight pitting	808.5	851.2	868.7
Spalling	979.2	1060	1060

generation stage of yielding stress, metal materials can produce high intensity acoustic emission signals. However, after entering the stage of slight damage, the activity of each index decreased.

(2) At the beginning of the stage of slight damage there usually has small oscillations witch is in the form of a letter V. It may be due to this stage has just entered the process of work hardening period. New damage at contact surface is flattened which is under high alternating stress, and then this new damage is reintegrated into the surrounding material environment. The signal becomes stable again over time.

(3) The pitting stage is usually a gradual and steady upward trend. Its duration at this stage is usually shorter than the more stable stage of slight damage. It can be seen that the starting point of upward trend of each index in C area is usually the sign of initial pitting stage combine with experimental observation.

(4) On spalling stage, all the indexes are replicated consistently with large upward jumps. The larger the jump amplitude is, the more serious the damage is. The more strain energy is released inside material.

13.4 Conclusion

In this paper, conventional double emission index is improved. It overcomes the shortcomings of conventional trend analysis with AE indexes, such as the introduction of subjective error, the large amount of displayed data, the unclear distinction of chaotic stages and the inability to achieve a good correspondence with statistical indexes. Trend analysis with multi-index from the collected AE data of ball bearings life-cycle is carried out. The results show that, the improved AE index can give a better fatigue evolution information. The display data is simplified and the stage identification accuracy is improved. Finally, the characteristics and evolution laws of the corresponding indexes from each fatigue process are summarized. A new reference basis for judging the fatigue process of ball bearing is provided.

Acknowledgements The research work is supported by the Education Department Foundation of Yunnan Province (Grant No. 2018JS025) and Provincial Education Program (Grant No. KKSY201701018).

References

1. J. Chen, *Mechanical Equipment Fault Diagnosis Technology and Its Application.* Shanghai Higher Education Electronic Audio and Video Publishing House (2003)
2. T.A. Harris, M.N. Kotzalas, *Rolling Bearing Analysis* (2010)
3. T. Yoshioka, T. Fujiwara, Application of acoustic emission technique to detection of rolling bearing failure. Am. Soc. Mech. Eng. **14**, 55–76 (1984)
4. A.M. Al-Ghamd, D. Mba, A comparative experimental study on the use of acoustic emission and vibration analysis for bearing defect identification and estimation of defect size. Mech. Syst. Signal Process. **20**(7), 1537–1571 (2006)
5. W. Achmad, Y.K. Eric, S. Jong-Duk et al., Fault diagnosis of low speed bearing based on relevance vector machine and support vector machine. Exp. Syst. Appl. Int. J. Arch. **3**(36), 7252–7261 (2009)
6. T. Yoshioka, T. Fujiwara, Paper II(i) “Measurement of propagation initiation and propagation time of rolling contact fatigue cracks by observation of acoustic emission and vibration”. Tribology **12**(2–3), 29–33 (1987)
7. M. Elforjani, D. Mba, Monitoring the onset and propagation of natural degradation process in a slow speed rolling element bearing with acoustic emission. J. Vib. Acoust. **130**(4), 1257–1261 (2008)
8. M. Elforjani, D. Mba, Observations and location of acoustic emission for a naturally degrading rolling element thrust bearing. J. Fail. Anal. Prev. **8**(4), 370–385 (2008)
9. M. Elforjani, D. Mba, Natural mechanical degradation measurements in slow speed bearings. Eng. Fail. Anal. **16**(1), 521–532 (2009)
10. A.W. Warren, Y.B. Guo, Acoustic emission monitoring for rolling contact fatigue of super finished ground surfaces. Int. J. Fatigue **29**, 603–614 (2007)
11. Z. Rahman, H. Ohba, T. Yoshioka et al., Incipient damage detection and its propagation monitoring of rolling contact fatigue by acoustic emission. Tribol. Int. **42**, 807–815 (2009)
12. H.P. Filip et al., Monitoring of acoustic emission signal of loaded axial bearings. J. Mater. Sci. Eng. **A1**(5), 717–724 (2011)

13. A.M. Al-Ghamd, D. Mba, A comparative experimental study on the use of acoustic emission and vibration analysis for bearing defect identification and estimation of defect size. Mech. Syst. Signal Proces. **20**(7) (2006)
14. W. Jialei, L. Shanjun, W.U. Lixin, et al., Comparative analysis on different AE parameters in biaxial loading of hole rock. J. Min. Saf. Eng. (2015)
15. X.L. Yao, Y.B. Zhang, X.X. Liu et al., Optimization method for key characteristic signal of acoustic emission in rock fracture. Yantu Lixue/Rock and Soil Mechan. **39**(1), 375–384 (2018)
16. J.K. Zhang, N. Wang, P. Lu et al., AE REE index to identify connecting state of a 2-bolt connected structure. Zhendong yu Chongji/J. Vibr. Shock **32**(8), 179–182 (2013)
17. G. Shen, *Acoustic Emission Detection Technology and Its Application.* Science Press (2015)
18. D.L. Donoho, De-noising by soft-thresholding. IEEE Trans. Inf. Theor. **41**(3), 613–627 (1995)

Chapter 14
Study on the Propagation Law of Lamb Wave in High Stiffened Panels

Yantao Liu, Guoliang Xu, Gang Sun, and Zhe Wang

Abstract The study of Lamb wave propagation law is of great significance for health monitoring and non-destructive testing of panel structures. However, in the panel with stiffeners, the propagation law of the Lamb wave is very complicated, and there are still some inadequacies in the current research, especially for the stiffened panel with multiple high stiffeners. In this paper, the propagation law of Lamb waves in panels with multiple high stiffeners is studied by finite element simulation. The time domain waveforms of received displacements are compared when the number of stiffeners is different, and the energy ratio curves are obtained. The results show that the number of stiffeners has little effect on the wave velocity of the Lamb wave. The Lamb wave decays when it passes through the stiffeners, and the more the number of stiffeners, the more obvious. In the 200–500 kHz band, the Lamb wave energy ratio curve is moderate and small, and the Lamb wave energy pass rate is high and stable in the 100–200 kHz band. This study can provide reference for signal analysis in the structural health monitoring and non-destructive testing of high stiffened panels.

14.1 Introduction

In the panel structure, the acoustic wave propagates mainly in the form of Lamb waves, and the study of the Lamb wave propagation law is of great significance for the monitoring of the health state of the structure [1, 2]. For example, the source is located by analyzing acoustic emission signals of impact and leakage [3–6]. However, some metal and composite panels are usually provided with periodic stiffeners structure on the surface in order to ensure sufficient mechanical strength. When the Lamb wave passes through the stiffeners, transmission, reflection, scattering, attenuation and modal transformation occur. And the higher the stiffeners, the larger the number of stiffeners, the more complex the Lamb wave, and the interference of these phenomena makes signal analysis more difficult. In recent years, some scholars have studied these effects.

Y. Liu (✉) · G. Xu · G. Sun · Z. Wang
Beijing Institute of Structure and Environment Engineering, Beijing 100076, China
e-mail: lytus@126.com

© The Author(s), under exclusive license to Springer Nature Singapore Pte Ltd. 2021

G. Shen et al. (eds.), *Advances in Acoustic Emission Technology*, Springer Proceedings in Physics 259, https://doi.org/10.1007/978-981-15-9837-1_14

Reusser et al. [7, 8] found that the Lamb wave has different transmission energy at different frequencies when passing through the stiffeners, and it has a tendency to oscillate. By comparing the signals through the 2 aspect ratio stiffeners, this phenomenon is more pronounced in stiffened panels with a large aspect ratio. When the S0 mode Lamb wave frequency is near the resonant frequency of the stiffened panel, the signal attenuation is severe. However, their research is mainly on the influence of a single stiffener on the Lamb wave signal, and the height of the stiffener is not high. Santhanam et al. [9] studied the relationship between the incident angle, frequency and reflection coefficient when the Lamb wave encounters the end of the panel. In addition, some scholars studied the modal transition when the Lamb wave passes through the notches [10].

However, the above scholars' research has the following inadequacies: Less research has been done on the variation law of Lamb waves after passing through multiple stiffeners; The height of the stiffeners studied is not too high; There are fewer studies on the S0 mode Lamb wave with fast wave velocity and less interference.

Based on previous studies, this paper studies the propagation law of Lamb waves after different number of stiffeners based on finite element simulation. The height of the stiffeners is up to 22 mm. The variation of Lamb wave velocity, attenuation and energy is analyzed in time domain and frequency domain. In the structural health state detection and non-destructive testing of the stiffened panel structure, the proposed method can provide reference for the selection of the Lamb wave frequency band.

14.2 Math

According to the motion mode of particles relative to the panel, Lamb waves can be divided into symmetrical mode (S) and antisymmetrical mode (A) Lamb waves. With the change of frequency, each form of Lamb waves can be further divided into multiple modes with different phase velocities and group velocities. This phenomenon is called dispersion characteristics. The dispersion curve of symmetrical and antisymmetrical mode are represented by (14.1) and (14.2)

$$\tan(qh)/q + 4k^2 p \tan(ph)/\left(q^2 - k^2\right)^2 = 0 \tag{14.1}$$

$$q \tan(qh) + (q^2 - k^2)^2 \tan(ph)/(4k^2 p) = 0 \tag{14.2}$$

where $h = d/2$, $p^2 = \omega^2/c_l^2 - k^2$, $q^2 = \omega^2/c_t^2 - k^2$, $k = \omega/c_p$, $c_l = \sqrt{E(1-\mu)/[\rho(1+\mu)(1-2\mu)]}$, $c_t = \sqrt{E/[2\rho(1+\mu)]}$. d is the panel thickness. k, ω, c_p are the wave number, the angular frequency and the phase velocity of Lamb wave, respectively. c_l is the longitudinal wave velocity in the material, and c_t is the transverse wave velocity. The parameters of the 5A06 magnesium-aluminum alloy are shown in Table 14.1.

Table 14.1 The material parameters of the 5A06 aluminum-magnesium alloy

Aluminum designation	Density, ρ (g/cm^3)	Young's modulus, E (MPa)	Poisson's ratio, μ
5A06	2.64	71,000	0.32

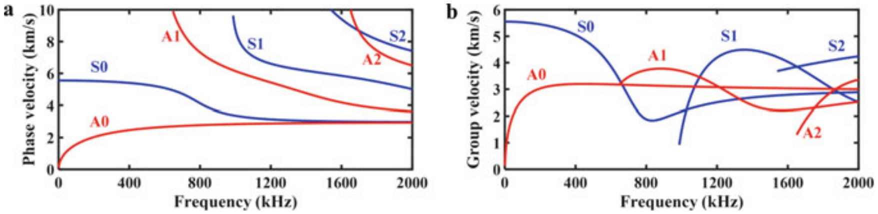

Fig. 14.1 The phase velocity and group velocity dispersion curves of Lamb waves in a 5A06 magnesium-aluminum alloy panel with a thickness of 3 mm: **a** Phase velocity, **b** Group velocity

The phase velocity and group velocity dispersion curves of Lamb waves in a 5A06 magnesium-aluminum alloy panel with a thickness of 3 mm are shown in Fig. 14.1.

In non-destructive testing, the frequency of interest is relatively low for Lamb waves in a panel structure, mainly because the high-frequency Lamb waves are seriously attenuated with increasing distance. At the same time, the high frequency Lamb wave contains more modalities and the signal is more complicated, which increases the difficulty of analysis. For the above reasons, it is usually mainly concerned with the S0 and A0 mode Lamb waves in the lower frequency band.

Compared with the S0 mode, the A0 mode Lamb wave has higher energy. However, the A0 mode Lamb wave has a slower speed than the S0 mode and reaches the receiving point after the S0 mode Lamb wave. In the flat structure, the characteristics of the S0 mode Lamb wave and the A0 mode Lamb wave in the time domain are relatively clear, and they can be distinguished according to the time of reaching the receiving point. However, in stiffened plats, Lamb waves undergo reflection and modal transitions when passing through the reinforcement stage. Some A0 modal Lamb waves convertes into S0 modal Lamb waves, making the characteristics of the A0 mode Lamb wave are not obvious in the time domain. It is difficult to obtain the exact arrival time of the A0 mode. In the frequency domain, the A0 mode Lamb wave overlaps with the S0 mode Lamb wave, and the A0 mode Lamb wave cannot be extracted from the S0 mode Lamb wave by filtering. The S0 mode Lamb wave is in a low frequency range and is less affected by the attenuation of the propagation distance. At the same time, the S0 mode Lamb wave has a fast speed and reaches the receiving point first. It is not easy to be interfered by other mode Lamb waves in the time domain.

Based on the influence of the above factors, this paper takes the S0 mode Lamb wave in the 0–500 kHz band as the research object.

In this paper, the energy ratio is used to measure the effect of the stiffeners on the Lamb waves of different frequencies. The energy ratio is expressed by the ratio of the energy of the Lamb wave with the frequency f propagating the same distance in the stiffened panel and the flat panel, which can eliminate the influence of propagation distance and measure the effect of stiffeners more accurately. The energy ratio is given by (14.3).

$$ER = FR_S^2 / FR_P^2 \tag{14.3}$$

where FR_S represents the frequency response of the Lamb wave in the stiffened panel and FR_P represents the frequency response of the Lamb wave after propagating the same distance in the flat panel.

14.3 Finite Element Simulation Model

In this paper, ABAQUS finite element simulation software is used to study the Lamb wave signal propagation law in stiffened panels. The ABAQUS software has a good simulation effect on the non-linear change of signals. Compared with the three-dimensional model, the two-dimensional finite element simulation parameters are simpler and more efficient. It is more suitable for multi-group control experiments with control variables. Therefore, the two-dimensional finite element simulation models were established based on the thickness, stiffener width and height and of the stiffened panels used in the spacecraft. The schematic diagram of the finite element model of stiffened panels with two stiffeners is shown in Fig. 14.2. The positions of each point in the model are recorded in Cartesian coordinate system.

The size of the panel structure is 2000 mm × 3 mm, and the material is 5A06 magnesium-aluminum alloy. The bottom edge of the panel coincides with the x-axis, and the axis of symmetry perpendicular to the bottom edge coincides with the y-axis. The height of stiffener is 22 mm, the width is 4 mm, and the spacing between the adjacent two stiffeners is 50 mm.

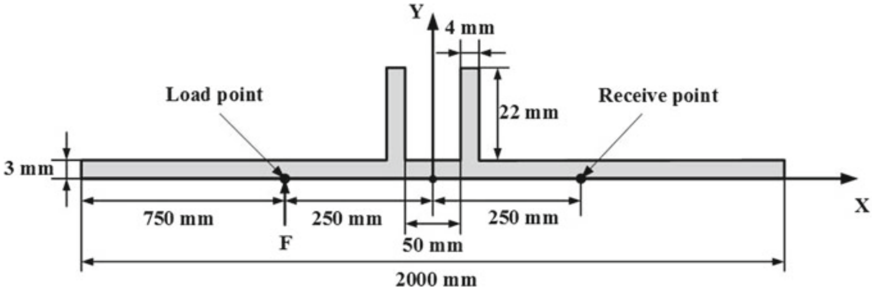

Fig. 14.2 The schematic diagram of the finite element model of stiffened panels with two stiffeners

The model uses a grid type of quadrilateral elements, and the grid size is determined according to the wavelength λ to ensure the accuracy of the simulation calculation. Since the maximum frequency f_m of the signal under study is 500 kHz and the shear wave velocity ct in the 5A06 magnesium aluminum alloy is 3198 m/s, the magnitude of the wavelength is c_t/f_m with a value of 6.396 mm. Dividing the model with a signal of 1 wavelength passing at least 10 grids as a standard, the size of the grid is not larger than 0.6396 mm. The smaller the grid size is, the higher the calculation accuracy is, and the longer the calculation time is required. If the grid size is too large, the simulation results will have greater errors. According to the above analysis, the mesh size is set to 0.5 mm, and the number of seeds required for each side is calculated based on the length of each side.

At the point (−250, 0), the load is applied in the positive direction of the y-axis, and the load is applied in the form of a concentrated force.

In non-destructive testing, the frequency of the acoustic emission signal of interest is below 500 kHz. In order to study the effect of stiffeners on the propagation characteristics of Lamb waves at different frequencies, the simulation signal is a broadband signal with a frequency of 0–500 kHz. The load is a superimposed sinusoidal signal with a frequency increasing from 1 to 500 kHz at a frequency of 1 kHz and a load duration of 20 μs. The load is expressed by (14.4).

$$F(t) = \begin{cases} \sum\limits_{f=1\,\text{kHz}}^{500\,\text{kHz}} \sin(2\pi f t) & t \in [0.20\,\mu\text{s}] \\ 0 & t > 20\,\mu\text{s} \end{cases} \tag{14.4}$$

The time and frequency domain characteristics of the load are shown in Fig. 14.3.

Set the receiving point at point (250, 0) to receive the displacement. Since the panel is long enough, it is not necessary to consider the influence of the left and right boundary reflection waves. In many application scenarios, the stiffeners on the surface of the stiffened panel are usually grid-like periodic distribution. In order to study the influence of the number of stiffeners on the Lamb wave, the finite element simulation models with the number of stiffeners of 1–6 were established respectively. The finite element models of the stiffened panel with 6 stiffeners and the flat panel of the control group are shown in Fig. 14.4. Based on the above settings, the simulation is carried out.

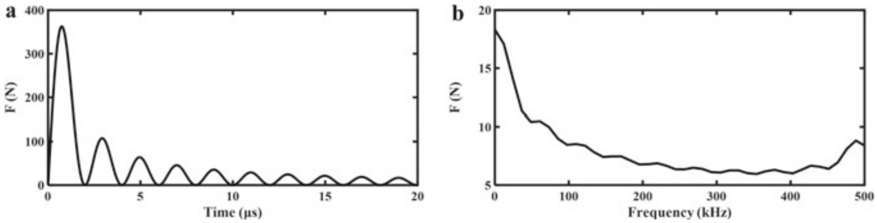

Fig. 14.3 **a** The time domain characteristics. **b** The frequency domain characteristics

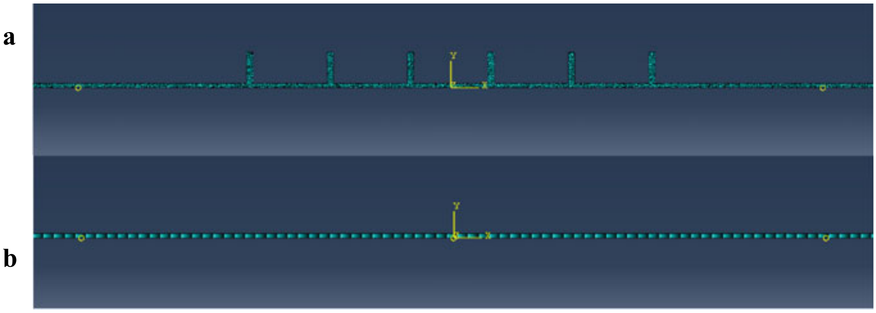

Fig. 14.4 **a** The stiffened panel with 6 stiffeners. **b** The flat panel

14.4 Result

14.4.1 Time Domain

The displacement time-domain waveform in the y-axis direction obtained by the receiving points of the flat panel and the 6 sets of stiffened panels are shown in Fig. 14.5. It can be seen from the figure that the time of the waveform in the 7 sets reaching the receiving point is about 95 μs, and the S0 mode Lamb wave velocity is calculated to be 5.26 km/s, indicating that the number of stiffeners is almost no effect on the Lamb wave velocity. At the same time, the first wave trough of the waveform in the flat panel is the largest. As the number of stiffeners increases, the first wave trough becomes smaller and smaller, indicating that the stiffeners attenuate the signal, and the more the number of stiffeners, the more severe the attenuation. The same conclusion applies to the first wave crest.

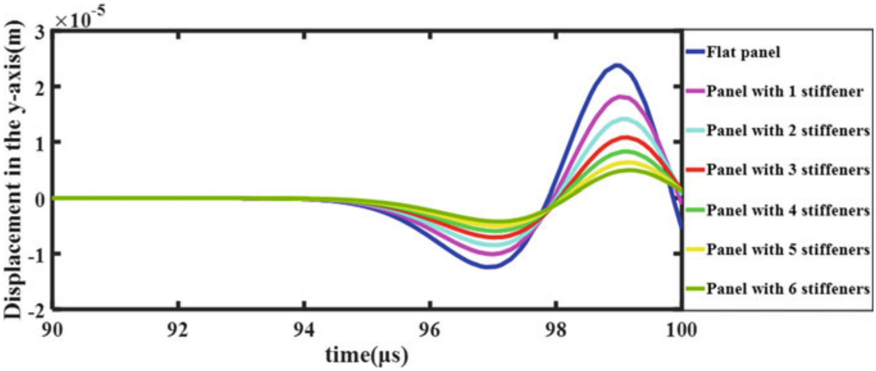

Fig. 14.5 The displacement time-domain waveform in the y-axis direction obtained by the receiving points of the flat panel and the 6 sets of stiffened panels

14.4.2 Frequency Domain

According to the obtained y-axis displacement waveform, the A0 mode Lamb wave reaches the receiving point around 160 μs. In this paper, the S0 mode Lamb wave before 160 μs is selected as the research object.

The energy ratio curves calculated from the simulation results of the six sets of stiffened panels are shown in Fig. 14.6. It can be seen from the figure that the energy ratio curve fluctuates with increasing frequency, and the effect of the stiffeners on the Lamb wave is equivalent to a comb filter. When the Lamb wave passes through the stiffeners, part of the A0 mode will be converted to the S0 mode. Since the S0 mode energy ratio is extremely small, although the Lamb wave energy is generally attenuated, there will be a large energy ratio curve. When the number of stiffeners is 1, the Lamb wave has an energy distribution in the 0–400 kHz band, and the energy passing rate is low in the 400–500 kHz band, which indicating that the high frequency signal is significantly attenuated after passing through the stiffeners. As the number of stiffeners increases, the energy ratio curve changes below 50 in the 200–500 kHz band, and the trend is gentle. In the 0–200 kHz band, the energy ratio curve changes drastically and has a significant pass band. In particular, the Lamb

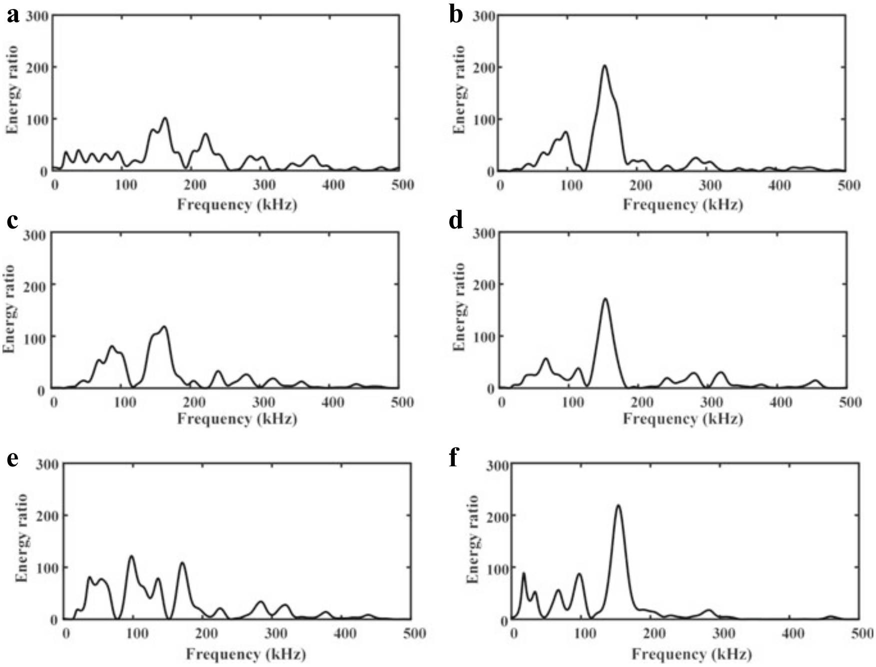

Fig. 14.6 **a** One stiffener. **b** Two stiffeners. **c** Three stiffeners. **d** Four stiffeners. **e** Five stiffeners. **f** Six stiffeners

waves in the stiffened panels with different number of stiffeners all have high energy passing rate in the 100–200 kHz band.

14.5 Conclusion

In this paper, the propagation law of Lamb wave in stiffened panels with high stiffeners is studied based on finite element simulation. The influence of the number of stiffeners on the Lamb wave signal is analyzed from the perspective of time domain and frequency domain. The results show that:

1. The time domain characteristics of the signal indicate that the Lamb waves arrive almost simultaneously in the models with different numbers of stiffeners, and the number of stiffeners has no effect on the wave velocity of the Lamb wave. The first wave trough of the Lamb wave will decay when passing through the stiffeners, and the more the number of stiffeners, the more obvious the attenuation. The same conclusion applies to the first crest.
2. The frequency domain characteristics of the signal indicate that the energy ratio curve fluctuates with increasing frequency, and the effect of the stiffeners on the Lamb wave is equivalent to a comb filter. Comparing the 6 models with different numbers of stiffeners, the energy ratio curve is more moderate in the 200–500 kHz band. In the 0–200 kHz band, the energy ratio curve changes drastically with an obvious pass band. At the same time, the Lamb wave energy passing rate in the 100–200 kHz band is high and stable.

According to the above conclusions, Lamb waves of appropriate frequency band can be selected to improve the signal to noise ratio and reduce the difficulty of analysis in structural health state detection and non-destructive testing of stiffened panel structures.

References

1. L. Zhang, D. Ozevin, D. He, W. Hardman, A. Timmons, A method to decompose the streamed acoustic emission signals for detecting embedded fatigue crack signals. Appl. Sci. **8**(1), (2018)
2. M.F. Haider, M.Y. Bhuiyan, B. Poddar, B. Lin, V. Giurgiutiu, Analytical and experimental investigation of the interaction of Lamb waves in a stiffened aluminum plate with a horizontal crack at the root of the stiffener. Sci. J. Sound Vib. **431**, 212–225 (2018)
3. X. Bian, Y. Zhang, Y.B. Li, X.Y. Gong, S.J. Jin, A new method of using sensor arrays for gas leakage location based on correlation of the time-space domain of continuous ultrasound. Sensors **15**(4), 8266–8283 (2015)
4. K. Grabowski, M. Gawronski, I. Baran et al., Time-distance domain transformation for Acoustic Emission source localization in thin metallic plates. Ultrasonics **68**, 142–149 (2016)
5. V. Meruane, P. Veliz, E.I. Droguett, A. Ortiz-Bernardin, Impact location and quantification on an aluminum sandwich panel using principal component analysis and linear approximation with maximum entropy. Entropy **19**(4), (2017)

6. Y.B. Li, Z. Wang, X.B. Rui, L. Qi, J.W. Liu, Z. Yang, Impact location on a fan-ring shaped high-stiffened panel using adaptive energy compensation threshold filtering method. Appli. Sci. **9**(9), (2019)
7. R.S. Reusser, D.E. Chimenti, R.A. Roberts, S.D. Holland, Guided plate wave scattering at vertical stiffeners and its effect on source location. Ultrasonics **52**(6), 687–693 (2012)
8. R.S. Reusser, S.D. Holland, D.E. Chimenti, R.A. Roberts, Reflection and transmission of guided ultrasonic plate waves by vertical stiffeners. J. Acoust. Soc. Am. **136**(1), 170–182 (2014)
9. S. Santhanam, R. Demirli, Reflection of lamb waves obliquely incident on the free edge of a plate. Ultrasonics **53**(1), 271–282 (2013)
10. F. Benmeddour, S. Grondel, J. Assaad, E. Moulin, Study of the fundamental Lamb modes interaction with asymmetrical discontinuities. NDT and E Int. **41**(5), 330–340 (2008)

Chapter 15
Research on AE Source Location and Identification Method of Tank Bottom Corrosion

Feng Qiu, Guang Dai, Mingjun Li, Dingrong Qu, and Yongliang Yu

Abstract As large storage tank has large diameter, the acoustic emission (AE) wave attenuation will increase. The number of location events may be lost. The activity of the defect cannot be understood. Reliability of safety assessment of tank bottom corrosion will be affected. In order to solve the problem, an acoustic source identification method is presented. Based on the AE source location theory of tank bottom, it is put forward that the sensors located on the tank bottom medium are employed together with the sensors arranged on tank outside wall near tank bottom to identify the acoustic source of tank bottom corrosion defects. Experiments of acoustic source location and identification for simulative tank bottom corrosion have been conducted. The results show that the method can help for recognizing acoustic source in arbitrary triangle and area location of tank bottom area; in addition, the sensor inside the tank is more sensitive to the identification of corrosion acoustic source than the external sensor. Therefore, the method can improve the reliability of results for the identification and location of tank bottom acoustic source.

F. Qiu · M. Li (✉) · D. Qu · Y. Yu
SINOPEC Qingdao Research Institute of Safety Engineering, Qingdao 266000, China
e-mail: ljmuma@outlook.com

F. Qiu
e-mail: qiuf.qday@sinopec.com

Y. Yu
e-mail: yuyongliang.ok@163.com

G. Dai
Northeast Petroleum University, Daqing 163318, China
e-mail: Gdai126@126.com

Y. Yu
Nanjing Boiler and Pressure Vessel Inspection and Research Institute, Nanjing 210000, China

© The Author(s), under exclusive license to Springer Nature Singapore Pte Ltd. 2021

G. Shen et al. (eds.), *Advances in Acoustic Emission Technology*, Springer Proceedings in Physics 259, https://doi.org/10.1007/978-981-15-9837-1_15

15.1 Introduction

Acoustic emission (AE) testing technology is a nondestructive testing method which can quickly evaluate the structural integrity of pressure vessels [1]. It can be used for on-line monitoring of storage tanks without stopping production, and finally make a reasonable safety evaluation for storage tanks. The acoustic source identification technology for tank floor corrosion can reflect the number of defect acoustic sources and the actual defect acoustic emission activity [2, 3]. Therefore, in the acoustic emission detection of tank corrosion state, the location source is an important index to evaluate the detection results, and the results have high reference value.

However, the acoustic source recognition technology of tank bottom corrosion still has some limitations. Tank bottom acoustic source localization is effect by complex sonic, multiple signals and threshold setting. At the same time, due to the design of the tank has tended to be larger, the acoustic wave from tank bottom defects maybe attenuate seriously. The number of acoustic position events will be lost. Acoustic activity cannot reflect the condition of defects reasonably. Safety assessment results of the tank bottom corrosion will not be accuracy [4]. Therefore, a new acoustic source identification method is need for these problem solution. Not only the reliability of position can be improved, and the activity of defects can be reflected reasonably. Both triangulation location and regional positioning applications can be combined for small tank detection, but also the requirements of regional location for large tanks can be met. Therefore, this paper proposes a method of tank bottom acoustic source identification to solve the above problems.

15.2 Acoustic Source Location and Identification Method of Tank Bottom Corrosion

In AE testing process, measure strategy of tank bottom location is setting several sensors uniform on tank wall outside nearby bottom based on the size of tank. Figure 15.1 is a triangle location map of tank bottom, setting six sensors around the tank uniformly. Triangle location are made up every three sensors location, forming a total of six groups.

Although the traditional location method can form multi triangle location group, missed inspection and misjudgment maybe appear. Because tank bottom corrosion signal is weak and large tank bottom has serious attenuation [5]. Therefore, it is necessary to place the sensor inside the tank. The sensor inside and the sensor outside the tank are in the same plane. For small storage tank, it can reduce the misjudgment of acoustic source and prevent the “loss” of AE signal. For large storage tanks, the detection coverage area can be increased in the area positioning. As shown in Fig. 15.2, No. 7 sensor is placed at the center of tank bottom plate to form triangle positioning with 6 sensors around the tank wall. S is an acoustic source setting at the tank bottom, the location is shown in Fig. 15.3.

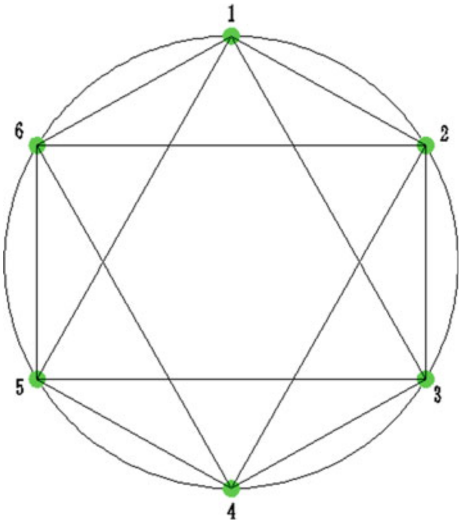

Fig. 15.1 Triangle location net of the tank

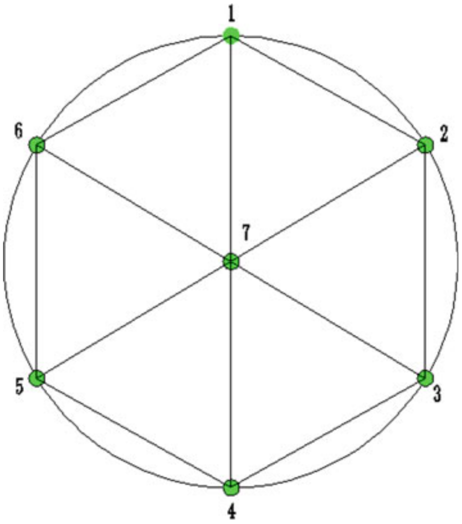

Fig. 15.2 Tank bottom center placement of a single sensor

In Fig. 15.3, the sensor No. 7 placed in the center of the tank bottom can form six positioning triangles with the surrounding six sensors, which reduces the attenuation by nearly half compared with the positioning shown in Fig. 15.1. The traditional positioning method is to identify the source S through the positioning triangle formed by sensors 1, 2 and 6. It can be seen from the figure that the acoustic source S is far away from sensor 6. When the acoustic wave propagates through the medium to the sensor 6, the amplitude of the wave attenuates greatly, even to zero. After the No. 7

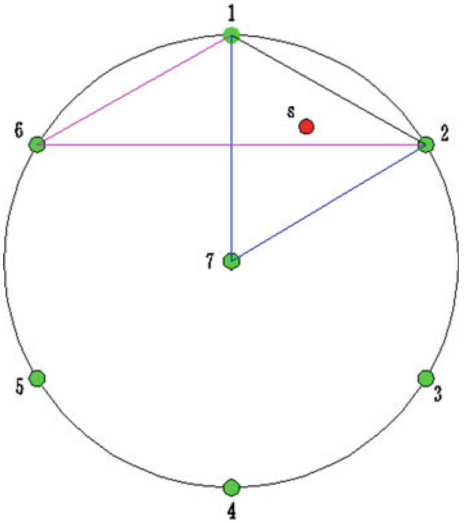

Fig. 15.3 S at the floor of the tank AE localization triangulation net

sensor is placed at the center of the tank bottom, it can form a triangle with the No. 1 and No. 2 sensors positioning, the attenuation of acoustic source S can be reduced.

15.3 Experiment of Acoustic Source Location and Identification Method for Simulated Tank Floor

15.3.1 Experimental System and Parameter Settings

In this experiment, the round steel plate made of Q235 carbon structural steel, which is commonly used in the bottom plate of atmospheric vertical storage tank, with the size of 1600 mm diameter and 8 mm thickness. DP3I sensor and the third generation full digital system produced by PAC are selected [6]. PDT is set to 300 μs, HDT is 600 μs, HLT is 1000 μs. Since the positioning acoustic source in this experiment comes from the 2H (0.5) lead breaking, the detection threshold is set to 40 dB [7].

15.3.2 Sensor Layout Program and Experiment

In this experiment, six sensors are evenly coupled to the periphery of the circular plate. At the same time, 1 sensor is coupled in the center of the circular plate. The sensor layout and lead breaking position are shown in Fig. 15.4. Table 15.1 shows the coordinates of sensors 1–6.

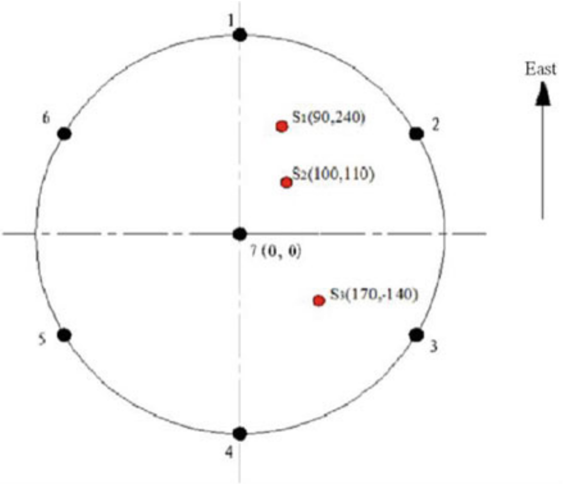

Fig. 15.4 Schematic diagram of sensor layout and lead breaking position

Table 15.1 Coordinate of each sensor

Senser number	1	2	3	4	5	6
Coordinates	(0, 400)	(346, 200)	(346, −200)	(0, −400)	(−346, −200)	(−346, 200)

As shown in Fig. 15.4, a sensor is placed on the center of simulated tank plate to form position triangle with the sensors on the outer circumference. Pencil lead fracture simulation source is triggered at three positions of the circular plate, which is compared with the results of the traditional positioning method no sensor is placed on the center of the simulated tank bottom plate. The coordinates of the three lead breaking positions are S1 (90, 240), S2 (100, 110) and S3 (170, −140). Figure 15.5 shows the circular plate with a sensor placed in the center.

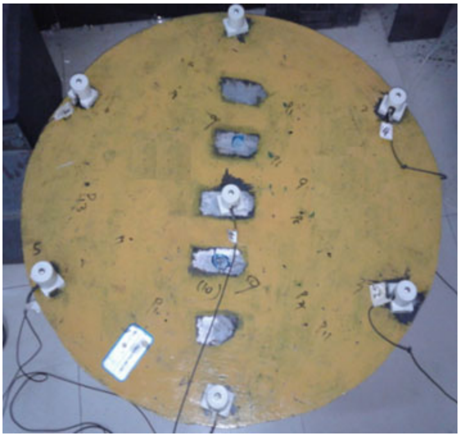

Fig. 15.5 Simulated tank bottom plate

15.3.3 Experimental Results and Analysis

When the AEwin tank bottom positioning software developed by PAC is used to locate the acoutic source of tank bottom, the No. 7 sensor on the center of the bottom plate in the experiment can not be listed as the positioning sensor. Therefore, a software system (NTBPT^{TM}, new tank bottom position testing) is developed to identify and locate the acoustic source by placing sensors in tank. Aewin system and ntbpttm system are used to locate the acoustic source in the experiment. Figure 15.6 shows AEwin tank bottom positioning software, and Fig. 15.7 shows the localization of NTBPT^{TM}.

The results of the two software systems show S1, S2, S3 locations. The result of AEwin software is with 1, 2, 6 sensor, and NTBPT^{TM} is with 1, 7, 2. The wave trigger 7 sensor cause 92 dB amplitude which is 1 dB higher than that of 6 sensor with 91 dB. The location results of other 2 acoustic source show the same condition. It can be seen that placing the sensor on the center of the tank bottom can improve the amplitude of the signal received by the sensor in the triangle forming positioning, and increase the recognition degree of the acoustic emission detection for the acoustic source in arbitrary triangle positioning, so as to improve the reliability of positioning results.

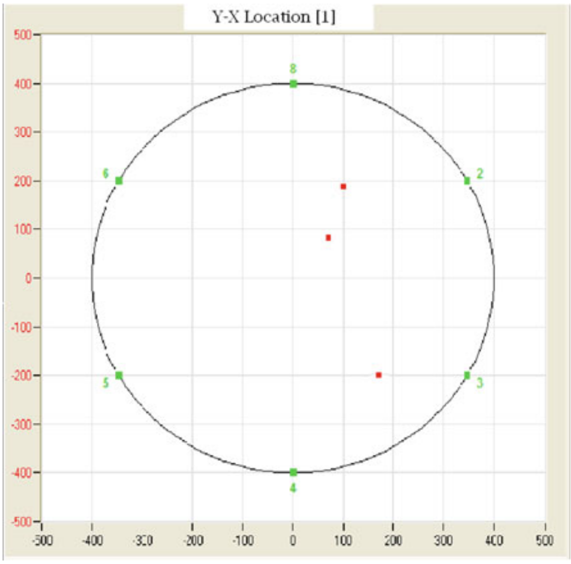

Fig. 15.6 Acoustic source location of traditional location method

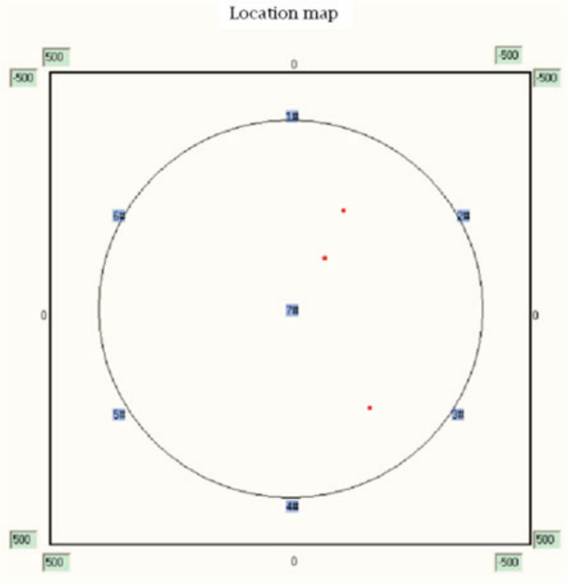

Fig. 15.7 Location method of sensors placed on the center of tank bottom

15.4 Experiment of AE Source Identification in Simulated Tank Bottom Corrosion Process

15.4.1 Experimental System

The simulated corrosion source device was put into the simulated tank and contacted with the tank bottom. The sensor was placed in the water medium in the tank. Sensors were evenly distributed around the tank wall near tank bottom. AE on-line monitoring of tank bottom corrosion was carried out for 12 h The simulated corrosion source device is made of a steel pipe with the same material as tank bottom. Its upper thread is connected with a PVC vent pipe. Steel pipe is filled with corrosion solution, and the bottom flange is fixed and sealed with a Q235 blind plate. Sensor arrangement is that six sensors (No. 1–6) are coupled at the same distance around the tank wall which is 50 mm away from the tank bottom plate; a sensor No. 7 is coupled at the outer bottom plate of the tank, and a sensor No. 8 is coupled to the outer wall of the steel pipe which is 50 mm away from the tank bottom; a sensor No. 9 is placed at the same height from the bottom as No. 8 in water. Sensor 8 and 9 are sealed with signal line. Experiment device is shown in Fig. 15.8.

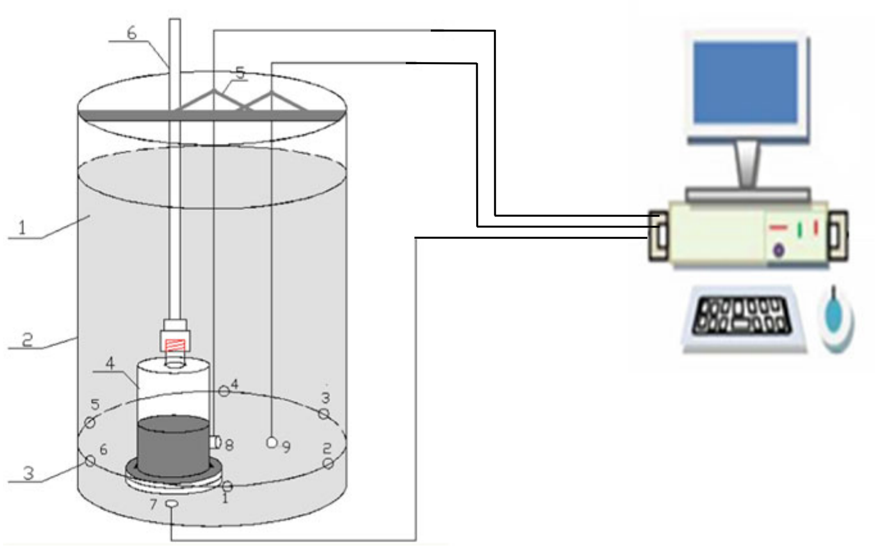

Fig. 15.8 Experiment device for AE testing of simulated tank bottom corrosion

15.4.2 Experimental Results and Analysis

According to the characteristics of acoustic wave propagation path of tank bottom corrosion, the corrosion AE signal was collected by placing sensors at three locations of tank outer wall, steel pipe wall and tank water. From Figs. 15.9, 15.10 and 15.11, the total history diagram of AE signal amplitude of channel 1 (representing 6 channels on tank outer wall), channel 8 and channel 9 collected during the 12 h monitoring process. Corrosion process of 12 h can be divided into three stages, initial stage, accelerated stage and stable stage. Signal amplitude is low, the main distribution range is 30–40 dB, and the impact number of AE signal is less during initial stage.

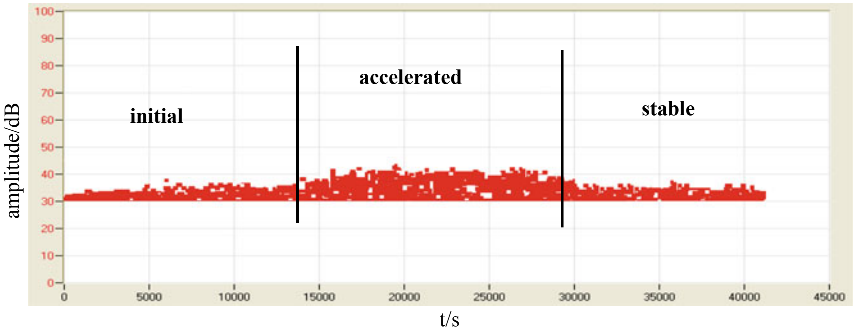

Fig. 15.9 AE signal amplitude of channel 1

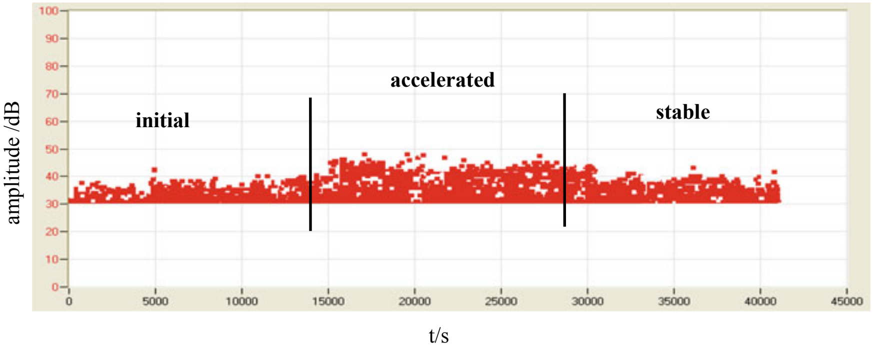

Fig. 15.10 AE signal amplitude of channel 8

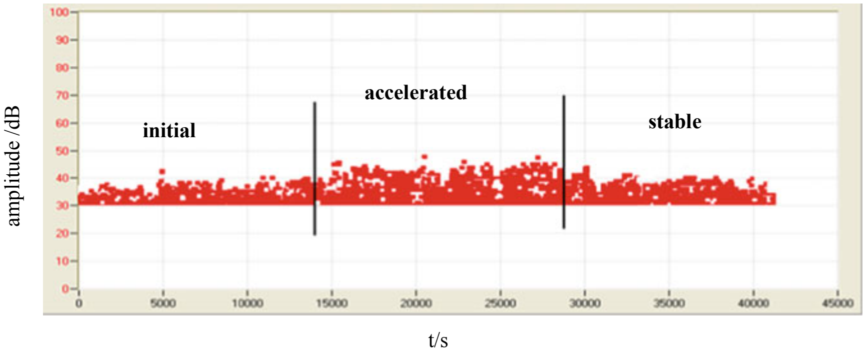

Fig. 15.11 AE signal amplitude of channel 9

Signal amplitude increases, the main distribution range is 40–48 dB, and the impact number of acoustic emission signal increases sharply during accelerated stage. Signal amplitude decreases, the main distribution range is 38–43 dB, the impact number of acoustic emission signal decreases, but the corrosion continues during stable stage. Table 15.2 lists the range of characteristic parameters of AE signals of the three channels in the whole corrosion monitoring process.

Table 15.2 Range of characteristic parameters of corrosion AE signal

Channel	AE signal characteristic parameters				
	Amplitude/dB	Hits	Energy	Duration/μs	Risetion/μs
1	30–43	20170	1–240	1–17000	1–3100
8	30–51	54552	1–70	1–20000	1–3500
9	30–48	39382	1–90	1–20000	1–5000

It can be seen from Table 15.2 that hits of AE signal received by sensor 1 arranged on the outer wall of the tank is less than that of sensors 8 and 9, and the value range of other parameters such as duration is the smallest. The parameters of AE signal received by sensor 8 coupled with the surface of simulated corrosion source device is the largest. Parameters of AE signal received by sensor 9 coupled with water is between parameters of sensor 1 and sensor 8.

The acoustic wave is generated by the corrosion of the simulated corrosion source device. Sensor 8 is coupled on the metal surface of corrosion device, and the AE signal received is the corrosion acoustic source signal. AE parameters can reflect the characteristics of the acoustic source. It can be seen that the signal characteristics received by sensor 9 are closer to that of corrosion acoustic source, with less signal loss. Amplitude, energy, rise time, duration and other parameter characteristics are closer to that of the source signals.

15.5 Conclusion

The sensor placed in the center of the tank bottom can improve the amplitude of the signal received by the sensor in the triangle array of time difference location, and increase the recognition degree of acoustic emission detection to the acoustic source in any triangle location.

It is feasible and testable to detect the corrosion defects of the tank bottom plate by using the underwater sensor. It can increase the positioning area of the tank bottom area and reduce the missed detection caused by signal attenuation. Because the water sensor is in the tank and surrounded by the medium, its ability to resist the influence of external interference on positioning is stronger than the sensor arranged outside the tank. The less interference signals received, the higher the reliability of location.

The AE signal characteristics received by the underwater sensor placed in the tank can reflect the corrosion process of the tank floor. Moreover, it is closer to the characteristics of corrosion sound source and less signal loss. Therefore, the research results of this paper can provide a method for acoustic emission detection of tank bottom corrosion.

Acknowledgements We would like to thank the “National Key R&D Program of China (2016YFC0801200)” for financial support. I would also like to thank the State Key Laboratory of Safety and Control for Chemicals SINOPEC Research Institute of Safety Engineering for their assistance and suggestions.

References

1. G. Dai, M. Zhang, G. Gao, F. Qiu, Analysis and experimental study on AE source characteristics of corrosion process in atmospheric vertical tank bottom. Chem. Eng. Mach. **39**(6), 704–708

(2012)

2. S. Park, S. Kitsukawa, K. Kato et al., AE source and relation between AE activity and rate of corrosion of oil tank bottom plate on acidic soils. Mater. Trans. **46**(11), 2490–2496 (2005)
3. SHEN. Gongtian, GENG. Rongsheng, LIU Shifeng. AE source location. Nondestr. Test. **24**(3), 114–117 (2002)
4. G. Li, G. Shen, H. Yan, Acoustic emission testing technique for atmospheric storage tanks. Nondestr. Test. **6**(3), 257–258 (2009)
5. J. Q. Zhong, Y. Liu, J. Yang, Acoustic emission testing technique for the corrosion destruction condition of vessels. Nondestr. Test. **33**(11), 24–28 (2011)
6. G. Li, G. Shen, H. Yan, Acoustic emission testing technique for atmospheric storage tanks. Nondestr. Test. **6**(3), 257–258 (2019)
7. NB/T 47013.9-2012, Pressure equipment destructive testing-acoustic emission testing

Chapter 16
Research on Extraction Method of Fatigue State Magneto Acoustic Emission Characteristic Parameters Based on CEEMD

Sha Wu, Gongtian Shen, Zenghua Liu, Yongna Shen, and Zhinong Li

Abstract In view of the strong background interference of (MAE) signal and the unique advantage of complementary ensemble empirical mode decomposition (CEEMD), CEEMD is introduced into magneto acoustic emission signal processing. A feature extraction method of MAE signal based on CEEMD algorithm is proposed. In the proposed method, the signal is decomposed by the method of CEEMD, the correlation coefficients of the decomposed eigenmode function (IMF) components and the original signal are analyzed, and the IMF component with a large correlation coefficient with the original signal is retained. Then the components with large correlation coefficients are reconstructed, and the feature parameters are extracted, so that the interference can be effectively suppressed. The CEEMD algorithm can reduce the energy difference between the reconstructed signal and the original signal while maintaining the signal characteristics of the original signal. Finally, when the characteristic parameter curve obtained from the reconstructed signal reaches the yield strength of the material, the trend of the whole graph becomes smooth and stable which accords with the actual situation and verifies the effectiveness of the method.

16.1 Introduction

Ferromagnetic metal materials are often subjected to repetitive loads during long-term service. Even if the load stress on a single cycle is safe, plastic deformation, creep and fatigue will often occur in the stress concentration area along with the

---

S. Wu · G. Shen (✉) · Z. Liu · Z. Li
College of Mechanical Engineering and Applied Electronics Technology, Beijing University of Technology, Beijing 100124, China
e-mail: shengongtian@csei.org.cn

S. Wu
e-mail: 597265536@qq.com

G. Shen · Y. Shen
China Special Equipment Inspection and Research Institute, Beijing 100029, China

© The Author(s), under exclusive license to Springer Nature Singapore Pte Ltd. 2021

G. Shen et al. (eds.), *Advances in Acoustic Emission Technology*, Springer Proceedings in Physics 259, https://doi.org/10.1007/978-981-15-9837-1_16

continuous accumulation of damage, or sudden fracture of components may even lead to catastrophic accidents. Therefore, it is extremely important to prevent fatigue damage of metal materials in service at an early stage. The characteristic parameters of the acoustic emission signal include ringing count, amplitude, RMS voltage, energy. Especially energy is widely used as a characteristic parameter. Here, these characteristic parameters are generalized to the characteristic parameter analysis of MAE signal. However, if the characteristic parameters of MAE signals interfered by strong background noise are directly extracted, the results obtained are not ideal or even contrary to the actual situation. Therefore, effective new methods must be sought to achieve the noise reduction function of MAE signal.

For non-stationary and nonlinear signals, the literature [1] presents a CEEMD method, which converts the white noise added in the EMMD algorithm into positive and negative pairs. It can better eliminate the residual noise of the reconstructed signal and improve the signal-to-noise ratio (SNR) of the signal. In the field of device diagnostics, the CEEMD algorithm is applied to the fault detection of induction motors [2], and the fault of the motor is detected by the method of spectrum analysis of the IMF component. In the field of geophysics, the CEEMD algorithm is applied to denoising seismic radar signals [3, 4], which successfully eliminates coherent noise in seismic radar signals and improves deeper response. CEEMD has been successfully applied to biomedical [5, 6] mechanical fault diagnosis [7–9], but its research in the field of MAE is relatively less. Based on the unique advantages of CEEMD and the characteristics of MAE signals with weak, low amplitude and easy to be submerged by noise, the CEEMD method is introduced into the characteristics extraction of MAE signals. A method for extracting characteristic parameters of MAE signals based on CEEMD is proposed, and experimental verification is performed under fatigue condition, which shows the unique advantages of this method.

16.2 Method and Experimental

Huang [10] first proposed a time-frequency analysis method of Empirical Mode Decomposition (EMD), which is an adaptive signal processing method. It decomposes the signal into a finite IMF, which can accurately express the different frequency components contained in the signal. Therefore, EMD is a time-frequency analysis method for nonlinear steady-state signals. It can repeatedly subtract the envelope mean to eliminate the oscillation and effectively reflect the transient characteristics of the signal. For a given MAE signal $x(t)$, firstly, select all the extreme points on $x(t)$ and connect the maxima with the cubic spline to form the upper and lower envelopes. Then take the median value $m_1(t)$ for the upper and lower envelopes, take the temporary local oscillation $h_1(t) = x(t) - m_1(t)$, replace $x(t)$ with $h_1(t)$, repeat the above two steps until $m(t)$ is equal to 0, the first IMF component is $c_1(t) = h_{1m}(t)$, the residual $r_1(t) = x(t) - c_1(t)$, and $x(t)$ is replaced by $r_1(t)$, repeat the above four steps until the decomposition cannot continue. There is a sum of n IMF components and a residual term:

$$x(t) = \sum_{i=1}^{n} c_i(t) + r_n(t) \tag{16.1}$$

Since this method produces modal aliasing problems, different frequency scales may appear in an IMF component, causing the IMF to lose its physical meaning and thereby reduce the performance of the method. In order to solve the problem of modal aliasing, Wu [11] proposed the EEMD method, which added the white noise of finite columns on the basis of EMD algorithm, so as to solve the problem of modal aliasing in EMD algorithm. Although this method improves the stability of EMD algorithm, the addition of a limited number of white noises limits the number of times it can be used in the set. On the contrary, the IMF obtained from EEMD algorithm is polluted by the added white noises, especially when the number of sets themselves is low, which leads to the problem of residual noise.

In view of the problems existing in the above two methods, Yeh [12] proposed a CEEMD method, which is an improved algorithm based on EMD and EEMD algorithm [13]. On the basis of EMD decomposition, n sets of positive and negative pairs of auxiliary white noise are added to obtain and obtained:

$$\begin{bmatrix} M_1 \\ M_2 \end{bmatrix} = \begin{bmatrix} 1 & 1 \\ 1 & -1 \end{bmatrix} \begin{bmatrix} S \\ N \end{bmatrix} \tag{16.2}$$

where: S is the MAE original signal; N is the added auxiliary white noise; M_1 and M_2 are the MAE signal after adding positive and negative paired noise, respectively. EMD decomposition is carried out on 2n signals, where each of the decomposed signals generates a group of IMF components, and the j IMF component of the i signal is decomposed into an imf_{ij}, finally taking the average of the above multi-component to obtain j imf components:

$$imf_j = \frac{1}{2N} \sum_{i=1}^{2N} imf_{ij} \tag{16.3}$$

By changing the white noise added in EEMD algorithm into the white noise with opposite phase, the problem that the added noise can not be neutralized is solved, so that when the decomposition effect of CEEMD is comparable to EEMD, the residual noise in the reconstructed signal can be eliminated accurately.

Figure 16.1 is a principle block diagram of characteristic parameter extraction of MAE signals based on CEEMD. The key point is to extract the characteristic parameters of the reconstructed signal (obtained from the correlation analysis between the IMF signal and the original signal), and verify the validity of the method based on the obtained characteristic parameter graph.

The application of MAE method to test specimen must have two conditions: a. magnetic field excitation conditions; b. detection conditions of elastic wave pulse. Therefore, the detection system can be divided into two parts, one is the excitation

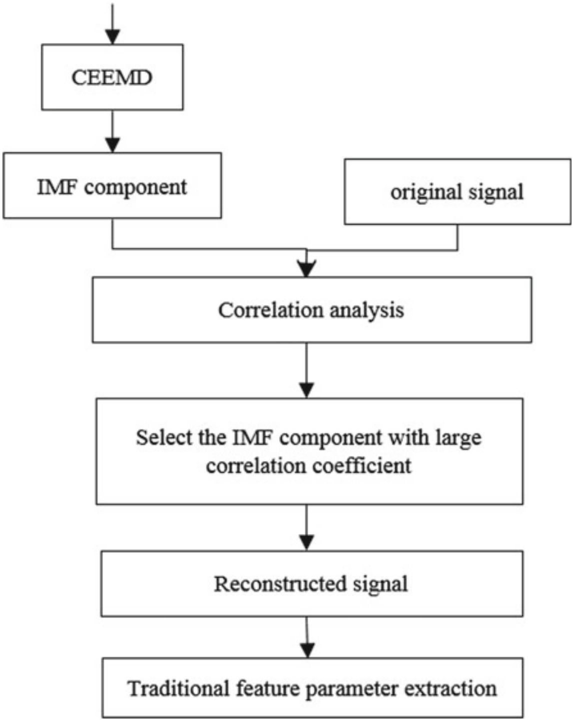
CEEMD
IMF component
original signal
Correlation analysis
Select the IMF component with large correlation coefficient
Reconstructed signal
Traditional feature parameter extraction

Fig. 16.1 Principle block diagram of characteristic parameter extraction of MAE signals based on CEEMD

magnetization module and the other is the signal acquisition module. The principle block diagram of the MAE detection system is shown in Fig. 16.2.

The excitation magnetization module is used to generate an alternating magnetic field, which enables the magnetization process of the test piece to be detected, thereby exciting the elastic wave pulse. The signal acquisition module is used to receive and process signals, and amplify the signals for subsequent research. In this test

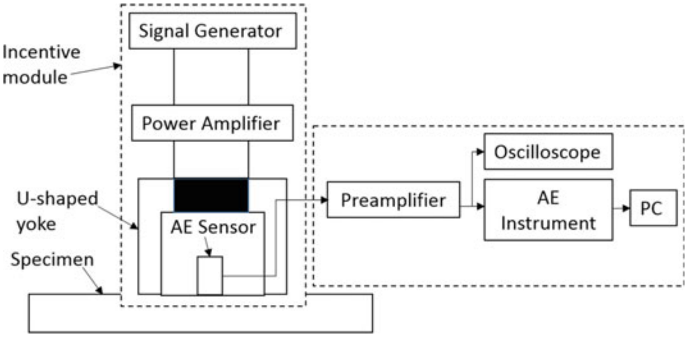
Incentive module
Signal Generator
Power Amplifier
U-shaped yoke
AE Sensor
Specimen
Oscilloscope
Preamplifier
AE Instrument
PC

Fig. 16.2 Block diagram of the MAE detection system

system, the signal generator is the Agilent 33220A signal generator, which produces a stable low distortion sinusoidal output signal [14]. The power amplifier is Newton N4L LPA05B amplifier, which has the advantages of high frequency, large current and low impedance, and has a fixed gain of 10 times [15]. The oscilloscope modle is DSO9064A [16] manufactured by Agilent Technologies. The acoustic emission detector is the SAEU2S acoustic emission detector manufactured by Shenghua Technologies [17]. Based on the experimental requirements of this paper, the sensor is SR150 sensor manufactured by Shenghua Technologies, and the preamplifier is broadband universal PAI preamplifier.

Based on the selection of the above experimental equipment, a complete MAE experimental test system was finally constructed. The experimental system is shown in Fig. 16.3.

In this experiment, the research material is Q235 steel, and the tensile sample is shown in Fig. 16.4. Before the start of the experiment, the specimen was placed in nitrogen at 550 °C for 2 h and cooled to room temperature with the furnace to eliminate residual stress. After processing by heat treatment, the yield strength of the material is 235 MPa and the tensile strength is 422 MPa.

Fig. 16.3 Physical diagram of MAE experimental test system

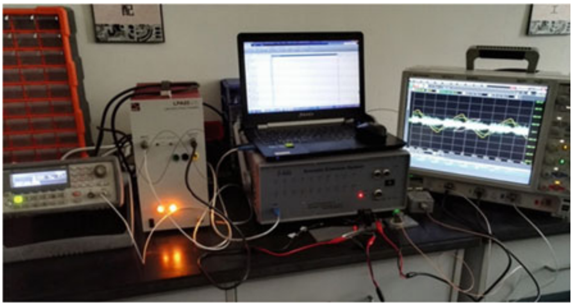

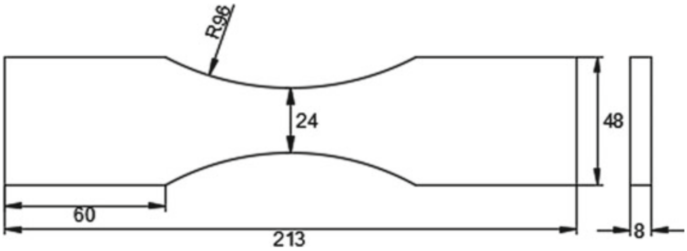

Fig. 16.4 Tensile specimen

16.3 Results and Discussion

The displacement rate of the chuck was set to 0.3 mm/min in the static load test, and the MAE signal of the specimen was collected before the stress was applied. Then MAE signal are collected with excitation frequencies of 10 and 50 Hz, output sinusoidal voltage amplitude of 0.5–3 V, and magnetic field direction parallel to the axial direction.

Firstly, this paper extracts one of the most representative characteristic parameters of the original signal, namely energy. As shown in Fig. 16.4a, when the excitation voltage is constant, the energy increases with the increase of the excitation frequency. With the excitation frequency unchanged, the energy increases with the increase of excitation voltage. According to MAE generation mechanism, excitation voltage directly affects the degree of magnetic domain structure change of ferromagnetic metal materials. With the increase of excitation voltage, irreversible movement of domain wall, generation and annihilation of domain wall and irreversible process of magnetic domain magnetization vector begin to generate MAE signal, thus making signal energy gradually increase [18]. As for the excitation frequency, it is related to the rate of change of the magnetic domain structure of ferromagnetic metal material. As the excitation frequency increases gradually, the energy increase rate of the MAE signal increases relatively. Although the increase of energy increase rate is beneficial to data analysis, the excitation frequency increases and the bimodal characteristics of the MAE signal are weakened to a certain extent, which is not conducive to data analysis. Therefore, when selecting the excitation frequency, the SNR and the shape characteristics of the signal should be considered at the same time.

In addition to energy as a characteristic parameter, Fig. 16.5b, c show the comparison of amplitude and RMS voltage with static tensile force. However, it is observed that the relationship between energy and static tensile force is not as obvious as that in Fig. 16.5a. Since the MAE signal contains a complex noise signal, in order to accurately extract the characteristic parameters, CEEMD algorithm will be used to denoise the MAE signal.

It can be seen from Fig. 16.6 that it is not ideal to extract the characteristic parameters of the original signal directly. Therefore, the CEEMD algorithm needs to be introduced to effectively improve the SNR of the signal while maintaining the characteristics of the signal. When using the CEEMD algorithm to process the MAE signal, firstly the signal needs to be decomposed into IMF components. Secondly, the correlation coefficients of each IMF component and the original signal are calculated, and the reconstruction signal is composed of two or three IMF components whose correlation coefficient cumulative value is close to 1. Finally, the characteristic parameters are extracted from the reconstructed signal.

It is found that the IMF1 and IMF4 components need to be accumulated in the static load experiment, and the obtained results are suitable for the extraction of characteristic parameters in the next step. Since it is easier to determine the threshold voltage value than the original signal, the characteristic parameters of the MAE signal can be accurately extracted. Therefore, using CEEMD algorithm to process the MAE

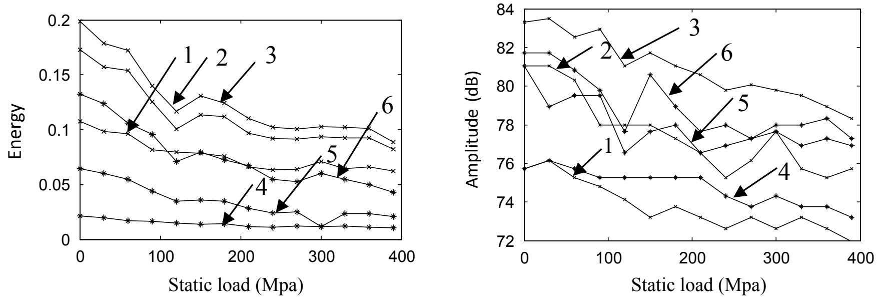

(a) Energy (b) Amplitude

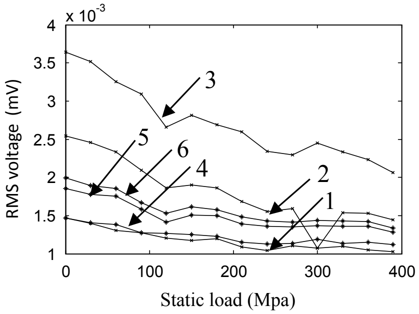

(c) RMS voltage

1. Excitation frequency 50HZ, excitation voltage 1V; 2. Excitation frequency 50HZ, excitation voltage 2V; 3. Excitation frequency 50HZ, excitation voltage 3V; 4. Excitation frequency 10HZ, excitation voltage 1V; 5. Excitation frequency 10HZ, excitation voltage 2V; 6. Excitation frequency 10HZ, excitation voltage 3V;

Fig. 16.5 Comparison graph of various parameters of original signal under different tensile forces of Q235 steel

signal has theoretical basis and support. In order to illustrate that the algorithm effectively improves the SNR of the signal, it can be seen from Fig. 16.7 that the SNR of the reconstructed signal obtained by CEEMD decomposition is higher than that of the MAE original signal when the fixed excitation frequency is 50 Hz and the excitation voltage is 1, 2 and 3 V. It is indicated that the CEEMD algorithm can reduce the energy difference between the reconstructed signal and the original signal while maintaining the signal characteristics of the original signal. At the same time, the SNR of the MAE signal is improved, which has a great influence on extraction of the characteristic parameters of the MAE signal.

Figure 16.8 shows the trend of the characteristic parameters of MAE under static tensile force. It can be seen that strength of the MAE signal decreases with the increase of the external tensile force. The reason for this trend is that there are a lot of dislocations in the material, which act as the pinning center and hinder the movement of domain walls. It can be seen from Fig. 16.5 that the values of the parameters of the

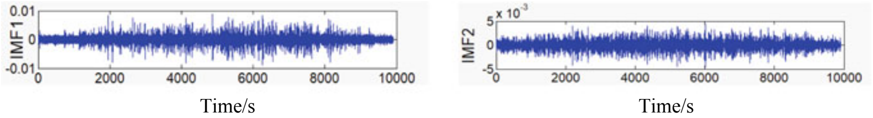

(a) the first IMF component (b) the second IMF component

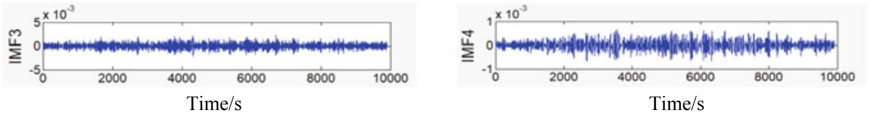

(c) the third IMF component (d) the fourth IMF component

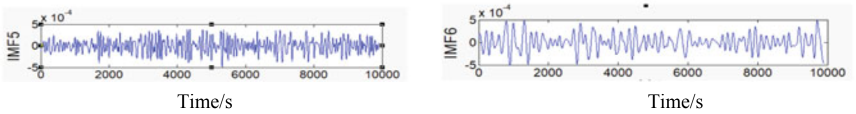

(e) the fifthIMFcomponent (f) the sixth IMF component

Fig. 16.6 CEEMD algorithm decomposition of each IMF component

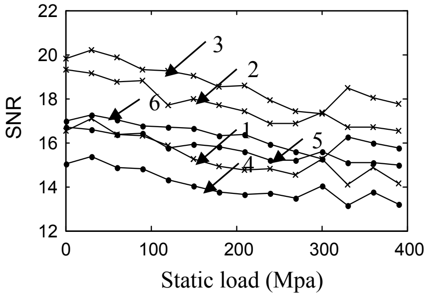

1. Excitation frequency 50HZ, excitation voltage 1V, SNR of reconstructed signal;
2. Excitation frequency 50HZ, excitation voltage 2V, SNR of reconstructed signal;
3. Excitation frequency 50HZ, excitation voltage 3V, SNR of reconstructed signal;
4. Excitation frequency 10HZ, excitation voltage 1V, SNR of original signal;
5. Excitation frequency 10HZ, excitation voltage 2V, SNR of original signal;
6. Excitation frequency 10HZ, excitation voltage 3V, SNR of original signal;

Fig. 16.7 Comparison graph of SNR of reconstructed signal and original signal under static load of Q235 steel

MAE signal are continuously decreasing, and strength of the MAE signal decreases rapidly during the elastic deformation stage where the tensile stress is small. When the yield strength reaches 235 Mpa, the MAE signal of tensile specimen tends to be stable, which accords with the actual situation and verifies the effectiveness of the method. Finally, the comparison between Figs. 16.8 and 16.5 shows that the trend of the characteristic parameter comparison graph obtained from reconstruction

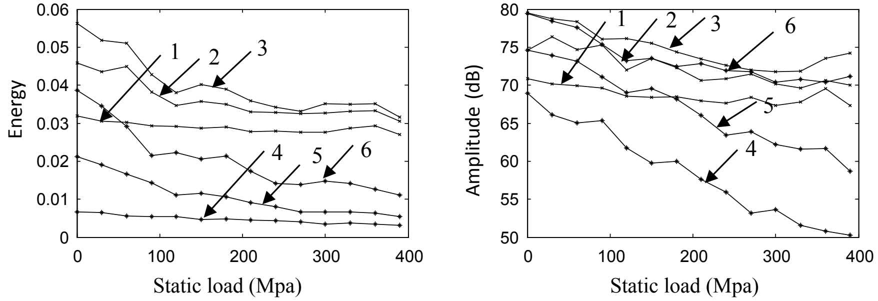

(a) Energy (b) Amplitude

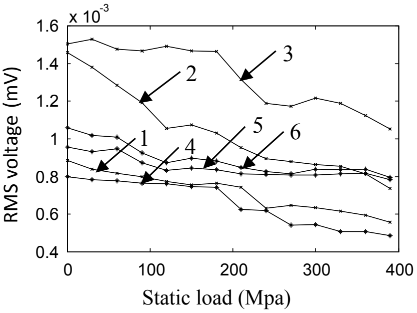

(c) RMS voltage

1. Excitation frequency 50HZ, excitation voltage 1V;
2. Excitation frequency 50HZ, excitation voltage 2V;
3. Excitation frequency 50HZ, excitation voltage 3V;
4. Excitation frequency 10HZ, excitation voltage 1V;
5. Excitation frequency 10HZ, excitation voltage 2V;
6. Excitation frequency 10HZ, excitation voltage 3V;

Fig. 16.8 Comparison graph of various parameters of reconstructed signal under different tensile forces of Q235 steel

signal is the same as that obtained from original signal. At the same time, when the characteristic parameter curve obtained from the reconstructed signal reaches the yield strength of the material, the trend of the whole graph becomes smooth and stable. Theoretically, the law of static load tensile force, excitation frequency and excitation voltage is more obvious. In other words, the CEEMD algorithm has practical significance in the processing of MAE signals under static load.

16.4 Conclusion

The CEEMD algorithm solves the problem of residual noise in the reconstructed signal by adding a pair of positive and negative relative noise and retains the useful information of the original signal well. Therefore, the method is referenced to the MAE signal processing. In the static load state, since the large amount of dislocations inside the material, the MAE signal strength continuously decreases as the tensile force of the static load increases. Moreover, when the curve obtained by the CEEMD algorithm is near the yield strength of 235 Mpa, the whole pattern trend becomes smooth and stable. According to the comparison of SNR, the proposed method effectively improves the SNR of the MAE signal. In summary, the CEEMD algorithm has a unique advantage in the extraction of MAE signal characteristic parameters under static load state.

References

1. J.-r. Yeh, J.-s. Shieh, N., Complementary ensemble empirical mode decomposition: a novel enhanced data analysis method. Adv. Adapt. Data Anal. **2**(2), 135–156 (2010)
2. P.A. Delgado-Arredondo, D. Morinigo-Sotelo, R.A. Osornio-Rios et al., Methodology for fault detection in induction motors via sound and vibration signals. Mech. Syst. Signal Process. **83**, 568–589 (2016)
3. M. Manataki, A. Sarris, A. Vafidis, Combining CEEMD and predictive deconvolution for the suppression of multiple reflections and coherent noise in GPR signals, in*International Workshop on Advanced Ground Penetrating Radar*, Florence, Italy. IEEE Press, pp. 1–4 (2015)
4. J. Li, C. Liu, Z. Zeng et al., GPR signal denoising and target extraction with the CEEMD method. IEEE Geosci. Remote Sens. Lett. **12**(8), 1615–1619 (2015)
5. C. Franco, J. Fontecave-Jallon, N. Vuillerme, et al.: Towards a suitable time-scale representation of cardio-respiratory signals through empirical mode decomposition algorithms: a simulation and validation tool, in*Conference Proceedings IEEE Engineering in Medicine and Biology Society*, Boston, MA, USA. IEEE Press, p. 802 (2011)
6. W. Zhao, Z. Wang, J. Ma et al., Fault diagnosis of a hydraulic pump based on the CEEMD-STFT time-frequency entropy method and multiclass SVM classifier. Shock Vibr. **1**, 8 (2016), 26 Sept. 2016
7. U. Satija, B. Ramkumar, M.S. Manikandan, Automated ECG noise detection and classification system for unsupervised healthcare monitoring. IEEE J. Biomed. Health Inform. **99**, 1–1 (2017)
8. M. Li, H. Wang, G. Tang et al., An improved method based on CEEMD for fault diagnosis of rolling bearing, in Advances in Mechanical Engineering, Hindawi Publishing Corporation, pp. 1–10 (2014)
9. L. Zhao, W. Yu, R. Yan, Rolling bearing fault diagnosis based on CEEMD and time series modeling. Math. Probl. Eng. (2014-7-7), **1**, 1–13 (2014)
10. N. Huang, Z. Shen, R. Long Steven et al., The empirical mode decomposition and the Hilbertspectrum for nonlinear and non-stationary time series analysis. R. Soc. **454**, 903–995 (1998)
11. Z.-h. Wu, N. Huang, Ensemble empirical mode decomposition: a noise-assisted data analysis method. Adv. Adapt. Data Anal. **1**(1), 1–41 (2008)
12. J.R. Yeh, J.S. Shieh, N.E. Huang, Complementary ensemble empirical mode decomposition: a novel noise enhanced data analysis method. Adv. Adapt. Data Anal. **2**(2), 135–156 (2010)

13. J. Lin, Overall empirical mode decomposition algorithm complementary gearbox fault diagnosis based on mechanical transmission **8**, 108–111 (2012)
14. S. Li, *Research on Key Technologies of Signal Interchangeable Virtual Instrument* (Harbin University of Technology, 2009)
15. W. Ke, *Magnetoacoustic Emission of Ferromagnetic Metallic Materials* (Nanchang University of Aeronautics, 2016)
16. P. Jiang, Power *Analysis and Defense Technology of Lightweight Block Cipher Algorithm* (Harbin University of Technology, 2013)
17. Y. Lai, X. Yan, L. Cheng, Band energy characteristics of acoustic emission signals in the whole process of loaded concrete failure. J. Vib. Shock **33**(10), 177–182 (2014)
18. Y. Shen, G. Shen, W. Ke, Advances in magnetoacoustic emission detection. Nondestruct. Test. **39**(5), 87–98 (2017)

Part IV
Material Characteristics

Chapter 17
Cluster Analysis of Acoustic Emission Signals on Tensile Damage Process of C/SiC Using an Improved K-Means Algorithm

Yongzhen Zhang, Xiaoyan Tong, and Leijiang Yao

Abstract C/SiC is one of most important thermal-structural materials for future aeronautical applications, but there is no consensus on the damage mechanism and pattern of it. To identify the failure processes under mechanical load is important to evaluate this material. In this paper, acoustic emission (AE), an effective continuous damage monitoring technique, is used to monitor tensile tests of 2D-C/SiC. An unsupervised clustering method based on the deep fusion of a genetic algorithm and a K-means algorithm is proposed to analyze the AE signals. Pattern recognition analysis of AE data was carried out to describe the evolution of various damage mechanisms during the failure process. According to the features of each class and associated SEM images of the fracture surfaces, a match between AE clusters and fracture mechanisms involved in the process, including matrix cracking, interface failure, interlaminar delamination, fiber breakage and bundle breakage, is established. It is found that the damage evolution of 2D-C/SiC under tensile loading can be divided into four stages at room temperature. The first stage and the third stage are the main development stages of matrix cracking and interface damage. The second stage and the fourth stage are the main damage periods of fiber, fiber bundle and interlaminar delamination. The damage pattern recognition and damage evolution process of 2D-C/SiC composites during tensile test are described.

Y. Zhang · X. Tong · L. Yao (✉)
National Key Laboratory of Science and Technology on UAV, Northwestern Polytechnical University, Xi'an 710072, China
e-mail: yaolj@nwpu.edu.cn

Y. Zhang
e-mail: zhangyongzhennpu@163.com

X. Tong
e-mail: tongxy@nwpu.edu.cn

© The Author(s), under exclusive license to Springer Nature Singapore Pte Ltd. 2021

G. Shen et al. (eds.), *Advances in Acoustic Emission Technology*, Springer Proceedings in Physics 259, https://doi.org/10.1007/978-981-15-9837-1_17

17.1 Introduction

As a typical ceramic matrix composite, continuous fiber reinforced silicon carbide (C/SiC) has excellent performance of high specific strength, corrosion resistance, oxidation resistance and high temperature resistance [1]. It has broad prospects in the application of thermal structures such as aeroengine, gas turbine, launch vehicle thermal protection system, and is an indispensable material for the development of aerospace and other high-tech fields [1–6]. Acoustic emission (AE) technology can monitor the development of material internal damage in real time and directly reflect the process of material damage generation and expansion. However, the AE signal of material damage is complex, and the parameters of the AE signal of damage types are not obvious, so it is difficult to directly associate the AE signal with the damage type [6, 7].

Previous research results show that the method of unsupervised clustering can identify the damage types of materials [8–12]. The damage modes of the composite under high temperature (700–1200 °C) were obtained by cluster analysis method by Momons et al. [9]; Tong et al. studied the AE signal parameters of C/SiC composite under room temperature tensile test by using k-means clustering algorithm [11]. Huang Xipeng, Wang Bo, etc. used the energy and amplitude of AE signals after wavelet denoising to carry out pattern recognition through K-means clustering analysis method, and studied the damage modes of 3D-N C/SiC and C/SiC composites with different densities under tensile load [11, 12]. At present, the unsupervised analysis of AE signals of tensile damage of C/SiC composite is mainly based on K-means algorithm and unsupervised clustering analysis of some characteristics of AE signal directly selected by researchers [9–12]. K-means clustering algorithm is a classical algorithm in cluster analysis, which has the advantages of simplicity and rapidity. However, K-means algorithm is a local search technology, which may converge prematurely due to the influence of initial clustering center [13]. At the same time, less AE signal characteristics can't reflect the AE events of materials completely. There is no an improved k-means algorithm to analyze the AE signal of C/SiC damage mode.

In this study, the genetic algorithm proposed by Holland is introduced to solve the problem of K-means algorithm in the clustering analysis of AE signals of 2D C/SiC tensile damage. The algorithm simulates the genetic and evolutionary process of biological species in nature, and it has strong robustness and global optimization ability [14]. Through the optimization of the common clustering algorithm for AE data processing in the tensile test of 2D C/SiC samples at room temperature, the more reliable clustering analysis results are obtained. At the same time, through the distribution of all kinds of damage types energy and the growth trend of accumulated energy in the process of tensile test, combined with SEM observation of sample fracture, the identification of damage types in the process of tensile loading is completed, which provides the basis for damage detection in the engineering application of 2D C/SiC composite materials.

17.2 Tensile Test

C/SiC was manufactured by the Science and Technology on Thermo-structural Composite Materials Laboratory of Northwestern Polytechnic University. The material mainly consists of C fibers, PyC and SiC matrix. The fiber volume content is about 40%, the porosity is about 15%, and the density is 2.1–2.2 g/cm^3.

The room temperature monotonic tensile test was carried out on Instron 8801 hydraulic servo fatigue testing machine. The loading rate was 0.5 mm/min. During the test, online monitoring was performed using the AE machine (PAC PCI-II) of the American Physical Acoustics Corporation (front amplification gain: 40 dB, signal threshold: 45 dB, sample rate: 1MSPS). After the tensile test, the specimen cut-off profile was observed using the Hitachi TM4000PLUS benchtop scanning mirror.

17.3 Clustering Analysis Based on Improved K-Means Algorithm

The most commonly used clustering algorithm in AE signal analysis of C/SiC material damage is K-means, however, it may convert accurately and lose the global optimal solution due to the influence of the initial clustering center. Therefore, this paper introduces genetic algorithm, through the deep fusion of genetic algorithm and K-means algorithm to solve the problem of K-means algorithm, so to achieve a more reasonable clustering of AE data. Through the unsupervised clustering method based on the improved k-means algorithm, the AE signals of 2D-C/SiC specimen in the process of tensile damage is analyzed, and the damage mode identification of the material under monotonic tensile load can be realized. To introduce genetic algorithm to unsupervised clustering analysis, the following problems should be solved: (1) the consistency of individual gene coding in genetic algorithm; (2) the construction of fitness function and genetic operation; (3) the selection of clustering effectiveness evaluation index. The flow of clustering analysis based on improved k-means algorithm is shown in Fig. 17.1.

17.3.1 Gene Label Conversion in Individuals

Before using genetic algorithm to get the final result, it is necessary to solve the problem of cluster label inconsistency. For example, the clustering {1, 1, 2, 2, 2, 3, 3, 3} and {2, 2, 3, 3, 3, 1, 1, 1}. Although their expressions are different, they represent the same result. The corresponding relationship between basic clusters must be established. For the clustering problem with m (m $\geq$ 2) base clusters, the relative position relationship between the cluster center and the coordinate origin is used to number all kinds of centers, then the corresponding element number of each

Fig. 17.1 The flow of clustering analysis based on improved k-means algorithm

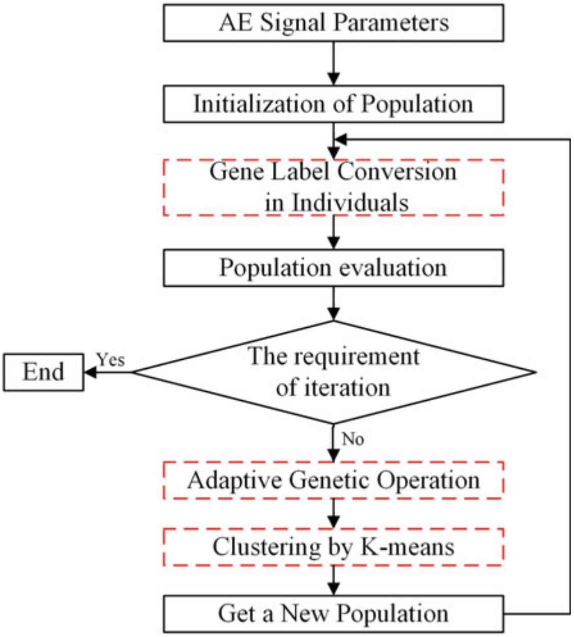
AE Signal Parameters
Initialization of Population
Gene Label Conversion in Individuals
Population evaluation
The requirement of iteration
Yes
End
No
Adaptive Genetic Operation
Clustering by K-means
Get a New Population

center is modified to the number of the cluster center to ensure that the labels of basic clusters are consistent.

17.3.2 Genetic Operation and Fitness Function Selection

The main genetic operations in unsupervised clustering based on improved genetic algorithm are crossover, mutation and selection operator selection. In this paper, single point crossing, random variation and roulette according to individual fitness are used to carry out genetic operation. Fitness is usually used to measure the degree of excellence of individual in the group to reach the optimal solution in the optimization calculation. In this paper, the fitness function is constructed by formula (17.1). The smaller the J value in formula (17.1) is, the better the clustering result is. Therefore, the following fitness function is selected:

$$f = \frac{c}{1 + J} \tag{17.1}$$

where c is a constant and J is a criterion function.

17.3.3 Evaluation Criteria of Clustering Effectiveness

Cluster validity evaluation is mainly a process of selecting the cluster validity index, evaluating cluster quality and determining the best cluster number [15]. Davies Bouldin index (DB) proposed by Davies et al. [16] is one of the most commonly used clustering effectiveness indexes. DB indexes estimate the compactness within a cluster by the distance between the sample points within the cluster and its cluster center and express the level of separation between clusters by the distance between the cluster centers. The relevant formula of DB value definition is shown in formula (17.2)–(17.4) The smaller the DB, the smaller the distance within the cluster, and the greater the distance between clusters, which means more clustering results. In this paper, the DB index is selected as the evaluation index of clustering effectiveness.

$$DB = \frac{1}{k}\sum_{i=1}^{K}\left(\max_{j=1,\ldots,j\neq i} R_{ij}\right) \tag{17.2}$$

$$R_{ij} = \frac{s_i + s_j}{D_{ij}} \tag{17.3}$$

$$s_i = \sqrt{\frac{1}{n}\sum \|x - m_i\|} \tag{17.4}$$

17.4 Results and Discussions

17.4.1 Tensile Test Results

The displacement loading curve of 2D-C/SiC specimen and the energy distribution of AE signals during stretching are shown in Fig. 17.2.

17.4.2 Acoustic Emission Signal Clustering Results

The results of previous studies on 2D-C/SiC ceramic matrix composites [10–12, 17–19] and SEM images of sample fracture (Fig. 17.3) show that there are five dominant failure modes in the damage and failure process of the material, including matrix cracking, interface failure, fiber fracture, interlayer peeling and fiber bundle fracture, and the parameters of the clustering center can represent the characteristics of AE signals under various damage modes [20, 21], so the cluster number K = 5 is selected for cluster analysis, and the result shown in Fig. 17.4 is obtained.

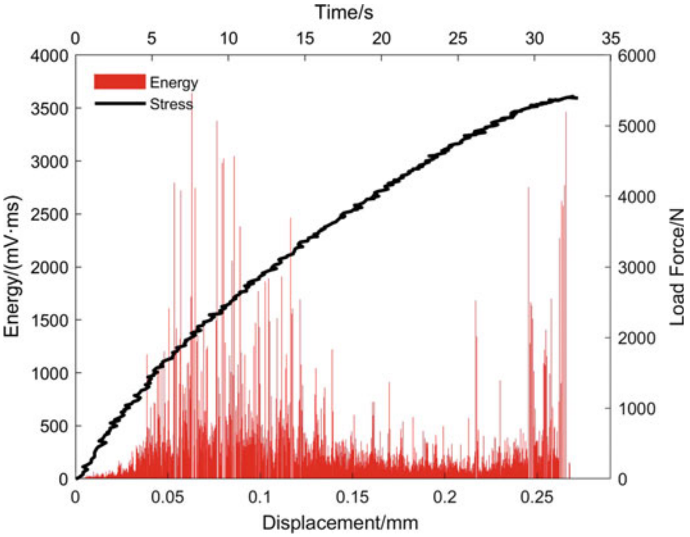

Fig. 17.2 Displacement loading curve and energy distribution of AE signals during tensile process

The acoustic emission parameters of each cluster center can be found in Table 17.2. The parameters of Cluster 1 are the smallest among all clusters. Considering the microcrack growth in matrix and the cracking characteristics of macro matrix in 2D C/SiC, Cluster 1 corresponds to matrix cracking; Cluster 2 and Cluster 3 have low energy, fiber fracture and interface debonding also have low energy characteristics, but the fiber's size is small, the stress is high during the loading process, resulting in a very short fracture time, and the corresponding AE signal frequency is also high [19]. It can be seen from Table 17.2 that the frequency of Cluster 3 is higher than that of Cluster 2, So Cluster 2 and Cluster 3 correspond to interface debonding and fiber breakage respectively. The fiber bundle is composed of fibers, so the fiber bundle and fibers should be similar in frequency. It is found that the frequency of Cluster 3 and Cluster 5 are both large and similar. The fiber bundle bears a larger load in the material. Generally, the single fracture of fiber bundle covers dozens or even hundreds of fibers, and the strain energy released when the fiber bundle breaks is higher [20], and the material will also produce a high energy AE signal, Therefore, Cluster 5 corresponds to fiber bundle breakage; In the process of material stretching, due to the high energy and a large number of interlaminar failure caused by the propagation and deflection of matrix cracks, Cluster 4 conforms to the AE signal characteristics of interlaminar delamination. The cluster center parameters and corresponding damage modes are shown in Table 17.2.

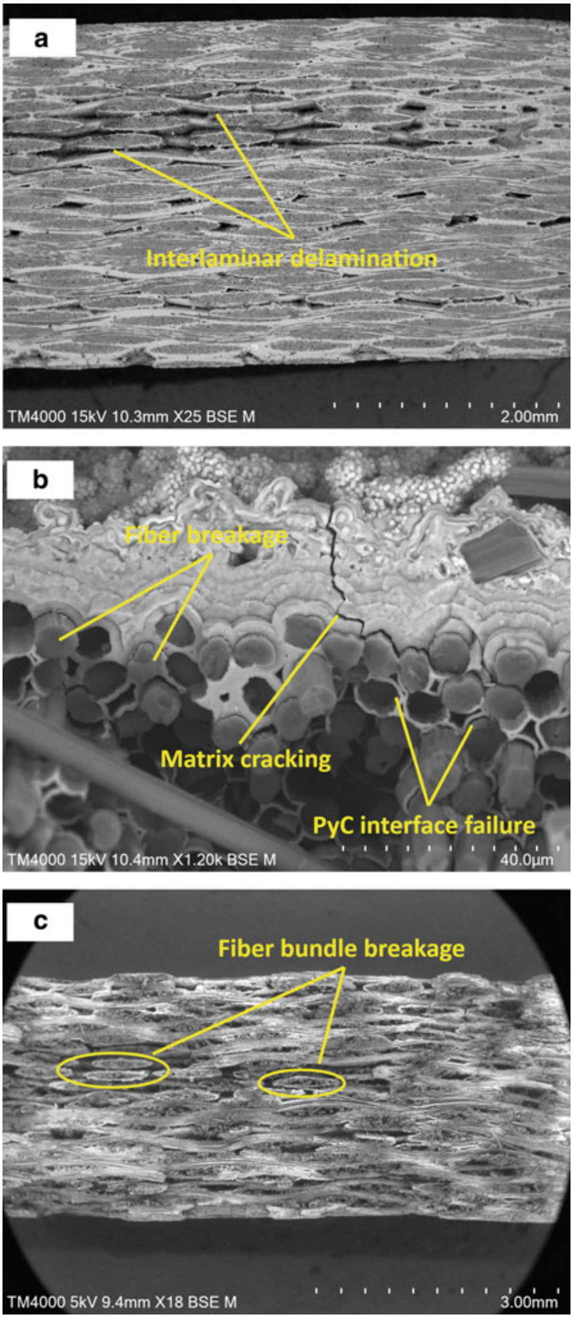
a
Interlaminar delamination
TM4000 15kV 10.3mm X25 BSE M
2.00mm
b
Fiber breakage
Matrix cracking
PyC interface failure
TM4000 15kV 10.4mm X1.20k BSE M
40.0μm
c
Fiber bundle breakage
TM4000 5kV 9.4mm X18 BSE M
3.00mm

Fig. 17.3 Fracture SEM images of sample. **a** Interlaminar delamination; **b** Fiber breakage, matrix cracking and PyC interface failure; **c** Fiber bundle breakage

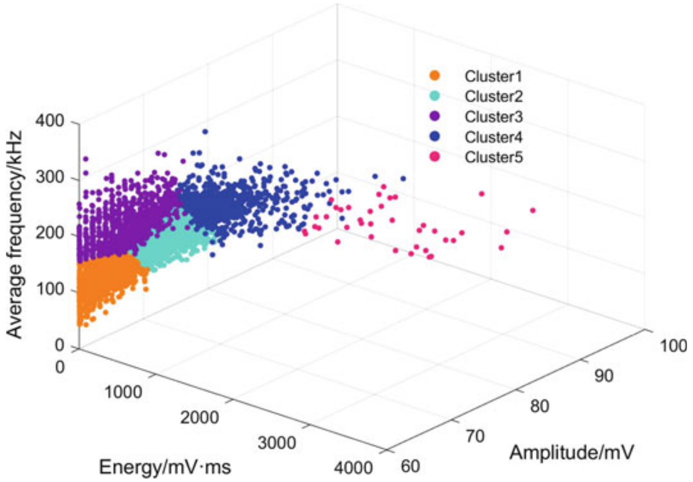

Fig. 17.4 Distribution of clustering results of acoustic emission signals

Table 17.2 Parameters value of the clustering center

Cluster	Average frequency	Amplitude	Count	Energy	Damage types
1	110	64	201	29	Matrix cracking
2	139	72	671	104	Interface debonding
3	183	67	340	48	Fiber breakage
4	172	79	2141	344	Interlaminar delamination
5	194	83	14077	2134	Fiber bundle breakage

17.4.3 Damage Evolution Analysis of C/SiC

The tensile failure process of C/SiC composites can be divided into three stages: damage initiation, damage acceleration and damage stability [18–22]. At the initial stage of loading, the stress-strain curve shows linear characteristics, almost no damage occurs; with the loading, the initial defects and cracks begin to grow and expand, resulting in the interface between the fiber and the matrix debonding, the material modulus gradually reduces, and the stress-strain curve of the material shows nonlinear characteristics; When the tensile stress reaches a certain value, the propagation of a large number of initial cracks ends, the crack density reaches saturation, and the damage enters a stable development period, and the stress-strain curve once again shows a nearly linear feature [21, 22]. Figures 17.5 and 17.6 are the evolution process of AE cumulative events total energy (count multiply energy) and event number of various damage modes in the tensile process based on AE pattern recognition. Figures 17.7 and 17.8 show the AE signal energy distribution of five damage

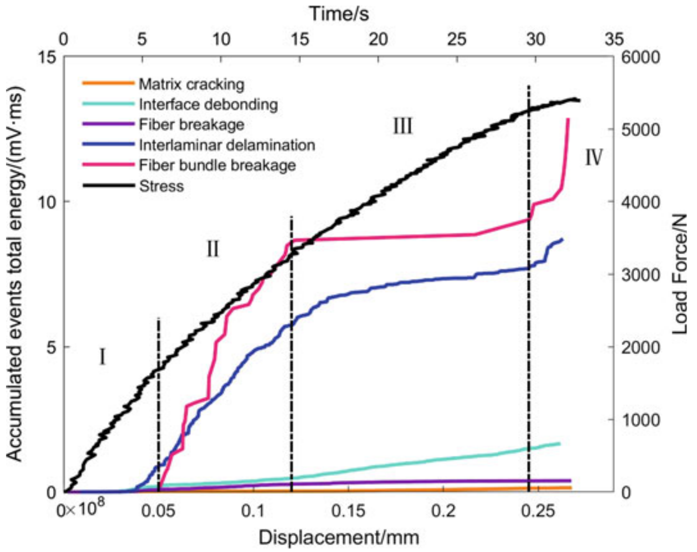

Fig. 17.5 Accumulated energy with strain and time

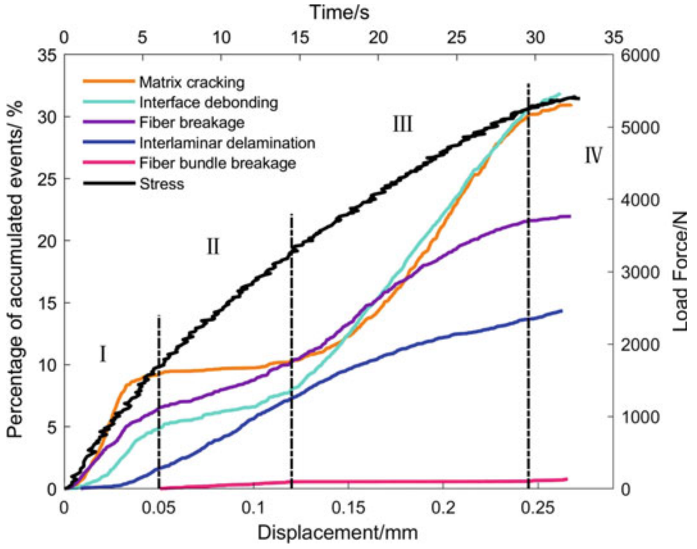

Fig. 17.6 Accumulated number of AE events with strain and time

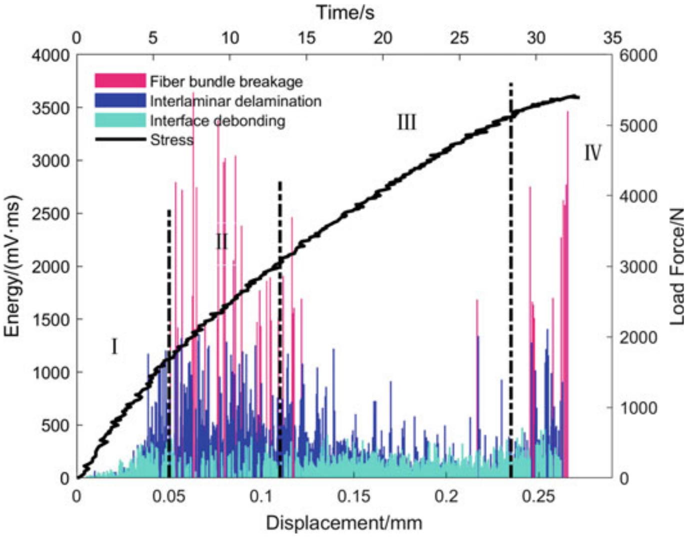

Fig. 17.7 Energy distribution of fiber breakage, interlaminar delamination and interface debonding

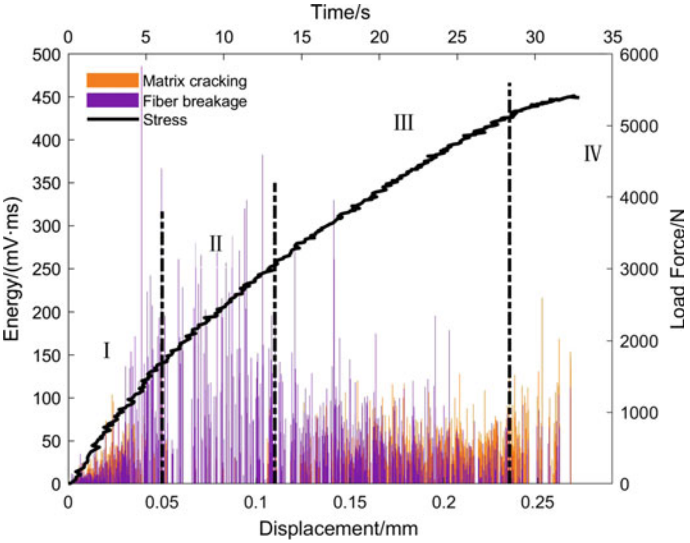

Fig. 17.8 Energy distribution of matrix cracking and fiber breakage during the tensile test

modes in the tensile process: matrix cracking, interface damage, fiber fracture, interlayer peeling and fiber bundle fracture. From Fig. 17.5, it could be seen that fiber bundle breakage, interlaminar delamination and interface debonding are the main factors of C/SiC specimen damage. Therefore, the whole loading process is divided into 4 stages according to the development law of main factors.

The first stage: it is generally considered that there is a damage initiation stage, but through the acoustic emission research method, it is found that even in the damage initiation stage, there are still obvious micro fracture events. At this stage, the main AE signals are matrix microcrack growth, pyrolytic carbon interface damage and filament fracture. During the preparation of C/SiC composite, thermal stress will be generated, and the pores in the microstructure will become the crack source, and expand under low stress. At the beginning of loading, the residual thermal stress of the material is released. When the local stress exceeds the bearing capacity of the SiC matrix, the pores of the SiC matrix as the crack source generate microcracks and expand. At the same time, with the increase of stress, matrix cracks begin to appear in the low strength SiC region. As the fiber blocks the growth of microcracks in the matrix, the cracks deflect along the interface, resulting in interface debonding, as shown in Fig. 17.3a. At the same time, a small number of weak fibers break in the fiber bundle.

The second stage: the number of high energy AE signals is increased rapidly, while the matrix cracking events and interface debonding events are very few, indicating that the stage of crack saturation has been entered. In two-dimensional plain weave composites, due to the extrusion between the fiber bundles, the braided joints are easy to produce hole defects, which is easy to cause matrix crack convergence and stress concentration of the fiber bundles in braided joints. In the crack saturation region, fiber and fiber bundle are the main bearing objects of tensile load. Strain energy is released more through fiber and fiber bundle fracture. Some fibers begin to break at the same time, and the AE energy is higher than that in the first stage (Fig. 17.8), and the AE events of fiber bundle breakage begins to appear (Fig. 17.7). It can be seen from Fig. 17.3c that the longitudinal fiber bundle breaks at the braided node, and there is obvious fiber pullout. In addition, during this period, due to the effect of fibers and fiber bundles on the matrix crack growth, cracks are generated in the cross area of longitudinal and transverse fiber bundles, and begin to extend along the longitudinal direction of fibers and fiber bundles, resulting in more interlaminar delamination. Meanwhile, It can be seen from Fig. 17.3a that most of the interlaminar delamination occurs in the cross area of fiber bundles. The interfacial slippage, fiber bundle fracture and interlaminar delamination in the process of fiber bundle pullout cause the elastic modulus of the material to decrease gradually at this stage, which is consistent with the existing understanding of the accelerated damage stage of the material.

The third stage: the fiber bundle breakage almost stopped, and other damage types continued to occur. This is due to the large number of fractures of fibers and fiber bundles as bearing parts in the saturated area of microcracks in the second stage; with the increase of stress, the matrix part begin to be the bearing object in the fracture area of fibers in this stage, and at the same time, the matrix cracks begin to form in the rich matrix area, as shown in Fig. 17.3b. With the growth of long cracks in the matrix, the interfacial debonding also increases continuously. The energy dissipation mainly depends on the surface energy formed by cracks and debonding and the friction of fiber pulling out, and the fiber bundle fracture almost stops.

The fourth stage: when the material enters the failure stage, the material reaches the maximum shape variable, the matrix, interface, interlayer and fiber continue to be damaged, the AE events of all kinds of damage continue to occur, the fiber bundle fracture event occurs again, and the material enters the serious damage stage until the specimen breaks. The highest point of displacement loading curve is regarded as the sign of material failure. However, from the perspective of AE analysis, the macroscopic failure of materials should have occurred before. The final fracture of the material can be forewarned by the surge of acoustic emission signals.

17.5 Conclusion

The results show that the AE pattern recognition method combined with fracture analysis can more accurately describe the evolution process of various damage mechanisms in the failure process than the stress-strain relationship alone. It is found that the matrix crack propagation and the fiber bundle breakage events occur alternately in the whole tensile test process, and the interface debonding and interlaminar crack continue to occur in the whole process; the matrix crack propagation exists in the early and later loading stages, but in the early stage, the microcrack propagation is dominant, in the later stage, the long crack propagation is dominant, and in the middle, the crack saturation stage is experienced.

Acknowledgements This work has been financially supported by the National Key Research and Development Project of China (2016YFB0700503) and the National Natural Science Foundation of China (51772244 and 11072195).

References

1. R. Naslain, Design, preparation and properties of non-oxide CMCs for application in engines and nuclear reactors: an overview. Compos. Sci. Technol. **64**(2), 155–170 (2004)
2. F. Christin, Design, fabrication, and application of thermostructural composites (TSC) like C/C, C/SiC, and SiC/SiC composites. Adv. Eng. Mater. (2002)
3. L. Zhang, L. Chen, Y. Xu, Progress in research work of new CMC-SiC. Aeronaut. Manuf. Technol. **1**, 24–32 (2003)
4. L. Zhang, L. Cheng, Discussion on strategies of sustainable development of continuous fiber ceramic matrix composites. Acta Materiae Compositae Sinica **24**(2), 1–6 (2007)
5. Q. Lu, G. Jiang, X. Luo, L. Hu, Lightweight and non-ablation new TPS for X-37B aerospace vehicle. Modern Def. Technol. **40**(1), 16–20 (2012)
6. L. Zhi Quan, M.A. Wu-Jun, Applied research of rocket engine thrusters made of ceramic matrix composite. J. Rocket Propuls. (2011)
7. N. Zarif Karimi, G. Minak, P. Kianfar, Analysis of damage mechanisms in drilling of composite materials by acoustic emission. Compos. Struct. **131**, 107–114 (2015)

8. Feasibility and limitations of damage identification in composite materials using acoustic emission. Compos. Part A: Appl. Sci. Manuf. **75**, 77–83 (2015)
9. H. Mei, Y. Sun, L. Zhang, et al., Acoustic emission characterization of fracture toughness for fiber reinforced ceramic matrix composites. Mater. Sci. Eng. A (Struct. Mater. Propert. Microstruct. Proces.) **560**, 372–376 (2013)
10. S. Momon, N. Godin, P. Reynaud et al., Unsupervised and supervised classification of AE data collected during fatigue test on CMC at high temperature. Compos. Part A: Appl. Sci. Manuf. **43**(2), 0–260 (2012)
11. X. Tong, J. Zhang, L. Yao et al., Cluster analysis of acoustic emission signals of 2D-C/SiC under tensile loading. Chin. J. Solid Mechan. **35**(2), 109–114 (2014)
12. X. Huang, B. Wang, C. Yang et al., Evaluating damage evolution of three-dimension needled C/SiC composite based on acoustic emission signal analysis. J. Inorgan. Mater. **33**(06), 609–616 (2018)
13. X. Huang, B. Wang, C. Yang et al., Damage evolution of C/SiC composite materials with different densities based on acoustic emission signal analysis. Acta Materiae Compositae Sinica **36**(02), 425–433 (2019)
14. J.A. Hartigan, M.A. Wong, Algorithm AS 136: A K-means clustering algorithm. J. Roy. Stat. Soc. **28**(1), 100–108 (1979)
15. J.H. Holland, Erratum: genetic algorithms and the optimal allocation of trials. SIAM J. Comput. **2**(2), 88–105 (1973)
16. K. Zhou, S. Yang, S. Ding, H. Luo, On cluster validation. Syst. Eng. Theor. Pract.
17. D.L. Davies, D.W. Bouldin, A cluster separation measure. IEEE Trans. Pattern Anal. Machine Intel. **PAMI-1**(2), 224–227 (1979)
18. G. Guan, G. Jiao, Z. Zhang, Uniaxial macro-mechanical property and failure mode of a 2D-woven C/SiC composite. Acta Materiae Compositae Sinica **22**(4) (2005)
19. P. Fang, L. Cheng, L. Zhang et al., Acoustic emission characteristics of C/SiC composite during tensile test. Nondestruct. Test. **28**(7), 358–361 (2006)
20. Y. Chang, G. Jiao, Y. Tao et al., Damage behavior of 2.5D-C/SiC composites under tensile loading. J. Inorg. Mater. **23**(3) (2008)
21. L. Li, S.V. Lomov, Y. Xiong et al., Cluster analysis of acoustic emission signals for 2D and 3D woven glass/epoxy composites. Compos. Struct. **116**(1), 286–299 (2014)
22. Y. Ech-Choudany, M. Assarar, D. Scida et al., Unsupervised clustering for building a learning database of acoustic emission signals to identify damage mechanisms in unidirectional laminates. Appl. Acoust. **123**, 123–132 (2017)

Chapter 18
Investigation of Flexural Progressive Damage of Three-Dimensional Braided Composites by Acoustic Emission and Micro-CT

Wei Zhou, Peng-Fei Zhang, Ran Liu, Ya-Ping Liu, Zhi-Yuan Wei, and Sa Yang

Abstract Three-dimensional four-direction is the most widely used braided structure in the field of three-dimensional braiding. For purpose of improving the mechanical properties of this kind of braiding in a certain direction, three-dimensional five-directional braid has been developed. The aim of this work is to investigate the progressive damage and failure behavior of three-dimensional five-directional braided composites subjected to three-point bending. To comprehensively analyzing the damage process of 3D five-directional braided composites, a variety of non-destructive testing methods is used, involving acoustic emission, digital image correlation and *X-ray* micro-computed tomography. Among them, the acoustic emission response behavior of the composite damage process is monitored in real time, and the displacement and strain field at different stages are calculated by the digital image correlation method. More importantly, the microscopic damage morphology of the materials is visualized by using *X-ray*, and the analysis results are supplemented and verified. Through analyzing the experimental results, the obvious *Kaiser* effect is observed, and the acoustic emission signals are concentrated in the middle and late stages of loading and directly related to the cumulative degree of damage. In addition, the position of the strain and displacement set from the deformation measurement is consistent with the damage evolution from the micro-computed tomography observation.

W. Zhou (✉) · P.-F. Zhang · Z.-Y. Wei · S. Yang
School of Quality and Technical Supervision, Hebei University, Baoding 071002, China
e-mail: zhouwei@hbu.edu.cn; zhouweihy@126.com

R. Liu
China Special Equipment Inspection and Research Institute, Beijing 100013, China

Y.-P. Liu
Hebei Province Special Equipment Supervision and Inspection Institute Baoding Branch, Baoding 071002, China

© The Author(s), under exclusive license to Springer Nature Singapore Pte Ltd. 2021

G. Shen et al. (eds.), *Advances in Acoustic Emission Technology*, Springer Proceedings in Physics 259, https://doi.org/10.1007/978-981-15-9837-1_18

18.1 Introduction

Three-dimensional (3D) textile structural composites reinforced with fibers, yarns and fabrics have enormous development potentials in the field of aerospace, military and marine industries owing to their little specific gravity, high specific strength, large specific modulus, fatigue resistance and strong designability [1–3]. In the long-term applications of the composite materials, the stiffness degrades with the external loading, and then results in the damage accumulation and destruction eventually [4]. Most researchers focus on the analysis of damage results for composite materials [5–7]. However, the research on 3D braided composites, especially the analysis of the effect of the binder yarns to prevent the delamination during the flexural progressive loading process, is relatively insufficient.

As one of the classic types of three-dimensional textile structural composites, the 3D five-directional braided composites have attracted a lot of attention due to their excellent mechanical properties. Liu et al. [8] investigated the high temperature compressive properties and failure mechanism of 3D five-directional braided composites. The results showed that the compressive modulus and strength decreased as temperature increased. Hu et al. [9] analyzed the strength characteristics of 3D braided composite specimens with different braiding angles in a three-point bending test based on the repeat unit cell model. It was found that the load-deflection curve and the progressive damage morphology are consistent with the numerical prediction results. Ouyang et al. [10] studied the bending fatigue behavior of 3D five-directional braided T-shaped composite from finite element analyses and experimental characterizations. In addition, Zhang et al. [11] and Wang et al. [12] analyzed the progressive damage behavior and the failure of 3D braided composites subjected to tension. In order to more accurately grasp the damage evolution process and mechanical properties of the composites, some effective detection methods are necessary to be taken.

Recently, a combination experimental mechanics and nondestructive evaluation (NDE) approach assisted has been widely applied to investigate aspects of the mechanical behavior and damage process of 3D braided composites, involving acoustic emission (AE) techniques [13–17], optical methods such as digital image correlation (DIC) [18], as well as others such as *X-ray* based micro-computed tomography (micro-CT). Zhou et al. [19] used a method combining AE with DIC to monitor the compressive buckling behavior of multi-delaminated composites. The analysis of the AE signal was based on a *k*-means algorithm and principal component analysis (PCA). The results showed that the AE signal of the compression process can be divided into three clusters. In addition, it has been found that the size and location of the delaminated defects results in a decrease in the mechanical properties of the composite. Castaneda et al. [20] used AE, DIC and micro-CT to investigate the role of z-binder for enhanced damage tolerance of 3D woven composites. The combined evaluation of globally calculated with locally resolved strain patterns which track the 3D damage evolution was realized and strain localizations related to damage were cross validated by the AE data and micro-CT analysis. Further, Zhang et al. [21] studied the effect of bearing direction on the progressive damage of 3D five-directional braided composites by three-point bending test. AE and micro-CT techniques were used to monitor the damage evolution behavior of the composites and the identification of internal damage initiation/evolution and distribution characteristics. The experimental results showed that the microscopic damage morphology observed by micro-CT can be well correlated with the variation characteristics of the collected AE parameters.

This paper is motivated by exploring the bending progressive damage mechanism of 3D five-directional braided composites. The novelty of the work presented stems from the combined use of multiple complementary methods including AE which is damage monitoring, DIC which provides full field and surface deformation information, and micro-CT which can provide the internal damage initiation/evolution. The mechanical curves, maximum stress value is recorded and discussed under flexural loadings. The progressive damage behaviors in composites are observed and evaluated. Furthermore, the failure mechanisms are analyzed.

18.2 Materials and Experimental Details

18.2.1 Specimens Preparation

In the present paper, Specimens provided by the Institute of Composite Materials of Jiangnan University (China) are fabricated by carbon fibers of Toray T700-12k as reinforcement and consolidated by TDE-85 epoxy resin using RTM (resin transfer molding) process [22, 23]. 3D five-directional braided preforms with the thickness of 4.7 ± 0.2 mm are cut into the size of 60 mm × 20 mm by cutting machine. Then, black/white paint is randomly sprayed on the side of the composite specimens to measure the displacement and strain fields of the composites. A total of three samples are employed.

18.2.2 Method

The three-point bending tests are conducted by a LD24 machine at a displacement-control velocity of 2 mm/min according to ASTM standard D790 partly. The span of two supporting rollers is set as 48 mm as shown in Fig. 18.1a. Meanwhile, AE signals and the speckle images are collected by a DS2A instrument and CMOS (MER-500-7UM-L) in real time, as shown in Fig. 18.1b–c. Two RS-54A AE sensors (the frequency range is 100–900 kHz) are used and their distance is 40 mm and preamplifier with the output of 40 dB. The threshold and the sampling frequency are fixed to 10 mV (40 dB) and 3 MHz by repeated tests. In addition, speckle images are scanned at 30.45 pixels/mm and collected twice per second by a CMOS camera

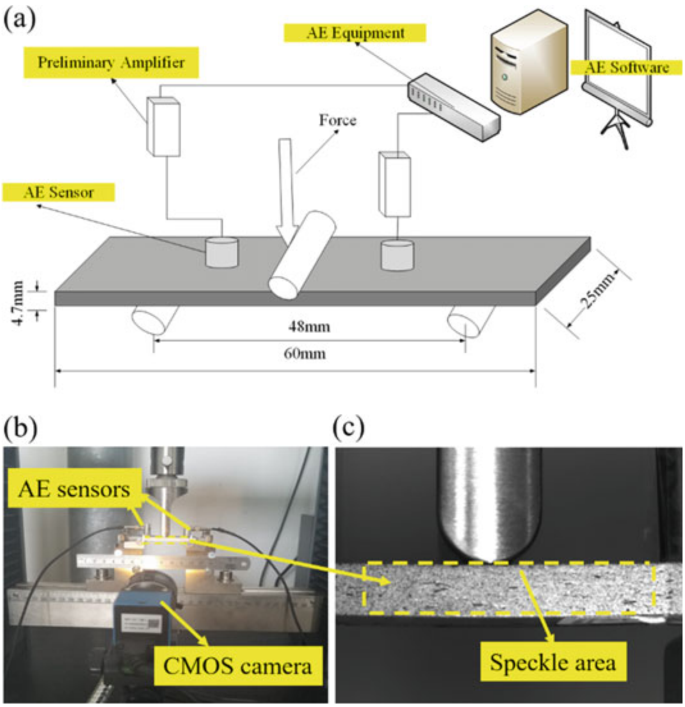
(a)
Preliminary Amplifier
AE Equipment
AE Software
Force
AE Sensor
4.7mm
48mm
60mm
25mm
(b)
(c)
AE sensors
CMOS camera
Speckle area

Fig. 18.1 **a** Specimens size and three-point bending diagram, **b** experimental system of measurement, **c** artificial speckle area

with a resolution of 2592 × 1944. Internal damage images at different stages are obtained by pausing the test and placing the specimens on a Skyscan 1172 X-ray computed tomography system. The specimens are rotated 180° (each rotation step is 0.2°) along the Y-axis and scanned layer by layer using a Micro-CT instrument with a resolution of 6.8 μm under conditions of 76 kW and 128 μA.

18.3 Results and Discussions

18.3.1 Mechanical Behavior

Table 18.1 shows Failure loads and AE distribution of the composite specimens. The typical load-displacement curves of the three specimens are presented in Fig. 18.2. As shown in Fig. 18.2, the mechanical curves of the composite demonstrate excellent repeatability. The damage initiation and growth, as well as changes in stiffness of the material can be fully described. At the initial loading stage, the load of the specimen increases linearly. As a typical stage of material damage evolution, select a Point

Table 18.1 Failure loads and AE distribution of the composite specimens

Group	Load/kN	Average failure loads/kN	Bending strength/MPa	Average bending strength/MPa	Amplitude range/dB	Accumulated counts
Group 1	6.51		848.7		40.06–95.76	14,097
Group 2	6.00	5.86	782.3	764.5	40.06–91.00	13,442
Group 3	5.09		663.6		40.06–97.58	14,686

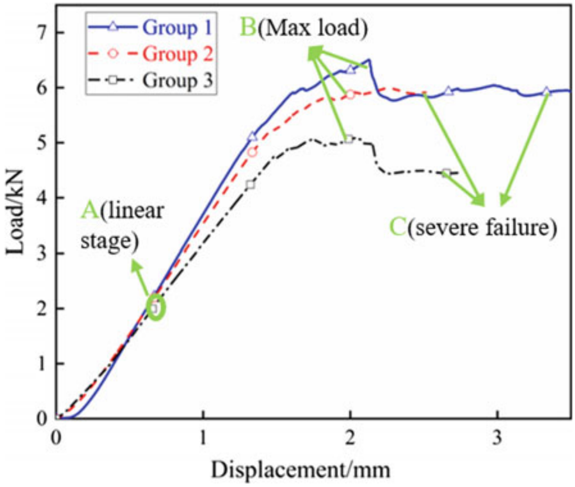

Fig. 18.2 The load-displacement curves for three groups of 3D five-directional braided composite specimens

A at this stage for the analysis of progressive damage. It can be detected whether the initiation cracks occur before the maximum load is reached. Then, with the load increases to the maximum (Point B), the slope of the curve (stiffness of the materials) decreases. It is noted worthy that to find that the load of the test piece does not decrease immediately and fluctuates up and down within a certain load range. This is because the composite only has the upper and lower surfaces of the yarn and the resin matrix damaged during the bending loading process, while the neutral layers of the axis yarn, braided yarn and matrix are still intact, so that part of the bearing capacity is still maintained. For purpose of research the characteristics under the final failure state, Point C is chosen just near the severe failure of the specimen. Afterwards, the first, second and third repeated loadings are performed at the positions of the three points.

18.3.2 Response Behavior of the AE Signal

Figure 18.3 shows the variation of the force-accumulated counts-amplitude over time for the specimen. As the progressive loading progresses, the AE amplitude and accumulated counts continue to increase, revealing a deeper degree of damage. In general, changes in AE amplitude and accumulated counts are associated with internal damage activity and damage behavior [24]. By the 1st loading, it can be found that the AE signal do not appear until loading for 45 s (2.58 kN), and the amplitude does not exceed 60 dB, and the AE accumulated counts value is low, indicating that the sample has almost no serious damage in the linear elastic stage. Then, performing the 2nd load, increasing the load to the maximum value, the characteristics of the corresponding AE signal are obtained. In fact, during the 2nd load, we find that there is no (or very little) AE signal before reaching the maximum of the first load. This interesting phenomenon of stress memory-damage is called the *Kaiser effect* [25]. By definition, little or no AE signal is recorded before reach any previous maximum stress level. Subsequently, when loading to 90 s (5.24 kN), the AE accumulated counts of the specimen increased significantly, the amplitude signal became richer and some AE signals greater than 60 dB appeared. The cause of this phenomenon may be several damage modes, such as matrix cracking, fiber debonding and delamination, occurring simultaneously [19]. Complex damage behavior is accompanied by rich AE signals.

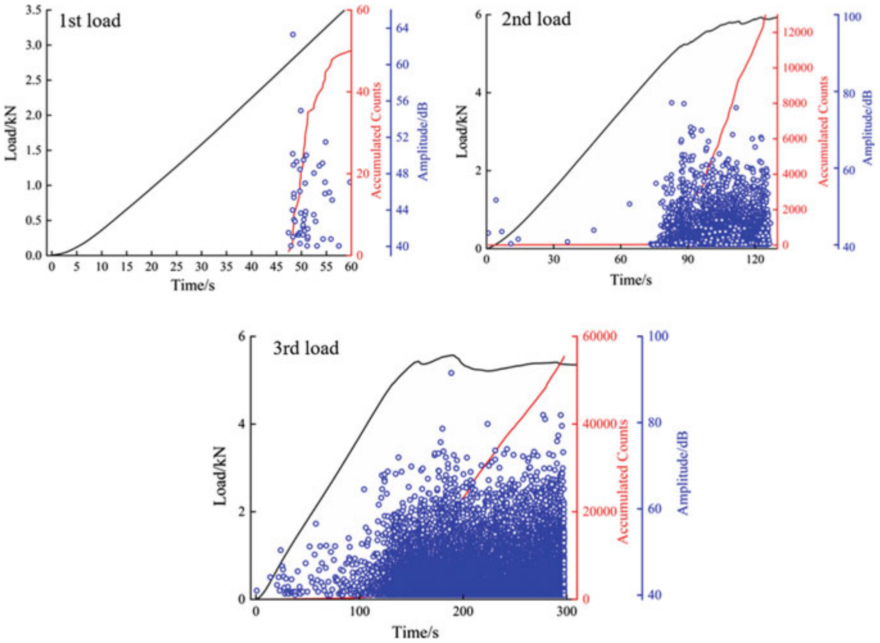

Fig. 18.3 Flexural load, amplitude and accumulated counts versus time of specimen

The purpose of the 3rd loading is to observe the damage evolution of the specimen after the failure point. It can be found that although the load does not continue to increase, the AE accumulated counts of the specimen still maintains an increasing trend. In addition, the amplitude signal distribution of the AE is more concentrated, and a large number of signals higher than 80 dB and even close to 100 dB appear. This phenomenon may be attributed to the fact that the previous two times loadings caused damage to the specimen mainly due to the fibers and matrix of the interface, while the internal axis yarn and the braided yarn does not completely break, which also reveal why the composites do not lose its bearing capacity immediately even after reaching the failure point. However, the last loading may cause the yarn to break and pull out, resulting in more and higher amplitude AE signals.

Figure 18.4 describes the distribution of AE amplitude and frequency varying with the duration of the composite samples. The responds of the AE signals at different loading stages can be seen from Fig. 18.4a–c, respectively. The frequency and duration of AE signals are related to the damage type of materials, while the

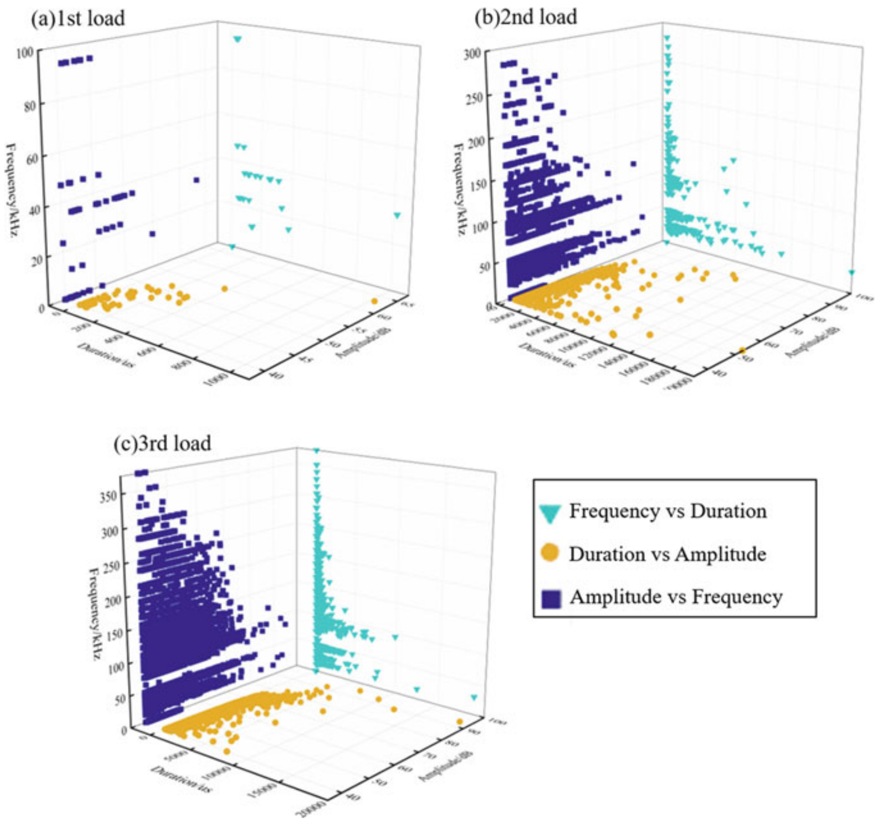

Fig. 18.4 AE amplitude and frequency with increasing duration for specimen in 1st load (**a**), 2nd load (**b**), 3rd load (**c**)

magnitude of amplitude reveals the damage degree of materials. It can be seen that after the first loading, the detected AE frequency do not exceed 100 kHz and the duration is concentrated within 4000 μs, while the amplitude signals are mainly distributed in the range of 40–45 dB, indicating that the damage of specimen is very slight at this time. Performed again loaded (see Fig. 18.4b), the values of duration, amplitude and frequency are significantly increased, and a large number of AE signals revealed the occurrence of damage of the specimen. In addition, it is found that the duration of the high frequency signal is short. These signals are primarily detected at the moment of matrix cracking and fiber breakage. After that, the 3rd load is executed, a large number of signals greater than 70 dB appear, the frequency and duration exceed 350 kHz and 20,000 μs respectively, and the distributions of AE signals are more dense and rich. On the other hand, AE signals of high amplitude and high duration appeared, indicating that continuous damage similar to debonding and delamination are aggravated in the specimen and combined with matrix cracking and fiber breakage resulted in failure of the material.

To sum up, the AE parameters such as accumulated counts, amplitude, duration and frequency can better describe the damage accumulation and failure process of composite. In order to understand the stress of the specimen more clearly, the strain field and displacement field of the material are obtained by calculating.

18.3.3 Displacement Field and Strain Field Distribution of Composite Specimens

The correlation coefficient $C(u, v)$ can be obtained using (18.1) [26]. From the maximum correlation coefficient C, the deformed image can be calculated. The surface deformation field shown by the deformed image can be used to describe the damage evolution of the specimens.

$$C(u, v) = \frac{\sum_{i=1}^{m}\sum_{j=1}^{m}\left[f(x_i, y_j) - f\right]\left[g\left(x'_i, y'_j\right) - \bar{g}\right]}{\sqrt{\sum_{i=1}^{m}\sum_{j=1}^{m}\left[f(x_i, y_j) - f\right]^2}\sqrt{\sum_{i=1}^{m}\sum_{j=1}^{m}\left[g(x'_i, y'_j) - \bar{g}\right]^2}} \tag{18.1}$$

where $f(x, y)$ and $g(x', y')$ are the gray value of the image of the undeformed and deformed patterns, f and g are the average gray value of $f(x, y)$ and $g(x', y')$, respectively.

Figure 18.5 show the distribution of strain field in the speckle zone of specimen in x direction and y direction at different loads and times, respectively. From Fig. 18.5a–b, the strain values in both directions gradually increase with the bending force increases. In the 1st load stage, the specimens only have relatively high strain values on the upper and lower surfaces, the overall strain value is small, and the strain value in the y direction is slightly larger than the strain value in the x direction. It can be seen that the surface of the specimen is the main force-bearing position at the beginning

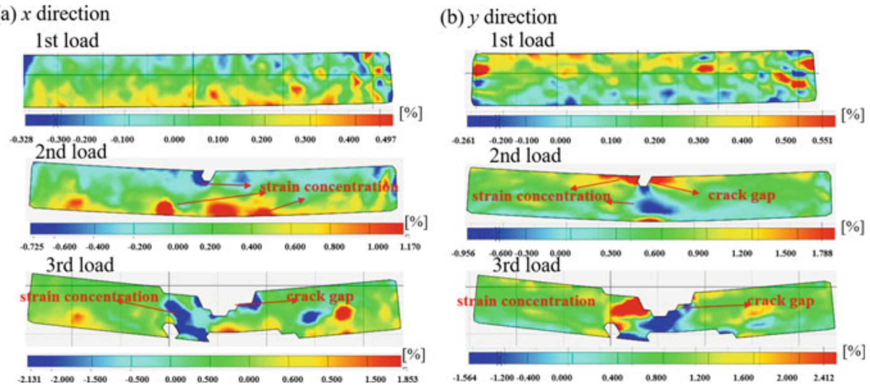

Fig. 18.5 The strain field distribution of the specimen after three times loading in x direction (**a**) and y direction (**b**)

of loading. After the 2nd loading, the upper and lower surfaces of the specimen show a significant strain concentration, and the closer to the center, the strain value is greater, which is due to the upper and lower surfaces of the specimen are subjected to greater pressure and tension, respectively. When the 3rd load is performed, crack gap appeared in the center of the specimen, indicating that specimens have completely failed. It can be observed that the value of high stress is distributed along the edge of the crack, extending from the surface to the neutral layer, and some damages such as matrix cracking, delamination and fiber breakage occurs at these stress concentration locations. This reveals the stress condition and damage evolution process of the specimen during loading.

The distributions of in-plane displacement fields of specimen after three times loading in *x* direction and *y* direction can be observed from Fig. 18.6. The distribution characteristics of the displacement deformation of specimens in *x* and *y* directions are consistent with the stress conditions in different directions, and the y displacement is greater than that of the *x* direction. This shows that the *y* direction is the main direction of force of the specimen subjected to bending loading. The displacement fields of the specimens in the *x* direction are layered, and higher displacement values appear on the upper and lower surfaces. From Fig. 18.6a, after the 2nd loading, the displacement deformation directions of the upper and lower surfaces are opposite, which fully prove that the upper and the lower surface of the specimen are subjected to different effects of compressive stress and tensile stress. In addition, it can be observed that after the 3rd loading is performed, the deformation band with a higher displacement value at the bottom disappears first, indicating that the tensile stress applied to the specimen was more obvious, and the bottom of the specimen fails first. The displacement fields of the specimens in the *y* direction are distributed in a ring shape, and the high displacement values are concentrated at the center position. The cracking of the matrix and the fiber fracture mainly occur in the region where the central displacement deformation value is high, and this phenomenon becomes more

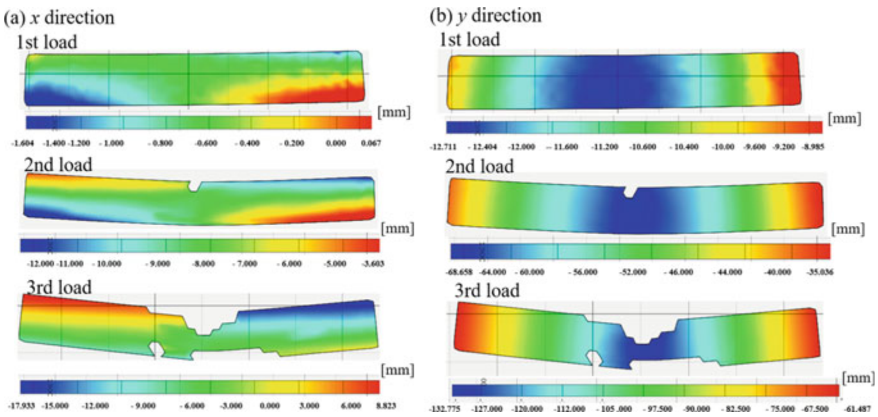

Fig. 18.6 The displacement field distribution of the specimen after three times loading in x direction (**a**) and y direction (**b**)

and more obvious as the loading strength increases. Further, we study the meso-damage morphology of the material by micro-CT to verify the correctness of the analysis.

18.3.4 Progressive Damage Morphology and Failure Analysis

Micro-CT is useful to analysis the damage evolution of composites under various damage modes at the microstructure level. Dark-grey areas in the images correspond to cracks and damage, while the light-grey areas represent higher-density material, i.e. carbon fiber tows [27]. The information obtained can be used for progressive damage analysis and material performance studies.

The internal damage evolution image of the specimen after three times loading at positions a, b and c is reflected in Fig. 18.7, and remarkable changes are observed. Position "a" represents the section inside the specimen, and it can be observed that the crack did not appear until the second loading and extended to the neutral layer. Finally, with the third loading is performed, these damages evolve into distinct bend band. "b" is the tomographic image on the side of the sample. After the first loading, the specimen shows no obvious damage, and only some void defects are found. The loading is completed again, some damage like the matrix cracking occurs. When the 3rd loading is performed, multiple severe damage modes occur simultaneously, and the previously generated cracks further deteriorate into delamination and debonding damage. Further, the occurrence of fiber breakage directly leads to material failure. "c" corresponds to the upper surface of the test piece. Due to the direct application of the compressive stress of the upper roller, the crack is formed in the width direction on the upper surface of the specimen after the two loads are performed. Continued to increase the loading force, debonding of the fiber bundle and the matrix occurred,

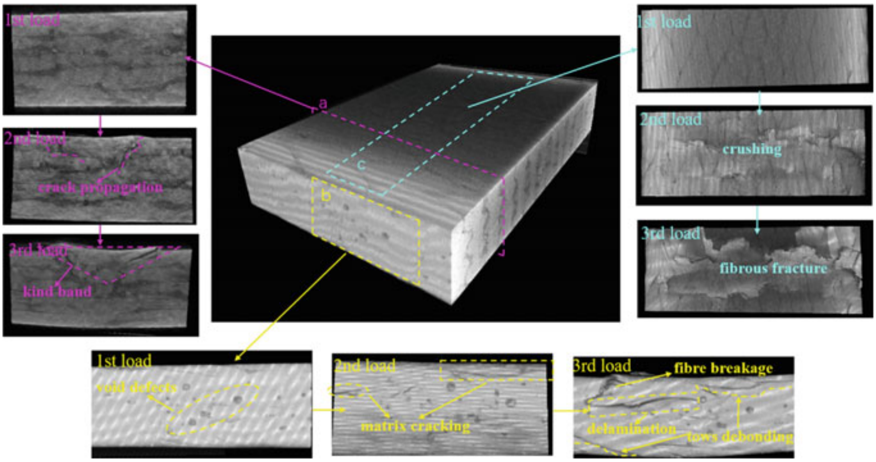
1st load
2nd load
crack propagation
3rd load
kind band
a
b
c
1st load
2nd load
crushing
3rd load
fibrous fracture
1st load
void defects
2nd load
matrix cracking
3rd load
fibre breakage
delamination
tows debonding

Fig. 18.7 Tomographic cross-sections images of the damage evolution at **a**, **b** and **c** position

and the surface of the sample exhibited a lattice-like protrusion, so that the upper surface became rougher and uneven. In addition, the buckling of the fibers affects adjacent fibers, creating a significant crushing phenomenon along the width of the sample.

To further confirm the damage distribution of the sample at the microstructure level, the four different positions of the cross section are scanned along the width direction of samples by Micro-CT as shown in Fig. 18.8. The kink band, matrix crack and fiber fracture as the main failure modes are indicated by a red mark in Fig. 18.8. It can be observed that the fibers are sheared at an angle and form a distinct bend band at a location near the center. In addition, it is found that the outer surface of the test piece is mainly distributed with transverse cracks, and the inside is mainly longitudinal cracks from top to bottom. As a conclusion, the damage of the specimen is mainly caused by the damage of the fiber and yarn, which proves that the axial yarn and the braided fibers have a supporting and reinforcing effect on the material.

18.4 Conclusions

The progressive damage behaviors and failure mechanisms of 3D five-directional braided composites under flexural loading are investigated by mean of AE, DIC and Micro-CT. A staged load is performed. Not only the AE response of the test pieces is monitored in real time, their deformation fields are calculated, and their internal damage morphology is visualized. Following conclusions are drawn from the study:

1. The mechanical curves of the 3D five-directional braided composite demonstrate excellent repeatability. The damage initiation and growth, as well as changes

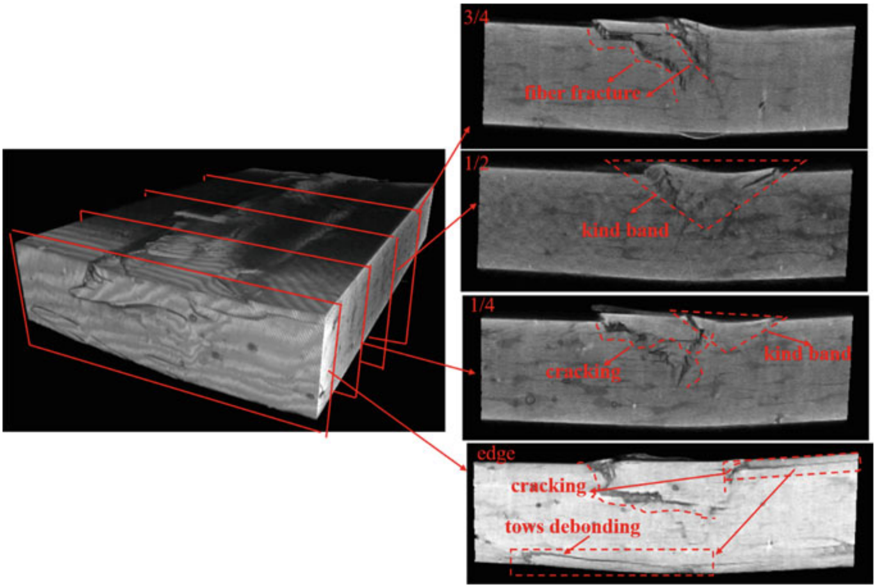

Fig. 18.8 Tomographic cross-sections along the width direction of samples

in stiffness of the material can be fully described. Here, the average failure loads and the average bending strength of specimen are 5.86 kN and 764.5 MPa respectively.

2. Through analyzing the experimental results, the obvious *Kaiser* effect is observed, and the AE signals is concentrated in the middle and late stages of loading and directly related to the cumulative degree of damage. Further, the AE parameters such as accumulated counts, amplitude, duration and frequency can better describe the damage accumulation and failure process of the composites.
3. The strain field distribution of the test piece reflects the stress of different loading stages, and the value of displacement deformation is related to the damage degree of the material. The cracking of the matrix and the fiber fracture mainly occur in the region where the central displacement deformation value is high, and this phenomenon becomes more and more obvious as the loading strength increases.
4. Micro-CT can be used to further observe the internal damage morphology. Some void defects are found in the initial stage, then, with the loading is completed again, some damage like the matrix cracking occurs. After the last loading, multiple severe damage modes occur simultaneously, and the previously generated cracks further deteriorate into delamination and debonding damage.

Acknowledgements The authors gratefully acknowledge the financial support of the National Natural Science Foundation of China (grant no. 11502064) and the project of China Special Equipment Inspection and Research Institute (grant no. 2018qingnian04).

References

1. Z.Y. Tian., Y. Yan, J. Li et al., Progressive damage and failure analysis of three-dimensional braided composites subjected to biaxial tension and compression. Compos. Struct. **185**, 496–507 (2018)
2. D.T. Zhang, L. Chen, Y. Sun et al., Meso-scale progressive damage of 3D five-directional braided composites under transverse compression. J. Compos. Mater. **50**(24), 3345–3361 (2016)
3. P. Turner, T. Liu, X. Zeng, Collapse of 3D orthogonal woven carbon fibre composites under in-plane tension/compression and out-of-plane bending. Compos. Struct. **142**, 286–297 (2016)
4. R.Q. Wang, L. Zhang, D.Y. Hu et al., Progressive damage simulation in 3D four-directional braided composites considering the jamming-action-induced yarn deformation. Compos. Struct. **178**, 330–340 (2017)
5. H. Ahn, W.R. Yu, Mechanical analysis of 3D braided and woven composites using fiber-based continuum analysis. Compos. Struct. **160**, 1105–1118 (2017)
6. G. Liu, L. Zhang, L. C. Guo, et al. Multi-scale progressive failure simulation of 3D woven composites under uniaxial tension. Compos. Struct. **208**, 233–243 (2019)
7. Y.M. Wan, B.Z. Sun, B.H. Gu. Multi-scale structure modeling of damage behaviors of 3D orthogonal woven composite materials subject to quasi-static and high strain rate compressions. Mech. Mater. **94**, 1–25 (2016)
8. J.Y. Liu, J.M. Zhou, Y. Wang, J. Mei, J.L. Liu, High temperature compressive behavior of three-dimensional five-directional braided composites. Compos. Struct. **226**, 111196 (2018)
9. L. Hu, Z.G. Liu, Y.B, Wang, Experiments and progressive damage analyses of three-dimensional full five-directional braided composites under three-point bending. Polym. Compos. **37**, 2478–2493 (2016)
10. Y.W. Ouyang, B.Z. Sun, B.H. Gu, Finite element analyses on bending fatigue of three-dimensional five-directional braided composite T-beam with mixed unit-cell model. J. Compos. Mater. **52**, 1139–1154 (2018)
11. C. Zhang, J.L. Curiel-Sosa, Q.B. Tinh, Meso-scale progressive damage modeling and life prediction of 3D braided composites under fatigue tension loading. Compos. Struct. **201**, 62–71 (2018)
12. B. Wang, G.D. Fang, S. Liu, Progressive damage analysis of 3D braided composites using FFT-based method. Compos. Struct. **192**, 255–263 (2018)
13. S.V. Lomov, A.E. Bogdanovich, D.S. Ivanov, D. Mungalov, M. Karahan, I. Verpoest, A comparative study of tensile properties of non-crimp 3D orthogonal weave and multi-layer plain weave E-glass composites. Part 1: Materials, methods and principal results. Compos. Part A: Appl. Sci. Manuf. **40**, 1134–1143 (2009)
14. A.E. Bogdanovich, M. Karahan, S.V. Lomov et al., Quasi-static tensile behavior and damage of carbon/epoxy composite reinforced with 3D non-crimp orthogonal woven fabric. Mech. Mater. **62**, 14–31 (2013)
15. W.F. Hao, Z.R. Yuan, C. Tang et al., Acoustic emission monitoring of damage progression in 3D braiding composite shafts during torsional tests. Compos. Struct. **208**, 141–149 (2018)
16. P. Lecomte-Grosbras, B. Paluch, M. Brieu, Characterization of free edge effects: influence of mechanical properties, microstructure and structure effects. J. Compos. Mater. **47**, 2823–2834 (2014)
17. L.J. Dong, Z. Wei, X.B. Ling et al., Collaborative localization method using analytical and iterative solutions for microseismic/acoustic emission sources in the rockmass structure for underground mining. Eng. Fracture Mech. **210**, 95–112 (2019)
18. L.J. Dong, Q.C. Hu, X.J. Tong et al., Velocity-free MS/AE source location method for three-dimensional hole-containing structures. Engineering, Available online (2020)
19. W. Zhou, W.Z. Zhao, Y.N. Zhang et al., Cluster analysis of acoustic emission signals and deformation measurement for delaminated glass fiber epoxy composites. Compos. Struct. **195**, 349–358 (2018)

20. N. Castaneda, B. Wisner, J. Cuadra et al., Investigation of the Z-binder role in progressive damage of 3D woven composites. Compos. Part A-Appl. Sci. Manuf. **98**, 76–89 (2017)
21. P.F. Zhang, W. Zhou, H.F. Yin, Y.J. Shang, Progressive damage analysis of three-dimensional braided composites under flexural load by micro-CT and acoustic emission. Compos. Struct. **226**, 111196 (2019)
22. D.T. Zhang, X.D. Liu, Y.H. Gu, Effects of off-axis angle on shear progressive damage of 3D woven composites with X-ray micro-computed tomography. Compos. Part A-Appl. Sci. Manuf. **115**, 311–320 (2018)
23. K. Bilisik, Multiaxis three-dimensional weaving for composites: a review. Textile. Res. J. **82**(7), 725–743 (2012)
24. W. Zhou, P.F. Zhang, Y.N. Zhang. Acoustic emission based on cluster and sentry function to monitor tensile progressive damage of carbon fiber woven composites. Appl. Sci. **8**(11), 2265 (2018)
25. L.S. Vladimir, V.N. Petr, Y.N. Zhang. Spectral characteristics of acoustic emission in carbon fiber-reinforced composite materials subjected to cyclic loading. Adv. Mater Sci. Eng. (2018)
26. W. Zhou, Z.H. Lv, Z.Y. Li. et al., Acoustic emission response and micro-deformation behavior for compressive buckling failure of multi-delaminated composites. J. Strain. Anal. Eng. **51**(6), 397–407 (2016)
27. Y. Wan, I. Straumit, J. Takahashi et al., Micro-CT analysis of internal geometry of chopped carbon fiber tapes reinforced thermoplastics. Compos. Part A-Appl. Sci. Manuf. **91**, 211–221 (2016)

Chapter 19
Fatigue Crack Growth of TC4 Titanium Alloy Using Acoustic Emission Technique

Wenjun Zhang, Gongtian Shen, and Yongna Shen

Abstract In this paper, the crack propagation process of TC4 titanium alloy was studied by using acoustic emission detection technology, and the trend analysis method and the correlation analysis method of the characteristic parameters of the acoustic emission are used to process and analyze the acoustic emission signal during the fatigue crack growth process. The results show that the acoustic emission counting parameters can well characterize the three stages of crack growth of TC4 titanium alloy: response to the initiation zone, steady-state extension zone and unstable fracture zone of fatigue crack. It provides a basis for the further use of acoustic emission technology for online monitoring and early warning analysis of TC4 titanium alloy.

19.1 Introductions

Fatigue damage is one of the main failure modes of aero-engine components. The basic process can be divided into three stages: crack initiation, stable crack propagation and unstable crack propagation [1]. First, the lattice structure of the material will generate stress concentration due to dislocation plugging, and then form a source of crack fatigue [2, 3]. This is the crack initiation stage; next, because the TC4 titanium alloy has a certain plasticity, the crack continues to expand after the crack is formed in a long time process. In this process, the local stress of the material is periodically released, and accompanied by the generation of acoustic emission signals. This process is the stage of stable crack growth. And the third stage is the unstable fracture stage of fatigue crack propagation. At the same time, this process occurs almost instantaneously. The energy released during this period is very large, which will produce a high-intensity AE signal. Due to the sudden type [4], it often causes catastrophic accidents. Therefore, in order to prevent early fatigue failure of materials, the detection and evaluation of the early fatigue state of materials is intuitively important.

W. Zhang · G. Shen (✉) · Y. Shen
China Special Equipment Inspection and Research Institute, Beijing 100029, China
e-mail: zwj787404079@163.com

© The Author(s), under exclusive license to Springer Nature Singapore Pte Ltd. 2021

G. Shen et al. (eds.), *Advances in Acoustic Emission Technology*, Springer Proceedings in Physics 259, https://doi.org/10.1007/978-981-15-9837-1_19

When the material is damaged by external or internal forces, it will release energy in the form of elastic waves [5, 6]. This is the acoustic emission phenomenon. The technique of using the acoustic emission sensor to collect the acoustic emission signals generated in this process and analyze the damage state is Acoustic emission detection technology. Compared with traditional nondestructive testing technology, AE testing has the advantages of dynamic detection and real-time monitoring of defects, and is not sensitive to the working environment [7].

The AE signal comes from the damage defect itself, so the evaluation of the test results also depends on the analysis of the corresponding AE signal characteristics of different damage modes of the structural material. A large number of research show that AE technology is very sensitive to the degree of steel structure crack damage [8–12], which means that it is feasible to apply AE technology to the detection and online monitoring of fatigue crack growth status. Based on the characteristics of the AE signal, Li [8] constructed a theoretical model of the AE signal generated when the fatigue cracks of the tooth surface of the gears expanded, which theoretically proved the feasibility of the acoustic emission technology for detecting fatigue wear. Mengyu [9] Conducted an AE study on the fatigue crack growth process of Q345R steel, and established the relationship between the AE count rate and energy rate and the fatigue crack growth rate, which provided a basis for the assessment of the remaining life of Q345R steel; Crivelli [10] applied AE testing in fatigue detection of gear tooth roots, providing support on the feasibility of system state tracking using continuous acoustic emission. Md Yeasin Bhuiyan [11] researched the effect of the acoustic emission sensor on the acoustic emission waveforms from fatigue crack growth in a thin aerospace specimen, It has been shown that the piezoelectric wafer active sensor transducer successfully captured the fatigue crack-related acoustic emission waveforms in the thin plate. AE Signal evolution is highly related to the physical boundary conditions of the cracks as well as the fatigue crack growth mechanism. Xie [12] and others also proved the feasibility of applying AE technology to fatigue damage detection by studying the crack initiation and propagation process of multi-layer tokamak magnets. This paper studied the relationship between fatigue crack propagation process and acoustic emission signal parameters for TC4 titanium alloy materials for aeroengines. In order to more clearly characterize the acoustic emission signal during the crack propagation of TC4 titanium alloy, this study selects energy and technical parameters for analysis, and analyzes the spectrum of the acoustic emission signal by FFT transformation.

19.2 Methods and Experimental Test Set-Ups

The material used in the test was a TC4 titanium alloy belonging to an equiaxed martensitic ($\alpha + \beta$) two-phase titanium alloy, and the chemical composition is shown in Table 19.1. According to the provisions of GB/T228.1-2010, a compact pull-up sample was produced, as shown in Figs. 19.1 and 19.2, according to the GBT6389-2000 crack extension standard [13], crack propagation test.

Table 19.1 Chemical composition of TC4 (wt%)

Main element	Alloying element content				Impurity element content			
Ti	Al	V	Fe	Si	C	N	H	O
margin	5.5–6.8	3.5–4.5	0.30	0.10	0.10	0.05	0.015	0.015

Fig. 19.1 Compact stretch pattern

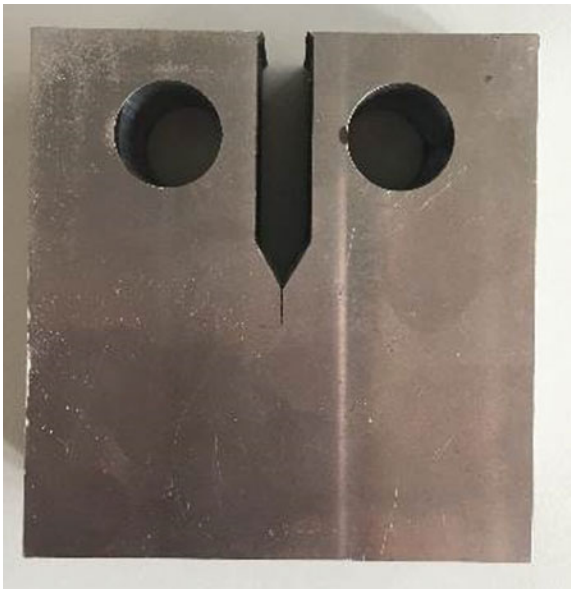

The acoustic emission detector uses the AMSY-6 acoustic emission detection system from Vallen, Germany, showed in Fig. 19.3. The acoustic emission signal is picked up by a VS150-M type resonant sensor (100–450 kHz), Fig. 19.4 shows its sensitivity curve. When setting the parameters of the acoustic emission detection system, open the host of the acoustic emission instrument and the supporting operating software. The noise at the test site is mainly concentrated at 35 dB. The noise mainly comes from the laboratory background noise and the friction between the test piece and the fixture. In order to eliminate the background noise, Set the threshold of the acoustic emission instrument to 35 dB during the experiment. The parameters of the acoustic emission system during the experiment are set as shown in Table 19.2. In this experiment, the COD gauge is used to measure the open displacement of the crack tip of the sample. At room temperature, the constant maximum load $P_{\max} =$ 11.11 kN is used to control the minimum load $P_{\min}$ to achieve different stress ratios. The load is constant $\triangle P$ and K is added. The test frequency is 10 Hz, Fig. 19.5 showed Experimental detection system (Fig. 19.5).

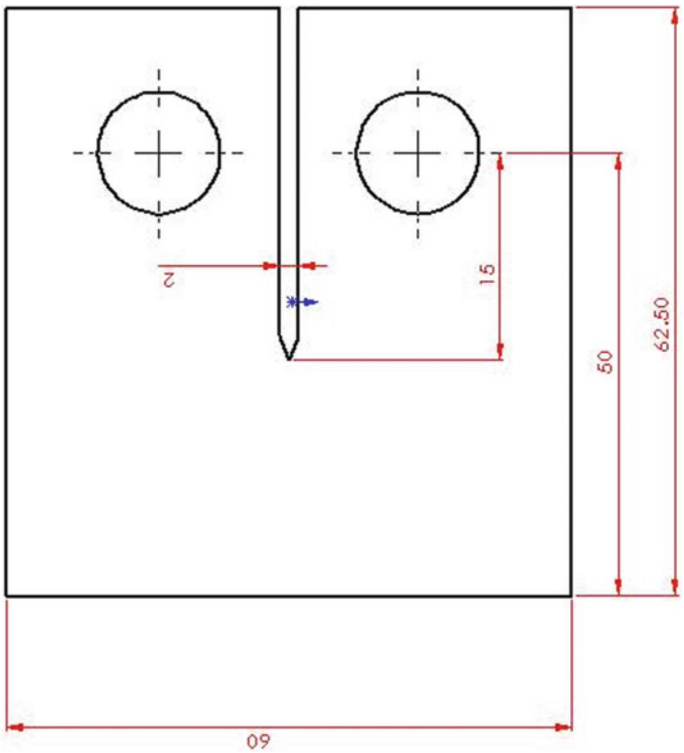

Fig. 19.2 Structure and grometry size of sample (mm)

19.3 Experimental Results and Analysis

The acoustic emission characteristics of crack propagation of TC4 titanium alloy materials are shown in Figs. 19.6. It can be clearly seen from the figure that the count value shows three acoustic emission stages, In the first stage (0–3775 S), the count value began to increase rapidly, This is because the formation of fatigue crack sources and the plastic deformation of the prefabricated crack tip will generate many acoustic emission signals, so that the count value will obviously increase in the short term after the experiment starts, and in the second stage (3775–5080 S), the count value began to decrease slowly, indicating that the acoustic emission signal strength at this stage was low. and then the count value monotonously increases Until the specimen breaks. These three stages correspond to the three stages of fatigue crack growth.

The logarithmic correlation diagram of energy and duration during fatigue loading is shown in Fig. 19.7, and the duration can reflect the ability release method of TC4 titanium alloy. Figure 19.7 shows that the energy remains unchanged at 100 eu at 0–10 μs, and starts to increase slowly after 100 μs, at which time the energy and

Fig. 19.3 AMSY-6 acoustic emission detection system

Fig. 19.4 Sensitivity of senser (VS150-M)

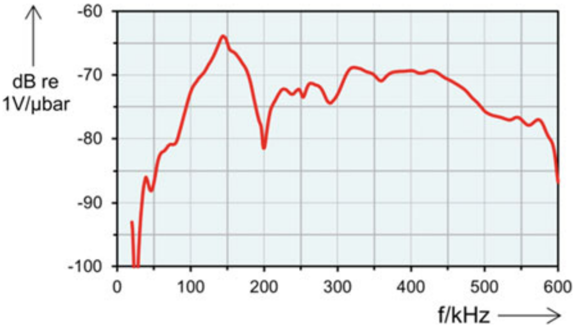

Table 19.2 Acoustic emission acquisition parameter setting

Threshold value (dB)	Sampling points	Sampling rate (MHz)	Pre-sampling pre-trigger
40	1024	2.5	200

duration are in a logarithmic relationship. At 105 μs, there are two branches of energy, which have been marked as a and b in the figure, means that there are more than one signal source at this stage. Considering the installation method of the test piece, it is speculated that this phenomenon is caused by the test piece and the pin. Caused by shaft friction.

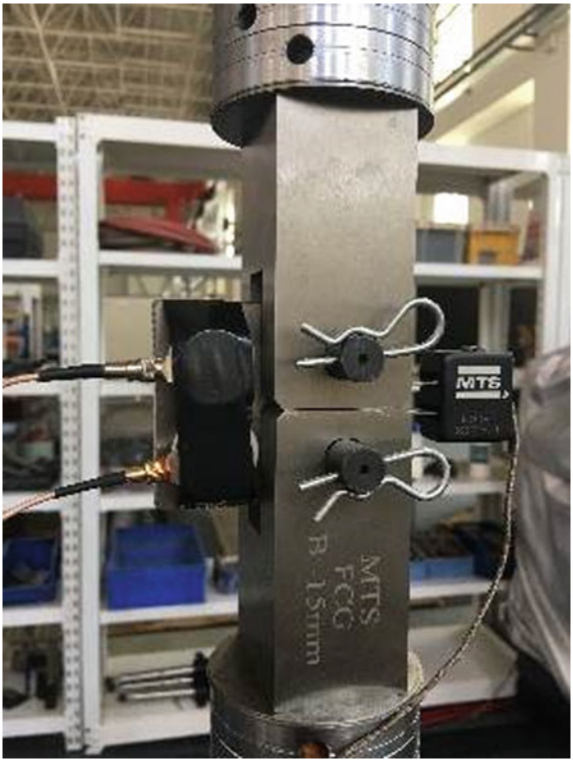

Fig. 19.5 Experimental detection system

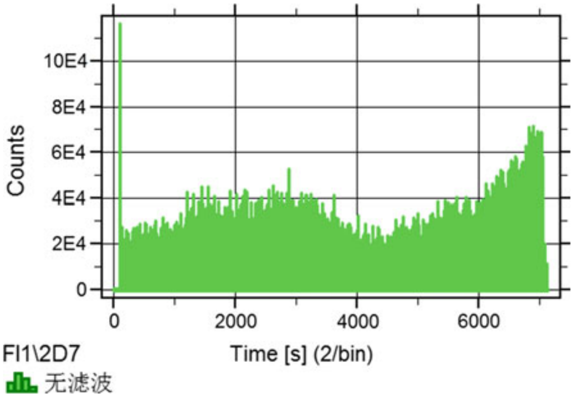

Fig. 19.6 Counts and Times correlation diagram

The typical waveform diagram of the fatigue crack propagation process of TC4 titanium alloy and the spectrum diagram obtained by fast Fourier transform are shown in Fig. 19.8. It can be clearly seen from the figure that the acoustic emission signal is mainly burst type signal, the main frequency band is 150–250 kHz, and the amplitude of the signal is mainly distributed in 0.006–0.018 mV, which is similar to the existing

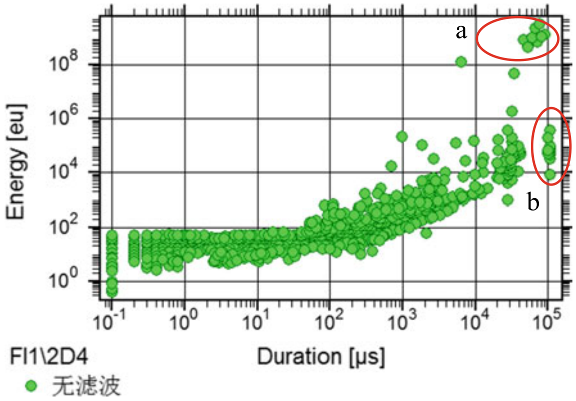

Fig. 19.7 Energy and duration correlation diagram

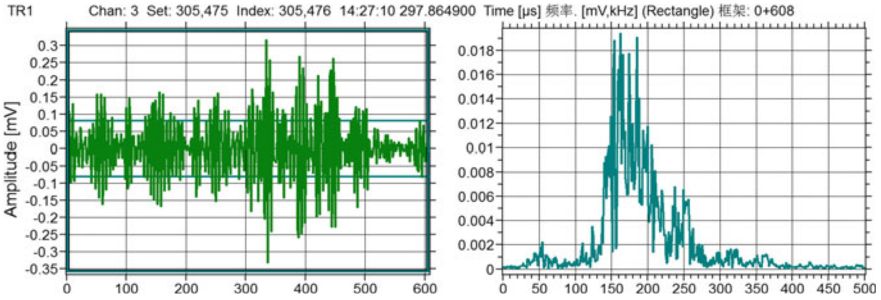

Fig. 19.8 Acoustic emission signal spectrogram

research features [6], Such signal characteristics can be used as a reference for crack propagation phenomena.

To study the relationship between acoustic emission signal characteristics and fatigue crack growth, it is important to investigate the acoustic emission signal source. In the existing research, it is generally pointed out that the acoustic emission source in the first stage of fatigue crack growth is the initiation of cracks, and the acoustic emission source in the second and third stages is crack propagation until the specimen breaks [9, 14]. In the first stage, because the TC4 titanium alloy is a polycrystalline metal material, elastic deformation is achieved by gradually moving the dislocation along the sliding surface. When the dislocation moves at a sufficiently high speed, the local stress around it causes AE to produce In the plastic deformation stage, due to the stress concentration, a large number of dislocations began to move [15, 16]. At this time, the AE signal showed a higher amplitude, and the ring count value also increased significantly. The first stage of Fig. 19.6 verified this; In the second stage, due to the increase in the density of dislocations inside the material, dislocations interact, and dislocation plug products, entanglements, and fixed cutovers occur, which makes the movement of dislocations difficult [17, 18]. Compared with the first stage, the sound The emission activity is reduced; the third stage is the stage of material fatigue crack instability expansion. At this stage, the specimen breaks rapidly, the material releases a large number of AE signals, and the count value increases significantly, which is consistent with the trend of Fig. 19.6. In addition, some studies have pointed out that if materials with different properties are subjected to different heat treatment processes, the acoustic emission source in the crack propagation stage will be inconsistent [19–21]. To explore the AE source in each stage of this process, further research is required Research to further determine the relationship between the AE signal and the fatigue crack growth mechanism of different heat treatment processes and materials with different properties.

19.4 Conclusion

1. The acoustic emission process of fatigue crack growth of TC4 titanium alloy can be divided into three distinct stages, corresponding to the initiation zone, steady-state extension zone and unstable fracture zone of fatigue crack. In the crack initiation stage, the AE signal exhibits higher activity, and the amplitude of the AE signal in the stable expansion stage decreases. It is presumed that due to the increase in the dislocation density and the difficulty of dislocation movement, the material in the crack instability expansion stage quickly breaks, and the AE signal amplitude Significantly increased.
2. The count value reflects the three stages of crack propagation, and the energy and duration correlation diagram reflects the material energy release mode. The spectrum diagram of the AE signal indicates that the AE signal in this process is mostly a burst signal.
3. The AE signal characteristics during the fatigue crack growth of TC4 titanium alloy provide a basis for applying AE detection technology to the fatigue crack damage detection and online monitoring.

Acknowledgements This work is financially supported by the Science and Technology Plan Project of State Administration for Market Regulation (No. 2020MK175), also the Internal Research Project of China Special Equipment Inspection and Research Institute (No. 2020QingNian02).

References

1. J.P. Zhong, *Cracking* (Higher education press, Beijing, 2014)
2. Z. Changwen, Ye. Hui, Li. Qiang, Acoustic emission characteristics of Q345 steel specimens with different defects. Petro-Chem. Equip. **000**(004), 5–9 (2013)
3. D. Soulioti, N.M. Barkoula, A. Paipetis et al., Acoustic emission behavior of steel fibre reinforced concrete under bending. Constr. Build. Mater. **23**(12), 3532–3536 (2009)
4. Z. Yihui, Z. Wenbin, X. Feiyun, Acoustic emission characteristics of Q235B steel plate tensile damage test. Vibr. Shock **34**(15), 156–161 (2015)

5. L. Zhang, L. Qin, Monitoring corrosion of steel bar using acoustic emission, in *IOP Conference Series Materials Science and Engineering* (2018), p. 452
6. E.V. Chernyaeva, P.A. Khaimovich, N.A. Shul'gin, Acoustic emission in commercial titanium after Barocryo deformation. Phys. Metals Metallogr. **115**(10), 1012–1016
7. W. Xianghogn, Z. Changming, M. Hanling, Experimental study on fatigue crack growth rate of hydraulic turbine runner blades based on acoustic emission technology. China Mech. Eng. **07**, 94–98 (2009)
8. Li. Lin, An acoustic emission model of fatigue crack growth on the surface of gears. Non-Destr. Test. **11**, 4–7 (2005)
9. C. Mengyu, D. Quan, Z. Zaojiao, Study on acoustic emission of Q345R fatigue crack growth process. J. Eng. Sci. **37**(260)(12), 56–61 (2015)
10. D. Crivelli, J. McCrory, S. Miccoli et al., Gear tooth root fatigue test monitoring with continuous acoustic emission: advanced signal processing techniques for detection of incipient failure. Struct. Health Monitor. **17**(3), 423–433 (2018)
11. M.Y. Bhuiyan, B. Lin, V. Giurgiutiu, Acoustic emission sensor effect and waveform evolution during fatigue crack growth in thin metallic plate. J. Intell. Mater. Syst. Struct. **29**(7), 1275–1284 (2018)
12. S. Xie, Acoustic emission monitoring of fatigue crack generation and propagation in multi-layer tokamak magnet, in *Abstract Book of World Conference on Acoustic Emission - 2017*. International Society on Acoustic Emission: Chinese Mechanical Engineering Society (2017), 15
13. General Administration of Quality Supervision of the People's Republic of Chin, *GB/T6398-2000 Standard Test Method for Fatufue Crack Grouth of Metallic Materials* (Standards Press of China, Beijing, 2001)
14. Z. Wang, G. Hu, H. Yu, Research on Q345B fatigue crack growth based on acoustic emission technology. J. Nanchang Hangkong Univ. (Natural Science Edition) (4) (2016)
15. Z. Han, H. Luo, Y. Zhang, et al., Effects of micro-structure on fatigue crack propagation and acoustic emission behaviors in a micro-alloyed steel. Mater. Sci. Eng. A (Struct. Mater. Prop. Microstruct. Process.), **559**(none):534–542 (2013)
16. A. Maslouhi, Fatigue crack growth monitoring in aluminum using acoustic emission and acousto-ultrasonic methods. Struct. Control Health Monitor. **18**(7), 790–806 (2011)
17. Z. Han, H. Luo, J. Cao et al., Acoustic emission during fatigue crack propagation in a micro-alloyed steel and welds. Mater. Sci. Eng. A **528**(25–26), 7751–7756 (2011)
18. J. Cao, H. Luo, Z. Han, Acoustic emission source mechanism analysis and crack length prediction during fatigue crack propagation in 16 Mn steel and welds. Procedia Eng. **27**(none), 1524–1537 (2012)
19. C.K. Lee, J.J. Scholey, P.D. Wilcox et al., Guided wave acoustic emission from fatigue crack growth in aluminium plate. Adv. Mater. Res. **13–14**, 23–28 (2006)
20. S. Shi, Z. Han, Quantitative monitoring of brittle fatigue crack growth in railway steel using acoustic emission. Proc. Inst. Mech. Eng. Part F J. Rail Rapid Transit. (2018)
21. J. Yu, P. Ziehl, B. Zárate, et al., Prediction of fatigue crack growth in steel bridge components using acoustic emission. J. Constr. Steel Res. **67**(8), 1254–1260 (2011)

Chapter 20
Experiment Research on Tensile Process of Glass Fiber Reinforced Plastics Basing on AE

Hui Luo, Wenchao Han, Yilin Yuan, Bo Ke, and Baodi Zhao

Abstract In this chapter, the tensile test has been carried out with three kinds of specimens, matrix specimen, and GFRP specimen (90°, 0°). Two AE sensors (VS150) were located at the end of the specimen, and one sensor (VS 900) was located in the middle of the specimen. At the same time acoustic emission equipment has been applied throughout the whole acquisition process of various emission signals. Amplitude, count, energy, duration, frequency distribution and other parameters as well as waveforms are analyzed to get the characteristic of fiber breakage. Frequency value of AE signals released by fiber breakage is between 100 and 400 kHz, duration is between 0.5 and 100 ms, and the amplitude is more than 80 dB. AE signals characteristics can provide a reliable reference for the study of the AE techniques in GFRP damage mechanism and relevant performance evaluation.

20.1 Introduction

Compared with metal materials, glass fiber reinforced plastics (GFRP) offer certain advantage in density, specific strength, good processability, corrosion resistance, and cheap price. With these advantages, GFRP has been widely used in the fields of aerospace, vehicle-making and pressure vessels. In recent years, tuber trailers assembled from glass fiber reinforced cylinders with large water capacity has a water capacity of 31.02 m^3, which lead to a 20% increase of transport efficiency and a 30% reduce of cost.

Affected by impact, wear damage, aging, etc., damage forms such as matrix cracking, fiber fracture, delamination, debebonding and others are easy to occur in the use of glass fiber reinforced large volume cylinders. Compared with metal material, damage modes are more complicated and simultaneous, and the internal damage in GFRP is often difficult to detect by visual inspection. Among these damage modes of f GFRP, fiber fracture has the greatest impact on the safety performance of

---

H. Luo (🖂) · W. Han · Y. Yuan · B. Ke · B. Zhao
China Special Equipment Inspection and Research Institute, Beijing 100013, China
e-mail: luohui@csei.org.cn

© The Author(s), under exclusive license to Springer Nature Singapore Pte Ltd. 2021

G. Shen et al. (eds.), *Advances in Acoustic Emission Technology*, Springer Proceedings in Physics 259, https://doi.org/10.1007/978-981-15-9837-1_20

materials. Therefore, it is very important to find fiber fracture by means of detection for safety evaluation of these large volume cylinders.

A number of researches have been reported about damage of glass fiber reinforced plastics detected via acoustic emission method. Researches by Fotouhi et al. [1, 2] showed that the fiber breaking frequency ranges from 350 to 450 kHz in the test of glass fiber/epoxy resin material. Nevertheless, Studies carried out by Pashmforoush et al. [3] showed that fiber breaking frequency ranges from 350 to 450 kHz in the test of glass fiber/epoxy resin material. Godin et al. [4] found that the fiber breaking signal has long duration and high amplitude according to the study of glass fiber/polyester material. Li et al. [5] carried out tensile test on glass fiber/epoxy ethylene resin material, and obtained that the fiber breaking signal frequency >150 kHz, and the amplitude was 0–80 dB. Therefore, the conclusions of current studies are quite different, and it is difficult to give guidance for the detection of cylinders.

20.2 Experiments

Large volume composite cylinders with steel liner are shown in Fig. 20.1. The structure is shown in Fig. 20.2.

Transverse cracking occurs because of the lower axial bearing capacity of the fiber layer in the use of cylinders, as shown in Fig. 20.3. The main performance of transverse cracking of the GFRP is matrix cracking, while part of fiber and resin were deboned and pulled out. In addition, when the GFRP layer is hit or worn, the

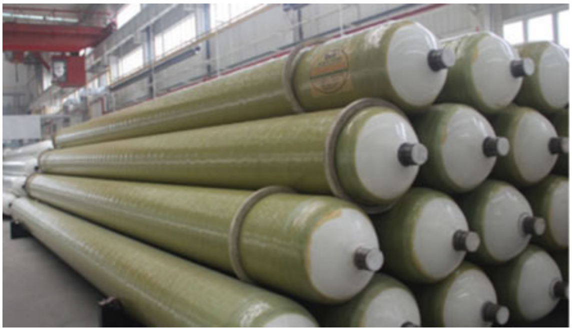

Fig. 20.1 Large volume composite cylinders with steel liner

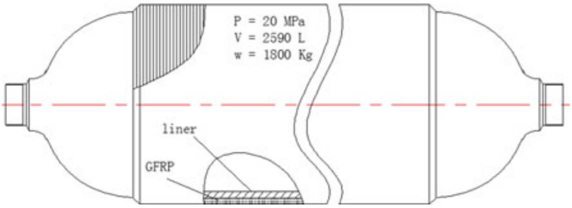

Fig. 20.2 Structure of large volume composite cylinders

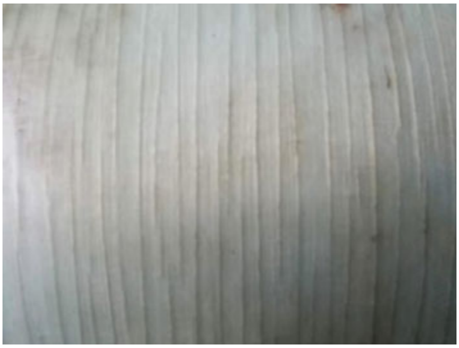

Fig. 20.3 Transverse crack

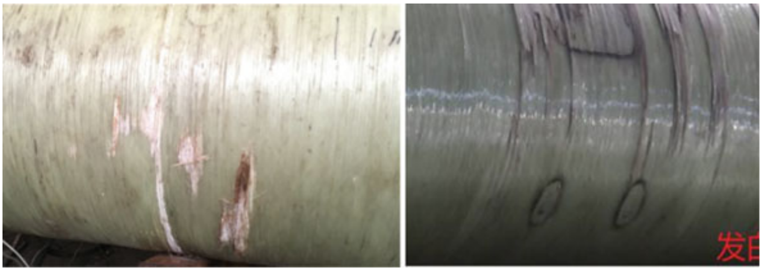

Fig. 20.4 Wear and fracture of wound layer

layer complete fracture or inner fiber fracture would happen, as shown in Fig. 20.4. In comparison with transverse cracking, fiber fracture has a great influence on the safety of gas cylinder, so it is very important to detect fiber fracture signal by acoustic emission.

20.2.1 Specimen Preparation

Three different specimens were used in the test. Specimen A was made by resin, with length size of 280 mm, 20 mm of width, 3 mm of thickness, as shown in Fig. 20.5. In the tensile test, this specimen was stretched until crack to obtained Acoustic emission signal during matrix cracking.

Specimen B was made by GFRP, with length size of 280 mm, 20 mm of width, 3 mm of thickness, as shown in Fig. 20.6. The tensile direction was perpendicular to the fiber direction, also known as the 90° specimen. The tensile test of specimen B was carried out to simulate the process of the matrix cracking, debebonding and pulled out, and obtained AE signals.

Specimen C was made by GFRP, with length size of 280 mm, 20 mm of width, 2 mm of thickness, as shown in Fig. 20.7. The tensile direction was parallel to the

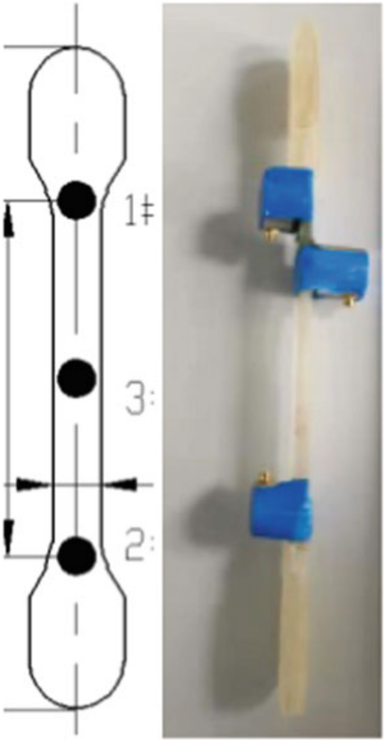

Fig. 20.5 Resin specimen (A)

fiber direction, also known as the 0° specimen. The test of specimen C was carried out to simulate the process of the resin cracking, debebondin, pulled out and fiber fracture, and obtained AE signals.

20.2.2 Equipment and Procedure

The acoustic emission device: AMSY-6, 22-channel, Germany. Both hardware system and software system were included, and it could display the waveform and parameter data list of acoustic emission signal and various types of charts in real time. The threshold value in the experiment is set as 40 dB.

The VS150 sensors were fixed at both ends of the specimen, with a bandwidth of 100–450 kHz, connected to the channel No. 1 and No. 2 of the device respectively ◦The VS900 sensor were fixed in the middle of the specimen, with a bandwidth of 100–1000 kHz, connected to channel No. 3 of the device. The sensors and specimen are coupled by grease and fixed by the tape.

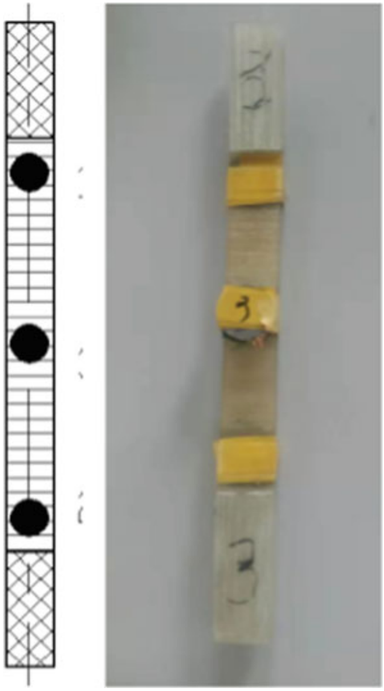

Fig. 20.6 Fiber reinforced resin specimen 90° (B)

The universal testing machine is used for the tensile test. The equipment model is bbsl-xs-30t, and the maximum tensile load of the equipment is 30 kN. The tensile rate in the test is less than 0.4 mm/min, as shown in Fig. 20.8.

Sensitivity tests are conducted after device connection and system setup, and broken lead test was carried out at the edge of the sensors with a Φ0.3–2H pencil. The response amplitude of each sensor is maintained above 99.0 dB. Then the attenuation was measured at a distance of 100 mm from the sensor. The attenuation of specimen A was 23 dB, that of specimen B was 18 dB, and that of specimen C was 14 dB.

20.3 Result

In the test, A tensile load was applied to the specimen slowly until the specimen broke. Specimen A broke at 3.0 kN and specimen B at 1.7 kN. During the tensile process of specimen C, the maximum load was 24 kN.

The fracture morphology of specimen A and B was brittle fracture. Without plastic deformation occurred during the specimen tensile process, and the fracture was flat. For specimen C, during the stretching process, transverse cracking first occurred, then the fiber continues to break under the tensile load until the fiber broke down (Fig. 20.9).

Fig. 20.7 Fiber reinforced resin specimen 0° (C)

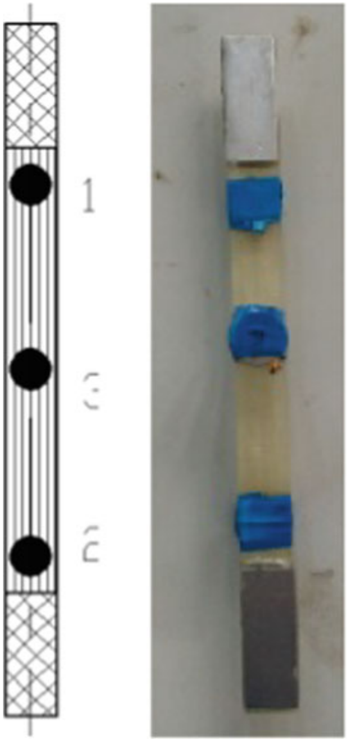

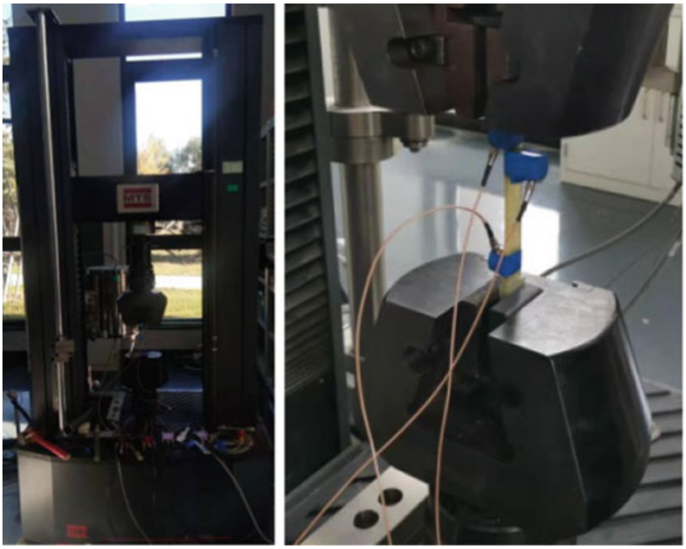

Fig. 20.8 Test machine and test process

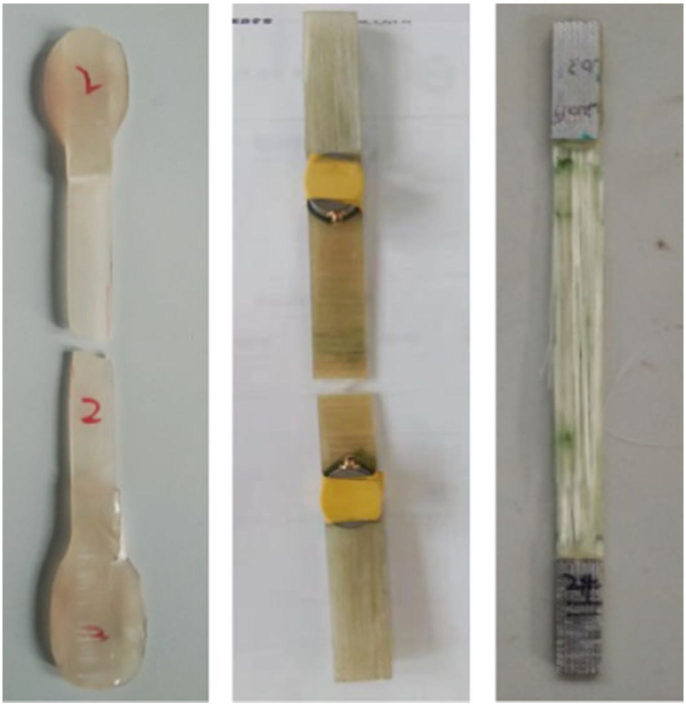

Fig. 20.9 Broken specimens (A/B/C)

20.3.1 Amplitude-Time in the Tensile Test

The amplitude-time diagram of specimens A, B and C during the tensile test is shown in Figs. 20.10, 20.11 and 20.12. In the process of specimen A and specimen B being stretched to fracture, the crack acoustic emission signal amplitude of the matrix was lower than 80 dB. During the tensile test of specimen C, the signal amplitude gradually increases with the increase of the tensile load. When the tensile force of the testing machine reaches 1/2 of the maximum load, the signal amplitude was greater than 80db, and when the tensile force reaches 2/3 of the maximum load, the signal amplitude reaches 100 db. After that, as the load continued to increase, the signal

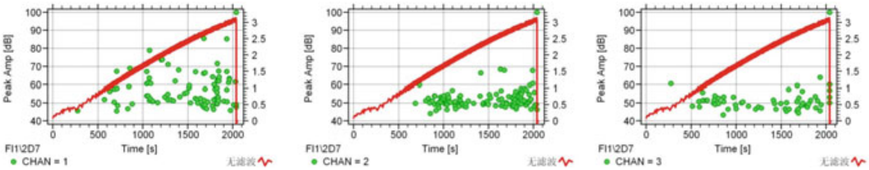

Fig. 20.10 Amplitude–time, specimen A (Channel No. 1/Channel No. 2/Channel No. 3)

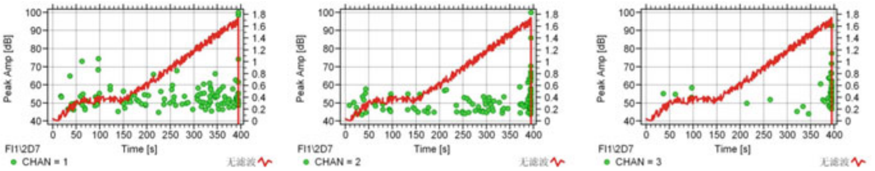

Fig. 20.11 Amplitude–time, specimen B (Channel No. 1/Channel No. 2/Channel No. 3)

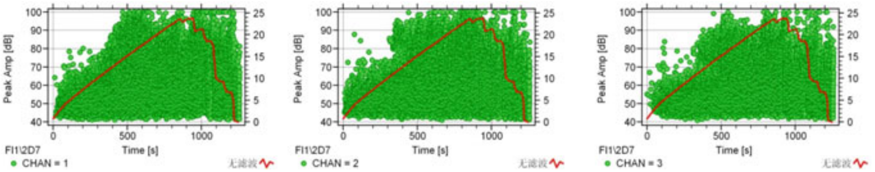

Fig. 20.12 Amplitude–time, specimen C (Channel No. 1/Channel No. 2/Channel No. 3)

amplitude would decrease slightly, and finally, the fiber in the fiber reinforcement material broken down. High-amplitude signals would appear during the breaking process. The amplitude distribution of specimens A and B were basically the same, and the amplitude distribution of signals collected by resonance sensor and broadband sensor is basically the same.

20.3.2 *Energy-Time in the Test*

The energy-time diagram of specimens A, B and C during the tensile test is shown in Figs. 20.13, 20.14 and 20.15. The fracture energy of specimens A and B was lower than 1.0 × 10^6 eu. During the tensile test of specimen C, the energy signal was over 1.0 × 10^6 eu when the tensile force of the testing machine reaches 1/2 of the maximum load. After that, the energy signal was greater than 1.0 × 10^8 eu due to the increasing load. When the fiber breaks, a higher energy signal appears, reaching 1.0 × 10^9 eu. Therefore, the energy of fiber fracture signal is much higher than that of resin cracking.

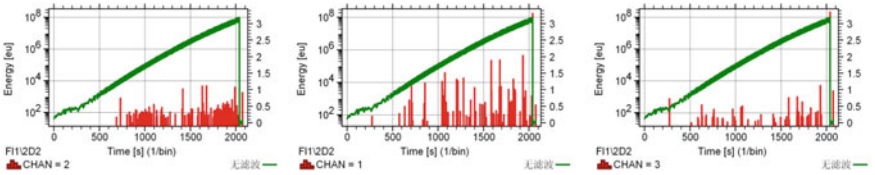

Fig. 20.13 Energy–time, specimen A (Channel No. 1/Channel No. 2/Channel No. 3)

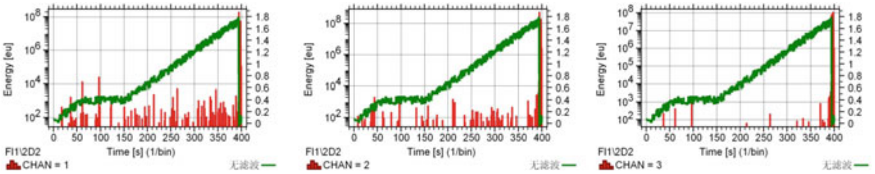

Fig. 20.14 Energy–time, specimen B (Channel No. 1/Channel No. 2/Channel No. 3)

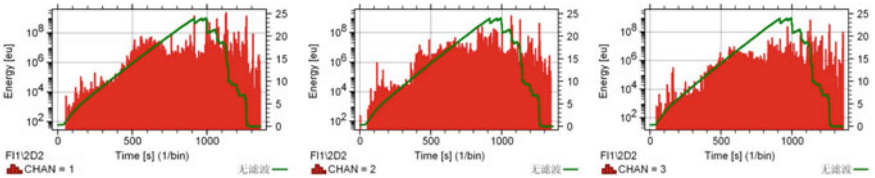

Fig. 20.15 Energy–time, specimen C (Channel No. 1/Channel No. 2/Channel No. 3)

20.3.3 Relationship of Energy- Duration

The relationship of Energy-duration in the test of specimen A, B and C is shown in Figs. 20.16, 20.17, 20.18. The duration was short than 5.0 × 10^2 μs in the fracture process of specimen A and specimen B. For specimen C, the acoustic emission signal with energy higher than 1.0 × 10^6 eu had a duration greater than 5.0 × 10^2 μs and a maximum of 1.0 × 10^4 μs. Therefore, the duration of fiber fracture signal is much higher than that of resin cracking.

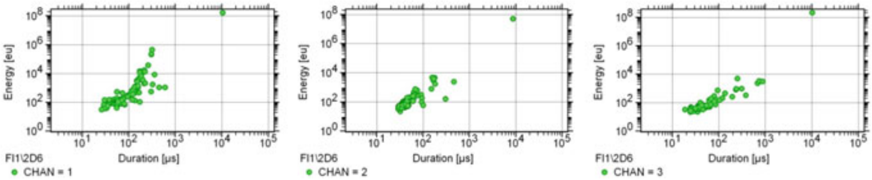

Fig. 20.16 Energy–time, specimen A (Channel No. 1/Channel No. 2/Channel No. 3)

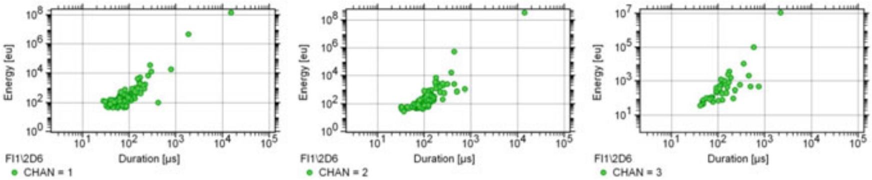

Fig. 20.17 Energy–time, specimen B (Channel No. 1/Channel No. 2/Channel No. 3)

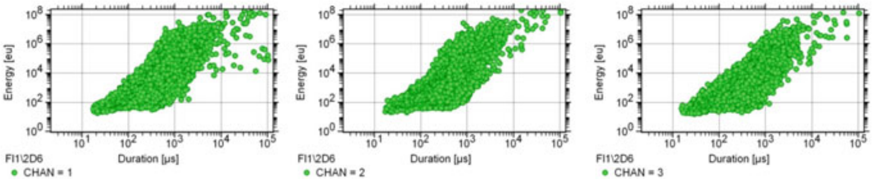

Fig. 20.18 Energy–time, specimen C (Channel No. 1/Channel No. 2/Channel No. 3)

20.3.4 Waveform and Spectrum

During the tensile test, the resin fracture signals and fiber fracture signals of specimens A, B and C are shown in Figs. 20.19, 20.20 and 20.21. The frequency distributions of specimens A and B are generally between 100 and 250 kHz, while the dominant frequency is 170 kHz. The frequency distribution range of specimen C is wide, ranging from 100 to 400 kHz, and the dominant frequency is the same as that of specimen A and B.

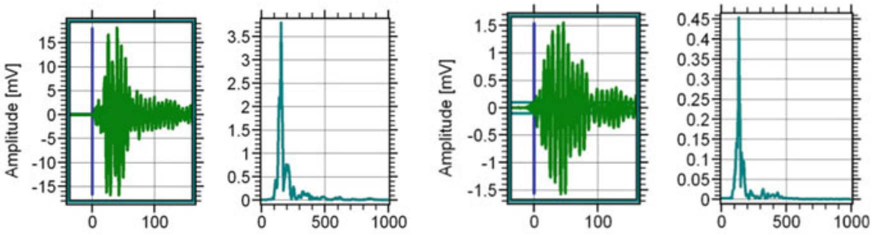

Fig. 20.19 Waveform and spectrum, specimen A (VS150/VS900/)

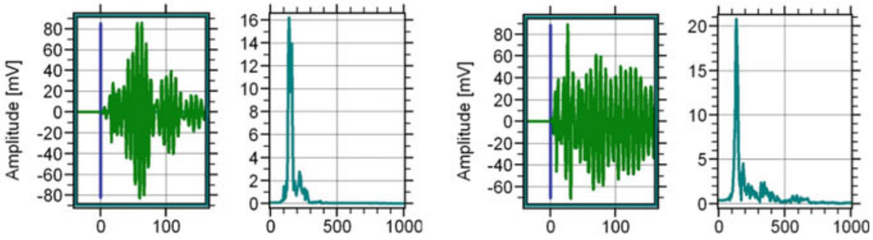

Fig. 20.20 Waveform and spectrum, specimen B (VS150/VS900/)

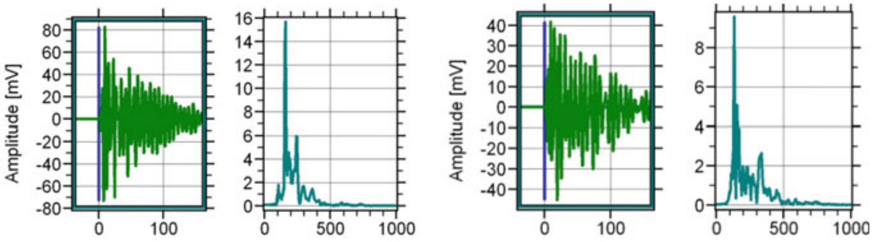

Fig. 20.21 Waveform and spectrum, specimen C (VS150/VS900/)

20.4 Conclusion

The test results of samples A, B and C show that acoustic emission can be used to detect fiber fracture in fiberglass reinforced resin materials, and has the following signal characteristics:

The frequency of resin cracking signal and fiber breaking signal are close to each other. The signal characteristics obtained by resonant sensor is similar to that obtained by wideband sensor, and the VS150 resonant sensor could be used to detect the acoustic emission of glass fiber reinforced plastics.

Compared with the matrix cracking signal, the fiber breaking signal has the characteristics of high amplitude, high energy and long duration, etc. These parameters can be used to distinguish the fiber breaking signal and to detect and evaluate the glass fiber reinforced resin material.

Acknowledgements This work is financially supported by National Key Research and Development Program of China (Grant No. 2017YFC0805604).

References

1. M. Fotouhi, M. Saeedifar, S. Sadeghi, et al., Investigation of the damage mechanisms for mode I delamination growth in foam core sandwich composites using acoustic emission. Struct. Health Monit. **14**, 265–280 (2015)
2. M. Fotouhi, S. Sadeghi, M. Jalalvand et al., Analysis of the damage mechanisms in mixed mode delamination of glass/epoxy composites using acoustic emission data clustering[J]. Thermoplast. Compos. Mater. **30**, 318–340 (2017)
3. F. Pashmforoush, M. Fotouhi, M. Ahmadi, Acoustic emission based damage classification of glass/polyester composites using harmony search k-means algorithm. J. Reinf. Plast. Compos. **31**(10), 671–680 (2012)
4. N. Godin, S. Huguet, R. Gaertner, Integration of the Kohonen's self organizing map and k-means algorithm for the segmentation of the AE date collected during tensile tests on cross-ply composites. NDT&E Int. **38**, 299–309 (2005)
5. L. Li, S.V. Lomov, Y. Xiong, Correlation of acoustic emission with optically observed damage in a glass/epoxy woven laminate under tensile loading[J]. Compos. Struct. **123**, 45–53 (2015)

Chapter 21
High-Temperature Creep Damage Evolution of C/SiC Based on Acoustic Emission

Guodong Bai, Xiaoyan Tong, and Leijiang Yao

Abstract C/SiC ceramic matrix composites are excellent high temperature resistant materials being light, with high strength and good toughness. It is necessary to understand the evolution of its characteristics before application. In this work, an acoustic emission (AE) signal is recorded for the creep damage process of C/SiC at high temperature, and the dual variable voting method and cluster analysis are applied to get the most suitable parameters for AE signal clustering analysis to provide optimal clustering. The clustering results of AE events were used to reproduce the evolution of typical damage, fiber breakage, matrix cracking and interface damage, and to compare the differences of the acoustic emission signals between different lifetime C/SiC samples. A relationship between the AE signal and the damage mechanism of C/SiC is constructed using AE events analysis and SEM observations, and finally the damage evolution and creep lifetime of C/SiC by pattern recognition is investigated. The results show that the sample with long creep lifetime has a longer pulled-out carbon fibers and a larger proportion of interface damage than short one, it is due to the difference of interface bonding. The interface damage leads to different types of creep rupture, and dominates the C/SiC high temperature creep lifetime.

21.1 Introduction

Carbon/Silicon Carbide (C/SiC) ceramic matrix composites (CMC) have excellent high temperature mechanical properties which are of particular use for high temperatures [1–5]. These include high strength and stiffness, and good thermal stability. It

---

G. Bai (✉) · X. Tong · L. Yao
National Key Laboratory of Science and Technology on UAV, Northwestern Polytechnical University, Xi'an 710072, China
e-mail: baiguodong@vip.qq.com

X. Tong
e-mail: tongxy@nwpu.edu.cn

L. Yao
e-mail: yaolj@nwpu.edu.cn

© The Author(s), under exclusive license to Springer Nature Singapore Pte Ltd. 2021

G. Shen et al. (eds.), *Advances in Acoustic Emission Technology*, Springer Proceedings in Physics 259, https://doi.org/10.1007/978-981-15-9837-1_21

has been used in aviation engines, supersonic aircraft, satellite orbital control engines, and it is considered to be one of the most promising thermal structural materials for the future [6, 7]. However, in addition to being subjected to continuous stress, CMC structures also need to be exposed to high temperatures and other environmental factors, so the damage and degradation processes of CMC are relatively complicated. Therefore, these processes are currently the subject of much research [8–10]. Revealing the damage mechanism and evolution of the material characteristics, and establishing the physical mechanism of the damage process are essential, since knowledge of these informs the basis of structural design, life prediction and application safety evaluation. In recent years, many researchers have conducted extensive research on the performance of CMC composite materials under service loading and the damage mechanism, and used this to predict cumulative damage, using fracture analysis, and stress/strain analysis [11, 12]. However, these cannot reveal the damage evolution process, while maintaining continuous monitoring of the source of the damage, and accurately record the complete process of material failure.

Acoustic emission (AE) arises from changes in the internal structure of a material leading to sources of local stress concentration. This energy is released rapidly in the form of an elastic wave. Different types of damage will give rise to different sources that produce distinct AE signals, and the basis of the AE technique is to distinguish the different signals as an indicator of the different types of damage within the material. AE technology has been widely applied to non-destructive testing, due to its real time continuous analytical capability. It is ideal for analyzing the thermal creep damage mechanism of C/SiC. In order to obtain as much information as possible, a large number of characteristic parameters are recorded. However, if the number of features is too high, the error rate for pattern recognition increases, which would reduce the effectiveness of the technique. Therefore, it is necessary to select and optimize these parameters. During pattern recognition, it is advantageous to use unsupervised identification algorithm in order to obtain known category samples, so that a clustering algorithm for AE signal analysis can be used.

It is known from previous studies and SEM analysis that damage to CMC can be mainly classified into three types: fiber breakage, matrix cracking, and fiber/matrix interface debonding. Momon [13] classified AE data from CMC fatigue testing by using unsupervised and supervised techniques, Racle [14] used mechanical parameters to investigate CMC damage factors, and Awaja [15] used a combination of four-point bending and X-ray radiography to study C/SiC damage. However, these studies did not analyze the time evolution of the damage how the materials eventually failed. Traditional AE pattern recognition methods, mostly based on the methods used to analyze metals are not well suited to providing CMC clustering analysis parameters.

This paper reports a method of determining a set of AE parameters suitable for C/SiC creep damage analysis by extraction from an AE signal, and establishes a relationship between the material damage mechanism and the AE signal. As a result, information is obtained on the dynamic evolution and Creep life of the damage process through cluster analysis.

21.2 Pattern Recognition Analysis Method

The creep failure process of C/SiC involves several different damage mechanisms, for example, fiber breakage, matrix cracking and interface debonding. The complex evolution of these damage modes determines the creep life of C/SiC. According to their physical background, different damage mechanisms exhibit different acoustic emission characteristics. Pattern recognition analysis is required to identify the damage mode of each acoustic emission event, and thus clarify the damage evolution during the whole creep experimental.

The K-means algorithm, an unsupervised pattern recognition method, was chosen to determine the clustering of the AE signals. This mainly consists of three parts: constructing a range of feature parameters, identifying the appropriate combination of these parameters and applying K-means clustering analysis on this combination. This protocol allows all relevant parameters to be included, and it avoids the impact of human factors such as bias and other spurious effects. The optimal combination of binary variables is determined through a voting method, thus the most reasonable feature parameters suitable for CMC AE signal pattern recognition are obtained. Different types of damage show different AE signal features, and different damage types can be identified through K-means clustering. All C/SiC acoustic emission pattern recognition analysis methods can be simplified as shown in Fig. 21.1.

21.2.1 AE Parameter Combination and k*-means Cluster*

In traditional AE pattern recognition, the selection of feature parameters is relatively fixed, and those parameters are determined by those arising from metals, which are not suitable for CMC. AE signals contain a lot of information, but much of this is invalid for pattern recognition, so it is essential to determine feature parameters suitable for CMC analysis.

Different parameter combinations have different effects on the eventual pattern recognition, so many different parameter combinations were constructed in order to create variables suitable for the following voting method. Before the parameter combinations optimization, it is necessary to construct a set of parameter combinations that all parameters could be built up, and all the parameter combinations can be obtained by method of the following.

The feature parameter combination is denoted a H and the number of clusters is denoted as I. Then we can obtain a cluster CL, where $CL = CL\,(H, I)$. The combined sum of number of variable H is N and the number of variable I is L

$$N = \sum_{X=M}^{K} \begin{bmatrix} K \\ X \end{bmatrix} \quad (K \text{ is max number of feature, } X \text{ is the feature selected})$$

$$L = P - 1 \quad P(\text{ is max number of clusters}).$$

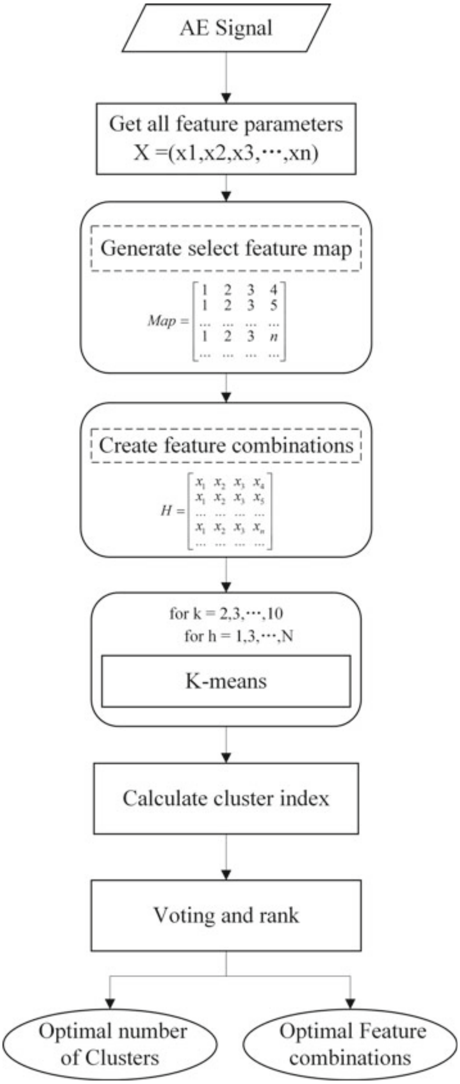
AE Signal
Get all feature parameters
X =(x1,x2,x3,⋯,xn)
Generate select feature map
Map =
Create feature combinations
H =
for k = 2,3,⋯,10
for h = 1,3,⋯,N
K-means
Calculate cluster index
Voting and rank
Optimal number of Clusters
Optimal Feature combinations

Fig. 21.1 Flowchart of pattern recognition

Therefore, the total number of combinations is $R = N \times L$. Then we can get the R parameter combinations through the traversal.

All the parameter combinations and their *IDs* can be obtained by the above method, then a prior *k*-means algorithm as the following was used to cluster.

1. Initialization: calculate the number of clusters according to the maximum-minimum distance criterion [16], and define the obtained K center as $C_{10}, C_{20}, \ldots, C_{K0}$.

2. Calculate the distance from the sample points which are undefined as the center-to-center of each category (the distance being the Euclidean distance), obtaining the minimum value, and putting it in the category where the shortest center is located.

   All samples are classified according to the method above, and the number of samples in all categories is recorded. Then each new cluster center is re-calculated.

$$C_{i1} = \frac{1}{n}\sum_{j=1}^{n} x_j \quad i = 1, 2, \ldots, K$$

(n is the number of samples belonging to class i),

   Then all the data points are divided into K classes, and the cluster centers were settled as the average of each cluster data.

3. By comparing the new category center and the old cluster center, if all the category centers are equal, namely $C_{im} = C_{i(m+1)}$, $i = 1,2, \ldots, K$, then the clustering process is finished, otherwise step (2) is repeated, the samples are reclassified until condition (3) is satisfied. When this occurs the clustering process is complete, with m representing the number of iterations.
4. When the best results are obtained, the entire iterative process is complete and the squares of the errors for all cluster categories are calculated.

21.2.2 *The Voting and Evaluation Criterion*

The key step in unsupervised analysis is to evaluate the validity of the reducing-order algorithm. We give three independent similarity criteria to evaluate the clustering. Then we use a voting rule to find the optimal value of the binary variable (*H, I*), with the rule given in Table 21.1.

It is important to note that the optimal value of the DB indicator is small, while the optimal value of the Dunn index and the Silhouette index is large. After the three votes were independently completed, the final total voting score Z is the sum of them:

$$Z = V\_DB(Z_1) + V\_\text{Dunn}(Z_2) + V\_\text{Slih}(Z_3)$$

The above formula is the final score function expression; the optimal feature combination and optimal clustering number are obtained as a function of the binary variable H and I.

Table 21.1 Voting criterion

Rank	I	II	III	IV
Score	30	15	10	5

The following is the method used to compute the three similarity criteria:

1. DB (Davies-Bouldin) Index
   The smaller the DB value the smaller the distance within the class, and the greater the distance between the classes. The *s* means average distance in the class data to the cluster centroid, the *D* means distance between cluster *i* and cluster *j*, and the DB index is defined as

   $$J_{DB} = \frac{1}{k}\sum_{i=1}^{K}(\max R_{ij}) \quad R_{ij} = \frac{s_i + s_j}{D_{ij}} \quad D_{ij} = \left|m_i - m_j\right| \quad s_i = \sqrt{\frac{1}{n}\sum |x - m_i|}$$

   The s means average distance in the class data to the cluster centroid, the *D* means distance between cluster *i* and cluster *j*.
   The smaller the DB value the smaller the distance within the class, and the greater the distance between the classes.
2. Dunn Index.
   The $d_{\min}$ represents the minimum distance between two classes, and the $d_{\max}$ represents the maximum distance between the same two classes, the Dunn index is defined as

   $$\text{Dunn} = \frac{d_{\min}}{d_{\max}}$$

   Obviously, Dunn $\in [0, \infty]$ has a larger value for better clustering results. The calculation of this index is easy to implement and has lower computational complexity, but it is more sensitive to a few border points.
3. Silhouette Index
   It shows the similarity evaluation criterion of each modes compared to other clusters of models. The larger the Silhouette value the better the classification. The *a* represents the average distance from sample to other samples in the same cluster, the *b* means the average distance from the sample to all the samples in some other cluster, and the Silhouette index is defined as

   $$\text{Sil} = \frac{b(x) - a(x)}{\max\{a(x), b(x)\}}$$

21.3 Experiment and Signal Acquisition

21.3.1 Sample Preparation and Creep Experiment

Firstly, T-300 carbon fiber [17] is woven into a plain weave by a two-dimensional cascade method. Then chemical vapor infiltration (CVI) is used to deposit an interface layer of Pyrolytic carbon (PyC) on the fiber surface using a propyne (C_3H_4) gas

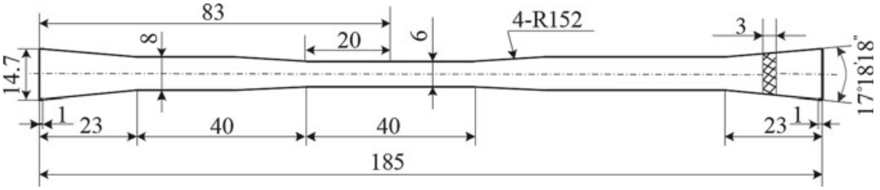

Fig. 21.2 The shape and basic dimensions of the specimen (all values are in mm)

source. The pyrolysis temperature was set at 960 °C at a pressure of 5 kPa. The SiC matrix was deposited using the CH_3SiCl_3 under condition of 1000 °C, 0.01 MPa vacuum and a 5 kPa deposition pressure. The fiber volume content was 40%, the density was 2.1 g/cm^3, and the porosity was 15%. Then the C/SiC composite material was cut into a dog-bone tensile specimen using a computer numerically-controlled machine, and its geometric dimensions are displayed in Fig. 21.2. Finally, chemical vapor deposition (CVD) was used to deposit 2 layers of SiC coating onto the sample surface in order to improve its oxidation and corrosion resistance.

Detailed information about the test equipment employed for creep testing in complex coupling environments of loading under a static atmosphere can be found in reference [18]. It includes a hydraulic universal servo tester (Model 8801, Instron Ltd., UK) and an environmental chamber, in which temperature, oxygen content and water vapor content can be controlled.

The creep tests were conducted using the above equipment at 700 and 1300 ºC in a wet oxygen atmosphere comprised of H_2O (5 Vol.%), O_2 (16 Vol.%) and Ar (79 Vol.%). The creep stresses were 75, 140 and 160 MPa, respectively. During the creep tests, the total pressure of the environment chamber was kept at 100 kPa, and the water-oxygen gas flow was slow. The creep tests continued until the sample failed catastrophically.

21.3.2 *Acoustic Emission Monitoring*

The AE sensor (Pico, Physical Acoustics Corporation) was positioned at the upper grip of catheter, deriving from the heating furnace. Vaseline was used as a coupling agent. Sensors were connected to a preamplifier (gain: 40 dB, frequency range: 1000–1600 kHz), which was connected to the data acquisition equipment (a four-channel MISTRAS 2001 system, Physical Acoustics Corporation). The threshold was set to 40 dB in order to filter out noise signals. The AE acquisition system as the Fig. 21.3.

The AEWin8 software was used to extract characteristic parameters from the AE waveforms. The characteristic parameters considered in this paper are listed in Table 21.2.

Experimental results as shown in Table 21.3. The table lists the temperature, the lifetime before failing, and a description of each specimen as well as additional

Fig. 21.3 AE acquisition system

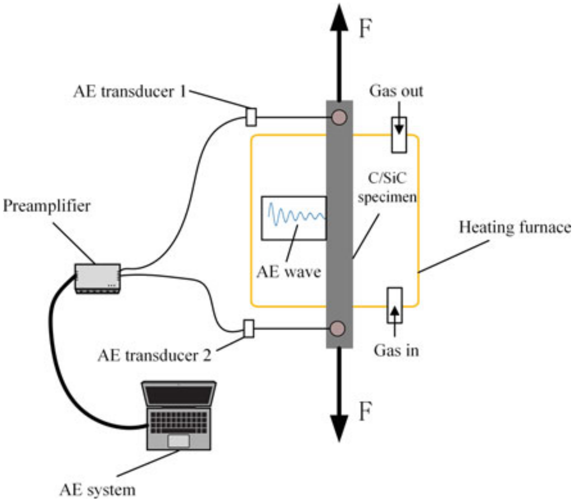

Table 21.2 The characteristic parameters

Feature	ID. Feature
Parameters	1. Time, 2. channel, 3. threshold, 4. extrinsic parameters
Time domain	5. Rise time, 6. number of counts, 7. energy, 8. duration time, 9. amplitude, 10. signal intensity, 11. absolute energy
Frequency domain	12. Average frequency, 13. peak frequency, 14. weighted frequency, 15., back-calculation frequency, 16. center frequency, 17. frequency band 1 (100–175 Hz), 18. frequency band 3 (175–250 Hz), 19. frequency band 2 (250–325 Hz), 20. frequency band 4 (325–400 Hz)

Table 21.3 Results and details of creep

Number	Temperature/°C	Stress/MPa	Specimens describe	Lifetime/min
1	1300	75	Tensile fracture, normal fracture	139
2	1300	140	Tensile fracture, normal fracture	62
3	1300	150	Tensile fracture, normal fracture	35
4	1300	160	Tensile fracture, normal fracture	15
5	1300	140	Tensile fracture, normal fracture	121
6	1300	140	Tensile fracture, normal fracture	90
7	700	140	Tensile fracture, normal fracture	622

information. The specimen lifetimes showed a large difference, and this variability may largely be due to C/SiC defects caused by the variations in the preparation process.

21.4 Results and Discussion

21.4.1 *C/SiC AE Signal Clustering*

The frequency domain and time domain parameters of the recorded AE signal can fully describe an acoustic signal accurately. However, in order to permit algorithmic comparison of signals, the following characteristic features of the AE signal from each sample were extracted as shown in Table 21.2.

Samples were analyzed using the method outlined in the previous section, with the algorithm parameters set to $K = 11$, $M = 5$, and $P = 6$ for the data set generated by each experiment (i.e. the set of AE events). The result of clustering analysis are shown in Table 21.3. In the table, the optimal cluster number and the optimal feature combination ID are obtained after the experimental data for each sample has been processed by clustering analysis, and the corresponding index values and voting scores of the three criteria are obtained.

The third column in Table 21.4 shows the distribution of the feature combinations after optimization, and different sample data correspond to different optimal feature combinations. It seems very irregular at first glance, however, as can be seen from Table 21.5, the feature combination of the optimal selections focus on the following 7 frequency features: weighted frequencies, central frequency, peak frequency and 4 frequency bands. Therefore, it can be said that the characteristic combination after optimization is based primarily on frequency. In the fourth column of Table 21.4, the optimal number of clusters after analysis is 4 clusters in experiment No. 3, and all others are 3 clusters, which corresponds to the number of main damage mechanisms of the material.

It can be gotten form the Table 21.4 the all three independent similar indices attain their optimal values for sample 6. Figures 21.4 and 21.5 show the distribution of each class after the AE data clustering analysis of sample 6 by two-dimensional and three-dimensional perspectives.

Figure 21.4 is composed of 16 subgraphs, they are symmetrical along the diagonals. In the subgraphs, each row has the same abscissa, and each column has the same ordinate axis and the subgraphs on the diagonals describe the distribution of

Table 21.4 The optimal parameter combination ID and cluster number

Sample	Features ID	Cluster number	DB index	Dunn index	Silh index	Score
2	5000014	3	0.680	1.334	0.494	50
4	5000010	3	0.505	1.492	0.559	60
5	5000005	3	0.631	1.942	0.547	60
7	5000016	3	0.643	1.909	0.505	60
3	5000003	4	0.593	1.307	0.546	60
1	5000008	3	0.536	1.739	0.643	75
6	5000009	3	0.264	3.186	0.798	90

Table 21.5 The parameter combinations of AE signals corresponding to IDs

ID	Elements of feature combinations				
ID.5000003	Weighted frequency	Frequency band 1	Frequency band 2	Frequency band 3	Peak frequency
ID.5000005	Weighted frequency	Frequency band 1	Frequency band 2	Frequency band 4	Peak frequency
ID.5000008	Weighted frequency	Frequency band 1	Frequency band 3	Frequency band 4	Peak frequency
ID.5000009	Weighted frequency	Frequency band 1	Frequency band 3	Center frequency	Peak frequency
ID.5000010	Weighted frequency	Frequency band 1	Frequency band 4	Center frequency	Peak frequency
ID.5000014	Weighted frequency	Frequency band 2	Frequency band 4	Center frequency	Peak frequency
ID.5000016	Frequency band 1	Frequency band 2	Frequency band 3	Frequency band 4	Peak frequency

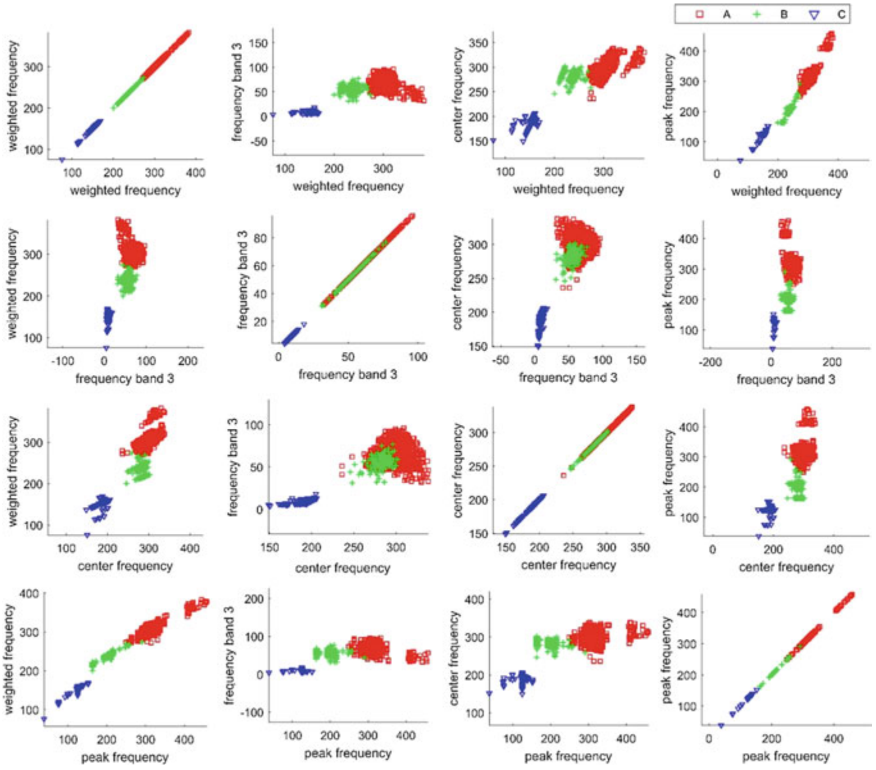

Fig. 21.4 Two-dimensional distribution of sample 6 cluster results

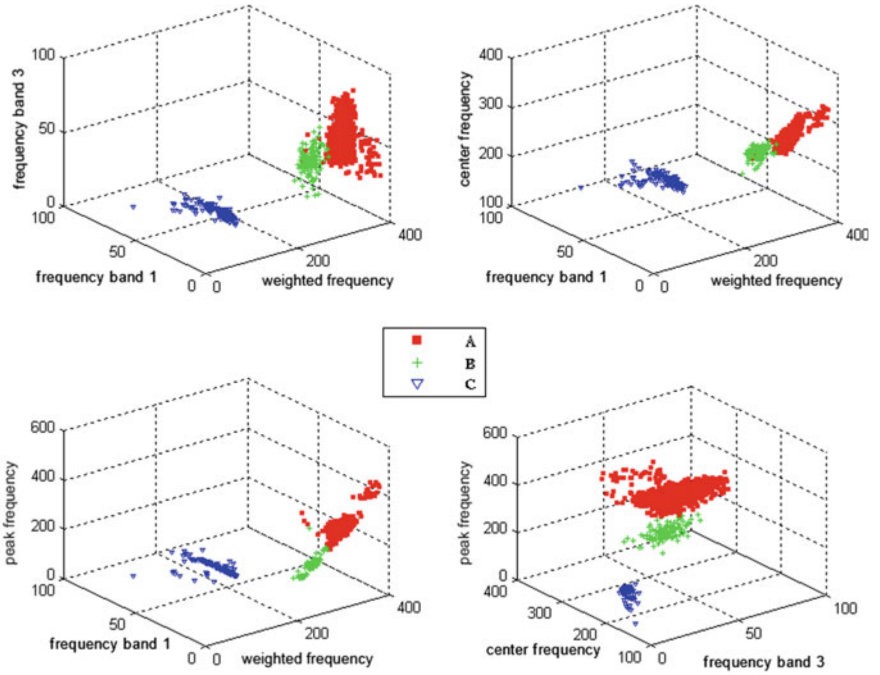

Fig. 21.5 Three-dimensional distribution of sample 6 cluster results

clustering for a single feature. The data in Fig. 21.4 are derived from sample No. 6, it may be observed that the overlap between different clusters is small. Clustering C, which represents low frequency signals, has a large separation distance from classes A and B, while the separation distance of class A and class B is relatively small. In subgraph (2, 3) (the subgraph of the third row in the second column), it is a subgraph of frequency band 3 and center frequency, which shows an obvious overlap between class A and class B. Other subgraphs can also clearly distinguish different types of data. Meanwhile, there are two small clusters in subgraphs (1, 3), (1, 4), (2, 4), and (3, 4), the distinguishing feature between them being peak frequency or weighted frequency. In addition, the subgraph on the diagonals shows that the peak frequency characteristics alone can distinguish different categories well. Therefore, peak frequency will be used as the main feature to identify the damage evolution process of materials in the subsequent analysis of material damages.

Figure 21.5 shows the clustering distribution map of different feature combinations. The data source is the same as Fig. 21.4, namely sample No. 6. It shows no overlapping data, and subgraph (2, 2) should be noted. It is a subset of Fig. 21.4 (2, 3), but the overlap that was present originally is no longer present in the three-dimensional subgraph. Therefore, it is more advantageous to use multiple variables with three-dimensional graphical representation for distinguishing different data samples.

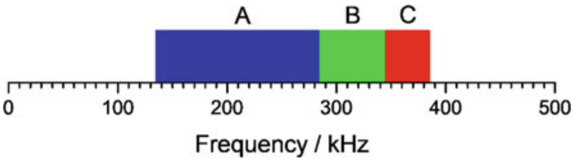

Fig. 21.6 The frequency domain of the peak frequency

After clustering analysis of the high temperature creep AE data, the optimal combination of clustering and clustering number (3 or 4) for each sample can be obtained. The aim is to identify the damage mechanisms and evolution of C/SiC composite materials, and it is necessary to link the information from this clustering analysis to the damage mechanism of the materials. However, there is no general criterion to evaluate the material damage caused by each damage mechanism identified by the AE signals from this material. In previous work, AE signals were clustered by clustering analyse with a voting rule and three similarity criterion.

The inherent relation between the AE signal and material damage to be elaborated. C/SiC composites processes can be divided into three types: fiber breakage, matrix cracking, and fiber/matrix interface debonding. The fiber/matrix interface debonding damage includes fiber debonding, fiber extraction and so on. These three damage modes correspond to the three clustering types A, B and C identified above. In order to find their corresponding relation, the characteristic parameters are analyzed. For instance, cluster centers labelled C have a similar peak frequency and are concentrated in the region [340, 370] kHz, B is distributed in the region [290, 340] kHz, occupying the middle-frequencies, and A is distributed between [150, 290] kHz, occupying the low-frequency region. Figure 21.6 shows more clearly the frequency domain of the peak frequency for each of the damage modes A, B and C.

The clustering centers are identified using the rule for the minimum sum distance from other clusters using Euclidean measure, so the center characteristic is the most representative. In Table 21.6, five characteristic with obvious steps can be found, peak frequency, weighted frequency, center frequency, frequency band 2 and frequency band 4. However, there are no obvious differences in other time-domain features, this also applies to other samples that are not listed in the table. The experimental and clustering process are carried out independently this result is obtained with any a priori knowledge. This reflects the priority of the frequency in the AE signal in material damage analysis, and it also demonstrates the objectivity of the clustering analysis algorithm used in this work.

21.4.2 C/SiC Damage Evolution and Creep Life Analysis

It is necessary that the class label must be given before the creep damage analysis. Different types of AE events correspond to different damage mechanisms and can be labeled based on signal energy, damage mechanisms, and SEM observations.

Table 21.6 Values of cluster centers

Sample	Cluster	Average frequency	Center frequency	Peak frequency	Frequency band 1	Frequency band 2	Frequency band 3	Frequency band 4
1	A	98.6	262.6	196.8	8.2	37	41	13
	B	111.7	287.9	290.4	4.4	17	57	20
	C	106.5	302.2	404.3	5.1	12	43	39
2	A	63	278	274	3	27	56	14
	B	116	290	296	5	13	58	24
	C	72	305	387	5	8	45	41
3	A	106.6	283	264	2	26	57	15
	B	119.9	294	282.1	2	13	64	20
	C	118.5	312.2	379.4	2	8	52	37
	D	104	296	403.5	3	13	61	41
4	A	98	281	230	2	34	52	12
	B	116	296	290	1	17	65	17
	C	231	309	362	2	10	61	27
5	A	114.1	288.7	289.4	3	24	56	18
	B	126.3	304.8	320.2	2	9	69	20
	C	118	312.7	352.5	3	9	51	37
6	A	109.1	284.9	270.8	4	25	49	22
	B	122.5	299.4	293.7	3	11	60	26
	C	116.9	305.4	403.8	4	12	42	42
7	A	86.9	189.7	121.7	44	42	9	5
	B	126.4	282.5	193.9	2	31	55	12
	C	123	296.7	313.9	2	15	66	17

For such CMC materials, the type of damage can be obtained by SEM fracture analysis. The C/SiC high temperature creep fracture surface with SEM observation is as shown in Fig. 21.7. It is known that the C/SiC creep damages mainly are (A) matrix cracking, (B) interface debonding (fiber extraction), and (C) fiber breakage. During the creep process, the material absorbs energy with the development of damage propagation, and the material will be destroyed until the strain reaches the limit.. The carbon fiber is the main carrier material in the C/SiC composites, which can characterize the breakage of the material, and the material is failed when it is destroyed abundantly.

AE energy is usually assumed proportional to the energy dissipated by the source, whatever the source mechanism. Hence the relationships between damages mechanisms and AE signals were established by analysis of energy, kinetics and location of signals for each cluster during all the mechanical tests performed. The AE energy distribution of different class is shown in the Fig. 21.8. The energy of class A signal is the lowest and the distribution interval is narrow, and this kind of signal produces the loading period, which corresponds to the characteristics of the matrix. The class

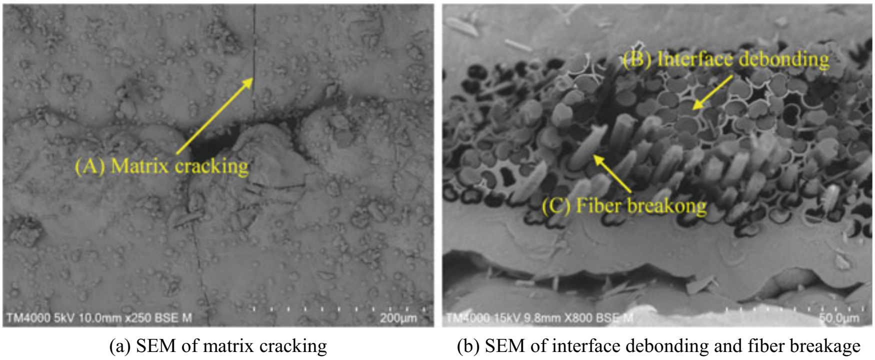
(A) Matrix cracking
TM4000 5kV 10.0mm x250 BSE M
200μm
(B) Interface debonding
(C) Fiber breakong
TM4000 15kV 9.8mm X800 BSE M
50.0μm

(a) SEM of matrix cracking (b) SEM of interface debonding and fiber breakage

Fig. 21.7 Fracture surface SEM of C/SiC

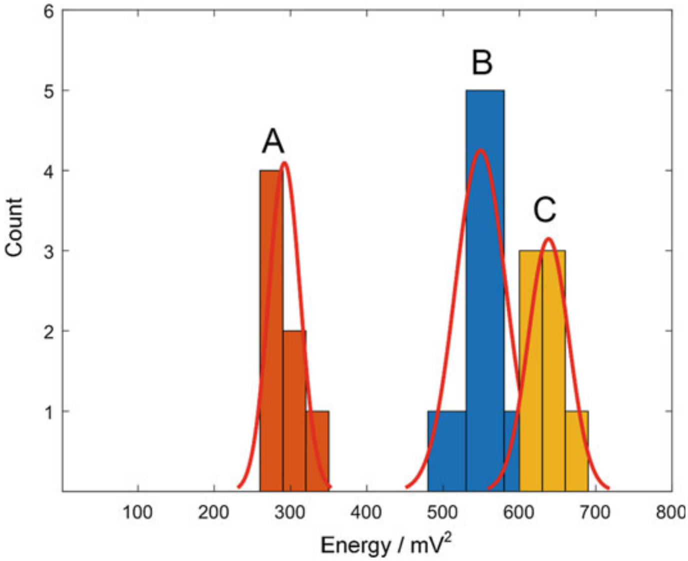

Fig. 21.8 Average energy distribution of different samples

B signals have a wide energy distribution and are generated throughout the creep process, it may respond to debonding. The Class C have the highest energy, so these class were attributed to the most important damage mechanisms observed in this type of composite during the creeping: fibre failures with maybe fibre band failures.

AE signals can reflect the damage evolution during the entire creep period before material failed, help to gain some insight into the high temperature creep behavior of C/SiC. As shown in Fig. 21.9, different damage modes accumulate with creep lifetime, they are derived from samples with long (Fig. 21.9a), medium (Fig. 21.9b), and short (Fig. 21.9c) creep lifetime respectively. The creep damage evolution of this

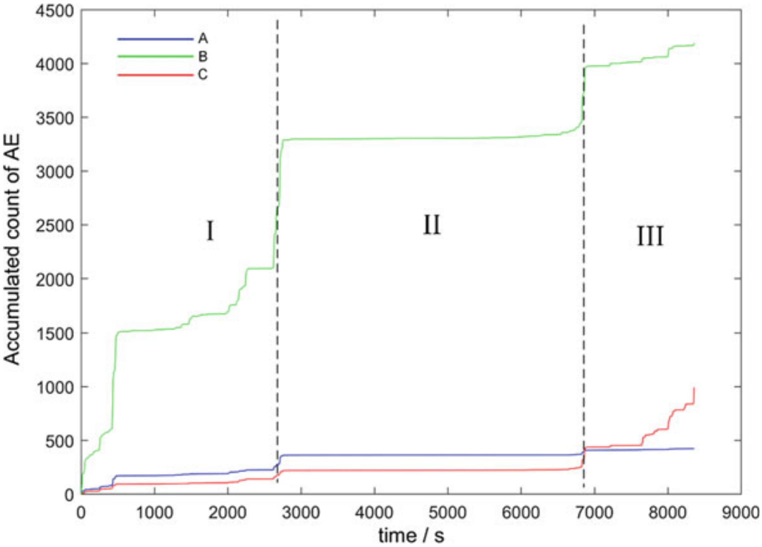

(a) AE events cumulative of long sample

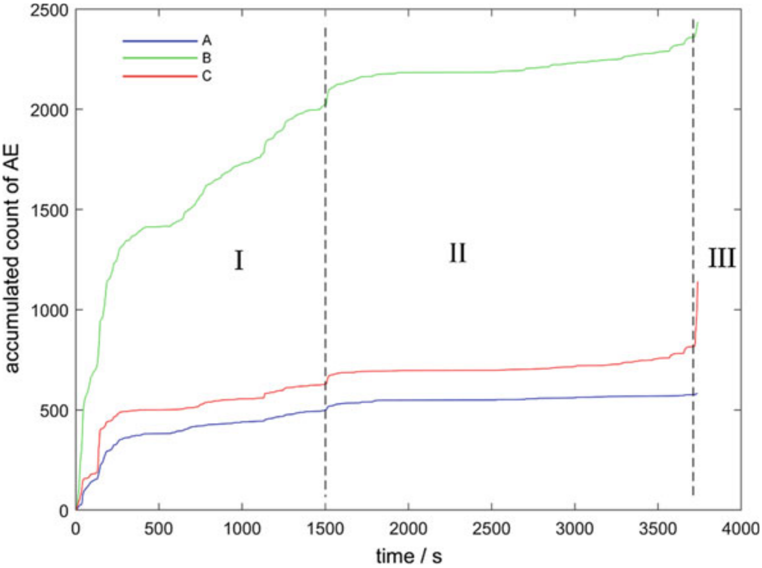

(b) AE events cumulative of medium sample

Fig. 21.9 Cumulative graphs of AE damage events

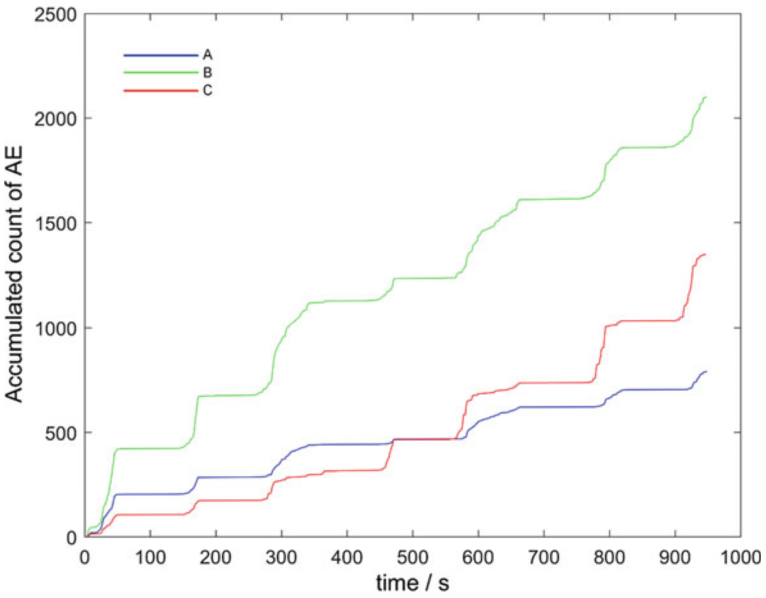

(c) AE events cumulative of short sample

Fig. 21.9 (continued)

material can be divided into three stages: (I) active initiation, (II) stable mid-life, and (III) accelerated damage at the end, these stages are elaborated in the following.

In each subgraph of Fig. 21.9, it is can be obtained that the class C has a steep increase in the accelerated damage phase. With the above analysis and the Table 21.6, the class C is the carbon fiber breakage. In each sample, it has the maximum energy and frequency since carbon fiber is C/SiC of the main carrier material, the material will failure when it has extensive damage. The class A is generated only in the loading phase, the duration is little, which corresponds precisely to the SiC matrix, a brittle material, elastic modulus and damage tolerance are small. It would be generated destroyed immediately when loading. The class B has a large proportion in each sample and generating at every stages of creep, which consistent with the characteristics of interface damage, the interface is PyC transferring the load from the matrix to the fiber. It must follow the equal strain criterion in composites, while the elastic modulus of the carbon fiber and the SiC matrix are different. Carbon fiber is the elastic material, having an increasing continuously strain under stress-oxidation conditions, but the SiC matrix is no longer increased when the strain reach to the damage tolerance. Therefore, during the whole creep process, the interface layer must be continuously damaged to adjust the strain between the fiber and the matrix.

It can be seen that the three stages of the long and medium life samples have a clear distinction in Fig. 21.9, while the short life samples do not. In Fig. 21.9a (the long life sample): all kinds of damage occurred in stage I; the interface damage is

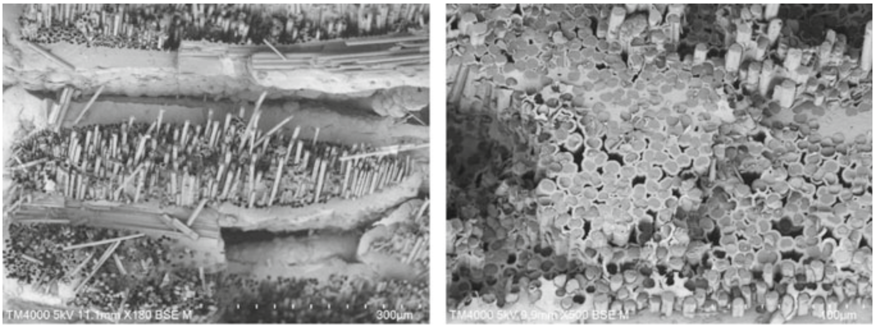

(a) SEM of long sample (b) SEM of short sample

Fig. 21.10 SEM of fracture morphology

continuously arisen in stage II, but fiber and matrix damage is hardly arisen; the fiber damage has a rapid increase with same interface damage in stage III, and the matrix damage is still little. In Fig. 21.9b (the medium life sample): the different stages also has a obvious distinction and it is similar to the long life sample, however, the I stage has more interface damage, the III stage is extremely short. In Fig. 21.9c (short life sample): there is no obvious distinction between the stages and all kinds of damages are arisen continuously by time, and the interface damage still accounts for a large proportion.

The difference of C/SiC creep lifetime is large indicating different damage mechanism. Through the SEM analysis as shown in Fig. 21.10, it can be seen that the different creep life has different fracture morphology. The sample with long life has a large number of fiber extraction due to interface debonding and a larger degree of fiber oxidation, but the short life samples has more tidy fracture and the fiber oxidation is little.

For long life sample, it can be obviously seen that fiber bundles are pulled out in Fig. 21.10a, which indicates that the interface bonding of C/SiC is weak. When loading, the interface absorb by damaged to adjust the strain of the carbon fiber and the SiC matrix to a continue the material. This also corresponds to the AE events accumulation of the good sample as the Fig. 21.9a, which interface damage events is much more than the number of fiber and matrix damage events tenfold, however, the short life samples is only twice. By Fig. 21.10b SEM of the poor sample, it can be seen that the fracture has no fiber pull-out, which indicates that the interface bonding of C/SiC is strong, the interface can not absorb the energy through the damage and then adjust the strain of the Carbon fiber and the SiC matrix, and it corresponds to the Fig. 21.9c AE events accumulation of the samples. Therefore, the damage of the interface is the main influencing factor of the life of C/SiC. For the sample with long life, in the stable creep stage, the interface can continuously absorbs energy through the damage, while the fiber and matrix damage hardly increase, so the life is longer. It also can explains why the same C-fiber and SiC matrix have different differences in the life of different samples.

21.5 Conclusion

The following conclusions are noted:

1. The dual variable voting method and clustering analysis are highly suitable for C/SiC CMC high temperature creep AE signal analysis, and *K*-means clustering is available in most samples and the optimal cluster classification is three.
2. There are three basic damage mechanisms of C/SiC composite samples in high temperature creep: fiber breakage, matrix cracking, and fiber/matrix interface debonding. They have significant differences in peak frequency, frequency band 2, and frequency band 4. It means that the AE signal is mainly related to the material damage mechanisms in the frequency domain.
3. The high temperature creep life of C/SiC composites mainly depends on the interface bonding strength, the samples with more interface damage have longer fiber extraction length, larger damage tolerance, and can obtain larger creep life.

Acknowledgements This work has been financially supported by the National Key Research and Development Project of China (2016YFB0700503) and the National Natural Science Foundation of China (51772244 and 11072195).

References

1. T. Li, D. Fan, L. Lu, J.Y. Huang, J. C.E.F.Zhao, et al. Dynamic fracture of c/sic composites under high strain-rate loading: microstructures and mechanisms. Carbon **91**, 468–478 (2015)
2. Y. Yang, Xu. Fei, X. Gao, G. Liu, Impact resistance of 2D plain-woven C/SiC composites at high temperature. Mater. Des. **90**, 635–641 (2016)
3. X. Luan, L. Cheng, C. Xie, Stressed oxidation life predication of 3D C/SiC composites in a combustion wind tunnel. Compos. Sci. Technol. **88**, 178–183 (2013)
4. H. Mei, L. Cheng, L. Zhang, Damage mechanisms of C/SiC composites subjected to constant load and thermal cycling in oxidizing atmosphere. Scripta Mater. **54**(2), 163–168 (2006)
5. S.Qiao, S. Du, G. Ji, D. Han, W. Li, Damage mechanism of 3D-C/SiC composite. J. Mech. Strength **26**(3) (2004)
6. 乔生儒, 杜双明, 纪岗昌, 韩栋, 李玫, “3D-C/SiC复合材料的损伤机理,” 机械强度, 26(3) (2004)
7. van Roode M, Ceramic gas turbine development: need for a 10 year plan. J. Eng. Gas Turbines Power**132**(1), 011301 (2010)
8. S. Pimenta, S.T. Pinho, Recycling carbon fibre reinforced polymers for structural applications: Technology review and market outlook. Waste Manage. **31**(2), 378–392 (2011)
9. T. Li, J. Mo, Yu. Xia, T. Suo, Y. Li, Mechanical behavior of C/SiC composites under hypervelocity impact at different temperatures: Micro-structures, damage and mechanisms. Compos. A Appl. Sci. Manuf. **88**, 19–26 (2016)
10. L. Salvo, M. Suéry, A. Marmottant, N. Limodin, D. Bernard, 3D imaging in material science: application of X-ray tomography. C R Phys. **11**(9–10), 641–649 (2010)
11. D. Frazer, M.D. Abad, D. Krumwiede, C.A. Back, H.E. Khalifa, C.P. Deck, P. Hosemann, Localized mechanical property assessment of SiC/SiC composite materials. Compos. A Appl. Sci. Manuf. **70**, 93–101 (2015)

12. Deju Zhu, Barzin Mobasher, S.D. Rajan, Non-contacting strain measurement for cement-based composites in dynamic tensile testing. Cement Concr Compos. **34**(2):147–155 (2012)
13. B. Nikolaos, M. Xie, X. Song, H. Fellx, A. Brian, J. Marrow, et al. Rich tomography techniques for the analysis of microstructure and deformation. Int. J. Comput. Methods **11**(03), 1343006 (2014)
14. S. Momon, M. Moevus, N. Godin, M. R'Mili, P. Reynaud, G. Fantozzi, Acoustic emission and lifetime prediction during static fatigue tests on ceramic-matrix-composite at high temperature under air. Compos. A Appl. Sci. Manuf. **41**(7), 913–918 (2010)
15. E. Racle, N. Godin, P. Reynaud, M. R'Mili, G. Fantozzi, L. Marcin, et al., Indicators for the damage evolution at intermediate temperature under air of a sic/[si-b-c] composite subjected to cyclic and static loading, in *Mechanical Properties and Performance of Engineering Ceramics and Composites*, hal-01814289, version 1 (2015)
16. F. Awaja, M.-T. Nguyen, S. Zhang, B. Arhatari, The investigation of inner structural damage of UV and heat degraded polymer composites using X-ray micro CT. Compos. A Appl. Sci. Manuf. **42**(4), 408–418 (2011)
17. C.M. Bishop, *Pattern Recognition and Machine Learning* (Springer Science+ Business Media, 2006)
18. S.R. Dhakate, V.K. Parashar, V. Raman, Influence of ceramic interphase on the mechanical properties of T-300 carbon fiber composites. J. Mater. Sci. Lett. **19**(17), 1575–1577 (2000)

Chapter 22
Acoustic Emission Monitoring of Pitting Corrosion on Zirconium Metal

Cheng Ye, Zhongzheng Zhang, Jun Jiang, Yongliang Yu, and Yu Xue

Abstract In order to study acoustic emission (AE) characteristics of pitting corrosion on zirconium metal, Pitting corrosion process of zirconium metal in 10% ferric chloride solution at 70 °C was monitored by AE technology. Two different types of sensors were used to record the AE signals, and conventional parameter-based approach and signal-based analysis were combined to deal with AE signals. The results showed that AE technology could better distinguish between the different stages of the zirconium metal pitting process. Compared with the signals of the nucleation stage, the signals of pitting propagation stage had greater activity, lower amplitude, higher count, rise time, duration time and energy. It contained two different types of signal waveforms corresponding to two phases pitting damage. Waveform mode was mainly composed of flexural wave and expansion wave, and the low frequency flexural wave was dominant in pitting propagation stage. Passivation film rupture and hydrogen bubbles breakdown were mainly AE sources of zirconium metal pitting. The research results had some certain reference value for AE monitoring of pitting corrosion on zirconium metal equipment.

22.1 Introduction

Acoustic emission (AE) is one phenomenon in which transient elastic stress waves are generated when material is damaged. AE detection technology established by applying this characteristic has been widely used in the field of non-destructive testing and material research of equipment. Pitting damage is one kind of common corrosion phenomenon in equipment of petrochemical enterprises, which can lead to leakage of equipment perforation and induced stress corrosion cracking. The application of AE technology to monitor the pitting process can achieve early warning of equipment safety. At present, there are many researches on AE pitting monitoring, but the research objects are mostly concentrated on austenitic stainless steel and aluminum alloy materials [1–5], a few researches on zirconium metal has been

---

C. Ye (✉) · Z. Zhang · J. Jiang · Y. Yu · Y. Xue
Nanjing Boiler and Pressure Vessel Supervision and Inspection Institute, Nanjing 210019, China
e-mail: anyan2227@163.com

© The Author(s), under exclusive license to Springer Nature Singapore Pte Ltd. 2021

G. Shen et al. (eds.), *Advances in Acoustic Emission Technology*, Springer Proceedings in Physics 259, https://doi.org/10.1007/978-981-15-9837-1_22

Table 22.1 Chemical composition of experimental zirconium plate

Element	C	Fe + Cr	H	Hf	N	O	Zr + Hf
Content	0.01	0.08	<0.0003	1.1	0.005	0.13	≧99.2

reported. Due to its excellent mechanical and corrosion resistance, zirconium metal has been used in important equipments in some harsh acid-base media environments in the petrochemical industry in recent years [6]. However, in some oxidizing medium solutions, such as in the ferric chloride solution, pitting corrosion occurs for zirconium metal [7]. The result may be more serious for equipments because zirconium metal is mainly designed for corrosion resistance purposes, therefore, the study of the AE characteristics of zirconium metal pitting corrosion has important application value for early warning of equipment safety.

22.2 Experiment

22.2.1 Experimental Equipment

The experimental sample was one small rectangular zirconium plate, the material was R60702, the specification was 200 × 40 × 3 mm, and the chemical composition was as shown in Table 22.1.

The experimental AE instrument is a two-channel AE instrument of American PAC Company, which can collect parameters and waveform data at the same time. The 1-channel sensor type is R15α, the response frequency band is 50–200 kHz the center frequency is 150 kHz, the 2-channel sensor type is R6α, the response frequency band is 35–100 kHz, and the center frequency is 55 kHz. The data acquisition threshold is set to 40 dB, the pre-gain is amplified by 26 dB, and the waveform sampling frequency is 5 MHz. The channel acquisition parameters are set to: peak definition time 200 μs, hit definition time 1600 μs, hit lock time 2000 μs. The heating and heat preservation equipment is a water bath type temperature control instrument for holding a 10% ferric chloride solution vessel as a jar and a sealed soft foam plug. The experimental setup is shown in Fig. 22.1.

22.2.2 Experimental Process

A 10% ferric chloride solution was placed, and a few drops of concentrated hydrochloric acid were added thereto, and the pH of the solution was measured to be about 1.2. The jar containing the ferric chloride solution was laced in a water bath temperature controller. When the temperature of the ferric chloride solution reaches 70 °C, the temperature was kept constant. Two sensors were placed at one

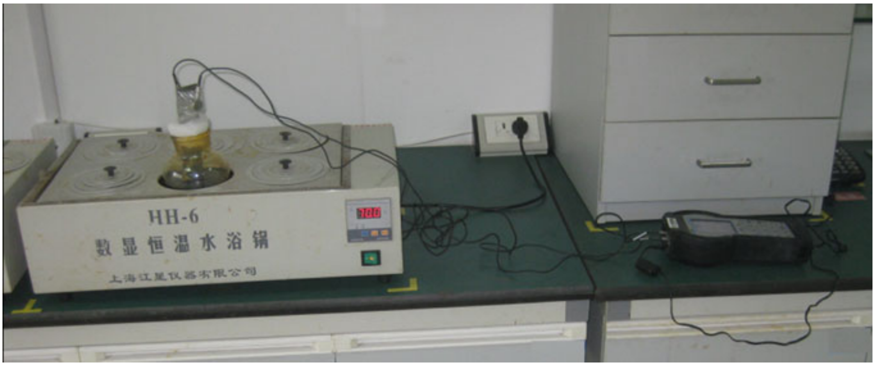

Fig. 22.1 Zirconium metal pitting corrosion AE monitoring test equipment

end of the sample, and the coupling agent was vacuum grease and fixed with plastic tape. The other end of the sample was inserted through a sealed foam plug into a jar solution to a depth of about 25 mm. The acoustic emission data was collected while acquiring characteristic parameters and waveforms. During the experiment, the data acquisition situation and the surface variation of the sample were observed. The experiment lasted for about 3.8 h, the experimental data collection was stopped, and the samples were taken for macroscopic observation. The surface solution of the sample was washed away with water and observed under an optical microscope. The above test procedure was repeated several times and the test results were basically the same.

22.3 Results and Discussion

22.3.1 Analysis of AE Activity and Characteristic Parameters

Figure 22.2 is a time history diagram of the cumulative AE signals of the two channels, reflecting the trend of AE activity during the test. It can be seen from the figure that

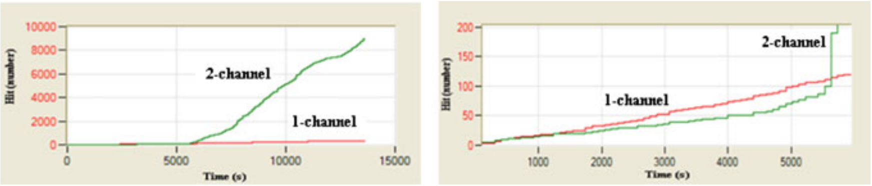

a cumulative AE hits time history plot

b cumulative AE hits time history plotin the first stage

Fig. 22.2 Cumulative AE hits history plot for two channels

the initial two-channel AE activity is similar and the value is small, wherein the channel 1 activity is slightly larger than the channel 2. At approximately 5632 s, the channel 2 AE signal activity increases rapidly, and remains substantially at this high activity value except for a slight decrease in the vicinity of 12,000 s. For channel 1, the AE activity remained essentially the same throughout the test. According to the signal activity distribution, the test process can be divided into two stages: 0 to 5632 s is one stage, and 5632 to 13,721 s is the second stage.

Figure 22.3 is a time history diagram of the characteristic parameters commonly used in AE technology. Through the time history distribution of the characteristic parameters, it can be found that, besides Fig. 22.3a, b, there are significant differences in signal characteristic parameters of each channel in different test phases during the test. In addition to the higher amplitude value, the first stage signal activity and hit number as well as the count, rise time, duration, and energy characteristic parameters are significantly smaller than the second stage. In addition, there are significant differences in the values of the characteristic parameters of the signals collected by the two different channels. In the first phase, the two channel characteristic parameters are basically the same. In the second stage, the 2-channel AE activity, the number of AEhit, the count, the energy, the rise time, and the duration time are significantly higher than 1 channel; and the amplitude is lower than 1 channel. The list of feature parameter distribution ranges is shown in Table 22.2.

Pitting corrosion of metals is generally considered to begin with the surface with an oxide film. Under the action of certain living anions (such as Cl^-) in the medium, the oxide film is first destroyed, and a passivation-activated battery is formed on the surface of the metal to be etched into small holes. As the Cl^- in the solution migrates into the pores, a concentrated solution of metal chloride (such as $FeCl_2$) is formed in the pores. Decomposition of the chloride solution leads to an increase in the acidity of the solution in the pores, which is further enhanced by corrosion [8]. Regarding the acoustic emission mechanism during pitting corrosion, Rongsheng and Gangqiang [9] believe that pitting corrosion is caused by film rupture, and a step pulse force is applied to the metal accompanying the film rupture process, thereby generating a stress wave, that is, AE phenomenon. The rupture of tiny hydrogen bubbles caused by corrosion will also produce AE signal with the same principle as membrane rupture.

Corresponding to the mechanism of pitting formation and the mechanism of pitting AE source, the time history distribution of the characteristic parameters of AE signals monitored by the experiment reflects the different stages of metal pitting damage. In this test, the AE signal was monitored by immersing the sample in the solution for about 25 s, indicating that the corrosion potential in the test corrosion system is higher than the pitting potential of zirconium. After the sample is immersed in the solution, the zirconium metal first acts on the surface passivation film and Cl^- in the solution. In the first stage (before 5632 s), the test solution system should mainly occur due to the destruction of the surface oxide layer of the zirconium metal leading to the continuous formation of the metal surface nucleation. At this stage, the AE signal source should be mainly destroyed by the passivation film on the surface of the zirconium metal, the AE activity is small, and the number of hit is small. The amplitude of the AE signal is relatively high, while the duration, rise time, count, and

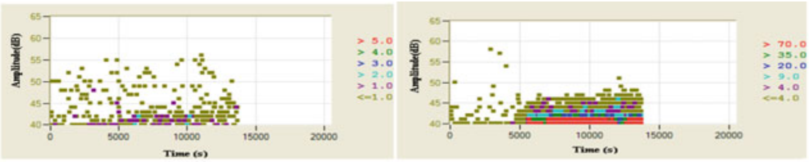

a 1-channel amplitude distribution time history plot b 2-channel amplitude distribution time history plot

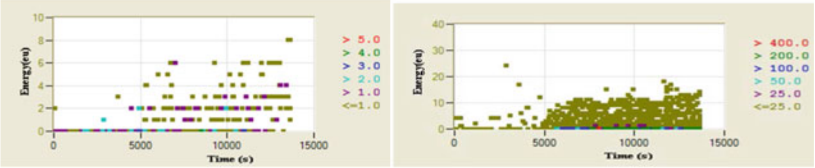

c 1-channel energy distribution time history plot d 2-channel energy distribution time history plot

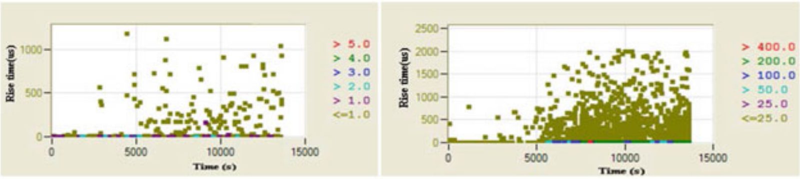

e 1-channel rise time distribution time history plot f 2-channel rise time distribution time history plot

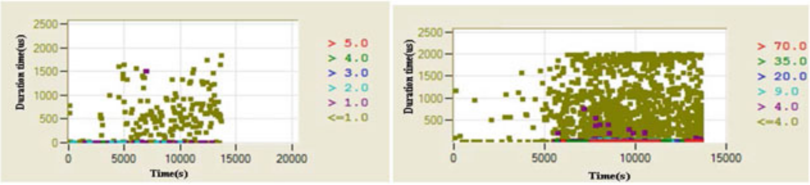

g 1-channel duration distribution time history plot h2-channel duration distribution time history plot

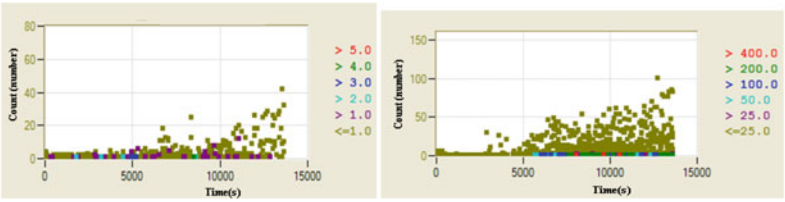

i1-channel count distribution time history plot j 2-channel count distribution time history plot

Fig. 22.3 AE characteristic parameters time history plot

energy are relatively small. As the reaction progressed, pitting gradually entered the expansion phase. In the second stage (after 5632 s), the zirconium metal reacts with the solution at the destruction of the oxide film to cause activation-passivation of the galvanic cell reaction, the metal begins to dissolve, hydrogen bubbles continuously evolve on the metal surface, and the electrochemical reaction begins to enter the active state. As the metal dissolves, the number of hydrogen bubbles increases, and the activity and hit of the corresponding AE signals also increase. The signal at this

Table 22.2 AE characteristic parameters distribution

Stage	Channel	Amplitude	Count	Rise time	Duration	Energy	Hit number
First stage	1	40–55	1–6	0–1179	0–1647	0–4	111
	2	40–58	1–30	0–779	0–1662	0–24	100
Second stage	1	40–56	1–42	0–1115	0–1835	0–8	232
	2	40–51	1–85	0–1999	0–2000	0–18	8914
Total	1	40–56	1–42	0–1179	0–1835	0–8	343
	2	40–58	1–85	0–1999	0–2000	0–24	9014

stage has a large activity, a large number of hits and small amplitude, while the duration, rise time, count, and energy are relatively high. Compared with the first stage, the activity and quantity of the second stage AE signal increase significantly, and the characteristics of the signal characteristic parameters are significantly different, indicating that the AE source should be different from the first stage.

Many literatures have reported that there is a silent period in the early stage of pitting corrosion of stainless steel and other materials [1, 2], that is, there is no phenomenon that AE signals occur for a period of time. This phenomenon did not appear in this test. Xu Jian believes that the silent period phenomenon reported in the above literature is mainly caused by the application of constant electromotive force method or moving current to control the electrochemical process during the experiment, and the corrosion potential does not reach the pitting potential [3]. In this test, the test corrosion system is an open circuit system, and the corrosion potential may be higher than the zirconium corrosion potential. The sample is immersed in the solution and pitting corrosion occurs very quickly, so no silent period occurs. If the passivation film failure reaction does not produce AE at the initial stage of metal pitting, the zirconium metal surface passivation film is more tightly bonded than the stainless steel material, and the passivation film destruction process time should be longer, and a longer silent period should occur. There was no silent period in this test, indicating that the passivation film destruction process did not occur during the silent period reported in the above literature.

In addition, there are significant differences in the signal activity and characteristic parameter distribution of the two channels during the pitting monitoring process, which is mainly caused by the difference in frequency response characteristics of different types of sensors. The 1-channel R15α sensor responds to the frequency band 50–200 kHz, and the 2-channel R6α sensor response band is 35–100 kHz. Resonant sensors with different frequency response characteristics are equivalent to different frequency band signal filters, and only the signals in the sensor response band are collected. The difference between the two channels of the collected signals in the experiment indicates that there are differences in the frequency distribution of the AE signals during the pitting process. In the first stage, the signal activity and quantity of the two channels are close, indicating that the signal frequency distribution in this stage is equivalent in the low frequency and high frequency range; in the second stage, the number and activity of the 2-channel are significantly higher than the 1-channel. It indicates that the signal frequency band at this stage should be mainly distributed in the low frequency range.

22.3.2 Signal Waveform Analysis

The signal waveform contains more acoustic emission source information than the acoustic emission characteristic parameters. Figure 22.4 shows the typical signal waveforms and their power spectrum distributions collected by two channels at different stages of the pitting process selected in the experiment. As can be seen from the figure, the signal waveforms are all bursty, and the signal frequency is mainly

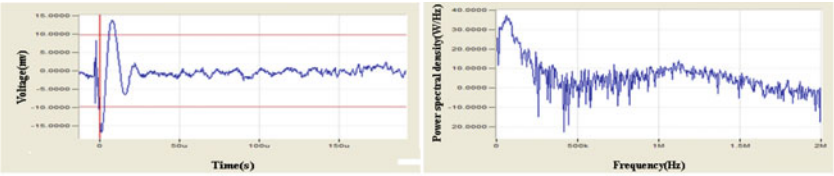

a 1-channel signal in the first stage

b 1-channel power spectrum in the first stage

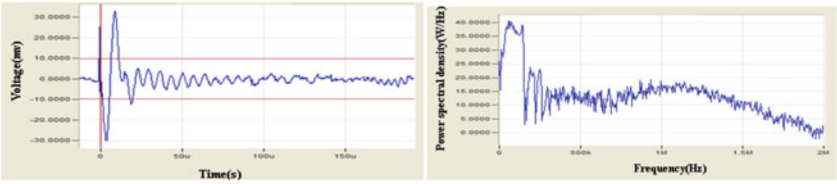

c 2-channel signal in the first stage

d 2-channel power spectrum in the first stage

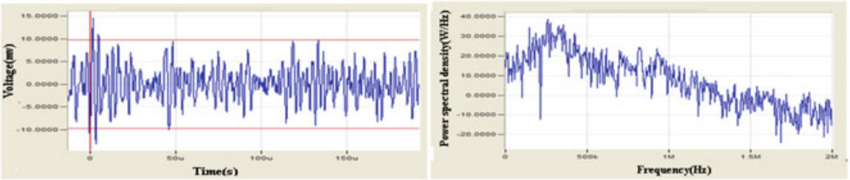

e 1-channel signal in the second stage

f 1-channel power spectrum in the second stage

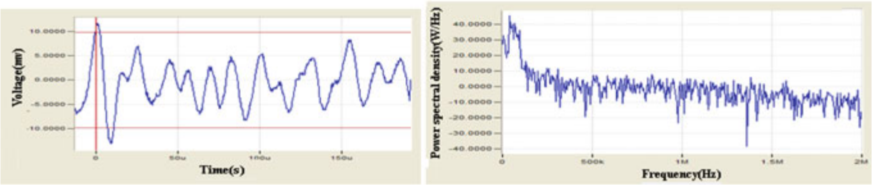

g 2-channel signal in the second stage

h 2-channel power spectrum in the second stage

Fig. 22.4 Typical AE signals and power spectrum of pitting corrosion

distributed between 20 and 500 kHz. Waveforms can be divided into two main types: the first stage signal waveform is a short signal with a short duration. The signal waveforms collected by the two channels are similar, and the peak frequencies are mainly distributed at 50–150 kHz; the second-stage signal waveforms are mainly resonant signals with longer durations. Among them, the peak-to-valley spacing of the 1-channel signal waveform is small, and the peak frequency is mainly distributed at 150–350 kHz. The peak-to-valley spacing of the 2-channel signal waveform is relatively large, accompanied by dispersion phenomenon, and the peak frequency is mainly distributed at 40–100 kHz.

Two types of waveform signals recorded during metal pitting have also been reported in previous studies [2, 5]. Fregonese et al. [2] studied the AE characteristics of 316L stainless steel in 3% NaCl solution, and recorded the short-wavelength and resonance-type waveforms with short duration and resonance waveforms using the R15α type sensor. They are distinguished by characteristic parameter rise time and count, the short signal waveform is corresponding to the formation and expansion of corrosion products on the surface of the sample, and the long-lasting resonance signal corresponds to hydrogen bubble formation and evolution. Two types of sensors were used in this test. The R15α sensor used the 1-channel was of the same type as in [2], and the two types of AE signal waveforms recorded were identical to those reported in the literature. The 2 channel uses R6α type sensor. The waveform recorded in the first stage is consistent with the literature report. There are some differences in the waveform of the second stage, which is mainly caused by the different frequency response characteristics of the sensor. The activity and number of the second-stage signals of the 2-channel are much higher than that of the 1-channel, indicating that the two-stage signal frequency is mainly distributed in the low-frequency response frequency band. In addition, different types of signal waveforms appear in different sequences in the experiment.

To further understand the waveform characteristics, a continuous wavelet is applied to the waveform signal to be transformed and superimposed with the material dispersion curve. The result is shown in Fig. 22.5. It can be seen from the figure that the distribution characteristics of the signal energy in the time domain and the frequency domain are basically consistent with the signal waveform and power spectrum analysis results. It can be seen from the superposition of the dispersion curve and the signal energy that the first-stage signal waveform is mainly expansion wave, the two-stage one-channel signal waveform mode is mainly expansion wave, and the two-channel waveform mode is mainly flexural wave. The wavelet transform result graph and the dispersion curve are not superimposed at the maximum energy of the signal, which may be related to the fact that the rectangular sample size is small and the wave propagation process is greatly affected by the boundary.

Based on modal AE theory and pitting corrosion AE source mechanism [9, 10], thin-plate metal pitting will mainly produce expansion wave and flexural wave. The expansion wave has the characteristics of fast propagation speed, low amplitude and high frequency (>100 kHz); while the flexural wave has slower propagation speed, larger amplitude, lower frequency (<100 kHz) and dispersion phenomenon. Comparing the signal waveforms collected by the two channels and the frequency

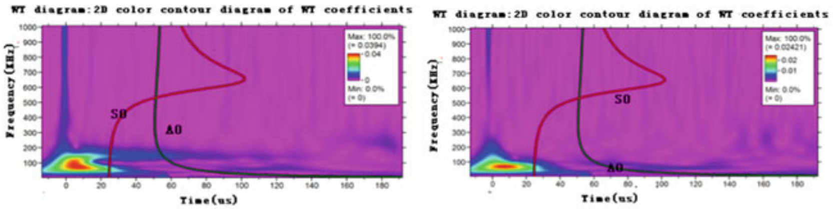

a Wavelet transform of 1-channel signal in the first stage b Wavelet transform of 2-channel signal in the first stage

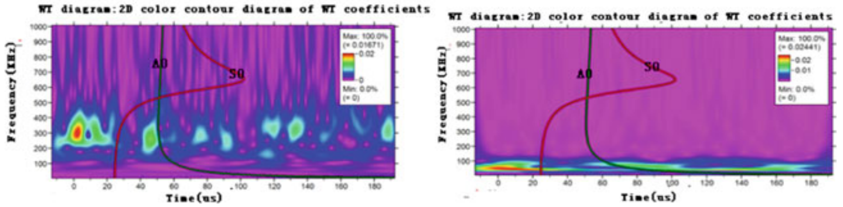

c Wavelet transform of 1-channel signal in the second stage d Wavelet transform of 2-channel signal in the second stage

Fig. 22.5 Wavelet transform and dispersion curve overlay

domain analysis results, it is found that the frequency band distribution of the signals collected by the sensor shows that the signals of the 2-channel are mainly composed of flexural waves, and the signal frequency band distribution is low; the signals of the 1-channel are mainly composed of expansionwave and high frequency. In the first phase of the test, the hit signals number of the 1-channel and the 2-channel is similar, but the number of the 1-channel signals is slightly higher than the 2-channels, and the signal waveform is dominated by expansion waves. In the second phase of the test, the number of the 2-channel signals is much higher than the 1- channel, and the signal waveform is mainly flexural waves.

22.3.3 Observation of Pitting Appearance of Zirconium Metal

After AE monitoring is completed, the sample is taken out and the surface of the immersed solution is observed. The surface of the sample is immersed in the surface of the solution, and the gray pits are densely covered, and the metallic luster has been lost. When the surface of the zirconium metal was magnified 200 times by an optical microscope, the microscopic morphology of the pit was as shown in Fig. 22.6. The macroscopic and microscopic morphology of the sample surface showed that the zirconium metal was pitting corrosion in the ferric chloride solution. In addition, a large amount of hydrogen bubbles were observed on the metal surface during the test. As shown in Fig. 22.7a, bubbles which grew on the surface of the sample observed during the test were observed. At the end of the test, several unbroken bubbles were still attached to the surface after the sample was taken out of the solution, as shown in

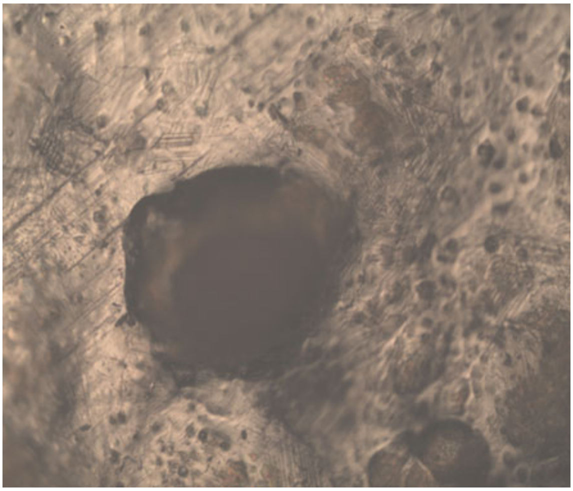

Fig. 22.6 Microscopic morphology of the sample surface

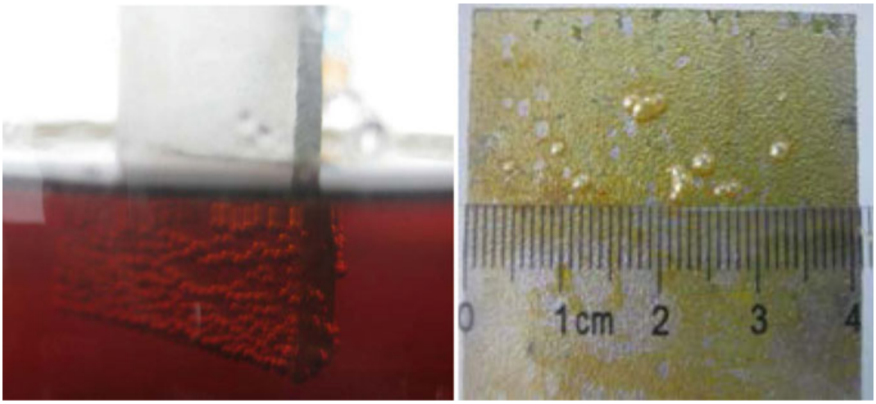

a bubble distribution in the test

b remaining ubble after the test

Fig. 22.7 Bubble distribution on the surface of the sample in the test

Fig. 22.7b. Part of the bubbles have been combined and aggregated, and the average diameter of the individual bubbles is about 0.5–2.0 mm.

Pitting AE source confirmation is an important part of the research on pitting corrosion AE. In the AE technology, the amplitude distribution analysis method is used to distinguish the AE source. $F(V) = (V/V_t)^{-b}$ is a commonly used mathematical model, where $F(V)$ is a normalized cumulative distribution function, indicating the probability that the amplitude of the acoustic emission signal exceeds V, and V_t indicates that the minimum amplitude is detected, b is the index [11]. By fitting calculation, the b values of the first phase and the second phase of the 1-channel are respectively 2.277 and 2.599, and the b values of the first phase and the second phase of the 2-channel are respectively 2.829 and 8.816. It can be seen that the *b* value corresponding to different stages of pitting corrosion is different, especially the difference of b value in the two stages of the 2-channel is large, indicating that the AE signals of different stages of pitting are different in the test.

Since there are few research literatures on zirconium metal pitting AE mornitoring, and there are relatively many researches on stainless steel and aluminum alloy, the test results are compared with the previous pitting corrosion signal characteristics of stainless steel materials. According to previous literature reports [3] pitting AE sources can be roughly divided into two categories: one is the formation and evolution of bubbles that are widely accepted by current researchers. Another type of AE source is considered to be a change in the surface of the material. Such as sample surface transient stress changes, passivation film damage, salt layer crack near the pit corrosion pit. During the test, it was found by observation of the surface of the sample that no visible bubbles existed on the surface of the sample at the initial stage, but AE signal was recorded. With the development of time, it can be observed that small bubbles appear on the surface of the sample and gradually grow and rupture. The rupture is accompanied by the AE hit signal, and some visible bubbles remain on the surface after the sample is taken out. No significant corrosion product accumulation was observed at the corrosion pit of the sample. In addition, the sample was not subjected to pre-strain stretching, and stress release due to dislocation of the metal caused by dissolving of the metal did not occur. Therefore, the passivation film rupture and hydrogen bubble rupture may be the source of AE at different stages during the test.

The membrane rupture process is generally considered to be a failure of the passivation film under the action of chloride ions. Sato [12] pointed out that the film may break into three modes: brittle cracking, plastic slip, plastic flow. In plastic flow, anodization induces sufficient membrane pressure to deform the membrane, and then the membrane begins to rupture, creating many fine pores at the top of the membrane, which are finally arranged into a close-packed model to stabilize the stress release. Similar results were reported by Xu et al. [3] and Jirarungsatian and Prateepasen [4]. It is believed that membrane rupture mainly occurs in the initial stage of passivation or pitting corrosion, the AE activity is low, and the signal amplitude signal is high. In this experiment, the first stage is the initial stage of pitting corrosion. The signal of this stage has a small activity and the higher amplitude is also consistent with the results reported in the literature. Therefore, the first stage of the AE signal source in the test should be the passivation film destruction.

The formation and evolution of hydrogen bubbles is considered by many scholars to be a widely accepted source of AE, but the exact mechanism remains unknown. An important requirement for the bubble to rupture is that the speed of sound must pass through the bubble. According to this theory and the observation of the bubble size, the bubble burst frequency can be calculated. $t = 2\pi R/V$, taking sound velocity $V = 340$ m/s, $R = 0.25-1$ mm, then the sound velocity needs to pass through the whole bubble as $t = 0.0046$–0.01847 µs, and the corresponding frequency is 54–217 kHz. In this test, the frequency distribution range of the second stage signal is basically consistent with the above calculation results. In addition, Fregonese [2, 5] reported that the hydrogen bubble burst AE signal has a longer rise time and a higher count with a longer duration resonant waveform. These characteristics are also consistent with the characteristics of the second phase of the AE signal of this test. In combination with the observation during the test, the AE source corresponding to the second stage AE signal should be bubble rupture.

22.4 Conclusion

1. AE technology has the ability to monitor the corrosion damage of zirconium metal and is a powerful tool for studying pitting corrosion of zirconium metal.
2. The characteristics of AE signals in different stages of pitting corrosion of zirconium metal are quite different, and different damage stages of pitting can be identified according to signal characteristics.
3. Compared with the pitting nucleation stage, the AE signal in the extended stage has large activity, low amplitude, and small counting, energy, rise time and duration.
4. There are two main types of zirconium metal pitting signal waveforms, in which the pitting nucleation stage mainly produces short-wavelengths with small duration, and the pitting extension stage mainly produces resonance waves with longer duration.
5. Zirconium metal pitting signal waveform mode is composed of flexual wave and expansion wave. During the pitting extension phase, the AE signal is dominated by the low-frequency bending mode.
6. Passivation film destruction and hydrogen bubble rupture are the two main AE sources of zirconium metal pitting process.

References

1. K. Darowicki, A. Mirakowski, S. Krakowiak, Investigation of pitting corrosion of stainless steel by means of acoustic emission and potentiodynamic methods. Corros. Sci. **45**, 1747–1756 (2003)
2. M. Fregonese, H. Idrissi, H. Mazille, L. Renaud, Y. Cetre, Initiation and propagation steps in pitting corrosion of austenitic stainless steels: monitoring by acoustic emission. Corros. Sci. **43**, 627–641 (2001)
3. J. Xu, X. Wu, E.-H. Han, Acoustic emission during pitting corrosion of 304 stainless steel. Corros. Sci. **53**, 1537–1546 (2011)
4. C. Jirarungsatian, A. Prateepasen, Pitting and uniform corrosion source recognition using acoustic emission parameters. Corros. Sci. **52**, 187–197 (2010)
5. M. Fregonese, H. Idrissi, H. Mazille, L. Renaud, Y. Cetre. Monitoring pitting corrosion of AISI 316L austenitic stainless steel by acoustic emission technique: choice of representative acoustic parameters. J. Mater. Sci. **36**, 557–563 (2001)
6. D. Changan, W. Wei, Ji. Langqin, Z. Meisheng, Corrosion resistance and application of zirconium in chemical media. Rare Metal Mater. Eng. **2**, 68–73 (1990)

7. L. Kechang, Zinc pitting corrosion. Rare Metal Mater. Eng. 884–885 (1985)
8. K. Ye, *Introduction to Metal Corrosion and Protection*, 3rd edn. (Higher Education Press, Beijing, 1980), pp. 105–106
9. G. Rongsheng, F. Gangqiang, Study on the mechanism of acoustic emission source in metal pitting process. Acta Acoust. Sinica **27**(4), 369–372 (2002)
10. Z. Rongsheng, S. Gongtian, L. Shifeng, Basic theory of modal acoustic emission. Non-Destr. Test. **24**(7), 302–306 (2002)
11. A. Pollock, International advances in nondestructive testing **7**, 215 (1981)
12. N. Sato, A theory for breakdown of anodic oxide films on metals. Electrochim. Acta **16**, 1683–1692 (1971)

Chapter 23
Acoustic Emission in Coatings—A Review

Yachen Zhang, Jia Meng, Liang Wang, and Lixin Song

Abstract Coating is fabricated on the substrate to protect the entire material. The failure of coatings can cause damage to material or structure. Acoustic emission (AE), as a non-destructive testing technology, can be used to get mechanical parameters and clarify the failure mechanisms. In this paper, metal coatings, ceramic coatings and thermal barrier coatings were taken as examples to introduce the research progress, existing problems and application prospects of acoustic emission technology on coatings.

23.1 Introduction

With the development of science and technology, people's requirements for the use of materials continue to increase. For general materials, it is often difficult to satisfy multiple conditions. The emergence of composite materials and coatings solved this

---

Funded by Advanced Space Propulsion Laboratory of BICE and Beijing Engineering Research Center of Efficient and Green Aerospace Propulsion Technology, No: LabASP-2018-08.

Y. Zhang · J. Meng (✉) · L. Song
Key Laboratory of Inorganic Coating Materials CAS, Shanghai Institute of Ceramics, Chinese Academy of Sciences, Shanghai 201899, China
e-mail: jiameng@mail.sic.ac.cn

Y. Zhang
e-mail: zhangych2@shanghaitech.edu.cn

L. Song
e-mail: lxsong@mail.sic.ac.cn

Y. Zhang
School of Physical Science and Technology (SPST), ShanghaiTech University, Shanghai 201210, China

L. Wang
Integrated Computational Materials Research Centre, Shanghai Institute of Ceramics, Chinese Academy of Sciences, Shanghai 201899, China
e-mail: L.Wang@mail.sic.ac.cn

© The Author(s), under exclusive license to Springer Nature Singapore Pte Ltd. 2021

G. Shen et al. (eds.), *Advances in Acoustic Emission Technology*, Springer Proceedings in Physics 259, https://doi.org/10.1007/978-981-15-9837-1_23

problem. Coatings are used in a wide range of applications especially in defense, machinery, and biology. As a material to protect the substrate, once the coating fails, the substrate will soon be ruined. In coatings, stress causes the initiation, propagation and spallation of cracks, which is the main inducement of coating failure. In the past, many research methods on the failure mechanism of coatings used time-sampling methods, which means take out a sample at regular intervals in a test. However, accidental introduction of new cracks and further expansion of original cracks during sampling make the results unreliable.

Acoustic emission (AE) is a type of non-destructive testing technology with a wide range of uses, which has made many contributions to the development of industrial manufacturing, petrochemical and aerospace since the birth of this technology. The distinguishing features of this method include dynamic, passive, and in-situ monitoring, which make it can reflect some physical damage of materials or parts in order to judge the internal state of them and even predict their life [1–5]. AE can be a suitable tool to detect the occurrence, development, and failure of cracks, which could help us study the failure process of coatings. Among a series of coatings, metal coatings, ceramic coatings and thermal barrier coatings have been thoroughly studied by AE. A large number of studies have shown that AE has great potential in the study of coating failure process. This article summarized some of the current status, existing problems and application prospects.

23.2 Metallic Coatings

Metallic coatings refer to the coatings of metal or alloy on the surface of the product by spraying, electroplating and other methods, which play a role of wear resistance and corrosion resistance.

Zhang et al. [6–10] used AE to systematically study the fatigue failure process of supersonic sprayed iron-based alloy coatings. The abrupt changes in the energy, amplitude and RMS (root mean square) of the acoustic emission signal were regarded as the basis for judging the critical failure state of the coating. According to the trend of the parameters and SEM photos of cross section, the entire failure process was divided into four stages: crack initiation, stable crack propagation, crack instability propagation, and spalling. A clear acoustic emission signal of fatigue damage was obtained by Empirical Mode Decomposition (EMD) and wavelet analysis. By changing the magnitude of contact stress, it was found that the amplitude of the acoustic emission signal has nothing to do with the magnitude of stress, but only with the failure mode. When the value of contact stress was low, pitting effect was likely to occur, and the amplitude of acoustic emission signal was also small; when the number was higher, spalling failure occurred, and the amplitude of AE signal was higher too; When the contact stress continued to increase, stratification failure occurred, and the amplitude of AE signal was at the same level as that of spalling failure.

Wang et al. [11] introduced acoustic emission technology into the microhardness indentation method when evaluating the toughness of the nickel-based alloy coating which was made by the vacuum melting method. The slope of accumulated energy counts (En) versus the load (P) was used as a parameter for qualitative determination of toughness. The larger the slope of the En-P straight line, the worse the toughness of the coating.

Sause et al. [12] conducted four-point bending experiments on nickel-copper-coated CFRP (carbon-fiber reinforced plastic). The process was divided into three stages: crack initiation, crack propagation and stratification by the combination of pattern recognition techniques and power spectrum analysis. RMS and acoustic emission localization can accurately distinguish the failure of coating and plastic substrate. The combination of pattern recognition technology and power spectrum analysis may be a powerful tool for identifying failure mechanisms in mixed materials, and AE analysis can often be used as an important tool for health monitoring and quality assurance of mixed materials.

Yang et al. [13] used AE technology as an auxiliary tool to judge the time point of coating crack initiation and matrix plastic deformation, and more accurately tested the fracture toughness of the material, when measuring the fracture toughness of chromium coating.

Gallego et al. [14] also used this technique to study the bonding strength of galvanized steel. When testing the mechanical properties of materials, AE is often used as an indicator of different deformations or failure stages. Since it can often detect the changes in materials earlier, more accurate values can be obtained.

To sum up, in the study of metal coatings, the role played by AE can be roughly classified into three. First, it can be used as an auxiliary tool to indicate the time points of deformation or failure when evaluating the mechanical properties. Second, the energy of AE signal was directly used as a parameter to evaluate the properties. Third, the whole failure process was segmented by the signal processing tool, and then with the help of SEM, the failure process of the coating was revealed.

23.3 Ceramic Coatings

Ceramic coatings, which are made by in-situ reaction, vapor deposition and other methods, are widely used because of its characteristics of wear resistance, corrosion resistance, anti-adhesion, high hardness and high temperature resistance.

Song et al. [15] evaluated the bonding strength of the coating by means of pressing experiment combined with AE technology. According to the time distribution curve of characteristic parameters such as energy, RMS, counts and amplitude of the signal, it can be found that energy was more sensitive to the failure of the coating, which was most suitable for evaluating the bonding strength of the coating. The trend of amplitude with time can better reflect the crack propagation process in the ceramic coatings.

Gong et al. [16] evaluated the mechanical properties of alumina coatings by tensile test. By analyzing the amplitude, energy, counts, the impact rate and the frequency domain waveform, the process of crack initiation and propagation in the coating during was pointed out. Meanwhile, the calculation method of mechanical parameters such as the strength in the coating layer and the bonding strength of the coating was given.

Watanabi et al. [17] studied the failure process of plasma sprayed alumina coatings under thermal cycling. The temperature range of the thermal cycle was from room temperature to 1000 °C, which was well beyond the use of AE probes. The introduction of laser technology solved this problem. Correspondingly, the surface velocity became the parameter to determine the fracture mode and the location of each AE events.

In summary, in the study of ceramic coatings, AE played a similar role in the study of metal coatings, including the determination of mechanical properties and the analysis of failure processes. In addition, because of that ceramic coatings are more likely used in high temperature, the use of laser technology is necessary to widened the temperature range of AE.

Because of the great difference in thermal expansion coefficient between metal and ceramic, ceramic coatings are easy to peel off under high temperature working environment. In high temperature applications, a metal transition layer is added between the ceramic and the metal. This special ceramic coatings are called thermal barrier coatings.

23.4 Thermal Barrier Coatings

Thermal barrier coatings (TBCs) are widely used in aerospace turbine engines for their outstanding performance in thermal, abrasion and corrosion resistance. However, the actual service environment of the thermal barrier coatings is awfully harsh, and its own structure is complicated, which causes the thermal barrier coating system to be prone to surface cracking and interface separation, and eventually lead to peeling failure of the coating [18]. Figure 23.1a shows a typical thermal barrier coating structure, which consists of three parts: a top ceramic coat (TC), bond coat (BC) and a substrate. Figure 23.1b shows that after undergoing a high temperature

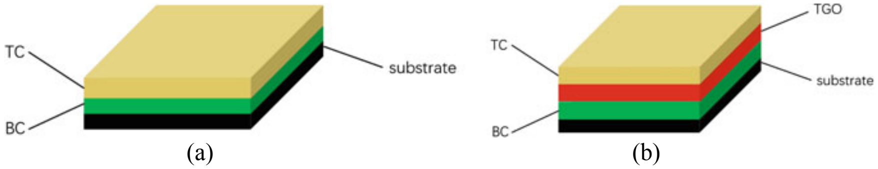

(a) (b)

Fig. 23.1 Typical structure of TBC before **a** and after **b** oxidation

oxidation process, a new layer of thermally grown oxide (TGO) will appear between TC and BC.

23.4.1 The Influence of Test Condition

A lot of studies have been done to explore the correlation between crack behaviors and AE signals. Tensile, compression, 3-point-bending, 4-point bending and thermal cycling were common test methods, especially tensile test.

Yao et al. [19] used the events and amplitude of the acoustic emission signal to divide the entire stretching process into five stages. According to the characteristics of the signals in the frequency domain, the signals were divided into three types, which are the substrate deformation signal, the surface vertical crack signal and the interface crack signal. The signals began with substrate deformation, then the surface vertical crack joined in, and finally interface crack, delamination came up. The quantitative relationship between the number of AE events and the interface crack size can be given with the help of a mechanical model.

Yang et al. [20–23] studied the failure process of thermal barrier coatings under many different external loads. In their study, the crack propagation process in *thermal cycle* was divided into three parts. At first, vertical cracks appeared on the surface of the TC layer, and then developed to the interface. At the same time, horizontal cracks also appeared at the interface. Finally, the interface cracks connected with each other led to the coating falling off. The quantitative parameters of surface crack length and interface crack length calculated from thermal stress and residual stress were in good agreement with the number of AE events. The life prediction was also consistent with the experimental results.

In the *three-point bending test*, surface crack and interface crack were dominant in the yield stage and plastic deformation stage, respectively. And the order and development of cracks was similar to that in thermal cycle.

As for *compress* load, the most prominent difference was the type of signal. There were two kinds of interface cracks. The one was caused by compress named opening interface cracks, and the other was caused by shear named sliding interface cracks. Only thermal change and compress load can lead to the former.

As the most dangerous failure mode for TBC, *molten calcium-magnesium-alumino-silicate* (CMAS) corrosion experiments was monitored by AE with the help of wave guide. Four kinds of signals were obtained by wavelet analysis, namely surface vertical crack, sliding interface crack opening interface crack and substrate deformation. Two types of interface crack predominated in the failure process, which was the cause of coating spallation.

It was worth noting that even if the external loads causing the coating failure were different, the crack types were similar and the frequencies of the acoustic emission signals were approximately the same. Figure 23.2 showed the 4 types of signals. Surface vertical crack was led by tensile stress in the TC, which existed earliest and generally in almost all failure processes. The Sliding interface crack was caused

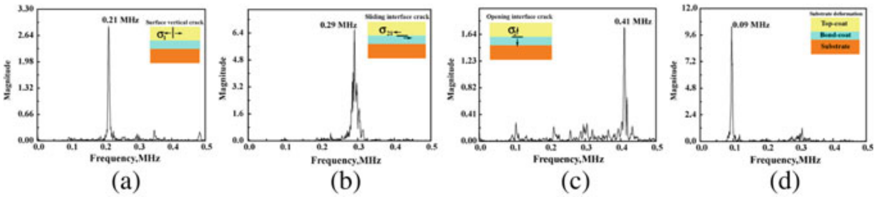

(a) (b) (c) (d)

Fig. 23.2 Typical frequency spectrum of the AE signal from **a** surface vertical crack **b** sliding interface crack **c** opening interface crack **d** substrate deformation [23]

sliding of the TC and BC due to the shear stress. Another interface crack was the opening interface crack. It was a horizontal crack that occurred at the interface due to tensile stress. Depending on the external force, the type of interface crack was different.

23.4.2 The Influence of Structure

It was mentioned above that in the thermal oxidation environment, the appearance of TGO would change the structure of TBC. Changes in structure can lead to different failure processes.

Park et al. [24] conducted a four-point bending experiment on TBC with different cycle times. The parameters of acoustic emission signals were analyzed. It was found that the number of thermal cycles was positively correlated with the number of events, while it was negatively correlated with amplitude, cumulative counts, cumulative energy, and mechanical strength. The AE signals of TBC which had exposed to oxidative environments for a long time in 4-point bending test can be classified into three categories in the frequency domain.

Li et al. [25] studied the Vickers-hardness of TBC before and after oxidation, it was shown that the appearance of TGO reduced the strength of the coatings and accelerated the destruction of it. Cluster analysis and wavelet were used and got the same result that there were 3 types of the signals.

The failure process under 3-point-bending test was different between TBC with and without TGO. Figure 23.3 showed the specific course. The failure began in TC. A surface vertical crack existed in TC at first, followed by many same cracks. With the conjunction of surface cracks, interface crack appeared. Finally, after the interface cracks elongated and merged, coatings failed down. Compared with Fig. 23.3a, b showed that when TGO was present, only one single vertical crack and one single interface crack appeared throughout the failure. It was worth caring that the external stress after oxidation is also at a low level.

Except for TGO, different substrates would also get different signals.

Wang et al. [26] performed 3-ponit bending tests on superalloy/BC/YSZ and stainless steel/BC/YSZ. The AE signals were distinguished easily. Figures 23.4, 23.5

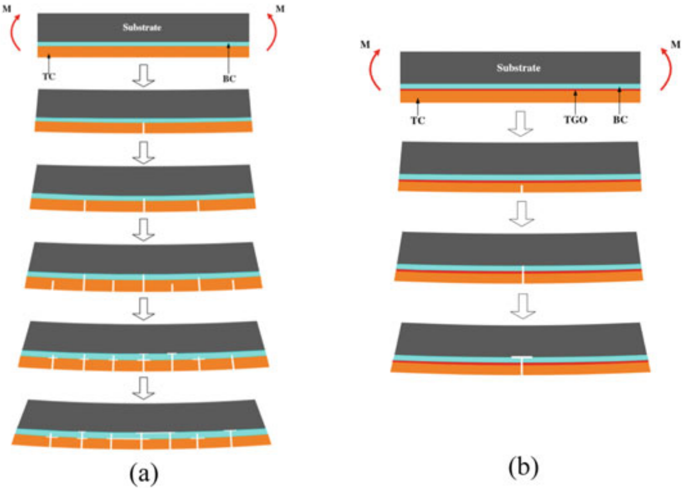

Fig. 23.3 Illustration of the failure process, of the **a** as-sprayed TBCs **b** pre-oxidized TBCs under three-point bending test [21]

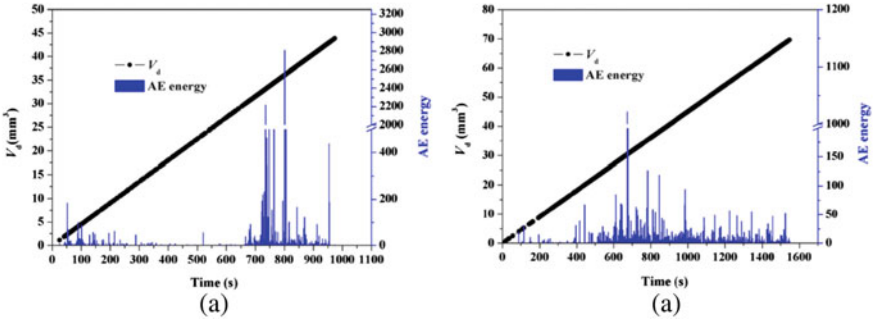

Fig. 23.4 Plot of deformed volume and AE energy as the function of loading time. **a** Superalloy/BC/YSZ. **b** stainless steel/BC/YSZ [26]

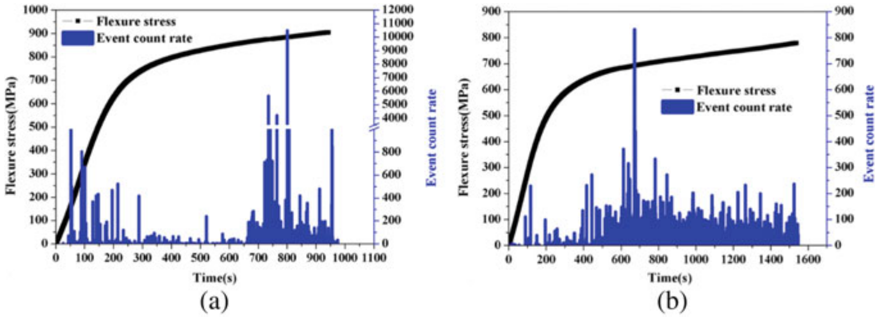

Fig. 23.5 Typical AE signal which corresponds to the plot of flexure stress versus time for the four coating systems. **a** Superalloy/BC/YSZ. **b** Stainless steel/BC/YSZ [26]

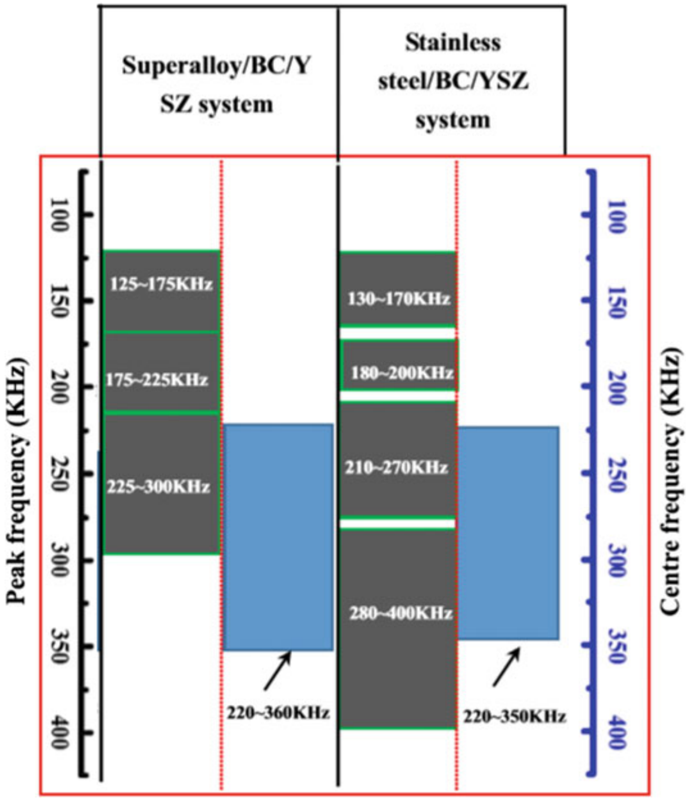

Fig. 23.6 Distribution of peak frequency and center frequency for the two coating systems [26]

and 23.6 illustrated the differences in energy, event count rate and peak frequency distribution, respectively. Because of the better deformation ability of stainless steel, the signal has lower energy, lower event count rate, and different distribution of frequency, compared with superalloy substrate.

23.4.3 AE Combined with Other Tools

Methods such as DIC (Digital image correlation) were also used as evidence in the study of the destruction process of coating materials.

Finite element analysis is a commonly used mechanical analysis tool. The residual stress obtained by finite element analysis can be used to obtain the location of the earliest failure from the perspective of mechanics. Moreover, the internal stress in different failure stages is also very helpful to judge the failure process [27].

Infrared imaging technology can be used to study the thermal barrier coating failure process in thermal cycling experiments, and successfully located defects by using heat flow distribution and acoustic emission signals [28].

Digital image correlation method which is as a tool can reflect material strain in real time. When it combined with acoustic emission, it can help study the coating damage process by displaying the deformation of materials in real time [26].

Since the conditions of use of the acoustic emission probe are limited, in some cases it is necessary to modify the experimental device. Testing at high temperatures requires a rod named wave guide, which can conduct AE signals. For ultra-high temperature conditions, for example during air plasma sprayed (APS), a non-contact laser AE instrument is needed [29].

23.5 Conclusion

Some progress has been made in mechanical property evaluation and failure process analysis. However, the current research was still in the preliminary stage, and there were still some problems to be solved.

1. The study on the failure process of coatings was incomplete and has no theoretical guidance.
2. Time-sharing sampling was still used to verify the acoustic emission results in most experiments, and the conclusions obtained from time-sharing sampling were not reliable.
3. At high temperatures, using a wave guide or laser AE may cause signal distortion.

Although there were still many technical challenges, AE still showed great vitality in coating research. From the analysis of single feature parameters to frequency domain analysis and wavelet analysis, with the development of signal processing technology, technologies such as artificial neural networks have begun to be applied to acoustic emission signal analysis [30, 31]. Technological innovations have injected new life into the acoustic emission studies of coatings. The development of coatings application and development will promote research on it as well.

Acknowledgements This paper was funded by Advanced Space Propulsion Laboratory of BICE and Beijing Engineering Research Center of Efficient and Green Aerospace Propulsion Technology, No: LabASP-2018-08.

References

1. N.J. Yang, C.J. Yao, X.J. Yuan, X.H. Long, *Material damage monitoring technology based on acoustic emission*, 1st ed., vol. 1 (Beihang University Press, Beijing, pp. 3–6, 2016)

2. F. Zhen, Simple talk about the forecast theory about coating's life. Coat. Paint. Electroplat. **1**, 3–5 (2005)
3. K. Ito, H. Kuriki, H. Araki, S. Kuroda, M. Enoki, Evaluation of generation mechanism of vertical cracks in top coat of TBCs during APS deposition by laser AE method. J. Therm. Spray Technol. **24**(5), 848–856 (2015)
4. F.H. Wang, H. Lou, S. Zhu, W. Wu, The mechanism of scale adhesion on sputtered microcrystallized CoCrAl films. Oxidat. Metals 39–50 (1996)
5. J. Valli, U. Mäkelä, A. Matthews, V. Murawa, TiN coating adhesion studies using the scratch test method. J. Vacuum Sci. Technol. A Vacuum Surf. Films 2411–2414 (1985)
6. H.D. Wang, Z.Q. Zhang, G.L. Wang, B.S. Xu, Z.Y. Piao, Investigation of contact fatigue failure mode and mechanism of plasma spraying coating. Tribology 251–257 (2012)
7. Z.Q. Zhang, G.L. Li, H.D. Wang, B.S. Xu, Z.Y. Piao, Acoustic emission wavelet analysis of coating during contact fatigue damage process. J. Mater. Eng. 48–53 (2012)
8. Z.Q. Zhang, G.L. Li, , H.D. Wang, B.S. Xu, Z.Y. Piao, Study on the microstructure and property of contact fatigue damage of plasma-sprayed Fe-based alloy coating. J. Mater. Eng. 59–62 (2012)
9. Z.Q. Zhang, G.L. Li, H.D. Wang, B.S. Xu, Z.Y. Piao, Monitoring fatigue wear of the coating based on acoustic emission. Tribology 89–95 (2012)
10. Z.Y. Piao, B.S. Xu, H.D. Wang, Behavior of rolling contact fatigue crack of plasma sprayed Fe-based coating. Tribology 56–60 (2011)
11. J.Y. Wang, Q.Z. Yang, X.H. Ni, Y. Shi, X.K. Du, The study of tenacity of Ni-based alloy composite coating using AE technology and micro-hardness method. New Technol. New Process 45–46 (2002)
12. M.G. Sause, D. Schultheiß, S. Horn, Acoustic emission investigation of coating fracture and delamination in hybrid carbon fiber reinforced plastic structures. J. Acoust. Emiss 1–13 (2008)
13. B.Q. Yang, K.Zhang, G.N. Chen, G.X. Luo, J.H. Xiao, An acoustic emission-based uniaxial tensile test method for evaluation of fracture toughness of a coating on its substrate. Acta Armamentarii 9 (2008)
14. A. Gallego, J.F. Gil, J.M. Vico, J.E. Ruzzante, R. Piotrkowski, Coating adherence in galvanized steel assessed by acoustic emission wavelet analysis. Scripta Materialia 1069–1074 (2005)
15. Y.N. Song, B.S. Xu, H.D. Wang, M. Liu, L.N. Zhu, Failure process analysis of plasma sprayed coatings under tip load based on acoustic emission signals. Surf. Eng. 675–682 (2014)
16. M.F. Gong, S.R. Qiao, H. Ji, C.Y. Zhang, D. Han, Acoustic emission testing of mechanical properties of electroplated-alumina coating. Nondestruct. Test. 22 (2008)
17. M. Watanabe, M. Enoki, T. Kishi, Fracture behavior of ceramic coatings during thermal cycling evaluated by acoustic emission method using laser interferometers. Mater. Sci. Eng. A 368–374 (2003)
18. R.A. Miller, Thermal barrier coatings for aircraft engines: history and directions. J. Thermal Spray Technol. 35–42 (1997)
19. W.B. Yao, C.Y. Dai, W.G. Mao, C.Lu, L. Yang, Y.C. Zhou, Acoustic emission analysis on tensile failure of air plasma-sprayed thermal barrier coatings. Surf. Coat. Technol. 3803–3807 (2012)
20. L. Yang, Y.C. Zhou, C.S. Lu, Damage evolution and rupture time prediction in thermal barrier coatings subjected to cyclic heating and cooling: an acoustic emission method. Acta Materialia 6519–6529 (2011)
21. L. Yang, Z.C. Zhong, J. You, Q.M. Zhang, Y.C. Zhou, W.Z. Tang, Acoustic emission evaluation of fracture characteristics in thermal barrier coatings under bending. Surf. Coat. Technol. 710–718 (2013)
22. L. Yang, Z.C. Zhong, Y.C. Zhou, W. Zhu, Z.B. Zhang, C.Y. Cai, C.S. Lu, Acoustic emission assessment of interface cracking in thermal barrier coatings. Acta Mechanica Sinica 342–348 (2016)
23. L. Yang, T.T. Yang, Y.C. Zhou, Y.G. Wei, R.T. Wu, N.G. Wang, Acoustic emission monitoring and damage mode discrimination of APS thermal barrier coatings under high temperature CMAS corrosion. Surf. Coat. Technol. 272–282 (2016)

24. J.H. Park, J.S. Kim, K.H. Lee, Acoustic emission characteristics for diagnosis of TBC damaged by high-temperature thermal fatigue. J. Mater. Process. Technol. 537–541 (2007)
25. C.C. Li, X. Qiao, T. Wang, W. Weng, Q. Li, Damage evolution and failure mechanism of thermal barrier coatings under Vickers indentation by using acoustic emission technique. Prog. Nat. Sci. Mater. Int. 90–96 (2018)
26. L. Wang, J.X. Ni, F. Shao, J.S. Yang, X.H. Zhong, H.Y. Zhao, D.Y. Li, Failure behavior of plasma-sprayed yttria-stabilized zirconia thermal barrier coatings under three-point bending test via acoustic emission technique. J. Therm. Spray Technol. 116–131 (2017)
27. L. Wang, C. Ming, X.H. Zhong, J.X. Ni, S.Y. Tao, F.F. Zhou, Y. Wang, Prediction of critical rupture of plasma-sprayed yttria stabilized zirconia thermal barrier coatings under burner rig test via finite element simulation and in-situ acoustic emission technique. Surf. Coat. Technol. 58–74 (2019)
28. D. Nies, B. Rehmer, B. Skrotzki, R. Vaßen, Damage characterization of thermal barrier coatings by acoustic emission and thermography. Adv. Eng. Mater. 790–794 (2012)
29. K. Ito, H. Kuriki, H. Araki, S. Kuroda, M. Enoki, Detection of segmentation cracks in top coat of thermal barrier coatings during plasma spraying by non-contact acoustic emission method. Sci. Technol. Adv. Mater. 035007 (2014)
30. S. M. Jafari, H. Mehdigholi, M. Behzad, Valve fault diagnosis in internal combustion engines using acoustic emission and artificial neural network. Shock Vibr. 1–9 (2014)
31. P. Ramasamy, S. Sampathkumar, Prediction of impact damage tolerance of drop impacted WGFRP composite by artificial neural network using acoustic emission parameters. Compos. Part B Eng. 457–462 (2014)

Chapter 24
Experiment Research on Tensile Process of Type IV Gas Cylinder Liner-HDPE Based on Acoustic Emission

Yilin Yuan, Gongtian Shen, Junjiao Zhang, Bo Zhao, Yongna Shen, and Ke Bo

Abstract The high-density polyethylene material (HDPE) of the plastic liner composite material full-wound gas cylinder (type IV gas cylinder) is made into three types of tensile samples, sample with no pre-defects and V-shaped notch sample and sample with preset round notch. Tensile tests were carried out on the three samples, and the tensile process was monitored by acoustic emission method to obtain the mechanical properties and acoustic emission signal characteristics of HDPE tensile damage. The research shows that when detecting and monitoring the acoustic emission of the plastic liner, the VS150 sensor can be selected with the amplitude and energy values as the characteristic parameters, and the acoustic emission signals at different stages of the tensile process are correlated with the structural changes inside the HDPE material molecules. The results of the study provide a basis for the fatigue monitoring of Type IV gas cylinder acoustic emission.

24.1 Introduction

Plastic liner composite material full-wound gas cylinder (type IV gas cylinder) appears as a new type of Compressed Natural Gas (CNG) gas cylinder due to its advantages of light weight, high strength, fatigue resistance and corrosion resistance. The bottle belongs to a high-pressure container for storing flammable and explosive media. The general design pressure is mostly 20 MPa, which is highly dangerous, and its explosion will cause casualties and property losses [1]. Due to the immature manufacturing process, an explosion occurred during the application of the Type IV gas cylinder. The Type IV gas cylinder was previously ordered to stop using and became a shortage in the production of domestic gas cylinders [2]. Therefore, the research on the safety technology of Type IV gas cylinder gave great significance to gain a place in the competition of CNG automobile market.

The structure of CNG gas cylinders mainly includes a fiber reinforced layer, an inner liner and an outer protective layer. At present, the non-destructive testing

---

Y. Yuan · G. Shen (✉) · J. Zhang · B. Zhao · Y. Shen · K. Bo
China Special Equipment Inspection and Research Institute, Beijing 100029, China
e-mail: shengongtian@csei.org.cn

© The Author(s), under exclusive license to Springer Nature Singapore Pte Ltd. 2021

G. Shen et al. (eds.), *Advances in Acoustic Emission Technology*, Springer Proceedings in Physics 259, https://doi.org/10.1007/978-981-15-9837-1_24

methods for composite material gas cylinders mainly include visual inspection, radiographic inspection, and ultrasonic inspection. Among them, visual inspection mainly performs visual inspection on the surface of the winding layer and the liner. Radiographic and ultrasonic inspections mainly detect the inside of the fiber layer and the adhesive layer of the liner [3]. In view of the relatively few domestic applications of Type IV gas cylinders, research on Type IV cylinders has focused on the design and numerical simulation of gas cylinder structures [1, 2, 4–8]. Abroad, represented by the United States, conducted acoustic emission testing research on fiber-reinforced composite materials, and successively formulated acoustic emission testing methods for composite pressure vessels, storage tanks, and pipelines, and included them in ASME standards [9], but no evaluation basis was given. In order to locate the damage source of composite materials, some researches have been done on the modal acoustic emission of composite materials at home and abroad. Since a large amount of data needs to be classified or clustered, the research mainly focuses on algorithms [10–20].

The above-mentioned conventional non-destructive testing methods for composite gas cylinders cannot dynamically monitor and evaluate the internal defects of the gas cylinders. Since modal acoustic emission can be used to identify material damage and distinguish the signal waveforms of fiber breakage and delamination, the IV gas cylinder can be monitored by acoustic emission detection method. However, the collected signal cannot be judged whether it is from fiber rupture, matrix cracking or liner rupture, and the fiber layer and liner signals need to be studied separately. In view of the fact that the glass fiber tensile test research is very mature, and the ASME standard also sets acoustic emission as one of the methods for detecting glass fiber vessel, and the acoustic emission characteristics of liner high-density polyethylene (HDPE) have not been reported. Therefore, this article takes HDPE material as the object, conducts a tensile test, and monitors the acoustic emission during the tensile process, so as to obtain the characteristics of the acoustic emission signal of the HDPE material of the liner of the type IV gas cylinders. To lay the foundation for the future research of acoustic emission detection and monitoring of Type IV gas cylinders.

24.2 Test Materials and Methods

Figure 24.1 is a typical plastic liner composite full-wound gas cylinder (type IV gas cylinder). The gas cylinder has a nominal working pressure of 2.1 MPa, a hydrostatic test pressure of 3.2 MPa, and a minimum design burst pressure of 8 Mpa. Diameter 293 mm, body length 385 mm, nominal volume 18.0 L, winding layer thickness 3 mm, gas cylinders thread PZ27.8, liner material HDPE, liner blow molding, as shown in Fig. 24.2, the liner design wall thickness 2.5 mm, liner outside Diameter 286 mm.

The HDPE material tensile process acoustic emission detection test system is shown in Fig. 24.3, which is composed of the tensile sample, tensile testing machine,

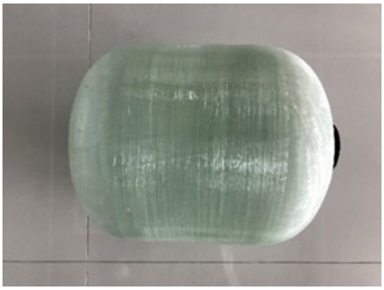

Fig. 24.1 Type IV gas cylinder

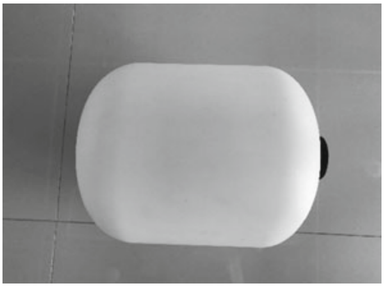

Fig. 24.2 High-density polyethylene liner

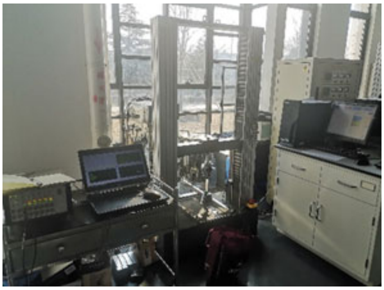

Fig. 24.3 Test system

acoustic emission sensor, and the acoustic emission detection device including a hardware system and a software system. The mechanical properties of HDPE materials are shown in Table 24.1 [21].

In this experiment, three different samples were monitored for acoustic emission during the tensile process, as shown in Figs. 24.4, 24.5 and 24.6. Sample A is a sample without pre-defects, the deformable part is the parallel segment of the sample 80 × 25 × 2.2 mm, B is the preset round notch sample, and the deformable part is the

Table 24.1 The mechanical properties of HDPE materials

Tensile strength/MPa	Elongation at break/%	Shore hardness	Maximum use temperature
≥18.5	≥100%	60–70	110–130

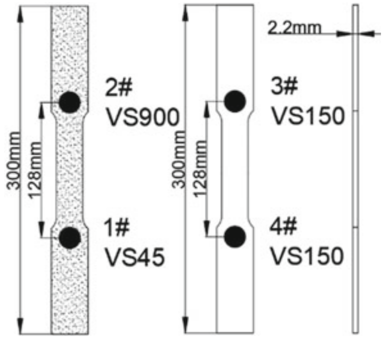
300mm
128mm
2#
VS900
1#
VS45
300mm
128mm
3#
VS150
4#
VS150
2.2mm

Fig. 24.4 Sample without pre-defects (A)

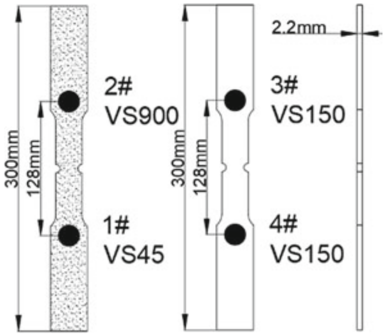
300mm
128mm
2#
VS900
1#
VS45
300mm
128mm
3#
VS150
4#
VS150
2.2mm

Fig. 24.5 Preset round notch sample (B)

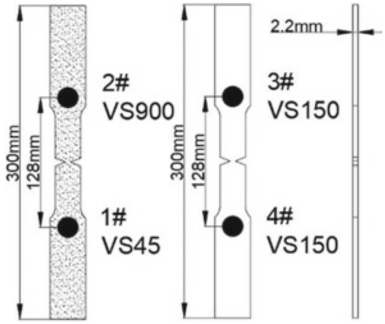
300mm
128mm
2#
VS900
1#
VS45
300mm
128mm
3#
VS150
4#
VS150
2.2mm

Fig. 24.6 Preset V-shaped notch sample (C)

circular notch segment 8 × 17 × 2.2 mm, C is the preset V-shaped notch sample, and the deformable part is 2 × 2 × 2.2 mm of V-shaped connecting segment.

The acoustic emission detector use the AMSY6 acoustic emission detection system of Vallen Company in Germany. It uses two VS150-M resonant sensors with a peak response frequency of 150 kHz (operating frequency range of 100–450 kHz) and one VS45-H broadband sensor (operating frequency range of 20–450 kHz), a VS900-M wideband sensor (working range 100–900 kHz) collects the signal, and the signal is amplified by a preamplifier with a 20–1000 kHz band-pass filter, the gain

Table 24.2 Acoustic emission acquisition parameter settings

Threshold value (dB)	Sampling points	Sampling rate (MHz)	Pre-sampling pre-trigger	Duration identification time (μs)
40	1024	2.5	200	400

is set to 34 dB. The sensor layout is shown in Figs. 24.4, 24.5 and 24.6, where the VS45 and VS900 sensors are fixed on one side of the sample, connected to channels 1 and 2 of the system, and the two VS150 sensors are fixed on the other side of the sample and connected to channels 3 and 4 of the system. The sensor and the sample are coupled by grease and fixed by adhesive tape. Acoustic emission acquisition parameter settings are shown in Table 24.2.

The E45.305-30t universal testing machine is used for the tensile test. The maximum tensile load of the equipment is 300 kN. In the test, the three types of tensile samples were stretched at a constant rate of 4 mm/min until the samples broke.

24.3 Test Results

24.3.1 The Tensile Properties of the Samples

Figure 24.7 shows the load-time relationship of the three samples. The black curve is the change of the load of the unpreset defect sample with the stretching time, the blue curve is the change of the load of the preset round notch with the stretching time, and the red curve is the load of the preset V-shaped notch with stretching time. It can be seen from the figure that the load has a nonlinear relationship with time.

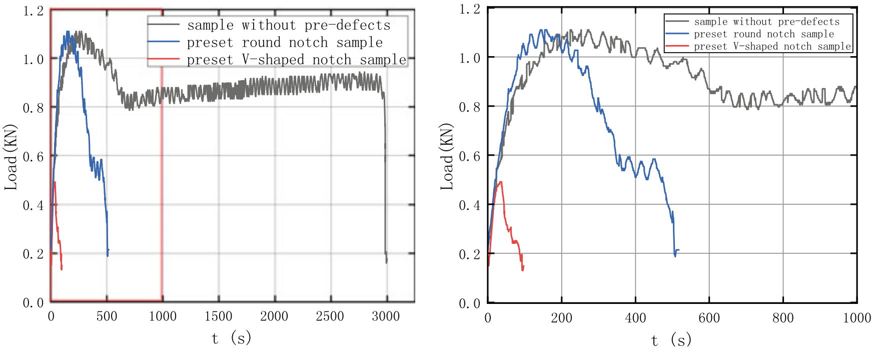

a)Load-time relationship of the three samples   b) Enlarged part of the red frame

Fig. 24.7 Load-time relationship of the three samples

Among them, the tensile time of the sample without pre-defect is much longer than that of the pre-made defect sample, and the tensile time of the preset round notch sample is longer than the preset V-shaped notch sample.

It can be clearly seen from the load-time relationship diagram that the tensile process of sample without pre-defects is divided into four stages: elastic deformation stage, yield stage, plastic deformation and fracture stage. The duration of the tensile process of the sample without pre-defects is 3000 s, and the plastic deformation stage, which is a "smooth line" in the figure, lasts for nearly 2600 s and the maximum force is 1.11 kN; The tensile process of the sample with the preset round notch is also the same that divided into four stages. The duration of the whole tensile process is 600 s, the maximum force is 1.11 kN, and the plastic deformation stage is relatively short. For the sample with preset V-shaped notch, the elastic stage and yield stage are obvious, the plastic deformation stage is very short, the maximum force is 0.49 kN, the duration of the tensile process is 120 s.

It can also be seen from Fig. 24.8 that during the tensile process, all three samples occurr plastic deformation. The entire parallel section of sample A occurs plastic deformation, and sample B occurs plastic deformation at the round notch section 8 × 17 × 2.2 mm only, and the sample C occurs only at the V joint which is 2 × 2 × 2.2 mm.

The mechanical properties of the samples are shown in Table 24.3. Yield strength refers to the maximum stress value of the material. Due to the different cross-sectional areas of the three samples, the V-shaped notch sample is the smallest, the round notch sample is the second, and the sample without pre-defect is the largest, resulting in the opposite relationship of yield strength. It can be seen from Fig. 24.8 and Table 24.3 that the yield strength of the sample with preset defects becomes larger, and the elongation and elongation rate become smaller.

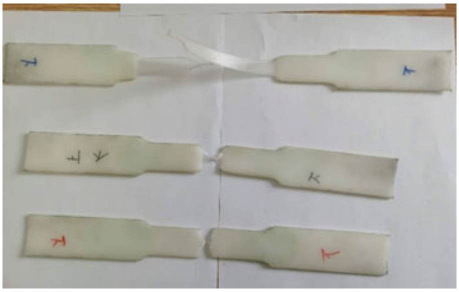

Fig. 24.8 Three broken samples

Table 24.3 The mechanical properties of the samples

Sample type	Elongation/mm	Elongation rate/%	Yield strength/MPa
Sample without pre-defects (A)	165	55	253
Preset round notch sample (B)	24	8	3710
Preset V-shaped notch sample (C)	12	4	55,682

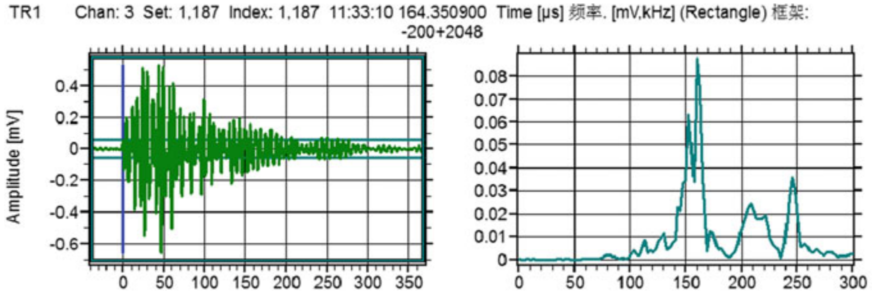

a) VS150-M

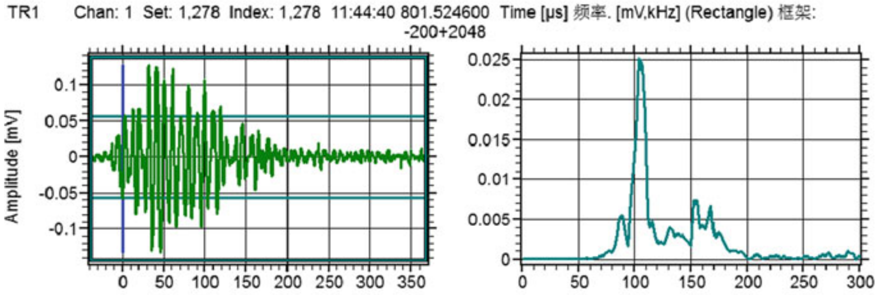

b）VS45-H

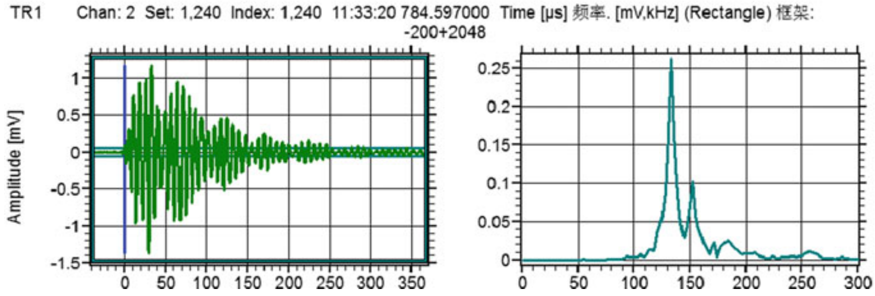

c）VS900-M

Fig. 24.9 The signal waveform and spectrum of the A sample in the DE segment

24.3.2 *Acoustic Emission Single Waveform and Spectrum Characteristics*

The acoustic emission single waveforms and spectrum diagrams of different stages of the three samples during the tensile process were analyzed.

The frequency distribution of the acoustic emission single of the three sensors of the A sample is shown in Table 24.4, and the different stages are shown in Fig. 24.10c; the frequency distribution of the acoustic emission signals of the three sensors of the Sample B are shown in Table 24.5, and the stages are shown in Fig. 24.11c; the

Table 24.4 The frequency distribution of the A sample (kHz)

Stage	VS150-M	VS45-H	VS900-M
Stage AB (elastic stage)	70–170	90–120	90–180
Stage BC (ascending stage of yield stage)	100–170	80–170	90–180
Stage DE (first half of plastic deformation stage)	130–260	90–180	120–170
Stage EF (the second half of the plastic deformation stage)	90–180	90–180	/
Point F (when pulled off)	80–250	90–140	80–160

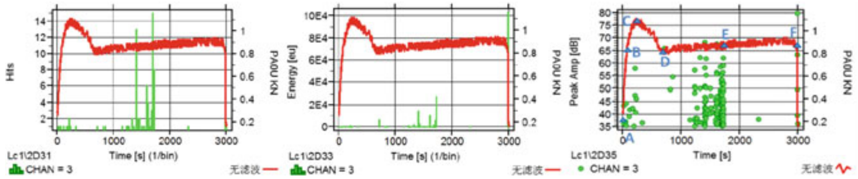

a)Hits-time b)Energy-time c) Amplitude-time

Fig. 24.10 A sample VS150-M acoustic emission characteristic parameter diagram

Table 24.5 The frequency distribution of the B sample (kHz)

Stage	VS150-M	VS45-H	VS900-M
Stage AB (elastic stage)	90–170	/	/
Stage BC (ascending stage of yield stage)	90–200	100–180	/
Stage DE (first half of plastic deformation stage)	80–170	/	70–120
Stage EF (the second half of the plastic deformation stage)	/	/	/
Point F (when pulled off)	80–250	70–150	80–250

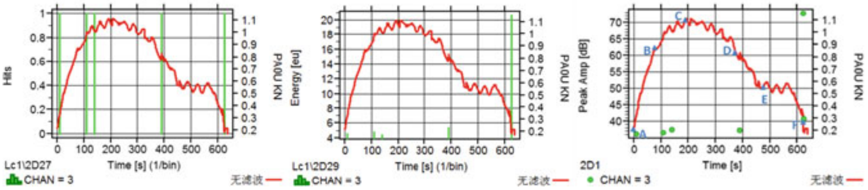

a)Hits-time b)Energy-time c) Amplitude-time

Fig. 24.11 B sample VS150-M acoustic emission characteristic parameter diagram

frequency distribution of the acoustic emission signals of the three sensors of the C sample is shown in Table 24.6, and the stage are shown in Fig. 24.12c.

The time-domain and frequency-domain diagrams of typical acoustic emission signals are shown in Fig. 24.9, which is the signal waveform and spectrum of the A sample in the DE segment (the first half of the plastic deformation stage). The acoustic emission signal frequency of the VS150-M sensor is distributed at 90–260 kHz,

Table 24.6 The frequency distribution of the C sample (kHz)

Stage	VS150-M	VS45-H	VS900-M
Stage AB (elastic stage)	/	/	/
Stage BC (ascending stage of yield stage)	90–170	/	90–220
Stage DE (first half of plastic deformation stage)	80–260	/	/
Stage EF (the second half of the plastic deformation stage)	/	/	/
Point F (when pulled off)	80–250	90–160	80–220

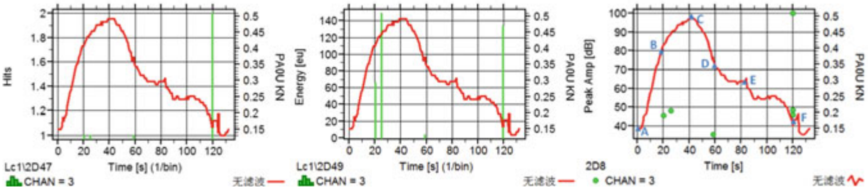

a)Hits-time b)Energy-time c) Amplitude-time

Fig. 24.12 C sample VS150-M acoustic emission characteristic parameter diagram

mainly distributed at 130–260 kHz, the acoustic emission signal frequency of the VS45-H sensor is distributed at 90-200 kHz, mainly distributed at 90–180 kHz, and the acoustic emission signal of the VS900-M sensor is distributed at 120–210 kHz, mainly distributed at 120–70 kHz.

According to the typical waveforms and spectrum of the three sensors, the frequency of HDPE material's acoustic emission signal is mainly distributed between 70 and 260 kHz. In some stages, when VS150 has an acoustic emission signal, the VS45-H and VS900-M sensors have no acoustic emission that exceeds the threshold. Which shows that the VS150 resonant sensor can be used to detect and monitor the HDPE material.

The following only analyzes the characteristic parameters of the acoustic emission signals collected by VS150.

24.3.3 Characteristic Parameters of Acoustic Emission Signals During Stretching

Acoustic emission monitoring was carried out on the tensile process of three kinds of samples. The parameters of acoustic emission signal collection were hits, RMS value, energy, amplitude, counts, duration time, etc. The main distribution range of acoustic emission parameters is shown in Table 24.7. From the table, it can be seen that the samples with preset defects have fewer hits than the samples without preset defects, and are accompanied by the appearance of high amplitude signals. The energy value of the sample with round notch is smaller than the energy value of

Table 24.7 The main distribution range of acoustic emission signal parameters

(a) Sample without pre-defects (A)					
Hits	Amplitude (dB)	Energy (eu)	Duration time (μs)	Duration time (μs)	Counts
181	35–78	1−9E4	1–2000	1–500	1–40
(b) Preset round notch sample (B)					
6	36.1;36.5;37.5; 37.3;72.7;40.7	4.56;4.78;4.38; 5.35;9.4E3;20.6	3.8;3.4;4.2; 4.8;472.3;50.8	0.3;0.6;3.5; 0.8;254.3;24.4	1;1;1; 1;46;5
(c) Preset V-shaped notch sample (C)					
6	45.6;48.2;35.5; 100;45.8;48.5	65.9;149;3.49; 7.57E6;27.2;107	107.7;134.1;0.5; 1808.4;32;165	42.5;33.7;0.2; 33.1;19.5;33.2	13;21;1; 215;4;17

a sample without pre-defect, and the energy value of a sample with preset V-shaped notch is greater than the energy value of a sample without pre-defect. Therefore, the hits and amplitude value are analyzed as characteristic parameters.

The hits-time charts collected by the three kinds of sample acoustic emission monitoring, as shown in Figs. 24.10, 24.11 and 24.12, and the energy-duration time correlation chart, as shown in Fig. 24.13.

It can be seen from the amplitude-time chart of the sample without pre-defects, as shown in Fig. 24.10c. There is a small part of the acoustic emission signal in the AB stage (elastic stage), and the amplitude of the acoustic emission signal is mainly distributed below 45 dB; In the BC stage (yield) Stage), there is a small peak, the acoustic emission signal is mainly distributed in 35–59 dB; In the CD stage (yield stage), the acoustic emission signal does not reach the specified threshold; In the DE stage (plastic deformation stage), the acoustic emission signal is from the pole very few and very rich, and appears a peak; In the EF stage (plastic deformation stage), the acoustic emission signal that basically does not reach the specified threshold appears; At the point F, which is the breaking point, the maximum value of the acoustic emission signal appears, with an amplitude of 35–80 dB.

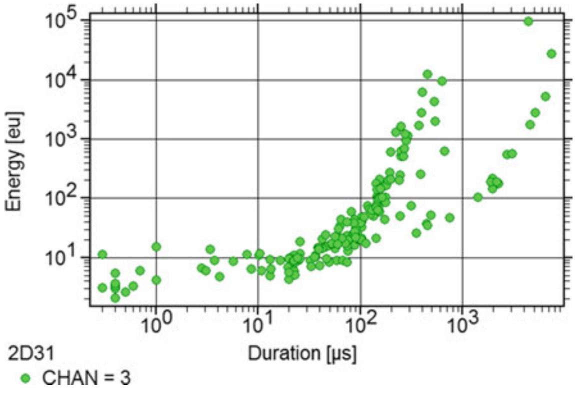

Fig. 24.13 Energy-duration time correlation diagram of sample A

It can be seen from the amplitude-time of the preset round notch sample, as shown in Fig. 24.11c. The acoustic emission signal appears in the elastic stage, the amplitude is 36.1, 36.5, 37.5 dB; An acoustic emission signal appears in the yield stage, the amplitude is 37.3 dB; In the plastic deformation stage, the acoustic emission signal that does not reach the specified threshold appears; At the break point, two acoustic emission signals appear and the maximum amplitude appears, the amplitudes are 72.7 dB and 40.7 dB, respectively.

It can be seen from the amplitude-time of the preset V-shaped notch sample, as shown in Fig. 24.12c.The acoustic emission signal appears in the elastic stage with amplitudes of 45.6 and 48.2 dB; The acoustic emission signal appears in the yield stage with amplitude 35.5 dB; In the plastic deformation stage, the acoustic emission signal that does not reach the specified threshold appears; At the breaking point, three acoustic emission signals appear and the maximum amplitude appears, the amplitudes are 100 dB, 45.8 dB and 48.5 dB, respectively.

From the energy-time correlation diagram, it can be seen that two kinds of acoustic emission signals appeared in the samples without pre-defects during the tensile process. When the duration was greater than 200 μs, a signal with low energy and long duration time appeared. Combining the graphs of tensile force and time, the signal appears when there are many acoustic emission signals during the plastic deformation stage at a tensile time of 1400 s, that is, the acoustic emission signals are the signals generated by the plastic deformation of the sample.

24.4 Analysis and Discussion

24.4.1 Discussion of Tensile Characteristics Analysis

The tensile process of HDPE material is divided into four stages: elastic deformation stage, yield stage, plastic deformation and fracture stage.

In the elastic deformation stage, the deformation is completely reversible, and the deformation occurs when the force is applied, and the deformation is completely restored after the force is released. From a microscopic point of view, the balance force between the molecules in the HDPE material is destroyed. In order to achieve a new balance, the position between the molecules is adjusted. After the external force is removed, the molecules returns to the original balance position.

In the yield stage, the HDPE material has thin necks during the process of forcing, and the narrow necks gradually expand. From the molecular mechanism, the movement of the HDPE material macromolecular segments (amorphous regions) begins to increase, and the stress is concentrated inside the grains;

In the plastic deformation stage, all the samples are drawn into thin necks, the strain hardening of the material and the softening caused by the geometric shape reach a balance, at this time, the force no longer increases, and tiny voids begin to appear in the center of the weakest section of the sample, expanding into small cracks, when the cracks propagate, thin neck deformation can be seen on the sample surface. From a microscopic point of view, the microcrystalline macromolecular structure begins to undergo orientation changes, and the degree of order changes from small to large, and then to decline.

24.4.2 Analysis and Discussion of the Characteristics of Acoustic Emission Signals

1. During the tensile process, the acoustic emission signals are detected in all three samples. The samples without pre-defects are mainly plastic deformation. The amount of deformation is large. The number of hits of the acoustic emission signal is large. The preset round notch sample is mainly a small amount of plastic deformation and fracture at the notch part, the amount of deformation is small, and the hits of acoustic emission signal is small. The preset V-shaped notch sample is mainly the fracture of the notch, accompanied by a very small amount of plastic deformation, the amount of deformation is smallest, and the hits of acoustic emission signal is least.

   The positive correlation between the hits and the amount of deformation shows that the signal detected by the acoustic emission signal is a plastic deformation signal.
2. A high amplitude signal appears in the preset V-shaped notch sample, indicating that the amplitude of the acoustic emission signal generated by the fracture is higher, and the amplitude of the acoustic emission signal generated by plastic deformation is lower; Compared with the sample without pre-defects, the high-energy signal appeared in the sample with the preset V-shaped notch, indicating that the energy of the acoustic emission signal generated by the fracture is relatively high.

   It can be concluded that the fracture signal has the characteristics of high amplitude and high energy compared with the plastic deformation acoustic emission signal.
3. By analyzing the acoustic emission waveform and spectrum, it is found that the frequency of the acoustic emission signal is mainly distributed between 70–260 kHz, the peak of the spectrum is around 140 kHz, and the frequency when broken is around 150 kHz.

Therefore, the selection of resonance sensor VS150-M can meet the requirements of detecting and monitoring the acoustic emission signal of HDPE material.

24.4.3 *Discussion on Generation Mechanism of Acoustic Emission Signal*

At different stages in the sample tensile process, the distribution of the characteristic parameters of the acoustic emission signal is very different.

In the elastic phase, the acoustic emission source is active, showing that the amplitude of the acoustic emission signal is small and the energy is low. The signal is basically at the beginning of the stretching, and it is inferred that it is the noise signal generated by the loading end when loading begins.

In the yield stage (ascending section), the acoustic emission source is active, which is manifested by a larger amplitude and higher energy of the acoustic emission signal. The signals are all located in the transition stage from the elastic stage to the yield stage. The generation mechanism is the internal segment of HDPE material (amorphous) Area) movement began to increase.

During the yield stage (descent), the source of acoustic emission is inactive.

In the first half of plastic deformation, the acoustic emission source is active, showing that the amplitude of the acoustic emission signal is large and the energy is high. The entire plastic deformation signal is concentrated in this stage, and the signal slowly increases at the beginning of plastic deformation. The signal amount reaches the maximum at Mid-term. The mechanism is that during the deformation of the thin neck, the orientation of the microcrystalline macromolecular structure begins to change, the order of the crystallites in the HDPE material in the early stage of the narrow neck changes is little, and the acoustic emission source is inactive. In the mid-term, as the crystallites began to occur large-scale slippage and other deformations, the degree of change in orderness was large.

In the second half of plastic deformation, the acoustic emission signal is inactive; as the change value of the order of crystallites decreases, the activity of the acoustic emission source decreases, and the signal is low;

During the fracture stage, the acoustic emission signal is active, which is manifested by the large amplitude and high energy of the acoustic emission signal, which is mainly the signal generated by the sample fracture.

24.5 Conclusion

1. HDPE materials produce acoustic emission signals during deformation and fracture, indicating that it is feasible to detect HDPE materials by acoustic emission methods;
2. The frequency of HDPE's acoustic emission signal is between 70–260 kHz, and VS150 resonant sensor can be used for the detection and monitoring of this material;

3. The amplitude and energy can be used as the characteristic parameters for distinguishing the signal acoustic emission caused by plastic deformation and fracture;
4. The characteristic parameter distribution of the acoustic emission signal at different stages of the tensile process is very different, and it is inferred that the structure of the HDPE material molecule is related.
5. Overall, the acoustic emission signal of the plastic liner is less than that of the fiber layer, indicating that most of the signals that appear during the monitoring of Type IV Gas Cylinder are from the fiber layer. This test can be a follow-up Type IV Gas Cylinder Provide a basis for fatigue monitoring.

Acknowledgements This work is financially supported by National Key Research and Development Program of China (Grant No. 2017YFC0805604).

References

1. T. Jie, *Research on Safety Technology of Fully Wound CNG Gas Cylinder with Plastic Liner Composite Material [D]* (Sichuan University, Chengdu, 2005)
2. G. Dong, *Structural Design of Non-Metallic Liner CNG Gas Cylinder and Research on Rapid Temperature Rise* (Northeast Petroleum University, Daqing, 2019)
3. W. Fei, Z. Jianping, T. Jun, et al., Research on acoustic emission testing technology of fiber-wound composite material cylinders. Aerospace Manuf. Technol. **3**, 59–63
4. L. Min, Safety analysis of full-complex winding gas cylinders for in-use vehicles. Saf. Spec. Equip. China **29**(11), 3–6 (2013)
5. Y. Zhong, Li. Xiaohui, Z. Shu, Safety research of CNG gas cylinders for automotive composite materials based on ANSYS. Chin. J. Saf. Sci. **21**(3), 77–82 (2011)
6. L. Min, Li. Wenchun, L. Yongjun, Defect analysis of fully compressed gas cylinders for compressed natural gas for vehicles. Press. Vessels **27**(3), 56–61 (2010)
7. Li. Xiaohui, *Safety and Reliability Analysis of All-Composite CNG Gas Cylinders for Vehicles* (Capital University of Economics and Business, Beijing, 2010)
8. X. Lirong, Failure mode analysis and prevention of CNG all-composite gas cylinders for vehicles. Pressure Vessels **26**(12), 51–61 (2009)
9. L. Zhejun, Ge. Li, W. Junfeng et al., Preliminary research on acoustic emission detection of composite gas cylinders. Aerosp. Mater. Technol. **2**, 120–123 (2011)
10. M. Surgeon, M. Wevers, One sensor linear location of acoustic emission events using plate wave theories. Mater. SxiEng. **265**(1–2), 254 (1999)
11. G. Caprino, V. Lopresto, Acoustic emission source location in unidirectional carbon fiber reinforced plastic plates with virtually trained artificial neural net works. J. Appl. Polym. Sci. **122**(6):3506 (2011)
12. M. Kaphle, A.C. Tan, Identification of acoustic emission wave modes for accurate source location in plate-like structures. Struct. Control Health Monitor. **19**(2), 187 (2012)
13. F. Dahmene, S. Yaacoubi, M. El Mountassir, Acoustic emission of composites structures: story, success, and challenges. Phys. Procedia **70**(2015), 599–603
14. W. Wang, Z. Zeng, Cluster analysis of acoustic emission signals during 304NG stainless steel stress corrosion process. J. Chem. Ind. Eng. **62**(4), 1027 (2011)
15. G. Kaloginnakis, J. Quintelier, Identification of wear mechanisms of glass/polyester composites by means of acoustic emission. Wear **264**, 235 (2008)

16. V. Kostopoulos, T.H. Loutas, On the identification of the fallure mechanisms in oxide composites using acoustic emission. NDT E Int. **36**(8), 571 (2003)
17. N. Godin, S. Huguet, R. Gaertner, Integration of the Kohonen s self-organising map and k-means algorithm for the segmentation of the AE data collected during tensile tests on crossply composites. NDT E Int. **38**(4), 299 (2005)
18. F. Pashmforoush, M. Fotouhi, M. Ahmadi, Acoustic emission based damage classification of glass/po1yester composites using harmony search K—means algorithm. J. Reinforced Plast. Compos. **31**(10), 671 (2012)
19. X. Wang, H.P. Zhang, X. Yan, Classification and identification of damage mechanisms in polyethylene self-reinforced laminates by acoustic emission technique. Polym. Compos. **32**(6), 945 (2011)
20. X. Wang, T.H. Zhang, X. Yan, Acoustic emission characteristic of damage modes on UHMWPE/LDPE laminates. In: Proceedings of the Fiber Society 2009 Spring Conference. Shanghai (2009)
21. Z. Xingmin, *Preparation and Mechanical Properties of Polyethylene Self-Reinforced Composites* (Donghua University, Shanghai, 2005)

Part V
Structure

Chapter 25
Detection and Evaluation of Vascular Network Based Self-healing Concrete Using Acoustic Emission

Y. Wang, R. Pullin, M. Pearson, R. Davies, and K. Holford

Abstract Given the very wide use of concrete within construction sectors, a huge amount of money has been spent to maintain and repair damage to infrastructure every year due to poor durability, construction methods, and quality control process of concrete structures. Then people started to investigate the "smart materials" that will adapt to their environment, including the self-healing concrete. In this study, totally four sets specimen (12 beams) has been tested and each whole testing process is divided into two parts. Acoustic Emission (AE) technique was applied to monitor the behaviour of self-healing concrete through whole testing process. The results have demonstrated that self-healing concrete based on vascular network is capable of restoring around 70% of the original concrete strength and bearing capacity. AE parameters can be effectively used to characterize the damage level of self-healing concrete. Experimental results also demonstrated that the use of Felicity effect could be promisingly applied to intuitively determine and evaluate the effectiveness of healing.

25.1 Introduction

As a kind of typical construction material, the durability, performance and service life of concrete used is of great importance regarding the reliability and safety of the structure. However, for a long time, a significant amount of money has been spent to maintain and repair damage to the concrete structures every year. Normally the repair and maintenance costs account for approximately half of the total expenditure on construction [1]. One of the biggest reasons is cracking of concrete. This is extremely common, and Especially the formation of microcracks can be caused by a number of factors including structural loading, plastic shrinkage, drying shrinkage, and thermal effects et al. Due to the reasons above, there are a lot of researchers starting to investigate the "smart materials" within the construction industry, including self-healing materials.

Y. Wang (✉) · R. Pullin · M. Pearson · R. Davies · K. Holford
Cardiff School of Engineering, Cardiff University, Cardiff C24 3AA, UK
e-mail: WangY219@cardiff.ac.uk

© The Author(s), under exclusive license to Springer Nature Singapore Pte Ltd. 2021

G. Shen et al. (eds.), *Advances in Acoustic Emission Technology*, Springer Proceedings in Physics 259, https://doi.org/10.1007/978-981-15-9837-1_25

25.1.1 Self-healing Materials

In recent years, since the degradation of material has been considered as an inevitable process which is commonly figured out through expensive maintenance cost, some researchers have gained the inspiration from biological systems and been developing materials which have the ability to adapt and respond to their environment. Since 2016, there is an ongoing programme of study regarding self-healing concrete and corresponding cementitious materials being undertaken by researchers at Cardiff, Bath, Bradford and Cambridge Universities in the UK.

25.1.2 Acoustic Emission

It has been long stated that it is of great importance to monitor the structural safety of concrete structures. One of the Non-Destructive Testing (NDT) methods used in recent years for real time monitoring is Acoustic Emission (AE), and it has been applied for damage detection in infrastructure and civil engineering for decades. The advantages of AE lie in its sensitivity to damage growth and corresponding changes occurred inside material which makes it promising for detection and quantification of damage in real time. In that case, AE is highly capable of monitoring the internal conditions of concrete structures under load and assisting in improving the efficiency of self-healing concrete. Associated AE parameters, such as amplitude, rise time, duration, signal strength and counts, can be extracted from AE waveforms. These types of parameters have been previously analysed to provide insight of damage mechanism and failure mode.

This study is trying to address detection of damage evolution both in concrete and self-healing concrete with focus on the mechanical properties and corresponding AE responses. The results could be utilized to provide information and guide for the design and improvements of performance end efficiency of self-healing concrete.

25.2 Materials and Experimental Setup

25.2.1 Preparation of Self-healing Concrete Specimens

Currently there are four kinds of self-healing techniques including: microcapsules releasing healing agents when damaged, bacterial healing filling cracks with calcium carbonate, shape memory polymers minimising the crack width after damage, and vascular flow networks supplying healing agents due to capillary force.

This study aims at studying the application of AE on self-healing concrete based on using the 2D vascular network in concrete as a system for hosting the self-healing agent. Cyanoacrylates were selected as an effective self-healing agent which were injected into the polyethylene based capillary tubes after damage.

25.2.1.1 Concrete Specimen Preparation

12 concrete beams of size 75 × 75 × 255 mm were cast in this study. The moulds used for beam casting contained pre-drilled holes, 4 at either end of each specimen. After curing for 5 days in a water bath and 1 day in the desiccator, a 6 mm rectangular notch was sawn at the centre line of the bottom surface of each beam. Then all the specimens were drilled at the channel openings to widen the diameter of the channel hole to 6 mm with a depth of 10 mm to fit the capillary network tubes. Two knife edges, which is used for the Crack Mouth Opening Displacement (CMOD) clip gauge, were glued on both sides of the notch on the bottom surface of the specimens. And a L-shaped deflection bracket, which is used for the measurement of central LVDT (Linear Variable Displacement Transducer), was glued onto a side surface, overhanging the bottom edge.

25.2.1.2 Healing Agents

More recently, researchers at Cardiff University have undertaken a substantial parametric study on adhesive-based self-healing of concrete beams. The main healing materials that have been proposed to date are epoxy resins, cyanoacrylates, and alkali–silica solutions, with the long-term aim of developing a material for this new composite material [2]. In this study, cyanoacrylate of type PC20 was used as the healing agent because of the main advantage of rapid curing due to acidity of glue and alkalinity of concrete (pH of approximately 13).

25.2.2 Testing Methods

25.2.2.1 Experiment Setup and Instrumentation

The experiments consisted of four sets of three beams. Apart from one set of three control beams, each set comprise three beams tested under three-point loading with different paused time with input of self-healing agent (cyanoacrylates) between 1st loading stage (initial loading) and 2nd loading (reloading) stage. The Test arrangement is shown below in Fig. 25.1. AE signals were recorded with a MISTRAS EXPRESS-8 Eight-Channel system. Steel pads were bonded to the concrete and magnetic clamps were used to hold the sensors on the surface of the specimens. Two R15I-AST sensors (70–200 kHz) were attached on one side of the specimen with 140 mm distance between each other, as shown in Fig. 25.2.

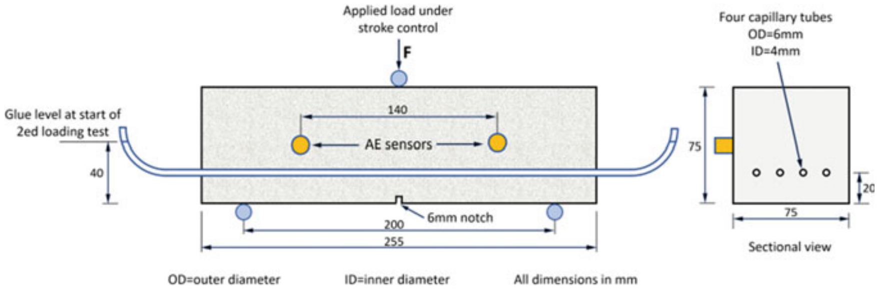
Applied load under
stroke control
F
Four capillary tubes
OD=6mm
ID=4mm
Glue level at start of
2ed loading test
140
AE sensors
40
75
20
200
6mm notch
255
75
Sectional view
OD=outer diameter
ID=inner diameter
All dimensions in mm

Fig. 25.1 Test arrangement for self-healing experiments on notched beams

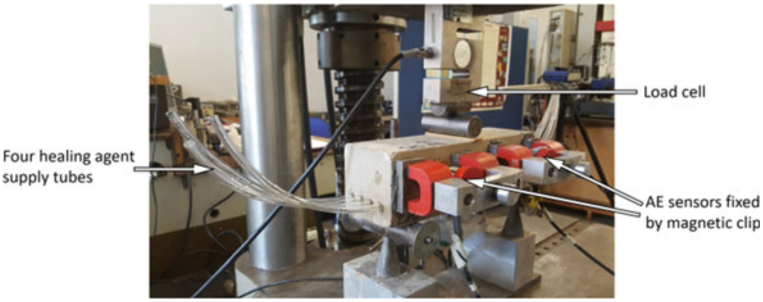
Load cell
Four healing agent
supply tubes
AE sensors fixed
by magnetic clip

Fig. 25.2 Experiment setup

25.2.2.2 Loading Conditions

As shown in Fig. 25.2, each specimen is subjected to three-point bending. The whole loading process is divided into two parts. Firstly, the load increased monotonically with a rate of 0.0002 mm/s until the CMOD reached 0.15 mm. After unloading, healing agent (cyanoacrylate PC20) was injected into all tubes to the height as shown in Fig. 25.1. Then the test was paused for different periods of time (1-h, 24-h and 3-days) before the reloading test. Secondly, after the specimen was healed, it was loaded monotonically again with the same rate of 0.0002 mm/s until the CMOD reached 0.30 mm.

25.3 Results and Discussion

As demonstrated in Fig. 25.3, the Load-CMOD curves for both control specimen (grey colour) and 24 h self-healing (blue colour) specimen are shown through the whole testing process (including the initial loading and reloading stages). According to the fracture theory for concrete [3], the crack propagation stages is highlighted (marked with Roman numerals in Fig. 25.3).

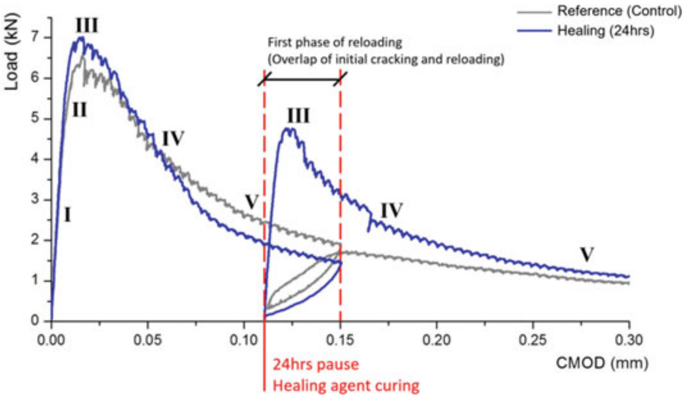

Fig. 25.3 Example of the Load-CMOD graphs for control specimen (grey curve) and 24 h self-healing (blue curve) specimen through the whole testing process

25.3.1 Strength Regained Ratio of Self-Healing Concrete

The results of the initial loading test (before the injection of healing agent) and the reloading test (after healing agent is injected and cracks are healed) are shown in Table 25.1. The control beams (C1 to C3) were already failed after the first three-points bending test. Therefore, the strength fell by an average of around 75% in the reloading process.

However, those specimens which were healed by cyanoacrylate with different healing time (1-h, 24-h, and 3-days) carried further loading in the reloading test.

Table 25.1 Mechanical results of initial loading and reloading

Healing agent	Specimen No.	1st loading/kN	Time of pause	2nd loading/kN	Strength recovery/%	Average/%
No	C1	6.55	No	1.73	26.4	25.5
	C2	6.11		1.47	24.1	
	C3	6.13		1.59	25.9	
Cyanoacrylate PC 20	SH-A1	6.67	1-h	4.44	66.	66.8
	SH-A2	6.09		4.36	71.6	
	SH-A3	5.98		3.72	62.2	
	SH-B1	7	24-h	4.81	68.7	65.9
	SH-B2	7.02		4.76	67.8	
	SH-B3	6.2		3.81	61.5	
	SH-C1	5.27	3-days	4.71	89.4	80.6
	SH-C2	6.18		4.92	79.6	
	SH-C3	5.35		3.9	72.9	

Around 60% ~ 80% original strength of specimens (batches of SH-A, SH-B and SH-C) were recovered and the maximum reached 89.4%.

25.3.2 Characteristics of AE Signals from Damage in Self-healing Concrete

25.3.2.1 The Amounts of AE Hits

Both of the four graphs in Fig. 25.4 show the load and distribution of AE hits amplitude against time during the reloading stage for (a) control beam, (b) 1-h healing beam, (c) 24-h healing beam, and (d) 3-days healing beam. In those graphs, each red dot represents an AE hit. The loading curve is represented in black lines corresponding to the *y*-axis on the right.

One critical point worth mentioning, considering as the CMOD during reloading stage reaching 0.15 mm (which is the previous unloading point), is indicated by a dotted line. Apparently, most of AE activities from healing products or consequences occur before the CMOD reached the previous maximum, which is 0.15 mm, and that's why most of attention should be placed on the reloading stage just before the dotted line.

For the control beam, it can be seen that only few AE hits were found before the dotted line. This is because that there is no healing occurred and barely no new host matrix damage as well. It's only the process of crack re-opening of the original crack and consistent with the Kaiser effect. But plenty of AE hits show up after the dotted line in both of them. Those AE activities can be mainly attributed to the damage of host matrix and formation of new microcracks and macrocracks.

In terms of those hits before the dotted line in Fig. 25.4b–d, it confirms that those emission are primarily attributed to the "healed damage". But the difficulties lie in that it's hard to recognize whether those signals originate from the reopening of healed cracks or the formation of new cracks due to the higher strength of the bonding surface, or both processes. However, the appearance of those hits before the dotted line can still qualitatively indicate the effect of healing consequences and it can also be found that the longer pause time left for healing, the more AE

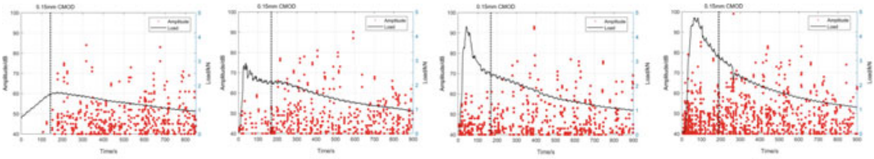

(a) (b) (c) (d)

Fig. 25.4 Amplitude of AE hits during the reloading stage for specimens: **a** control; **b** 1-h healing; **c** 24-h healing; **d** 3-days healing

hits are produced with relatively higher energy. That phenomenon matches with the mechanical response as well.

During the stage of overlap of precracking and reloading, theoretically the AE activities from this period of time are supposed to be coming from two different type of damage sources before the previous damage level (recognized by the value of CMOD) is exceeded after the specimens are healed. One of them is resulting from the sources of generation of new cracks formation. This is simply due to the fact that the healing effect, such as the healing agent available in the vascular network based specimen, possess a much stronger bond effect with original host matrix, which result in the bonding surface of cracked area possess higher strength than the surrounding original host material, and compel the new cracks to be occurred aside in a different position. Another type is primarily the sources from the damage of healed crack surfaces. These healed cracks, result from the filling of the adhesive in the vascular network due to the capillary force when microcracks appear, can fill those tiny interspaces very well. However, in terms of the recovery of mechanical properties and the effect of healed area to the overall structure has been less investigated. Therefore, the bonded crack surfaces by the filling adhesive agents could still be weaker regarding the mechanical properties than that of the original host matrix. Thus, it is potentially to be damaged again before the maximum load reached.

It also presents a relative dense area of AE hits for each self-healing specimen compared with control beams before the dotted line due to the new damage after the injection of healing agent. Moreover, from those self-healing specimens, the longer the healing time, the more hits are, which reflect better healing effect. Therefore, from the perspective of AE hits, the level of healing effect could be qualitatively assessed in the order of healing time 1-h < 24-h < 3-days. These results demonstrate that the self-healing capability is indeed related to different reaction time of the adhesive and host matrix.

25.3.2.2 Evolution of AE Hits

The variation and evolution of AE hits for one of the control specimen and one of the self-healing specimen before and after different healing time are shown in Fig. 25.5. As can be seen from the graphs, a large amount of AE signals was generated both during the initial loading and reloading stages. Obviously, the amount of AE hits in the

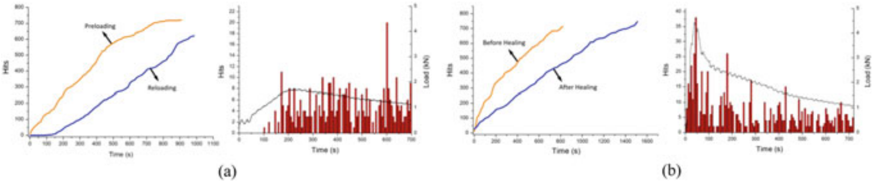

Fig. 25.5 Examples of evolution of cumulative AE hits and load curve during reloading stage for: **a** control beam; **b** 24-h healing beam

reloading stage is relatively less than that in the initial loading stage no matter for the healed beams or the control beams. For those healed beams, with the increase of load, the number of AE signals increases gradually from beginning, which is against the Kaiser Effect of AE. This is because that although there are already loads of cracks and damage occurred after the initial loading stage, the healing agent is injected afterwards and outflow rapidly from the tubes to those macrocracks and microcracks due to capillary force. Thus, most of the cracks in the specimen have been restored as well as the regained strength to make the concrete specimen as original as ever. In that case, during the reloading stage to evaluate the healing effectiveness, the healed concrete follows a similar damage process to the specimen before healing. It also can be illustrated from the AE monitoring results. More specifically, at the beginning of initial loading, the number of AE hits increase slightly due to the own properties of concrete. As a kind of porous material, there are still many micro-cavities and holes in concrete even though the concrete has cracked and damaged already. Under the action of external load, the micro-cavities and holes around the main cracks are squeezed compacted which result in the mortar particles rub and collide with each other and will generate a small amount of AE signals.

Subsequently, the amount of AE hits goes up significantly as the load increases, indicating that the interior structure of the specimen starts to change and produce new microcracks and damages. When the peak load is reached, the AE characteristic parameters increased dramatically because of the brittleness of concrete. Thus, the cracks will expand unstably when the load reaches the maximum value and the specimen will be failed due to the brittle fracture.

25.3.2.3 The Absolute Energy of Fracture

Figure 25.6 displays the evolution of AE hits cumulative absolute energy of both the initial loading and reloading stage for (a) control beam, (b) 1-h healing beam, (c) 24-h healing beam, and (d) 3-days healing beam. The cumulative absolute energy of initial loading and reloading stage for specimen is represented in blue and red curves respectively. Again, the most important point-in-time as the CMOD value during reloading stage reaching 0.15 mm (the previous unloading point), is indicated

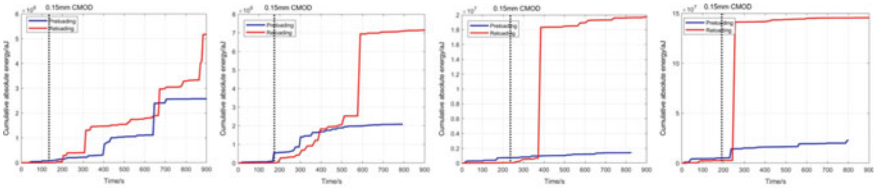

(a) (b) (c) (d)

Fig. 25.6 Cumulative energy during the initial loading and reloading stage for specimens: **a** control; **b** 1-h healing; **c** 24-h healing; **d** 3-days healing

by dotted line, which is consistent with the distribution of AE hit and amplitude as discussed above.

As can be seen from Fig. 25.6, a different pattern worth noting between the cumulative absolute energy generated from reloading of control beam and other self-healing beam tests after the dotted line. The energy released from control specimen during reloading increases gradually over time as similar as the initial loading stage. In terms of the self-healing specimens, however, as can be seen from both self-healing specimens, the most distinguished feature is that the energy generally stays at higher value during reloading than that of the initial loading after passing the previous damage level. This can be attributed to the breakage of ultimate failure caused by either the reopening of healed crack or the formation of new damage because of the higher bonding strength of the healed area.

Both the self-healing specimens show a similar pattern as there is a burst of energy. As shown in the Fig. 25.6, the order of magnitude is 106 for the control beam, and the order of magnitudes are 106, 107 and 108 for (b) 1-h healing beam, (c) 24-h healing beam, and (d) 3-days healing beam respectively. Based on the result above, it demonstrate that the self-healing specimens has possessed much higher cumulative energies than the control specimen, and that is in the order of control beam <1-h self-healing beam <24-h self-healing beam <3-days self-healing beam, which matched well with the results of the amounts of AE hits above as well.

On the other hand, it also demonstrates that the AE energy is indeed related to the healing effect and its corresponding time to some extent. Moreover, the amount of AE hits for 3-days self-healing beam is about twice than that of control specimen, but the cumulative energy for 3-days self-healing beam is about 28 times larger than that of control beam. It shows that the cumulative energy is not only related to the length of healing time, other factors such as the micropore structures of the material itself, bonding quality and healing degree, also have significant effect on the cumulative energy during the reloading stage. For instance, the higher the bonding quality is, or the less unhealed area left, the more fracture energy could be needed when cracks and damages occurred.

One thing noticed and worth mentioning is, for example as shown in Fig. 25.7, because of that the main crack occurred in the initial loading stage with a lot of microcracks surrounded, the new crack during the reloading process would initiate to the sides of the main crack after the initial cracks were healed and closed. To

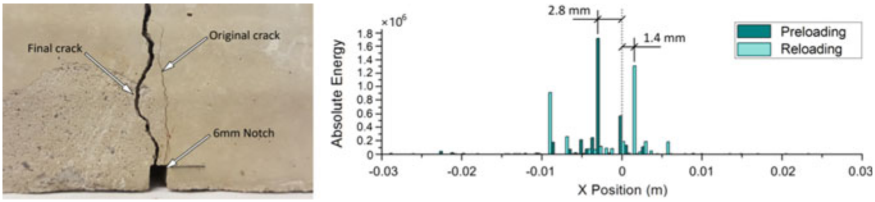

Fig. 25.7 Original cracks and new crack occurrence on side face of self-healing beam with its AE energy distribution from a 24-h healing test

some extent, that phenomenon could be reflected on the graphs of the distribution of absolute energy. The distance between energy peaks of initial loading and reloading indicates that the two main cracks generated during each loading stages are not in the same place. Even some of the specimens cannot be visualized from the surface but still can be verified by the energy distribution, which would be helpful to the damage location of new cracks. Since most of the energy is generated in the middle-notched area of each specimen, the range of X-axis of the graphs shown below has been shortened to 60 mm for a more focused and clear representation. The middle of specimen is signed by a grey dotted line and the distance from each energy peak to the centre line has been labelled.

25.3.3 Evaluation of Self-healing Efficiency Based on AE Felicity Effect

25.3.3.1 Kaiser Effect and Felicity Effect

Generally, the loading path history of the material has an important impact on the AE characteristics during the repeated loading. The Kaiser effect was put forward by the German scholar Kaiser in the first place [4]. It was discovered in a test of loading metal materials. The Kaiser Effect is manifested and defined as the absence of AE signals (or no obvious AE signals) at loads not exceeding the previous maximum load level when material undergoes repetitive loading. In other words, material has a memory for the historical load with respect to the presence of Acoustic Emission phenomenon. Conversely, if the material gives off significant AE signals at a lower load than the one previously reached in an increasing repeated loading, then this phenomenon is defined as Felicity Effect.

During the two stages of loading of self-healing concrete beams, it can be observed that all the specimens generated AE signals from the very beginning until they were unloaded before the pause. Then those specimens which were healed during the pause generated AE signals again before the unloading point (i.e., the maximum loading level during initial loading stage) was exceeded. The presence of this phenomenon is called “Felicity effect” and it can be manifested as the occurrence of “detectable and effective AE activities” during repeated loading of the material before the load level reaches the previous maximum applied load. The criteria used to determine the “effective AE signal” are discussed in the next section.

Meanwhile, the Felicity effect can also be quantified using the Felicity Ratio (FR), which is the ratio of load where considerable AE resumes during reloading, divided by the previous maximum load applied as shown below:

$$\mathrm{FR}(i) = \frac{P_{\mathrm{AE}}(i+1)}{P_{\mathrm{MAX}}(i)} \tag{1}$$

where

$\mathrm{FR}(i)$ is the Felicity Ratio of the ith loading during a cyclic loading;

$P_{\mathrm{MAX}}(i)$ is the maximum load during the ith loading;

$P_{\mathrm{AE}}(i+1)$ is the loading level when considerable AE resumes at the $i+1$th load.

From previous study, combination use of the Kaiser effect and Felicity effect can be efficiently used to determine whether major structural defects are present. Furthermore, Felicity Ratio can become an important criterion for evaluating the severity of material defects. It is complied with Kaiser effect when Felicity Ratio is greater than 1, or against the Kaiser Effect when Felicity Ratio is less than 1.

25.3.3.2 Determination of Valid Emission Signals

In terms of concrete, because of its complexity and it's a kind of polyphase and compound material, can be influenced by many factors. So many different kinds of defects, cracks and microstructural inhomogeneity are already contained inside before any load applied. In that case, some microcracks will deform and propagate even under relatively low stress condition. Therefore, it is of great importance to determine whether there are "effective AE signal" received and corresponding loading magnitude during the process of cyclic loading. However, up to now there is no agreed definition about the concept of "effective AE signal". Normally researchers just distinguish the signals by using their own experience and properties of corresponding material.

During the experiments, it was observed that occasionally some cement paste caused by spalling may peel and the AE amplitude will increase significantly. But this kind of signal is very short and therefore it cannot be regarded as the valid AE signal as a sign of AE recovery. Hongguang and Zaoding [5] conducted an experimental study with respect to the relationship of Kaiser and Felicity effect in concrete material. According to his findings, the following two criteria can be considered to use as the determination for "effective AE signal" in concrete:

1. AE signals has been continuously increasing when load increases;
2. More than 10 AE hits are received in the process of increasing the load by 10%.

25.3.3.3 Healing Performance Evaluation

To more intuitively characterize and better quantify the degree of self-healing, another index HI, called "Healing Index", is introduced and defined as the following equation.

$$\mathrm{HI}(\%) = 100 \cdot (1 - \mathrm{FR}) \tag{2}$$

According to these two criteria, the results of Facility Ratio calculated are shown in Table 25.2.

As shown in Table 25.2, the Felicity Ratio is related to different healing time and relatively decreases with the increasing strength recovery of healing. This is because the specimen is internally microcracked and damaged during the first loading, and

Table 25.2 Strength recovery and felicity ratio

Specimen No.	Strength recovery/%	Felicity ratio	Healing index
C1	26.4	0.8135	18.65
C2	24.1	0.8221	17.79
C3	25.9	0.6989	30.11
SH-A1	66.6	0.7379	26.21
SH-A2	71.6	0.6887	31.13
SH-A3	62.2	0.5738	42.62
SH-B1	68.7	0.0580	94.20
SH-B2	67.8	0.0616	93.84
SH-B3	61.5	0.0982	90.18
SH-C1	89.4	0.2385	76.15
SH-C2	79.6	0.1406	85.94
SH-C3	72.9	0.0515	94.85

the healing agent will flow to the section of fracture surface due to the capillary action, which enables it to be repaired timely and promptly, so the strength of the specimen is regained and improved.

During the reloading stage, the position of crack occurred would be different according to the bonding quality of fracture surface. If the bond strength is greater than the original, it is more likely the microcracks would occur in a different location. Opposingly, if it is less than the original strength, then the previous microcrack surface will get cracked again. Therefore, the Felicity Effect is shown in that case. Furthermore, it can be concluded that the use of Facility Ratio could be promisingly used to determine and evaluate the effectiveness of healing. However, it still needs to be further studied about whether there is a quantitative relationship between the Facility Ratio and quality of healing effectiveness.

25.4 Conclusion

1. Self-healing concrete based on vascular network is capable of restoring around 70% of the original concrete strength and bearing capacity. AE parameters could be used to highly potentially characterize the damage degree of self-healing concrete.
2. The amount of AE hits and absolute energy before and after healing can be qualitatively assessed by AE signals. The AE results indicate that the cracked specimen after healing possessed larger amount hits and much higher energy from the ultimate failure.
3. Kaiser effect and Felicity effect are of great potential to be applied to intuitively evaluate the severity of material defects. It provides a promising way to determine

the healing efficiency regarding the self-healing materials. The higher the healing efficiency, the more obvious the Felicity Effect; the lower the healing efficiency, the more obvious the Kaiser Effect.

Acknowledgements The authors would like to thank all the members in CUSP lab and technicians in Cardiff School of Engineering both for their massive guidance and help. The authors also appreciate the support from the RM4L (Resilient Materials for Life) project, funded by EPSRC (EP/P02081X/1), which enabled these advances to be made.

References

1. S. Liu, M.R. Pearson, M. Eaton, R. Pullin. Correlation between acoustic emission distribution and stress variation through the depth of RC beam cross sections. Constr. Build. Mater. **150**(Supplement C), 634–645
2. C. Joseph, *Experimental and Numerical Study of the Fracture and Self-healing of Cementitious Materials* (Cardiff University, 2008)
3. JGM van Mier, *Fracture Processes of Concrete* (CRC Press, 2017)
4. E.J. Kaiser, A study of acoustic phenomena in tensile tests. Dissertation. Technische Hochschule Munchen, Munich, FRG (1953)
5. J. Hongguang, L. Zaoding, Experimental study on the relationship of Kaiser and Felicity effect in concrete material. Appl. Acoust. **16**(6), 30–33 (1997)

Chapter 26
Damage Evaluation Inside the Concrete Dam by Tomography and AE Analysis

Y. Yang, H. Asaue, T. Shiotani, and K. Hashimoto

Abstract Although the elastic wave method has received much attention as a promising NDT method, the utilization of elastic wave on the damage evaluation of concrete dams still needs in-depth research. Therefore, in this research, the feasibility of the elastic wave method inside the damage evaluation of concrete dams, including characterization of the cracks appearing on the dam surface and the automatic continuous monitoring by AE activities were carried out. Sensors were arranged both in the inspection gallery and the surface of the dam, and the elastic wave was excited by steel balls of several diameters both in the inspection gallery and the surface of the dam body. Both elastic wave tomography and surface wave tomography were conducted. In addition, AE measurement has been conducted in this research, in which the sensors were arranged horizontally in the inspection gallery. As a result, the length and the depth distributions of the crack were revealed by elastic wave tomography and surface wave tomography. In addition, it was confirmed that the sensors arranged in the inspection gallery could measure AE inside the dam, indicated the possibility of damage monitoring by AE analysis.

26.1 Introduction

The application of non-destructive inspection (NDT) for damage evaluation of concrete has been studied all over the world, for it can save both time and money

---

Y. Yang (✉) · T. Shiotani · K. Hashimoto
Department of Civil and Earth Resources Engineering, Kyoto University, Kyoto, Japan
e-mail: yang.yitao.77r@st.kyoto-u.ac.jp

T. Shiotani
e-mail: shiotani.tomoki.2v@kyoto-u.ac.jp

K. Hashimoto
e-mail: hashimoto.katsufumi.8a@kyoto-u.ac.jp

H. Asaue
Department of Urban Management, Kyoto University, Kyoto, Japan
e-mail: asaue.hisafumi.7a@kyoto-u.ac.jp

© The Author(s), under exclusive license to Springer Nature Singapore Pte Ltd. 2021

G. Shen et al. (eds.), *Advances in Acoustic Emission Technology*, Springer Proceedings in Physics 259, https://doi.org/10.1007/978-981-15-9837-1_26

while avoiding damage toward the concrete structure. And the elastic wave method, since its characteristics of circumventing and scattering when deterioration such as crack exists inside the concrete, has received much attention as a promising NDT method. With the analysis of the parameters of elastic wave, such as velocity and energy (amplitude), it is possible to evaluate the deterioration of concrete structure [1, 2]. However, the utilization of elastic wave method on the damage evaluation of concrete dams still needs in-depth research.

In this research, the characterization of the crack appearing on the surface of concrete dam by tomography and the feasibility of the automatic continuous monitoring by AE activities have been studied. To investigate the crack appearing on the surface of the dam, sensors have been arranged and the elastic wave was excited by steel balls of several diameters both in the inspection gallery and the surface of the dam body. The elastic wave tomography and surface wave tomography are applied for detect of crack distribution. AE measurement has been also conducted in this research. As a result, the length and the depth distribution of the crack was revealed by elastic wave tomography and surface wave tomography. In addition, it was confirmed that the sensor arranged in the inspection gallery could measure AE activities inside the dam, which indicated the possibility of damage monitoring of the concrete dam by AE analysis.

26.2 Methodology of Tomography

With the elastic wave tomography, the p-wave velocity distribution in the concrete structure can be calculated and visualized as a tomogram. First of all, the excitation time T_s and arrival time T_o of the elastic wave are recorded during the measurement. And the observed travel time T_{obs} can be calculated by Formula (26.1):

$$T_{obs} = T_o - T_s \tag{1}$$

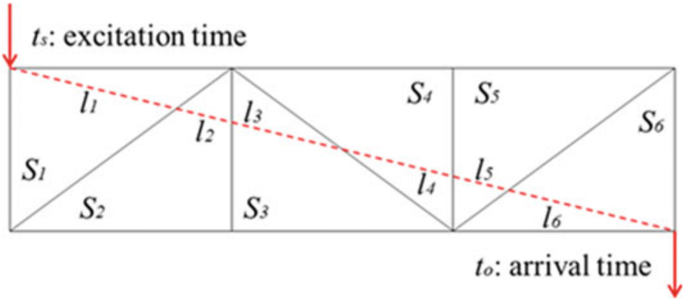

Fig. 26.1 Slowness for calculation of propagation time

Meanwhile, as shown in Fig. 26.1, the target area is divided into several elements and the "slowness", which means the inverse of the velocity, is given into each element as an initial parameter.

With the initial value of the slowness, the theoretical travel time T_{cal} for each wave path can be obtained by Formula (26.2).

$$T_{\mathrm{cal}} = \sum_{j} s_j \cdot l_j \tag{2}$$

where s_j is the slowness of j-element and l_j is the length of the wave path crossing j-element. Then, as shown in Formula (26.3), the difference between the observed and theoretical travel time ΔT can be obtained.

$$\Delta T = T_{\mathrm{obs}} - T_{\mathrm{cal}} \tag{3}$$

Next, in order to eliminate the difference between the observed and theoretical travel time, the correction value of slowness Δs_j and the revised slowness s'_j are calculated by Formulas (26.4) and (26.5):

$$\begin{bmatrix} \Delta s_1 \\ \Delta s_2 \\ \vdots \\ \Delta s_j \end{bmatrix} = \begin{bmatrix} \sum_i \frac{\Delta T_i * l_{i1}}{L_i} / \sum_i l_{i1} \\ \sum_i \frac{\Delta T_i * l_{i2}}{L_i} / \sum_i l_{i2} \\ \vdots \\ \sum_i \frac{\Delta T_i * l_{ij}}{L_i} / \sum_i l_{ij} \end{bmatrix} \tag{4}$$

$$s'_j = s_j + \Delta s_j \tag{5}$$

where ΔT_i is the difference between the observed and theoretical travel time for i-wave path, l_{ij} is the length of the i-wave path crossing j-element, and L_i is the total length of the i-wave path. Then, every wave path can be updated with the revised slowness by the ray tracing algorithm. By iterations of the calculation above, accurate slowness/velocity for each element can be obtained, resulting in forming the tomogram of the elastic wave velocity over the target area. And with the tomogram, the velocity distribution of the target area can be visualized.

26.3 Target Area

26.3.1 *Elastic Wave Tomography*

In this research, to investigate the cracks on the surface of the dam (within the red box in Fig. 26.2), elastic wave tomography was conducted in this research, and the target area is shown within the blue line in Fig. 26.2.

The measurement was conducted on October 30, 2018. A wide band data recorder (WX-7000SYR by TEAC CORPORATION), as an acceleration measurement system, was used for the measurement. Piezoelectric acceleration sensors (707 IS by TEAC CORPORATION) were used, of which frequency response of the sensor is around 3 Hz to 20 kHz and the sampling rate was 50 kHz. To determine the proper size of the steel ball, steel balls of $\varphi 30$ mm, $\varphi 50$ mm, and $\varphi 100$ mm were used to excite the elastic wave in the inspection gallery and the waveforms were recorded from the surface of the dam. As shown in the Fig. 26.3, the amplitude by $\varphi 30$ mm and $\varphi 50$ mm steel balls were small, which indicated that it would be difficult to recognize the arrival time of the wave, especially when the wave pass through deteriorated area. Therefore, a steel ball of $\varphi 100$ mm was used for the excitation of the elastic wave.

The elastic wave was excited from both the inspection gallery and the surface of the dam body. The locations of the measurement points and the crack on the dam

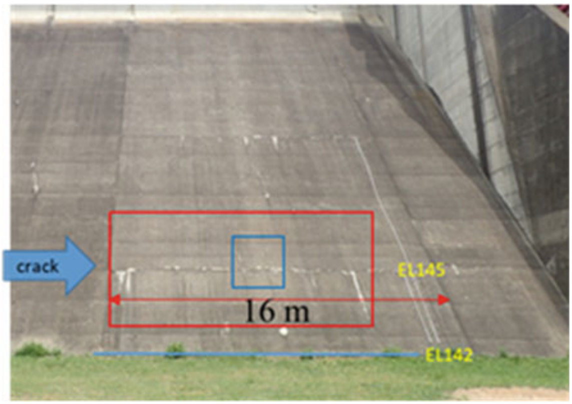

Fig. 26.2 Measurement target appearance

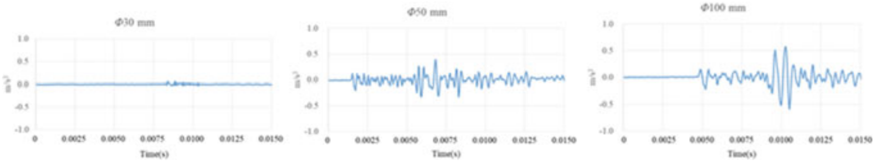

Fig. 26.3 Waveform by impacting of steel balls of φ30 mm, $\varphi 50$ mm and $\varphi 100$ mm

surface are shown in Fig. 26.4. 15 (3 × 5) sensors were set on the measurement points and the sensor interval was 400 mm.

The locations of the measurement points in the inspection gallery are shown in Fig. 26.5. 5 sensors were set on the wall of the inspection gallery with an interval of 3000 mm in the horizontal direction. Also, since it is in the stairs area of the

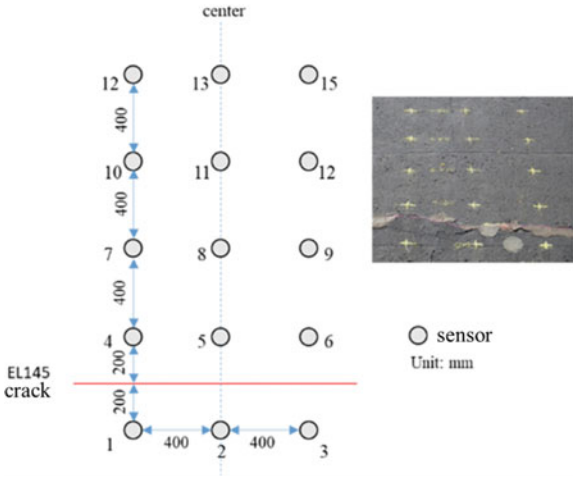
center
12
13
15
10
11
12
7
8
9
4
5
6
1
2
3
400
400
400
200
200
400
400
EL145
crack
sensor
Unit: mm

Fig. 26.4 Dam surface measurement point and crack position

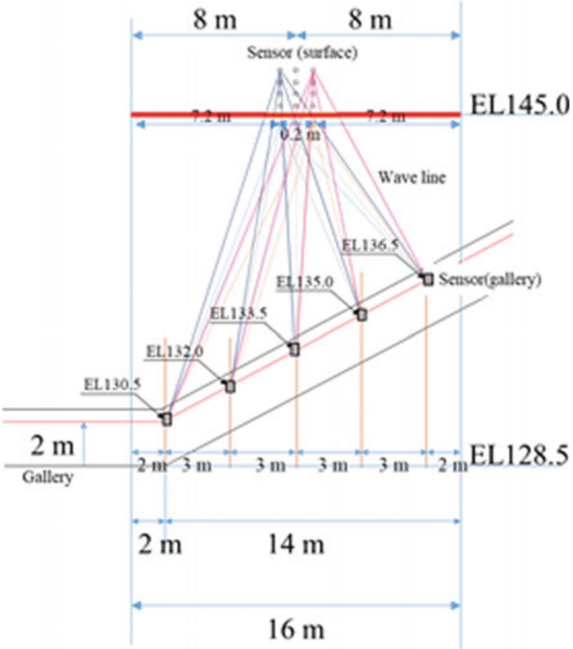
8 m
8 m
Sensor (surface)
EL145.0
7.2 m
7.2 m
0.2 m
Wave line
EL136.5
Sensor(gallery)
EL135.0
EL133.5
EL132.0
EL130.5
2 m
Gallery
2 m
3 m
3 m
3 m
3 m
2 m
EL128.5
2 m
14 m
16 m

Fig. 26.5 Measurement points in the dam gallery

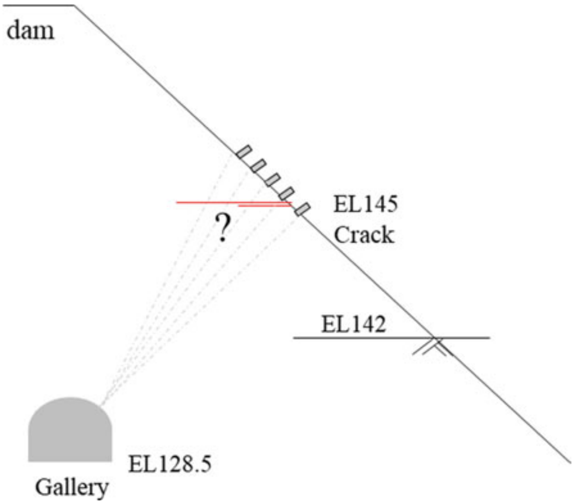

Fig. 26.6 The positional relationship between the gallery and the surface of the levee

inspection gallery, the sensors had to be arranged to be rising up with an interval of 1.5 m. Figure 26.6 shows the positional relationship between the measurement points of the dam surface and the inspection gallery. The elevation of the bottom floor of the inspection gallery is 128.5 m, and the elevation of the crack on the dam surface is 145 m.

Various coordinate such as the coordinates of measurement points were derived from simple measurement and drawings and detailed measurement of coordinates has not been performed. The propagation distance of the elastic wave in this measurement was about 25–30 m.

26.3.2 Surface Wave Tomography

In the elastic wave tomography, it is necessary that the elastic wave path passes through the structure. However, for some situations such as tunnel lining concrete, bridge slab and retaining wall, the sensor arrangement is limited to the surface and the elastic wave tomography will be difficult to conduct. Meanwhile, the Rayleigh wave, is a kind of surface wave, propagates near the surface of the medium. Also, the Rayleigh wave carries more energy and has lower attenuation than *P* wave and *S* wave. Most importantly, the propagation depth of the Rayleigh wave depends on the wavelength or frequency. With all of these characteristics, Rayleigh wave is regarded as a promising tool of the damage evaluation near the concrete surface. In this research, the phase velocity of Rayleigh wave was obtained and the tomography analysis same as the elastic wave tomography was conducted.

The measurement equipment such as wide band recorder and sensor were same as those used in the elastic wave tomography. The sampling rate was 50 kHz. And

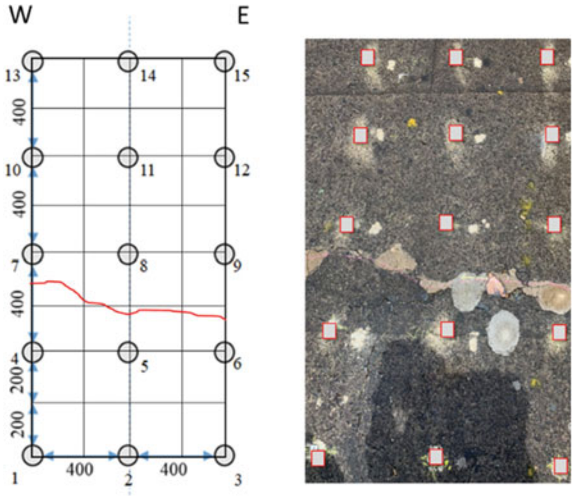

Fig. 26.7 Sensor arrangement in surface wave tomography

the measurement was conducted on October 31, 2018. Steel balls of $\varphi 30$ mm and $\varphi 75$ mm were used to excite the surface wave. The predominant frequencies were obtained from the FFTs of the waveforms. The Rayleigh wave velocity is assumed 2000 m/s in the concrete, the wavelengths λ of $\varphi 30$ mm and $\varphi 75$ mm were 29 cm and 80 cm. The sensors were arranged to 15 (3 × 5) points and the sensor interval was 400 mm, as shown in Fig. 26.7. The position of the crack was also shown in Fig. 26.7. The impact was performed in the vicinity of each sensor.

26.3.3 AE Analysis

Acoustic Emission (AE) is the phenomenon of radiation of elastic waves in solid materials that happens when the elastic energy accumulated inside the materials is released rapidly in the processes such as the occurrence of cracks. Since it is highly related to the occurrence and development of the cracks, AE is widely used in health monitoring of concrete structures.

The AE is applied to the health monitoring of concrete structures mainly by the AE parameters, including number of hits, maximum amplitude, etc. One waveform of the AE signal input to the AE sensor is called one hit. And the number of hits is usually used for estimating the occurrence frequency and the occurrence form of cracks. The maximum amplitude means, literally, the maximum value of the AE waveform.

In this research, AE measurement was conducted in order to detect the AE that possibly occurs inside the dam. Since there is no example of steady AE observation in a concrete dam, whether AE could be detected was still unknown. To increase the detection rate of AE, the sensors were arranged in the inspection gallery horizontally

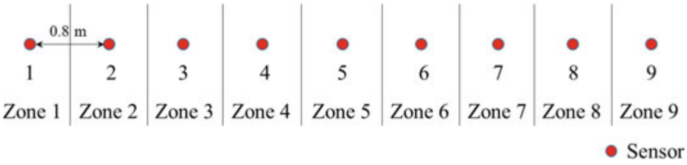

Fig. 26.8 Sensor position in AE measurement

with an interval of 0.8 m, as shown in Fig. 26.8. The sensors were attached to the pedestals that were bonded to the upstream wall of the inspection gallery by adhesive, at a height of 2 m from the floor. Since the large size of the dam, it was thought that the distant AE would be attenuated and only nearby AE could be detected when the normal AE measurement frequency band (tens of kHz to several MHz) is used. Therefore, the AE measurement was carried out in the acceleration range in this research. The measurement equipment such as wide band recorder and sensor were same as those used in the elastic wave tomography and the sampling rate was also 50 kHz. The fluctuation of water level of the reservoir was considered to be one of the possible reasons for the occurrence of AE inside the dam. Therefore, the measurement time were set to be *A*: 12:43–16:45 (about 4 h) on December 17, 2018, *B*: 16:50–19:04 (about 2 h) on the same day, and *C*: 8:55–13:02 (about 4 h) on December 18, 2018, when the water level were changing continuously.

26.4 Results

26.4.1 Velocity Distributions by Elastic Wave Tomography

Figure 26.9 shows the velocity distribution obtained by three-dimensional elastic wave tomography analysis from the obtained data, and Fig. 26.10 shows the location of the elastic wave tomography results. The velocity distributions from a to d are cross-sectional views taken in the vertical direction of the three-dimensional elastic wave tomography result, at interval of 200 mm from the western side (cross section a) to the eastern side (cross section d). In section a, velocity of about 3600 m/s is distributed to about 1.5–2.0 m in the depth direction. In section b, a velocity boundary can be confirmed near the red line which was drawn horizontally from the position of the crack in the surface and the low velocity area (about 3700 m/s) appears similar distribution as section a. This tendency can also be found in the sections c and d. Therefore, it can be estimated that the cracks appearing on the surface are also distributed continuously to the depth of about 1.5–2.0 m. And the red line of cross-sectional a to d in Fig. 26.9 was the estimation of the crack's location. The cracking range was estimated to be about 1.3 m by the coring test.

Considering that the size of the mesh was 500 mm in the depth direction (*Z* axis), the result of elastic wave tomography and the coring test were similar. In addition,

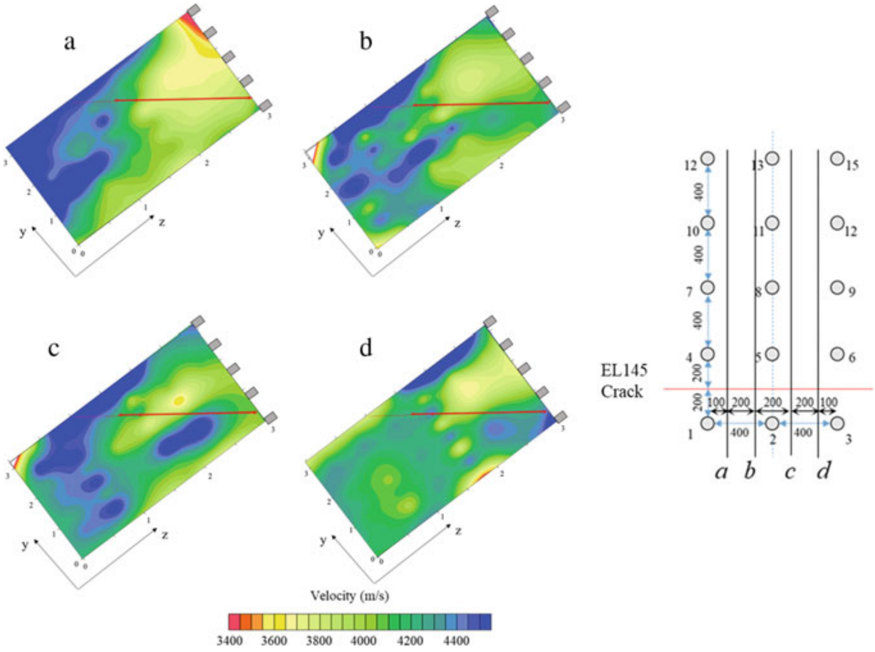

Fig. 26.9 Velocity distribution by elastic wave tomography

Fig. 26.10 Position of relationship between velocity distribution and dam

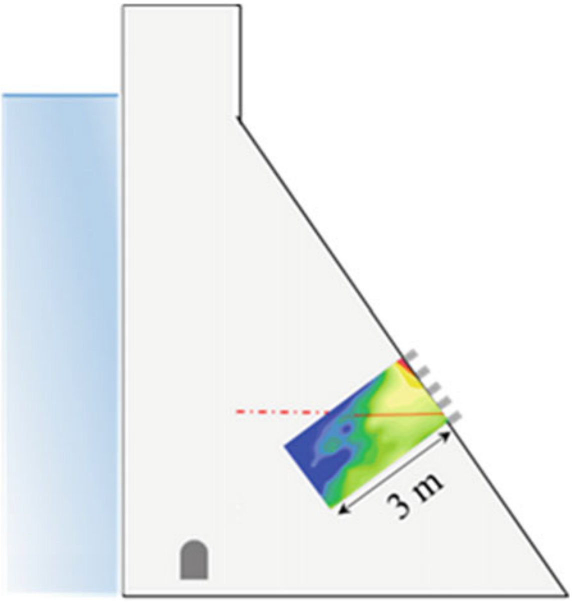

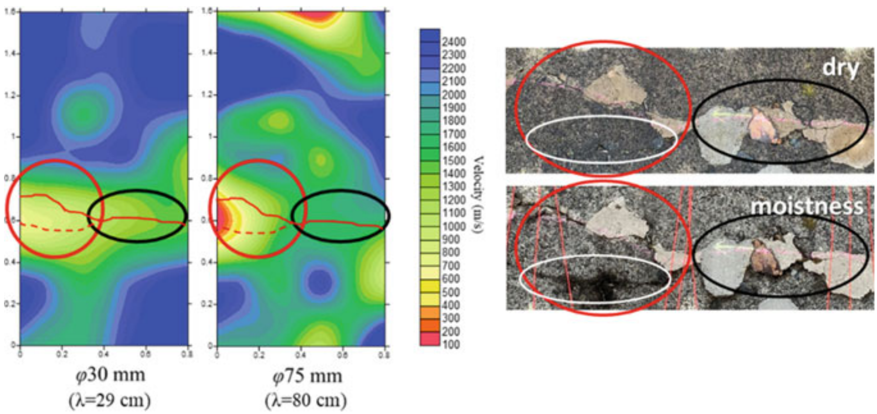

φ30 mm
(λ=29 cm)

φ75 mm
(λ=80 cm)

Fig. 26.11 Velocity distributions by surface wave tomography and the condition of cracks

since the low velocity area is prominent on the west side (section a and b), the crack condition is considered to be more severe in the western side.

26.4.2 Velocity Distributions by Surface Wave Tomography

The velocity distributions by surface wave tomography and the photographs of the cracks are shown in Fig. 26.11. It can be confirmed that low velocity area under 1300 m/s appears in the location of cracks. Furthermore, lower velocity area appears in the left side in both results for φ30 mm and φ75 mm, indicates the severe damage conditions in the western side cracks (left side in the photographs). As shown in the photographs in Fig. 26.11, it can be confirmed that two main cracks appear in the western side, which were not well repaired by the mortar, compared with the cracks of the other side, which may cause the lower velocity in western side. In addition, in the velocity distribution of φ75 mm, of which the Rayleigh wave propagates deeper than that of φ30 mm, the velocity of the western side appears to be lower than the velocity distribution of φ30 mm, while the velocity of the eastern side appears to be higher. Therefore this indicates that the crack depth of the western side is larger.

26.4.3 AE Analysis

Figure 26.12 shows the result of AE zone location for each hour. The AE zone location was performed for each zone shown in Fig. 26.8. The zone location was for AE events of 2 or more hits. The distribution of AE zone locations highly depended on the located zone (1–9) and the variation of AE zone locations with time was not

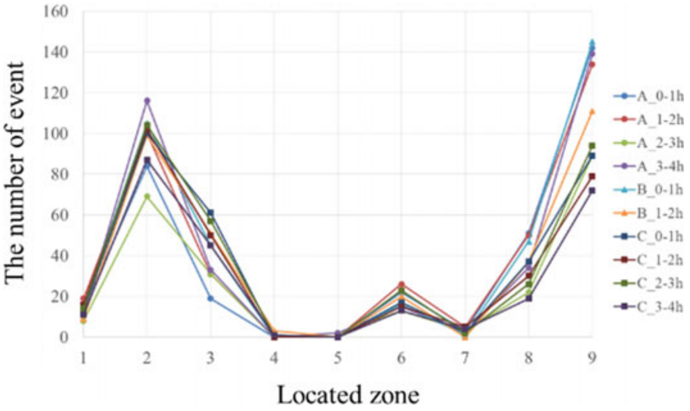

Fig. 26.12 AE zone location

confirmed. A lots of AE occurred in zone 2 and zone 9, while in zones such as zone 4 and zone 5 almost no AE zone locations were detected. AE events appeared to occur about 5 events per minute constantly. And no clear relationship was confirmed between the short-term changes of the reservoir water level and the number of AE zone location.

26.5 Conclusions

The feasibility of elastic wave tomography and surface wave tomography on concrete dam was confirmed in this research. As a result, the depth distribution of the crack was revealed by elastic wave tomography even if the propagation distance was long. Also, the surface wave tomography revealed the depth distribution of the crack that the crack was deeper in the western region.

In addition, it was confirmed that the sensor arranged in the inspection gallery could measure AE activities inside the dam, which indicated the possibility of damage monitoring of the concrete dam by AE analysis.

Acknowledgements This research is supported by the “Grant for R&D on River and Sabo Engineering Technologies” from the Ministry of Land, Infrastructure, Transport and Tourism (MLIT), Japan.

References

1. Y. Kobayashi, T. Shiotani, H. Shiojiri, Damage identification using seismic travel time tomography on the basis of evolutional wave velocity distribution model, in *Proceedings of Structural Faults and Repair 2006* (CD-ROM) (2006)
2. D.G. Aggelis, T. Shiotani, Repair evaluation of concrete cracks using surface and through-transmission wave measurement. Cement Concr. Compos. **29**, 700–711 (2007)

Chapter 27
Evaluation of Fatigue Damage in RC Slabs Considering Water Infiltration by Means of 3D AE and Elastic Wave Tomography

H. Asaue, T. Shiotani, S. Fukumoto, and T. Maeshima

Abstract To maintain civil engineering infrastructures reasonably, proper maintenance programs shall be implemented before remarkable damage/deterioration. As for RC slabs of road bridges, an evolutional process of fatigue damage shall be studied to establish the proper maintenance program. The authors have enthusiastically studied the mechanism of fatigue failure of the RC slabs; however, there is still space to clarify internal fatigue damage progress in consideration of water infiltration. In the study, to know the fatigue failure mechanism of RC decks in consideration of water infiltration, a wheel loading test of the RC slab filled with water on the surface is conducted systematically. Numerous numbers of repetition of the wheel load are conducted by several loads' step and after each designated cycle e.g., 100, 200 and 250 k cycles, the specimen is subject to static load with monitoring AE activity. With using AE activity namely AE sources located, 3D AE tomography is implemented to identify the damage with elastic wave velocity distributions (tomogram). Based on the tomograms obtained each loads' step, failure mechanisms in consideration of water infiltration is discussed in comparison with the cases without infiltration. Through the study, very unique failure progress, being different from dry condition, which expands from first-introduced cracks comes to light.

H. Asaue (✉) · T. Shiotani
Graduate School of Engineering, Kyoto University, C3-b4S15, Katsura Campus, Nishikyo-Ku,
Kyoto 615-8540, Japan
e-mail: asaue.hisafumi.7a@kyoto-u.ac.jp

S. Fukumoto
IHI Inspection and Instrumentation Co., Ltd., 2-6-17, Fukuura kanazawa-ku, Yokohama,
Kanagawa, Japan

T. Maeshima
College of Engineering, Nihon University, 1, Nakagawara Tokusada Tamuramachi, Koriyama,
Fukushima, Japan

© The Author(s), under exclusive license to Springer Nature Singapore Pte Ltd. 2021

G. Shen et al. (eds.), *Advances in Acoustic Emission Technology*, Springer Proceedings
in Physics 259, https://doi.org/10.1007/978-981-15-9837-1_27

27.1 Introduction

Nowadays, as road infrastructures have been constructed intensively since 1960s, almost those are reaching their life-span 50 years recently in Japan. Accordingly ageing rate of more than 50 years old shifted to 43% in coming 10 years from 18% of 2013 [1]. Replacement of those aging infrastructures with new ones would be the most ideal measure; however, due to decrease of construction budget, life-prolonging tactics are appeared to be the most adaptable for those existing aging infrastructures. Among the infrastructures, concrete bridge decks hold many difficult problems, resulting in taking a lot of cost to maintain. Specifically, it is planned by three major expressway companies that more than 90% of the renewal budget for 15 years will be used for bridge slabs. The RC bridge slabs are so principal members of road infrastructures to maintain that many organizations have studied intensively for their deterioration mechanisms, countermeasures against deterioration, and so forth. In order to simulate the peculiar failure process of the bridge decks experimentally, test slabs have been subjected to wheel loading tests with NDT approaches [2]. A three-dimensional approach using AE tomography [3] have been applied recently, and fatigue failure mechanisms could be explained by a velocity distribution of elastic waves [4]. In addition, acceleration of deterioration due to water infiltration is a problem in actual RC slabs. In this study, 3D AE and elastic wave tomography was applied to the wheel load running test on the RC slabs with submerged upper surface. As a result, clarified the relationship between deterioration progress and velocity distribution of RC slabs with water effect.

Final form of deterioration specified in RC decks namely 'aggregation' is discussed by the findings. Note 'aggregation' is the final form of deterioration of RC decks, remaining only aggregate from concrete where cement hydrated matrix is washed out by excessive water pressures filled in the cracks due to mobile loads.

27.2 AE and Elastic Wave Tomography

AE and Elastic wave tomography can estimate internal velocity distribution of the structure, analysis procedure is shown as follows, some sensors can record arrival time of elastic wave when the wave is generated by an AE activity or a hammering. After each arrival time is determined, the propagation velocity of through the path of elastic wave is calculated by both of the distance from the excitation point to the receive point and T_{obs} (observed propagation time) which is obtained by Formula (27.1):

$$T\text{obs} = To - Ts \tag{1}$$

where T_s is the excitation time and T_o is the arrival time. On the other hand, in the algorithm of the tomography, the inverse of velocity which is specifically referred

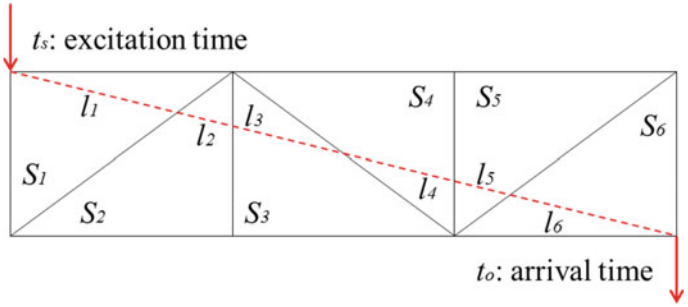

Fig. 27.1 Slowness for calculation of propagation time

to as the "slowness" is given as an initial parameter into each element as shown in Fig. 27.1. Next, T_{cal} (theoretical propagation time) obtained by a finite element model is the total of the propagation time calculated by the slowness and the distance in each element [refer Formula (27.2)]. Where s_j is the slowness of each element and l_j is the length crossing each element. ΔT is defined by observed propagation time (T_{obs}) and theoretical propagation time (T_{cal}) in Formula (27.3):

$$T\text{cal} = \sum_j sj * lj \tag{2}$$

$$\Delta T = T\text{obs} - T\text{cal} \tag{3}$$

Then the slowness in each element is revised in order to reduce ΔT. The slowness correction amount and the revised slowness are obtained by Formulas (27.4) and (27.5) respectively:

$$\begin{bmatrix} \Delta s1 \\ \Delta s2 \\ \vdots \\ \Delta sj \end{bmatrix} = \begin{bmatrix} \sum_i \frac{\Delta Ti * li1}{Li} \Big/ \sum_i li1 \\ \sum_i \frac{\Delta Ti * li2}{Li} \Big/ \sum_i li2 \\ \vdots \\ \sum_i \frac{\Delta Ti * lij}{Li} \Big/ \sum_i lij \end{bmatrix} \tag{4}$$

$$s'j = sj + \Delta sj \tag{5}$$

where L_i is the total distance of the wave in the i-element. The iteration calculation from Formulas (27.4)–(27.5) enables to obtain the accurate slowness and finally the velocity in each element corresponding to the observed propagation time of multiple waves over the structure, resulting in forming the tomogram of the elastic wave velocity over the target area [5]. Through these steps, velocity distributions were determined in the structure.

27.3 Measurement Condition

Wheel loading apparatus as shown in Fig. 27.2 has been used. The wheel is made by steel of 0.3 m diameter and 0.4 m width. The load repetition was set at 8.97 rpm in the available range of 0.897–9.97 rpm in this apparatus. The maximum vertical load of 250 kN for dynamic and 534 kN for static condition can be applied. In this unique device, the basement put on concrete slabs is repeatedly moved in a lateral direction, while the loading point is movable for conventional apparatus [6]. The loading program is exhibited by Fig. 27.3. The load of 98 kN is repeatedly applied

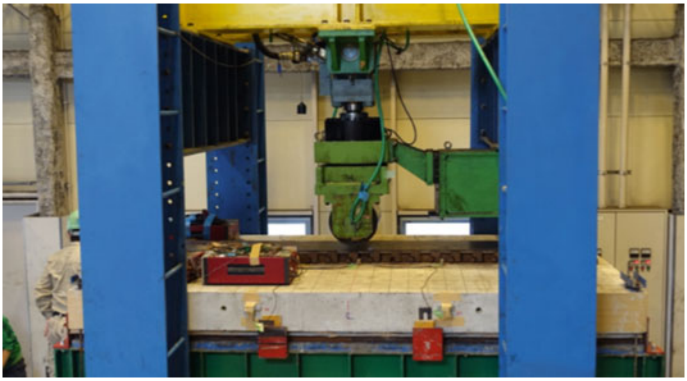

Fig. 27.2 Wheel loading apparatus

Fig. 27.3 Loading step

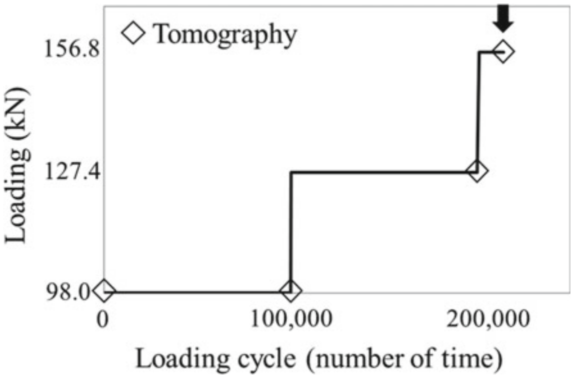

for 100 k times for the first step. Then the load is increased to 127.4 kN and repeatedly applied for another 100 k times. Finally, the load of 156.8 kN is applied until the limitation of fatigue failure. The eventual load cycles in this experiment is 214,194 times. In this study, static loads are each applied just before going to the next step i.e., after load cycles of 100 k times of 98 kN, the load is unloaded and reloaded again to 98 kN with static manner. The same goes for the further cases of 127.4 kN and 156.8 kN. The specimen of concrete slab is 3.0 × 2.0 × 1.6 m with a mixture proportion as in Table 27.1. The compression strength is 20.7 N/mm^2. A central area of the top surface (see the bold blue rectangle in Fig. 27.4) is kept saturated by continuous water pouring to acertain height. Strain gauges are embedded in the specimen. Arrangement of AE sensors and excitation locations are demonstrated as in Fig. 27.4. 36 AE sensors of 60 kHz resonance are arranged onto the specimen, namely 10 for top, 18 for bottom and 8 for sides. For elastic wave tomography, excitations are made by a 35 mm diameter. Steel ball for 18 points on the top as avoiding the loading area depicted by a green broken rectangle, and 28 points on the bottom. Measurement of elastic wave excitations are conducted three times: before loading, after 100 k load applications, after 200 k load applications, and after failure. Detected signals by the sensors are amplified by 40 dB at preamplifier and acquired by the monitoring system of 48-channel Express-8 (Physical Acoustics Corp) with a 1 MHz sampling rate.

27.4 Results and Discussions

Density of the wave paths in expected aggregation area becomes smaller because excitation points cannot be set under the wheel guide plate. So the lower of the resolution resulted by the elastic wave tomography. To understand this fact as well as to know the analytical resolution of the tomography, elastic wave/ray paths formed by combinations between excitation points and sensor positions are depicted as in Fig. 27.5. Accordingly, to suffice the density of wave paths beneath the loading area, AE sources obtained during the static loading applied after every wheel loading cycles are utilized in addition to the data derived by the elastic wave tomography.

Tomograms by each step are shown in Fig. 27.6. In the case before loading (see 0 cycles), areas of slightly small velocity of 3300 m/s are obtained, whereas overall velocity exhibits 4400 m/s, and therefore the specimen is appeared to be intact at this moment. In the case of 100 k cycles, the areas of small velocity less than 3000 m/s become more distinctive and continuously emerged in the transversal direction, resulting in the average velocity of 4000 m/s. In the case of 200 k cycles, areas of small velocity less than 3000 m/s widely evolve to the right sides of interest, and damage areas evaluated by the velocity less than 2700 m/s, which is concluded by our past paper [2], are observed. As areas demonstrating large velocity of more than 4000 m/s are still remained in places at this step, this appears to be the stage where damage and intact areas are mixed. After the fatigue limit, middle and upper areas are damaged widely of interest. In consideration of the velocity decrease with

Table 27.1 Mixture proportion of concrete slab

Max. gravel size (mm)	Slump (cm)	W/C (%)	Volume ratio of sand s/a (%)	Air (%)	Unite weight per 1 m^3 concrete (kg/m^3)				
					Water: W	Cement: C	Sand: S	Gravel: G	Admixture
20	12	64.3	46.6	4.5	178	277	839	1055	2.27

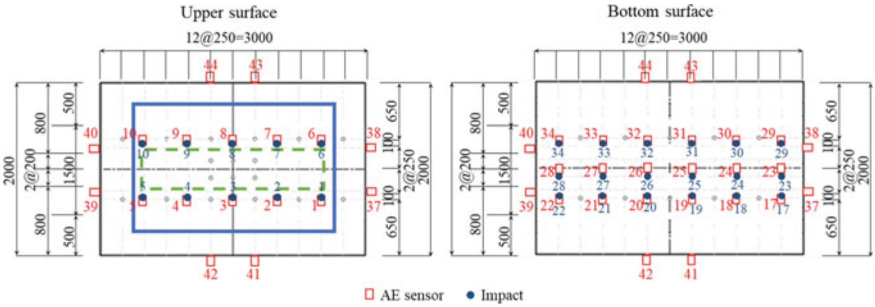
Upper surface
12@250=3000
Bottom surface
12@250=3000
AE sensor
Impact

Fig. 27.4 Location of AE sensors and excitation points denoted by red squares and blue circles

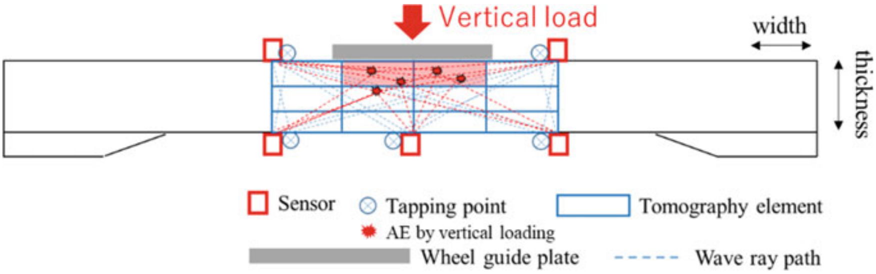
Vertical load
width
thickness
Sensor
Tapping point
Tomography element
AE by vertical loading
Wheel guide plate
Wave ray path

Fig. 27.5 Ray paths in the specimen

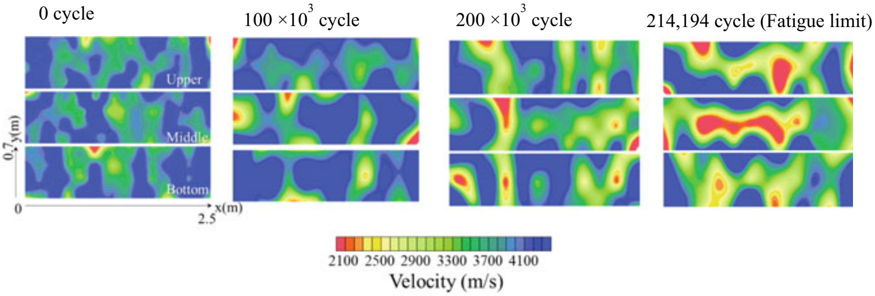

Fig. 27.6 Tomograms by elastic wave tomography combined with AE activity

steps as well as specific distributions of small velocity, it is implied that the damage is only generated at the specific areas. Comparison of the velocity distribution of RC slab in the dry and infiltration conditions is shown in Fig. 27.7. According to the result, low velocity area spreads with loading step in dry condition. On the other hand, it seems that velocity area in part is getting down in dry condition. In addition, the number of steps in the wet condition that reach the fatigue limit is about half times of the dry condition.

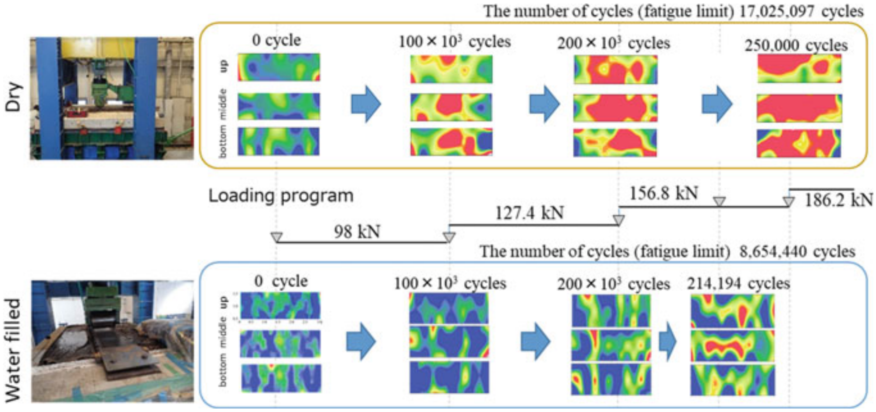

Fig. 27.7 Comparison of the velocity distribution of RC slab in the dry and infiltration conditions

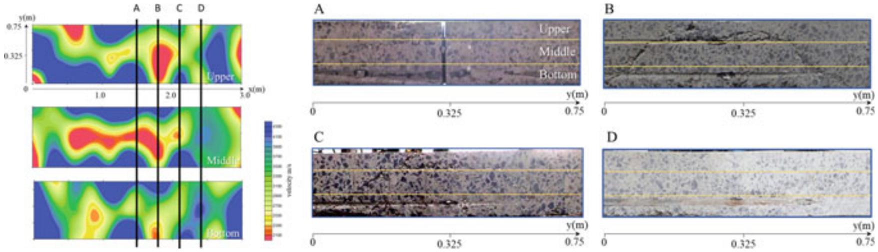

Fig. 27.8 Tomograms in the fatigue limit and sectional phots after the wheel loading test

The cross section of the RC slab in fatigue limit in dry condition and the velocity distribution at that time are Shown in Fig. 27.8. In section A of Fig. 27.8, the aggregation area can be appeared in the boundary between upper and middle layers, corresponding well to the areas showing the small velocities less than 2700 m/s in section A in the fatigue limit of Fig. 27.8. Specifically, the area suggesting the aggregation assumed by the tomogram has velocities smaller than 2300 m/s. In section B of Fig. 27.8, extraordinary aggregation can be observed in the boundary between the upper and middle layer, and moreover diagonally developed cracks heading to the bottom are distinctly observed. In addition, the cracks lay more in the left side namely 0–0.325 m in section B of Fig. 27.8. Surprisingly these crack conditions accord pretty well to the concentrated damage areas evaluated by tomogram in section B in the fatigue limit of Fig. 27.8 (see 0–0.325 m in Y). In section C, the area of aggregation becomes unclear and more difficult to identify the area from section D in Fig. 10. From tomograms of these sections C and D, the same estimation of damage can be conducted i.e., slight damage in section C and no remarkable damage in section D. Through the above comparison between sectional observation and corresponding tomograms, it can be concluded that the location of aggregation can be reasonably estimated by the velocity smaller than 2300 m/s, which is obtained from the tomography with sufficient density of wave/ray paths. For the in-situ bridge deck evaluation, when sufficient AE sources are obtained, spreading over the area of measurement, resulting in a reliable ray paths density, identification of aggregation can be implemented with the AE and elastic wave tomography.

27.5 Conclusions

In this study, to know the fatigue failure progress of RC deck in consideration of water infiltration, a wheel loading test of a RC slab filled with water on the surface is carried out with elastic wave tomography combined AE activity. The obtained results are shown below.

1. According to tomograms by steps of wheel loading test with water, low velocity zones continued to transversal direction until fatigue limit. As a result, in the case of water infiltration, fatigue damage progresses from the cracks developed initially.
2. In tomographic approaches, elastic wave/ray path density is crucially important to provide accurate and reliable results. By the tomograms obtained by the combination of elastic wave tomography and AE tomography, Aggregation which is one of the most nuisance forms of the damage peculiarly in concrete slabs, is successfully evaluated as velocity areas smaller than 2300 m/s.

Acknowledgements This study is implemented under the support of The Cross-Ministerial Strategic Innovation Promotion Program (SIP). The experiment was conducted in College of Engineering, Nihon University. We would like to express our sincere appreciation to Prof. Iwaki of Nihon University for his experimental support as well as vital discussions.

References

1. The Ministry of Land, Infrastructure, Transport and Tourism: Annual report 2015 on Maintenance of Roads, Japan, 2015, https://www.mlit.go.jp/hakusyo/mlit/h26/hakusho/h27/index.html (in Japanese)
2. T. Shiotani, H. Ohtsu, S. Momoki, H.K. Chai, H. Onishi, T. Kamada, Damage evaluation for concrete bridge deck by means of stress wave techniques. J. Bridge Eng. **17**, 847–856 (2012)
3. Y. Kobayashi, T. Shiotani,Seismic tomography with estimation of source location for concrete structure, in*Structural Faults and Repair 2012* (CD-ROM, Edinburgh, Scotland, 2012)
4. T. Shiotani, H. Asaue, T. Nishida, T. Maeshima, Y. Tanaka, Evolution of fatigue damage in wheel-loading tests evaluated by 3D elastic-wave tomography. J. Disaster Res. 487–495 (2017)
5. Y. Kobayashi, T. Shiotani, H. Shiojiri, Damage identification using seismic travel time tomography on the basis of evolutional wave velocity distribution model, in *Proceedings of Structural Faults and Repair 2006* (CD-ROM, 2006)

6. T. Shiotani, S. Yoshimi, T. Kamada, H. Ohnishi, S. Momoki, H. K. Chai, Visualization of fatigue damage for concrete bridge deck with stress wave techniques, in *Structural Faults and Repair 2010* (CD-ROM, 2010)

Chapter 28
Research on Acoustic Emission Technology for Tank Floor Under Interference of Nitrogen Sealing System

He Yan, Gongtian Shen, Liang Du, Wenjing Zhao, and Shu Xing

Abstract Noise interference caused by the nitrogen seal system is an important factor affecting the acoustic emission inspection effect of the floor of the atmospheric storage tank. How to effectively reduce the impact of nitrogen seal system noise on the detection results and obtain effective and real acoustic emission data is the key to the acoustic emission inspection of this kind of equipment. In this paper, the acoustic emission inspection system based on three point positioning algorithm is used, and three kinds of arrangements are used, including the main acquisition sensor, the main acquisition sensor + part guard sensor, the main acquisition sensor and all the guard sensors, and acoustic emission inspection is carried out for the atmospheric storage tank with nitrogen seal system, and the protection sensor is verified. Suppressing effect and optimizing arrangement of noise signal in nitrogen sealing system. The test results show that the strong noise caused by the nitrogen seal system can be effectively filtered through the layout of the main acquisition sensor and the guard sensor. It is of practical significance to solve the acoustic emission inspection problem of the atmospheric storage tank under the on-line condition of the nitrogen seal system and improve the acoustic emission detection ability of the floor of the atmospheric storage tank.

With the rapid development of petrochemical industry and the increasing demand for energy, petrochemical raw material reserves have attracted the attention of all countries in the world. At present, China has built dozens of national strategic and commercial petroleum reserves. Storage tank is an important storage equipment for crude oil and product oil. Although the failure probability is low, the failure consequence is serious. Leakage of large atmospheric storage tank will not only cause environmental pollution such as soil, river and groundwater, but also easily cause fire, explosion, and unimaginable consequences. According to relevant data, 80% of tank accidents are caused by corrosion and perforation leakage of bottom plate. The detection methods for floor leakage are generally divided into open tank detection

---

H. Yan (✉) · G. Shen · L. Du · W. Zhao · S. Xing
China Special Equipment Inspection and Research Institute, Beijing 100029, China
e-mail: Peteryan76@126.com

© The Author(s), under exclusive license to Springer Nature Singapore Pte Ltd. 2021

G. Shen et al. (eds.), *Advances in Acoustic Emission Technology*, Springer Proceedings in Physics 259, https://doi.org/10.1007/978-981-15-9837-1_28

and online detection. Open tank inspection is a method to detect the bottom plate of the tank after the tank is shut down and cleaned by using the macro, magnetic leakage, thickness measurement and other non-destructive testing methods. Due to the process of tank opening detection, such as shutdown and tank cleaning, this method will require a lot of manpower, material and financial resources. Relevant statistics show that at present, only 9% of the open tanks do have serious corrosion or leakage, and the open tank detection of other tanks has different degrees of waste. In view of the problems such as high cost of open tank maintenance, serious over time storage tank, and severe impact of imported crude oil with low oil price on tank corrosion, it is urgent to detect and evaluate the tank with a fast and online detection method. With the popularization and application of acoustic emission detection technology in the corrosion detection of the bottom plate of atmospheric storage tank, more and more atmospheric storage tanks first use acoustic emission detection technology to classify and grade the bottom plate, and then select the targeted open tank detection according to the rating results. This method greatly overcomes the time-consuming caused by blind open tank detection such as shutdown replacement, cleaning the bottom of the tank, point by point scanning inspection Lack of effort [1, 2].

The so-called acoustic emission is the phenomenon of transient elastic waves generated by the rapid release of energy from local sources in materials, also known as stress wave emission or micro vibration activity [3, 4]. In an ideal situation, the acoustic emission detection of the bottom plate of atmospheric storage tank is to use the acoustic receiving sensor arranged at a certain height from the bottom plate to receive the corrosion signal from the bottom plate, and use the coaxial cable to transmit the acoustic signal from the receiving sensor to the data processing center. The processing center positions and correlates the collected signal according to a certain calculation method, and finally gives different correlation results. The inspector grades the results according to relevant standards, determine the corrosion condition of the bottom plate of the tank to be inspected, and put forward reasonable maintenance strategies. However, when using AE online detection, a lot of noise will seriously affect the acquisition, analysis and discrimination of real signals, such as wind and rain will affect the acquisition of signals; vibration and electromagnetic interference will affect the analysis and discrimination of signals. For light oil and volatile, flammable and explosive media, the corresponding nitrogen sealing system is often used on the top of the tank during storage, which can not only prevent the top of the tank from emitting combustible gas, but also prevent the air from entering the tank, forming an explosion [5–7]. Nitrogen sealing system can effectively reduce the volatilization of organic gases and prevent the pollution of toxic gases to the surrounding environment. However, if nitrogen sealing system is used, noise interference caused by pressure change will occur when nitrogen is replenished. If this interference source cannot be effectively prevented or eliminated in the detection, the detection result will not reflect the real situation of the tested object, so that how to effectively reduce is the key to obtain effective and real acoustic emission data for the impact of noise of nitrogen sealing system on the test results. In this paper, the acoustic emission detection system based on three-point positioning algorithm is used to detect the on-line acoustic emission of atmospheric tank with nitrogen seal system

Table 28.1 Basic information of atmospheric sewage tank for test

Serial number	Floor material	Tank type	Diameter (m)	Height (m)	Floor thickness (mm)	Storage medium	Date of putting into use
5412A	Q235-B	Vault	20	17.7	12.0 (edge plate)	Sewage	2005
					10.0 (Middle plate)		

by using three sensor arrangements: main collection sensor, main collection sensor + part of guard sensor and main collection sensor + all guard sensors, respectively, to verify the effect and advantages of the guard sensor in suppressing noise signals of nitrogen seal system In order to solve the problem of acoustic emission detection of atmospheric storage tank under the condition of nitrogen sealing system online, and expand the application scope of acoustic emission online detection of atmospheric storage tank floor.

28.1 Test Object and Instrument

28.1.1 Test Object

The tank selected in this test is a sewage tank that has been in service for 12 years. See the following Table 28.1 for specific parameters.

28.1.2 Test Instrument

(1) An acoustic emission detection system (Samos) with guard sensor;
(2) Low frequency sensor, frequency range: 20–100 khz;
(3) Data connection line and coaxial cable;
(4) 0.5 mm HB lead core and standard lead breaking equipment.

28.2 Test Plan

This test adopts three forms: no guard sensor, main sensor + partial guard sensor and main sensor + global guard sensor. The arrangement height of the main acquisition sensor is 300 mm from the bottom plate, and the arrangement height of the guard sensor is 1300 mm. The test process is as follows:

28.2.1 System Building

The 16 sensors are distributed on the wall plate of the inspected tank in two layers (the distance between layers is 1 m), and the location and number are shown in Figs. 28.1 and 28.2. Connect the sensor to the acoustic emission host with coaxial cable and data

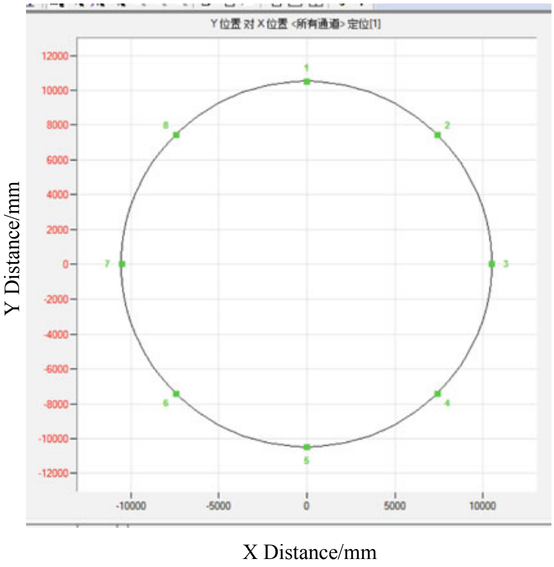

Fig. 28.1 Layout of main sensor

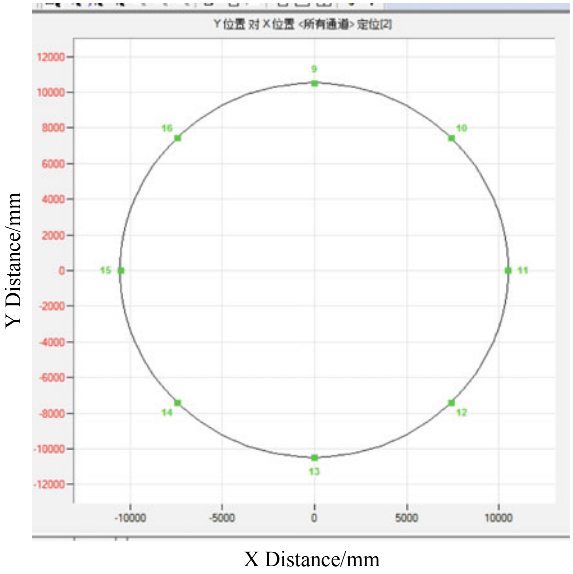

Fig. 28.2 Layout of guard sensor

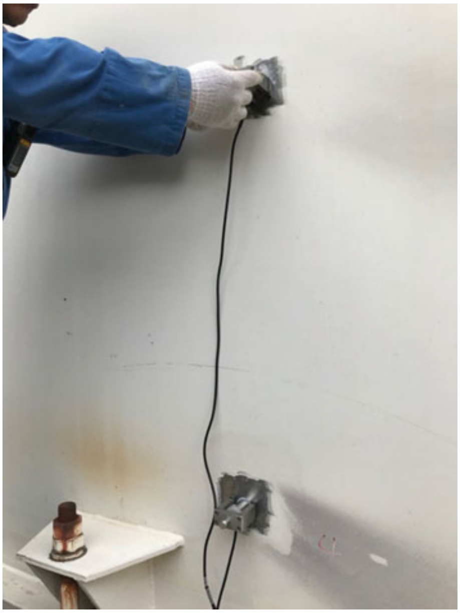

Fig. 28.3 Location of main sensor and guard sensor

connection line, connect the power line and ground zero line, open the host preheating for 10 min, enter the data acquisition interface, set the relevant parameters, and collect the corresponding data under three different sensor arrangements.

28.2.2 Sensor Sensitivity Test

The sensitivity of the installed sensors is tested one by one by using the lead breaking method specified in the standard. Considering the small difference in the length of the coaxial cable, the change of the average peak amplitude of each sensor should not exceed ±4 dB.

28.2.3 Function Test of Guard Sensor

According to the relevant provisions of standard JB/t10764, the acoustic emission on-line test is carried out under three working conditions: no guard sensor (8 main sensors), partial guard sensor (8 main sensors + 4 guard sensors) and global guard sensor (8 main sensors + 8 guard sensors). The test time is not less than 30 min each time, and the corresponding collected data is recorded.

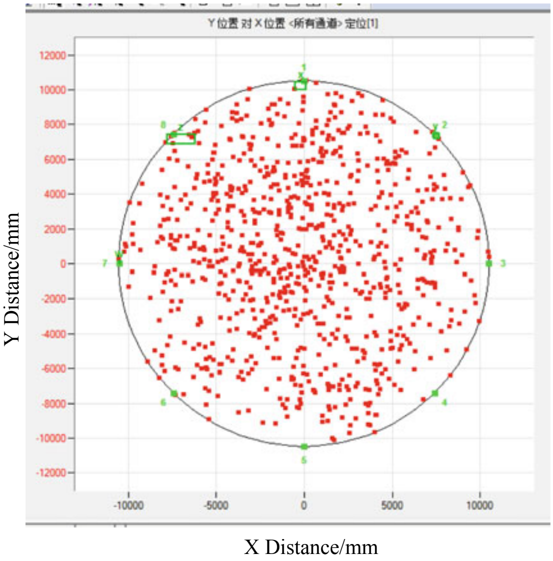

Fig. 28.4 Event plane location without guard sensor

28.3 Data Collection and Result Analysis

28.3.1 Data Acquisition Without Guard Sensor

In order to test whether the installed guard sensor has a certain blocking effect on the noise from the nitrogen sealing system, firstly, the acoustic emission signal acquisition is conducted for the tested object without guard sensor. During the 30 min acquisition process, 4180 events are formed, with an average of 139 events per minute. The relevant acquisition results are shown in Figs. 28.4, 28.5 and 28.6.

28.3.2 Data Acquisition Under Some Escort Sensors

In order to test whether it can be blocked by the installation of local guard sensors, the local guard is used for data collection in this test. In the 30 min collection process, 678 events are formed, with an average of 22.6 events per minute. The relevant collection results are shown in Figs. 28.7, 28.8 and 28.9

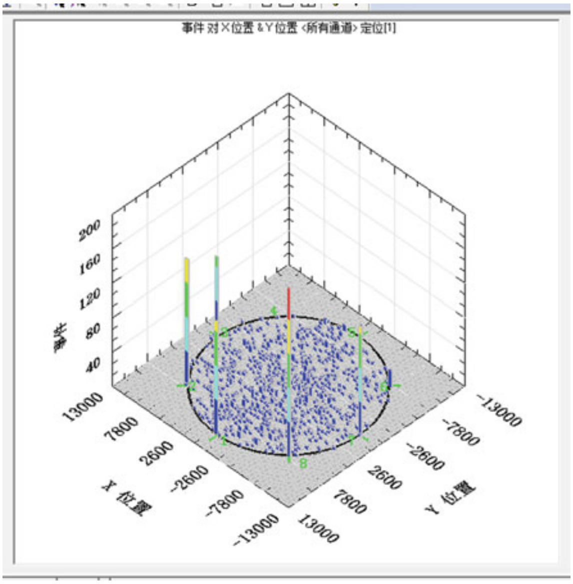

Fig. 28.5 Event stereo location without guard sensor

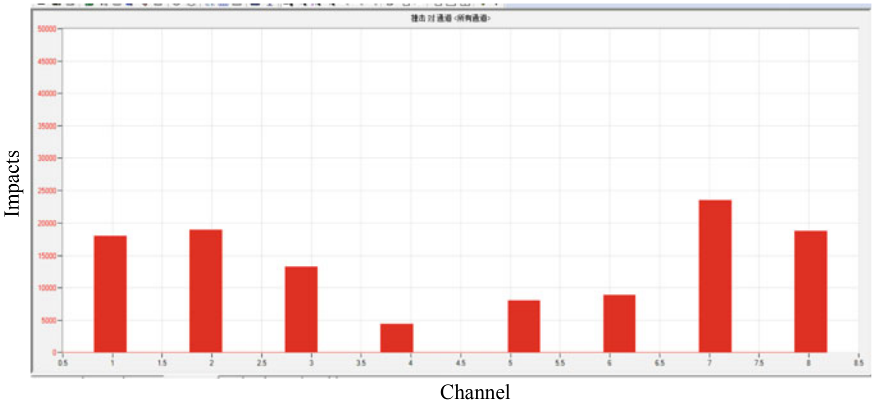

Fig. 28.6 Impact number of channel without guard sensor

28.3.3 *Data Acquisition Under Global Protection Sensor*

The noise from the nitrogen sealing system is blocked by a global guard sensor. In the 30 min acquisition process, 29 events are generated by the main sensor, with an average of 1 event per minute. 1924 events are generated by the guard sensor, with an average of 64.1 events per minute. The relevant acquisition results are shown in Figs. 28.10, 28.11, 28.12, 28.13 and 28.14.

Fig. 28.7 Event plane location under some guard sensors

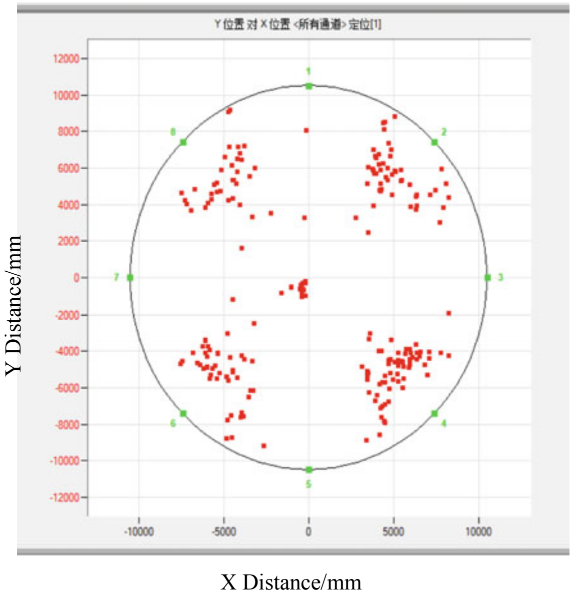

Fig. 28.8 Event stereo location under some guard sensor

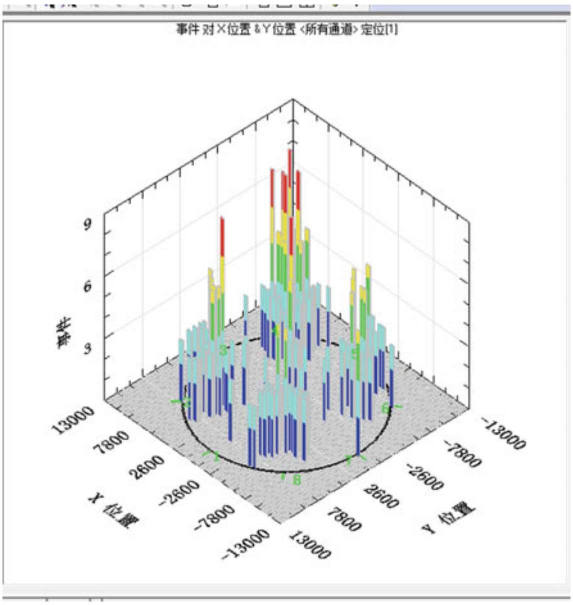

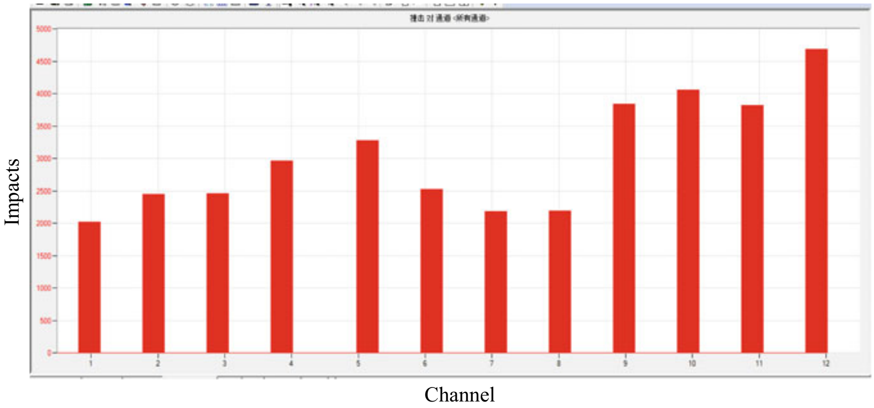

Fig. 28.9 Impact number of channel under some guard sensor

Fig. 28.10 Event plane location under global guard sensor

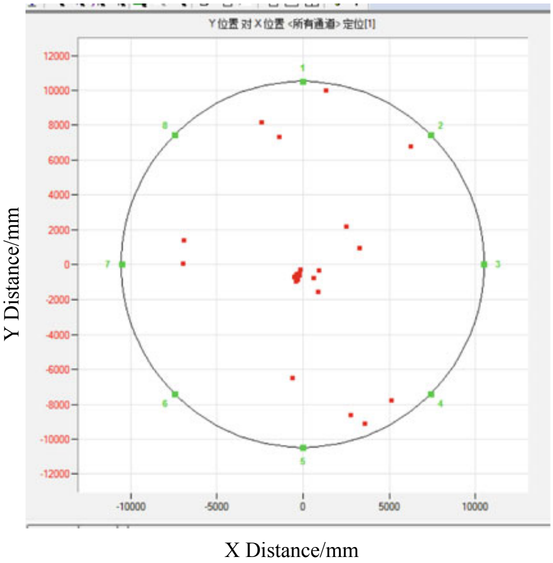

28.3.4 Result Analysis

(1) From Figs. 28.4, 28.5, 28.7, 28.8 and 28.10, 28.11, it can be seen that for the same tank and the same operation condition, the number of event location under three different working conditions decreased significantly, from 139 per min to 1 per minute on average. It can be seen that the guard sensor can effectively block the noise from the nitrogen sealing system;

(2) It can be seen from Figs. 28.4 and 28.7 that the location map in the mode of local guard sensor presents petal shape, that is, there is no location event in the

Fig. 28.11 Event stereo location under global guard sensor

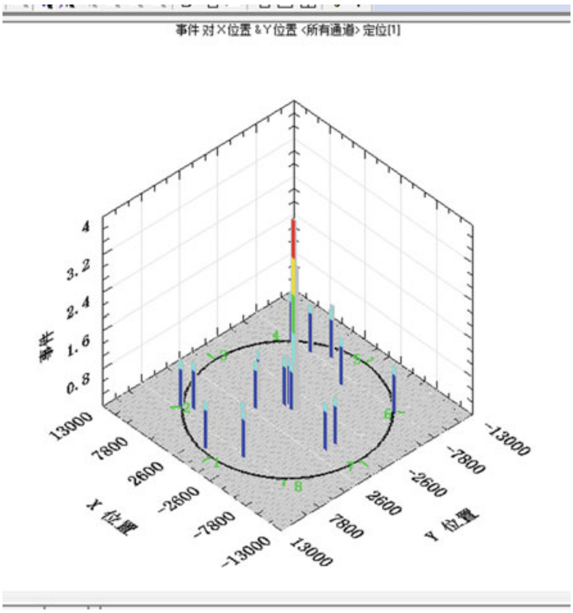

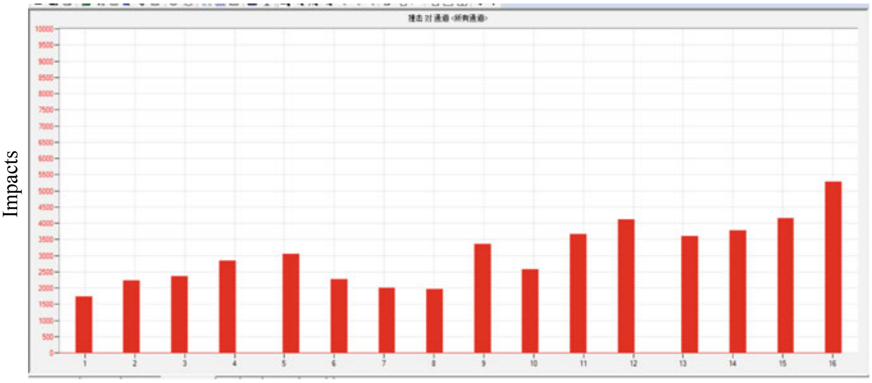

Fig. 28.12 Impact number of channel under global guard sensor

part with guard sensor and there are location events in the part without guard sensor. It can be seen that the coverage of the guard sensor is the same as that of the main sensor. When applying the guard sensor, one-to-one correspondence with the main sensor is needed to play the role of full guard.

(3) It can be seen from Figs. 28.9 and 28.12 that there is a slight difference between the channel impact number of the guard sensor and that of the main sensor, but it can be seen from Figs. 28.10 and 28.13 that the number of positioning events of the guard sensor is much higher than that of the main sensor. It can be seen

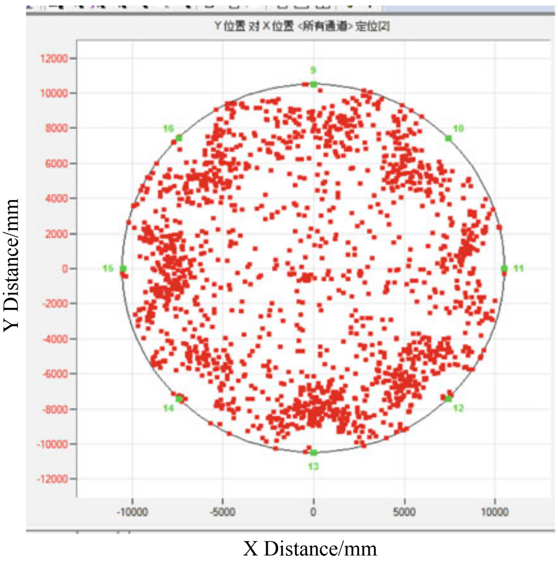

Fig. 28.13 Event plane location of guard sensor under global guard

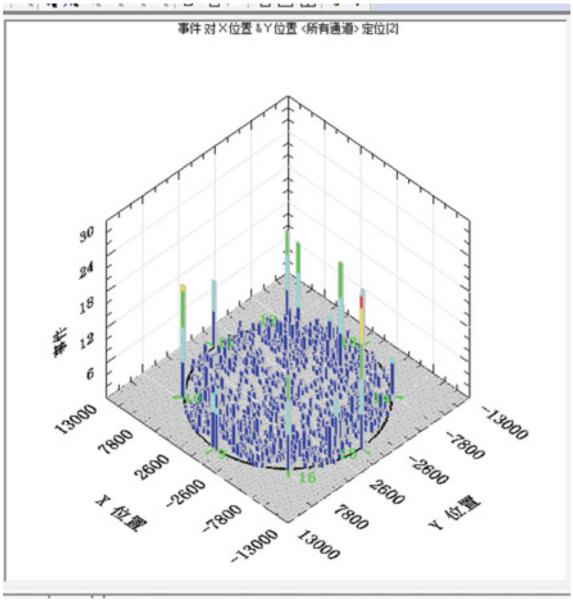

Fig. 28.14 Event stereo location of guard sensor under global guard

that the function of the guard sensor is not to block the signal acquisition of the main sensor, but to block the positioning of the main sensor. Therefore, it is not recommended to use the area positioning method when using the guard sensor.

28.4 Conclusion

1. Using the guard sensor can effectively block the noise from outside the guard sensor, so that the on-line acoustic emission detection problem under the noise interference can be solved by using the guard sensor;
2. The coverage of the guard sensor is the same as that of the main sensor. Therefore, the number of guard sensors should be the same as the number of the main sensors;
3. When using guard sensors for on-line acoustic emission detection, it is not recommended to use regional positioning method for conclusion evaluation.

Acknowledgements This study was financially supported by the research project of Research on the key technologies of social emergency service system (2018YFC0810604).

References

1. B. Li Yi, L.Y Sun, et al., On line acoustic emission inspection method for large normal pressure storage tank bottom. J. Tianjin Univ. **41**(1), 11–16 (2008)
2. P. Sosoon, K. Shigeo, K. Kenji, et al., AE source and relation between AE activity and rate of corrosion of oil tank bottom plate on acidic soils. Mater. Trans. **46**(11), 2490–2496 (2005)
3. ASME-E1316-06a, Standard terminology for nondestructive examinations[s]
4. JB/T10764-2007, Non-destructive testing—acoustic emission testing and evaluation of atmospheric pressure metal storage tanks[s]
5. X.f. Liang, Design and application of nitrogen sealing system for raw material storage tank in chemical industry. Ningbo Chem. Ind. (1), 27–29 (2013)
6. L.l. Fan, X.j. Yan, Application of nitrogen sealing technology in light oil tank. Sci. Technol. Inf. 33, 86–87 (2015)
7. C.f. Fan, M.h. Zhang, Design of nitrogen sealing system and calculation of breathing gas volume for low pressure storage tank of combustible medium. Shandong Chem. Ind. **46**(6), 114–115 (2017)

Chapter 29
Difference Analysis of Acoustic Emission Testing Methods on Storage Tank Floor

Huatian Xu, Yewei Kang, Zhenghong Guo, Wei Yang, Jinggang Cao, and Linjie Duan

Abstract Acoustic emission testing (AE) on storage tank floor is a beneficial method for tank owners to obtain information about possible corrosion or even leakage of the floor without opening the tank, so it is widely used. However, it can be seen from the literature published internationally that different countries or different companies have great differences in parameter setting and data evaluation methods when performing AE testing on the oil tank floor, which can lead to different results. Nowadays there is no universal standard on AE test procedure and data evaluation methods for oil tank floor testing. The purpose of this paper is to summarize the difference in AE testing of tank floor, especially in parameter setting and data processing method, in order to provide a guideline for peers.

29.1 Introduction

Aboveground storage tanks (ASTs) are widely used in petroleum industry. PetroChina Pipeline Company has more than 200 large-scale ASTs and there are more tanks will be constructed in next several years. If it carries on the conventional tank maintenance plan, a lot of money will be wasted, because there are many "good" tanks found during the maintenance [1]. So how to evaluate the corrosion situation of tank floor and provide maintenance guidance for storage tank floors is an urgent problem.

AE provides an advanced method to inspect the tank floor while filled with the oil and enables tank operator to monitor tank condition in-service [2]. AE are stress waves produced by sudden release of the elastic energy in stressed materials. When defect-related processes such as corrosion, crack growth, hydrogen blistering, and leakage and so on take place in and on the tank floor, stress waves will be produced.

H. Xu (✉) · Y. Kang · Z. Guo · J. Cao · L. Duan
PetroChina Pipeline R&D Center, Langfang 065000, China
e-mail: xuhuatian@petrochina.com.cn

W. Yang
China Petroleum Pipeline Engineering Corporation, Langfang 065000, China

© The Author(s), under exclusive license to Springer Nature Singapore Pte Ltd. 2021

G. Shen et al. (eds.), *Advances in Acoustic Emission Technology*, Springer Proceedings in Physics 259, https://doi.org/10.1007/978-981-15-9837-1_29

The sensors mounted on the external surface of tank near the tank floor can detect these stress waves, and the corrosion situation of the tank floor can be priority classified by data analysis.

However, it can be seen from the literature published internationally that different countries or different companies have great differences in data acquisition and data evaluation methods when performing AE testing on the oil tank floor, which can lead to different results. Nowadays there is no universal standard on AE test procedure and data evaluation methods for oil tank floor testing. The purpose of this paper is to summarize the difference in AE testing of tank floor, especially in parameter setting and data processing method, in order to provide a guideline for peers in performing AE testing on storage tank floors.

29.2 Methods

AE testing technique consists of two steps: (1) Testing procedure to set up and to perform the measurement. (2) Data evaluation and grading the corrosion condition of the tank floor. By summarizing domestic and foreign literature, we have compared the similarities and differences of data acquisition and evaluation in these 2 steps in AE testing.

29.2.1 Difference Analysis of Data Acquisition

The key to a successful test is always a proper set-up. In the process of data acquisition, the main content is testing procedure to set up and to perform the measurement, so we have summarized five aspects that can affect the AE testing of the tank floor according to the open literature.

29.2.1.1 Requirements of Liquid Level of the Tank

The requirement of liquid level of the tank is inconsistent. Such as in inspectahire company [3], they fill oil to the tank at least 50% full before testing. In Iran [2], they need the tank 70% full. And in the standard of ASTM [4], tank should load oil to its maximum capacity, and in Chinese standard JB/T 10764-2007 [5], the liquid level of the tank should be loaded to its 85–105% of the operation level.

In PetroChina Pipeline Company, tank was filled with product level of 80% which provides the required load pressure for AE testing. We have had an experiment, the results is that number of signals decreased 37% if the liquid level from 81 to 60% full, as shown in Fig. 29.1. So it is important that liquid level of the tank should be consistent with the data evaluation method.

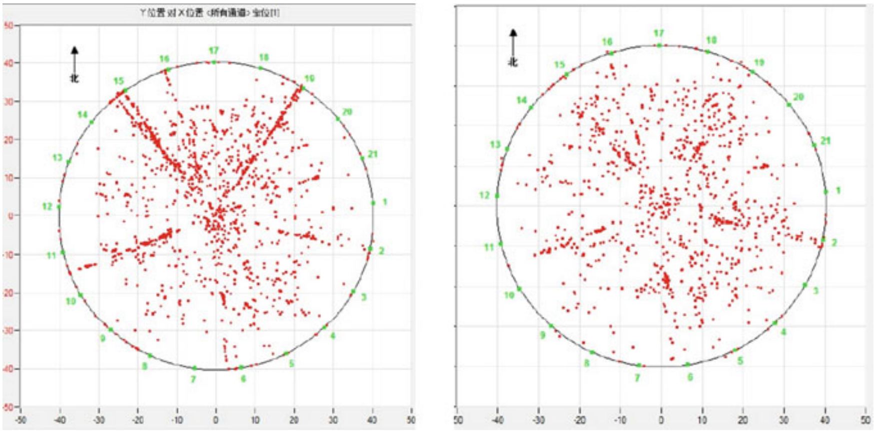

a) Liquid level at 81% full

b) Liquid level at 60% full

Fig. 29.1 Number of signals decreased when liquid level was set from 81–60%

29.2.1.2 Height Setting Requirement of Guard Sensor

The height setting requirement of guard sensors is different. In Austria, the height of guard sensors is set from 3 to 5 m above the tank floor [1], and in Britain standard the height of guard sensors is from 4 to 6 m above the tank floor [6]. In Japan, the author Shigenori yuyama in his paper [7] suggests the height of guard sensors is 1–3 m above the main sensors.

As shown in Fig. 29.2, it is an experiment on the fixed roof of tank that number of signals decreased when the tank had guard sensors. According to our research,

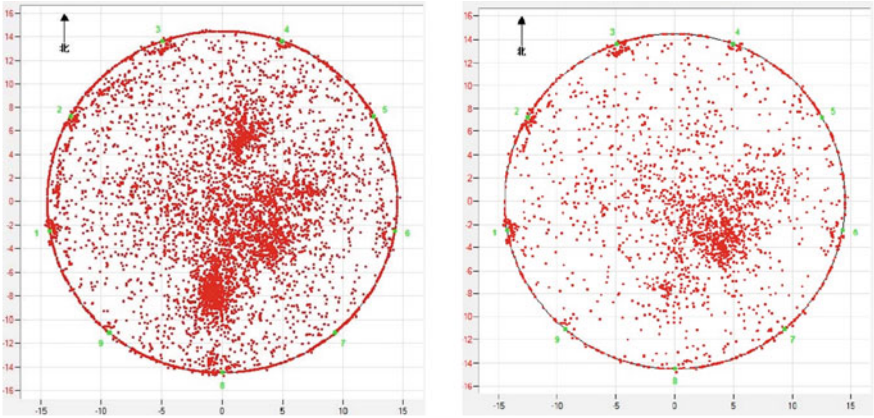

a) No guard sensors

b) Using guard sensors

Fig. 29.2 Signals decrease when use guard sensors

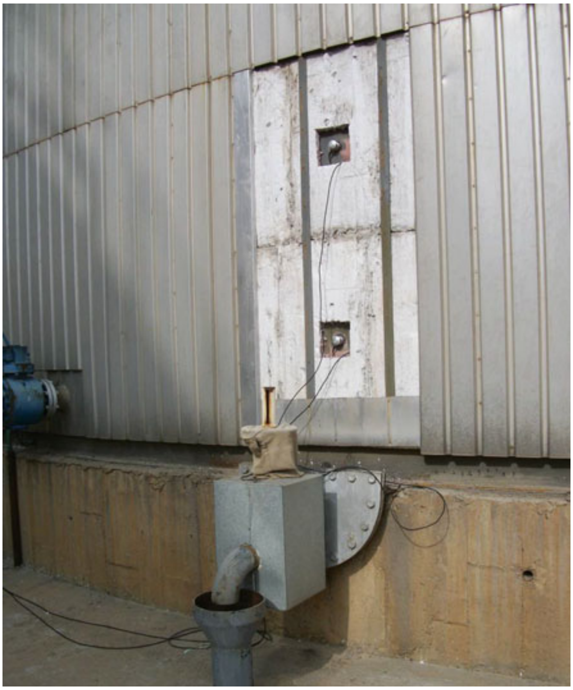

Fig. 29.3 Position of the guard sensor and the main sensor

the height of guard sensors are 1–2 m by the results of field testing in PetroChina Pipeline Company. The advantage of this height is easy to install guard sensors.

In most situations, fixed roof of tank should have guard sensors in order to eliminate noise from condensation drops. Because the liquid drops can be formed on the tank inner roof due to the change of temperature, when it drops to the surface of liquid, the noise is produced. Figure 29.3 shows the relative position of the guard sensor and the main sensor in field testing.

29.2.1.3 Height Setting Requirements of Main Sensors

Height setting of main sensors in most companies is 1 m [1, 2, 7]. In the Chinese standard JB/T 10764-2007 [5], AE sensors should be installed on the outside surface of the tank wall approximately 0.1–0.5 m from the bottom, we think this height is a bit low. And the reasonable height is from 0.5 to 1 m in PetroChina Pipeline Company, which ensures that the overall corrosion of the tank floor is evaluated even in the presence of sludge and heating coil.

29.2.1.4 The Rest Time Before Inspection

The oil stored in the tank is fluctuating when the oil is pumped into or out the tank, and a large amount of noise signals will be received by the AE sensors on the surface of the tank wall, so it will affect the evaluation results of the corrosion state of the tank bottom.

The rest time of the oil before inspection is more than 12 h in most companies. In ASTM, the suggested rest time for oil is 24 h [4]. In PetroChina, the time is 12–24 h, and crude oil needs a longer period of time for rest, light oil is allowed a shorter period of time.

29.2.1.5 Data Acquisition Time

The data acquisition duration varies greatly in different companies. Such as in Austria, the acquisition duration is 24 h, and in European standard [6] is at least 1 h. Some companies suggest the data acquisition duration is 2 h [8]. In PetroChina, acoustic emission testing experiments show that most of the data collected during the daytime are affected by noise signal by comparing the AE data collected during day time with the one collected during night time.

So we collected 12 h of the data at night in order to avoid noise interference in the daytime, such as the irradiation of the sun, vehicles, and so on.

29.2.2 Difference Analysis of Data Evaluation

Data evaluation has much difference in different countries or companies, so we have summarized four aspects that affected the accuracy of the evaluation results respectively.

29.2.2.1 Data Processing Method is Different

Data processing methods are different according to the published papers. Paper [9] said that overall corrosion grading is based on the total number of AE hits accumulated during the test, and potential leak sources are identified by clusters of events.

Paper [10] said that AE parameters like signal duration or peak amplitude were used for data processing. And one weak point of this approach was that the dependence of these parameters on the distance between AE source and sensors had to be estimated.

Paper [8] said that the most important parameter is the number of registered hits, which depends on tank size, viscosity of the product, applied threshold, etc.

Table 29.1 Data processing method with leakage probability and events activity

Leakage probability	Events activity				
	I	II	III	IV	V
I	A	B	B	C	D
II	B	C	C	C	D
III	C	D	D	E	E
IV	D	E	E	E	E

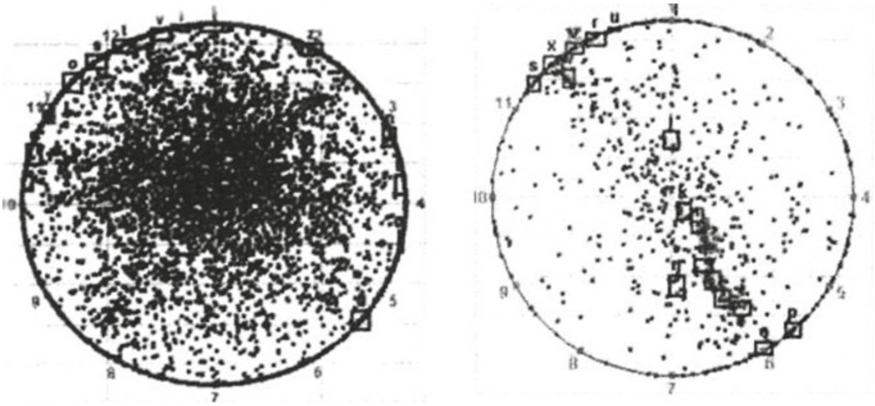

Fig. 29.4 Different location graph are all rated as grade C

In PetroChina, we use leakage probability and events activity to evaluate the corrosion severity of the tank floor, as shown in the Table 29.1.

29.2.2.2 The Grade Criteria is Different

Data evaluation results show that the location graph is different for the same AE grade, such as these four different pictures in Fig. 29.4 are all rated as grade A.

In two different pictures of events activity are all evaluated as grade C.

So the rating of the AE results cannot just been evaluated by the event location graph.

29.2.2.3 The Number of Grades of AE Results is Different

The number of grades of AE results is different. In ASTM [4], the data evaluation results are divided into 3 grades. Paper [1] shows data evaluation results into 4 grades [1]. And many companies have divided the AE results into 5 grades [2, 8, 9].

Table 29.2 Recommended service period in different companies

Grade	Description	Recommended service period		
		PetroChina Pipeline Company	Company B	Company C
A	Very minor/no damage	5 years	4 years	4 years
B	Minor damage	3 years	3 years	2 years
C	Intermediate damage	2 years	2 years	1 year
D	Active damage	Require internal inspection in 1 year	1 year	0.5 year
E	Highly active damage	Internal inspection immediately	0.5 year	Require internal inspection

So we should use the reasonable method of data evaluation to divide the number of AE grade so as to provide practical maintenance advice for tank owners.

29.2.2.4 Recommended Service Period is Inconsistent

The recommended service period is inconsistent. There are three different recommended service period obtained from the published papers [1, 2, 7], as shown in Table 29.2.

So we should consider the basis theory of recommended service period for tank re-inspection in the future.

29.3 Conclusion

1. Height setting of liquid level, data acquisition time, data processing method and so on can affect the accuracy of AE inspection of the tank floor.
2. Reliable AE evaluation can be a reality if the inspectors had a lot of experiences, and the suitable data analysis method and data acquisition methods were adopted.
3. Comparing between AE in-service inspection and non-destructive testing on aboveground storage tank floors will make AE testing more and more accurate in the future.
4. It is important to summarize the scientific and reasonable practices of AE testing in the petroleum industry, and to form a unified standard on data acquisition and data evaluation in order to promote the application of AE on tank floor evaluation.

References

1. G. Lackner, P. Tscheliesnig, Field testing of flat bottomed storage tanks with acoustic emission—a review on the gained experience, EWGAE 2004, Lecture 18.E
2. H.M. Javadi, A. Broumandnia, H. Sadeghi, Evaluation of acoustic emission inspection of oil tank floor via tank bottom plates thickness measurement. J. Mech. Res. Appl. **4**(3), 37–44 (2012)
3. Inspectahire company, Tank assessment with acoustic emission. https://www.inspectahire.com. 11/5/2018
4. ASTM E1930-02, Standard Test Method for Examination of Liquid Filled Atmospheric and Low Pressure Metal Storage Tanks Using Acoustic Emission. ASTM International, West Conshohocken, PA (2002)
5. JB/T 10764-2007, Acoustic emission testing and evaluation of atmospheric pressure metal storage tanks. China Special Equipment Inspection and Research Institute, Beijing (2007)
6. BS EN 15856-2010, Non-destructive testing-Acoustic emission-General principles of AE testing for the detection of corrosion within metallic surrounding filled with liquid. 11/28/2009
7. S. Yuyama, M. Yamada, K. Sekine, High-Pressure Inst of Japan Recommend AET for corrosion in tank bottom plate of AST, Materials Evaluation (2007), pp. 888–892
8. P.J. van de Loo, D.A. Kronemeijer, Screening of tank bottom corrosion with a single point, in *European Conference on Acoustic Emission* (2002)
9. D. Papasalouros, K. Bollas, D. Kourousis, Acoustic emission tank floor testing: a study on the data-base of tests and followup inspections, in *31st Conference of the European Working Group on Acoustic Emission* (EWGAE) (2014)
10. G. Lackner, P. Tscheliesnig, Acoustic emission testing on flat-bottomed storage tanks: how to condense acquired data to a reliable statement regarding floor condition, EWGAE 2002

Chapter 30
Waveguide Methods for AE Online Testing of Several Cryogenic Vertical Double-Wall Tanks

Yanting Xu, Yadong Wang, and Jianyong Zheng

Abstract Three kinds of cryogenic and atmospheric vertical double-wall storage tank structures are studied in this paper. Some external structural parts of a storage tank or specially designed auxiliary components are used as the waveguide rods of AE on-line detection. The waveguide effect is verified by transmitting analog signals between adjacent waveguide poles. Some tanks have been inspected by means of these waveguide methods. The results show that these waveguide methods can basically meet the requirements of AE online detection of these kinds of tanks. Therefore, the technical problems of AE on-line detection of such tanks have been finally solved.

30.1 Introduction

In recent years, AE technology has been widely used in the on-line inspection of single-wall vertical atmospheric storage tanks in the normal temperature range, and good results has been achieved. It not only solves the safety inspection problem of storage tanks, but also saves the overhaul time and enormous cost of open inspection for enterprises [1, 2]. For double-wall cryogenic storage tanks, AE detection is needed for the inner tank, but AE sensors are usually difficult to be mounted directly on the inner tank wall because of the double-wall tank structure feature, and then AE on-line detection cannot be directly implemented. Therefore, through the research and field investigation of several typical types of double-wall cryogenic tank structures, we designed special acoustic wave guide device or used some structures of the tank to assist AE on-line detection of these tanks. These practices have proved that the technical problems of AE on-line detection of these storage tanks have been well solved.

Y. Xu (✉) · Y. Wang · J. Zheng
Zhejiang Academy of Special Equipment Science, Hangzhou 310020, China
e-mail: 657311787@qq.com

Y. Xu · Y. Wang
Key Laboratory of Special Equipment Safety Testing Technology of Zhejiang Province, No. 211, Kaixuan Road, Hangzhou, China

© The Author(s), under exclusive license to Springer Nature Singapore Pte Ltd. 2021
G. Shen et al. (eds.), *Advances in Acoustic Emission Technology*, Springer Proceedings in Physics 259, https://doi.org/10.1007/978-981-15-9837-1_30

30.2 Structural Characteristics of Common Double-Wall Cryogenic Vertical Storage Tanks

A double-wall cryogenic vertical storage tank consists of an inner tank and an outer tank. A thick rigid insulating plate is usually used between the inner bottom plate and the outer bottom plate. The space between the inner and outer cylinders is usually filled with pearlite sand and inert gas. In this way, the inner tank can be kept at a certain deep cold temperature. The foundation of this kind of tank is usually overhead. Because it is very difficult to open and repair this kind of tank, stainless steel is usually chosen as the material of the inner tank to facilitate long-term operation. For the on-line AE detection of such tanks without opening tanks, the key technical problem to be solved is how to transmit AE signals from the inner tank. Therefore, it is necessary to adopt some effective acoustic wave transmission method according to the different actual structure characteristics of storage tanks.

30.3 Waveguide Methods for Three Double-Wall Tanks with Different Infrastructures

In recent years, according to the foundation structure characteristics of several common double-wall cryogenic tanks, we have adopted different acoustic conduction methods to effectively realize AE on-line monitoring of these tanks.

30.3.1 Method One: Probe Waveguide Rods

A 15,500 m^3 double-wall cryogenic ethylene storage tank (T7001) of a large petrochemical enterprise in Jiangsu Province is based on an overhead structure. By consulting the drawings and field observation, no exposed metal components welded with the inner tank wall can be used for acoustic wave transmission of the inner tank. However, we found that a certain number of instrumentation nozzles were distributed along the outer tank wall circumference about 1 m from the bottom plate of the outer tank. We specially designed the carbon steel probe waveguide rod as shown in Fig. 30.1, so that the acoustic signals from the internal storage tank can be received by the sensors mounted on the probe waveguide rods. The photo of a waveguide rod is shown in Fig. 30.2.

The total length of the waveguide rod is determined by the distance between the inner and outer tank walls, the thickness of the outer wall and the length of the instrumentation nozzle. In order to maintain close coupling between the waveguide rod and the inner tank wall, the waveguide rod is threaded to the center hole of the outer flange. Before the implementation of AE testing, we temporarily remove the instrumentation device, insert the waveguide rod into the nozzle and make it close

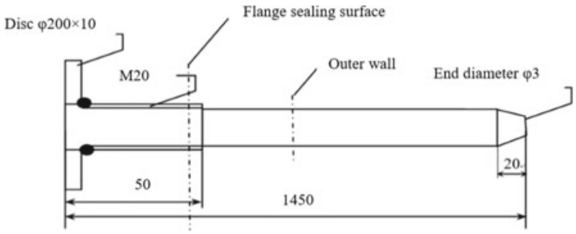

Fig. 30.1 Structure diagram of a probe waveguide rod

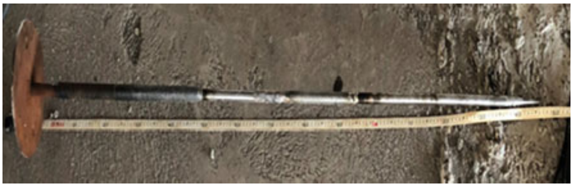

Fig. 30.2 Photo of a probe waveguide rod

contact with the inner tank wall. In this way, the acoustic signals from the inner tank can be transmitted to the sensor coupled on the waveguide rod disc. Figure 30.3 is the photo of a sensor, a waveguide rod and an instrumentation nozzle which have been installed together.

In order to test the acoustic attenuation of the waveguide rod itself, the pencil core (2H, φ0.3 mm) breaking signals are emitted at different positions of the waveguide rod. The signals are received by the sensor installed on the waveguide rod disc. The test results are shown in Table 30.1. The results show that the acoustic attenuation of the waveguide rod is small, so it can satisfy the AE testing.

In order to test the acoustic wave conduction effect of the coupling between the waveguide rod and the inner tank wall, lightly tap the disc of each waveguide rod

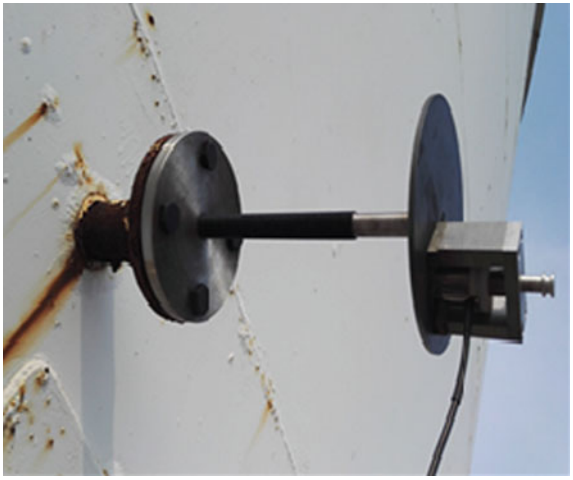

Fig. 30.3 Photo of a sensor, a waveguide rod and an instrumentation nozzle

Table 30.1 The attenuation testing result of the waveguide rod

Location of the analog source	10 mm sensor edge	80 mm starting point of thread	500 mm end of thread	1000 mm	1450 mm end point
Average response amplitude (dB)	94.5	83.9	85.5	80.5	84.1

Table 30.2 Comprehensive sound wave conduction on inner tank wall after installation of guide rod

Response amplitude of knocking near a certain sensor	Triggered sensors and their response amplitudes			
2#: 96 dB	9#: 71 dB	4#: 57 dB	5#: 56 dB	11#: 67 dB
5#: 98 dB	11#: 64 dB	4#: 58 dB	9#: 56 dB	1#: 56 dB

several times with a metal member like a screwdriver. If the adjacent sensor receives the mechanical tap signals, it is considered that the waveguide rod is well coupled with the inner tank wall, and AE signals from the inner tank can also be received. Some conductivity test results are shown in Table 30.2. The results show that the waveguide method basically meets the requirements for AE on-line detection of such tanks.

30.3.2 Method Two: The Fixed Accessories of Storage Tank [3]

Figure 30.4 shows the overhead foundation of an 8800 m^3 double wall cryogenic storage tank (4118-v4) in a large petrochemical company in Zhejiang Province. Through drawing review and site investigation, it is found that there are several

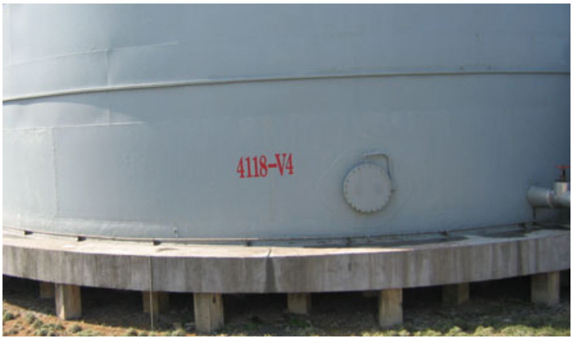

Fig. 30.4 Photo of 4118-v4 tank bottom

evenly distributed fixed rods welded with the inner tank wall, and that they pass through the outer tank bottom plate and the concrete foundation and are fixed with metal base plates, as shown in Fig. 30.5. Thus, we can directly couple the sensor to the metal base plate of the fixed rod, as shown in Fig. 30.6. With the help of these fixed accessories as waveguide rods, AE signals from the inner tank can be received by the sensors. The test method of acoustic conduction effect is similar to the above method. The acoustic source positioning results of AE on-line detection of the inner tank bottom plate are shown in Figs. 30.7 and 30.8. The test results show that this method also basically meets the requirements of AE on-line detection of such tanks.

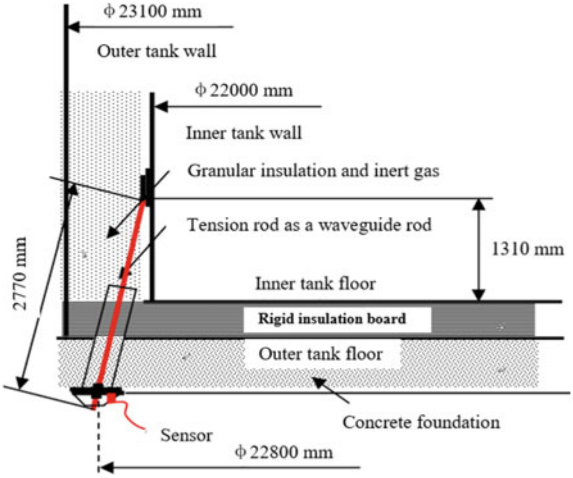
Φ23100 mm
Outer tank wall
Φ22000 mm
Inner tank wall
Granular insulation and inert gas
Tension rod as a waveguide rod
1310 mm
2770 mm
Inner tank floor
Rigid insulation board
Outer tank floor
Concrete foundation
Sensor
Φ22800 mm

Fig. 30.5 Structural drawing of 4118-v4 double wall cryogenic storage tank

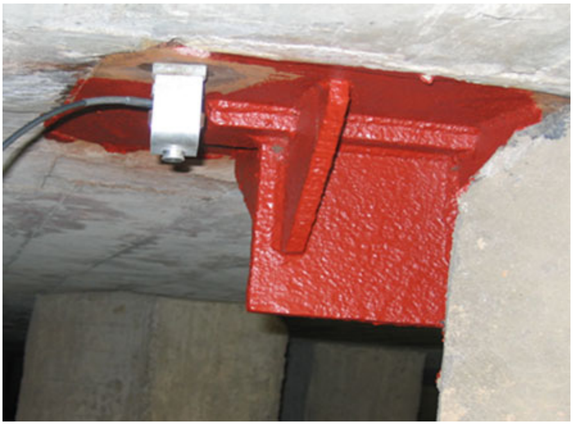

Fig. 30.6 Photo of the sensor installation position of on overhead floor

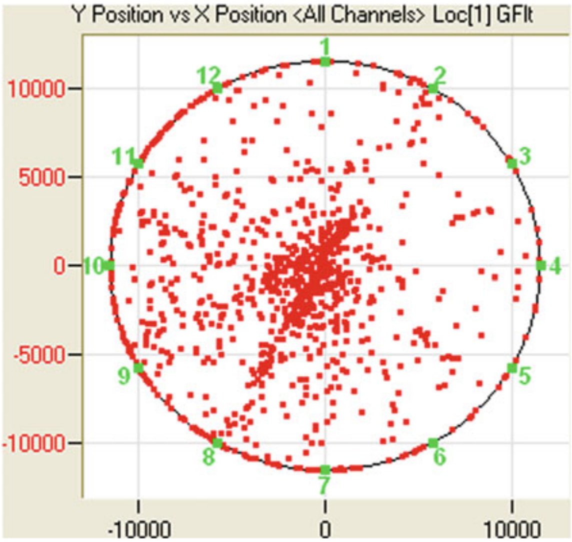

Fig. 30.7 Two dimensional positioning diagram from the inner tank floor

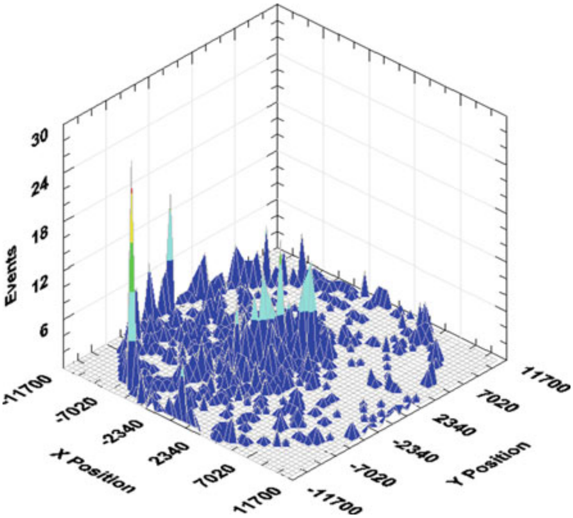

Fig. 30.8 Two dimensional positioning diagram from the inner tank floor

30.3.3 Method Three: The Fixed Rod and Its Special Clamp

Figure 30.9 shows the overhead foundation of a 7000 m^3 double wall cryogenic ethylene storage tank (T701) in a large petrochemical enterprise in Jiangsu Province. The structure of the overhead foundation is similar to the above, except that the fixed rods extending from the inner tank wall are vertically anchored in the underground concrete foundation. Due to the large surface curvature of these fixed rods,

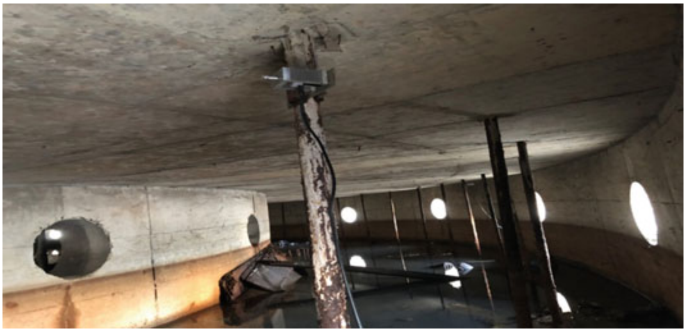

Fig. 30.9 Photo of T701 tank bottom

the coupling effect of directly installing the sensor is very poor. If the steel rod is ground out of the plane to improve the coupling effect, the strength of the fixed rod will be reduced. For this reason, we specially designed sheet metal clamps as shown in Fig. 30.10. The clamp is made of carbon steel plate with thickness of 2–3 mm and width of about 50 mm.

Polish the fixed rod surface where the clamp is installed, apply some couplant to the polished area, and then fasten the clamp on the fixed rod. The sensors are mounted on the clamps. The test method of acoustic conduction effect is similar to the above method. The test results show that this method also basically meets the requirements of AE on-line detection of such tanks.

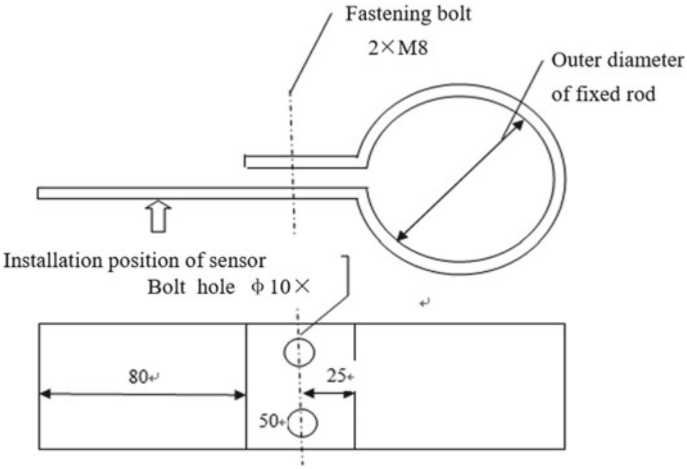
Fastening bolt
2×M8
Outer diameter
of fixed rod
Installation position of sensor
Bolt hole Φ10×
80
25
50

Fig. 30.10 Structural drawing of a sheet metal clamp

30.4 Results and Conclusions

According to the structural characteristics of three kinds of common double wall cryogenic tanks, different acoustic conduction methods are adopted in this paper to realize on-line AE detection of these kinds of tanks. These practices have proved the practicability and effectiveness of these acoustic conduction methods. Thus, the technical problems of AE on-line detection of these vertical double-wall cryogenic storage tanks have been well solved. It is believed that these methods and solutions on acoustic conduction can provide some reference for colleagues engaged in AE detection.

In addition, when designing and selecting the appropriate acoustic conduction mode for vertical double-layer cryogenic tanks, the following suggestions can be taken:

1. If some components of the tank can transmit the acoustic wave from the inner tank, and it is also suitable for direct sensor installation to receive these AE signals, the most direct mode of acoustic transmission should be preferred.
2. When it is necessary to design and make a special wave guide rod or its auxiliary structure, its structure shall be as simple as possible and easy to make and install, and its acoustic attenuation shall be as small as possible. At the same time, good coupling between the waveguide rod and the inner tank wall or between the auxiliary structure and the fixed rod shall be ensured. After the installation of the waveguide rod or its auxiliary structure, the overall acoustic conduction effect still need to be tested.

Reference

1. Y.T. Xu, X.W. Wang, Effectiveness of AE on-line testing results of atmospheric vertical storage tank floors. PVP2012-78067, Toronto, Ontario, Canada (2012)
2. H.G. Li, G.P. Peng, AE on-line testing of liquid ammonia tanks. Nondestructive Test. Technol. (04) (2008)
3. Y.T. Xu, Y.D. Wang, Acoustic emission in-service detection of cryogenic storage tank floors, in *17WCNDT World Nondestructive Testing Congress*, Shanghai, China (2008)

Chapter 31
Research on Immersion-Type Acoustic Emission Detection and Location Method for Large Tank Bottom

Junwei Gao, Ying Zhang, Shi Liu, and Zidong Zhu

Abstract When the acoustic emission technology is used to detect the corrosion of the large tank bottom plate, it is not easy to collect information in the central area of the floor due to the attenuation of the corrosion acoustic emission signal, and the detection blind zone is formed. Immersion acoustic detection technology is an effective method to solve the above problem. By using the detector to carry several immersion acoustic sensors into the tank from the manhole, the tank bottom plate is detected in different regions according to the preset route, so as to realize the global detection of the large tank bottom plate. The location of the corrosion source of the tank floor is a key technology when using immersion acoustic testing. To this end, sound source passive positioning method based on time delay estimation, combined with the characteristics of tank bottom immersion acoustic detection, a planar small array unit acoustic positioning method is established. By simulating the tank bottom plate positioning experiment, it can be known that the error of the positioning method in the direction finding accuracy and the ranging accuracy meets the requirements. Using the experimental data, the maximum effective radius R of the immersed acoustic detection unit was determined. According to the large-scale tank immersion acoustic detection method, a prototype of the tank bottom plate acoustic detector was designed.

Y. Zhang (✉)
College of Environmental and Safety Engineering, Changzhou University, Changzhou, Jiangsu, China
e-mail: aezy163@163.com

J. Gao
College of Mechanical Science and Engineering, Northeast Petroleum University, Daqing, Heilongjiang, China

S. Liu · Z. Zhu
Shenyang Longchang Pipeline Testing Center, Shenyang, Liaoning, China

© The Author(s), under exclusive license to Springer Nature Singapore Pte Ltd. 2021

G. Shen et al. (eds.), *Advances in Acoustic Emission Technology*, Springer Proceedings in Physics 259, https://doi.org/10.1007/978-981-15-9837-1_31

31.1 Introduction

With the rapid development of the petroleum industry, the reserves of crude oil and refined oil are crucial. In the oil reserve system, the tank is the core equipment, and the corrosion of the tank floor is the main factor affecting its safe operation. At present, the detection method of the storage tank is mainly combined with the on-line detection of acoustic emission and the magnetic leakage scanning detection, and is supplemented by other conventional non-destructive testing methods [1–3]. Although the acoustic emission on-line detection can realize the hierarchical quantitative evaluation of the corrosion state of the tank bottom plate, when the large-scale storage tank (volume is above 20,000 m^3) is in-line detection, the acoustic emission signal generated in the middle area of the bottom plate is affected by attenuation and other factors. It cannot be received by sensors coupled to the outer wall of the tank, forming the blind zone for detection. The detection blind zone increases with the increase of the diameter of the tank bottom plate. Therefore, when acoustic emission online detection is adopted for large storage tanks, due to the blind area of detection, it is impossible to evaluate the corrosion defect activity of the whole bottom plate of storage tanks, resulting in inaccurate evaluation results, affecting the final tank inspection and maintenance decision, and bringing safety risks.

Immersion acoustic detection method can solve the above problems [4]. By placing an automatic detector equipped with acoustic sensors from the manhole above the tank and controlling the detector to walk along the preset route to complete the area detection of the tank bottom plate, the global detection of the tank bottom plate can be realized. In this method, the location of corrosion sound source is the key. In this paper, the acoustic positioning method of planar small array unit is established, and the validity of the method is verified by experimental simulation. Finally, according to the immersion detection method, a prototype of tank bottom plate global detector is designed.

31.2 Large-Scale Tank Floor Immersion Acoustic Global Detection Method

31.2.1 Problems in Online Detection of Acoustic Emission from Large Tank Bottom Plates

At present, the most effective detection method for tank bottom plate corrosion is acoustic emission online detection technology. The method utilizes a plurality of acoustic emission sensors equally coupled to the outer wall of the tank and receives corrosion acoustic signals from the tank floor. Then, the position of the sound source is located by the corrosion acoustic emission signal received by sensors, and the corrosion state of the sound source is evaluated according to the detection standard.

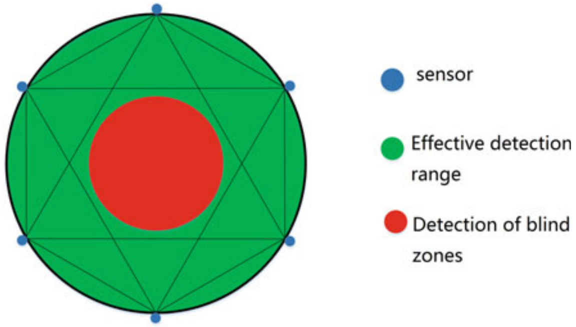

Fig. 31.1 Schematic diagram of detection blind zone of tank sound source localization technology

According to statistics, the on-line detection technology of acoustic emission has high detection accuracy in the routine detection of small and medium-sized storage tanks, which significantly reduces the detection cost of the storage tank and improves the detection efficiency.

However, at present, the main problem of this detection technology is that as the storage tank tends to be large-sized and coupled with weak corrosion intensity of the acoustic emission signal itself. The sound waves emitted by the corrosive acoustic emission source causing the tank bottom plate, especially in the central region, are greatly attenuated by the medium propagation signal, and it is difficult to trigger the sensor disposed on the outer wall of the tank. The existing tank acoustic emission on-line detection technology is difficult to obtain the corrosion acoustic signal in the central area of the large tank bottom plate (Fig. 31.1), which cannot fully reflect the activity of corrosion defects of the large tank bottom plate, and significantly affects the reliability of corrosion safety evaluation results of the bottom plate of large storage tanks.

31.2.2 Immersion Acoustic Emission Global On-Line Detection Method

The basic idea of immersion acoustic universal detection method for corrosion of bottom plate of large storage tank is realized by placing automatic detector into the tank. The automatic detector is equipped with acoustic detection sensors and acquisition equipment, which can realize the overall detection of the corrosion state of the bottom plate of the storage tank through patrol inspection according to the preset route.

The specific working principle and process are shown in Fig. 31.2. The immersion acoustic automatic detector is placed on the bottom of the tank from the manhole at the top of the tank and moved to the designated starting position by the positioning control system, as shown in point A of Fig. 31.2. At point A, the detector is stationary, and the mounted acoustic detector starts to work, and the corrosion acoustic signal in the

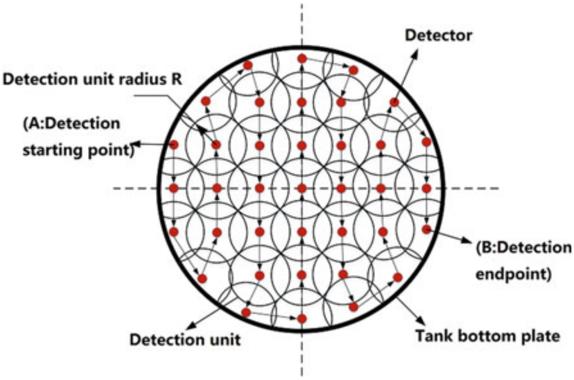

Fig. 31.2 Schematic diagram of the immersion acoustic whole field detection process of the tank bottom plate

tank bottom detection unit with radius R is collected, and the acquisition time is Δt. After the data acquisition of the first detecting unit is completed, the detector moves to the center of the next detecting unit according to the predetermined detecting path, and the above detecting process is repeated. According to this process, the detection is performed unit by unit according to the predetermined detection path shown in Fig. 31.2, and until the detection end point B is moved, the global acoustic on-line detection of the entire tank bottom plate can be realized.

In addition to the hardware design, how to use acoustic sensors on the detector to locate and evaluate the corrosion condition of the detection unit is a key issue. This involves the selection of the positioning method, the determination of the number and arrangement of the acoustic sensors, and the determination of the radius R of the detection unit.

31.3 Planar Small Array Unit Positioning Method

The immersion acoustic detector enables global detection of the bottom plate by walking on the tank floor in a specified path. However, how to use acoustic sensors mounted on the detector to accurately locate and evaluate the corrosion source in each detection unit is a key issue for the application of this method. Based on the TDOA (Time Difference of Arrival) passive time difference positioning method [5, 6], the acoustic positioning method for the planar small array unit suitable for the tank bottom plate is established [7] to effectively locate the corrosion source in the tank bottom detection unit.

A planar array of small array elements composed of five acoustic emission sensors was established, as shown in Fig. 31.3. Where S is the sound source signal, N_1–N_5 are five acoustic emission sensors respectively, wherein the sensor N_1 is placed at the origin as the reference array element, and the sensor N_2–N_5 is distributed on the coordinate axis of the XOY plane in a counterclockwise direction. The distance between the sensors N_2–N_5 and the base element N_1 is $D/2$.

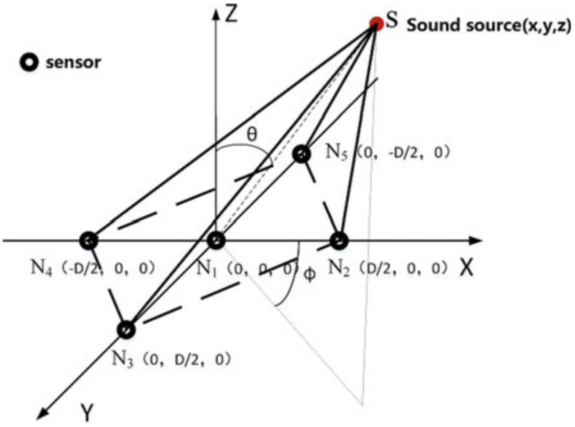

Fig. 31.3 Small array unit sound source localization model

According to the geometric relationship between the sound source and the small array unit and the TDOA principle, the following equations can be obtained:

$$\begin{cases} x^2 + y^2 + z^2 = r_1^2 \\ \left(x - \dfrac{D}{2}\right)^2 + y^2 + z^2 = r_2^2 \\ x^2 + \left(y - \dfrac{D}{2}\right)^2 + z^2 = r_3^2 \\ \left(x + \dfrac{D}{2}\right)^2 + y^2 + z^2 = r_4^2 \\ x^2 + \left(y + \dfrac{D}{2}\right)^2 + z^2 = r_5^2 \end{cases} \tag{31.1}$$

$$\begin{cases} r_2 - r_1 = c\tau_{21} \\ r_3 - r_1 = c\tau_{31} \\ r_4 - r_1 = c\tau_{41} \\ r_5 - r_1 = c\tau_{51} \end{cases} \tag{31.2}$$

$$\begin{cases} x = r_1 sin\theta \cos\varphi \\ y = r_1 sin\theta \sin\varphi \\ z = r_1 \cos\theta \end{cases} \tag{31.3}$$

In these formulas, r_1–r_5 are the distances of the sound source S to the sensors N_1–N_5 respectively; τ_{21}–τ_{51} are the delay differences of the sensors N_2–N_5 and the reference sensor N_1 respectively; c is the sound speed; φ is the azimuth angle; θ is the elevation angle.

When the immersion acoustic detector is used to monitor the corrosion state of the tank bottom plate, in order to ensure the receiving effect, the acoustic emission sensor carried by the detector should be as close as possible to the tank bottom plate. At this time, the elevation angle of the tank bottom corrosion source and the sensor array $\theta \approx 90°$. Therefore, the positioning of the small matrix unit of the corrosion source of the tank floor can be regarded as the two-dimensional plane positioning in the XOY plane, and the above three equations are connected, and when the sound source conforms to the far-field model, that is $r_1 \gg c\tau_{i1}$ $(i = 2, 3, 4, 5)$, the sound source localization of the planar small array unit is available:

$$\begin{cases} r_1 = \dfrac{D^2 - c^2 \sum\limits_{i=2}^{5} \tau_{i1}^2}{2c \sum\limits_{i=2}^{5} \tau_{i1}} \\ \varphi = \arctan\left(\dfrac{\tau_{51} - \tau_{31}}{\tau_{41} - \tau_{21}}\right) \end{cases} \tag{31.4}$$

31.4 Verification Experiment of Plane Small Array Unit Positioning Method

31.4.1 Experiment System

The sound source localization test system for the verification plane small array unit positioning method is composed of a Q235 carbon structural steel plate with a size of 2800 mm × 1600 mm × 16 mm (for simulating the tank bottom plate) and a PAC acoustic emission signal acquisition system (SAMOS system)., 5 acoustic emission sensors (R3α), 5 preamplifiers and signal lines, the experimental system is shown in Fig. 31.4.

31.4.2 Experimental Protocol

The verification experiment scheme is as follows: On the simulated tank bottom plate, according to the requirements of the plane small array unit positioning method, five acoustic emission sensors are arranged, and a HB $\varphi = 0.5$ mm automatic pencil is used to break the given position on the simulated tank bottom plate. Data are collected by positioning array of small array elements, and the positioning calculation is carried out by using Formula (31.4), and the accuracy of the positioning method in distance positioning and direction positioning is analyzed.

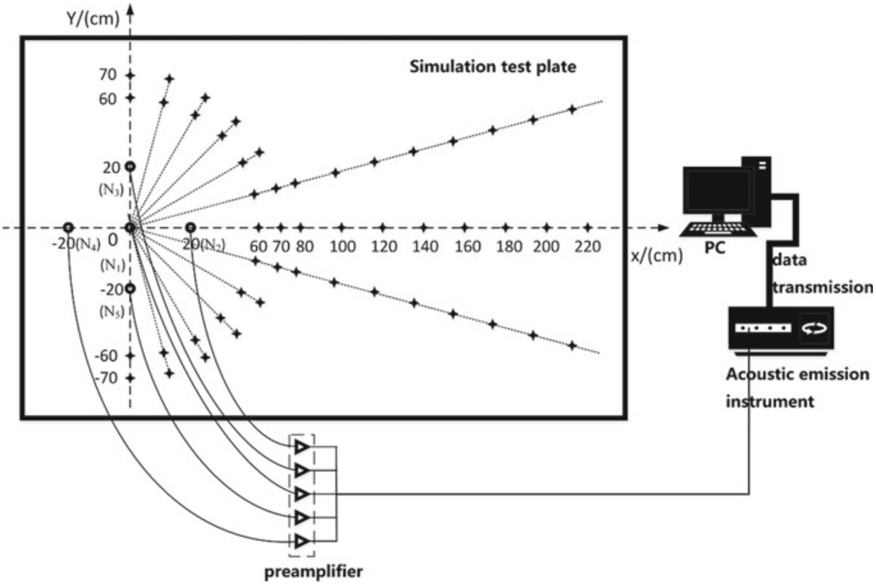

Fig. 31.4 Sound source localization test system for planar small array unit positioning algorithm

The sensor array is arranged as shown in Fig. 31.4, wherein the N_1 sensor is placed on the coordinate origin in the XOY plane, and the remaining four sensors N_2, N_3, N_4, and N_5 are arranged counterclockwise. The coordinates of the five sensors are N_1 (0, 0), N_2 (20, 0), N_3 (0, 20), N_4 (−20, 0), and N_5 (0, −20), respectively. Accuracy analysis mainly includes direction finding sound source localization analysis and ranging sound source localization analysis. (1) Direction finding sound source: When $r = 60$ cm and $r = 70$ cm, respectively, a sound source is set every 15° from $\varphi = -90°$ until $\varphi = 90°$. (2) Ranging sound source: When $\varphi = 0°$, $\varphi = 15°$ and $\varphi = -15°$, a sound source is set every 20 cm from $r = 60$ cm until $r = 220$ cm.

31.4.3 Experimental Results Analysis

According to the above experiments, the experimental data acquisition of direction finding and ranging is completed, and the influence of two factors of sound source angle φ and distance r on the direction finding accuracy and ranging accuracy of sound source localization is analyzed.

(1) Direction finding results and accuracy analysis
Firstly, the influence of different sound source angles on the direction finding accuracy of small array unit positioning method is analyzed. In the case that the ranging r is constant, the acoustic signal from different angles is received and positioned by the planar small array positioning method, and the measured

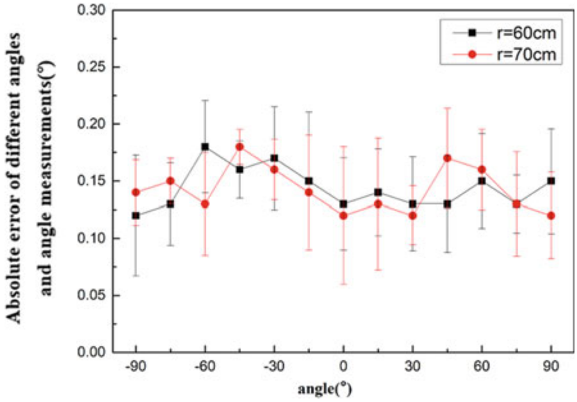

Fig. 31.5 Absolute error of different angles and angle measurements

value and accuracy analysis are obtained. The sound source angle is calculated using (31.4). The specific calculation and error analysis results are shown in Fig. 31.5.

It can be seen from Fig. 31.5 that under different sound source angles φ and different sound source distances r, the absolute errors of the sound source angle measurement values are small, and the values are distributed 0.1°–0.2°. It is shown that the direction finding accuracy of the planar small matrix unit sound source localization method is not affected by the sound source angle φ and the distance r.

(2) Ranging results and accuracy analysis

According to the above method, the influence of different sound source positions on the ranging accuracy of the small array unit positioning method is analyzed. It mainly analyzes the influence of two factors of different sound source angle φ and distance r on the accuracy of sound source ranging.

In the case where the sound source angle φ is constant, the relationship between the relative error of the sound source distance measurement value and the sound source distance is as shown in Fig. 31.6.

It can be seen from Fig. 31.6 that when the sound source angles are $\varphi = 0°$,15° and $-15°$, the relative error of the ranging based on the planar small array unit sound source localization method increases with the increase of the sound source distance. But the value of the increase is small, and the relative error of the ranging at the sound source distance of 220 cm is only about 6.5%, indicating that the positioning method has higher positioning accuracy.

(3) Determination of the effective radius R of the detection unit

According to the above experimental data analysis, when the sound source localization method using the planar small array unit is used to locate the sound source, the positioning accuracy decreases as the distance of the sound source from the sensor array increases. The distance between the sound source and the sensor

Fig. 31.6 Relative error of different distance and distance measurements

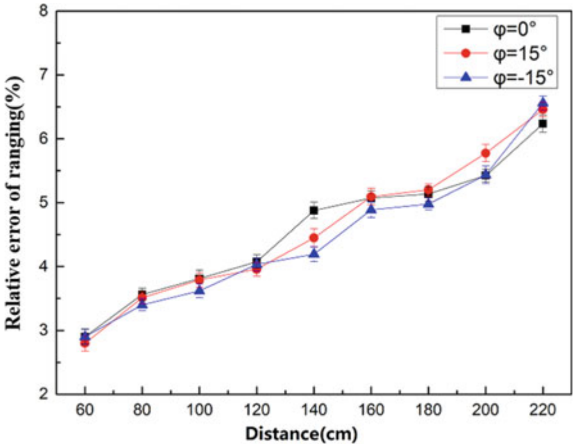

array is the effective radius R of the detection unit, and the effective radius R can be determined by the relative error analysis method of the sound source ranging.

In this paper, the mean value fitting method is used to average the relative error values of the sound source ranging under the three sound source angles of $\varphi = 0°$, 15° and −15°. Then the fitting relationship between the relative error of the ranging and the distance r of the sound source is obtained. The fitting curve is shown in Fig. 31.7. The fitting formula can be obtained (31.5).

$$y = 0.24x^2 + 1.35x + 2.1 \tag{31.5}$$

Fig. 31.7 Fitting curve of relative error of sound source localization and sound source distance

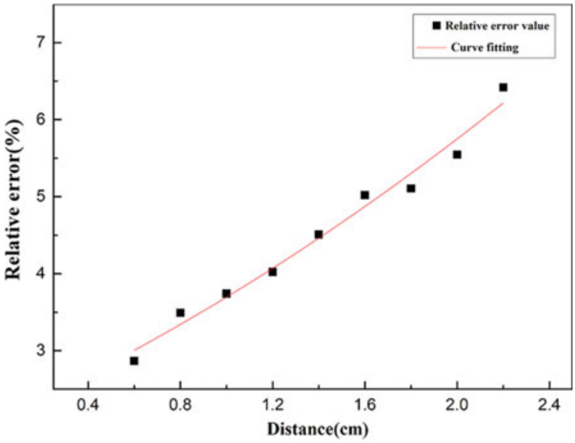

In the above formula, x is the sound source distance; y is the relative error of the sound source ranging. The R-square (that is, the coefficient of determination) of the equation is 0.98, indicating that the fitting effect is better.

When the relative error of the ranging is 20%, the distance of the sound source from the center of the sensor array is calculated by (31.5) to be 6.27 m. Therefore, through the verification experiment, when the above method is used for the immersion acoustic detection of the tank bottom plate, the maximum effective radius R of the detecting unit can be 6 m.

31.5 Immersion Automatic Acoustic Detector Prototype Design

Considering the detection environment of the large tank bottom plate and the online detection of acoustic emission, the design must ensure that the detector can be smoothly recovered after the floor is inspected smoothly according to the preset route and the inspection is completed. The main design components include the design of motion, inspection, and recycling modules. The composition of each module of the detector is shown in Fig. 31.8.

31.5.1 Design of the Motion Module

The motion module is the key to whether the immersed automatic acoustic detector can smoothly walk on the inner bottom plate of the tank and successfully complete the

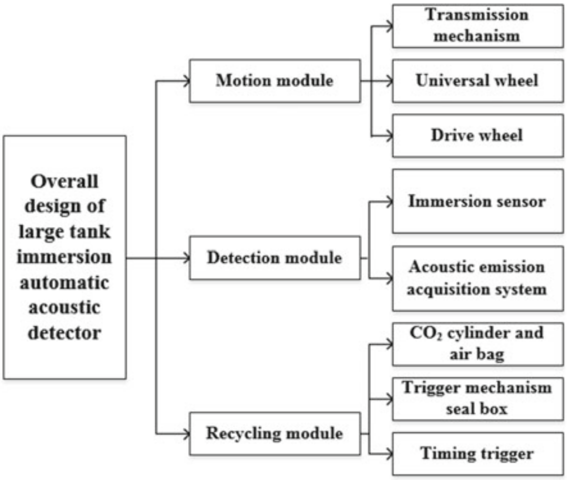
Overall design of large tank immersion automatic acoustic detector
Motion module
Transmission mechanism
Universal wheel
Drive wheel
Detection module
Immersion sensor
Acoustic emission acquisition system
Recycling module
CO_2 cylinder and air bag
Trigger mechanism seal box
Timing trigger

Fig. 31.8 Immersion automatic acoustic detector overall design

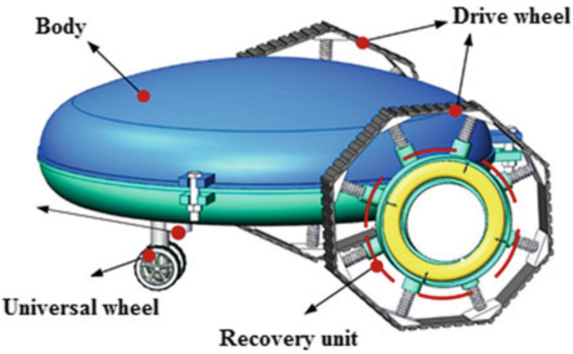

Fig. 31.9 Detector motion module schematic

inspection task. The bottom of the tank used for long-term use is often accompanied by high-viscosity sludge such as sludge and old emulsified oil. These deposits are easy to change the trajectory of the detector, easy to slip, etc., in order to ensure the detector walks smoothly at the bottom of the tank. The motion mechanism designed in this paper adopts wheel drive. The detector installs two independent drive wheels symmetrically on the left and right sides of the machine body. A universal wheel is installed at the front end of the detector as the driven wheel and the front end support, as shown in Fig. 31.9. The detector relies on the difference in rotational speed between the two drive wheels to achieve steering, thereby enabling free travel of the test instrument.

31.5.2 Design of the Test Module

In order to meet the detection efficiency and detection accuracy of the detector in the tank bottom plate, the planar small array unit positioning model of Fig. 31.3 is adopted, and the detection module of the immersion automatic acoustic detector is composed of an acoustic emission acquisition system and five immersive acoustic sensors. As shown in Fig. 31.10. N_1, N_2, N_3, N_4, and N_5 are respectively five acoustic emission sensors, wherein the sensor N_1 is placed at the origin as a reference array element, and the sensors N_2, N_3, N_4, and N_5 are sequentially distributed in the counterclockwise direction on the lower casing of the detector.. The distance between the sensors N_2, N_3, N_4, and N_5 from the reference array element N_1 is 200 mm.

31.5.3 Design of the Recycling Module

The recycling module means that the immersed automatic acoustic detector can be self-recovered after the completion of the detection of the whole tank bottom plate for subsequent signal analysis. The recycling module designed in this paper includes

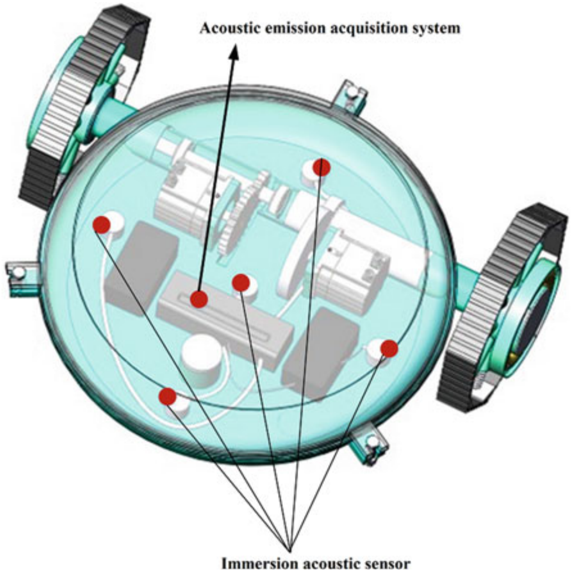
Acoustic emission acquisition system
Immersion acoustic sensor

Fig. 31.10 Detector detection module schematic

a timing trigger mechanism, a CO_2 cylinder, a gas bladder with a gas core, and a drive wheel. The airbag on the driving wheel will be turned on by the timing triggering device according to the preset time. The control module drives the motor to rotate to drive the rack to puncture the CO_2 cylinder seal. The cylinder will quickly inflate the recovery airbag. Open the airbag box and float the detector to the manhole recovery position by the buoyancy generated.

31.6 Conclusion

In order to realize the global inspection of large tank bottom plate, a large-scale tank bottom corrosion immersion acoustic global detection method and planar small array unit positioning method are proposed, and the maximum effective radius R of the detection unit in the immersion acoustic detection of large tank bottom is determined. According to the immersed global detection method of large storage tanks. An immersed automatic acoustic detection prototype is designed. The prototype is currently in the preliminary stage of thinking, and a lot of follow-up work is needed on the design of the prototype.

Acknowledgements This study was financially support by the national "13th Five-Year" national key R&D program (2017YFC0805804).

References

1. G. Du, S. Jin, C. Zhang, A study on acoustic emission technology for tank bottom corrosion inspection. Anti-Corr. Methods Mater. **57**(6), 605–610 (2010)
2. Z. Xu, W. Wang, Y.Wang, Application of online comprehensive detection technology for large crude oil storage tanks. Non-Destr. Test. **41**(2), 52–55 (2019)
3. L. Luo, Y. Li, A literature review of failure prediction and analysis methods for composite high-pressure hydrogen storage tanks. Int. J. Hydrogen Energy **44**(46), 25188–25198 (2019)
4. J. Lu, J. Xu, Research progress on domestic tank bottom corrosion detection technology. China Storage Transp. **05**, 116–118 (2018)
5. Z. Zhang, D. Sun, X. Zhang, Statistical model on the time and time difference error of arrival in TDOA location estimation. J. Chongqing Univ. **176**(3), 1511–1526 (2006)
6. S. Kwon, D. Kim, J. Lee, Performance analysis of 3D localization for a launch vehicle using TOA, AOA, and TDOA. Wireless Pers. Commun. **103**(2), 1443–1464 (2018)
7. M. Jia, J. Sun, C. Bao, Real-time multiple sound source localization and counting using a soundfield microphone. J. Ambient Intell. Humanized Comput. **8**(6), 829–840 (2017)

Chapter 32
Study on a Method of Corrosion Acoustic Emission Location for the Tank Floor

Zhihai Hu, Keqin Ding, Huazhong Wei, and Jiwang Zhang

Abstract Storage tank is one of the most important equipment for oil and gas storage and transportation. With the increase of the running time, a lot of harmful substances are deposited on the bottom of the tank. When acoustic emission is used to monitor corrosion defects on the floor of storage tank, there are many interfering factors, which make it difficult to locate corrosion defects. In order to accurately locate the acoustic emission signals source in the damaged part of tank floor, a positioning method is proposed. This method analyzes the propagation mode of the source signals from the corrosion defect, and then establishes an appropriate three-dimensional cylindrical coordinate system based on the relative position of the sensor and the corrosion space on the geometric relation between them in the coordinate system, the relation between the position of the sound source and the time difference of the sound signals is deduced. And to simplify the calculation, after the position of the coordinate system is determined, the Angle between the sensors is changed to make its relative position a special Angle, which makes the calculation faster. Before the monitoring, the layout of acoustic emission sensors in the corrosion monitoring of tank floor was determined to increase the positioning accuracy. It provides some guidance for monitoring tank floor corrosion location by acoustic emission.

32.1 Introduction

Atmospheric pressure storage tank plays an important role in oil and gas storage and transportation. The corrosion of tank floor is often complicated and changeable, and there are many inducing factors. This makes the oil and gas storage process has a huge safety hazard [1–3]. In the current nondestructive testing, acoustic emission monitoring method has the advantages of convenience, rapidity, low cost and high

Z. Hu · H. Wei
School of Mechanical and Electrical Engineering, Wuhan Institute of Technology, Hubei, Wuhan 430205, China

Z. Hu · K. Ding (✉) · J. Zhang
China Special Equipment Inspection and Research Institute, Beijing 100013, China
e-mail: kqding@sina.com

© The Author(s), under exclusive license to Springer Nature Singapore Pte Ltd. 2021
G. Shen et al. (eds.), *Advances in Acoustic Emission Technology*, Springer Proceedings in Physics 259, https://doi.org/10.1007/978-981-15-9837-1_32

sensitivity [4, 5]. However, acoustic emission signals have uncertainty and randomness, and the detected signal is mixed with various noise interference, which makes it difficult to locate acoustic emission signal [6–9]. Common acoustic emission signal positioning methods include one-dimensional linear positioning method [10], plane triangle positioning method [11, 12] and parallelogram positioning method [13]. Which methods are plane positioning. However, when acoustic emission corrosion monitoring is used in the field. Acoustic emission sensors are mostly arranged around the tank wall and not in the same plane as the floor. The sound source signal propagates along the surface of a metal sphere. Space metal it is broken down into various wave forms for conduction. Therefore, according to the same plane positioning calculation has a large error.

Based on the acoustic emission monitoring process of tank floor corrosion, the general placement characteristics of acoustic emission sensors, and the time difference of signals reception, a new three-dimensional geometric positioning calculation method was established in this study. This method can provide accurate results for spot monitoring of corrosion location of tank floor.

32.2 Positioning Principle

Establish a three-dimensional cylindrical coordinate system at the center of the base plate. The inner surface of the floor is in the xy plane. Place two sensors at the same height: 1#(R_1, θ_1, z_1) and 2#(R_2, θ_2, z_2). 3#$(R_3, \theta_3, 0)$ is located at the origin of coordinates (not drawn). And the rectangular coordinates of the three sensors 1#(x_1, y_1, z_1), 2#(x_2, y_2, z_2) and 3#$(x_3, y_3, 0)$. Suppose there is an acoustic emission source $S(r, \theta, 0)$ at the floor. The distances between the sound source and the sensors 1#, 2# and 3# are r_1, r_2 and r_3. Fig. 32.1 is a space diagram.

Meanwhile, t_1 and t_2 are respectively the time taken by AE sources to reach sensor 1 and sensor 2. v is the locating sound velocity, and its size is the propagation velocity of acoustic emission signal. The distance between the sound source signals and the sensor r_1 and r_2 can be expressed as:

$$r_1 = r_3 + \delta_1, \quad r_2 = r_3 + \delta_2 \tag{32.1}$$

Type of $\delta_1 = \Delta t_{1.3} v$, $\delta_2 = \Delta t_{2.3} v$. If the sensor is immersed in any position of the oil in the tank, the positioning geometric relationship of signals source can be expressed as:

$$\begin{aligned} r_1^2 &= z_1^2 + \left[r^2 + \left(\frac{z_1}{\tan \phi_1} \right)^2 - 2r \left(\frac{z_1}{\tan \phi_1} \right) \cos(\theta - \theta_1) \right] \\ r_2^2 &= z_2^2 + \left[r^2 + \left(\frac{z_2}{\tan \phi_2} \right)^2 - 2r \left(\frac{z_2}{\tan \phi_2} \right) \cos(\theta - \theta_2) \right] \end{aligned} \tag{32.2}$$

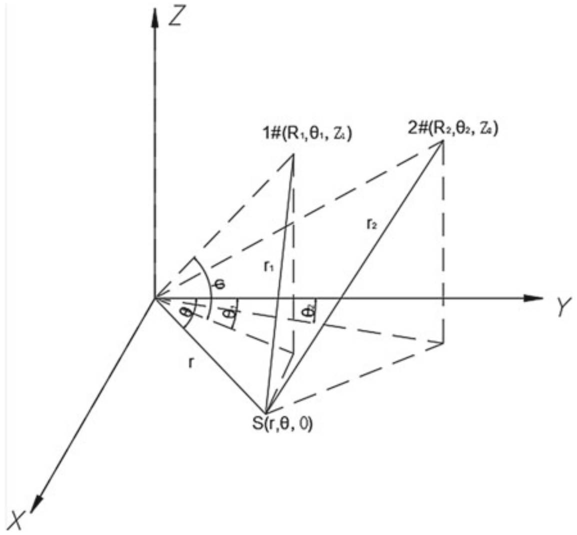

Fig. 32.1 Positioning space diagram

Generally, acoustic emission sensors are arranged at the same height on the outer surface of tank wall. The $R_1 = R_2 = R$. Where R is the height of the sensor from the floor, and is the radius of the floor of the storage tank.The geometric relationship can be simplified as follows:

$$\begin{aligned} r_1^2 &= z_1^2 + \left[r^2 + R^2 - 2rR\cos(\theta - \theta_1)\right] \\ r_2^2 &= z_1^2 + \left[r^2 + R^2 - 2rR\cos(\theta - \theta_2)\right] \end{aligned} \tag{32.3}$$

In combination with (32.1), (32.2) and (32.3), it can be known that:

$$\begin{aligned} (r_3 + \delta_1)^2 - \left(z_1^2 + R^2\right) &= r^2 - 2rR\cos(\theta - \theta_1) \\ (r_3 + \delta_2)^2 - \left(z_1^2 + R^2\right) &= r^2 - 2rR\cos(\theta - \theta_2) \end{aligned} \tag{32.4}$$

As in (32.4), v and t are measured by acoustic emission signals. Under the cylindrical coordinate system established at the center of the inner surface of the base plate. z_1, R and θ_i are determined by arranging acoustic emission sensors and relative positions of the coordinate system.

To determine the time t from the 1#, 2# sensors to the sound source, r_1 and r_2 were projected into the xy plane. The calculation method of plane triangle is adopted. Place sensor no. 3 at the origin of the coordinates. At this point, the calculation formula of r_3 can be obtained according to the calculation method of plane triangle positioning:

$$r_3 = \frac{L_1}{2\left(x_2\cos\theta + y_2\sin\theta + \delta_3'\right)} = \frac{L_2}{2\left(x_3\cos\theta + y_3\sin\theta + \delta_2'\right)} \tag{32.5}$$

In the formula, the calculation formula of L_1 and $\delta_3^{'}$ is:

$$L_1 = x_2^2 + y_2^2 - \delta_1^{'2}, L_2 = x_3^2 + y_3^2 - \delta_2^{'2} \tag{32.6}$$

$$\delta_3^{'} = r_3 - \sqrt{(r_3 + \delta_1)^2 - z_1^2}, \delta_2^{'} = r_3 - \sqrt{(r_3 + \delta_2)^2 - z_2^2} \tag{32.7}$$

From this, the simultaneous equations can be solved to find r and θ in accordance with the actual situation. The coordinates of acoustic emission sound source S at the damaged part of the floor were obtained, and the damage location was completed.

32.3 Sensor Layout

According to the positioning principle, for small storage tanks. During acoustic emission monitoring, in order to calculate the location of acoustic signals source conveniently. The number of acoustic emission sensors should be at least 3. The monitoring area is the triangular circumscribed circle of the three sensors on the projection surface of the tank floor. In order to improve the accuracy of positioning, set the number of sensors to 4. one of each set of sensors must be in the same horizontal plane as the inner surface of the floor. At this point, the origin of the cylindrical coordinate system is placed in the center of the floor. If the Angle between two adjacent sensors is 90°, as in (32.4) can be written as 90°, 180° and 270°. As shown in Fig. 32.2, the equation calculation can be simplified in this way.

For large tanks. The central part of the floor is the weak area for detection, and the corrosion signals at the bottom of the tank is small. In the process of propagation, the signals will be attenuated again, which may result in corrosion leakage detection. A sensor is placed in the center of the tank bottom and monitored together with the sensor on the outer wall of the tube. At this time, the middle position sensor is taken as the origin of cylindrical coordinates and combined with any two sensors. In

Fig. 32.2 Positioning of small tank sensor

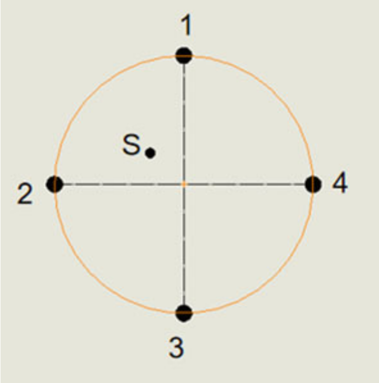

Figure 32.3 Positioning of large storage tank sensor

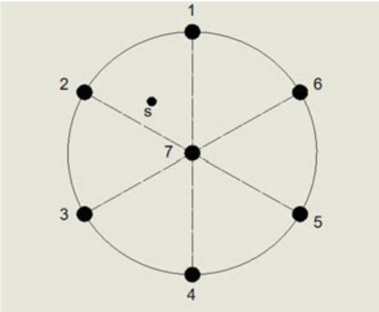

this cylindrical coordinate system, the positioning of sound source can simplify the calculation. Since the monitoring range of the sensor is generally limited. According to the monitoring range, the sensor is arranged as an equilateral triangle in a large area. While improving the recognition accuracy and reliability as much as possible, a larger monitoring area is obtained. Three sensors on the same line cannot be positioned. As shown in Fig. 32.3. Generally, the sensor can be arranged at a special Angle, the (32.4) can be simplified again.

32.4 Conclusion

Based on the arrangement of general acoustic emission sensors in the localization of corrosion acoustic emission source signals on tank floor and the localization method of time difference of acoustic emission source signals, the position relationship between acoustic emission source signals and acoustic emission sensor in three-dimensional cylindrical coordinate system is established. The relation between the time difference of the sound source signal and the position of the sensor is derived. The specific location of corrosion damage was calculated. In addition, the most effective sensor position distribution can be arranged according to this relation.

Acknowledgements This research was supported by the Research on Cloud Service Technology for Testing and Monitoring of Typical Industrial Equipment and Products (2018YFF0214700).

References

1. C. Xiao,*Corrosion Behavior of Carbon Steel Q235B in Sedimentary Water at the Bottom of Crude Oil Storage Tank*. China University of Petroleum (east China), 2016.
2. H. Bi, H. Wang, H. Wang, Z. Li, D. Hu, J. Chen,Uniform corrosion characteristics of floor steel based on acoustic emission and electrochemistry. Corrosion Sci. Prot. Technol. **29**(04), 381–386 (2017)

3. J. Shuai, K.J. Han, X.R. Xu, Risk-based inspection for large-scale crude oil tanks. J. Loss Prev. Proc. Ind. **25**, 166 (2012)
4. L. Jiang, W. Han, Z. Xu, Z. Wang, B. Su,Research status of acoustic emission on-line detection technology for tank floor. Corrosion Protec. **37**(05), 375–380 (2016)
5. H. Yan, G. Shen, G. Li, Y. Zhang,Acoustic emission detection of floor characteristics of atmospheric pressure storage tank. Pressure Vessel (02), 53–57 (2008)
6. F. Qiu,G. Dai, Y. Zhang, D. Qu, X. Huang, Experimental study on acoustic emission monitoring of multi-source corrosion on tank floor. Pressure Vessel **33**(11), 1–6 (2016)
7. H. Li,L. Kong, X. Lin, R. Li, Acoustic emission detection and application of floor of atmospheric metal storage tank. Energy Saving **36**(07), 73–76 (2017)
8. Z.W. Li,S. Yuyama, M. Yamada, et al., Investigation on AE signal/noise processing in corrosion damage evaluation of tank bottom. J. Acoust. Emiss. **23**, 233 (2005)
9. J.F. Chen, H.S. Bi, Q. Wang et al., The application of acoustic emission technology in oil and gas storage and transportation equipment. Adv. Mater. Res. **807–809**, 2652 (2013)
10. Y. Chen Yuan,*Study on Acoustic Emission Signal Processing and Source Location* (Southeast university, 2017)
11. R. Gong,Z. Cheng, J. Qu, Y. Luo, Z. Liu, The study of modal acoustic emission in defect location of structural materials. Vibration Shock (03), 176–179+192+216 (2006)
12. H. Bi,Z. Li, Y. Cheng, J. Wang, H. Rong, Application of acoustic emission detection technology in oil and gas storage and transportation system. Chem. Mac. **41**(03), 286–290 (2014)
13. F. Qiu,G. Dai, Y. Zhang, Y. Zhao, M. Zhang, Identification and location of corrosion acoustic emission sources on tank bottom. Nondestructive Test. **37**(02), 14–19 (2015)

Chapter 33
Experiment Research on Acoustic Emission of Impact-Damaged Fully-Wrapped Composite Gas Cylinder with Non-metallic Liner

Ke Bo, Sanjiang Liu, Liang Cheng, Yilin Yuan, and Hui Luo

Abstract The acoustic emission (AE) was used to monitor the impact damage of full-wrapped composite cylinder with non-metallic liner. The results showed that AE technique was capable of monitoring the accumulation of impact damage events in this type of cylinder. Hit number and AE energy were the effective AE signal discriminators. The results provided an experimental basis for cylinder impact damage evaluation of full-wrapped composite cylinder with non-metallic liner.

33.1 Introduction

Fully-wrapped composite gas cylinders with non-metallic liner (type 4 cylinders) are widely used for filling LPG gas in the world, because of their attractive advantages, such as light weight, high strength, good fatigue and anti-corrosion performance.

For type 4 cylinders, composite was a key factor to ensure safety due to non-load sharing of liner materials. Impact damage, cuts and abrasions were the common damage modes of type 4 cylinder. The fiber was directly cut or removed in the laminate and laminate strength was reduced at the points surrounding the damage [1]. Fatigue crack may generate nearby the damage and develop as the cylinder undergoes in-service pressure cycles [2]. Cuts and abrasions could be inspected by visible inspection. However, impact damage which was not inspected easily by general tests might cause matrix cracking, delamination and fiber fracture, which will directly affected the safety of impact damaged cylinder. It's well known that failure of composite was not an abrupt and catastrophic event, but instead damage develops progressively in service by the accumulation of fibre failures and other microstructural failure events [3]. Therefore, acquiring information of development of impact damage to evaluate the structural condition and determine that whether the cylinder can be used safely is essential.

K. Bo · S. Liu (✉) · L. Cheng · Y. Yuan · H. Luo
China Special Equipment Inspection and Research Institute, Beijing 100013, China
e-mail: boke2@163.com

© The Author(s), under exclusive license to Springer Nature Singapore Pte Ltd. 2021

G. Shen et al. (eds.), *Advances in Acoustic Emission Technology*, Springer Proceedings in Physics 259, https://doi.org/10.1007/978-981-15-9837-1_33

An important damage monitoring technique for composite pressure vessel was acoustic emission (AE). In the application of composite materials for AE technique, many of the researches involving AE monitoring had concentrated on the understanding and differentiating the failure processes, prediction of residual strength, the extent of damage and damage location [4]. Many studies were performed into the AE analysis of carbon fiber and glass fiber composites [5, 6]. Lin et al. [7] explored the thermo-mechanical properties under hydraulic and atmospheric fatigue cycling by using AE technique. Mohammadi et al. [8] evaluated damage under impact loads in composite structures. But few studies were involved in detecting impact damage and their accumulation in different cycle times by AE testing on type 4 cylinders.

In this paper, a study involving AE testing was conducted to a type 4 cylinder with artificial impact damage. Impact damage of cylinder accumulated gradually with increasing of cycle times, which changed the safety performance and condition of the cylinder. AE testing was performed on the cylinder after different cycle times to determine that wether it can be used to assess the extent of impact damage. Different parameters of AE signals collected were discussed and analyzed in details. The conclusion of our study can provide an experimental basis for type 4 cylinder impact damage evaluation.

33.2 Experiment Program

The overall process of experiment designed was as follows:

1. Prefabricated an impact damage in a type 4 cylinder.
2. Cycled the cylinder from 0.2 MPa to working pressure.
3. After a certain number of cycle times, detected the cylinder by AE testing.
4. Repeated operation of cycle and AE testing until the cylinder was cycled to failure.

33.2.1 Details of the Cylinder in the Test

A fully-wrapped glass fiber composite gas cylinder with non-metallic liner designed for filling LPG was used in the test, which dimension was 290 × 440 mm (D × L), capacity of 18L. The working pressure was 2.1 MPa. Impact damage was made as enterprise standards QB101-2017 Fully-wrapped Composite Gas Cylinder with Non-metallic Liner. Cylinder was filled with water until its weight was the same as filling weight with LPG (7.56 kg). Then the cylinder was dropped to a punch from a height of 1.2 m. Drop test was shown in Figs. 33.1 and 33.2a. This operation caused a impact damage with a length of about 100 mm in cylindrical portion and dome region of the cylinder. Its appearance was shown in Fig. 33.2a.

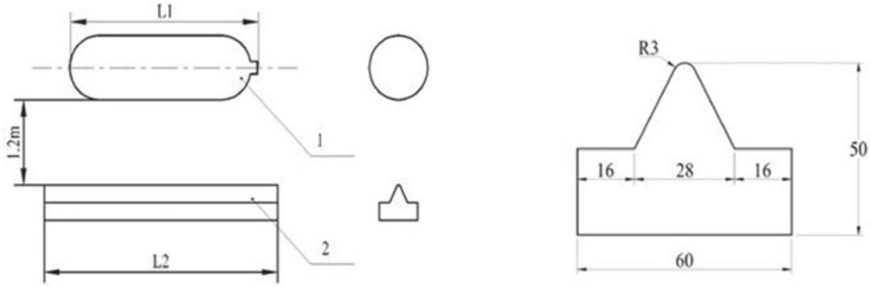

Fig. 33.1 Drop test and punch designed for this work

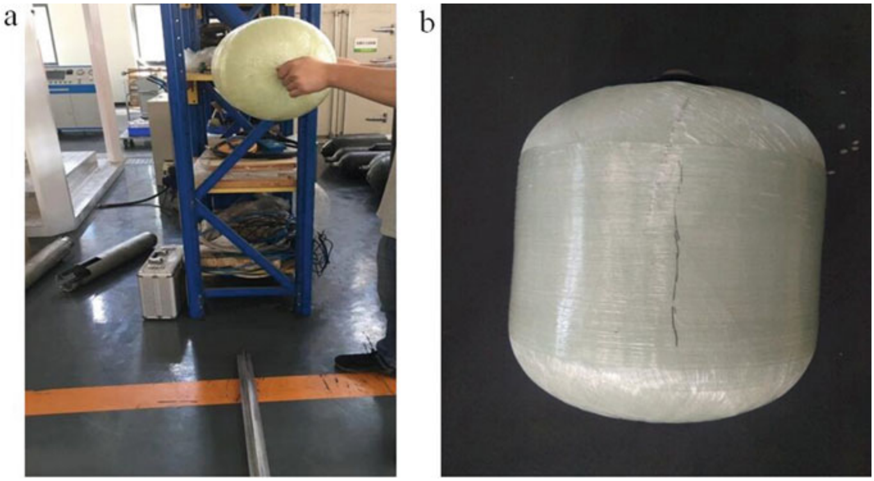

Fig. 33.2 **a** Actual drop test, **b** impact damage in surface of cylinder

33.2.2 Cycling Test and AE Testing Procedure

To replicate the in-service condition of repeated depressurization-pressurisation, cylinder with artificial impact damage was subjected to pressure cycles ranging from a lower pressure of 0.2 MPa to a upper pressure of 2.1 MPa at a constant frequency of 7.5 cycles per minute by a 10 MPa fatigue testing machine. The upper pressure was the same as working pressure of the cylinder. More information of cycle test was shown in Table 33.1.

Cycle testing was suspended after a certain number of cycles and detected the cylinder by AE testing. In AE testing, pressurization was from 0.2 to 2.4 MPa by a manual pump, then decompressed the cylinder after holding for 10 min in the pressure of 2.4 MPa. AE signals were collected during this overall process. The project of cycle and AE testing was shown in Table 33.2 and Fig. 33.3.

Table 33.1 Details of cycle test

Testing medium	Lower pressure (MPa)	Lower pressure holding time (s)	Upper pressure (MPa)	Upper pressure holding time (s)
46# hydraulic oil	0.2	2.5	2.1	2.5

Table 33.2 Project of cycle and AE testing

Order for collecting AE signal	Cycle times[1]	Order for collecting AE signal	Cycle times
1	500	11	17,000
2	1500	12	19,000
3	2500	13	21,000
4	3500	14	23,000
5	5000	15	25,000
6	7000	16	27,000
7	9000	17	29,000
8	11,000	18	31,500
9	13,000	19	34,000
10	15,000		

Note 1: After certain number of cycle times given in this column, cycle testing was suspended and detected cylinder by AE testing

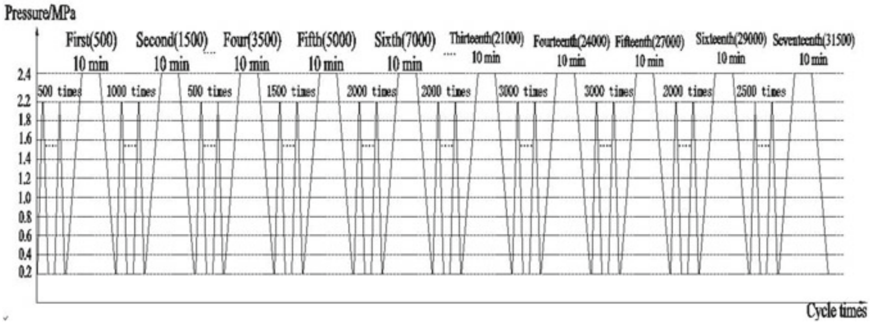

Fig. 33.3 The graph of cycle and AE testing project

Thresholds were settled at 40 dB. Eight sensors with 150 kHz frequency were used. Each sensor was connected with a 40 dB pre-amplifier, as shown in Fig. 33.4a. The coupling agent was vacuum grease. From Fig. 33.4b, sensors were fastened firmly with scotch tape and fixed with elastic rubber belt. The maximum distance between two sensors was 303 mm.

In the process of cycling and AE testing, cylinder appearance was monitored and the AE data was recorded by AE system.

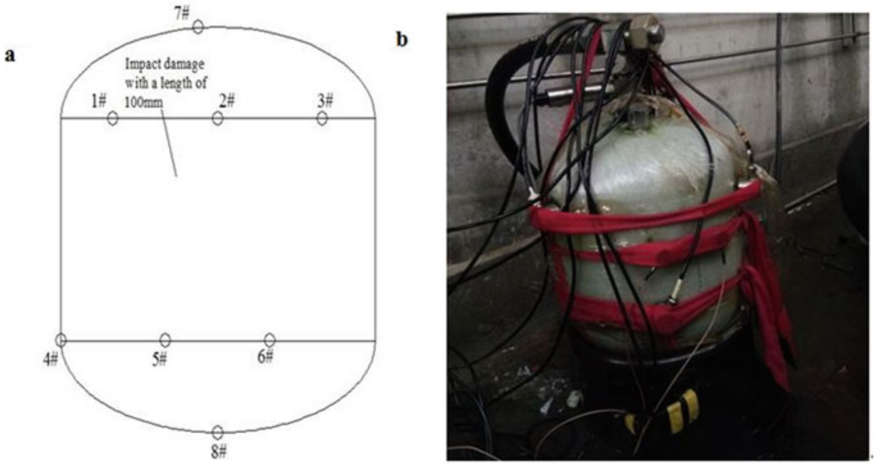

Fig. 33.4 **a** Distribution of sensors, **b** sensors fastened on the cylinder

33.3 Results and Discussion

33.3.1 Changes of Cylinder Appearance During Testing

There were not visible changes in cylinder appearance before 29,000 cycle times. Trivial damage was found in the region of impact damage after 29,000 cycle times, as shown in Fig. 33.5a. The liner began to deform locally after 31,500 cycle times and cylinder leaked after 34,800 cycle times, as shown in Fig. 33.5b, c.

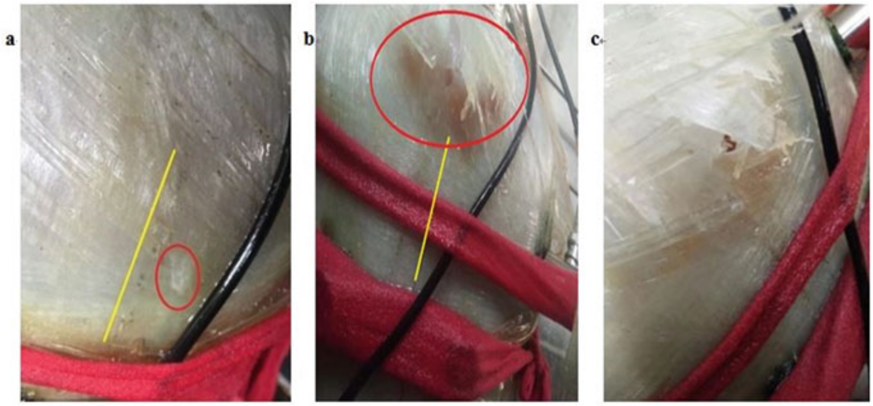

Fig. 33.5 **a** Trivial damage after 29,000 cycle times, **b** deformation of liner after 31,500 cycle times, **c** Leakage of cylinder after 34,800 cycle times

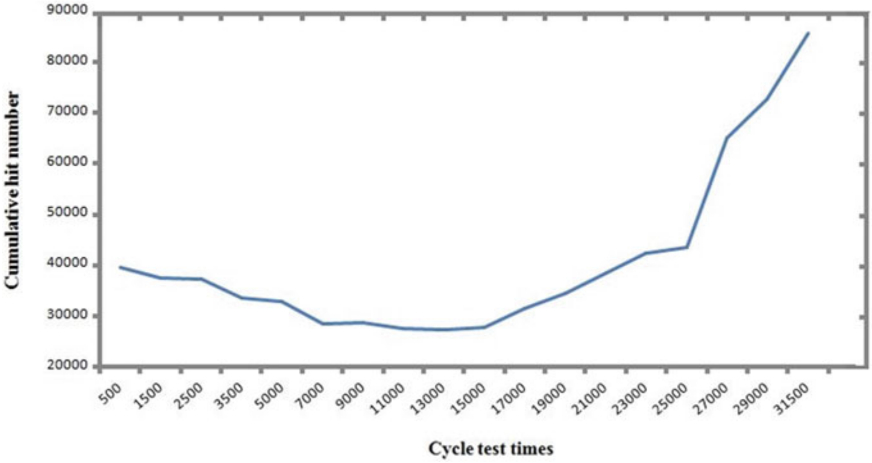

Fig. 33.6 AE cumulative hit number Versus cycle test time of eight sensors with pressurization

33.3.2 Characteristics of AE Cumulative Hit Number

Hit number from eight sensors were added up in AE testing after different cycle times and plotted these points in a diagram, as shown in Fig. 33.6. Cumulative hit number decreased gradually before 7000 cycles from the diagram. From 7000 to 15,000 cycles, the cumulative hit number was maintained in a relatively low level. From 15,000 to 25,000 cycles, the hit number increased with the cycle testing proceeding, which indicated that damage was accumulated in cylinder composite. Therefore, cumulative hit number was regarded as a feature to identify damage in cylinder. The trend of cumulative hit number with the cycle testing proceeding was an important reference to determine development of impact damage in cylinder composite.

33.3.3 Characteristics of AE Energy

The AE signal with relatively high energy occurred in the AE testing after 1500 cycle times, see Fig. 33.7a. The value of energy was higher than 15×10^7 eU. Subsequently, there were no AE events with high energy occurred until the cylinder was cycled to 23,000 times(as shown in Fig. 33.7b–d). After 23,000 times, both the number of signals and the value of signals' energy increased, especially in the AE testing after 34,000 cycle times, see Fig. 33.7e, f. A large number of signals with higher energy were collected and the cylinder made sound of fiber fracturing during AE testing after 34,000 cycle times. It demonstrates that a large range of fiber bands fractured. Fiber bands may facture with these high energy releasing. Therefore, high energy can be regarded as a feature to identify the cylinder fiber fracturing signals.

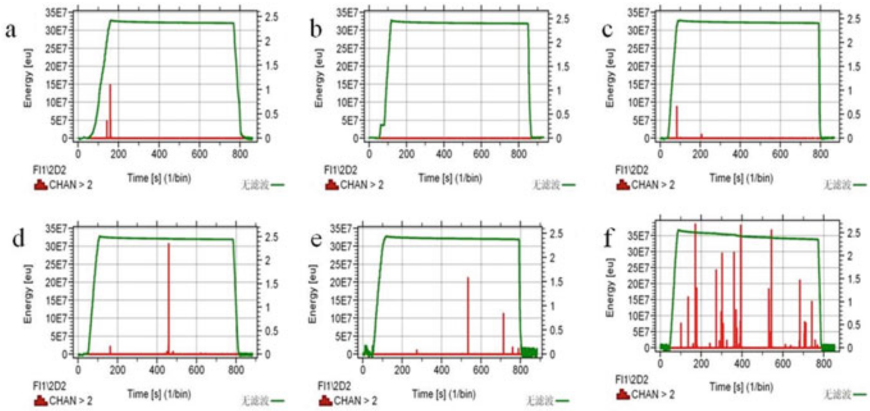

Fig. 33.7 AE energy VS time of pressurization after **a** 1500 cycle times, **b** 7000 cycle times, **c** 19,000 cycle times, **d** 23,000 cycle times, **e** 31,500 cycle times, **f** 34,000 cycle times

33.3.4 Comparisons and Analysis

According to the results above listed, characteristics of AE cumulative hit number were closely in accordance with characteristics of AE energy.

Combining with results of cumulative hit number and AE energy, more information can be acquired. Overall process could be divided in four phases according to the diagram of Fig. 33.6. At initial phase(i.e. 0–1500 cycles), because of impact damage in cylinder, stress distribution was uneven and cylinder composite had stress concentration in site of impact damage, fiber bearing high stress in the location of stress concentration may fracture when pressured, accounting for the relatively high AE cumulative hit number and energy of signals.

In the second phase (1500–15,000 cycles), localized high stress released in previous phase and new damage had not initiated or propagated to a certain degree, so cylinder was in a stable state with less and less AE hit number and few signals with high energy. In the third phase (17,000–25,000 cycles), AE hit number increased and signals with high energy were captured again. It was a gradual process of accumulation of damage.

Through the diagram in Fig. 33.6, cumulative hit number which reflected AE activity after 1500 cycle times was nearly the same as the number after 23,000 cycle times. There were AE signals with high energy in AE testing. AE testing results showed certain damage in cylinder composite in two cases. One case was that impacted damage and other case was that damage accumulated with cycle testing. Therefore, AE testing is an effect method to detect potential impact damage in full-wrapped composite cylinder with non-metallic liner.

In the four phase (26,000–31,500 cycles), slope of the curve, which represents growth rate of AE cumulative hit number was more steep. More signals with high energy were collected. Damage was propagating severely and cylinder was very dangerous for service in this phase. After 34,000 cycle times, more AE signals with higher energy were collected and the pressure was decreasing in pressure holding stage, which demonstrates that the cylinder was cycled to failure and fiber fractured at a large range.

In our study, the cylinder was cycled to failure and its pressure history in overall life was known. After different cycle times, AE testing was performed to the cylinder. By combining with results of cumulative hit number and AE energy after different cycle numbers, accumulated impact damage of the cylinder leaded to a dramatic increase in the amount of AE activity. A consistent correlation was obtained between the structural condition of the cylinder and AE cumulative hit number and energy. Therefore, AE testing can be used to detect impact damage of type 4 cylinder and assess the extent of the damage in different stage.

33.4 Conclusions

The acoustic emission (AE) was used to monitor the impact damage of full-wrapped composite cylinder with non-metallic liner after different cycle times. The following conclusions can be drawn:

(a) AE technique can be capable of monitoring the initiation and accumulation of impact damage events in this type of cylinder.
(b) The trend of cumulative hit number can directly reflect the accumulation of impact damage in type 4 cylinder with impact damage after different cycle times.
(c) Energy and cumulative hit number are effective AE signal discriminators for impact damage evaluation.

Acknowledgements This work is financially supported by National Key Research and Development Program of China (Grant No. 2017YFC0805604).

References

1. ISO/TR 13086-4:2019, Gas cylinders-Guidance for design of composite cylinders-Part 4: Cyclic fatigue of fibres and liners
2. G. Richard, F. Richard, Periodic inspection of composite wrapped pressure vessels using acoustic emission. CINDE J. 5–13 (2005)
3. H.Y. Chou, A.P. Mouritz, Acoustic emission analysis of composite pressure vessels under constant and cyclic pressure. Compos. Part A **70**, 111–120 (2015)
4. L. Dong, J. Mistry, Acoustic emission monitoring of composite cylinders. Compos. Struct. **40**(2), 149–158 (1998)
5. P.J. de Groot, P.A.M. Wijnen, R.B.F. Janssen, Real-time frequency determination of acoustic emission for different fracture mechanisms in carbon/epoxy composites. Compos. Sci. Technol. **55**(4), 405–412 (1995)

6. T. Krietsch, J. Bohse, Selection of acoustic emissions and classification of damage mechanisms in fiber composite materials. J. Acoust. Emis. **16**(1–4), 233–242 (1998)
7. L. Li, S.V. Lomov, X. Yan, V. Carvelli, Cluster analysis of acoustic emission signals for 2D and 3D woven glass/epoxy composites. Compos. Struct. **116**, 286–299 (2014)
8. M. Ghayoomi Mohammadi, A. Mahdian Ahi, J. Yousefi, M. Ahmadi Najafabadi, AE-based damage investigation in unidirectional composite laminates under low-velocity impact tests, Modares Mech. Eng. **17**(7), 91–100 (2017) (in Persian)

Chapter 34
Application and Research of Acoustic Emission in Using Hoop-Wrapped Composite Cylinders

Yaping Liu, Ruipeng Zhang, Wei Zhao, and Kai Zhao

Abstract Hoop-wrapped composite cylinders for Automotive Vehicles increase rapidly in recent years. At present, several major accidents of hoop-wrapped composite cylinders for vehicles has happened in China, therefore the compressed natural gas cylinders is the most serious. In the regular inspection, the higher ratio of surface defects have been found in Hoop-wrapped composite cylinders for Automotive Vehicles, at the same time, the surface of broken hoop-wrapped composite damage in cylinders is much higher than in the past few years. In use, hoop-wrapped composite cylinders will be defected which is caused by collision with the vehicle surface damage, affected the hoop-wrapped composite cylinder's safety. Therefore, it is necessary to find an on-service nondestructive testing method for the hoop-wrapped composite cylinders. Consequently, we study the Acoustic Emission (AE) signals characteristics of the hoop-wrapped composite cylinders during the fatigue process and the air tightness process, and using process, and defects recognition method preliminarily is advanced. These studies have important significance for realization of AE on-line detection and fault diagnosis of the hoop-wrapped composite cylinders.

34.1 Introduction

The hoop-wrapped composite cylinders have been widely used in various industries such as aerospace, petrochemical and automotive industries [1, 2]. However, in the recent years, there were been several serious major vehicle compressed natural gas cylinders accident, in which the hoop-wrapped composite cylinders is the most serious. In the regular inspection, the certain ratio of harmful surface damage has

---

Y. Liu (✉) · W. Zhao · K. Zhao
Hebei Special Equipment Supervision and Inspection Institute Branch of Baoding, Baoding 071000, China
e-mail: liuyaping_2008@126.com

R. Zhang
China Construction Installation Group Beijing Company, Beijing 100013, China
e-mail: zrp641534652@126.com

© The Author(s), under exclusive license to Springer Nature Singapore Pte Ltd. 2021

G. Shen et al. (eds.), *Advances in Acoustic Emission Technology*, Springer Proceedings in Physics 259, https://doi.org/10.1007/978-981-15-9837-1_34

been also found in the hoop-wrapped composite cylinders. Usually, after the certain cycle of filling, the metal lining may be broken or even leaked, and after a certain use and wear, the wound layer may have a series of damages. So these damages lead to limit the life of hoop-wrapped composite cylinders. Meanwhile, there is currently no means to detect the hoop-wrapped composite cylinders.

Acoustic emission (AE) which have advantages of dynamic testing, testing without material restrictions and high sensitivity, can be monitored in real time with equipment in use. Experimental study on acoustic emission of composite pressure vessels at home and abroad is in progress [3]. It can be concluded that it is feasible to evaluate AE as a dynamic evaluation method for hoop-wrapped composite pressure vessels. In the evaluation, the damaged of the hoop-wrapped composite cylinders will release the transient elastic wave when it is loaded, meanwhile the sensors receives and analyzes the parametric characteristics of the elastic wave to evaluate the activity of the defect. The time difference of the waveform received by the sensors can be used to locate the defect. Therefore researches of the acoustic emission signals characteristics of the hoop-wrapped composite cylinders which are running are necessary to improve the safety of CNG vehicles.

34.2 Fatigue Experiment

34.2.1 Fatigue Experiment in Liner

In the fatigue experiment, the two sensors VS150 were arranged in the head and tail of the liner of the hoop-wrapped composite cylinders and the sensor VS900 was arranged at the tail, as is shown in Fig. 34.1. The distance between two VS150 sensors was 600 mm, which was arranged in a straight line. In this experiment, the acoustic emission signal was continuously collected until the liners of the hoop-wrapped composite cylinders were leaked.

In the experiment, the liner shows significant acoustic emission signals characteristics after the fatigue cycle reaches 15,000 times which we can see in Fig. 34.2.

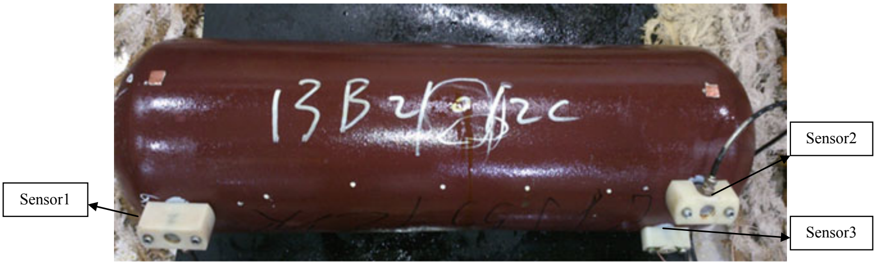

Fig. 34.1 Two sensors VS150 were arranged in the head and tail

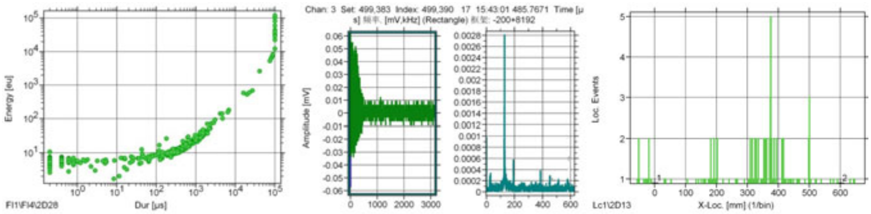

(a) (b) (c)

Fig. 34.2 Significant acoustic emission signals characteristics

The crack signals appears in the liner is obvious which is basically concentrated in the middle area of 200–300 mm after the fatigue cycle reaches 30,000 times. The signal of leakage reaches the maximum value which is relatively higher of the energy and amplitude. The RMS is mainly concentrated between 5 and 9 µV and the duration time reaches 50,000 µs. It is observed with us that the acoustic emission signal location is consistent with the same leaking position as shown in Fig. 34.2c.

34.2.2 Fatigue Experiment in Hoop-Wrapped Composite Cylinders

In the experiment, the two sensors VS150 were arranged in the head and tail of the hoop-wrapped composite cylinders and the sensor VS900 was arranged at the tail which is shown in Fig. 34.3. The distance between the two VS150 sensors was 1600 mm, which is arranged in a straight line. In the fatigue experiment, the pressure cycle is 7.89 time/min, and the acoustic emission signal is continuously collected until the hoop-wrapped composite cylinders are leaked.

In the fatigue, the acoustic emission system monitored the cracks in the inner liner or the composite layer. In this process, it can be shown the acoustic emission signal characteristics of cracks of the hoop-wrapped composite cylinder which are generated and extended and the distribution characteristics of the positioning signals

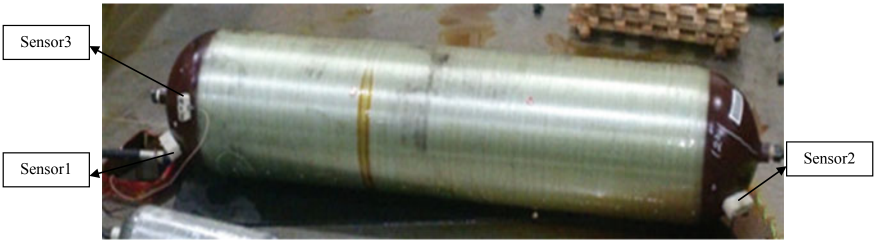

Fig. 34.3 The two sensors VS150 were arranged in the head and tail

through analyzing the experimental data. In the entire fatigue cycle, through calculating the sum of hits and the mean value of other acoustic emission parameters from the statistical analytical method, we can obtain the characteristic parameters of the acoustic emission signal of the hoop-wrapped composite cylinders. During the fatigue experiment of the hoop-wrapped composite cylinders, the acoustic emission signals are also changed greatly with the increasing of the fatigue cycle.

Figure 34.4 shows that the characteristics of the collected signals. In the experiment, the acoustic emission signal shows obvious characteristic discipline after the fatigue cycle was 30,000 times, and each parameter shows a sharp rising trend which is shown in the below Fig. 34.4. During the fatigue cycle of 70,000 times of the hoop-wrapped composite cylinders, the crack signal of the hoop-wrapped composite cylinders is strong. From the location in Fig. 34.4c, it can be found that the location signal is much more, and there are positioning signals in both positions. One is in the range of 200–300 mm, where is the head of the hoop-wrapped composite cylinders, and the other is mainly concentrated in the 800 mm, where is the middle of the hoop-wrapped composite cylinders. As a matter of fact, with the increasing of fatigue cycles, it can be found that the location signals is increasing, which is mainly concentrated in the middle area of 800–900 mm. From the RMS parameter, it can be found that the characteristic of peaking is obvious, and the largest RMS signal is generated. It can be seen from the figure that there is a signal generated after the hoop-wrapped composite cylinders leaks. In the fatigue experiment, the hoop-wrapped composite cylinders leaks which the leaking signals is relatively larger of hits, ringing count, duration time, rise time, amplitude, RMS and energy, especially the rise time reaches 100,000 μs and the range of the amplitude is in 35–80 dB. Compared the location of the signal of Fig. 34.4 with the actual leaking location of the hoop-wrapped composite cylinders, it can be discovered that they are basically the same location. By observing leakage signals, there may be multiple cracks, but it is most likely to happen to leak in the middle of the hoop-wrapped composite cylinders. As shown in Fig. 34.4b, the acoustic emission signals cover the frequency range of 100–200 kHz and are mainly concentrated at 150 kHz. Through analyzing the acoustic emission signals, it can be found that the acoustic emission technique could be used as an effective means for the safety evaluation of the hoop-wrapped composite cylinders.

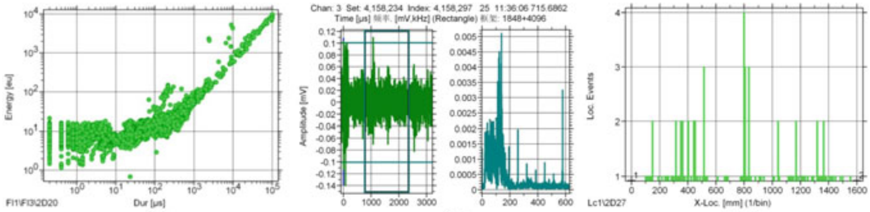

(a) (b) (c)

Fig. 34.4 Characteristics of the collected signals

34.3 Air Tightness Experiment

According to the standard GB 24162–2009 “Periodic inspection and evaluation of hoop wrapped fibre reinforced composite gas cylinders with metal liners of compressed natural gas for automotive vehicles”, the fiber-wound gas cylinders for vehicles are mandatory to be inspected once every five years. The experiment of the hoop-wrapped composite cylinders was carried out in accordance with the two experimental standards: GB/T 9252-2001 “Method for cycling test of gas cylinders” and GB 24160-2009 “Hoop-wrapped Composite Cylinders with Steel Liner for the On-board Storage of Compressed Natural Gas As A Fuel for Automotive Vehicles”.

In the air tightness experiment, the sensors received the changes in the signals of the hoop-wrapped composite cylinders, and then analyzed the signals. Through the air tightness experiment, it is possible to monitor the germination micro cracks in the inner liner or hoop-wrapped composite layer by the acoustic emission [4, 5]. In this paper, the acoustic emission is experimented of a large number of the gas hoop-wrapped composite cylinders for the automotive vehicles.

In this experiment, the two sensors VS150 were arranged in the head and tail of the hoop-wrapped composite cylinders as shown in Fig. 34.5. The distance between the two VS150 sensors was 1300 mm, which was arranged in a straight line. In the process of the air tightness experiment, the pressure was generally 7–20 MPa. In the pressurization process, it was obvious to obtain the characteristic discipline from the acoustic emission signals through collecting and analyzing the acoustic emission signal. In the process of pressurization, it was the rapid pressurization which was rapidly pressurized to 20 MPa, and then kept the pressure for five minutes.

34.3.1 *Air Tightness Experiment in Defected Hoop-Wrapped Composite Cylinder*

In the experiment, the volume of the hoop-wrapped composite cylinders was 90 L which was broken in the hoop-wrapped composite. The following Figs. 34.6 and 34.7

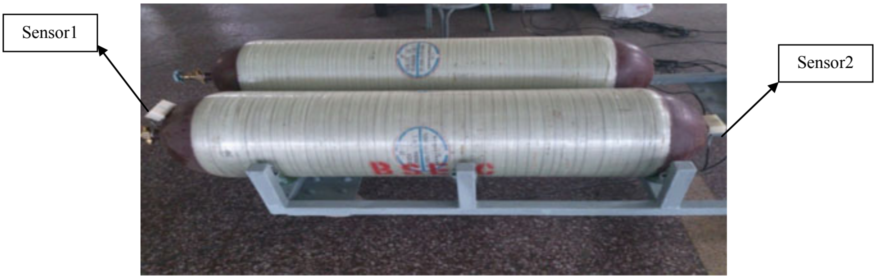

Fig. 34.5 The two sensors VS150 were arranged in the head and tail

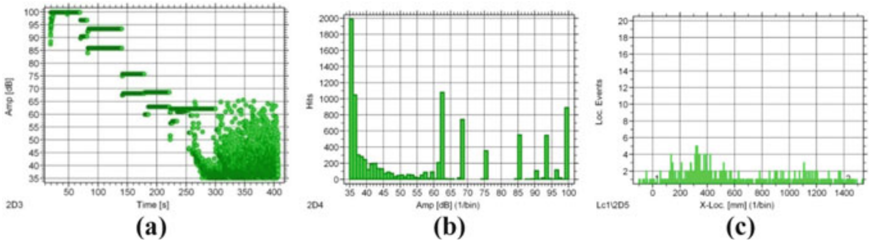

(a) (b) (c)

Fig. 34.6 The pressurization process

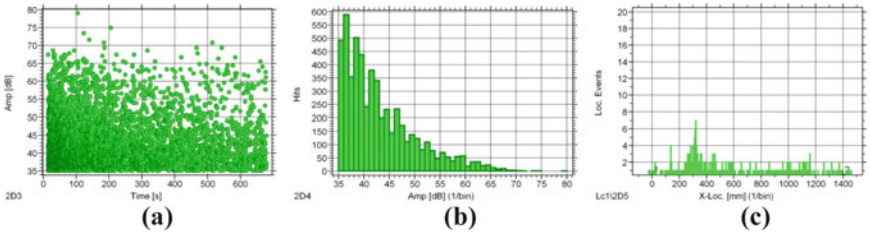

(a) (b) (c)

Fig. 34.7 The keeping pressure process

are the acoustic emission parameters diagrams of the acoustic emission signals during the pressurization and keeping pressure process of the hoop-wrapped composite cylinders. The relationship diagram between acoustic emission parameters is usually used to show the features of the acoustic emission sources.

In the pressurization process, from the location diagram in Fig. 34.6c, we can see that there are many positioning signals in the hoop-wrapped composite cylinders which have broken defects in the head. The Fig. 34.6 shows much hits signals in the range of 35–40 dB and 60–99 dB. In this process, there are much mechanical signals which is shown in the Fig. 34.6. In the waveform and frequency spectrum, the acoustic emission signals scatters and is also no convergence in the defected hoop-wrapped composite cylinders.

In the keeping pressure process, by observing the amplitude diagram, it can be found that the amplitude is generally maintained in 35–70 dB which is mainly centered in 35–45 dB which the change is relatively large. Through observation of the waveform and frequency spectrum, it can be seen that the waveform converges after 1200 μs. There are much more positioning signals in the defective location at the same time a few signals are in other parts.

As a result of this process, we can see the activity of the acoustic emission signals can effectively be used for monitoring and quantifying which can be seen in the Table 34.1. From the Figs. 34.6 and 34.7, it has relatively a large number of changes in the amplitude signals between 7 and 15 MPa which is retained generally between 99 and 60 dB in the broken hoop-wrapped composite of the cylinders. We can clearly see that many signals are always the same amplitude, such as 99 dB in the Fig. 34.6a.

Table 34.1 The AE parameter distribution of AE signals

AE parameters	Range	Distribution rang	AE parameters	Range	Distribution rang
Amplitude (dB)	35–84	35–70	Duration time(μs)	1–99,999	1800–99,999
Energy (eu)	1–629,758.4	1–650	Rise time (μs)	1–99,999	1–1800
Hits	1–12,500	1–12,500	RMS (μV)	2.0–84	2.0–11

From the diagrams for the acoustic emission amplitude and hits, they are reflected that the signals are generally between 35–70 dB after 15 MP. After the rise time of 350 s, the signals are began to become flat. It is clearly seen that the signals are scattered and the changes are relatively large in the waveform diagram during the pressurization process.

34.3.2 Air Tightness Experiment in Intact Hoop-Wrapped Composite Cylinder

The acoustic emission experiment was performed after the internal appearance test, bottle thread test, and water pressure test in the air tightness experiment of the intact hoop-wrapped composite cylinders. In the experiment, the acoustic emission signals of the cylinders was active which the pressure is between in 8 and 20 MP. The following parameters diagrams show that the characteristics of the collecting signals during the pressurization process and keeping pressure process. The parameters diagrams are usually used for showing the features of the acoustic emission sources.

In the pressurization process which is shown in Fig. 34.8, it can be seen that the amplitude is gradually reduced in 50–150 s, and the trend is stable after 150 s which is basically focused on the range between 35 and 45 dB. From the Fig. 34.8c, the positioning signals of the hoop-wrapped composite cylinders are rare which is

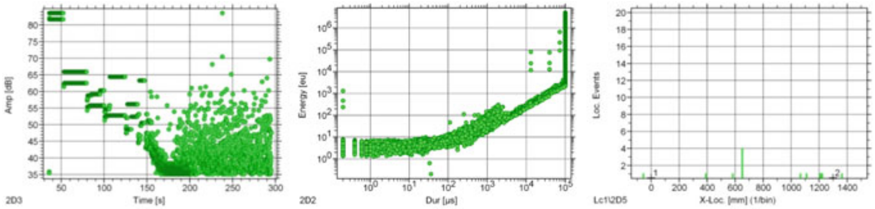

(a) **(b)** **(c)**

Fig. 34.8 The pressurization process

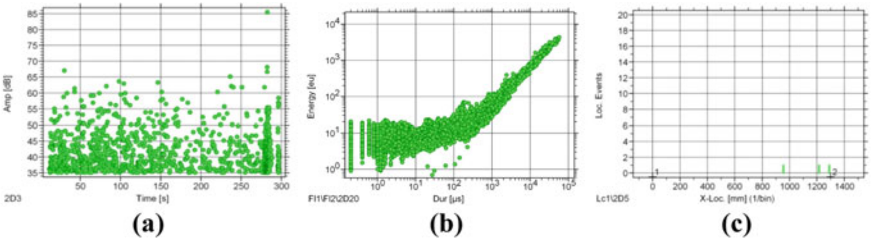

(a) (b) (c)

Fig. 34.9 The keeping pressure process

indicated that the hoop-wrapped composite cylinders have no defects in the pressurization process. The signals are generally stabilizes after the pressure is raised to 15 MPa. By observing the waveform and frequency spectrum, it can be found that the signals are convergent and not obviously abnormal.

In the keeping pressure process which is shown in Fig. 34.9, it can be known that the amplitude is obviously stable, and there is basically no signals of locations. It can be seen from the frequency diagram that the acoustic emission signals are convergent and not obviously abnormal. From the amplitude parameters diagrams in Fig. 34.9a, there are much more acoustic emission signals after the rise time of 250 s. In the energy diagram, the signals are less than the energy signals in the pressurization process.

From the above parameters diagrams, the activity of the acoustic emission signals can effectively be used for monitoring and quantifying of the air tightness experiment. As shown in the parameters diagrams that there have relatively a large number of changes in the amplitude signals between 7 and 15 MPa which are retained generally between 60 and 99 dB in the intact hoop-wrapped composite cylinders. As a result, it can be seen that the acoustic emission experiment of the 90 L gas cylinders which is inspected has a relatively large change of the amplitude. Between 8 and 15 MPa, the amplitude is generally in the range of 55 and 90 dB, and a part of the acoustic emission signals is always the same for example the amplitude is 84 dB. From the amplitude and hits diagram, it is reflected that the amplitude is generally between 35 and 45 dB after 15 MPa in the pressurization process. Moreover, the amplitude of the signals during the keeping pressure are also generally 35–45 dB. There is less positioning signals during the air tightness experiment. It is clearly seen that the signals are in the frequency converges well and there is no abnormal signal from the waveform diagram in the air tightness experiment. As a matter of fact, the acoustic emission signals are indicated that the used hoop-wrapped composite cylinders which are ready for inspection are no abnormal, and the performance is relatively stable.

From observing the parameters of each diagram, it can be found that the characteristics parameters of the experiment are fluctuated up and down within the certain range, and there is no obviously changing trend. Through analyzing and comparing each parameter, it is concluded that the distribution range of the acoustic emission parameters signals of the intact hoop-wrapped composite cylinders after many experiments are shown in Table 34.2. It can be seen from the above Table 34.2 that the

Table 34.2 The AE parameter distribution of AE signals

AE parameters	Range	Distribution range	AE parameters	Range	Distribution range
Amplitude (dB)	35–84	35–45	Duration time (μs)	1–220	1–100
Energy (eu)	1–300	70–222	Rise time (μs)	1–1400	1–600
Hits	1–12,000	1–200	RMS (μV)	2.0–9	2.0–3

used hoop-wrapped composite cylinders in the experiment are no defects which can be used normally. The data can be used as the basic data in the air tightness test in the detection for the using hoop-wrapped composite cylinders which are intact.

34.4 Conclusion

From the fatigue experiments in the laboratory and the air tightness of the hoop-wrapped composite cylinders, it can be obtained the following conclusions by analyzing the collected acoustic emission signals:

(1) The broken hoop-wrapped composite cylinders have relatively a large number of changes in the amplitude signals between 7 and 15 MPa which is retained generally between 60 and 99 dB. Moreover the signals are generally between 35 and 70 dB after 15 MP in the pressurization process. The signals are scattered and the changes are relatively larger in the waveform diagram during the pressurization process.

(2) The Intact hoop-wrapped composite cylinders have relatively a large number of changes in the amplitude signals between 7 and 15 MPa which are retained generally between 99 and 60 dB. The amplitude and hits are reflected that the signals are generally between 35 and 45 dB after 15 MPa in the pressurization process. Moreover, there are less positioning signals during the air tightness process. The AE signals are indicated that the used hoop-wrapped composite cylinders which were ready for inspection are not abnormal, and the performance is relatively stable.

(3) Through analyzing the AE signal, it can be found that the AE technique could be used as an effective means for the safety evaluation of the hoop-wrapped composite cylinders. Observing the trend of statistical parameters of the AE signal of the fatigue of the hoop-wrapped composite cylinders, it can be analyzed the characteristic changes of defects or without defects.

(4) The method is preliminarily proposed to detect of the hoop-wrapped composite cylinders by the AE. The data of this experiment can provide the experimental data for the on-line testing of the hoop-wrapped composite cylinders by AE.

References

1. F.W. Sexton, D.M. Fleetwood, M.R. Shaneyfelt, P.E. Dodd, G.L. Hash, Single event gate rupture on thin gate oxides. IEEE Trans. Nucl. Sci. **44**(6), 2345–2352 (1997)
2. J. Clerk Maxwell, *A Treatise on Electricity and Magnetism,* 3rd edn., vol. 2 (Oxford: Clarendon, 1892), pp 68–73
3. I.S. Jacobs, C.P. Bean, Fine particles, thin films and exchange anisotropy, in *Magnetism*, vol. III, ed. by G.T. Rado, H. Suhl (Academic, New York, 1963), pp. 271–350
4. K. Elissa, Title of paper, unpublished
5. R. Nicole, Title of paper with only first word capitalized. J. Name Stand. Abbrev., submitted for publication

Chapter 35
Acoustic Emission Testing of Energy Field Objects

V. V. Bardakov, S. V. Elizarov, V. A. Barat, D. A. Terentyev, V. G. Kharebov, and K. A. Medvedev

Abstract This article presents the work carried out on the energy field objects of the thermal power plants (TPPs) by means of acoustic emission (AE) method. In total, 5 examples of AE method applications on TPP are presented in the article, such as pipelines testing during hydraulic pressure test, valve leak detection, inflow detection of vacuum equipment, testing of cooling tower support columns, testing of power transformer insulation.

35.1 Introduction

Energy field is one of the most important in modern life, because it provides heat and power supply. The main power generation sources in this field are TPPs. TPP combines a large number of equipment involved in its work at various stages. At that uninterrupted operation of TPP is necessary. In the result, there is need to assess the technical state of all its equipment in operation mode. The AE method is a good method which can be used for decision of this task.

The AE method can be used on TPP to solve at a least the next list of tasks:

- Testing of pipelines during hydraulic pressure test;
- Valve leak detection;
- Air inflow detection of vacuum equipment (research task);
- Testing of cooling support columns (research task);
- Testing of power transformer insulation.

V. V. Bardakov (✉) · S. V. Elizarov · V. A. Barat · D. A. Terentyev
INTERUNIS-IT LLC, Moscow 111024, Russia
e-mail: BardakovVV@interunis-it.ru

V. G. Kharebov · K. A. Medvedev
LLC Research and Development Centre EGIDA, Moscow 101000, Russia

© The Author(s), under exclusive license to Springer Nature Singapore Pte Ltd. 2021

G. Shen et al. (eds.), *Advances in Acoustic Emission Technology*, Springer Proceedings in Physics 259, https://doi.org/10.1007/978-981-15-9837-1_35

35.2 AE Testing of Pipelines During Hydraulic Pressure Test

Pipeline testing on TPP during hydraulic pressure test is typical task which is decided by means of AE method, but for extended objects testing, such as pipelines it is not convenient to use standard systems with parallel channels connection. The good decision is using AE systems with serial connection of channels. The example of such type of systems is DDM type systems with digital data transfer channel, produced by INERUNIS-IT company (Fig. 35.1).

At this moment 2 version of system exist (DDM1 and DDM2). For example, for basic configuration of systems with 2 lines, it is possible to connect up to 32 channels for DDM1 and up to 40 channels for DDM2 (Table 35.1). By means of serial modules connection, with distances between 2 nearest modules up to 100 and 150 m for DDM1 and DDM2, it is possible to test long sections of pipelines by 1 loading cycle.

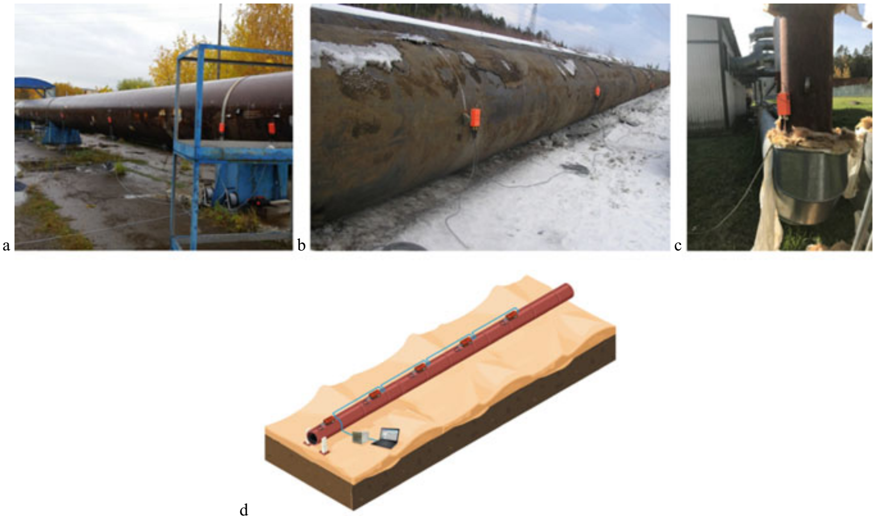

Fig. 35.1 **a–d** Examples of DDM system appliance

Table 35.1 Main parameters of DDM systems

Parameter	DDM1 system	DDM2 system
Maximum channels number per 1 line	16	20
Maximum cable length between 2 modules	100	150
Lines number for basic configuration	2	

35.3 AE Valve Leak Detection

In addition to pipelines there are a lot of valves units on TPP. One of the main operation parameters of valve is tightness. In the result, detection of valve tightness and leakage value of valve is relevant task. As it is known AE method has high sensitivity for detection of gas and liquid leak [1].

Automatic leak detection function, realized in portable 2 channel device UNISCOPE can be used for leakage detection of valve (Fig. 35.2) [1, 2].

This function consists of 3 stages (Fig. 35.3). The first stage consists of setting valves characteristics and parameters of their operation (Fig. 35.3a). At the second stage, data are collected in accordance with the measurement scheme (Fig. 35.3b). The data are collected by change the sensor position to the points indicated in the schematic drawing, which is located on the device screen. At the same time, automatic noise filtering, identification of the leakage signals and calculation of the leakage value on the basis of the empirical equation are carried out. And at the last, third stage, a report is generated (Fig. 35.3c), with a conclusion about the tightness/non tightness of the valves, and the leakage value (if the valves are non-tight).

At that, testing time of valve unit depends from flow diameter and takes from 1 to 15 min. Minimal value of leakage which can be detected is about 1 l/min for gases and 0.2 l/min for liquids. The relative error is about 20%.

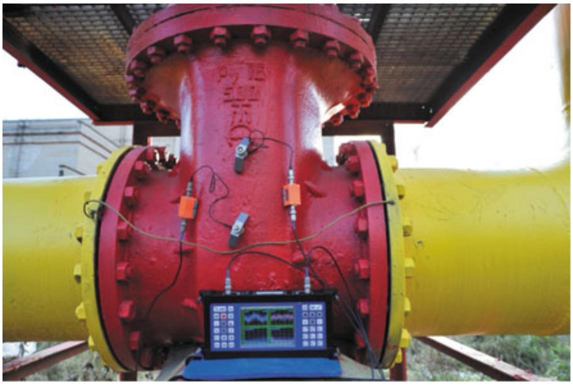

Fig. 35.2 UNISCOPE device

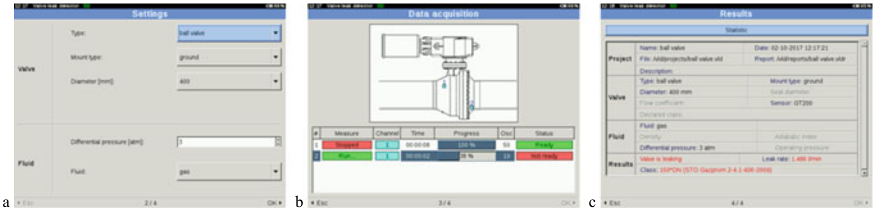

Valve
Type: ball valve
Mount type: ground
Diameter [mm]: 400
Fluid
Differential pressure [atm]: 3
Fluid: gas

Project
Name: ball valve
Valve
Type: ball valve
Mount type: ground
Diameter: 400 mm
Sensor: GT200
Fluid
Fluid: gas
Differential pressure: 3 atm
Results

Fig. 35.3 **a–c** Examples of UNISCOPE software in leak detection mode

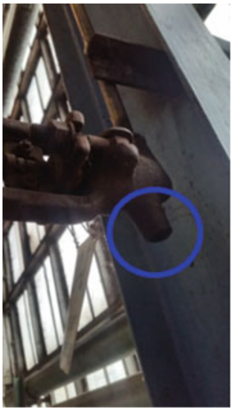

Fig. 35.4 Vent valve on vacuum equipment

35.4 AE Air Inflow Detection of Vacuum Equipment

In addition to leak detection, the AE method also makes it possible to detect air inflows of vacuum equipment. Air inflows occur in vacuum pipelines of TPP in turbine and condenser sections. The pressure in such pipes is lower than atmospheric. In the result penetration defects create air inflow, which reduces the installation efficiency of vacuum equipment. Therefore, the relevant task is air inflow detection.

For investigation of AE method application in this direction, one air inflow simulation experiment was carried out. During that experiment the air inflows were simulated by vent valve opening on vacuum equipment in turbine section (Fig. 35.4).

The portable device UNISCOPE produced by INTERUNIS-IT company was used as AE acquisition system with GT200 AE sensor, which was mounted on the tube. The data was recorded in frequency range from 100 to 400 kHz. Typical results are presented in Fig. 35.5.

Figure 35.5a shows the signal waveforms which correspond of air inflow with a small opening of vent valve, and Fig. 35.5b shows noise signal for closed valve. Air inflow (in opposite of noise signal) is characterized by shift of the spectrum to the low frequency region (Fig. 35.5c, d) and can be detected as a source of correlated noise with a width of autocorrelation function about 300 mks (Fig. 35.5e, f).

The next step is to carry out additional investigation to determine of air inflows on vacuum pipelines with vapor and different values of acoustic noises.

35.5 AE Testing of Cooling Tower Support Columns

Cooling tower is a big block (Fig. 35.6a) which is used to cool a big flow of water, which fall from top to the bottom of the tower (in the pool), by means of directed air steam.

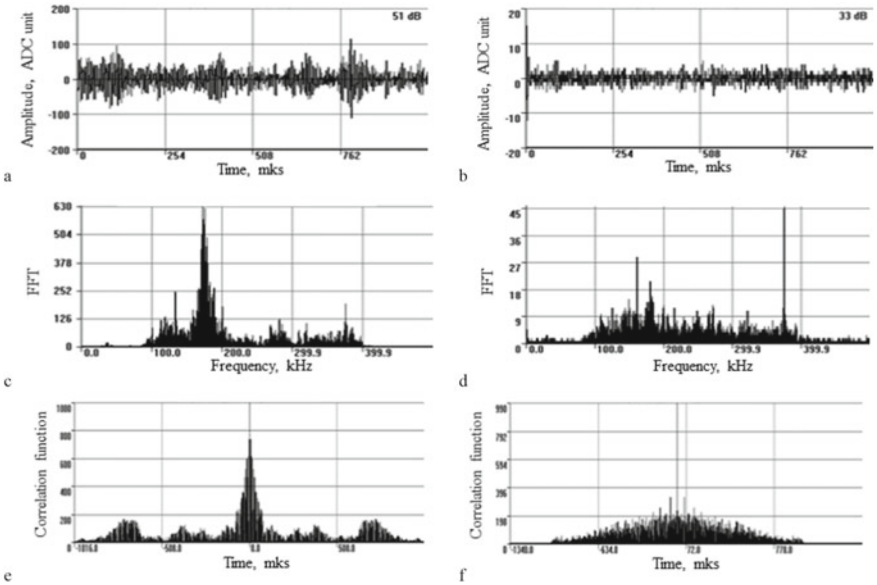

Fig. 35.5 Waveform, spectrum and autocorrelation function of **a**, **c**, **e** air inflow, **b**, **d**, **f** noise

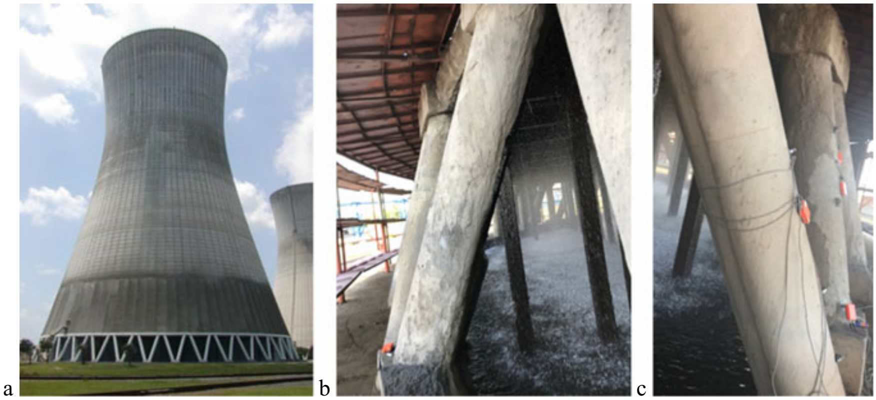

Fig. 35.6 **a** Example of water cooling tower, **b**, **c** cooling tower support columns

This large-scale structure is based on reinforced concrete (RC) support columns around the perimeter (Fig. 35.6b, c). The length of the column is about 4 m. In addition to the continuous static load, the columns are under humid environment and concrete corrosion occurs. In the result there is need to monitoring of RC support columns. For investigation of AE method in this direction the experiment was carried out. The work objective of experiment is investigation of reinforced concrete cooling tower support columns monitoring possibility by means of AE method.

Table 35.2 Damage levels of columns

Damage level of column	Existing defects
Heavy	Destruction of concrete protection layer Concrete corrosion Cracks with a width up to 6 mm
Intermediate	Partial destruction of concrete protection layer Cracks with a width up to 7 mm
Minor	Minor cracks in concrete protection layer

Support columns of cooling tower which have been operated since the second half of the last century were tested. Summary 3 columns with different damage levels—heavy, intermediate and minor were investigated (Table 35.2).

3 AE sensors with operation frequency band from 30–300 kHz were mounted on each column at a distance of 1 m between each other. The duration of data acquisition was about 15 h. This time period included day-night and night-morning temperatures changing which were used as a load in additional to the static load.

First of all noise level was investigated. This type of object has high level of acoustic noises in sound range due to falling water and strong wind flows, but in the frequency band from 30 to 300 kHz the noise level is low enough and does not exceed 30 dB.

Figure 35.7 shows the dependence of cumulative hits on air temperature over 15 h period for the most active channels of each column.

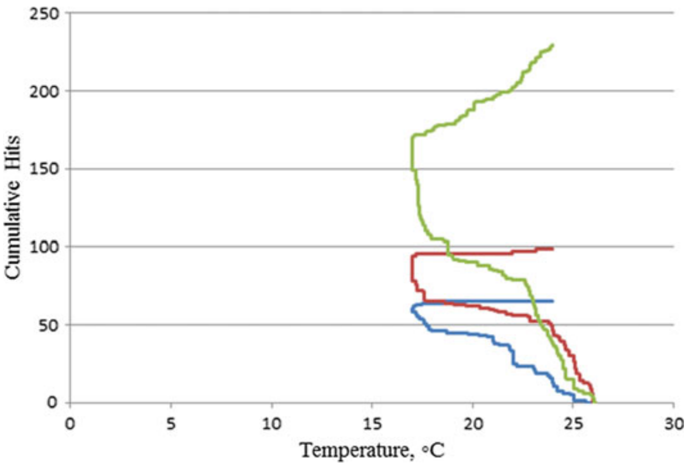

Fig. 35.7 Dependence of cumulative hits on air temperature for most active channels for 3 columns with different damage levels (blue—minor, red—intermediate, green—heavy)

At that the temperature decreasing period duration was about 4 h, constant temperature period was about 8 h and duration of temperature increasing was 3 h. This graph demonstrates that temperature changing could be used as load in addition to static load. In particular, the graphs show a correlation between the slope ratio of the dependence and damage level of the columns.

Based on the obtained results, monitoring possibility was confirmed.

35.6 AE Testing of Power Transformer Insulation

Deterioration of power transformers insulation technical state is a serious problem reducing lifetime of transformers. In places where insulation is weakened or has defects, partial discharges (PD) occur, which lead to insulation destruction with subsequent breakdown of transformer [3]. Therefore, it is important to detect transformer insulation defects as well as their position.

2 power transformers (110 kV) with different lifetime 10 (first transformer) and 25 years (second transformer) were tested. According to the preliminary information, based on periodic oil sample inspections from the tank of transformers, the second transformer had insulation defects. The first transformer had a good condition.

18 AE sensors GT200 with resonant frequency of 180 kHz were used for testing. Sensors were mounted on the tank of transformer around the perimeter in 2 levels. The A-Line 32D DDM system with digital data transfer channel and high noise immunity was used in these experiments to avoid electrical noises. The duration of data acquisition was 2 h for each transformer.

The main problem during power transformer testing is high level of acoustic noises from its operation and vibration due to cooling systems operation. So, as an example Fig. 35.8 demonstrates dependences of AE activity and average amplitudes for 2 transformers for 10 min period.

Second (older) transformer has higher values of parameters, but first transformer also has high enough values. It was found that the AE data of second transformer has one feature in comparison with first transformer. This feature is hits witch were registered with certain periodicity. The most common periodicity value is 10,000 mks. At 50 Hz of power voltage frequency, the value of 10,000 mks corresponds to one action of PD source per half of a power voltage period (Fig. 35.9).

Figure 35.9 shows dependence of amplitudes for 3 sensors located near each other. Also, it is important to note, that these periodic signals are characterized by constant of waveforms within each sensors. This fact may means that they are from one source. But for most channels in addition to these periodic signals, there are a lot of noise signals. These noise signals can break periodicity and results of the location (Fig. 35.10a, b).

So, filtration was carried out based on AE parameters of periodic signals. Filtration consists of preliminary amplitude filtration and filtration based on parameter Counts/Duration. Filtration results are presented in Fig. 35.10c, d.

The winding insulation defect was found based on result of location.

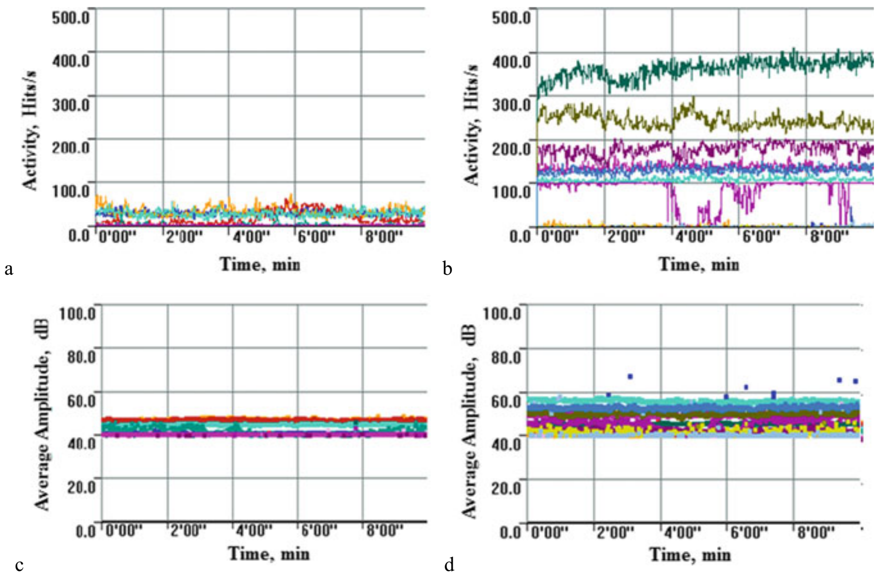

Fig. 35.8 Dependences of activity and average amplitude for **a**, **c** first transformer and **b**, **d** second transformer

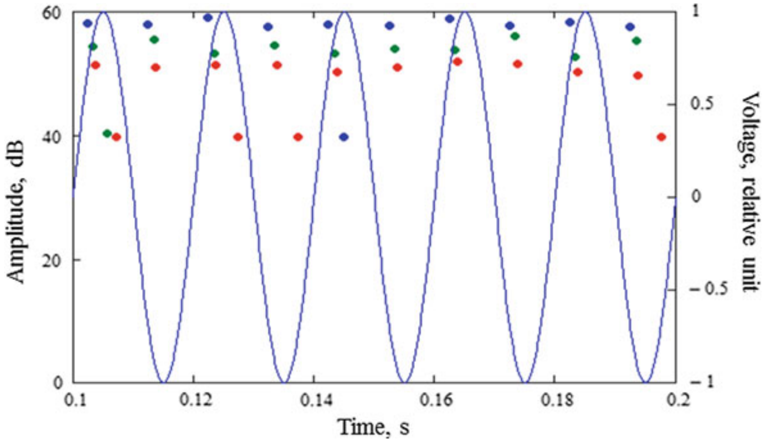

Fig. 35.9 Dependence of amplitudes and voltage on time

35.7 Conclusions

The article describes the application of AE method on TPP objects, namely:

1. Pipeline testing during hydraulic pressure test by means of AE systems with serial channel connection was presented.

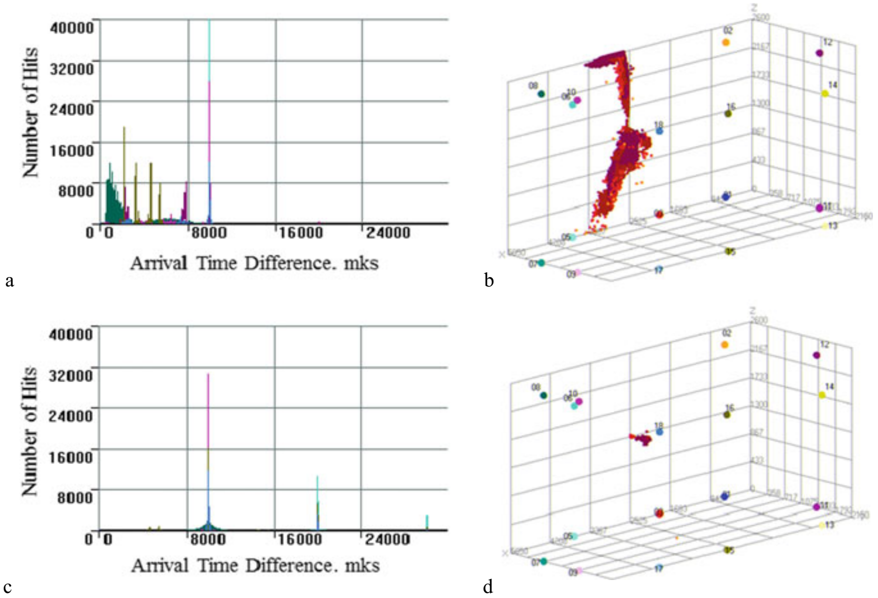

Fig. 35.10 Dependences of arrival time difference and volume locations. **a**, **b** Before filtration, **c**, **d** after filtration

2. Valve leakage detection by means of UNISCOPE devise was presented.
3. Investigation of air inflow detection possibility on vacuum equipment was carried out. Air inflow detection possibility was confirmed.
4. Investigation of RC cooling tower support columns monitoring possibility was carried out. Monitoring possibility was confirmed.
5. AE testing of 2 power transformers was carried out. Insulation defect was found based on the results of testing.

Reference

1. S. Elizarov, V. Barat, D. Shchelakov, Checking of the shut-off valves tightness using a portable multifunctional device "UNISCOPE" . NDT World **1**, 22–24 (2012)
2. S. Elizarov, V. Bardakov, A. Shimanskiy, A. Alyakritskiy, D. Terentyev, V. Barat, A. Gogin, V. Koltsov, UNISCOPE: instrument integrating NDT methods, in *WCAE 2017: Advances in Acoustic Emission Technology, Part of the Springer Proceedings in Physics Book Series* (SPPHY), vol. 218 (2017), pp. 65–74
3. W. Sikorski, K. Walczak, Power transformer diagnostics based on acoustic emission method. Acoust. Emission Res. Appl. 91–116 (Chapter 5)

Chapter 36
AE Detection of Leakage Location in an Ethylene Oxide Reactor

Yanting Xu, Yadong Wang, Gangyi Cai, and Jiele Xu

Abstract The imported ethylene oxide (EO) reactor in the EOEG unit of a petrochemical company has been leaking internally since it was put into operation. Before we tried to locate the leak by AE technology this time, the foreign technicians from the manufacturer had come to the company several times to find out the leak location, but they did not determine the location of the leak. Due to the limitation of its complex structure and inaccessibility, it is impossible to use other methods for leak detection. By taking some correction measures for the sound source location or other setups, we finally located two highly suspected sound sources. After partial removal of the half pipes, one of them was identified as the leakage point, and another is a very serious crack defect.

36.1 Introduction

In recent years, AE technology has been widely used in the monitoring or testing of pressure vessels or pipes, and usually good detection results has been achieved. It not only solves the safety inspection problem of special pressure equipment, but also saves the overhaul time and enormous cost of open inspection for enterprises. One of the applications is to identify the leakage signals and locate the leakage source [1, 2]. When AE testing is carried out for such equipment, it is generally required to apply a test load that exceeds the maximum operating pressure in the near future, so that serious defects in the equipment can emit acoustic signals, which are then received by AE testing system for source positioning and analysis. Compared with other detection methods, one of the advantages of AE technology is its insensitivity to complex structures and accessibility.

Y. Xu (✉) · Y. Wang · G. Cai · J. Xu
Zhejiang Academy of Special Equipment Science, Hangzhou 310020, China
e-mail: 657311787@qq.com

Y. Xu · Y. Wang
Key Laboratory of Special Equipment Safety Testing Technology, No.211, Kaixuan Road,
Hangzhou, China

© The Author(s), under exclusive license to Springer Nature Singapore Pte Ltd. 2021

G. Shen et al. (eds.), *Advances in Acoustic Emission Technology*, Springer Proceedings
in Physics 259, https://doi.org/10.1007/978-981-15-9837-1_36

The EO reactor introduced in this paper is a bi-conical shell structure with internal metal supporting structures to strengthen its rigidity. There are indications that the container has been leaking for several years. The leakage position is suspected to be on the vessel wall under the welded heating pipe (half pipe). It is impossible to enter the container for internal inspection during shutdown inspection, because all four manholes have been welded after the installation and acceptance of the vessel. The outside of the conical shell is welded with dense heating pipes, so most of the inspection methods cannot be implemented because of the small space. Technicians from foreign manufacturers have come to China several times and have not found out the location of the leakage. This technical problem has been puzzling the owners for several years.

Finally, AE technology becomes the only possible way to solve this problem. The external shell does not bear the internal pressure, only bears the local external pressure from the heating pipe, and the shell thickness is up to 100 mm, so it is very likely that the defect (leaking) cannot be excited to send detectable signals or cannot be further accurately located. Therefore, it brings a great challenge to the application of AE detection technology. By making a detailed inspection plan and taking some targeted technical measures, we finally succeeded in finding out the leakage and positioning it accurately. At the same time, we have also found another very serious crack with a depth 80 mm.

36.2 AE Testing Process of the EO Reactor

36.2.1 The Structure of the EO Reactor

The structure of the EO reactor is shown in Fig. 36.1. The vessel is composed of two conical shells, which are fixed by metal supporting members inside, and three heating pipes (half pipes) are densely coiled and welded on the outside of the conical shell. The thickness of the outer conical shell is 100 mm, the outer diameter of the

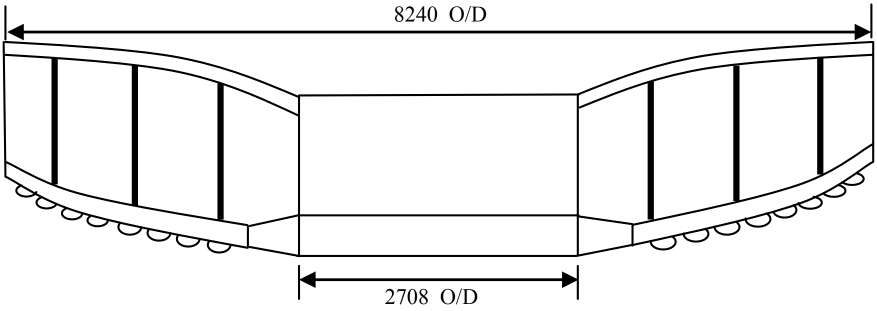

Fig. 36.1 The structure of the EO reactor

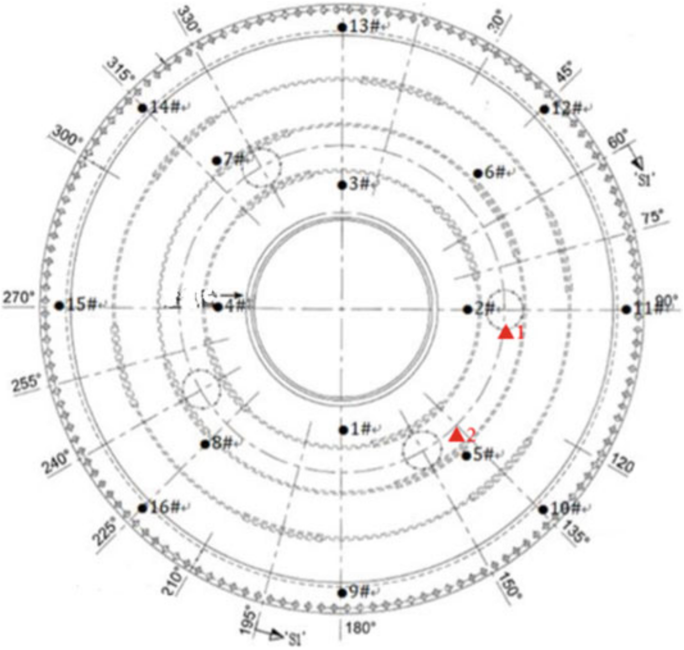
330°
30°
315°
45°
300°
60°
'S1'
75°
270°
90°
255°
240°
120
225°
135°
210°
150°
195°
'S1'
180°
1#
2#
3#
4#
5#
6#
7#
8#
9#
10#
11#
12#
13#
14#
15#
16#
▲1
▲2

Fig. 36.2 The arrangement of the sensors (upward view)

large end is 8240 mm, and the outer diameter of the small end is 2708 mm. The material is carbon steel.

36.2.2 Arrangement of Sensors

The arrangement of the sensors is shown in Fig. 36.2 (upward view). Four sensors are equally distributed on the circumferences of the small end and the middle end of the conical shell respectively, and eight sensors are evenly distributed on the circumference of the large end. Sensors on two adjacent circles are staggered.

36.2.3 Loading Mode

The external conical shell is loaded by the hydrostatic test of the heating pipes, and the loading curve is shown in Fig. 36.3. Hold for 20 min at the highest pressure of 4.0 MPa.

Fig. 36.3 The loading curve

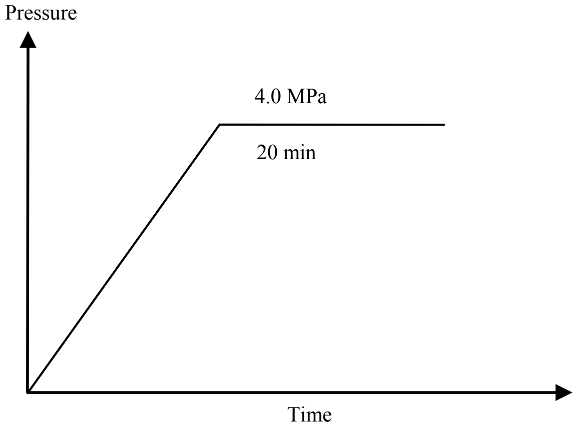

36.2.4 Parameter Setting of Acquisition and Data Analysis Display

There is no conical shell positioning software in our AE detection system. In order to locate the sound sources more accurately, we expand the external conical shell into a sector plan, as shown in Fig. 36.4. D1 and D2 in Fig. 36.4 are the outer shell diameters at the first circle of sensors (1#–4#) and the third circle of sensors (9#–16#) respectively, and H is the vertical height between the first and third circles of sensors.

As can be seen from the figure,

$$\mathrm{D1/D2} = \mathrm{X/(X + H)}, \text{ that is, } \mathrm{X} = \mathrm{D1} \times \mathrm{H/(D2} - \mathrm{D1)}$$

$\pi \times \mathrm{D1} = 2\pi \times \mathrm{X} \times \theta/360$, that is, the center angle θ of the sector circle is $180 \times (\mathrm{D2} - \mathrm{D1})/\mathrm{H}$.

D1, D2 and H can be measured on site, so after getting θ, the plane coordinates of each sensor can be calculated further and then entered into the positioning setup.

According to the test of background noises, the lower threshold is selected. The wave velocity is measured several times on the conical shell, and the average value

Fig. 36.4 The conical shell and its expanded sector plan

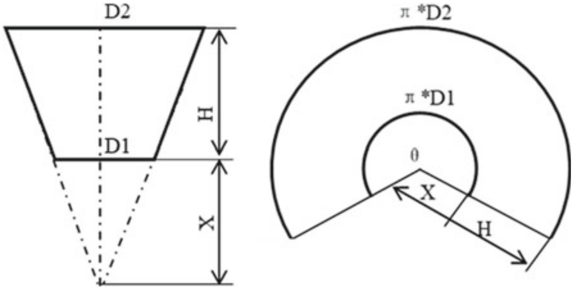

is taken. In addition, regional positioning, linear positioning and the correlation diagrams of related parameters are also set as auxiliary observation means.

36.2.4.1 AE Test and Retest Results

Two meaningful acoustic source locations (S1 and S2 in Fig. 36.5, respectively corresponding to ▲1 and ▲2 in Fig. 36.2.) were obtained during AE monitoring. A penetrating crack (verified by UT) in the conical shell was found after partial removal of the half tube at S1. Another crack was found after polishing the outer surface of the shell at S2 for 20 mm, which was verified by UT to extend to the inner surface. In other words, there is an internal surface crack with a depth of up to 80 mm at the source S2. Photos of two defects are shown in Figs. 36.6 and 36.7.

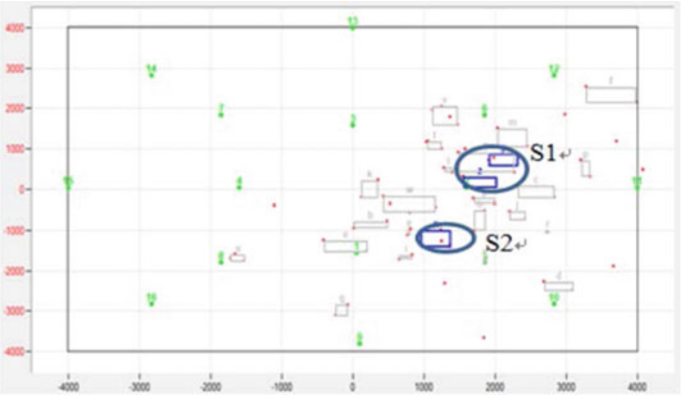

Fig. 36.5 Sound source location

Fig. 36.6 The penetrating crack with a depth of 100 mm

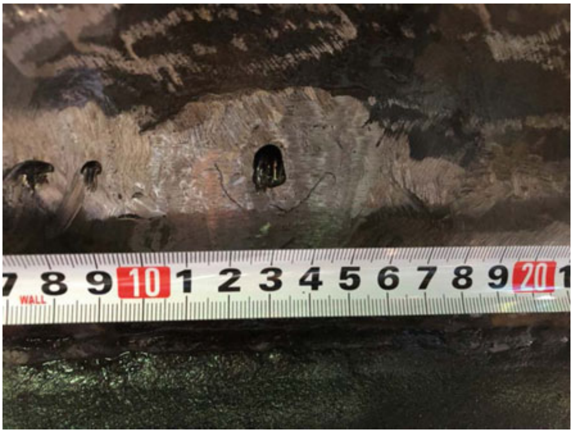

Fig. 36.7 The inner surface crack with a depth of 80 mm

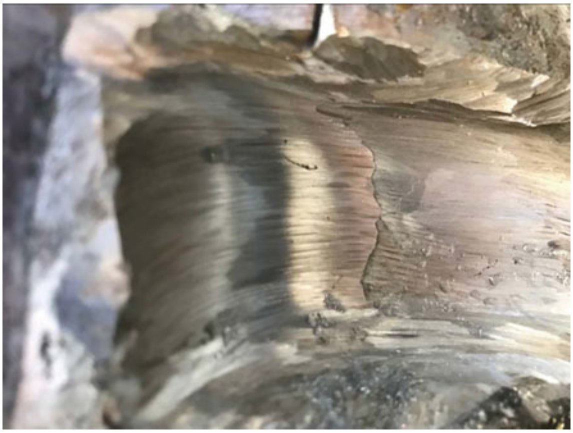

36.3 Conclusions

In this paper, AE technology is used to solve the technical problem of finding out the internal leakage of a non- internal pressure structure which has been bothering the owner for many years. We not only successfully found the penetrating crack which caused the internal leakage, but also unexpectedly found another internal surface crack which is about to penetrate.

The test case shows that for some technical problems of "unsatisfactory" or "unconventional" AE test conditions, if other methods cannot be implemented or invalid, we can boldly try to use AE technology to solve it through careful analysis and detailed targeted detection scheme. How can you know if you don't try?

References

1. W. Y. Wang, Acoustic emission detection technology of pressure pipeline leakage. Chin. J. Nondestruct. Testing **03** (2016)
2. G.T. Shen, R.S. Geng, S.F. Liu, Source location technology of continuous acoustic emission signals. Chin. J. Nondestruct. Testing **04** (2002)

Chapter 37
A Method of Vacuum Leak Detecting Based on Acoustic Emission Characteristics Analysis

Qi Lei, Sun Lichen, Liu Gaotong, Rui Xiaobo, Liu Tao, and Wang Lina

Abstract In the view of space science and technology is developing, the number of spacecraft in orbit is increasing. Space environment including vacuum, vibration, alternating temperature, micro-meteorites and space debris threatens the structure safety of spacecraft. Once a leak in the spacecraft structure occurs, the pressure of the capsule will drop, which will have a significant impact on the safety of the astronauts. When a leak occurs, the acoustic signal is generated and a method for vacuum leak detection can be used based on characteristics analysis. In this paper, the vacuum leak detection principle is described, and tested by the proposed experimental platform. By characteristic analysis, the signals generated by three different leak holes of 1.0, 1.5 and 2.0 mm are collected and compared with the background acoustic signal by the pump without leakage. The Experiment data show that the signal frequency of the pump running is below 20 kHz. The leak signal is above 20 kHz, which is obviously distinguished from the background noise. When the diameter of the leak hole increases, the energy of leak signal becomes larger, but the high frequency component in the signal decreases. The characteristics analysis of leak acoustic emission signal in this paper is meaningful to the leak detection of spacecraft.

37.1 Introduction

With the increase of human space activities, more and more space debris are left in earth orbit. Once space debris collides with spacecraft, the spacecraft cabin damage and gas leak prone to occur. Therefore, it is very important to detect the leak of spacecraft in orbit. Leak location and leak rate assessment are two major tasks of leak detection. The gas leak of spacecraft cabin is from atmosphere to vacuum. The pressure difference is small and the acoustic signal generated by the leak is extremely weak mixed with the background noise of pump running, which increases the difficulty of acoustic leak detecting. After 2000, NASA, ESA and other institutions have studied a series of on-orbit leak detection methods [1, 2], including optical method, acoustic

---

Q. Lei (✉) · S. Lichen · L. Gaotong · R. Xiaobo · L. Tao · W. Lina
Institute of Spacecraft Environment Engineering, Beijing, China
e-mail: qilei511@126.com

© The Author(s), under exclusive license to Springer Nature Singapore Pte Ltd. 2021

G. Shen et al. (eds.), *Advances in Acoustic Emission Technology*, Springer Proceedings in Physics 259, https://doi.org/10.1007/978-981-15-9837-1_37

emission method, pressure change method, resistance change method, etc. All of these methods have unique advantages, however, the acoustic emission detection method is more suitable for engineering applications because of its simple principle and high detecting sensitivity [3, 4].

Acoustic emission leak detection is a kind of nondestructive testing technology, which is mainly used by the amplitude, frequency, energy and other parameters of the acoustic emission signal generated by the leak to locate and evaluate the leak. Acoustic emission detection can be divided into two types according to the signal type [5, 6], burst signal detection and continuous signal detection. The former mainly focuses on the number of ringing, rise time and other parameters detection, while the latter mainly focuses on the detection of amplitude, energy and other parameters. In recent years, with the development of digital acquisition technology, acoustic emission leak detection has developed rapidly and achieved certain research results. In 1999, Hunaidi and Chu [7] simulated a variety of leak forms of plastic pipes under certain experimental conditions, and studied the acoustic characteristics of the leak signals, including the characteristics of each frequency component of the acoustic signal or vibration signal. They studied the relationship between the frequency components and the leak form, flow rate, pipe pressure, and the relationship between attenuation rate, wave velocity and frequency. In 2006, Jingpin et al. [8] and others studied the application of modal acoustic emission technology in the field of pipeline leak detection, established the model of pipeline leak modal acoustic emission localization, and successfully solved the problem of one-dimensional pipeline leak location. In 2014, Avramchuk et al. [9] and others studied the application of the new cross-correlation method to leak location, and solved the problem of pipeline leak detection through time-frequency correlation function. However, most of these methods are aimed at the location of leak points, and there are few studies on leak rate assessment, especially gas leak rate assessment. In the paper, the spectrum analysis method combines with the characteristic parameter analysis method to study the characteristics of acoustic emission signals produced by gas leak of different sizes of leak holes, and the spectrum and characteristic parameters of acoustic emission signals of gas leak are obtained.

37.2 Detection Principle

When there is a leak in the sealed cabin of a spacecraft, the gas leaks from the sealed structure along the leak path to the vacuum environment outside the cabin under the action of the pressure difference. When the gas medium passes through the tiny aperture, its velocity is high. It is in a turbulent state with a large number of turbulence. The internal stress of the interaction between the turbulence of the gas causes their respective volume elements to be subjected to equal and opposite undulating forces, which causes the gas to produce a quadrupole sound source. At the same time, the interaction of the gas and the channel structure of the leak will produce a dipole sound source, and the superposition of the two forms the generation of gas leak ultrasound [10, 11].

In this paper, the acoustic emission sensors are installed on the spacecraft bulkhead structure to collect the leak acoustic emission signal and perform characteristic analysis, which can realize leak location and leak rate evaluation. However, because the spacecraft leak is from the atmosphere to the vacuum, the pressure difference is small and the acoustic signal generated by the leak is extremely weak. The CFD simulation of gas leak from the atmosphere to the vacuum is shown in Fig. 37.1. The leaked gas in the vacuum environment will expand rapidly when entering the vacuum environment, forming a supersonic jet with a higher flow rate. At the same time, the signal is also mixed with the background noise of the running pump, which increases the difficulty of the acoustic leak rate evaluation. In this paper, firstly the frequency spectrum of the leak acoustic signals from leak holes of different diameters are analyzed. The suitable comparison frequency band is selected to overcome the influence of low-frequency pump noise. Then, the characteristics of the leak acoustic signal to effectively extract the characteristic parameters of the signal are analyzed. The analysis results are more scientific and useful by the combination of spectrum analysis and characteristic parameter analysis.

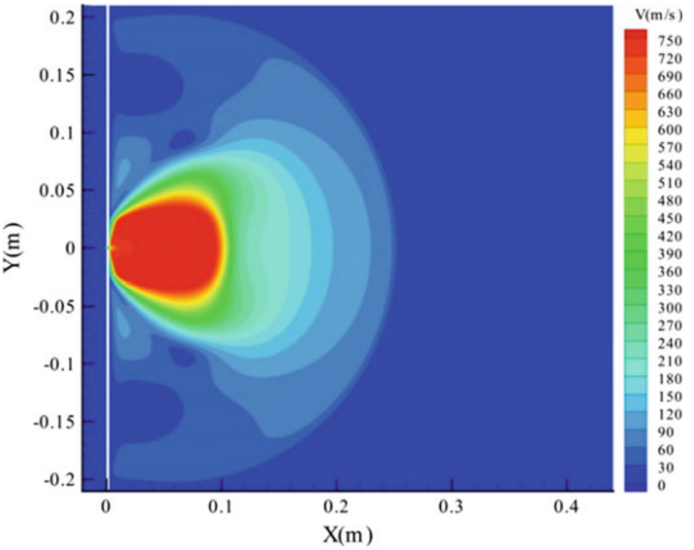

Fig. 37.1 CFD simulation of gas leak from the atmosphere to the vacuum

37.3 Experimental Platform and Experimental Program Design

In order to carry out the principle experiment research, a leak detection experimental platform was built, which is composed of a leak generating system and a signal acquisition system. The leak generating system is mainly composed of a vacuum pump, a bellows, a vacuum-to-plate adapter and a test plate with leak holes, as shown in Fig. 37.2. Three circular leak holes with different sizes of 1.0, 1.5 and 2.0 mm are premade on the test plate. The minimum leak rate of this system is about 1 Pa m^3/s.

The signal acquisition system realizes the acquisition, analysis and processing of the leak acoustic signal, which is composed of some sensors, some preamplifiers, an acoustic emission acquisition instrument and a computer. The RS-2A acoustic emission sensor is used in the experiment and its effective frequency band is 100–400 kHz, and the frequency response curve is shown in Fig. 37.3. The preamplifier can achieve 40 dB gain amplification; the acoustic emission acquisition instrument

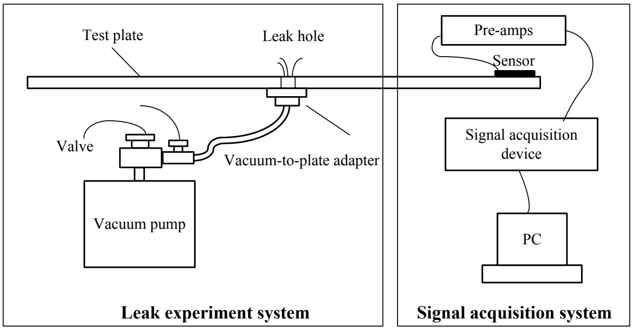
Test plate
Leak hole
Pre-amps
Sensor
Valve
Vacuum-to-plate adapter
Signal acquisition device
Vacuum pump
PC
Leak experiment system
Signal acquisition system

(a) Schematic diagram

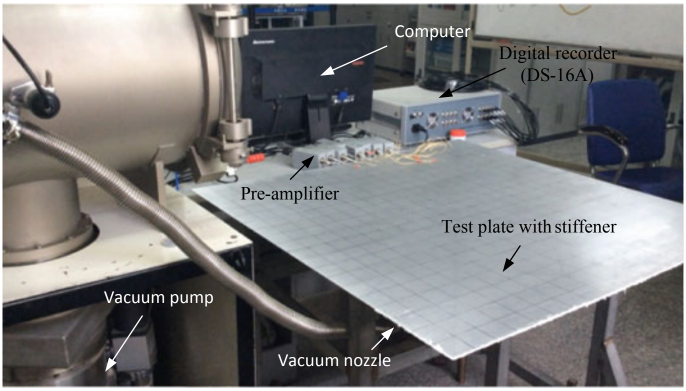
Computer
Digital recorder (DS-16A)
Pre-amplifier
Test plate with stiffener
Vacuum pump
Vacuum nozzle

(b) Physical map

Fig. 37.2 Leak detection experiment platform

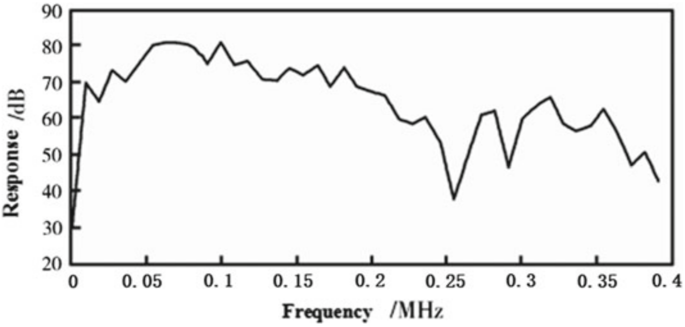

Fig. 37.3 Frequency response curve of sensor RS-2A

has a sampling rate of 3 MHz per channel and a sampling accuracy of 16 bit. The experiment data can be stored in the computer in real- time and processed using the MATLAB program.

In the leak experiment, the sensor is installed at a position 20 cm away from the leak hole. By changing the position of the vacuum adapter, the leak from three different sizes leak holes of 1.0, 1.5, and 2.0 mm can be realized. The no-leak state can be produced with tape covering as a comparative experiment. The sensor layout is shown in Fig. 37.4.

37.4 Leak Signal Characteristics Analysis

As the background noise will be produce by the vacuum pump during the experiment, it is necessary to eliminate the noise before processing characteristic analysis of the leak signal. In order to acquire the distribution of the background noise, three sensors are used to collect the signals in the condition that the vacuum pump is running while the leak hole is covered. To keep the experiment conditions consistent, the sensors are placed as Fig. 37.4 shows. The vacuum adapter is placed on different leak holes each time to generate the background noise at different conditions. The background noise is shown in Fig. 37.5.

It can be seen from the above figure that the background noise produced by the operation of the vacuum pump is basically the same. And the noise amplitude is less than 10 mV, while the frequency is mainly distributed below 20 kHz. Therefore, the background noise can be eliminated by using 20 kHz high pass filter before the analysis of the characteristics of the leak signals.

The acoustic emission signals excited by three different leak holes are collected. The time domain and frequency domain signals after 20 kHz high pass filtering are shown in Fig. 37.6.

As can be seen from the above figure, the signal frequencies for different leaks are mainly concentrated below 400 kHz. With the increase of the leak holes diameter,

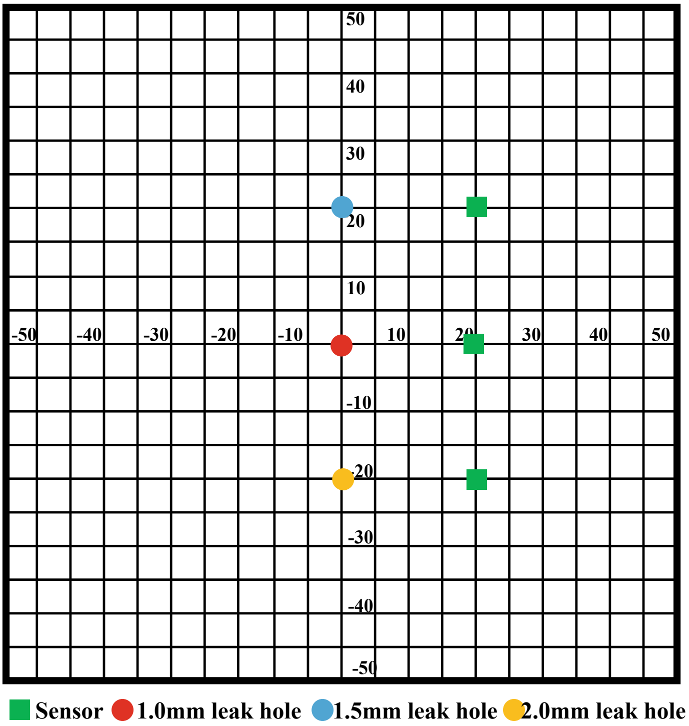
50
40
30
20
10
-50
-40
-30
-20
-10
10
20
30
40
50
-10
-20
-30
-40
-50
Sensor
1.0mm leak hole
1.5mm leak hole
2.0mm leak hole

Fig. 37.4 Sensor layout

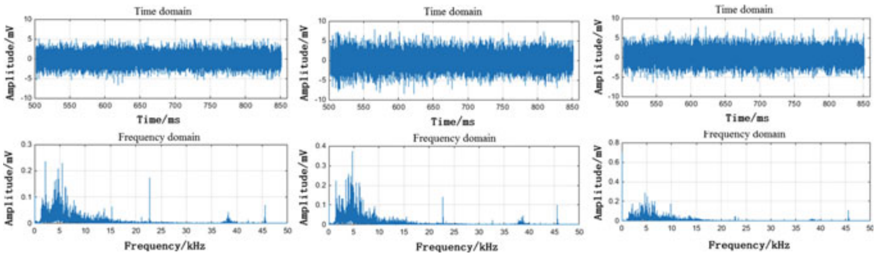

（a）1.0 mm （b）1.5 mm （c）2.0 mm

Fig. 37.5 The background noise signal of the running vacuum pump in three conditions

the signal amplitude increases and the frequency band distribution expands. The leak signal of 1 mm leak hole has obvious peaks near 290 and 400 kHz. The leak signal of 1.5 and 2.0 mm leak holes also have a peak near 270 kHz, but less obvious than that of 1.0 mm leakage hole. As a result, the frequency domain characteristic of leak signals can be used to analysis the leak rate.

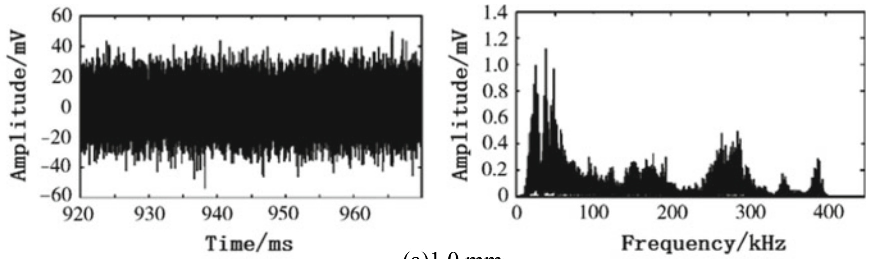

(a)1.0 mm

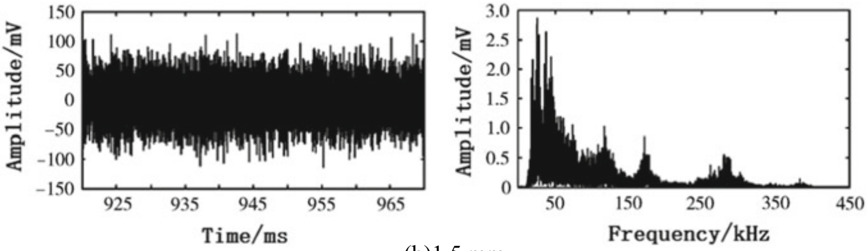

(b)1.5 mm

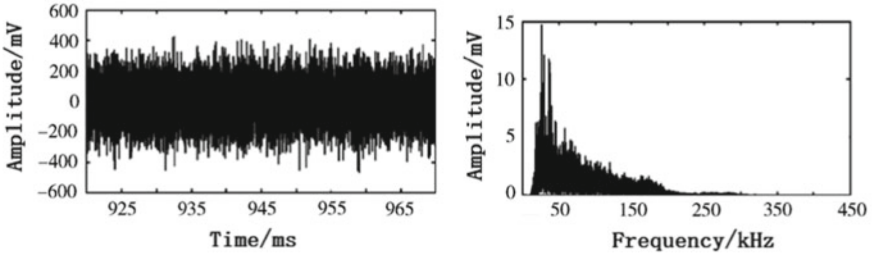

(c)2.0 mm

Fig. 37.6 The acoustic emission signals of three different leak holes

The commonly used characteristic parameters of continuous acoustic emission signals are including signal amplitude (Amplitude), average signal level (ASL), signal energy (Energy), root mean square of signal voltage (RMS) and so on. To increase the stability of feature parameter identification of different leak signals, the signal is first filtered by 20–250 kHz. Then, the collected leak signals with a total length of 8 ms are divided into 25 segments. The analyzing results are shown in Fig. 37.7. As can be seen from the figure, all of the four parameters is able to distinguish three different kinds of leak effectively, and the results are more stable and clear by using the ASL, Energy and RMS parameters.

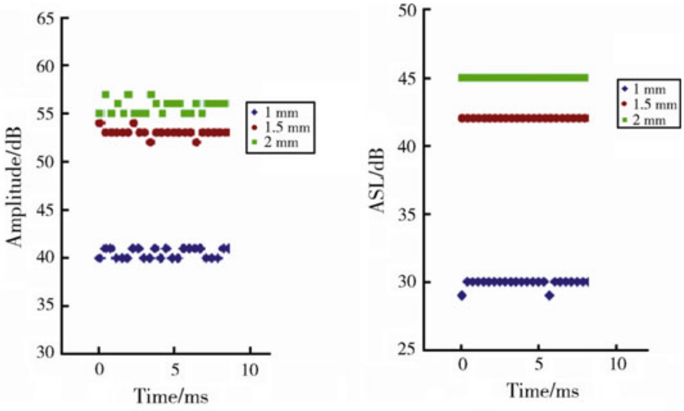

(a) Amplitude (b) ASL

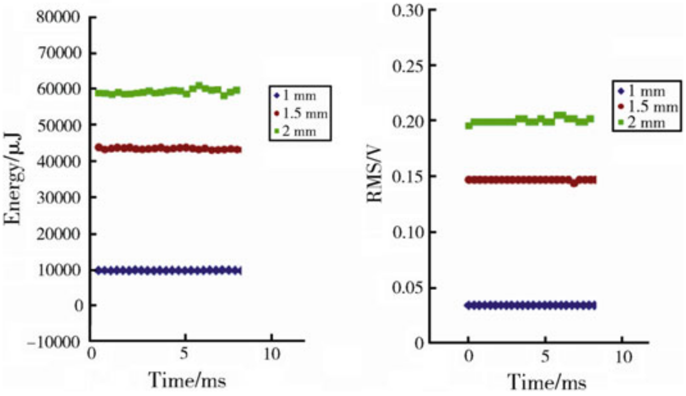

(c) Emergy (d) RMS

Fig. 37.7 Characteristic parameters of leak acoustic emission signals

37.5 Conclusion

The leak problem in spacecraft in-orbit is very serious, which threatens the spacecraft in-orbit operation and the life safety of astronauts. It is very important to judge the leak accurately and in time, determine the leak location and evaluate the leak rate for the disposal of leak accidents. In this paper, the acoustic emission signals of three typical kinds of leak are analyzed through spectrum analysis and characteristic parameter analysis. The following conclusions are drawn:

1. The leak acoustic emission signal is a broadband signal whose energy is mainly concentrated below 400 kHz. The larger the leak hole is, the larger the amplitude is, but the frequency band of leak signal with small leak hole is wider than that with a large leak hole.

2. The frequency band of background noise caused by vacuum pump operation is less than 20 kHz, which can be removed by high pass filtering in the analysis of leak signal. By analyzing ASL, Energy and RMS parameters of the leak signal, different leak holes can be identified and the leak rate can be evaluated.

Acknowledgements This research was supported by National Nature Science Fund of China (No. 61903040), the Open Foundation of State Key Laboratory of Precision Measurement Technology and Instrument (Tianjin University) (No. pilab1706).

References

1. A.J. Hyde, A. Davis, E. Christiansen, International space station hand rail and extravehicular activity tool impact damage. Orb. Debris Quart. News **12**(3), 3–6 (2008)
2. L. Qi, Z. Zeng, L. Sun et al., An impact location algorithm for spacecraft stiffened structure based on posterior possibility correlation. Sensors **20**(2), 368 (2020)
3. C. Clark, L. Labonte, J. Castro, et al., Wireless leak detection using airborne ultrasonics and a fast-bayesian tree search algorithm with technology demonstration on the ISS, in *IEEE International Conference on Wireless for Space and Extreme Environments (WiSEE), Orlando, FL, USA* (2015)
4. L. Qi, Z. Zeng, Y. Zhang et al., Research on leakage location of spacecraft in orbit based on frequency weighting matrix beamforming algorithm by lamb waves. Appl. Sci. **10**(4), 1201 (2020)
5. K.M. Holford, M.J. Eaton, J.J. Hensman, et al., A new methodology for automating acoustic emission detection of metallic fatigue fractures in highly demanding aerospace environments: an overview. Prog. Aerosp. Sci. (2017)
6. D. Ozevin, J. Harding, Novel leak localization in pressurized pipeline network using acoustic emission and geometric connectivity. Int. J. Press. Vessels Pip. **92**(2), 63–69 (2012)
7. O. Hunaidi, W.T. Chu, Acoustical characteristics of leak signals in plastic water distribution pipes. Appl. Acoust. **V58**, 235–254 (1999)
8. J. Jingpin, H. Cunfu, W. Bin, et al., A new acoustic emission source location technique based on wavelet transform and mode analysis. Chin. J. Sci. Instrum. **26**(5), 482–485 (2005)
9. V.S. Avramchuk, A.A. Yefremov, et al., New calculation method of correlation function applied to leak localization, in 2014 *International Conference on Mechanical Engineering, Automation and Control Systems* (2014), pp. 1–4
10. A. Nilsson, B. Liu, Vibro-acoustics vol. I and II. Chin. J. Acoust. **2014**(3), 335–336
11. L. Lin, L. Xiao-Dong, Assessment of fine-scale turbulence noise source models for jet noise prediction. J. Eng. Thermophys. **30**(4), 588–590 (2009)

Chapter 38
Acoustic Emission Testing for the Large Vacuum System and Analysis of Signal Source Data

Yue Kaibai, Ma Xuerong, Lu Jun, Zuo Jifeng, Yao Li, and Chen Xiaohui

Abstract For the large vacuum systems, which is in the condition of vacuum testing, acoustic emission testing and stress–strain test were implemented in the areas of stress concentration. Elimination of noise by interference, combined stress–strain test results, the data of signal source was analyzed. Results show that the monitoring for the areas of stress concentration and structure instability, forecast can be achieved effectively. And then, an effective security evaluation method, which is applied to the online testing and later inspecting of the large vacuum system, is proposed.

38.1 Introduction

Acoustic emission testing has been widely used in many fields. For the typical equipment in the pressure-resistant test or in the service state, such as the pressure vessel, the acoustic emission testing can carry out the whole process and real-time structural integrity evaluation, the activity monitoring of key defects, and the monitoring and prediction of structural instability and damage. Compared with other nondestructive testing methods, acoustic emission testing has obvious and unique advantages in real-time, nondestructive safety evaluation, defect activity monitoring, structural instability and failure prediction. For metal pressure vessels, acoustic emission testing technology is a new nondestructive testing method which is gradually becoming more and more mature.

Y. Kaibai (✉) · M. Xuerong · L. Jun · Z. Jifeng · Y. Li · C. Xiaohui
China Aerodynamics Research and Development Center, Mianyang 621000, China
e-mail: yuekaibai64256@163.com

© The Author(s), under exclusive license to Springer Nature Singapore Pte Ltd. 2021

G. Shen et al. (eds.), *Advances in Acoustic Emission Technology*, Springer Proceedings in Physics 259, https://doi.org/10.1007/978-981-15-9837-1_38

A large-scale vacuum system is a research and development device composed of two vacuum spherical tanks with a volume of 20,000 m^3 and supporting pipelines. The inner wall of the ball shell is provided with longitudinal and circumferential T-shaped reinforcing ribs, which are welded with the ball shell plate to form a combined ball shell structure resistant to external pressure. In case of no test, the spherical tank is in vacuum state for a long time unless equipment maintenance is carried out. The main technical parameters of the large vacuum system are shown in Table 38.1, and its physical object is shown in Fig. 38.1.

Compared with the conventional pressure vessel, the large vacuum system has the characteristics of large geometry size, internal stiffener, obvious difference in stress distribution, numerous noise interference effects, and difficulty in retesting results.

Table 38.1 The main technical parameters of the large vacuum system

Working temperature	77 °C (350 K)	Working medium	Dry air	Connecting pipe	DN3000/DN3600 mm
Nominal volume	20,000 m^3	Effective volume	20,040 m^3	Spherical tank inner diameter	33,700 mm
Structural type	Seven-band hybrid	Pillar type	Skirt	Ball shell material	Q345R
Corrosion allowance	1.7 mm	Test gas pressure	0.115 MPa	Vacuum test	10 Pa (A)

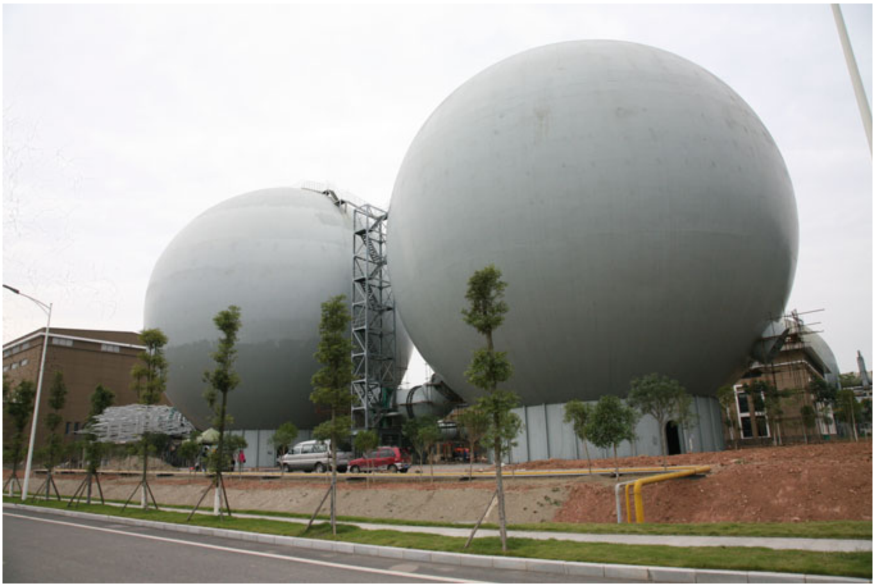

Fig. 38.1 Physical object of the large vacuum system

According to NB/T 47013.9-2012 “Nondestructive Testing of Pressure Equipment Part 9: Acoustic Emission Testing”, GB/T 18182-2012 “Acoustic Emission Testing and Results Evaluation Methods for Metal Pressure Vessel”, JB/T 1076 4-2007 “Acoustic Emission Testing and Evaluation Methods of Nondestructive Testing for Normal-pressure Metal Storage Tanks” and other standards, the existing mature acoustic emission testing technology of pressure vessels is very difficult to be directly applied to the acoustic emission testing of the large vacuum system under the vacuum test state.

In order to carry out acoustic emission monitoring on key parts or typical defect parts, explore the real-time monitoring and prediction methods for the evaluation of defect activity, hazard degree and structural integrity. In order to improve the pertinence of safety state monitoring and regular maintenance after the large vacuum system is put into use, so as to effectively prevent the occurrence of various failure and damage accidents, this paper aims at. Acoustic emission monitoring has been carried out for the large vacuum system under the condition of vacuum pumping in this paper.

38.2 Equipment Setup

This test is mainly aimed at the acoustic emission testing of the large vacuum system in the vacuum test state. Before the vacuum test, the stress analysis and calculation have been carried out by the Chinese Academy of special inspection, relevant design and scientific research personnel, and the high stress distribution area of the whole system has been determined. Under the vacuum test state, the inspection and detection items carried out synchronously include the acoustic emission monitoring for the stress concentration parts. Measurement, stress testing and strain monitoring.

The main location of acoustic emission monitoring is a high stress distribution area, which is fillet weld connection of the pipe and the two billiard tanks. The process adopts the characteristic parameter method. The pipeline part uses the triangle surface positioning to arrange the sensor, and the ball tank part uses the area positioning due to the complex structure with the internal existence of reinforcing ribs. There are 12 sensors arranged around the fillet weld connection of the V-06 vacuum ball tank and the pipeline. It is divided into two regions. Two sensors are symmetrically arranged at 2700 mm away from the fillet weld on the pipeline, and the first region is formed by arranging five sensors equidistant from the edge of the fillet weld. Five sensors are arranged equidistant on the circumference of 2800 mm with the center of the pipeline as the circle point, and the second region is formed by arranging five sensors equidistant from the edge of the fillet weld. Similarly, the third and fourth region are arranged around the fillet weld of the V-05 vacuum ball tank and pipeline. The arrangement of sensors in Region II is shown in Fig. 38.2.

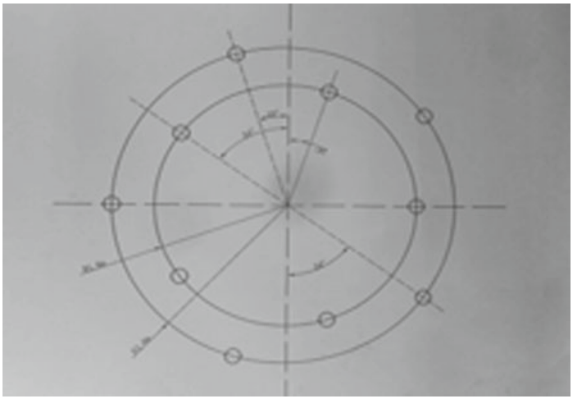

Fig. 38.2 The arrangement of sensors in Region II

38.3 System Debugging

The 32 channel AMSY5 ASIP-2 system of acoustic emission acquisition and analysis, the resonant narrow-band integrated probe VS150-RIC, the AMSY5 acoustic emission software (including BDSWB acquisition, VAELP analysis, BDSWLOC1 positioning and other software) from Germany Vallen company are used. The AMSY5 ASIP-2 system has ultra-high speed, all digital, all waveform and strong anti-interference. According to NB/T 47013.9-2012 "Nondestructive Testing of Pressure Equipment Part 9: Acoustic Emission Testing" and other standards, the testing process is prepared. The simulation source is L2.5mmΦ0.3mm30°2H lead core breaking, self calibration pulse signal. At the position 100 mm away from the probe, the surface coating shall be removed and the metal background shall be exposed by the angle grinder. The simulated acoustic emission signal shall be used for 3–5 times of repeated measurement, and the sensitivity verification of each channel shall be carried out one by one, which shall not be less than 76 dB. In principle, the sensitivity variation range of each measurement shall not be more than ±4 dB.

The large vacuum system has the large size, the internal existence of reinforcing ribs, the obvious difference of stress distribution and the influence of noise interference. In order to find out the effective methods of noise suppression and elimination, and to ensure the smooth extraction and detection of effective acoustic emission signals, the following measures are taken: one is to carry out repeated, multiple and different conditions experimental debugging on the simulated test piece and the real object; the other is to carry out the final measurement on the tank structure; thirdly, the method of characteristic parameters is used to filter out the irrelevant noise signals.

38.4 Test Process and Result Evaluation [1–3]

The acoustic emission test is carried out in combination with the vacuum test of the ball tank system. The two ball tanks are tested separately. First, we close the gate valve FM-02 between the two ball tanks and the gate valve FM-04 between the V-06 vacuum ball tank and the wind tunnel, and carry out the vacuum test on the V-06 vacuum ball tank. The specific vacuum test is carried out in stages according to 50,000, 10,000, 5000 Pa and 23.7 Pa, and enough inspection time is kept at all levels. After the vacuum test of V-06 vacuum ball tank, the pressure of V-06 ball tank and connecting pipes is maintained, and then the vacuum test of V-05 vacuum ball tank is conducted according to the same stage. According to the measurement of sound velocity, the result is 4900 m/s in Region I and III, and 4700 m/s in Region II and IV. The attenuation curve and pulse table are shown respectively in Figs. 38.3 and 38.4.

During the acoustic emission monitoring of V-06 vacuum ball tank, according to NB/T 47013.9-2012 “Nondestructive Testing of Pressure Equipment Part 9: Acoustic Emission Testing”, no effective acoustic emission source is found that increases continuously with the increase of negative pressure. The situation of acoustic emission activity source above level II is shown in Table 38.2. At the stage of pumping to 50,000 Pa, two acoustic emission activity sources are found in region I and three acoustic emission activity sources are found in region II, At 50,000 Pa in the pressure maintaining stage, one acoustic emission active source is found in region I and region II respectively. At the 50,000–10000 Pa stage, three acoustic emission active sources are found in region I and four acoustic emission active sources are found in region II. At the 10,000–5000 Pa stage, one acoustic emission active source is found in region I and region II respectively. At the 5000–5000 Pa stage, one acoustic emission active

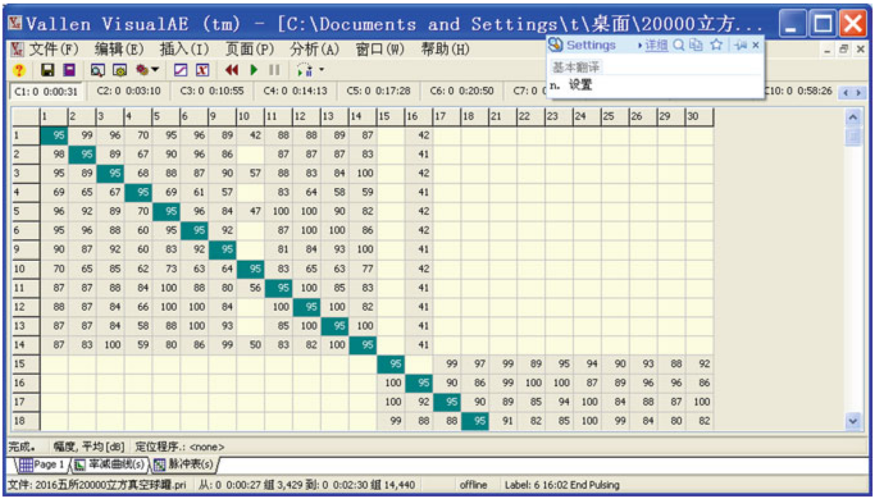

	1	2	3	4	5	6	9	10	11	12	13	14	15	16	17	18	21	22	23	24	25	26	29	30
1	95	99	96	70	95	96	89	42	88	88	89	87		42										
2	98	95	89	67	90	96	86		87	87	87	83		41										
3	95	89	95	68	88	87	90	57	88	83	84	100		42										
4	69	65	67	95	69	61	57		83	64	58	59		41										
5	96	92	89	70	95	96	84	47	100	100	90	82		42										
6	95	96	88	60	95	95	92		87	100	100	86		42										
9	90	87	92	60	83	92	95		81	84	93	100		41										
10	70	65	85	62	73	63	64	95	83	65	63	77		42										
11	87	87	88	84	100	88	80	56	95	100	85	83		41										
12	88	87	84	66	100	100	84		100	95	100	82		41										
13	87	87	84	58	88	100	93		85	100	95	100		41										
14	87	83	100	59	80	86	99	50	83	82	100	95		41										
15													95		99	97	99	89	95	94	90	93	88	92
16													100	95	90	86	99	100	100	87	89	96	96	86
17													100	92	95	90	89	85	94	100	84	88	87	100
18													99	88	88	95	91	82	85	100	99	84	80	82

完成。 幅度, 平均 [dB] 定位程序.: <none>

文件: 2016五所20000立方真空球罐.pri 从: 0 0:00:27 組 3,429 到: 0 0:02:30 組 14,440 offline Label: 6 16:02 End Pulsing

Fig. 38.3 The attenuation curve

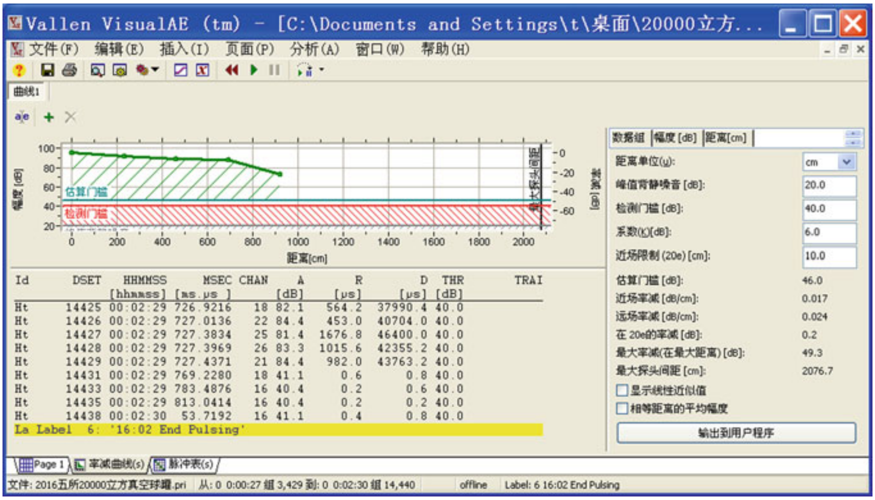

```
Id        DSET    HHMMSS      MSEC CHAN     A        R        D   THR        TRAI
                [hhmmss] [ms.μs ]        [dB]     [μs]     [μs]  [dB]
Ht       14425 00:02:29 726.9216   18 82.1    564.2  37990.4 40.0
Ht       14426 00:02:29 727.0136   22 84.4    453.0  40704.0 40.0
Ht       14427 00:02:29 727.3834   25 81.4   1676.8  46400.0 40.0
Ht       14428 00:02:29 727.3969   26 83.3   1015.6  42355.2 40.0
Ht       14429 00:02:29 727.4371   21 84.4    982.0  43763.2 40.0
Ht       14431 00:02:29 769.2280   18 41.1      0.6      0.8 40.0
Ht       14433 00:02:29 783.4876   16 40.4      0.2      0.6 40.0
Ht       14435 00:02:29 813.0414   16 40.4      0.2      0.2 40.0
Ht       14438 00:02:30  53.7192   16 41.1      0.4      0.8 40.0
La Label   6: '16:02 End Pulsing'
```

距离单位(u): cm
峰值背静噪音 [dB]: 20.0
检测门槛 [dB]: 40.0
系数(K)[dB]: 6.0
近场限制 (20e) [cm]: 10.0
估算门槛 [dB]: 46.0
近场衰减 [dB/cm]: 0.017
远场衰减 [dB/cm]: 0.024
在 20e的衰减 [dB]: 0.2
最大衰减(在最大距离) [dB]: 49.3
最大探头间距 [cm]: 2076.7
□ 显示线性近似值
□ 相等距离的平均幅度

文件: 2016五所20000立方真空球罐.pri 从: 0 0:00:27 组 3,429 到: 0 0:02:30 组 14,440 offline Label: 6 16:02 End Pulsing

Fig. 38.4 The pulse table

source is found in region II. At the 5000–23.7 Pa, two active sources of acoustic emission were found both in region I and region II. At the pressure maintaining stage of 23.7 Pa, no active source of acoustic emission was found. Through the field inspection and routine non-destructive testing spot check and re inspection of the parts comprehensively evaluated as level III, it is confirmed that there are no over standard defects in the effective acoustic emission source area, the acoustic emission test of vacuum pumping test is qualified, and the acoustic emission monitoring results are consistent with the stress–strain monitoring results and the actual situation of vacuum pumping test.

During the acoustic emission monitoring of V-05 vacuum ball tank, according to NB/T 47013.9-2012 “Nondestructive Testing of Pressure Equipment Part 9: Acoustic Emission Testing”, the situation of acoustic emission activity sources above level II is shown in Table 38.3. At the stage of pumping to 50,000 Pa, one acoustic emission activity source is found in Region IV. At the stage of pressure maintaining at 50,000 Pa, no acoustic emission activity source is found. At the stage of 50,000–10,800 Pa, one active sources of acoustic emission is found in Region III and four active sources were found in Region IV. When the reading of the vacuum gauge is 10,800 Pa, a signal with a source strength of 99.4 dB was detected by acoustic emission, and the acoustic emission monitoring data is shown in Table 38.4. At this time, the stress value of the connecting pipe between the two ball tanks, i.e. the upper end of the connection between the V-06 ball tank and the pipe, reached 191 MPa, exceeding the warning value of 158.4 MPa; after on-site inspection, It is measured that the gate valve FM-02 on the pipeline between the two ball tanks is lifted up for 15 mm and moved to the direction of V-05 vacuum ball tank for 15 mm. The universal corrugated expansion joint on the pipeline between the gate valve and V-05 vacuum ball tank is bent and deformed near the lower part. According to the finite

Table 38.2 The situation of acoustic emission activity sources (V-06)

ID	Pressure stage	Region No.	Position	A(dB)	D (μs)	E (eu)	R (μs)	Remarks	Activity	Strength	Comprehensive evaluation
1	Pumping to 50,000 Pa	I	2/1/9	80.2	38,003.2	136E04	565.2	×2	Medium	High	III
2		I	1/6/9	73.8	34,636.8	478E03	709.8		Medium	Medium	II
3		II	3/14/10	87.4	79,436.8	232E05	954.4		Medium	High	III
4		II	6/9/5	60.7	14,067.2	216E02	859.6	×2	Medium	Medium	II
5		II	6/3/9	62.6	22,963.2	837E02	844.8		Medium	Medium	II
1	50,000 Pa in the pressure maintaining stage	I	2/1/6	78.0	35,750.4	547E03	562.2		Strong	Medium	III
2		II	6/9/5	64.4	21,184.0	743E02	878.0		Strong	Medium	III
1	50,000 – 10,000 Pa	I	2/1/9	78.7	37,491.2	689E03	570.8		Medium	Medium	II
2		I	1/6/5	70.5	30,131.2	590E03	726.2		Medium	Medium	II
3		I	1/3/9	72.7	33,830.4	292E03	428.8		Medium	Medium	II
4		II	5/6/3	73.1	36,979.2	715E03	861.6		Medium	Medium	II
5		II	3/9/6	78.4	52,838.4	202E04	712.0		Medium	Medium	II
6		II	3/10/14	75.7	41,548.8	683E03	988.4		Medium	Medium	II
7		II	9/6/5	78.0	46,169.6	188E04	1168.0	×5	Medium	Medium	II
1	10,000–5000 Pa	I	9/6/2	84.4	32,204.8	212E04	279.8		Medium	High	III
2		II	5/6/9	71.2	29,248.0	325E03	846.0		Medium	Medium	II
1	5000 Pa in the pressure maintaining stage	II	3/10/14	79.1	28,416.0	102E04	791.0		Strong	Medium	III
1	5000 –23.7 Pa	I	2/1/6	83.6	32,204.8	212E04	1231.6		Medium	high	III
2		I	3/9/1	76.1	20,102.4	386E03	512.0		Medium	Medium	II
3		II	10/4/3	81.7	18,636.8	463E03	195.8		Medium	high	III
4		II	3/14/10	77.2	24,467.2	566E03	490.6	×5	Medium	Medium	II

Table 38.3 The situation of acoustic emission activity sources (V-05)

ID	Pressure stage	Region No.	Position	A (dB)	D (μs)	E (eu)	R (μs)	Remarks	Activity	Strength	Comprehensive evaluation
1	Pumping to 50,000 Pa	IV	22/23/29	71.2	23,731.2	318E03	436.4		Medium	Medium	II
2	50,000–10,800 Pa	IV	17/23/30	83.6	42,560.0	529E04	190.4	×9	Super	High	IV
3		IV	21/22/26	93.8	80,640.0	718E05	236.6	×4	Medium	Medium	II
4		IV	18/21/24	82.9	29,491.2	181E04	1161.6		Medium	High	III
5		IV	18/17/24	80.2	42,022.4	222E04	198.0	×2	Medium	Medium	II
6		III	15/18/21	90.8	42,073.6	168E05	1260.0	×3	Medium	High	III

Table 38.4 The situation of acoustic emission activity sources (V-05, pumping to 10,800 Pa)

ID	Pressure stage	Position	X (cm)	Y (cm)	A (dB)	D (μs)	E (eu)	R (μs)	CNTS	Activity	Strength	Comprehensive evaluation
1	Pumping to 10,800 Pa	5/12/6	201.7	−114.72	99.4	61,542.4	875E05	122.0	4544	Medium	Super	III

element analysis and calculation, the maximum stress of this section of pipeline is 321.08 MPa, which is located at the lower end of the horizontal axial bellows short section, i.e. near the lower part of the bellows, there is a bolt bending and deforming position. Through the analysis, the phenomenon of gate valve lifting and displacement is due to the difference of single upper and lower surface area of 144° elbow of DN3600 connecting pipeline between two ball tanks, which is about 62,000 cm^2, and the edge is generated when it is close to the vacuum state. The upward thrust of the elbow angle split line is about 620 KN, and the total upward thrust of the two elbows is about 1240 KN. The pipe support between the two ball tanks is a sliding support, which has no restriction on the pipe and the gate valve, so the gate valve is lifted up and displaced horizontally.

38.5 Existing Problems

1. Due to the positioning method, rib plate structure, large skirt and other reasons, it is difficult to locate. The pipeline part can realize the triangle surface positioning, and the ball tank part can only realize the regional positioning.
2. There are noise signal sources such as personnel inspection and inspection in some vacuum stages.
3. The stress release of the rib plate inside the tank body becomes the acoustic emission signal source, causing interference.
4. The vacuum test belongs to the negative pressure test, which is different from the usual pressure rise test.

38.6 Conclusion

In view of the acoustic emission testing of the large vacuum system under the vacuum pumping test state, the following conclusions with engineering significance can be drawn:

1. Acoustic emission testing can monitor the vacuum test process of spherical tank and pipeline system in real time, and evaluate the results effectively and reliably.
2. The large vacuum system can effectively carry out acoustic emission monitoring on the stress concentration part in the vacuum test state, and realize the instability prediction and integrity evaluation of the whole structure through the measures of noise elimination and routine nondestructive testing retest.
3. Acoustic emission testing can monitor the deformation and stress release of the stiffened plate structure in real time.
4. Because of the complex structure and the stiffener inside, it is difficult to realize the plane positioning in all monitoring areas of the vacuum ball tank. Acoustic emission testing can provide an effective method for monitoring and post inspection of the large vacuum system.

References

1. Y. Li, Characteristic parameter distribution of several typical acoustic emission signals. Nondestruct. Testing **28**(2), 19–22 (2004)
2. Y. Kai-bai, Y. Li, M. Xue-rong, L. De-ming, Experimental research on large wind tunnel pressure shell using acoustic emission. Nondestruct. Testing **34**, .61–65 (2012)
3. Y. Li, Acoustic emission signal detection of fatigue cracks in 16Mn steel, in *Proceedings of the Eighth National Conference on Nondestructive Testing, Chengdu* (2003)

Chapter 39
Study on AE Detection Signal of Composite Barrel Under Axial Compression Failure Load

Xiaolin Li, Wei Yin, Hao Chen, Gang Sun, and Lixia Wang

Abstract AE detection is performed in the axial compression failure test of composite barrels. Through analysis of AE signals such as energy, hits, amplitude and duration, it is concluded that the AE signals can accurately reflect the load change and damage of the test piece. By analyzing the signal frequency, the correspondence between the damage type of the test piece and the signal frequency is obtained. AE detection can effectively monitor the elastic deformation stage and damage development and accumulation process of cylindrical parts, and can provide reference for the analysis of AE signals during the test of test pieces of similar materials and similar structure.

39.1 Introduction

Composite structures are more prone to various micro or macro defects than metal structures in the manufacturing and use process [1]. They have unique damage mechanisms and the damage process is more complicated [2]. It can be known from the literature that the damage and fracture of composite materials mainly include three types of damage modes: substrate cracking, interface damage, and fiber breakage. Among them, interface damage includes detachment of the substrate and fiber interface, fiber pull-out, and interlayer separation; Fracture includes normal and split modes of fiber [3]. At present, the commonly used methods for composite damage detection are: X-ray, UT, A-UT, AE, etc. [4]. AE detection refers to the phenomenon of transient stress waves generated when a material or a component enters the irreversible plastic deformation stage due to stress exceeding the yield limit, or cracks are formed and propagated, and strain energy is rapidly released during fracture. This technology can diagnose the damage condition through the stress wave released by the material or component, and has become an important non-destructive testing method for studying the damage failure of composite materials [5].

X. Li (✉) · W. Yin · H. Chen · G. Sun · L. Wang
Beijing Institute of Structure and Environment Engineering, Beijing 100076, China
e-mail: 49150575@qq.com

© The Author(s), under exclusive license to Springer Nature Singapore Pte Ltd. 2021

G. Shen et al. (eds.), *Advances in Acoustic Emission Technology*, Springer Proceedings in Physics 259, https://doi.org/10.1007/978-981-15-9837-1_39

In this paper, the AE signal is collected through the AE instrument during the axial compression failure test of the composite barrel. By analyzing the AE signal such as energy, AE hits, amplitude, and duration, it is concluded that the AE signal can accurately reflect the load change and damage of the test piece. By analyzing the signal frequency, the correspondence between the damage type of the test piece and the signal frequency is obtained.

39.2 Test Method

39.2.1 Test Products

The test product is a composite cylindrical part. The total height of the test part is 700 mm and the diameter is 1000 mm. An axial compression failure test is required for the test product. During the test, the test piece is placed vertically and fixed on the test bench, and a 200 T material testing machine is used to apply the axial load to the test piece.

39.2.2 AE Instrument and Probe Arrangement

The AE loading test was performed at the same distance from the upper surface to the lower surface in the middle of the fourth quadrant, and a total of four sensors were installed. The four sensor locations were square and the side length was 400 mm. The loading schematic of AE is shown in Fig. 39.1. The AE detection instrument

Fig. 39.1 Relative position diagram of sensor arrangement

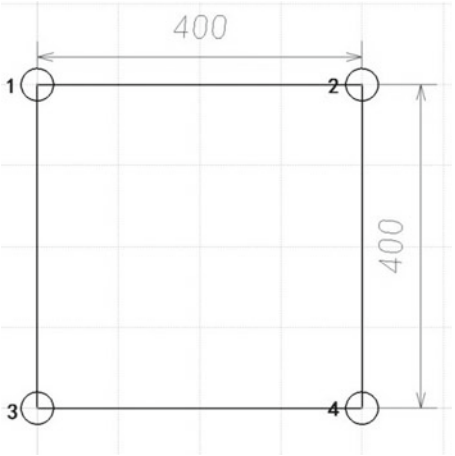

uses Vallen's acoustic emission detection system. VS150 is selected as sensors with 4 channels and 4 acquisition channels.

Each sensor is connected to the instrument channel through a single-ended preamplifier. Medical Vaseline is used as the coupling agent between the probe and the test piece. The instrument settings and probe parameters are: instrument main amplifier gain 20 dB; gain threshold 40 dB; front amplifier gain 40 dB; sensors center frequency 150 kHz; no pre-filtering.

39.2.3 Test Process

The loading process: 200 kN → 400 kN → 600 kN → 700 kN → 800 kN → 900 kN → 950 kN → 1000 kN → 1050 kN → 1100 kN. AE signal waveform and characteristic parameters were collected during the test.

39.3 Test Result and Analysis

The failure load is 1000.80 kN. During the first six level loading, the test piece was normal. During loading level 7, Slight sound detected. During loading level 8, A loud sound after a click before the final failure, which caused product failure results. when the load was unloaded to 0, the deformation of the test piece restored basically.

Figure 39.2 is the AE process diagram, The entire axial pressure failure stage is mainly divided into three stages, the threshold value is 40 dB, During the entire axial pressure failure process, the amplitude distribution of AE time is 40–100 dB, and the energy distribution is 0–2.6×10^9, the duration is between 0 and 1.29 S.

In the first stage (0–193 s), it can be seen from the AE process diagram that the hits at this stage is little and the amplitude of this stage is small, most of which are below 70 dB, and the corresponding energy is also small. The duration is basically below 500 μm, and the duration of individual signal points is between 500 and 1000 μm. This is mainly due to the bearing capacity of the test piece. In the initial stage of the axial compression test, the deformation of the material is mainly the elastic deformation of the matrix in the composite Mainly, there are fractures of individual microfibers. From the displacement data during the test, it can be seen that during the loading process of the first three stages, the test piece has a deformation of about 1.2 mm.

Analysis of the waveforms at this stage shows that there are two types of waveforms at this stage. One is that the frequency is around 500 kHz (Fig. 39.3), the amplitude is below 60 dB, and the duration is relatively short. This type of signal is mainly used in combination with the above analysis. According to preliminary judgment, this type of waveform should be a waveform signal generated by the elastic deformation process of the composite matrix during loading; the other is a frequency of about 140 kHz (Fig. 39.4), and the duration is Between 500 and 1000 μm, the

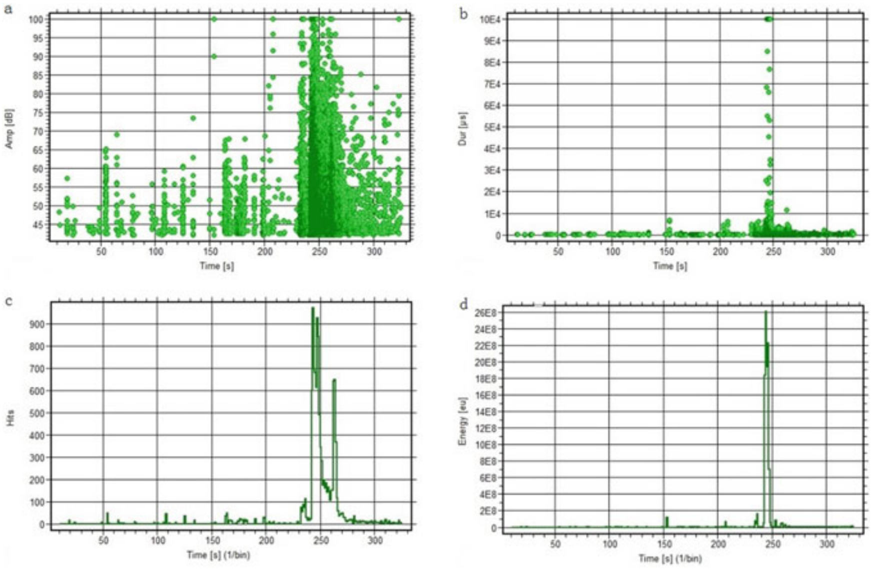

Fig. 39.2 AE process diagram

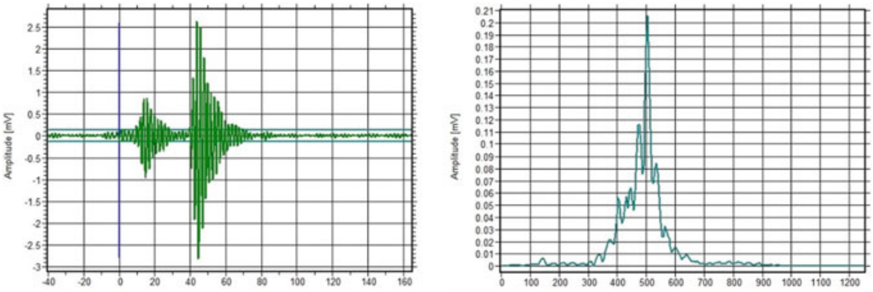

Fig. 39.3 Stage 1 waveform with a frequency of 500 kHz

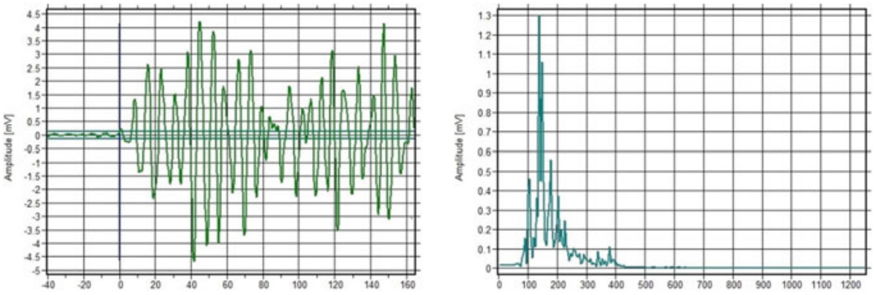

Fig. 39.4 Stage 1 waveform with a frequency of 140 kHz

number is relatively small. It is preliminarily judged that such waveforms should be the fracture waveform signals of individual microfiber filaments.

The second stage (198–240 s), this stage is the loading stage 6 and 7 of the axial compression test. During the loading stage 7. It can be seen from the AE process diagram that the hits at this stage has begun to increase, and the amplitude of this stage has increased significantly. During the loading process, the amplitude value of the AE signal has been increasing. The amplitude of individual signals reaches 100 dB, but during the loading process, the amplitude value returns to below 60 dB. Comparing the duration process chart, we can see that the duration of AE signal with amplitude above 80 dB is also relatively large. It is preliminary judged that during this process, obvious damage occurred in the test piece, but the damage did not expand with the progress of the load. According to the reference given in [6], it shows that high amplitude (>80 dB) signals are more related to fiber damage modes, while medium amplitude signals (60–80 dB) may be related to interface damage, and low amplitude signals (<60 dB) are related to substrate damage. this process should be a macro separation of the interface and resin macro crack growth.

The waveforms of this stage can be divided into two types. One is a frequency of around 140 kHz (Fig. 39.5), the amplitude is below 60 dB, and the duration is below 1000 μm. The waveform signal is dominant, and this type of waveform should be the signal of the fracture waveform of the microfibril. The other is that the frequency is around 140 kHz (Fig. 39.6), the duration is relatively long, and the amplitude is above 80 dB. This AE signal appears during the loading of each stage, it is initially determined that this kind of waveform corresponds to macroscopic separation of interface and macroscopic crack propagation of resin.

Stage 3 (240–264 s failure) is the 8th stage of axial compression test loading. During the loading process, the test piece made a "crack, crack" sound, and then suddenly made a loud noise, the test piece was damaged. As can be seen from the acoustic emission history chart, both energy and ringing counts increase rapidly, and a large number of AE signals with duration and amplitude reaching display limit appear between 243 and 248 s. In addition, the number of acoustic emission signals below 80 dB is also increasing rapidly, which indicates that at this stage a large number of macro-cracks and macro-expansion of the resin interface were produced,

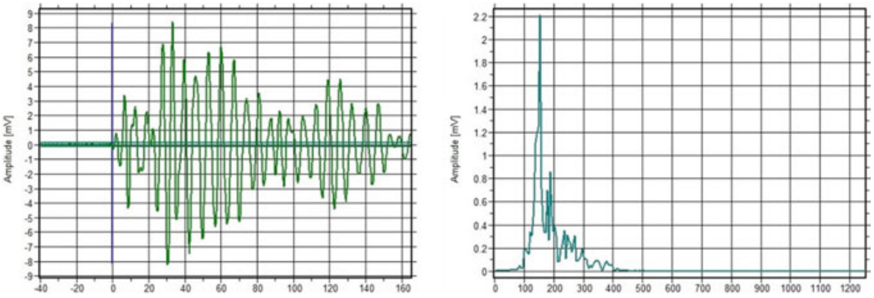

Fig. 39.5 Stage 2 waveform with a frequency of 140 kHz (Low amplitude)

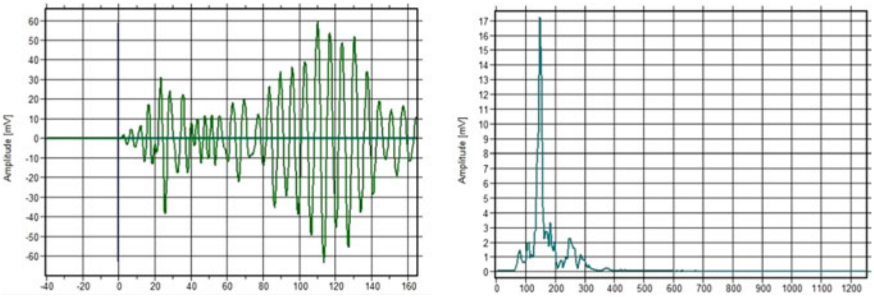

Fig. 39.6 Stage 2 waveform with a frequency of 140 kHz (high amplitude)

accompanied by a considerable number of single-filament breaks and tow breaks. At this stage, the composite materials have been overall failure. During the subsequent compression process, the test piece can't support the axial compression loading and destabilization occurs.

The waveforms of this stage can be divided into two types, one is the frequency around 140 kHz (Fig. 39.7) and the amplitude is above 80 dB. This type of waveform corresponds to the macro separation of Macro crack growth of the resin. The other is a frequency of around 140 kHz (Fig. 39.8), the amplitude is less than 80 dB, and the duration is less than 1000 µm. this type of waveform is a fracture waveform signal of microfiber filaments.

Figure 39.9 shows the morphology of the test piece under axial pressure, of which Fig. 39.9a is the morphology of the test piece under axial pressure, and Fig. 39.9b is the morphology of the basic recovery of the test piece after axial pressure unloading. Figure 39.9c deformation of the internal reinforcement ribs of the test piece. The failure morphology of the test piece also verified the relationship between the acoustic emission signal and the failure mode of the test piece from the side.

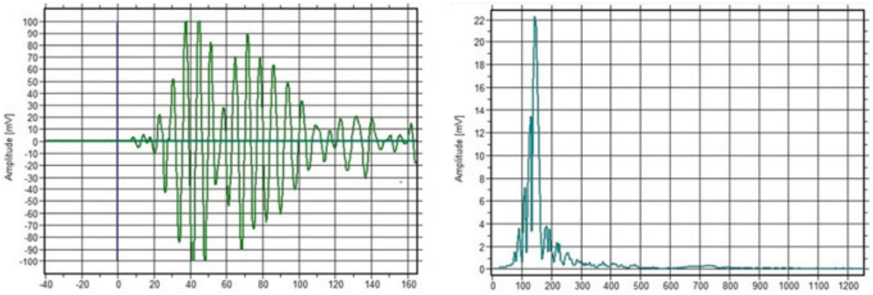

Fig. 39.7 Stage3 waveform with a frequency of 140 kHz (high amplitude)

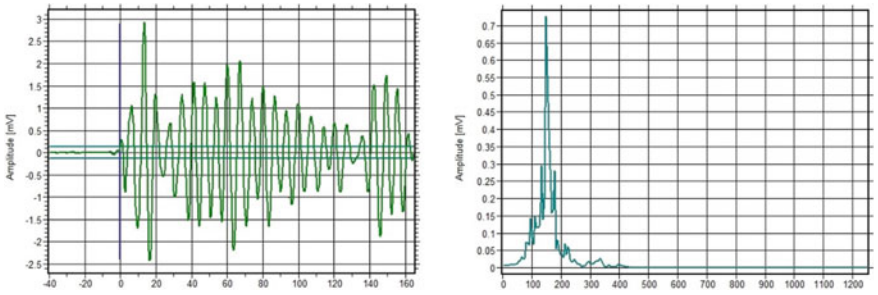

Fig. 39.8 Stage 3 waveform with a frequency of 140 kHz (Low amplitude)

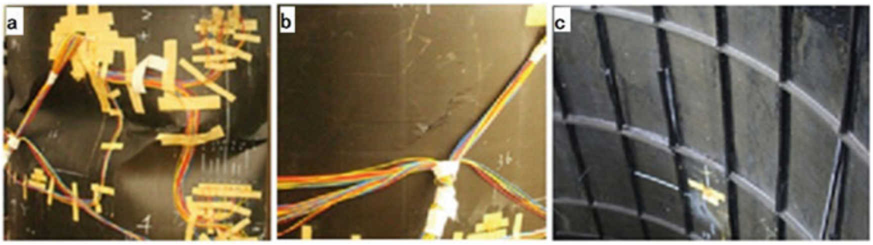

Fig. 39.9 Axial compression failure of test piece

39.4 Conclusion

1. AE detection of the axial failure process of the composite cylindrical parts, analysis of AE signals, the axial pressure failure is divided into three stages, the first stage is the elastic deformation stage of the composite matrix; the second stage is the stage of macro cracks in the composite test piece and the macro separation of the interface; the third stage is the stage where the composite test piece has a large number of defects and damage. Different stages have different damage modes and produce different characteristics of acoustic emission signals.
2. From the frequency analysis of the signal, it is known that the AE signal with a frequency of 500 kHz, an amplitude below 60 dB, and a relatively short duration is a waveform signal generated by the elastic deformation process of the composite matrix during loading; the AE signal with a frequency of 140 kHz, an amplitude below 80 dB and a duration below 1000 μm is a waveform signal of microfiber filaments; the frequency is around 140 kHz and the amplitude is above 80 dB is the waveform signal corresponds to the macroscopic separation of the interface and the macroscopic crack propagation of the resin.

References

1. Z. Huang, C. Huang, J. Zhang, D. Jiang, S. Ju, Advances in the application of acoustic emission technology in damage detection and failure process analysis of fiber reinforced composites. Mater. Rep. Rev. **32**(4), 1122 (2018)
2. W. Liang, Damage mechanics and nondestructive testing of composites. Mater. Sci. Eng. **1**, 22 (1990)
3. S. Meng, X. Tian, S. Du, et al., Mechanical properties testing and failure mechanisms of three-dimensional braided carbon/epoxy composites. J. Compos. **21**, 1261–1266 (2002)
4. T.J. Chotard, New applications of acoustic emission technique for real-time monitoring of material processes. J. Mater. Sci. Lett. **21**, 1261–1266 (2002)
5. B. Zhu, P. He, L. Zhu, et al., Study on the application of polymer composites in transfer joints. Fluid Mach. **41**(11), 52–55 (2013)
6. Z. Liu, *Acoustic Emission Detection*, vol. 106 (Acoustic Emission Training Textbook for Space Accreditation Committee, Beijing, 2017).

Chapter 40
Localization of Acoustic Emission Sources in the Steel Bifurcated Pipe of Hydropower Station

Weiping Wu, Zhejun Liu, Shulin Cao, Donfeng Li, and Zhen Huo

Abstract The paper analyzes and studies the acoustic emission localization of the irregular-shaped and thick-wall steel plate bifurcated pipe of hydropower station. The paper analyzes the effect of acoustic velocity and structural irregularity on localization accuracy of AE source. On the basic of time–frequency analysis of the AE signals, drawing of the Lamb wave dispersion curves, calculation of the group velocity and the phase velocity of the Lamb wave, meanwhile, considering the characteristics of multi-mode and variable velocity of the wave, the paper proposes a method to measure the sound velocity based on linear fitting of TDOA (time difference of arrival) versus distance difference of respective source distances from the two sensors. The Location Uncertainty (LUCY) and location error (LE) analysis of AE location source are also implemented. At the end the proposed velocities of the different area of the steel bifurcated pipe are calculated.

40.1 Introduction

The location of time difference of arrival (TDOA) in acoustic emission detection is based on the measurement of the TDOA, sound velocity, sensor position and other parameters, as well as the complicated geometric calculation in the sensors array, therefore, the parameters mentioned above will affect the accuracy of AE sources location. It is usually assumed that the material is isotropic, the sound velocity in the material is constant and the path of propagation between the source and the sensor is straight, in location of TDOA. Linear location (one-dimensional location) and plane

W. Wu (✉) · S. Cao · D. Li
National Center of Quality Inspection and Testing for Hydraulic Metal Structure Ministry of Water Resources, Zhengzhou 450044, China
e-mail: wp.wu@163.com

Z. Liu
Aerospace Research Institute of Materials & Processing Technology, Beijing 100076, China

Z. Huo
Wuhan Boiler and Pressure Vessel Inspection Institute, Wuhan 430040, China

© The Author(s), under exclusive license to Springer Nature Singapore Pte Ltd. 2021

G. Shen et al. (eds.), *Advances in Acoustic Emission Technology*, Springer Proceedings in Physics 259, https://doi.org/10.1007/978-981-15-9837-1_40

location (two-dimensional location such as plane and cylinder location) are the most common AE sources localization methods at present.

Location of AE sources is usually based on simple geometric models: line, plane, cylinder, sphere, and cone. However, as a matter of fact, this approach does not always obtain good results for the following reasons [1]:

1. In many cases, irregular and complicated geometry of an object cannot be reduced to simple shapes.
2. The complex characteristics of acoustic wave propagation (such as sound velocity, attenuation, waveform, propagation path and so on).
3. The properties of the materials and the internal medium.

Therefore, the simple location schema on irregular-shaped objects often leads to chaotically placed AE sources.

Due to the complicated geometry, irregular shape and thick-wall steel plate of the steel bifurcated pipe in hydropower station, the acoustic velocity and structure directly affect the location accuracy of AE source. In this paper. the location accuracy of AE sources in hydraulic test of steel bifurcated pipe is analyzed from the point of view of sound velocity and irregularity of structure.

40.2 The Structure of Steel Bifurcated Pipe and AE Sensors Layout

The arrangement of AE sensors of a steel bifurcated pipe of asymmetric Y-shape in hydraulic test is taken as a case study. The inner diameters of the main pipe, branch pipe, and inscribed sphere are 3200 mm, 2200 mm and 3840 mm respectively, and the bifurcation angle is 77°; The thickness of the bifurcated pipe varies from 42 to 50 mm and the thickness of the crescent rib is 120 mm; the material is steel 07MnCrVR of 600 MPa grade strength. The main areas of AE detection are the key load-carrying parts, the parts of stress concentration due to large geometric constraints, and the parts with high difficulty coefficient of welding: the crescent rib, and the main cone as well as the transitional cone, which are shown in Fig. 40.1b named area A1 and A2.

AMSY-6 (38 channels) detection system of Vallen Systeme GmbH is used to carry out the AE monitoring of the steel bifurcated pipe in hydraulic test. The type of sensor is VS150-RIC, high sensitivity resonance sensor (100–400 kHz) with a center frequency of 150 kHz, and with a built-in preamplifier gained 34 dB. The working parameters of the AE system during the test are set as shown in Table 40.1. The AE signals generated during the hydraulic test are transient, so location of TDOA is calculated.

Sensors are arranged on the external surfaces of the bifurcated pipe, channel group I of 11 sensors are placed in the area of A1. Among them, 9 sensors are arranged on both sides of the combined welds between the crescent rib and the shell plate of the branch pipes, 260 mm away from the center of the rib. The space between

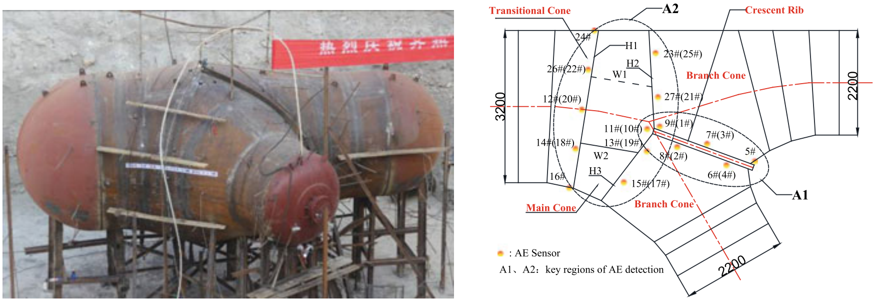

(a) The steel bifurcated pipe (b) Assignment of the AE Sensors

Fig. 40.1 The steel bifurcated pipe and AE sensors assigned

Table 40.1 Parameter setting of the AE system

Threshold/dB	Sample frequency /MHz	Sampling point	Filter (kHz)	Pretrigger	Dur. disT. (μs)	RearmT. (μs)
40	10	8192	25–850	200	400	3200

two adjacent sensors on the same side is about 1500 mm. The sensors are arranged alternately on both sides in isosceles triangle as far as possible. 2 sensors are arranged near the top apex and bottom apex of the crescent rib.

Channel group II of 18 sensors are placed in the area of A2. Among the array, 8 sensors are arranged at 200 mm upstream of the circumferential weld (H1) between the main cone and the transitional cone, and the spacing between the adjacent two sensors is 1351 mm. 10 other sensors are arranged at downstream of the circumferential welds (H2, H3) between the main cone and the two branch cones (two sensors 10#, 12# are shared in channel group I). Plane location method is applied in channel group II.

The bifurcated pipe was assembled and welded by a large number of steel shell plates, and the geometry is complicated and irregular; thus, the possible acoustic transmission paths are complicated and uncertain. The area surrounding the line of welding fusion is high risk zone of welding cracks. AE signals from the welding fusion region can be received by a certain sensor without transmitting through the thick-wall weld and/or the irregular structure, but can be received by the other sensor just by transmitting through the weld or the irregular structure, which lead to serious distortion and attenuation of acoustic waveform [2], in addition to the velocity variation and complicated transmission paths of acoustic wave. At the same time, the varying sound velocity caused by dispersion also reduces the location accuracy.

40.3 Sound Wave Transmission and Measurement of Sound Velocity in Steel Bifurcated Pipe

The location accuracy of AE sources in location of TDOA is directly affected by the sound velocity, as well as the structure shape which result in the uncertainty and complication of sound transmission paths.

Sound velocity is affected by material type, anisotropy, structure shape and size, AE source property, distance between the AE sources and receiving sensor, gate threshold, container medium and other factors.

The modes of sound waves received by the sensors may be longitudinal, shear, surface, lamb waves (symmetric or asymmetric)etc., therefore, sound velocity variation is often encountered, as well as dispersion phenomenon under which the sound velocity is a function of the frequency of the sound wave.

At present, the mainstream AE detection system can't deal with the condition of variable sound velocity. If the true sound velocity in the detected component is constant but different from the value entered in the location calculation software, the location error will depend on the measured time difference of arrival. If the AE source is in the middle of the sensor array, TDOA of the sensors is very small and it is not easy to detect the difference in sound velocity. Nevertheless, the closer the AE source is to the sensor, the greater the time difference is, and the greater the error of AE source location is due to velocity error.

40.3.1 Diversity of Acoustic Transmission Paths in Thick-Wall Plate of Bifurcated Pipe

The welds and obstacles (the crescent rib protrudes from the weld, and the K-shaped groove angle of rib changes gradually) result in the interface reflection of the wave, and each reflection generates wave model conversion besides superposition due to the complicated acoustic transmission paths.

The possible acoustic transmission paths in a cylinder of thick-wall plate are very complicated [3, 4], shown as Figs. 40.2 and 40.3.

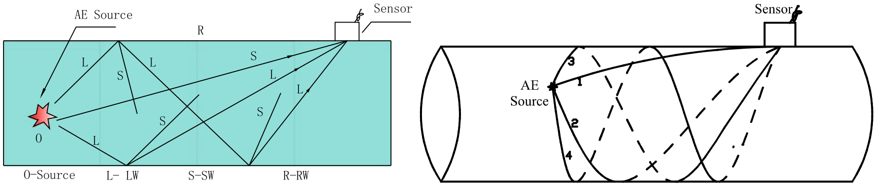

(a) in thick-wall plate

(b) in a cylinder

Fig. 40.2 Possible propagation paths of the wave in the bifurcated pipe

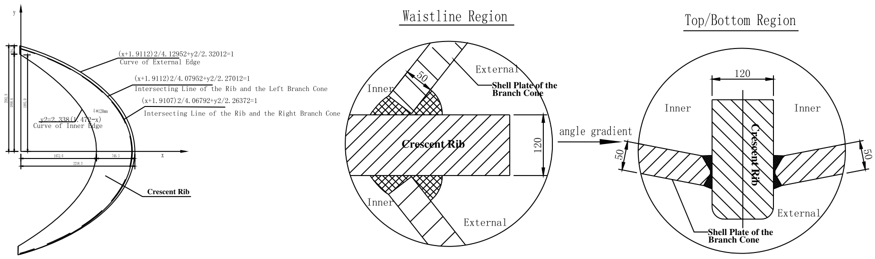
y
x
(x+1.9112)2/4.12952+y2/2.32012=1
Curve of External Edge
(x+1.9112)2/4.07952+y2/2.27012=1
Intersecting Line of the Rib and the Left Branch Cone
(x+1.9107)2/4.06792+y2/2.26372=1
Intersecting Line of the Rib and the Right Branch Cone
δ=120mm
y2=2.338(1.472−x)
Curve of Inner Edge
2062.9
1998.6
1885.0
1472.0
746.3
2218.3
Crescent Rib
Waistline Region
External
Inner
50
Shell Plate of the Branch Cone
Crescent Rib
120
Inner
External
angle gradient
Top/Bottom Region
120
Inner
Inner
50
Crescent Rib
50
External
Shell Plate of the Branch Cone

Fig. 40.3 Crescent rib and K-shaped weld

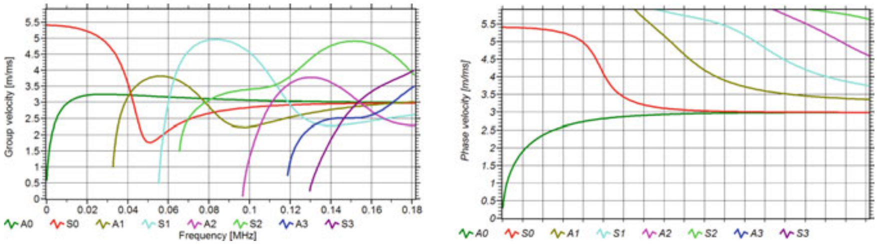

(a) Group velocities **(b)** Phase velocity

Fig. 40.4 Dispersion curves for a steel plate thickness of 50 mm ($V_L = 5900$ m/s, $V_S = 3230$ m/s)

Fig. 40.5 Source location for two sensors

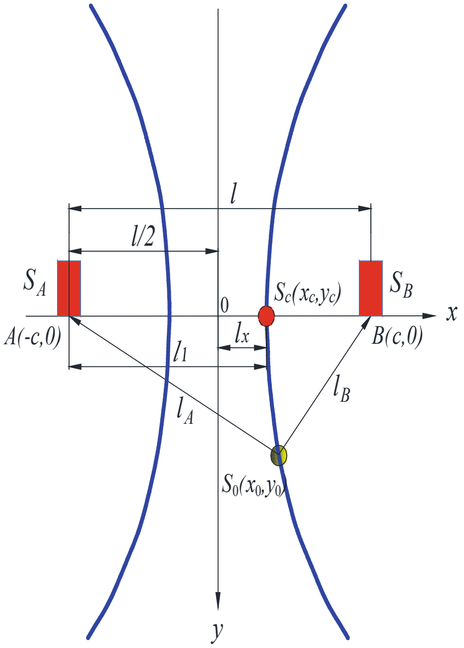
l
l/2
S_A
$S_c(x_c,y_c)$
S_B
0
x
$A(-c,0)$
l_x
$B(c,0)$
l_1
l_B
l_A
$S_0(x_0,y_0)$
y

Fig. 40.6 Velocity calculation- error bar and regression line

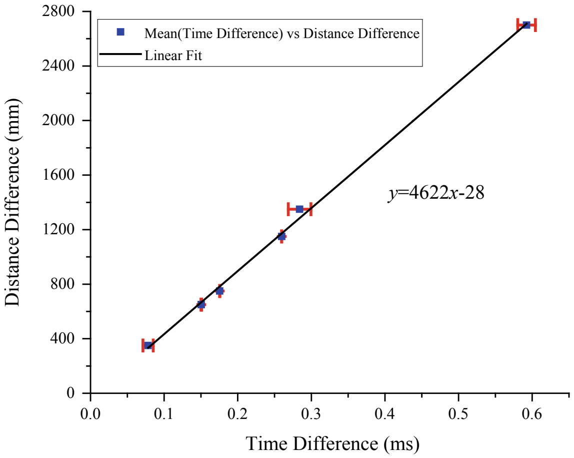

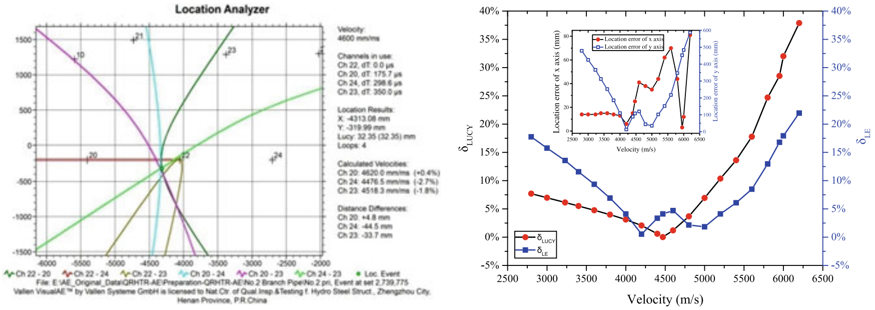

```
Velocity:
4600 mm/ms

Channels in use:
Ch 22, dT: 0.0 µs
Ch 20, dT: 175.7 µs
Ch 24, dT: 298.6 µs
Ch 23, dT: 350.0 µs

Location Results:
X: -4313.08 mm
Y: -319.99 mm
Lucy: 32.35 (32.35) mm
Loops: 4

Calculated Velocities:
Ch 20: 4620.0 mm/ms  (+0.4%)
Ch 24: 4476.5 mm/ms  (-2.7%)
Ch 23: 4518.3 mm/ms  (-1.8%)

Distance Differences:
Ch 20: +4.8 mm
Ch 24: -44.5 mm
Ch 23: -33.7 mm
```

```
File: E:\AE_Original_Data\QRHTR-AE\Preparation-QRHTR-AE\No.2 Branch Pipe\No.2.pri, Event at set 2,739,775
Vallen VisualAE™ by Vallen Systeme GmbH is licensed to Nat.Ctr. of Qual.Insp.&Testing f. Hydro Steel Struct., Zhengzhou City,
Henan Province, P.R.China
```

(a) Location analysis

(b)LUCY and LE analysis

Fig. 40.7 Location analysis in region of A2

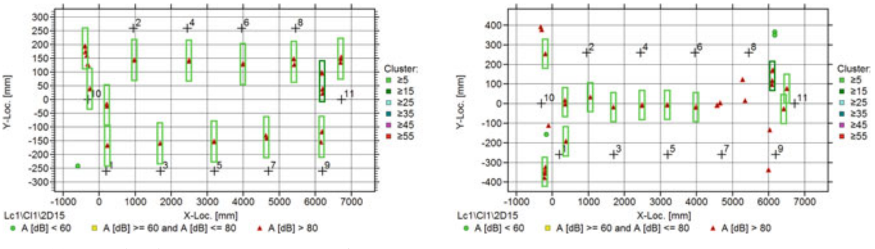

(a) Location by AST at V_u=4500m/s

(b) Location by AST at V_u =4000m/s

Fig. 40.8 Location diagrams generated by automatic sensor test(AST) at different sound velocities

The parts of the rib protruding from the shell plate may cause the change of the acoustic propagation paths, and the acoustic velocity may also vary greatly after transmitting through the weld or rib. In particular, the location accuracy of the AE source will be lower in the small triangular area composed of the apexes of the crescent rib and the intersecting curves of the main cone and the branch cones (that is the intersection area of A1 and A2), and in the area of the combined welds of the crescent rib and branch pipes which is near the waist line.

40.3.2 Dispersion Curves of AE Signals

Dispersion is a physical phenomenon while the sound velocity varies in function of frequency. Since the actual AE signal includes components of various frequencies, and the sound velocity depends on frequency, hence the components of different frequencies in the AE signal will propagate at different speeds in the medium. The velocity of longitudinal, shear, surface waves is independent of wave frequency, while the velocity of plate wave is related to the frequency of the wave, dispersion occurs, and the sound velocity in the plate is approximately distributed between the longitudinal velocity and the shear velocity.

The dispersion curves(the steel plate with a thickness of 50 mm, longitudinal wave velocity of 5900 m/s, shear wave velocity of 3230 m/s) are obtained from Wavelet software[5, 6] of Vallen Systeme GmbH, in which A0, A1, A2 and A3 represent zero-order, first-order, second-order and third-order asymmetric lamb waves, respectively, while S0, S1, S2 and S3 represent zero-order, first-order, second-order and third-order symmetric lamb waves respectively (Fig. 40.4).

40.3.3 Principle of AE Location for Two Sensors and Sound Velocity Measurement

When the AE source lies in the line between the two sensors, the location of TDOA for two sensors is the usual linear location, but most of the time, the AE source is not aligned between the two sensors. As shown in Fig. 40.6, the trajectories of all points with the same time difference is a hyperbola. For the calculated coordinate axis x, only when the AE source aligned between the two sensors, the calculated results of the AE location is true (ignoring the velocity changes). For AE sources deviating from the connection between the two sensors, the linear location result tends to the center of the connection between the two probes. The larger the deviation value (y_0) is, the greater the location error will be [7]. Formula (40.1) shows the calculation of location of TDOA for two sensors (Fig. 40.5).

$$\begin{cases} \Delta l = l_A - l_B = \sqrt{(x+c)^2 + y^2} - \sqrt{(x-c)^2 + y^2} = v \cdot \Delta t \\ \dfrac{x^2}{\Delta l^2/4} - \dfrac{y^2}{c^2 - \Delta l^2/4} = 1 \end{cases}$$
$$\Rightarrow \begin{cases} \text{if } \Delta l = 0, \text{ then } x = 0 \\ \text{if } y = 0, \text{ then } x = \pm\dfrac{\Delta l}{2} \text{ and } l_1 = \dfrac{l + v \cdot \Delta t}{2}, l_x = \dfrac{v \cdot \Delta t}{2} \end{cases} \tag{40.1}$$

The method of sound velocity measurement proposed in this paper is based on the fact that the distance between the AE source and the sensor directly affects the measured sound velocity, this method takes into account the difference of the sound velocity calculated by the signal received by the sensor near or far from the AE source. A ring of sensors array is arranged around the circumference of the steel bifurcated pipe, pencil lead breaks (PLBs) are implemented at a certain position where is in the connection line of the two sensors selected. The time when the PLBs signal arrive at the two sensors respectively is recorded and TDOA (Δt) is calculated, Δl is the distances difference of respective source distances from the two sensors. The mean value of the TDOA of the three PLBs signals at the same position is $\overline{\Delta t}$, and a data point ($\overline{\Delta t}$, Δl) is obtained.

The equation of linear regression of a series of data points ($\overline{\Delta t_i}$, Δl_i) is $y = ax + b$, where a is the slope and b is the intercept.

In the experiment, 18 data points of (Δt_i, Δl_i) and 6 data points of ($\overline{\Delta t_i}$, Δl_i) were obtained, as shown in Table 40.2 (The maximum sensors space involved in the calculation of sound velocity is 2700 mm). The time error bars and linear regression line of the data are shown in Fig. 40.6.

The analysis shows that when Δl is small, the variance of the time difference(the time error bar) is short relatively, when Δl increases, the time error bar is longer and the time difference is larger.

The regression equation is: $y = 4622x - 28$, so the value of 4600 m/s can be taken as the sound velocity.

Table 40.2 Velocity Measurement

Δl (mm)	Δt_1 (ms)	Δt_2 (ms)	Δt_3 (ms)	$\overline{\Delta t}$ (ms)	Velocity (m/s)
350	0.0825	0.0820	0.0701	0.0782	4488
650	0.1502	0.1510	0.1502	0.1505	4313
750	0.1753	0.1757	0.1757	0.1756	4278
1150	0.2597	0.2598	0.2596	0.2597	4432
1350	0.2662	0.2930	0.2929	0.2840	4756
2700	0.5994	0.5786	0.5992	0.5924	4509

40.4 Analysis of Location Accuracy of AE Sources

Location Uncertainty (LUCY for short) and Location Error (LE for short) are considered as criteria to evaluate the location accuracy of AE sources in the paper.

40.4.1 Definition of Location Uncertainty and Location Error

Location uncertainty (**LUCY**) describes how well a calculated source position fits with the measured arrival time differences. **LUCY** is basically the standard deviation from a set of measured values to a set of calculated values.

LUCY can only be calculated if the system of equations considered by the location algorithm is overdetermined, E.g. if for linear location an event consists of 3 hits, LUCY can be calculated.

Assuming that the calculated coordinate of AE source is (x_s, y_s), the sound velocity entered in the location calculation software is $\boldsymbol{v}_{\mathbf{u}}$, that is, the sound velocity of the first hit is $v_f = v_{\mathrm{u}}$, and the coordinate of the sensor receiving the hit first is (x_f, y_f).

The time of flight (TOF) of the first hit is t_f:

$$t_f = \frac{\sqrt{(x_f - x_s)^2 + (y_f - y_s)^2}}{v_u} \tag{40.2}$$

The coordinate of the No. i-th sensor in the channel group is (x_i,y_i), and the time difference of i-th hit and the first hit is $\mathrm{dT_i}$, then the time of flight (TOF) of the i-th hit t_i is:

$$\begin{aligned} t_i &= t_f + dT_i \\ &= \frac{\sqrt{(x_f - x_s)^2 + (y_f - y_s)^2}}{v_u} + dT_i \end{aligned} \tag{40.3}$$

The measured value of distance D_i represents the distance between the sensor (x_i, y_i) and the calculated location of the AE source:

$$D_i = \sqrt{(x_i - x_s)^2 + (y_i - y_s)^2} \tag{40.4}$$

The calculated value of distance between the sensors (x_i,y_i) and the calculated location of the AE source is:

$$\begin{aligned} P_i &= v_u \times t_i \\ &= \left[\frac{\sqrt{(x_f - y_s)^2 + (y_f - y_s)^2}}{v_u} + dT_i \right] \cdot v_u \\ &= \sqrt{(x_f - y_s)^2 + (y_f - y_s)^2} + v_u \cdot dT_i \end{aligned} \tag{40.5}$$

The distance deviation of the measured value and the calculated value is $\Delta_i = D_i - P_i$。

Location Uncertainty (**LUCY**):

$$\text{LUCY} = \sqrt{\frac{\sum_{i=1}^{n} (D_i - P_i)^2}{n - 1}} = \sqrt{\frac{\sum_{i=1}^{n} \Delta_i^2}{n - 1}} \tag{40.6}$$

where:n is the number of the sensors of the channel group.

Relative location uncertainty δ_{LUCY} is defined as:

$$\delta_{\text{LUCY}} = \frac{\text{LUCY}}{L_{max}} \tag{40.7}$$

where:

L_{max} represents the maximum sensor spacing among the channel group;

If the real physical position of AE source is $(x_{0,}y_0)$, then the location error (LE) is:

$$\text{LE} = \sqrt{(x_0 - x_s)^2 + (y_0 - y_s)^2} \tag{40.8}$$

The location error calculation formula of one-dimensional linear location is a special case of Eq. (40.8). Location errors in x-direction and y-direction can be defined respectively as: $\text{LE}_x = |x_0 - x_s|$, $\text{LE}_y = |y_0 - y_s|$, then $\text{LE} = \sqrt{\text{LE}_x^2 + \text{LE}_y^2}$.

Relative positioning error δ_{E} is defined:

$$\delta_E = \frac{\text{LE}}{L_{max}} \tag{40.9}$$

Similarly, relative location error δ_{Ex} in x-direction and relative location error δ_{Ey} in y-direction can be defined respectively as: $\delta_{Ex} = \text{LE}_x / L_{max}$, $\delta_{Ey} = \text{LE}_y / L_{max}$,Then $\delta_E = \sqrt{\delta_{Ex}^2 + \delta_{Ey}^2}$.

40.4.2 The Example Analysis

The AE sources location in the two cases of the lowest location precision is discussed: the physical source is very close to one of the sensors (i.e. if the physical source is far away from the center of the sensors array, then, the greater the time difference is, and the higher the location error of AE source is, due to the velocity variation), the most complicated and irregular parts of the detected component.

40.4.2.1 Location Analysis in Region of A2

In region of A2, the planar location array is composed of sensors $20^{\#}$(−5405, −200), $21^{\#}$(−4729,1400), $22^{\#}$(−4054, −200), $23^{\#}$(−3378, 1290), and $24^{\#}$ (−2703, −200). The simulated source of Pencil lead breaks(PLBs) are implemented at the point that is in the connection line of the sensor $20^{\#}$ and sensor $22^{\#}$ and 300 mm away from the sensor $20^{\#}$, and its coordinates is (−4354, −200). The maximum sensors space among the sensors array is about 2700 mm. In order to reduce the influence of velocity variation and complicated transmission paths of sound wave due to the wave transmitting through the longitudinal weld W1, sensor $21^{\#}$ does not participate in location calculation. According to Formulas (40.6), (40.7), (40.8) and (40.9), the calculation results are obtained shown in Table 40.3.

When LUCY (or δ_{LUCY}) is relatively small, the corresponding sound velocity value is defined as the ideal sound velocity value V_{i}. It is indicated from Table 40.3 and Fig. 40.7 that 4200–4800 m/s is assigned to V_{i} in order to control the relative LUCY (δ_{LUCY}) and relative LE(δ_{LE}) below 5%.

When V_{u} is less than V_{i}, LUCY is less than LE; when V_{u} is greater than Vi, LUCY is greater than LE. The change rule of relative $\boldsymbol{\delta}_{\mathbf{LUCY}}$ and the δ_{LE} is constant with the change of sound velocity.

Therefore, although it is difficult to find the actual physical location of the AE source, a proper value of V_{u} can be selected by means of LUCY analysis to improve the location accuracy.

From the sub-figure in Fig. 40.7b, it can be found that the location error in the *x*-direction (circumferential direction) is generally smaller than that in the *y*-direction (longitudinal direction, the wave received the sensor should transmit through the circumferential weld), indicating that the weld has obvious influence on the sound velocity and AE location.

40.4.2.2 Location Analysis in Region of A1

Planar location is adopted in region of A1. The AST (Auto Sensor Test) function is applied, each channel transmits 8 standard pulse signals with a frequency of 150 kHz and a width of 5.2 ms successively as the simulated source, and the other channels receive the signals for location analysis.

Table 40.3 LUCY and LE analysis in region of A2

Velocity (m/s)	LUCY (mm)	δ_{LUCY}(%)	LE (mm)	$\mathrm{LE}_{x(\mathrm{mm})}$	$\mathrm{LE}_{y(\mathrm{mm})}$	δ (%)	Velocity (m/s)	Lucy (mm)	δ_{Lucy}	LE (mm)	$\mathrm{LE}_{x(\mathrm{mm})}$	LE_y(mm)	δ
2800	208.0	7.56	479	14	479	17.75	4600	32.4	1.18	127	41	120	4.70
3000	188.2	6.84	425	14	425	15.75	4800	99.1	3.60	58	38	44	2.15
3230	165.6	6.02	366	14	366	13.57	5000	187.3	6.81	49	35	35	1.83
3400	148.8	5.41	312	15	312	11.57	5200	279.5	10.16	111	44	102	4.11
3600	128.6	4.67	252	15	252	9.35	5400	367.4	13.35	164	62	152	6.08
3800	107.5	3.91	187	14	186	6.91	5600	479.9	17.44	229	70	218	8.48
4000	84.2	3.06	111	13	110	4.10	5800	666.6	24.22	350	44	347	12.95
4200	55.8	2.03	14	6	13	0.53	5950	770.3	27.99	453	3	453	16.78
4400	16.1	0.59	90	15	89	3.34	6000	864.4	31.41	484	12	484	17.93
4470	0.4	0.02	111	25	108	4.11	6200	1022.8	37.17	593	81	587	21.95

The location maps of AE sources at the two different acoustic velocities V_u in Fig. 40.8 is analyzed respectively. When the deviation between the sound velocity value entered in the location software (V_u) and the actual velocity is too large (Fig. 40.8b), the deviation of the location source and the physical source is large as well, meanwhile, the location tends to be close to the middle of the sensors array, what' worse, even the effective locations can't be achieved in some areas (such as the positions sensors $7^{\#}$ and $8^{\#}$ placed). The multiple locations where the sensors $10^{\#}$ and $11^{\#}$ arranged are not concentrated and fails to achieve effective locations,which is caused by the irregular geometry of the region: in the small triangular area composed of the apexes of the crescent rib and the intersecting curves of the main cone and the branch cone(that is the intersection area of area A1 andA2), the surfaces is complicated with large local curvature, in addition, the inner edge and external edge of the rib protruding from the shell plate may cause the change of the acoustic propagation paths and great change of the acoustic velocity after the wave transmitting through the weld or rib, therefore the location precision of AE sources will be lower.

Channel $3^{\#}$ is selected as the transmit of AE signals, and the planar location array is composed of sensors $1^{\#}$, $2^{\#}$, $3^{\#}$ and $4^{\#}$.

The location of AE signals generated successively by the same AE source is not a point, but a location group around the physical position of the source. Therefore, cluster analysis is used to take the center of the location group in the rectangular cluster as the position of the physical source, and the size of the rectangular cluster is 300 × 300 (mm). The coordinate of the physical source is (1700, −260), and the maximum sensor spacing of the location group is 3000 mm.

If the location of *y*-direction, that is, the thickness direction of the rib, is ignored, linear location algorithm can be carried out by channels $1^{\#}$, $3^{\#}$and $5^{\#}$. Figure 40.9 shows the LUCY and LE curves corresponding to the plane location and linear location.

According to the sub-graph in Fig. 40.9a, the location error in the *y*-direction (the direction of rib thickness) is greater than that in the *x*-direction (the direction of

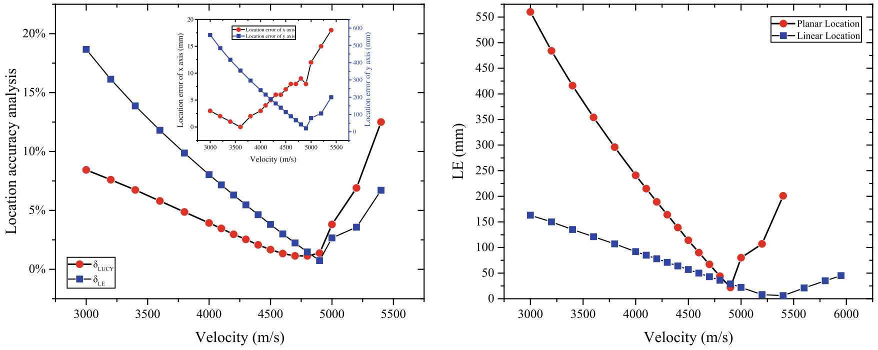

(a) Planar Location

(b) Linear Location

Fig. 40.9 LUCY and LE analysis in region of A1

intersection line between rib and shell plates on both sides). That is due to the fact that the sound wave transmit through the crescent rib with a thickness of 120 mm in the *y*-direction, and the angle between the crescent rib and the shell plate of the branch pipes changes along the direction of the intersection line, which affects the sound transmission paths and wave velocity. The proposed V_u varis from 4400 to 5000 m/s. According to Fig. 40.9b, in linear location, because the simulated AE source is in the center of the connection between the two sensors and the time difference is small (zero in theory), thus, it is not easy to recognize the difference in sound velocity, and the effect of sound velocity on location precision is not obvious.

According to the principle of linear location shown in Fig. 40.5, the sensors in the area with combined welds of the crescent rib and the branch pipes(region of A1) are arranged in one-dimensional linear location mode. As for the AE source deviating from the line between the two sensors, if the offset y_0 in *y*-direction is small (by arranging the sensors close to the combined welds on the same side of the shell plate in *y*-direction), the theoretical location error in the *x*-direction is very small. Therefore, the planar or linear location modes can be used to monitor the area A1 of the steel bifurcated pipe, on one hand, the former location mode has a higher location accuracy in *x*- direction than the latter in spite of high location error in *y*-direction; on the other hand, although the latter ignores the location in *y*-direction, it needs fewer sensors and the location calculation is more simple.

40.5 Conclusion

In this paper, the influence of acoustic velocity and structural irregularity on the location accuracy of AE sources of steel the bifurcated pipe is analyzed. On the basis of time–frequency analysis of AE signal and dispersion analysis of lamb wave, a linear regression method is proposed to measure the sound velocity by considering the multi-mode of sound waves and the characteristics of sound velocity variability. Through the analysis of localization uncertainty (LUCY), the ideal value of sound velocity entered in the location calculation software is selected to reduce the localization error (LE) and improve the accuracy. The following conclusions are obtained:

1. The irregular-shaped structures result in the change of the acoustic propagation paths and great change of the acoustic velocity after the wave transmitting through the welds or the rib.
2. Linear fitting of TDOA (difference time of arrival) versus distance difference of respective source distances from the two sensors is a good method to obtain the ideal value of sound velocity and the proposed sound velocity is about 4600 m/s.
3. The selection of velocity by LUCY analysis induces less loation eroor(LE). As for the irregular geometry region of A1 and A2 of the steel bifurcated pipe, the proposed velocity varies from 4400 to 5000 m/s and 4000 to 4800 m/s, respectively.

4. The linear location can be odopted instead of planar location in the AE location of the irregular region of A1.

References

1. A.B.Samokhvalov, AE source location on irregular-shaped objects using 3D grid method. *Advances in Acoustic Emission Technology :Proceedings of the World Conference on Acoustic Emission-2013*, vol. 158 (Springer Proceeding in Physics, 2015), pp. 103–113
2. W. Wu, S. Cheng, D. Li, S. Cao, B. Lü, Study of Acoustic Emission Attenuation Characteristics of the Steel Bifurcated Pipe in Hydropower Station. *Advances in Acoustic Emission Technology: Proceedings of the World Conference on Acoustic Emission-2017*, vol. 218 (Springer Proceedings in Physics 2019), pp. 317–326
3. Y. Promboon, *Acoustic Emission Source Location* (The University of Texas at Austin, 2000)
4. E. Dehghan Niri, A. Farhidzadeh, S. Salamone, Determination of the probability zone for acoustic emission source location in cylindrical shell structures. Mech. Syst. Signal. PR 60–61, 971–985 (2015)
5. J. Vallen, H. Vallen, Latest improvements on freeware AGU-Vallen-Wavelet, *in Proceedings of 31st Conference of EWGAE (EWGAE 2010)* (2010), pp. 1–8
6. A. Mostafapour, S. Davoodi, M. Ghareaghaji, Acoustic emission source location in plates using wavelet analysis and cross time frequency spectrum.Ultrasonics 54, 2055–2062 (2014)
7. Y. Yue, B. Xu, J. Leng, S. Li, A generalized linear—location method of acoustic emission source. J. Ship Mech. **6**(5), 70–79 (2002)

Chapter 41
Study of Acoustic Emission Response to Vortex Shedding of a Bluff Body

Fatematuz Zohora, David Holmes, Pietro Borghesani, Michael Cholette, and YuanTong Gu

Abstract Acoustic emissions (AE) have been used to detect fluid flow disturbances such as leaks in pipes and turbulence. In such scenarios, fluid dynamics characteristics can be observed at a pipe wall using an AE sensor as a result of complex mechanical interactions. The purpose of this study is to understand the relationship between fluid dynamic force (lift force) at a circular bluff body inside a pipe, and the AE response to this force. Both experimental and numerical studies were conducted to understand this relationship. This investigation reveals that the generated lift force was weak. As a result, the pipe wall response in terms of deformation, velocity, and acceleration was small, and the AE sensor failed to detect the signals. The findings indicate that numerical study can be used as a guide to design AE condition monitoring strategies and to understand what type of disturbance profiles can and cannot be detected.

41.1 Introduction

Acoustic emission (AE) is a popular non-destructive testing technique used in condition monitoring. An AE generating event causes surface motion of a structure in the form of elastic waves. An AE sensor plays a critical role as it records this surface motion and converts it into a voltage–time waveform. Importantly, AE has been used to detect fluid flow disturbances like leaks in pipes or high turbulent flow [1]. AE technique thereby can be used for investigating the relationship between fluid dynamics, and the corresponding mechanical phenomenon at the pipe wall.

When flow passes over a body, the body creates an obstacle to the flow path and generates a wake region downstream. In this scenario, the body is known as a bluff

---

F. Zohora · D. Holmes (✉) · M. Cholette · Y. Gu
School of Mechanical, Medical and Process Engineering, Queensland University of Technology, Brisbane, QLD 4000, Australia
e-mail: d.holmes@qut.edu.au

P. Borghesani
School of Mechanical and Manufacturing Engineering, University of New South Wales, Sydney, NSW 2052, Australia
e-mail: p.borghesani@unsw.edu.au

© The Author(s), under exclusive license to Springer Nature Singapore Pte Ltd. 2021

G. Shen et al. (eds.), *Advances in Acoustic Emission Technology*, Springer Proceedings in Physics 259, https://doi.org/10.1007/978-981-15-9837-1_41

body. Flow over a bluff is a classical problem in the fluid dynamic research area and has practical engineering applications. Flow over high-rise buildings, marine risers, bridges, cooling towers, chimneys, airfoils, tube bankers in heat exchangers, are a few of many practical engineering examples of flow over a bluff body. This type of flow often includes many complex fluid phenomena such as vortex shedding, wake flow, separation and high turbulence [2]. When the flow is obstructed by a bluff body, two types of fluid dynamic forces are generated: lift and drag force (Fig. 41.1). The drag force acts in the direction of the fluid flow, while the lift force is generated perpendicular to the flow direction. The fluid dynamic phenomenon changes depending on the value of these two fluid dynamic forces. The lift and drag force on a bluff body, and vortex shedding frequency are calculated from well-established equations:

$$F_D = C_D S q_{inf} \tag{41.1}$$

$$F_L = C_L S q_{inf} \tag{41.2}$$

$$q_{inf} = \frac{1}{2}\rho v^2 \tag{41.3}$$

$$f_s = \frac{S_t v}{d} \tag{41.4}$$

where F_D and F_L are drag and lift forces on the whole cylinder in the x-direction and y-direction respectively;q_{inf} is free stream fluid dynamic pressure, f_s is the vortex shedding frequency, S_t is Strouhal number, d is dimension of the bluff body, v is fluid velocity in the pipe, S is the surface area of the bluff body.

This study aims to understand the relationship between fluid dynamic phenomenon occurring due to fluid disturbances around the bluff body—(vortex shedding in this study) and mechanical phenomenon—(responses of fluid force on the pipe wall) using AE testing technique. From Fig. 41.1, a circular bluff body inside a pipe generates vortices in the downstream flow. Lift and drag forces are generated at the bluff body. The force of interest in this study is lift force as it acts on the pipe wall, and vibration generates from the vortex shedding. Both events have influences

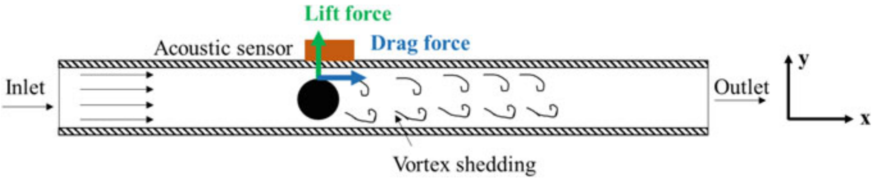

Fig. 41.1 Fluid dynamic forces around a bluff body

on the pipe wall which can be recorded by an acoustic sensor. The extensive literature [3–5] on flow over a bluff body and the equations are helpful to estimate the lift force and vortex shedding, while the numerical and experimental study is beneficial to estimate the AE detectability.

41.2 Method

The method of this study (Fig. 41.2) involves an experimental study, and a numerical study consisting of computational fluid dynamics (CFD) and finite element analysis (FEA) simulation of flow over a cylinder. An experimental study was conducted to observe the response of the expected vortex shedding frequency in the frequency domain and then compared with the numerical study. A CFD simulation was conducted since CFD is a powerful tool that can demonstrate the fluid dynamic phenomenon occurred at the cylinder wall inside the pipe, while a FEA was performed to observe the mechanical phenomenon as a result of the fluid dynamic at the pipe wall. ANSYS Fluent and ANSYS Harmonic Response were used as CFD solver and FEA mechanical solver to investigate the fluid dynamic phenomenon and mechanical response at pipe wall respectively.

The experimental data were collected from the test-rig with an AE data acquisition system. The AE data was used for appropriate signal processing to get the response of the pipe wall in the frequency domain. The CFD study of a three-dimensional cylinder inside a pipe calculates lift force and vortex shedding on the cylinder. The lift force is then applied to the FEA model to get the response quantities (deformation, velocity and acceleration) at the pipe wall in the predetermined frequency range (around vortex shedding frequency) found from CFD simulation. The excitation frequency and magnitude of mechanical response at the pipe wall were compared from AE lab tests and FEA model.

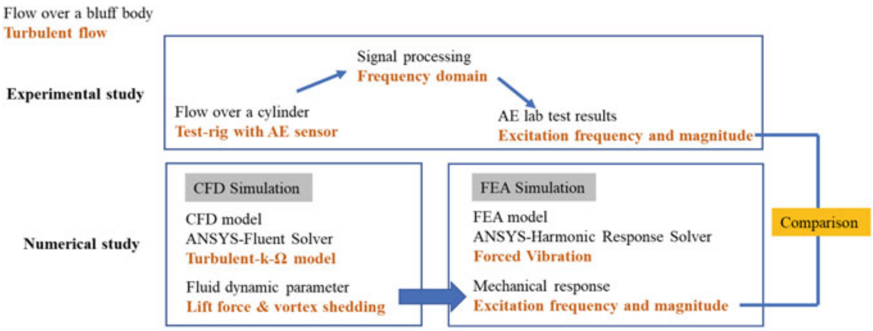
Flow over a bluff body
Turbulent flow
Experimental study
Signal processing
Frequency domain
Flow over a cylinder
Test-rig with AE sensor
AE lab test results
Excitation frequency and magnitude
Numerical study
CFD Simulation
CFD model
ANSYS-Fluent Solver
Turbulent-k-Ω model
Fluid dynamic parameter
Lift force & vortex shedding
FEA Simulation
FEA model
ANSYS-Harmonic Response Solver
Forced Vibration
Mechanical response
Excitation frequency and magnitude
Comparison

Fig. 41.2 Flow diagram of the method of this study

41.3 Numerical and Experimental Test Set-Ups

41.3.1 Experimental Test Set-Up

The experimental set-up has two parts: test-rig and AE data acquisition equipment. The pipe dimension was 1.2 m long and 125.4 mm inner diameter with 1.6 mm wall thickness and the cylinder diameter was 25 mm. A flow meter and a pressure gauge were used to measure the fluid flow rate and pressure at pipe outlet respectively. A flow stabilized zone was introduced to the inlet of the pipe to make the fluid stable before it passes over the cylinder. A higher flowrate was selected to generate turbulent flow inside the pipe. Physical acoustic corporation (PAC) resonance sensor (AE R15 α) with resonance frequency 150 kHz was mounted on the surface of the pipe for capturing AE signals. The AE sensor was connected to a high-pass (100 kHz) amplifier via a pre-amplifier. The gain of the amplifier and pre-amplifier was 0 dB and 60 dB respectively. LabVIEW software was used for signal recording through communication with *NI 9223* module and MATLAB was used for signal post-processing. The sampling frequency for data acquisition was selected manually to 1 MHz for R15α.

41.3.2 Numerical Test Set-Up

A three-dimensional circular cylinder (as a bluff-body) inside a pipe was selected in this study as a vortex generator to obtain vortex shedding frequency and lift force. The geometry domains of interest for CFD and FEA study are shown in Fig. 41.3. The pipe and cylinder dimensions were adopted from the experimental test-rig. The material for the pipe and cylinder was Stainless steel. A high flow rate was considered for this study to ensure the flow inside the pipe is turbulent. The turbulent flow was selected because it generates higher vortex shedding frequency compared to laminar regime. A transient turbulent model (Standard k-omega) was selected for this study with velocity inlet and pressure outlet boundary condition. The Reynolds number, Re was 1.6e4 based on the mean inlet velocity inside the pipe and given dimension. The time step set to 0.001 s for the study. Mesh and time sensitivity tests were performed to select converged mesh size and time resolution for this study (Figs. 41.4 and 41.5).

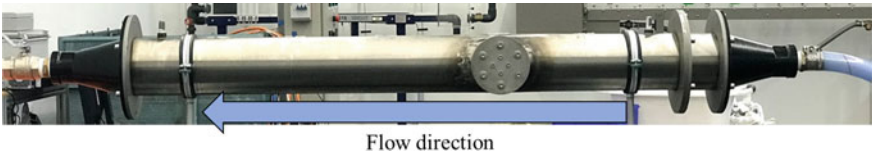

Fig. 41.3 Flow over a cylinder test-rig

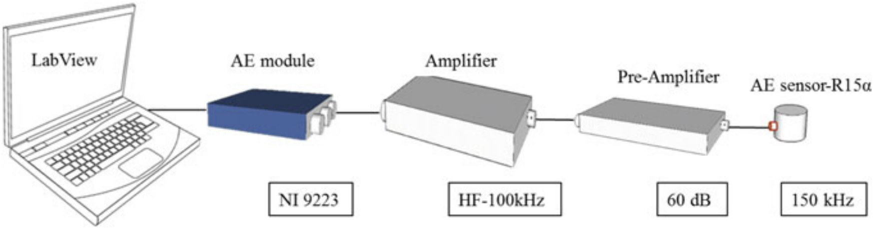
LabView
AE module
Amplifier
Pre-Amplifier
AE sensor-R15α
NI 9223
HF-100kHz
60 dB
150 kHz

Fig. 41.4 AE data acquisition set-up

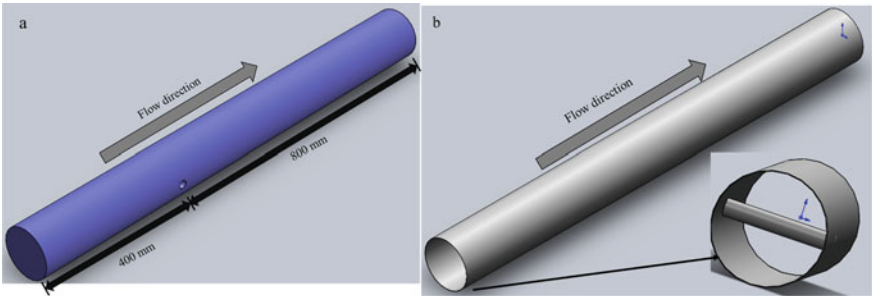
a
Flow direction
800 mm
400 mm
b
Flow direction

Fig. 41.5 **a** CFD geometry domain, **b** FEA geometry domain

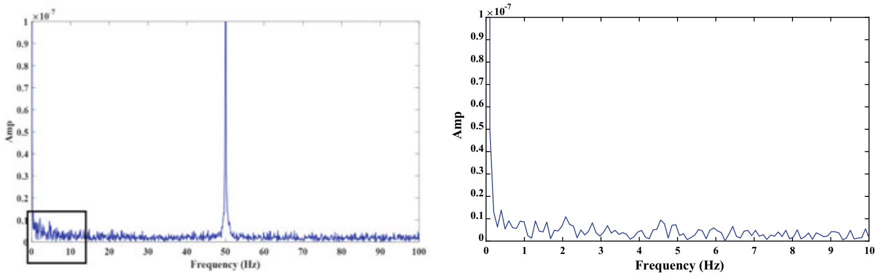

Fig. 41.6 Left: Frequency domain of raw AE signal, Right: Zoom around low frequency domain of raw AE signal

41.4 Results and Discussion

41.4.1 Experimental Results and Discussion

The experimental study was conducted to get AE voltage–time waveforms. As the area of the interest in this study is frequency, therefore, the AE response was observed in the frequency domain. The measured AE data are used to calculate fast Fourier transform (FFT) which does not show any specific frequency rather shows noise, refer

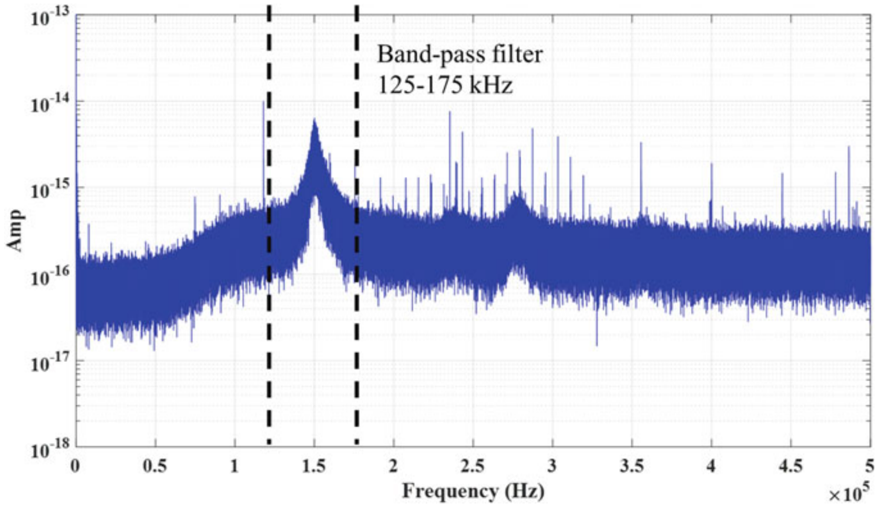

Fig. 41.7 PSD of raw AE signal

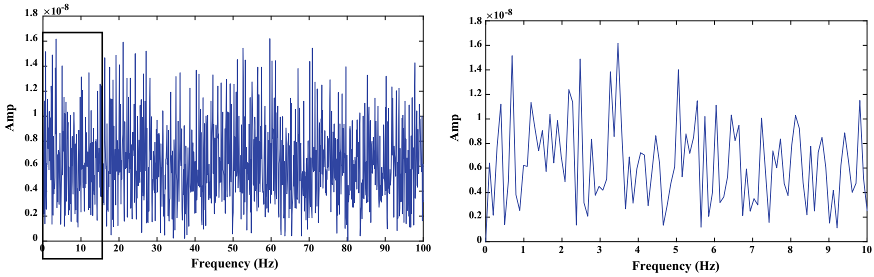

Fig. 41.8 Left: Frequency domain of envelope AE signal, Right: Zoom around low frequency domain of envelope AE signal

to Fig. 41.10 Left. Vortex shedding frequency can be calculated analytically from (41.3) that gives 0.987 Hz. To have a closer look at the lower frequency, Fig. 41.10 Right plot is obtained. Yet, no specific information is extracted from the signal in the frequency domain. To get some idea of the overall frequency trend, PSD of the raw AE signal is calculated. The plot (Fig. 41.11) shows that the signals are amplified around 150 kHz range which is the resonance frequency range of the AE sensor used for this study. Since the analytical vortex shedding frequency is low, demodulation of the signal can help us to find the frequency. A filter-band of 125–175 kHz around the resonance frequency of the sensor is selected. The filtered signals are then used for envelope analysis using Hilbert transform.

The demodulated signal of AE can be found in Fig. 41.12. The frequency range over the 100 Hz shows no specific frequency peak that can be related to the vortex shedding frequency. Hence, the results arise a few questions. Is the excitation

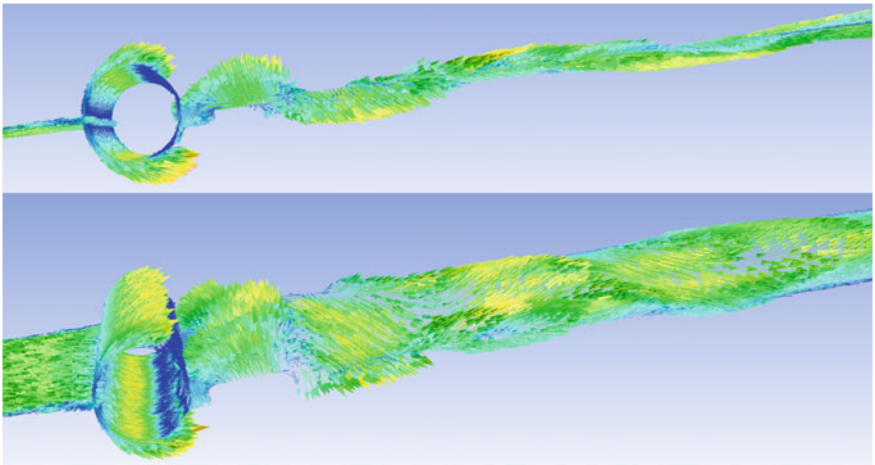

Fig. 41.9 Vortex shedding around a cylinder from CFD simulation

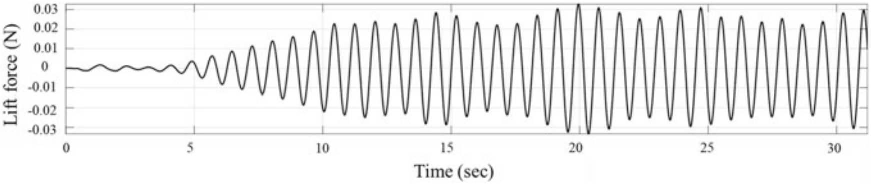

Fig. 41.10 Lift force generated due to vortex shedding

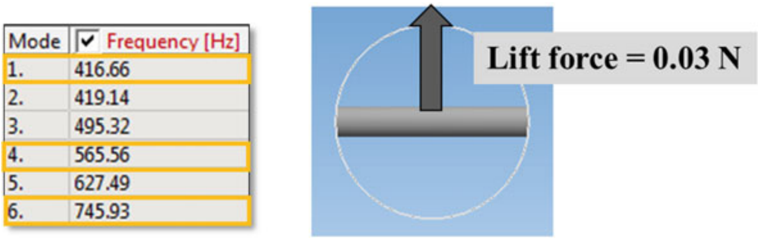

Mode	☑ Frequency [Hz]
1.	416.66
2.	419.14
3.	495.32
4.	565.56
5.	627.49
6.	745.93

Fig. 41.11 Left: Natural frequencies of the system, Right: direction of lift force acting on the cylinder

frequency due to vortex shedding low and buried into the background noise? Is the vortex shedding generated at all in the pipe? Is the generated lift force weak that can have less impact on the pipe wall? To find the answers to these questions, a numerical study will be a helpful tool.

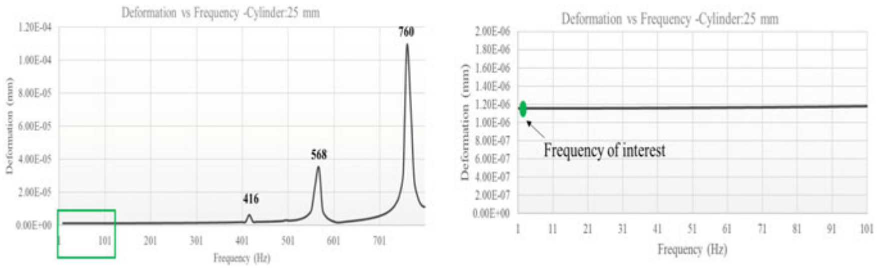

Fig. 41.12 Left: Deformation of pipe wall over a wide range of force vibration frequency, Right: deformation of pipe wall over frequency of interest (1–101 Hz)

41.4.2 Numerical Results and Discussion

It was found that smooth surface circular cylinder generates stronger dynamic force and vortex shedding than rough surface circular cylinder [6]. Thus, a circular smooth surface cylinder is selected to generate a strong vortex shedding in this study. A higher Reynolds number ensures higher vortex shedding frequency refers to (41.3). On the other hand, it is found from (41.2) that lift force is function of lift coefficient in the case of the same fluid properties and geometry domain. A theoretical vortex shedding frequency value (0.9871 Hz) can be found from (41.3), provided that an infinite channel/pipe wall was considered. Figure 41.6 demonstrates that an alternating vortex shedding is generated from the current domain. The magnitude and frequency of this alternating vortex shedding are 0.03 N and 1.249 Hz (from Fig. 41.7). The calculated value is accurate enough as the value is considered for a finite pipe wall (125.4 mm). The study reveals that the generated lift force was weak.

It is expected that this lift force and frequency of the vortex shedding have influences on the pipe wall. To obtain this influence, the lift force is applied to the pipe wall using ANSYS Harmonic Response solver. This solver solves the forced vibration equation. As per [7, 8] the input of an AE sensor is either velocity or displacement or force, while the output is voltage over time. AE wave such as lamb wave or bulk wave is complex for simulation. A simplified case considered where the mechanical response qualities deformation, velocity and acceleration are obtained as an effect of lift force on the pipe wall. So, the deformation and velocity are of great interest in this study. Before finding the forced vibration response, the natural frequency of the system is important to know. An analytical calculation shows that the weight of the test-rig is 4 kg (approx.) and the natural frequency is 579 Hz. To avoid the resonance of the system, it is essential to identify the natural frequency of the system. Through the ANSYS Modal analysis, a list of natural frequencies (Fig. 41.8 Left) is determined for the current system. Thereby, the natural frequency of the system can be verified. Further validation can be obtained once the system is under force vibration and shows the resonance frequency. As to determine the pipe wall response, the ANSYS Harmonic Response solver is used applying lift force to the pipe wall as can be seen from the Fig. 41.8 Right. The pipe responses are obtained as deformation,

Table 41.1 Deformation, Velocity and Acceleration at pipe wall due to lift force

	Lift force (N)	Vortex shedding frequency (Hz)	Displacement (mm)	Velocity (mm/s)	Acceleration (mm/s^2)
Cylinder: 25 mm	0.03	1.249	1.15e−6	7.25e−6	4.56e−5

velocity and acceleration at the pipe wall due to the applied lift force. As expected, the responses of the weak force are insignificant. Figure 41.9 left shows the deformation of the system over a range of 1–800 Hz. The resonance frequency is at 568 validate the analytical calculated natural frequency. As the frequency of the interest for this study is low (referring to previous section, vortex shedding frequency 1.249 Hz), the deformation of the pipe is observed in the range of 1–101 Hz (Fig. 41.9 Right). The plot shows that the magnitude of the excitation frequency is constant over the frequency range and the value is 1.15 nm. The mechanical response qualities are summarised in Table 41.1. The magnitude of the responses is so insignificant that the visible response on the pipe wall is not expected. The sensitivity of the resonance sensor used for this study is 75 kHz 1 V/(m/s). Thereby, the velocity (from Table 41.1 7.25e−6 mm/s) that is generated due to the lift force cannot be recorded with sensor (Figs. 41.10, 41.11 and 41.12).

Answering to the questions in Sect. 4.1 that a vortex shedding is generated downstream of the pipe with a low frequency and a weak lift force is present. The mechanical response quantity (velocity) of this weak force on the pipe wall is insignificant to excite the AE sensor which has a sensitivity 1 V/(m/s)) for recording the signals.

41.5 Conclusion

The vital outcome of this study is the amount of force which is generated due to the fluid disturbance is critical to detect the AE signals in the pipe wall. The findings demonstrate that the vortex shedding induced vibration is too weak to record for a resonant AE sensor at the Reynolds number tested. The excitation frequency range was beyond capturing the AE signals. Yet, this study is valuable to understand the fluid dynamic-mechanical phenomenon relationship at the pipe from computer modelling. Understanding this relationship is of major importance in the condition monitoring fields involve fluid dynamics phenomenon, for instance, leaks in pipe, pressure tank.

Acknowledgements The authors gratefully acknowledge the supports given by Queensland University of Technology (QUT) for experimental test-rig and providing High-Performance Computing facilities for the numerical study.

References

1. X. Cui, Y. Yan, M. Guo, Y. Hu, X. Han, Localization of continuous gas leaks from a flat-surface structure using an acoustic emission sensor array . IEEE International Instrumentation and Measurement Technology Conference Proceedings **2016**, 1–5 (2016)
2. A. Sohankar, Flow over a bluff body from moderate to high Reynolds numbers using large eddy simulation. Comput. Fluids **35**, 1154–1168 (2006)
3. T. Sarpkaya, Vortex-induced oscillations: a selective review (1979)
4. D.M. Sallet, The lift force due to von Karman's vortex wake. J. Hydronaut. **7**, 161–165 (1973)
5. M. Matsumoto, Vortex shedding of bluff bodies: a review. J. Fluids Struct. **13**, 791–811 (1999)
6. B. Zhou, X. Wang, W. Guo, W.M. Gho, S.K. Tan, Experimental study on flow past a circular cylinder with rough surface. Ocean Eng. **109**, 7–13 (2015)
7. J. Keprt, P. Benes, Primary calibration of acoustic emission sensors, in *Fundamental and Applied Metrology*, Lisbon, Portugal (2009)
8. I. 12713, Non-destructive testing—acoustic emission inspection—Primary calibration of transducers (1998)

Chapter 42
Damage Localization of Debris Cloud Hypervelocity Impact Based on Acoustic Emission

Kai Zhang, Runqiang Chi, and Baojun Pang

Abstract With the increase of the human aerospace activities, space debris environment is seriously threatening on-orbit spacecraft safe operation. It is necessary to monitor the occurrence and location of impact. In this paper, two stage light gas gun is used for launching spherical projectile to impact on double-layer plates. The projectile penetrates the front plate to form debris cloud, and the debris cloud further impact the rear plate. Ultrasound sensors are used to gain impact signals on the rear plate. According to the morphology of debris cloud, the damage center are located by the conventional triangulation technique. Unlike single-point impact, debris cloud impact is a sequence of impacts by multiple particles in a short time, the impact damage is a certain area. As the initial velocity increases, the impact area becomes larger. The characteristics of the acoustic emission (AE) signals are analyzed by using wavelet packet technology and energy entropy principle. A characteristic parameter related to the impact area is constructed. An empirical formula for predicting the damage diameter is established by using exponential fitting method.

42.1 Introduction

With the increase of human activities in space exploration, the number of space debris in low earth orbit is increasing. The collision velocity between space debris and spacecraft belongs to the category of HVI. In low earth orbit, the average collision velocity is about 10 km/s. When the space debris size is in the range of 1–10 mm, the spacecraft may be penetrated. With the debris size increases, the impact even causes the spacecraft to disintegrate. In reality, long-term manned spacecraft is unavoidable

---

K. Zhang (✉)
Changshu Institute of Technology, Changshu 215500, China
e-mail: bluerobbin@163.com

Dalian University of Technology Changshu Research Institute Co., Ltd, Changshu 215500, China

R. Chi · B. Pang (✉)
Harbin Institute of Technology, Harbin 150001, China
e-mail: pangbj@hit.edu.cn

© The Author(s), under exclusive license to Springer Nature Singapore Pte Ltd. 2021

G. Shen et al. (eds.), *Advances in Acoustic Emission Technology*, Springer Proceedings in Physics 259, https://doi.org/10.1007/978-981-15-9837-1_42

to be impacted by space debris, penetration will cause leakage of gas in the enclosure. To ensure the safety of astronauts, space debris impact sensing system is proposed. The sensing system is accompanied by some measurable physical phenomena during HVI, such as electromagnetic radiation (visible light, infrared light, microwave), AE wave, plasma, impact acceleration, secondary debris cloud, impact cratering or perforation damage. Since on-orbit sensing system was put forward, series of related work were carried out. Many on-orbit sensing methods based on different principles were designed, including impact acceleration sensing method [1–3], thermal imaging detection method [4], resistance film sensing method [5], microwave sensing method [6], PVDF sensor sensing system, etc. Among them, AE technology were attracted much attention, such as Prosser compared the difference of AE signals between low-velocity and high-velocity impacts [7], it was concluded that low-velocity impacts produced signals with little extensional mode and large flexural mode components, and high-velocity impacts had large extensional mode components. Schäfer used this technology to locate the impact of space debris on aluminum alloy plate and honeycomb aluminum plate [8].

Time difference of arrival (TDOA) source location problem has been studied in isotropic and anisotropic structures [9–12]. For an isotropic plates with the known wave speed, locating an AE event is traditionally done by trilateration. The triangulation technique works very well when the velocity of the signal in the medium and the time of arrival of the signal at all three sensor locations are known. Kundu proved that small variations in the wave speed estimation can significantly alter the predicted source location. This ambiguity in the source location prediction can be reduced by increasing the number of receiving sensors [13].

For manned spacecraft, adding protective structure is an effective protective method. The double-layer aluminum alloy plate structure is a typical protective structure. When the space debris penetrates the front plate, it breaks into many fragmentation called secondary debris cloud. This process reduces the impact energy density and also reduces the degree of impact damage. But it also brings new problems for localization. Most of the works focus on single point source localization, the AE signals of the second debris cloud impact are produced by multiple particles hitting a certain area in a short time. How to locate this kind of impact is a new problem. This paper presents a method to locate debris cloud impact events. Simulation of space debris impact by launching projectile with two-stage light gas gun. The debris cloud impact damage is an area. By analyzing the motion characteristics of debris cloud, the damage center is located by TDOA method. The spectrum characteristics of impact signals with different initial velocities are analyzed. The relationship between AE signals and damage area is analyzed. The characteristic parameter used to estimate the size of impact damage area is constructed.

42.2 HVI Experiment

A typical double-layer Whipple shield, as the impact target is designed as shown in Fig. 42.1. The front plate as a bumper used in the experiment is 6061-T6 Aluminum alloy plate. The plate dimension is 200 × 200 mm, its thickness is 1 mm, fixed on a frame. The rear plate is 5A06 aluminum alloy plate, its dimension is 500 × 500 mm, its thickness is 3 mm, suspended in the target chamber. The distance between them is 100 mm. The projectile impacts the front plate normally and penetrates it to form the debris cloud. Four ultrasonic sensors are fixed on the back plate with clamps, the sampling frequency of the oscilloscope is 25 M/s.

When the projectile impacts the front plate normally, the secondary debris cloud is symmetrically distributed. Figure 42.2a is the schematic diagram of debris cloud impact condition. The velocity of debris cloud includes the normal velocity of trajectory axis and the radial velocity (perpendicular to trajectory axis). In order to describe the motion characteristics of debris cloud, representative points are usually selected for analysis, as shown in the Fig. 42.2a. The central point 1 shows the point with the fastest moving speed of the debris cloud, which contains only normal velocity v_{1a}.

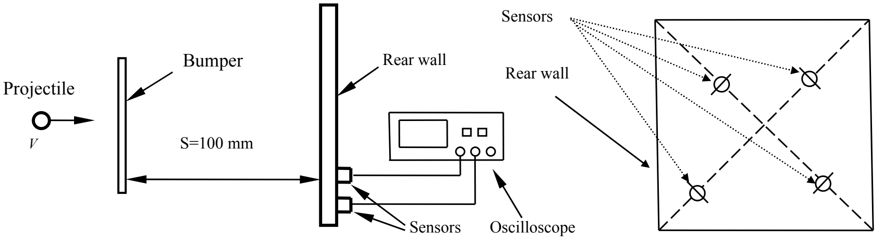
Projectile
V
Bumper
S=100 mm
Rear wall
Sensors
Oscilloscope
Sensors
Rear wall

Fig. 42.1 Schematic of debris cloud impact signal acquisition experiments

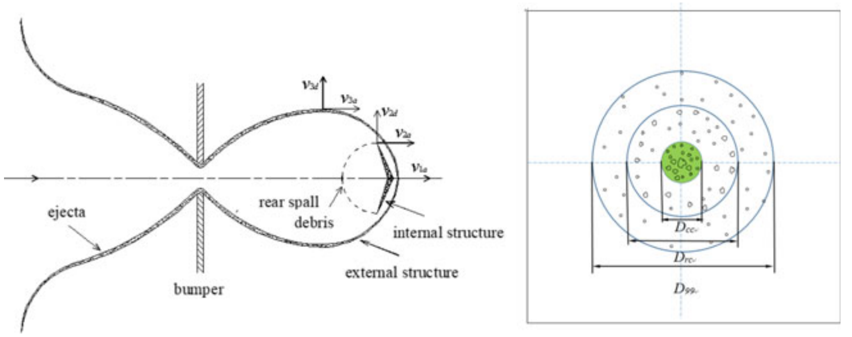
v_{3d}
v_{3a}
v_{2d}
v_{2a}
v_{1a}
ejecta
rear spall
debris
internal structure
external structure
bumper
D_{cc}
D_{rc}
D_{99}

(a) Schematic of debris cloud configuration

(b) Schematic of debris cloud impact damage in the rear plate

Fig. 42.2 Schematic of double layer plate impacts by projectile. **a** Schematic of debris cloud configuration. **b** Schematic of debris cloud impact damage in the rear plate

Table 42.1 Experimental results of debris cloud impact

Experiment	Impact velocity (km/s)	D_{99} (mm)	Damage mode
No. 1	2.50	102	NP
No. 2	3.05	126	P
No. 3	3.65	133	NP
No. 4	4.00	152	NP
No. 5	4.45	159	NP
No. 6	5.05	165	NP

The point 3 shows the point with the outermost radial direction of the debris cloud, which has the normal velocity v_{3a} and the radial velocity $v_{3\mathrm{d}}$ parallel to the target plate. The damage area in rear plate can be broadly classified into three areas: the central cratered area (D_{cc}), the ring cratered area (D_{rc}), and the spray area (D_{99}), as interpreted in Fig. 42.2b [14].

The experimental results are shown Table 42.1. Six HVI experiments are carried out. The impact velocity is in the range of 2.50–5.05 km/s. The spay area D_{99} increases with the impact velocity. The central cratered area D_{cc}, the ring cratered area D_{rc} are not listed in this table, as it is difficult to confirm the boundary. There are two damage modes on the rear plate, penetrated or not penetrated (P/NP).

Figure 42.3 are the morphology of debris cloud impact damage. In Fig. 42.3a, the rear plate is not penetrated, and a crater damage is in the impact center. There are a few small craters around it. In Fig. 42.3b, the initial velocity is 3.05 km/s, the projectile is partially broken, and the rear plate is penetrated. There is a non-circular perforation in the impact center. Around the perforation, there are several impact craters. In Fig. 42.3c, the initial velocity of the projectile is 3.65 km/s. the damage degree of the rear plate reduced, the rear plate is not penetrated, but the number of craters is increased, and the damage area of debris cloud is increased. With the further increase of the initial velocity of the projectile, the damage degree of rear plate decreased, as shown in Fig. 42.3d–f. The reason is with the increasing of the initial velocity, the size of the small fragments in the debris cloud decreases, and the distribution area increases. The fragmentation of the projectile consumes the impact energy.

42.3 Analysis of Debris Cloud Impact AE Signals

Figure 42.4 shows the time history curve of AE signal at 150 mm away from the center of rear plate. The sensor here is farthest from the edge, so we can gain long time non reflection signals. When the rear plate impact by debris cloud, there are two kind of force, the radial expansion force normal impact force. The former excites symmetric S_0 and S_2 mode plate waves, and the latter excites the antisymmetric A_0 mode plate waves [15]. With the increase of the initial velocity, the projectile breaks

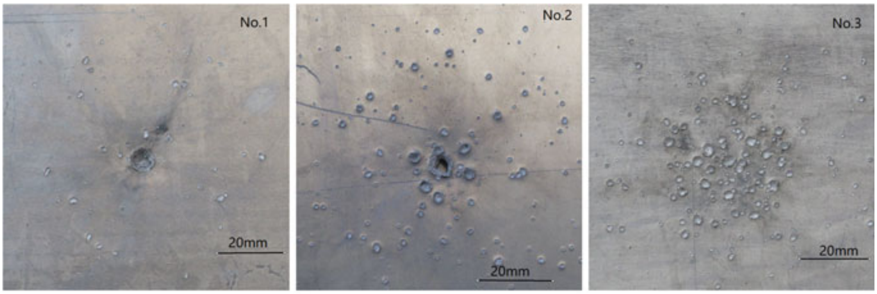

(a) *V*=2.50 km/s (b) *V*=3.05 km/s (c) *V*=3.65 km/s

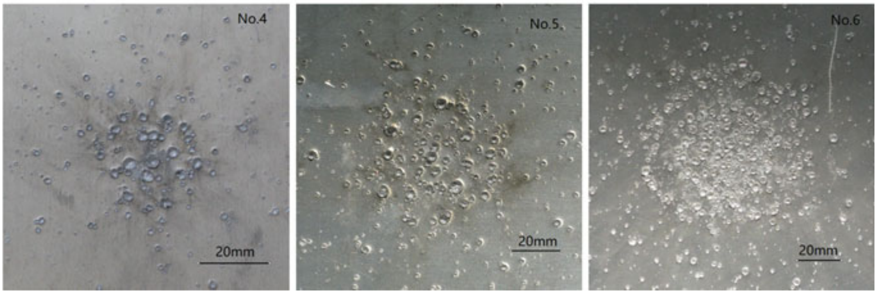

(d) *V*=4.00 km/s (e) *V*=4.45 km/s (f) *V*=5.05 km/s

Fig. 42.3 Morphology of debris cloud impact damage in rear wall

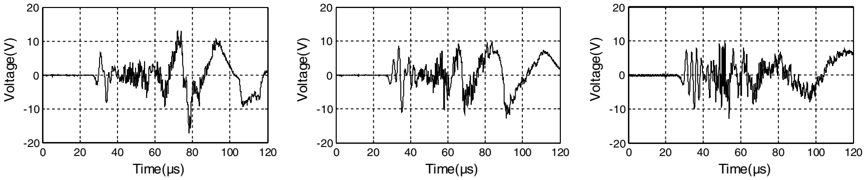

(a) *V*=2.50 km/s (b) *V*=3.05 km/s (c) *V*=3.65 km/s

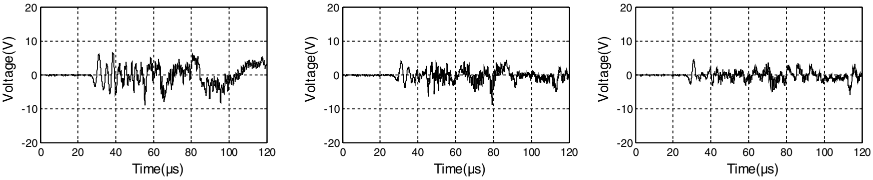

(d) V=4.00 km/s (e) V=4.45 km/s (f) V=5.05 km/s

Fig. 42.4 Debris cloud impact signals with different projectile initial velocity

into smaller particles in the debris cloud, as a result the impact force load on the target plate becomes smaller. As can be seen from the figure, the amplitude of signals tends to decrease.

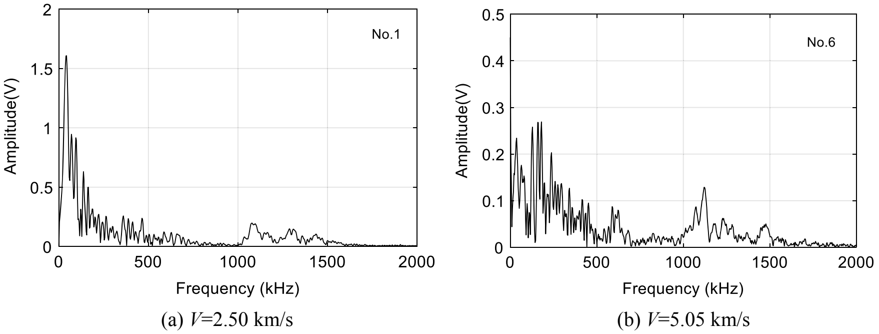

(a) V=2.50 km/s (b) V=5.05 km/s

Fig. 42.5 Frequency spectrums of debris cloud impact signals

The fast Fourier transform results of the signals in Fig. 42.4a and f are shown in Fig. 42.5. The energy of debris cloud impact AE signals are concentrated in two frequency bands, 0–500 kHz and 1000–1500 kHz, the former corresponds to S_0 and A_0 modes in 3 mm aluminum alloy plate, and the latter corresponds to S_2 mode. Furthermore, with the increase of projectile velocity, the energy of AE signals decreases gradually. In addition, when the initial velocity of the projectile is low, the energy lower than 500 kHz is significantly higher. With the increase of the initial velocity, the energy of the two frequency bands in the signal spectrum becomes closer.

Through the spectrum distribution characteristics, we can see that with the increases of the initial velocity, the proportion of low-frequency component energy in the signals tends to decrease, and the energy is evenly distributed in the whole frequency domain. With the help of wavelet packet technology [16], the phenomenon can be analyzed more clearly. The process of wavelet packet decomposition of signals is as follows: if the j-layer wavelet packet decomposition sequence of signal S_{jk} ($k = 0\text{–}2^{j}-1$), then it divides $0 \sim f_{\max}$ into $(0 \sim f_{\max}/2^j)$, $(f_{\max}/2^{j} \sim f_{\max}/2^{j-1})$, …, $(f_{\max}\text{-}f_{\max}/2^{j-1} \sim f_{\max})$ 2^{j} parts in total. According to the above decomposition process, the AE signals can be decomposed by wavelet packet. The db8 wavelet is selected as the wavelet base, which has good compactness. According to the characteristics of signal spectrum, the decomposition level is taken as 8 layers, and the corresponding bandwidth of each frequency band is 48.825 kHz.

After wavelet packet decomposition, the energy $E_{j,k}$ of each reconstructed signal are set as

$$E_{j,k} = \sum_{l=1}^{N} \left|x_{k,l}\right|^2 \tag{42.1}$$

where, j is the number of decomposition layers; k is the order signal after signal decomposition, ($k = 0, 1, 2\ 2^{j-1}$); x_{kl} is the amplitude of discrete point of reconstruction signal; l is the first sampling point in signal; N is the number of signal samples.

In the J-scale, the total energy E of the signal is the sum of the energy of each sub-bands, that is

$$E = \sum_{k=0}^{2^j - 1} E_{j,k} \tag{42.2}$$

The first 10 sub-bands wavelet packet energy are calculated, and the proportion of each frequency band are obtained, as shown in Fig. 42.6. From the results we can see that with the increase of the initial velocity, the energy of each sub-band gradually becomes uniform [17].

In order to describe this characteristic quantitatively, the concept of entropy, which is commonly used in information theory, is introduced to deal with the signals. Entropy represents the amount of information output by the source, which is a measure of the degree of signals confusion. The more concentrated the signal distribution in each frequency band, the smaller the entropy value; otherwise, the more uniform the signal distribution in each frequency band, the greater the entropy value.

Shannon entropy is defined as follows:

$$H(X) = -\sum_{j=1}^{L} p_j \log(p_j) \tag{42.3}$$

where, $p_j \in [0, 1][0, 1]$ is the eigenvalue of the signal; L is the number of eigenvalues of the signal, when $p_j = 0, p_j \log(p_j) = 0$.

According to the spectrum characteristics of the signals, A_0 mode lamb wave is concentrated in the frequency band lower than 100 kHz, so after 8-layer wavelet packet decomposition, the first 2-order sub-bands can better reflect the A_0 mode characteristics. Five eigenvalues are obtained by summing the decomposed sub-bands energy percentages one by one in Fig. 42.6.

$$p_j = E_{i,j}/E(j = 1 - 5) \tag{42.4}$$

These eigenvalues are related to the signals below 500 kHz, as the high frequency part are also an important factor to reflect the damage characteristics, the proportion of energy in other frequencies is summed as another eigenvalue,

$$p_6 = 1 - \sum_{j=1}^{5} p_j \tag{42.5}$$

The energy entropy of the signals are calculated by substituting the six eigenvalues into (42.3). According to the definition of entropy, when the six value is the same, the entropy is the largest. For comparison purposes, the entropy value is normalized. The wavelet packet energy entropy of debris cloud impact AE signal is defined as

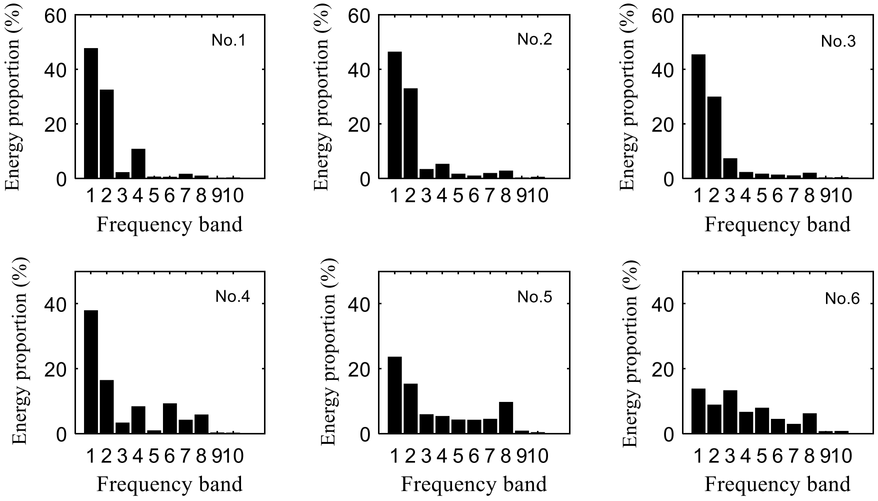

Fig. 42.6 The distribution of frequency bands energy of AE signals caused by debris cloud impact

$$W_{EE}=\frac{-\sum_{j=1}^{6} p_j \log_2(p_j)}{-\log_2(1/6)} \tag{42.6}$$

The characteristic value changes with the impact velocity is shown in Fig. 42.7. The entropy value increases with the initial velocity of the projectile. The value reflects the spectrum characteristics of debris cloud impact signals: the closer the value is to 0, the more concentrated signals distribution in frequency domain; the closer the value is to 1, the more uniform signals distribution in frequency domain.

Fig. 42.7 Wavelet packet energy entropy versus projectile initial velocity

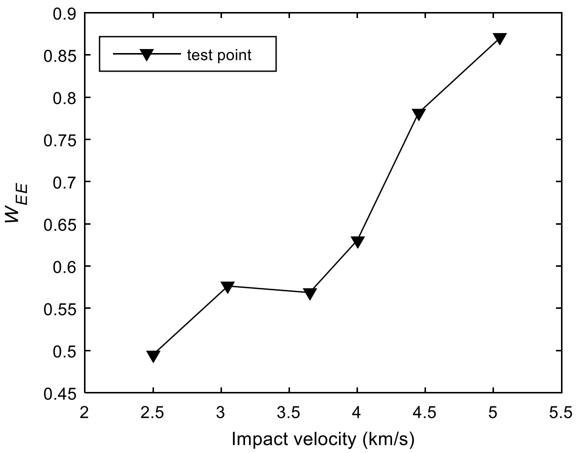

42.4 Debris Cloud Impact Localization

In this paper, the projectile impacts the double-layer plate structure normally. In this condition, the damage on the rear plate is symmetrical. The signals received by sensors may be from the impact damage center, or from the damage boundary, or between them. It is difficult to confirm where the first arrival signals from. But due to the symmetry of debris cloud structure as shown in Fig. 42.2, the location should be the damage center, as shown in Fig. 42.8. We assume the first arrive signals from the dotted line in the graph. As the dotted line is the same distance from the center, the difference of the arrival time to each sensor is the same. So we can conclude that the location of the damage center can be calculated by using conventional location method.

Using the first trough of wave as the arrival time in the experiment. The results are shown in Fig. 42.9. They are the signals received by the sensors 150 and 250 mm away from the center of the target plate. The wave propagation velocity c is obtained by lead break test. Five repetitive tests are carried out on the target plate, the mean value of velocity c is 5.47 km/s calculated by least squares method.

Impact localization are achieved by using a simple algorithm. The number of sensors is N ($N > 2$), the coordinate of the impact source are (x_0, y_0), the coordinate of the sensors location are (x_i, y_i). The exact clock time of the acoustic event is t_0, the arrival time to each sensor is t_i. Then the distance of the ith sensors from the impact point is given by

Fig. 42.8 Schematic of wave propagation

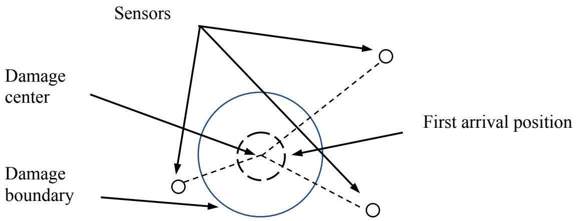

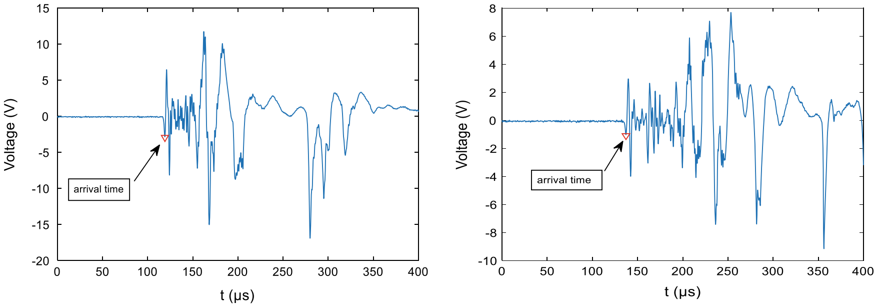

(a) d=150 mm

(b) d=250 mm

Fig. 42.9 The arrival time of AE signals

$$(x_i - x_0)^2 + (y_i - y_0)^2 = c^2 (t_i - t_0)^2 \tag{42.7}$$

Consider the predicted location are (x, y), then the predicted impact time t_0' can be calculated as

$$t_0'(x, y) = t_i - \frac{\sqrt{(x_i - x)^2 + (y_i - y)^2}}{c} \tag{42.8}$$

For each sensors, the impact time t_0 should be the same, it is mean that for the true impact location (x_0, y_0)

$$t_0(x_0, y_0) = t_i - \frac{\sqrt{(x_i - x_0)^2 + (y_i - y_0)^2}}{c} \tag{42.9}$$

When (x, y) take other value, t_0' would not be the same. Then the error function $E(x_0,y_0)$ can be defined as

$$E(x_0, y_0) = \sum_{i=1}^{N} (t_i - \frac{\sqrt{(x_i - x_0)^2 + (y_i - y_0)^2}}{c} - \tilde{t}_0)^2 \tag{42.10}$$

The variable $\tilde{t}_0$ is the arithmetic mean of t_0. Ideally, for the correct values of (x_0, y_0), the error function should give a zero value. Therefore, we need to minimize the value of this error function. The results are shown in Table 42.2.

The debris cloud impact source location problem is a little different from the traditional one. We analyze the impact damage area of debris cloud using the spectrum distribution characteristics of AE signals. As the energy entropy of wavelet packet of AE signals increases with the increase of initial velocity and the spay area D_{99} also increases with the velocity. The distance S between the two plates is a factor of D_{99} [14]. The impact damage area is described by dimensionless composition as follows:

$$\frac{D_{99}}{S} = X_1 \cdot W_{EE}^{X_2} + X_3 \tag{42.11}$$

Table 42.2 Localization results

Experiment	Damage center (measured)	Damage center (predict)	D_{99}(mm)	D_{99}(mm)(predict)
No. 1	(10.0, 0.2)	(7.28, −0.57)	102	101.11
No. 2	(5.3, 20.3)	(5.9, 23.14)	126	133.50
No. 3	(15.5, 15.2)	(10.31, 25.40)	133	131.35
No. 4	(15.2, 18.3)	(10.22, 12.54)	152	145.21
No. 5	(12.2, −6.3)	(11, −7.66)	159	160.84
No. 6	(10.3, −5.0)	(7.88, −9.23)	165	164.88

Fig. 42.10 Damage area prediction and experimental results

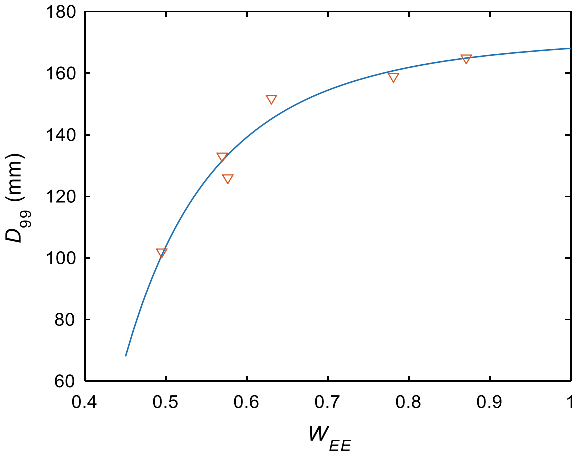

Fit the data according to the experimental parameters, we obtain

$$\frac{D_{99}}{S} = -\,0.04322 \cdot W_{EE}^{-3.988} + 1.724 \tag{42.12}$$

The predict results are shown in Table 42.2 and Fig. 42.10. It should be noted that the fitting formula is not considered the projectile size, bumper thickness, etc. The scope of application of the formula has some limitations and needs to be further improved.

42.5 Conclusion

A new technique to locate debris cloud impact damage is proposed. The proposed technique is first to locate the damage center based on minimizing an error function. According to the change of signal spectrum characteristics with impact velocity, the characteristic parameter of the signals are constructed to estimate the damage area. Experimental results show the damage center and damage area fit well with the prediction.

Acknowledgements This study is supported by a Grand of Changshu Institute of technology (No. KYZ2016003).

References

1. D. Pavarin, A. Francesconi, R. Destefanis et al., Analysis of transient vibrations on complex targets representing elementary configurations of Goce satellite. Int. J. Impact Eng. **35**(12), 1709–1715 (2008)
2. J.B. Vergniaud, M. Guyot, M. Lambert et al., Structural vibrations induced by Hvi—application to the Gaïa spacecraft . Int. J. Impact Eng. **35**(12), 1836–1843 (2008)
3. G. Parzianello, A. Francesconi, D. Pavarin, An estimation method for the shock response spectrum propagating into plates subjected to hypervelocity impact. Measurement **43**(1), 92–102 (2010)
4. P. Howell, W. Winfree, K.E. Cramer, Infrared on-orbit inspection of shuttle orbiter reinforced carbon-carbon using solar heating, in *SPIE Optics and Photonics* (San Diego CA USA, 2005), pp. 1–11
5. S. Fukushige, Y. Akahoshi, T. Koura et al., Development of perforation hole detection system for space debris impact. Int. J. Impact Eng. **33**(1–12), 273–284 (2006)
6. E. Soma, K. Maki, T. Takano et al., Study on an impact detection of space debris via microwave. Jpn. Soc. Aeronaut. Space Sci. **56**, 105–109 (2008)
7. W.H. Prosser, M.R. Gorman, H.H.D.Acoustic emission signals in thin plates produced by impact damage. J. Acoust. Emiss., **17**, 29–36 (1999)
8. F. Schäfer, R. Janovsky, Impact sensor network for detection of hypervelocity impacts on spacecraft . Acta Astronaut. **61**(10), 901–911 (2007)
9. D. Aljets, A. Chong, S. Wilcox et al., Acoustic emission source location on large plate-like structures using a local triangular sensor array. Mech. Syst. Sig. Process. **30**, 91–102 (2012)
10. T. Kundu, S. Das, K.V. Jata, Point of impact prediction in isotropic and anisotropic plates from the acoustic emission data . J. Acoust. Soc. Am. **122**, 2057 (2007)
11. T. Kundu, H. Nakatani, N. Takeda, Acoustic source localization in anisotropic plates. Ultrasonics **52**(6), 740–746 (2012)
12. L. Dong, X. Li, G.J. Xie, An analytical solution for acoustic emission source location for known P wave velocity system. Math. Probl. Eng. (2014)
13. T. Kundu, Acoustic source localization. Ultrasonics **54**(1), 25–38 (2014)
14. H. Guan Gongshun, B. Pang, N.G. Cui, Crater distribution on the rear wall of aluminum dual-sheet structure under hypervelocity normal impact. J. Mech. Eng. **45**(3), 246–251 (2009)
15. Q. Tang, B.J. Pang, Z.Y. Han et al.,Analysis of frequency spectrum character of acoustic emission wave from hypervelocity impact on single-sheet plate, **28**(4), 609–611 (2007)
16. B.J. Pang, K. Zhang, M. Lin et al., Characteristic analysis of acoustic emission signals caused by debris cloud impact. Chin. J. High Pressure Phys. **28**(6), 661–670 (2014)
17. K. Zhang, B.J. Pang, M. Lin, Wavelet packet analysis for acoustic emission signals caused by debris cloud impact. J. Vibr. Shock **31**(12), 125–128 (2012)

Chapter 43
The Influence of Rod Waveguide on Acoustic Emission Signal of Different Frequencies

Xianglong Zeng, Qiong Deng, Bo Wang, Zhilun Deng, Xudong Wang, and Chengyu Zhang

Abstract In this study, the influence of rod waveguide on the acoustic emission (AE) signals of different frequencies was investigated. Two influential factors were considered: the rod waveguide and the interface between specimen and rod waveguide. Firstly, the attenuation effects of AE signals with different frequencies transmitting in rod waveguide were studied. Secondly, the variation of the wave when the AE signal went through the interface was studied. The results were compared to the data gotten in the first step. According to these experiments, the following experimental phenomena can be observed: the energy and amplitude of the acoustic signal are attenuated by the rod waveguide more strongly with the increase of frequency; The maximum rates of attenuation respectively reach 98.81% and 99.18%; When the frequency of signal is less than 300 kHz, the rate of attenuation is within 30%; On the contrary, the interface enhances the energy and amplitude. According to further analysis, it can be drawn that when the AE signal is lower than a certain frequency, the energy, amplitude and frequency are all can be used as characteristic parameters under the condition of rod waveguide is used. Besides, frequency is a better parameter than energy and amplitude when the AE signal is higher than the threshold.

43.1 Introduction

As a nondestructive testing (NDT) method, AE detection is widely used to investigate material damage at elevated temperature. When AE detection is carried out at elevated

---

X. Zeng · Q. Deng · B. Wang (✉) · Z. Deng
School of Aeronautics, Northwestern Polytechnical University, Xi'an 710072, China
e-mail: b.wang@nwpu.edu.cn

X. Wang
Beijing Softland Times Scientific & Technology Co. LTD, Beijing 100083, China
e-mail: AE1616@163.com

C. Zhang
School of Materials Science and Engineering, Northwestern Polytechnical University, Xi'an 710072, China
e-mail: cyzhang@nwpu.edu.cn

© The Author(s), under exclusive license to Springer Nature Singapore Pte Ltd. 2021

G. Shen et al. (eds.), *Advances in Acoustic Emission Technology*, Springer Proceedings in Physics 259, https://doi.org/10.1007/978-981-15-9837-1_43

temperature, the heat is harmful for the sensors. For the reason, rod waveguides are typically mounted between the materials being inspected and the sensor. However, after using the waveguide, the characteristic parameters of AE signal may be changed. So, the results according to these parameters will be influenced.

There are many studies about the influence of rod waveguide on AE signal. Zelenyak et al. [1] built a finite element method (FEM) model for AE signal propagation in an aluminum plate. A rod waveguide was attached to the plate. The model was validated by experimental data lastly. In the study, the geometry, material and temperature of the waveguide are systematically changed to investigate the influence on the detected signals. The conclusion shows that: the diameter, length and material of the rod waveguide will predominantly affect the signal, but the temperature has no significant influence. Sikorska et al. [2] presented the influences of varying waveguide material and/or shape on traditional AE characteristics of pulsed events. Results show that although ceramic waveguides attenuate the signals more than commonly used grades of steel and aluminum, waveform fidelity is less affected.

In the above studies, the change of detected signal was studied when the geometry, material and temperature of the rod waveguide was varied. However, according to some researches, different frequency signals have different attenuation rules in the same medium. Besides, the law will have significant impact on the detected signal transmitting on the waveguide. There are few studies on this aspect. As these factors, it is necessary to study the influence of a waveguide on AE signals. Besides, as the waveguide and specimen are made of different materials, the wave will have a significant change with the variation of frequency when it goes through the interface between waveguide and specimen. Therefore, it is essential to study the influence of rod waveguide on AE signal of different frequencies. It was studied in consideration of the rod waveguide and the interface between rod waveguide and specimen in this research.

43.2 Relevant Ultrasonic Theory

43.2.1 The Variation of the Attenuation Coefficient with Frequency for AE Signals

Based on the frequency-power-law dependence phenomenon, Szabo [3] proposed a generalized frequency-domain model. The model was from the frequency-domain form of the thermal viscous wave model and the damped wave model. Then, the frequency-domain acoustic wave model was transformed into a convolution integral acoustic wave equation in the time domain:

$$\frac{1}{c_0^2}\frac{\partial^2 P}{\partial t^2} + \frac{2\alpha_0}{c_0}L_\eta(P) = \nabla^2 P \tag{43.1}$$

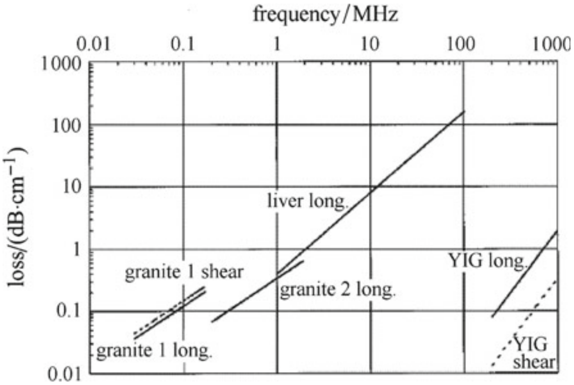

Fig. 43.1 The relationship between the attenuation and frequency for various materials

In which, the dissipation term $L_\eta(P)$ is a convolution operator.

According to (43.1), it is found that when sound waves transmit in media, their attenuation coefficients show a power law dependence of frequency [4]:

$$\alpha = \alpha_0 \omega^\eta \tag{43.2}$$

In which, ω is angular frequency; α is attenuation coefficient; α_0 and ω are the parameters obtained by experimental data fitting, between 0 and 2.

In Szabo and Wu [5] study, experimental data of the relationship between frequency and attenuation coefficient of a group of different materials were given, as shown in Fig. 43.1 [4]. The relation between attenuation coefficient and frequency is described on the double logarithmic coordinate. The slope of the straight line is the parameter η. For ideal solids and liquids, η is 0 or 2.

In acoustical theory, the attenuation of the wave partly results from physical dispersion when it propagates in rod waveguides. In solids, the scattering attenuation caused by the heterogeneous properties of polycrystalline metals (such as impurity, coarse crystal, internal stress and the equality of the second) is the most obvious.

On the other hand, geometrical dispersion is another more important cause that will influence the amplitude of AE signal [6]. Because of AE wave's geometrical dispersion and multimode, the envelope of a mode wave is elongated with the increase of propagation distance in time domain. So, the amplitude of this AE signal will decrease. It will be more difficult to detect the AE signal for the reason. In the following, a geometrical dispersion curve of an infinitely long cylinder waveguide was analyzed. This model has the same diameter and material with the one used in our study. The dispersion was mainly considered in geometric.

43.2.2 Dispersion Curve Analysis

According to Silk and Bainton's theory [7], the guide wave in the cylinder is divided into three modes: axisymmetric longitudinal mode $L(0,m)$, axisymmetric torsion mode $T(0,m)$ and axisymmetric bending mode $F(n,m)$ ($n,m = 1,2,3\ldots$). The modes reflect the different propagation modes and vibration modes of guided waves in the cylinder. The phenomenon that phase velocity varies with frequency of wave is called dispersion [3]. Figures 43.2 and 43.3 show the frequency dispersion curve diagram of phase speed and group speed for an infinite cylinder with diameter $D = 10$ mm. Its material density is 7.932 g/cm^3, p-wave velocity is 5738.92 m/s, the shear wave velocity is 3067.6 m/s. The material that used in the calculation is 304 stainless steel, which is the one made up of the rod waveguide used in our study.

In the dispersion curve shown in Figs. 43.2 and 43.3, at least two or more modes exist at the same frequency of the wave, which is called multi-mode phenomenon [8]. As it can be seen from Figs. 43.2 and 43.3, the number of guided wave modes is the least when the frequency is smaller than 300 kHz. Therefore, in the frequency region, the signal of AE has the least attenuation when the waves propagate in the infinite cylinder.

All above analysis were based on infinite cylinder, but in a finite rod, wave motion becomes even more complicated due to reflection and resonance [9]. Acoustic waves are partially reflected and transmitted at every interface, the relative amounts of which depend on the ratio of the relative characteristic impedances of each pair of boundary materials. This impedance is a function of material density and the speed wave hitting the interface. If material attenuation is low, these reflections will combine with late

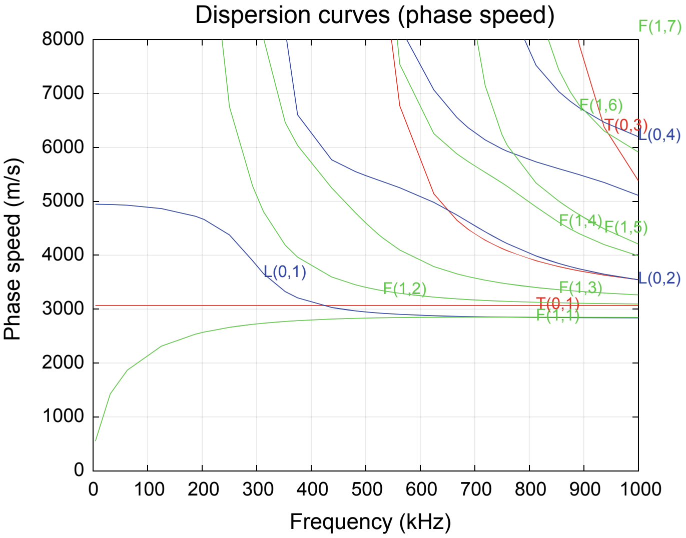

Fig. 43.2 The dispersion curves of phase speed for infinitely long rod waveguide

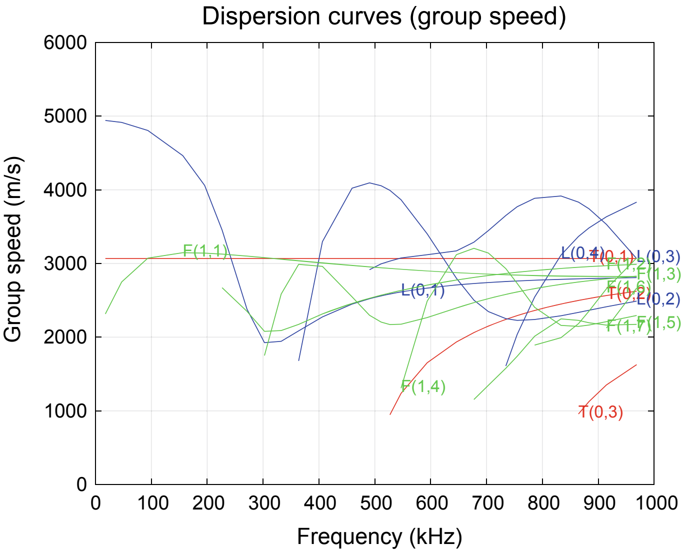

Fig. 43.3 The dispersion curves of group speed for infinitely long rod waveguide

arriving components of the original signal, complicating feature identification. For the above reasons, the rod waveguide is used to study its effect on the signal in Part 3.

43.2.3 Reflection and Transmission of Ultrasonic Waves at Heterogeneous Interfaces

When an ultrasonic wave travels through an infinite medium, it will travel straight ahead without changing direction. However, when encountering a heterogeneous interface (the acoustic impedance of the heterogeneous interface is quite different), reflection and transmission phenomena will occur. When these phenomena occur, a part of ultrasonic wave is reflected back to the first medium on the interface, and another part enters the second medium through the interface of the medium.

As the ultrasonic wave is incident to a sufficiently large smooth interface, a reflection wave in the first medium is generated in the opposite direction of the incident wave. At the same time, a transmission wave in the second medium is generated in the same direction as the incident wave. This distribution is represented by the sound pressure transmittance. The ratio of acoustic pressure for transmitted wave to it of incident wave on the interface is called the acoustic pressure transmittance of the interface, which is expressed by t:

Table 43.1 The parameters that used in the calculation of the sound pressure transmittance

The density of C/SiC composite (kg/m^3)	The speed of sound in C/SiC composite (m/s)	The density of stainless steel (kg/m^3)	The speed of sound in stainless steel (m/s)
1.9×10^3	8388	7.9×10^3	5738

$$t = \frac{p_i}{p_0} = \frac{2Z_2}{Z_2 + Z_1} \tag{43.3}$$

which Z_1 represents the acoustic impedance of the first medium and Z_2 represents the acoustic impedance of the second medium. The acoustic impedance Z is equal to the density times velocity of wave. In the Part 3, the theory was used to study the influence of the interface between the specimen and rod waveguide on signal.

C/SiC composites, a kind of ceramic matrix composite, is widely used at elevated temperature structural of aviation and aerospace. The study for the high temperature performance of the composites is essential. AE detection is widely used to investigate C/SiC composites damage at elevated temperature. In this research, the material was used to study the influence of the interface between rod waveguide and specimen on AE signal. According to the theory, the sound pressure transmittance is equal to 1.44, and the parameter that used in the calculation is shown in Table 43.1. This result shows that as the wave impedance of 304 stainless steel is greater than C/SiC composites, the interface strengthens the signal. It was verified in the Part 4.

43.3 The Influence of Rod Waveguide on AE Signal

43.3.1 Experimental Method

In this part, the variation for parameters of AE signals after the waves spread through the rod waveguide was studied. The holographic AE signal analyzer DS5-16C manufactured by Beijing Softland Times Scientific & Technology Co. LTD was used in these researches.

Firstly, in order to determine the actual influence of rod waveguide on AE signal, the characteristic parameters of AE signal directly emitted from the simulated source should be measured. For this purpose, the received R54A probe was coupled directly with the excitation probe. The characteristic parameters of excitation signal can be gotten according to the received signal. Secondly, a sensor was fixed at one end of a rod waveguide and another sensor was fixed at the other end. This 600 mm long rod waveguide was made of 304 stainless steel. The size of the rod waveguide is shown in Fig. 43.4 and the way of sensors fixed is shown in Fig. 43.5, which Fig. 43.5b is a partial enlarged drawing for sensor. Lastly, bunches of sinusoidal signals were sent at an end, the frequencies of the signal were 100–900 kHz. The sinusoidal signal was a bunch of pulse signal which was stopped sending after 10 cycles per second and

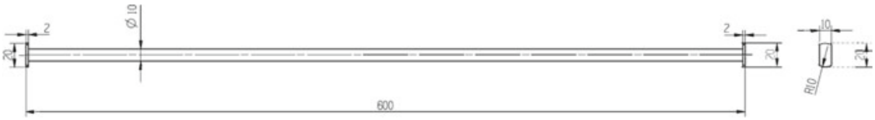

Fig. 43.4 The size of the rod waveguide

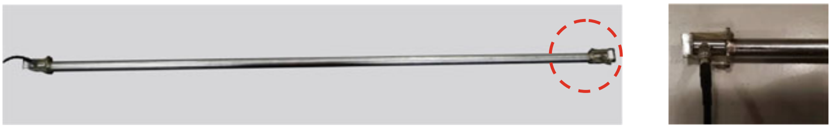

a. The photographof rod waveguide **b. The enlargement of sensor**

Fig. 43.5 The way of sensors fixed

the waveform is shown in Fig. 43.6. At the same time, the AE signals were gathered by sensors and the parameters of AE signals were extracted. AE signal acquisition system parameters are shown in Table 43.2.

AE signal processing and analysis methods can be roughly divided into three categories: single parameter analysis method, waveform analysis technology and pattern recognition method based on multi-parameter analysis. In recent years, the

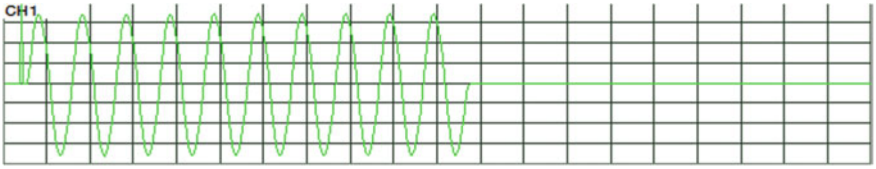

Fig. 43.6 The waveform of sending signal

Table 43.2 AE signal acquisition system parameters

Parameter	Value
Type of acoustic AE analyzer	DS5-16C
Preamplifier (dB)	40
Peak detect time (μs)	30
Hit detect time (μs)	150
Hit lock time (μs)	300
Type of sensor	R54A
The diameter of sensor (mm)	8
The range of frequency for sensor (kHz)	Broadband
Sampling frequency (MHz)	3
Band-pass filters	Direct through

theory of wavelet analysis, modern spectral analysis and neural network analysis have also been applied. In this study, the analyses of AE characteristic parameters and waveform were carried out.

43.3.2 The Analysis of AE Characteristic Parameters

In traditional AE processing, various AE parameters are used for describing AE signals. AE energy is calculated by integrating the signal over time. Amplitude and frequency are more meaningful parameters for measuring continuous emissions, whilst count rate and energy analysis are useful for burst emission characterization [10]. A burst is defined as an event that exceeds a certain threshold. For an event, the features were extracted and analyzed in this part of this study: peak amplitude, up time, ring count, energy, peak frequency. The characteristic parameters of excitation signal are shown in Table 43.3 and the parameters of received signal are shown in Table 43.4. The first column of two table is the frequency of electrical signal produced by AE signal analyzer. As the conversion error of piezoelectric ceramic, there is a little difference in the frequencies between electrical signal and received signal.

The variation of three characteristic parameters are shown in Table 43.5. According to the table the following results can be gotten: (1) The peak amplitude and energy are changed more significantly with the increase of frequency, which the maximum decrease of peak amplitude is 98.81% and that of energy is 99.18%; They are consistent with the attenuation law for acoustic wave that given in Part 2; (2) The frequency is changed less with the increase of frequency and the variation is within 6%; (3) When the frequency is less than 200 kHz, the changes of the peak amplitude, the energy and the peak frequency are mild; It is consistent with the dispersion law that is deduced in Part. 2.

Table 43.3 The characteristic parameters of excitation signal

Frequency of electrical signal (kHz)	Peak amplitude (mV)	Up time (μs)	Ring count (μs)	Energy (mV*mS)	Peak frequency (kHz)
100	8510.75	6.33	35	738.85	102.539
200	8432.62	5	46	730.02	190.429
300	8442.39	4.33	65	702.39	307.617
400	8461.92	3.67	69	482.32	410.156
500	8369.15	3.33	59	322.70	495.117
600	7501.53	7	49	106.1	585.937
700	4442.45	3.33	41	66.62	679.687
800	3840.95	12.00	38	42.70	773.437
900	3451.54	13.67	32	35.47	890.625

Table 43.4 The characteristic parameters of received signal

Frequency of electrical signal (kHz)	Peak amplitude (mV)	Up time (μs)	Ring count	Energy (mV*mS)	Peak frequency (kHz)
100	8295.90	20	290	690.2	102.539
200	6074.22	27	1292	510.8	192.626
300	2475.59	24.33	1748	205.96	290.039
400	1708.99	29.67	1323	97.41	385.986
500	297.82	29.67	1538	11.25	515.300
600	252.69	16	154	9.74	603.515
700	125.73	24	19	7.34	703.125
800	111.69	21.33	4	2.17	796.875
900	41.2	16.33	4	0.29	937.50

Table 43.5 The variation of characteristic parameters

Frequency of electrical signal (kHz)	The variation of peak amplitude (%)	The variation of energy (%)	The variation of peak frequency (%)
100	−2.52	−6.58	+ 0.00
200	−27.97	−30.03	+ 1.15
300	−70.68	−57.86	−5.71
400	−79.80	−79.80	−5.89
500	−96.44	−84.43	+ 4.08
600	−96.63	−85.16	+ 3.00
700	−97.17	−88.98	+ 3.45
800	−97.09	−94.92	+ 3.03
900	−98.81	−99.18	+ 5.26

43.3.3 Waveform Analysis

As the middle of the frequency band, 500 kHz was chosen as a representative frequency in this study. In this part, the signal of 500 kHz was used as an example to performed a time–frequency analysis. The complete waveforms of about 6 ms long before and after passing through the rod waveguide were selected. Then wavelet transform was performed for these waveforms. The wavelet scalogram is shown in Fig. 43.7. The following results can be gotten: (1) According to the waveform, the duration time increases a lot after the signal going through the rod waveguide, which results from the dispersion in rod waveguide; (2) In the wavelet scalogram, the number of peaks increases. It is shown that the bunch of acoustic waves disperses and becomes multiple modes after propagating through the rod waveguide, which is consistent with the theory that is given in Part 2; (3) Comparing the two figures, the

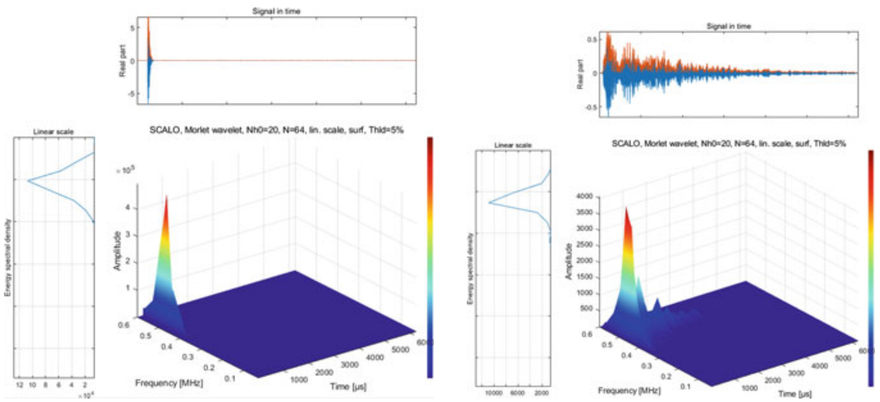

a. The wave before the waveguide **b.** The wave after the waveguide

Fig. 43.7 Wavelet scalogram

maximum amplitude decreases greatly in the wavelet scalogram, which proves the attenuation of signal after passing through the rod waveguide.

43.4 The Influence of the Interface Between Waveguide and Specimen on AE Signal

43.4.1 Experimental Method

In this part, the influence of the interface between waveguide and specimen on AE signal was studied. The holographic AE signal analyzer that applied in Part 3 was used for this research.

At first, a sensor was fixed at one end of a C/SiC specimen and a waveguide with another sensor at the end was fixed aside. This waveguide is the one used in Part 3. Besides, the third sensor was fixed at the other end of the specimen. The third one was the emission sensor and the other two was received sensor. The way of sensors fixed is shown in Fig. 43.8, which Fig. 43.8b is a partial enlarged drawing for sensor. Next, in order to determine the influence of the interface between waveguide and specimen on AE signal, the characteristic parameters of AE signal before the interface were needed to acquire. For this purpose, the probe was coupled directly aside the connecting area of the waveguide and the specimen. Last, a bunch of sinusoidal signals were sent at an end, the frequencies of which were 300–900 kHz. The frequency band is usually acquired in C/SiC failure experiment.

According to the placement of three sensors, in this part, the variations of the characteristic parameters for the AE signal detected by two received sensors result from the rod waveguide and the interface. And the influence of the waveguide on

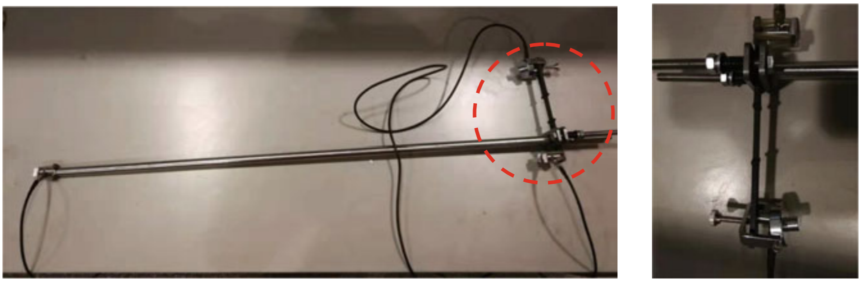

a. The photograph of waveguide with specimen **b.** The enlargement of sensor

Fig. 43.8 The way of sensors fixed

AE signal has been discussed in Part 3. So, the influence of the interface between waveguide and specimen on AE signal can be gotten by the comparison between Part 3 and Part 4.

43.4.2 The Analysis of AE Characteristic Parameters

The characteristic parameters of the signal before the interface are shown in Table 43.6 and the parameters of received signal after the interface are shown in Table 43.7. The first column of two table is the frequency of electrical signal produced by AE signal analyzer. As the signal was too weak to detect, the wave of the frequency greater than 650 kHz was not given in the table.

The variations of three characteristic parameters are shown in Table 43.8 and compared the results with Table 43.5. As the lack of test data for 650 kHz in Part 3, some results are not listed. Comparing with the acoustic pressure transmittance calculated in Part 2, the measured values of interface enhancement in the test are different from the theoretical values. The differences result from the unsatisfactory bonding between the specimen and the waveguide rod as well as the conduction effect of the coupling agent. According to the data in two tables, the following

Table 43.6 The characteristic parameters of the signal before the interface

Frequency of electrical signal (kHz)	Peak amplitude (mV)	Up time (μs)	Ring count (μs)	Energy (mV*mS)	Peak frequency (kHz)
300	326.23	57.00	32	13.29	292.968
400	112.30	91.33	44	6.22	398.437
500	158.39	97.00	184	10.11	536.132
600	41.81	16.67	134	5.65	597.656
650	19.84	14.33	114	2.18	662.109

Table 43.7 The characteristic parameters of the signal after the interface

Frequency of electrical signal (kHz)	Peak amplitude (mV)	Up time (μs)	Ring count	Energy (mV*mS)	Peak frequency (kHz)
300	270.77	60.67	30	10.54	292.968
400	87.89	30.67	20	2.21	398.437
500	20.75	75.00	39	1.2	492.187
600	10.99	0.00	22	1.27	580.078
650	5.19	0.00	4	0.15	632.812

Table 43.8 The variation of characteristic parameters after the signal going through the interface and waveguide

Frequency of electrical signal (kHz)	The variation of peak amplitude (%)	The effect of interfacial enhancement (%)	The variation of energy (%)	The effect of interfacial enhancement (%)	The variation of peak frequency (%)
300	−16.39	285.16	−20.69	188.21	0.00
400	−21.74	387.43	−64.47	175.89	0.00
500	−86.90	367.98	−88.13	76.24	−8.20
600	−73.71	780.12	−77.52	151.48	−2.94
650	−73.84	–	−93.12	–	−4.42

results can be gotten: (1) The changes of the frequencies are less after the wave going through the interface and the variations are all within 10%; (2) The maximum amplitude and energy increase a little, which consists with the theory given in Part 2; (3) The maximum amplitude and energy are changed significantly with the increase of frequency, which the maximum decrease of amplitude is 73.84% and that of the energy is 93.12%; It is consistent with the attenuation law for acoustic wave that given in Part 2.

43.4.3 Waveform Analysis

In common with Part 0.3, the signal of 500 kHz was used as an example to performed a time–frequency analysis. The waves about 3.5 ms long before and after passing through the interface were selected. Then wavelet transform was performed for these waves. The wavelet scalogram is shown in Fig. 43.9. The following results can be gotten: (1) According to the waveform, the duration time increases a lot after the signal going through the rod waveguide. It results from the dispersion in rod waveguide; It is the same with Part 3; (2) In the wavelet scalogram, the number of peaks increases. Compared with Fig. 43.7, it is shown that the number of peaks increased

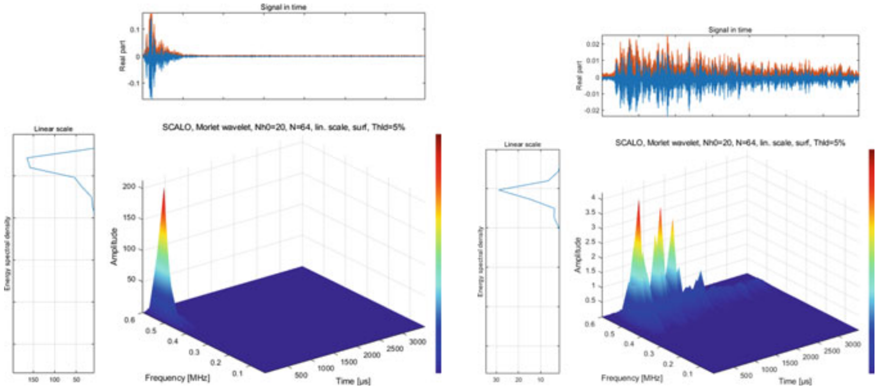

a. The wave before the interface **b.** The wave after the interface

Fig. 43.9 Wavelet scalogram

more. Besides, the amplitudes of wave in newly emerging modes are changed more obviously. It owes to the amplifying effect of interface between the rod waveguide and C/SiC composite.

43.5 Analysis and Discussion

When the signal frequency is greater than 300 kHz, the rod waveguide has a dispersion effect on the sound wave. The wavelet scalogram shows that the sound wave is dispersed into multi-mode sound wave with the same frequency. However, these waves have different wave velocity. It is an important factor causing the decrease of the amplitude and the energy of the received signal. The other effect of dispersion is the duration extension of AE bursts, which are made up of numerous waves of different modes. Different modes will lead to different speeds, the wave will be lengthened in time domain as they move further from the source. Besides, as the frequency increases, the amplitude and energy decrease more. The largest drop of them respectively reach 98.81% and 99.18%. In addition to dispersion, AE bursts are attenuated as they travel through the material. Particularly in compounds with larger grain sizes, frequency-dependent attenuation can increase significantly. For these reasons, as a traditional AE characteristic parameters analysis method, the cluster analysis based on amplitude and energy will be greatly affected. On the other hand, the peak frequency is less affected and the variation is within 10%. It is a more accurate clustering parameter.

Different from the attenuation effect of rod waveguide, the amplitude and energy will increase when the AE signal transmits into the rod waveguide. The enhancement effect results from that the wave impedance of rod waveguide is higher than the specimen. It indicates the strengthening effect of the interface.

As a kind of AE detection tool at elevated temperature, the rod waveguide can be used to get clear signal when the concerned frequency is less than a certain threshold. According to the Figs. 43.2 and 43.3, when the frequency of the signal is less than 300 kHz, there are less modes. Besides, the attenuation of energy is smaller. In view of the above reasons, for the rod waveguide made of 304 stainless steel, the threshold is about 300 kHz.

43.6 Conclusion

According to this study, the following conclusions can be drawn:

1. The influence of the rod waveguide on the AE signal comes from two aspects: the rod waveguide and the interface between the rod waveguide and specimen. In these factors, the rod waveguide attenuates the energy and amplitude of the acoustic signal. Besides, the attenuation degree increases with the rise of frequency. However, the energy and amplitude will increase after the wave goes into the waveguide with higher wave impedance. In addition, the variations of frequency are small.
2. When a rod waveguide is used in AE detection, the clustering method based on energy and amplitude is not accurate and the peak frequency is a good choice.
3. The rod waveguide can be used in AE detection when the concerned frequency of wave is less than certain threshold. For different materials, the thresholds may be different.

Acknowledgement The study is supported by the 111 Project, No. BP0719007.

References

1. A.M. Zelenyak, M.A. Hamstad, M. Sause, Modeling of acoustic emission signal propagation in waveguides. Sensors-Basel **15**(5), 11805–11822 (2015)
2. J. Sikorska, J. Pan, The effect of waveguide material and shape on acoustic emission transmission characteristics. J. Acoust. Emission **22**, 264–273 (2004)
3. T.L. Szabo, Time domain wave equations for lossy media obeying a frequency power law. J. Acoust. Soc. Am. **96**(1), 491–500 (1994)
4. W. Cai, W. Chen, Fractional derivative modeling of frequency-dependent dissipative mechanism for wave propagation in complex media. Chin. J. Theor. Appl. Mech. **48**(6), 1265–1280 (2016)
5. T.L. Szabo, J. Wu, A model for longitudinal and shear wave propagation in viscoelastic media. J. Acoust. Soc. Am. **107**(5), 2437 (2000). (Pt 1)
6. Z. Lu, N. Zou, S. Li, Y. Liu, Z. Liu and S. Jin, “Analysis of modes and dispersion for ultrasonic guided wave detection in pipes,” *Nondestructive Test*, 2016.
7. M.G. Silk, K.F. Bainton, The propagation in metal tubing of ultrasonic wave modes equivalent to Lamb waves. Ultrasonics **17**(1), 11–19 (1979)

8. L.I. Long-TaoH.E. Cun-Fu and W.U. Bin, “Research on Restraining Dispersive Characteristics of Ultrasonic Guided Wave in a Long Pipe,” *Journal of Data Acquisition & Processing*, 2004.
9. YAMASAKITAMAI and HIRAO, Optimum excitation signal for long-range inspection of steel wires by longitudinal waves. Ndt&E Int. **34**(3), 207–212 (2001)
10. M. Wevers, Fundamentals of acoustic emission (1996)

Chapter 44
Acoustic Emission Characteristics of Defects in Crawler Crane Truss Beam

Zhanwen Wu, Gongtian Shen, Daihua Sun, Yongna Shen, and Junjiao Zhang

Abstract In order to carry out the application of acoustic emission technology in the structural inspection of crawler crane truss beam, this paper studies the AE attenuation characteristics and AE location method in the crawler crane truss beam. The destructive test process of the truss beam was monitored by using AE instruments. And the AE characteristics during the loading process of the truss beam were analyzed. The results show that the acoustic emission sources in chord and web rod can be accurately located by cylindrical location method. In the process of destructive test, the AE sources can be located, and the amplitude distribution of AE location events is between 40 and 64 dB. The AE signal of crack propagation is a burst signal, and its frequency mainly distributes in the range of 100–450 kHz, and the peak frequency is 170 and 350 kHz. In the truss beam of crawler crane, the weakest parts are web rods. The results show that AE technology can be used to detect the defects and early deformation in the truss beam of crawler crane.

44.1 Introduction

In manufacturing process of modern industry, the cranes are the indispensable equipments and used extensively in hoisting, transporting, loading, installation, carriage of persons and so on. There are more than 2440 thousands of cranes in China at the end of 2019. The security and reliability of the crane are significant for the society. The metal structure supports the whole self-weight of the crane and the outside load, forming the working system and movement space to accomplish all of the functions of the machine. So, the state of the crane's metal structure affects the security and reliability of the whole machine directly.

Z. Wu · G. Shen (✉) · Y. Shen · J. Zhang
China Special Equipment Inspection and Research Institute, Beijing 100029, China
e-mail: shengongtian@csei.org.cn

D. Sun
Beijing Special Equipment Inspection & Testing Center, Beijing 100029, China

© The Author(s), under exclusive license to Springer Nature Singapore Pte Ltd. 2021

G. Shen et al. (eds.), *Advances in Acoustic Emission Technology*, Springer Proceedings in Physics 259, https://doi.org/10.1007/978-981-15-9837-1_44

Truss structure is a common type of crane boom structure. It is often used in crawler crane, wheel crane, tower crane, portal crane and other cranes. The truss structure is complex, and composed of upper chord, lower chord and web rod. And the web rod is divided into oblique web rod and straight web rod. As the truss boom is mostly welded by K-type, T-type and other types of pipe joints, there are a large number of welds. Also, due to its large slenderness of the member itself and its large structure, it is difficult to detect its defects or may be missing by using the normal method.

The nondestructive testing techniques used in cranes ordinary are visual inspection, ultrasonic flaw detection, stress testing, etc., which will be conducted for sampling parts of steel structure. But this method only can detect in a small range with low speed and low efficiency, also do not have the ability to discover early damage. It is easy to cause missed inspection, and the inspection cost is higher. The cracks are one of the familiar faults in crane structures. The acoustic emission (AE) is a supplemental technique for the testing. The activity defects in the whole structure can be found in once loading test, and also can be supervised on line, which will reduce the inspecting cycle, cost and has potential of early damage forecasting [1–5]. Therefore, the purpose of this study was to explore the feasibility of applying acoustic emission technology to detect and evaluate the structural integrity of the crawler crane truss beam.

At present, the research and application of acoustic emission of crane steel beam is mainly box beam, and the study on truss beam structure is rarely reported. In order to achieve the purpose of acoustic emission technology in crane field inspection, it is necessary to study the acoustic emission characteristics of defects on the crane truss beam.

In this paper, the acoustic emission attenuation characteristics and source location characteristics of truss beam are studied firstly. And then, the three-point bending test is carried out on the crane truss beam, and the acoustic emission signal is collected by the acoustic emission instruments during the test. Through the test, the AE characteristics of the destructive test process of the truss beam are obtained, including the characteristics of AE parameters, frequency spectrum and location. The results of this study provide a new method and basic data for the overall rapid detection of the crawler crane truss beam.

44.2 Study of AE Attenuation and Source Location in Truss Beam

44.2.1 AE Attenuation Characteristics of Truss Structure

In order to collect effective AE signals in the AE testing of crane truss beam, it is necessary to arrange sensors reasonably. Usually, there are four main chords in the truss beam, and the main chords are tubular structures. We test the attenuation

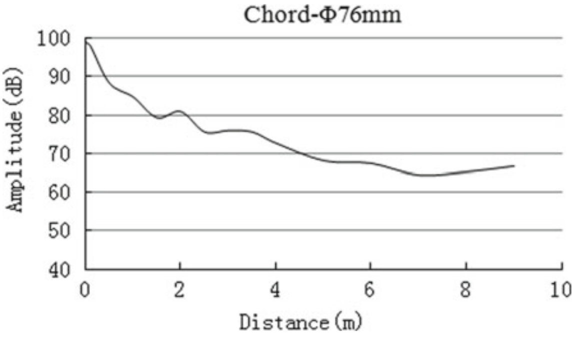

Fig. 44.1 AE attenuation curve of Distance versus Amp

characteristics of acoustic emission signals on the main chord, which material is made of BJ770 steel tube, and its nominal diameter is Φ 76 mm.

An acoustic emission sensor is arranged at the end of a chord. Taking this as the origin, and a HB Φ 0.5 mm pencil lead is used as the simulation source. The lead is broken three times at every 500 mm interval along the extension direction of the chord. The average AE amplitude value of AE signals of simulation sources at different positions is obtained, and the attenuation characteristic diagram of AE signals is drawn, as shown in Fig. 44.1. As shown in Fig. 44.1, the AE amplitude value shows a trend of attenuation with the increase of propagation distance. When the distance is more than 6000 mm, the AE amplitude value changes little, and its value is 67 dB.

44.2.2 AE Source Location in Truss Structure

The acoustic emission positioning test is carried out on a real truss girder of crawler crane. The dimension is 9000 mm * 1350 mm * 1350 mm. Its shape is shown in Fig. 44.2. Firstly, the feasibility of linear positioning method is tested, and the algorithm is time difference of arrival (TDOA) method. The distance between sensors is not more than 4.5 m. If a group of sensors are arranged on any one chord of the four main chords, the acoustic emission sources on the two adjacent chords can be located correctly. For the diagonal main chord, due to the complex propagation path of AE signals, the location error is larger, about 45%, which cannot meet the needs of engineering application. If the sensors are arranged on the diagonal top chord and

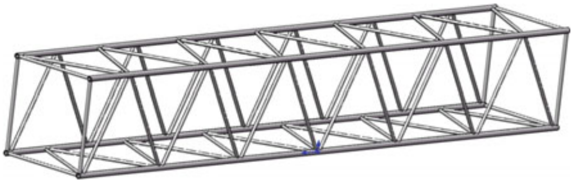

Fig. 44.2 The test truss girder

bottom chord, and the distance between sensors is also not more than 4.5 m, the simulated AE sources on the web rods can only be located at the welding point of the web rod with the main chord. The AE sources location error is large and can't reflect the real positioning. This is mainly because using the TDOA algorithm for the linear positioning. The arrival time difference between the simulated acoustic emission sources on the web rod to a group of adjacent sensors is the same as that of its welding point of web rod and main chord. And the AE source location calculated according to TDOA is the same. Therefore, for the large truss beam, the linear positioning method can't correctly locate the AE sources in the web rod.

In order to precise locating the AE source in the web rod of truss beam, the cylindrical location method is adopted. The AE sensors are arranged alternately on the four chords, and a total of 10 sensors are arranged to form a cylindrical location. The layout diagram of the truss beam is shown in Fig. 44.3. As the same with linear location method, the AE simulation sources on the main chord can be accurately located. The accuracy is about 200 mm. There are total 9 AE simulated sources on the web rod from 1 to 9, shown in Fig. 44.3. The AE sources location results are shown in Fig. 44.4. The maximum error is 450 mm, which is 10% relative to the distance between the adjacent sensors. This could be met to the overall testing requirements in

Fig. 44.3 The layout diagram of the truss beam

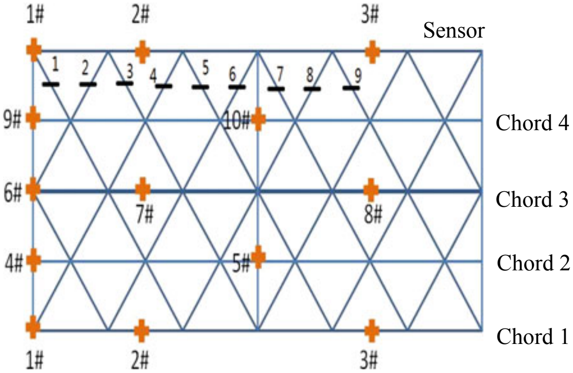

Fig. 44.4 The AE sources location results of the truss beam

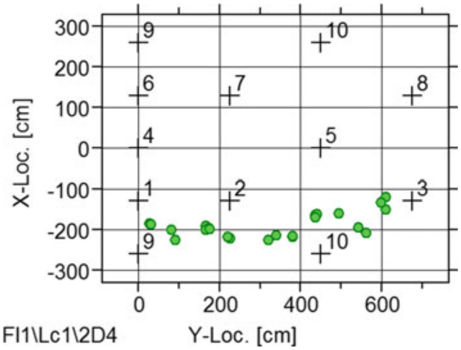

engineering application for this lager truss beam. Therefore, the cylindrical location method can be used to locate the acoustic emission sources for the truss beam.

44.3 Experiments

44.3.1 Instruments

The loading device is YE-5000 four-column hydraulic pressure testing machine used for the three-point bending test. The maximum test load is 23t.

The AE measurements were realized with the AE system AMSY-6 (Vallen-System, Icking, Germany) including sensors, preamplifiers, computer software, cables etc. The broadband AE sensors are VS900-M, VS45-H and resonant sensor is VS150-RIC. The bandwidths of the VS900-M, VS45-H and VS150-RIC are 100–900 kHz, 45–450 kHz and 100–450 kHz, respectively. The preamplifiers had 40 dB gains with a 20–1000 kHz bandpass filter. The AE acquisition settings threshold is 39 dB used for the test.

44.3.2 Specimen

The test specimen used in this test is a section of a real crawler crane beam, which is made up of four tubular chords and multiple web rods. The truss beam length is 9000 mm, and the side length of cross section is 1350 mm. The beam is in the state of new manufacture delivery, and its appearance and test site are shown in Fig. 44.5. The material of the truss beam is BJ770, which yield strength is 770 MPa and tensile strength is 820 MPa.

44.3.3 AE Sensors Layout and Artificial Defect

During the test, a total of 10 AE sensors are arranged on the specimen, and the layout of AE sensors is shown in Fig. 44.6. At the same time, in order to study the acoustic emission signal characteristics of crack propagation, three artificial cracks were prefabricated on the main chord and web rod respectively. The location of three artificial cracks is shown in Fig. 44.6. The coordinates of the three artificial defect centers are (0, 420), (0, 520), (200, 480). The location of each channel and artificial defect were located correctly. Figure 44.7 shows the location results of each AE sensor, and Fig. 44.8 shows the location result of defect 2.

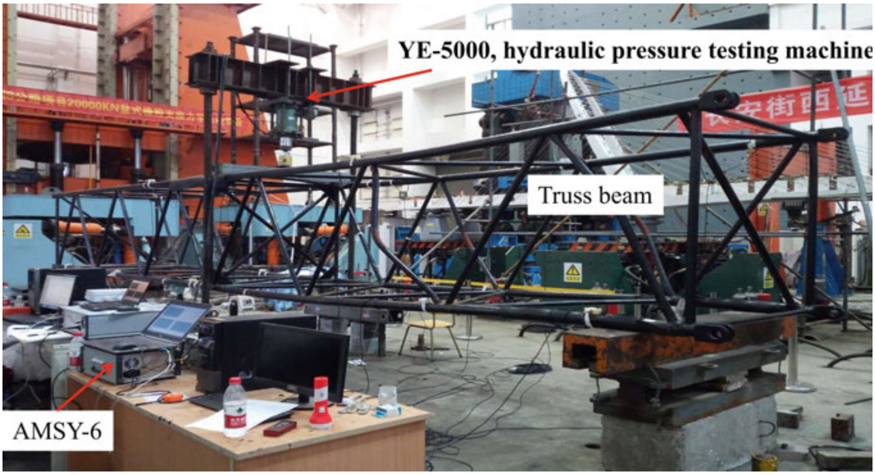
YE-5000, hydraulic pressure testing machine
Truss beam
AMSY-6

Fig. 44.5 The test specimen and test site

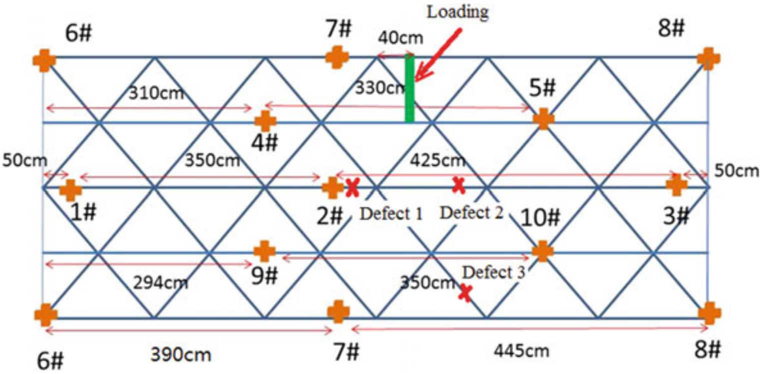
Loading
6#
7#
8#
40cm
310cm
330cm
5#
4#
50cm
350cm
425cm
50cm
1#
2#
Defect 1
Defect 2
10#
3#
294cm
9#
350cm
Defect 3
6#
390cm
7#
445cm
8#

Fig. 44.6 Layout of AE sensors and artificial defects

Fig. 44.7 Location of sensors

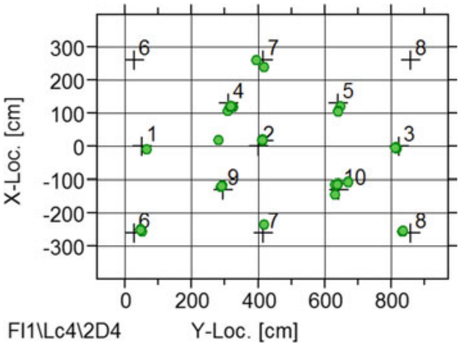

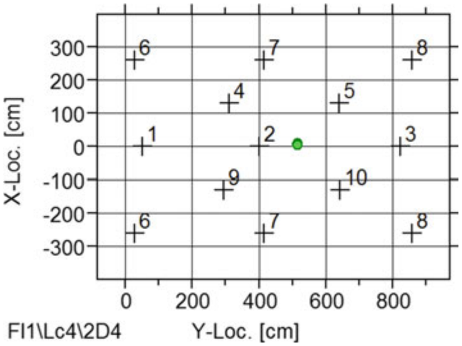

Fig. 44.8 Location of defect 2(0, 520)

44.3.4 Loading Procedures

The YE-5000 four-column hydraulic pressure testing machine is used to load the truss beam, and the loading position is 400 mm away from the middle position of the beam, as shown in Fig. 44.6. Before loading, the Polyvinylchloride (PVC) plastic plates were coated on the beam, support structure and loading point to reduce the acoustic emission signal caused by friction during loading.

This test adopts step by step loading. Under the load of 50 kN, 70 kN, 90 kN, 110 kN, 120 kN, 140 kN, 160 kN and 180 kN, keep the load separately, and observe the activity of acoustic emission signals. When the load increases to more than 180 kN, the web rod deforms obviously. Drops the load to 110 kN, and then loads to 180 kN, until another web rod deforms. Drops the load to 135 kN, and then loads until deforms, and then finished the test. During the loading process, the acoustic emission signals of the crane truss beam were collected.

44.4 Results and Discussion

44.4.1 AE Source Location During the Test

During the whole loading process, AE location events are generated in the loading stage. Except for a small amount of AE location events at 140 kN holding load, there are no AE location events in other holding load and unloading stages. The AE location events in each stage are shown in Fig. 44.9. In the first loading process, before the load increases to 140 kN, the number of AE location events in each stage is less than 40, and its distribution is more scattered. With the increase of load, AE location events increase. During the loading process after 140 kN, AE location events increases rapidly and the distribution is relatively concentrated. At the same time, during the second and third loading process, a large number of AE location events were produced, and the distribution was concentrated.

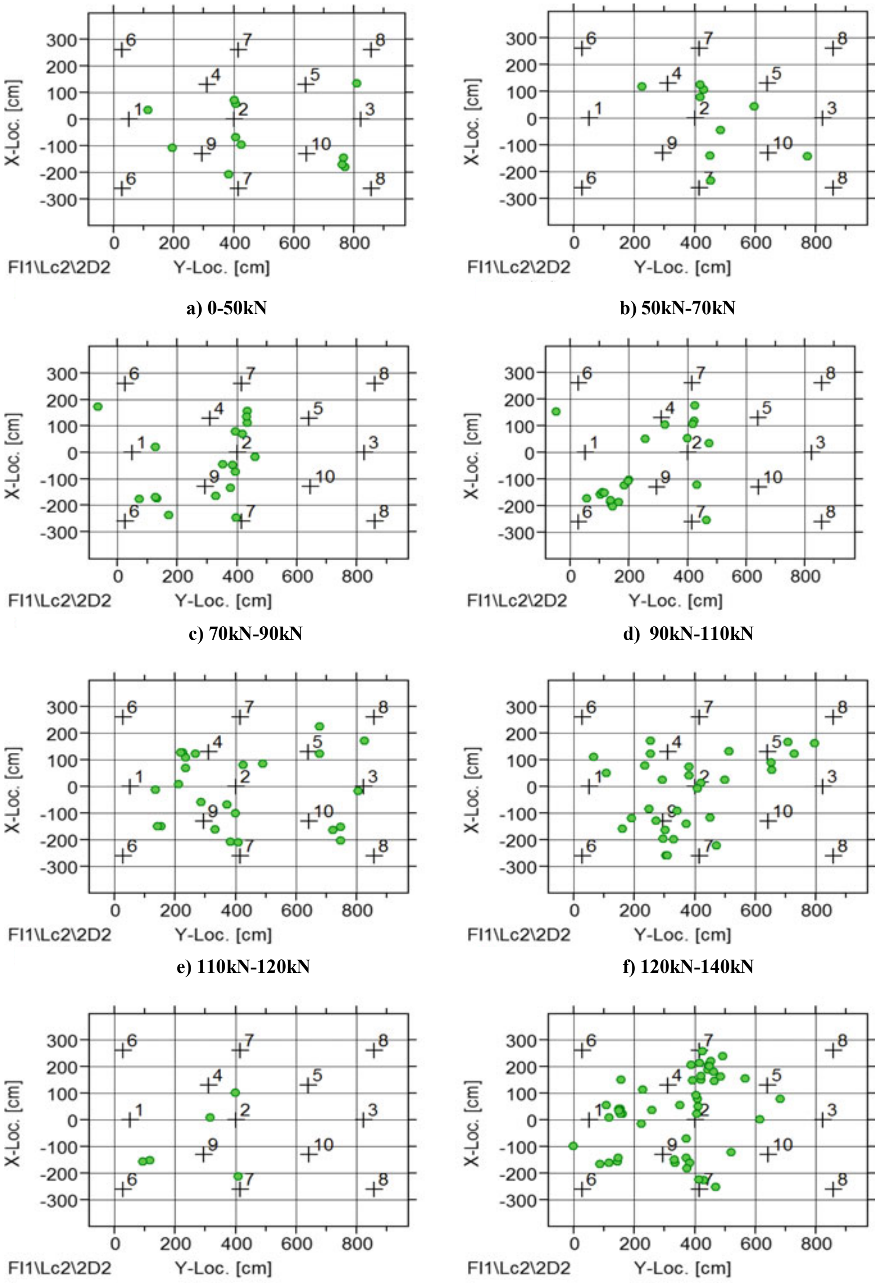

a) 0-50kN

b) 50kN-70kN

c) 70kN-90kN

d) 90kN-110kN

e) 110kN-120kN

f) 120kN-140kN

g) 140kN

h) 140kN-160kN

Fig. 44.9 Distributive AE events versus Location

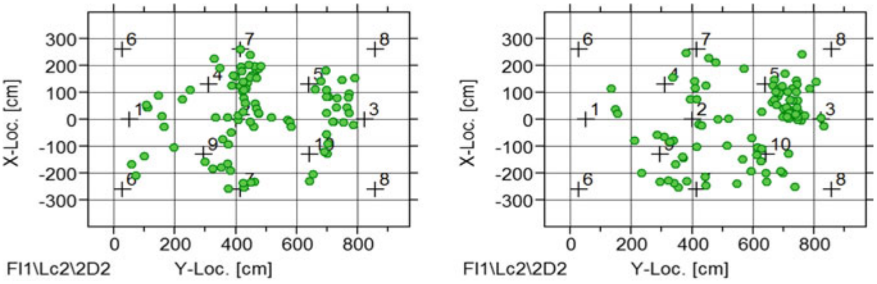

i) 160kN-180kN

j) 110kN-180kN

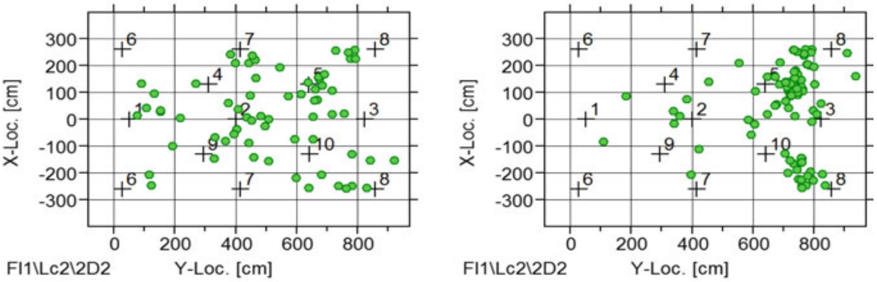

k) 180kN- plastic deformation

l) 135kN- plastic deformation

Fig. 44.9 (continued)

In the first loading process, before 140 kN, the signal distribution is relatively scattered, and the main chords and web rods of the beam have no obvious deformation or cracking. After 140 kN, a large number of AE location events occurred in the middle of the beam, and obvious plastic deformation occurred in the web rod of this section, and its y coordinate was in the range of 3500–4500 mm. In the second loading process, due to the existence of Kaiser Effect, only a small amount of AE location events are generated before 140 kN. With the increase of load, except for a large number of AE location events in the range of 3500–4500 mm in y-coordinate, a large number of AE location events are generated between sensor 3 and sensor 5. The coordinates are in the range of 0–1350 mm in x-coordinate and 6500–7500 mm in y-coordinate. There is obvious deformation of web rod. Before the third loading, the depth of artificial defect 2 was increased, and the broadband sensors VS900-M and VS45-H were added near the artificial defect 2 to obtain the AE signals of crack propagation. In the third loading process, a large number of AE location events appeared between sensor 8 and sensor 10, and the web rod was obviously deformed.

These show that the cylindrical location method can detect and locate the deformation area before the obvious deformation of the web rod occurs in the truss beam. In the loading process, even if the main chord is processed with artificial defects, the web rod still has obvious plastic deformation firstly, which indicates that the web rod is the weakest link of the whole truss beam. The strength margin of the main chord is greater.

44.4.2 AE Parameters Characteristics of AE Location Events During the Test

Figure 44.10 shows the typical parameter distribution of acoustic emission signal which is obtained by VS150-RIC sensor. In the experiment, a large number of acoustic emission signals are generated, and the signal has high amplitude and energy. Table 44.1 shows the parameter distribution ranges.

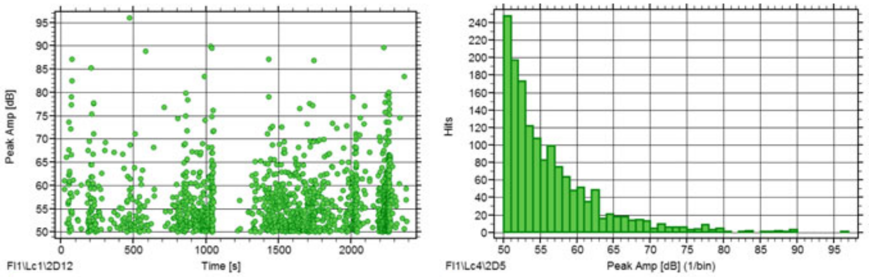

a) Amplitude-time b) Hits-Amplitude

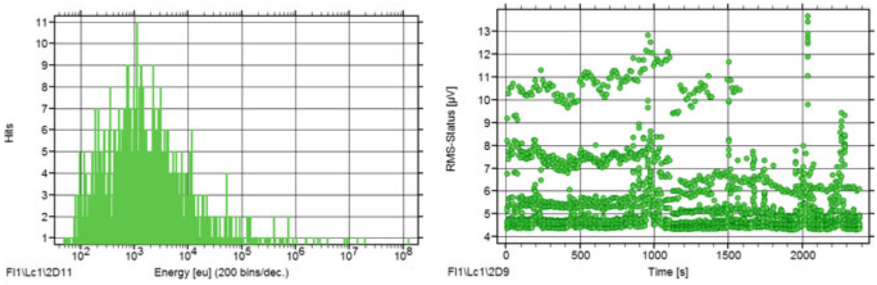

c) Hits-Energy d) RMS-time

Fig. 44.10 Location AE signals parameter distributions (0–180 kN)

Table 44.1 Parameter distribution of AE signals

AE parameter	Distribution	AE parameter	Distribution
Amp (dB)	50–70	Dur (µs)	100 to 5 × 104
Energy (eu)	10–10^5	Rise time (µs)	4 to 1 × 103
Counts	1–1600	RMS (µV)	4.5–12

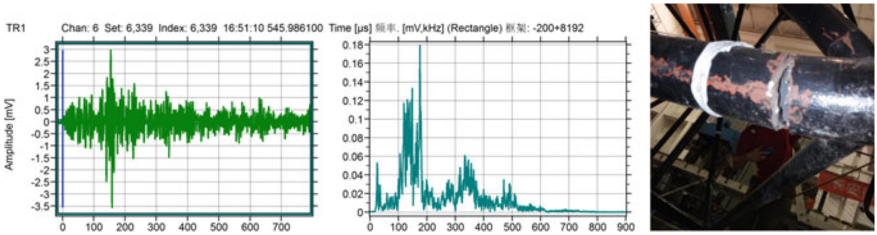

Fig. 44.11 Waveform and spectrum of crack propagation AE signal (VS 900-M)

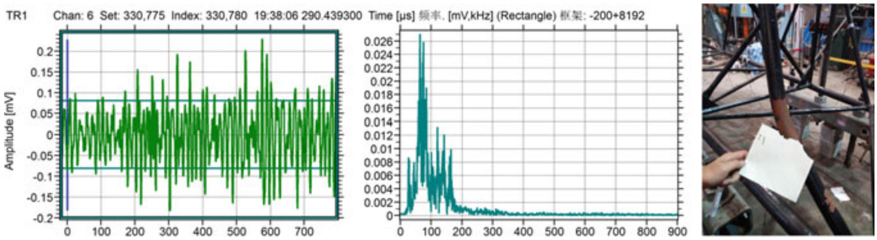

Fig. 44.12 Waveform and spectrum of plastic deformation AE signal (VS 900-M)

44.4.3 Frequency Spectrum Feature of AE Signals

In order to obtain the acoustic emission signals of crack cracking and plastic deformation accurately, the VS900-M sensors were arranged near the crack and plastic deformation regions in the loading test. Figures 44.11 and 44.12 are typical waveforms and spectrum of crack propagation AE signals and plastic deformation AE signals during the test, which are obtained by wide band sensor VS900-M. Figure 44.11 shows that the crack propagation AE signals waveform is a typical burst signal, its frequency is mainly distributed in the range of 100–350 kHz, and the peak frequency is rich near 170 and 350 kHz. However, the plastic deformation AE signals waveform is a mixture of continuous and burst signals. Its frequency range is mainly less than 150 kHz, and its peak frequency is rich near 70 kHz.

44.5 Conclusions

Through the research of this study, the defect location method and the acoustic emission characteristics of truss structure in AE test are obtained. It lays a foundation for field AE test and provides a possibility for defect evaluation.

1. The AE attenuation in steel tube is not too large. The average amplitude is greater than 65 dB at 8 m away from the sensor.

2. The AE cylinder location method is applicable for the AE test of truss beam of the crane.
3. The AE signals of crack, plastic deformation could be located during the test.
4. In the truss beam of crawler crane, the weakest parts are web rods.
5. AE technique provides a possibility for defect inspection and evaluation method for crane's truss beams in once loading.

Acknowledgement This study was financially supported by the National key research and development plan project 2017YFC0805703.

References

1. G.T. Shen, Z.W. Wu, Investigation on acoustic emission source of bridge crane. Insight **52**(3), 144–148 (2010)
2. G.T. Shen, *Acoustic emission technology and application* (Science Press, Beijing, 2015), pp. 152–159
3. L. Hongyun, Z. Zheng, Z. Qunpeng, et al., The application of AE technique in the safety assessment on handling facility. Hoisting Conveying Mach. **1**, 36–39 (2005)
4. G.R. Drummond, K.F. Fraser, et al., in *Assessing the structure integrity of crane booms using acoustic emission*. EWGAE 2002 25th European Conference on Acoustic Emission Testing Prague, Czech Republic, 11–13 Sept 2002
5. T. Jian-jun, W. Fu, D. Yong-gang, et al., Application of acoustic emission testing technology in truck crane girder detection. China Measur. Technol. **33**(4), 30–32 (2007)

Part VI
Condition Monitoring and Diagnosis

Chapter 45
Identification of Acoustic Emission Signals for Bearings Fault Based on Neural Network of Cuckoo Search Algorithm

Ping Yang, Yun Li, and Yang Yu

Abstract As the key component of rotating machinery, rolling bearings often fail to the wear during the long-term operation which directly affects the safe and stable operation of the units. In this paper, the acoustic emission equipment is used to collect signals from the rolling bearing fault, and an intelligent fault diagnosis method based on Cuckoo search (CS) Algorithm optimization neural network is proposed. The acoustic emission signal analysis from the measured rolling bearing shows that the stability and accuracy are high by this algorithm, and the average accuracy reached 93% in the classification. The effectiveness of the newly proposed algorithm is verified by examples of roller bearing fault diagnosis.

45.1 Introduction

Rolling bearings are one of the important components of rotating machinery. In rotating machinery, rolling bearing failure can account for up to 30% [1]. The failure information can be obtained by collecting the state data of rolling bearing, which can effectively reduce economic losses and accidents. Acoustic emission technology can obtain early failure information of rolling bearings.

Acoustic emission (AE) is the phenomenon of parts of materials emitting instantaneous elastic waves due to quick release of energy [2]. Acoustic emission characteristic parameters have amplitude, duration, energy count, rise time, count and so on. The characteristic parameters of acoustic emission are different due to different faults of the rolling bearing.

The fault diagnosis of rolling bearing has always been concerned by researchers. Therefore, bearing fault identification has great significance, and the recognition accuracy of the feature set to the bearing fault is improved while reducing the time consumption. According to research findings at home and abroad, BP neural network is the most used and most mature training algorithm for neural network training [3,

---

P. Yang · Y. Li (✉) · Y. Yu
Shenyang University of Technology, Shenyang 110870, China
e-mail: 1786308837@qq.com

© The Author(s), under exclusive license to Springer Nature Singapore Pte Ltd. 2021

G. Shen et al. (eds.), *Advances in Acoustic Emission Technology*, Springer Proceedings in Physics 259, https://doi.org/10.1007/978-981-15-9837-1_45

4]. However, there are also some problems, such as low learning efficiency, slow convergence, and easy to fall into local minima. In order to solve these problems, domestic and foreign scholars have continuously improved the BP neural network from genetic algorithm, particle swarm optimization and adaptive particle swarm optimization [5–7]. Particle swarm optimization (PSO) algorithm has faster calculation speed, the better global search, avoiding complex genetic crossover and mutation algorithms, and fast convergence. The local convergence problem arises because the particle swarm algorithm converges too fast.

In order to solve the above problem, an intelligent fault diagnosis method based on Cuckoo search (CS) Algorithm optimization neural network is proposed. The Cuckoo search algorithm is a parasitic and Levi fly parallel mechanism [8]. This mechanism determines the efficient optimization mode, compensates for the local convergence problem, and converges to the global optimum. Then, the characteristic parameters of the acoustic emission of rolling bearing are trained, and the effectiveness of the proposed algorithm is verified.

45.2 Cuckoo Search Algorithm Method

In the way of reproduction, the cuckoo bird is different from other birds. The cuckoo bird does not nest and hatch, and does not feed the offspring. Instead, they produce the eggs in other nests, deceive other hosts, and raise them from the host bird, a breeding method called nest parasitism. Cuckoo search (CS) algorithm, the cuckoo species combining with the Lévy flight behavior, proposed by Yang and Deb in 2009 [9]. In order to describe the behavior of cuckoo bird nesting, Yang and Deb proposed three principles in CS [10]:

1. Each cuckoo lays one egg each time and dumps it in a randomly selected nest.
2. The best nests with high-quality eggs will pass onto the next generation.
3. The number of available bird nests is certain. Under this condition, the owner of the bird's nest will find the eggs. Once the egg is found, the host bird will discard the cuckoo bird eggs or abandon the bird's nest to build a new nest. In other words, the bird's nest will be replaced with a certain probability.

45.2.1 Cuckoo Search Algorithm Theory

Based on the three principles proposed by Yang and Deb, the cuckoo optimization path and position update by the following equation:

$$x_i^{t+1} = x_i^t + \delta \oplus levy(\beta) \tag{45.1}$$

where x_i^t is the position of the ith ($i = 1, 2, \ldots$, n) nests in the t generation;δ is the step factor, which is used to control the size of the step. δ is usually expressed as follows:

$$\delta = \delta_0 \left(x_i^t - x_{best} \right) \tag{45.2}$$

where δ_0 is a constant and generally takes the value $\delta_0 = 0.01$. x_{best} is the current optimal value. $levy(\beta)$ is a step size of Lévy flight, a Lévy flight is performed as follows:

$$levy(\beta) \sim \mu = t^{-\beta}, \quad 1 < \beta \leq 3 \tag{45.3}$$

However, in order to make the calculation simple in practice, $levy(\beta)$ is also expressed as follows:

$$levy(\beta) = \frac{\phi * \mu}{|\nu|^{-\beta}} \tag{45.4}$$

where μ, ν obey the normal distribution of the standard vertebra, such as $\mu \sim N(0, 1)$ and $\nu \sim N(0, 1)$; β is a Lévy flight parameter ($\beta = 1.5$). ϕ is usually expressed as follows:

$$\phi = \left(\frac{\Gamma(1+\beta) * \sin\left(\pi * \frac{1}{2}\beta\right)}{\Gamma\left(\left(\frac{1+\beta}{2}\right) * \beta * 2^{\frac{\beta-1}{2}}\right)} \right)^{-\beta} \tag{45.5}$$

In summary, the expression of the new position in the cuckoo algorithm as follows:

$$x_i^{t+1} = x_i^t + \delta_0 \frac{\phi * \mu}{|\nu|^{-\beta}} \left(x_i^t - x_{best} \right) \tag{45.6}$$

In addition, a fraction of the solution are abandoned and build a biased random walk shown as follows:

$$x_i^{t+1} = x_i^t + \gamma \left(x_g^t - x_k^t \right) \tag{45.7}$$

where $\gamma \in [0, 1]$ denotes scaling factor; x_g^t, x_k^t are the locations of two nests randomly selected in the tth generation. The pseudocode of cuckoo search (CS) is illustrated in Fig. 45.1.

45.2.2 *Cuckoo Search Algorithm Optimization BP Neural Network*

The BP network structure is initially determined based on the data sample dimension, and the total number of weights and thresholds is determined, then the code length

```
Begin
Set the parameters and initialize the population of Np nests xi(i=1,···, Np);
While (stop criterion is not met)
    For each nest, perform Lévy flight to generate new solutions with Eq.(1);
    Evaluate its fitness;
    Abandon a fraction of solutions with a probability p0 and build new one with Eq.(7);
    Evaluate its fitness;
    Rank the solutions and keep the bestnest;
End
Output the best solution;
End
```

Fig. 45.1 The pseudocode of cuckoo search (CS)

of the individual cuckoo is determined by CS. In the process of optimizing the BP neural network by the cuckoo search algorithm, each cuckoo individual represents a combination of weights and thresholds, in other words, a neural network construction method, and the merits of each individual are determined by the fitness function. The cuckoo search algorithm finds the optimal fitness value corresponding to the individual from performing the CS optimization process, and obtains the optimal weight and threshold combination to construct the CSBP neural network. The flow chart of CSBP is shown in Fig. 45.2.

45.3 Experiment

45.3.1 Experiment Platform

This experiment uses QPZZ-II type rotating machinery fault simulation platform. The experimental platform is shown in Fig. 45.3. The experimental platform can simulate various fault states of rotating machinery and provide the basic conditions for comparative analysis and diagnosis of various states. As Fig. 45.3 shows, (a) is the experimental platform, (b) is a normal bearing, (c) is the control platform.

45.3.2 Experiment Setup

In this experiment, the acoustic emission detection system adopts the US PCI-2 acoustic emission acquisition system, in which the gain of the pre-amplifier is 40 dB,

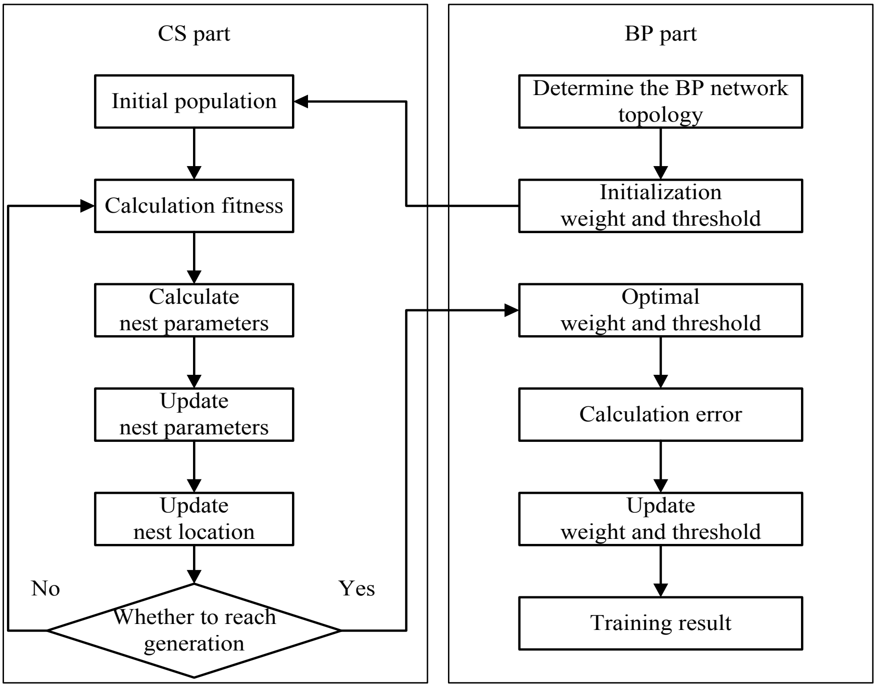
CS part
Initial population
Calculation fitness
Calculate nest parameters
Update nest parameters
Update nest location
No
Yes
Whether to reach generation
BP part
Determine the BP network topology
Initialization weight and threshold
Optimal weight and threshold
Calculation error
Update weight and threshold
Training result

Fig. 45.2 The flow chart of CSBP

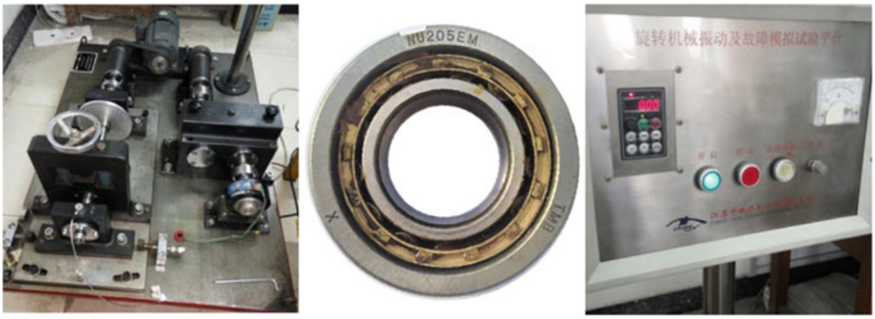
NU205EM
TMB

(a) (b) (c)

Fig. 45.3 Vibration and fault simulation test platform for rotating machinery

the sampling frequency is 3 MHz, the threshold value is 40 dB, and other parameters are selected as the default parameters of the PCI-2 acquisition card. The parameters are shown in Table 45.1.

Table 45.1 PCI-2 acquisition card parameters

Parameter	Value
Time driven rate	1000 ms
RMS/AST time constant	500 ms
Channel gain	40 dB
HLT	1000 ms
HDT	800 ms
Analog filter	100–400 kHz

45.3.3 Experimental Design

The characteristics of the original acoustic emission signals collected by the PCI-2 system are more than 20 kinds, which can complete the adaptive extraction and intelligent diagnosis of the rolling bearing fault characteristics. In this experiment, 8 parameters of acoustic emission signals were selected as the input sample feature vectors of the network model, such as rise time, count, energy, duration, amplitude, RMS, ASL and peak frequency. Reasons for selecting acoustic emission characteristic parameters are shown in Table 45.2. In the experiment, the NU205EM rolling bearing was selected, with an inner diameter of 25 mm, an outer diameter of 52 mm, a pitch diameter of 39 mm, a number of rolling elements of 13, and a rolling body diameter of 7.5 mm. Samples setting under training conditions are shown in Table 45.3. The rolling bearing fault types are shown in Fig. 45.4. As Fig. 45.4 shows, (a) is the inner ring failure, (b) is outer ring failure, (c) is the cage failure, (d) is the rolling element failure.

Table 45.2 Reasons for selecting AE characteristic parameters

AE characteristic parameters	Select reason
Rise time	Can be used for motor noise identification
Count	Widely used for evaluation of AE activity and positioning concentration
Energy	Reflect the relative energy and intensity of the event
Duration	Commonly used for class discrimination amplitude of wave source
Amplitude	Directly determine the measurability of time, often used for class identification, intensity and attenuation identification of wave sources
Peak frequency	Can roughly reflect the frequency of the signal
RMS	Simple measurement and unaffected by thresholds
ASL	Similar to RMS, also used for background noise level measurement

Table 45.3 Sample setting under training conditions

Training label	Rolling bearing operating condition	Number of training samples	Number of test samples
00001	Normal	30	6
00010	Outer ring failure	30	6
00100	Inner ring failure	30	6
01000	Rolling element failure	30	6
10000	Cage failure	30	6

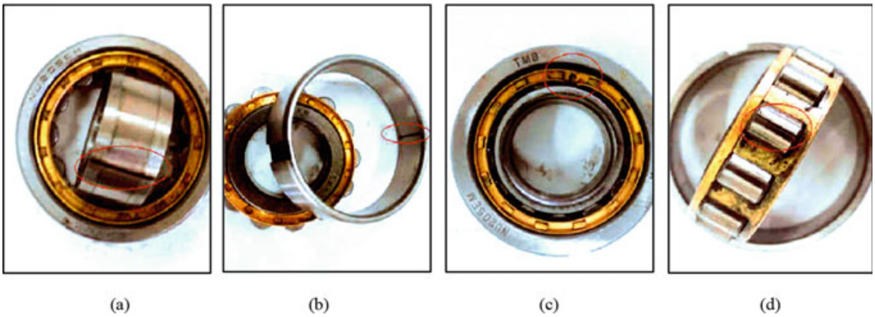

Fig. 45.4 Rolling bearing fault types

45.4 Result

The result of the fitness evolution curve of four network models is shown in Fig. 45.5.

As Fig. 45.5 shows, (a) is the fitness evolution curve of the GA-BP network model, (b) is the fitness evolution curve of the PSO-BP network model, (c) is the fitness evolution curve of the APSO-BP network model, (d) is the fitness evolution curve of the CS-BP network model in this paper. As can be seen from the figure, Fig. 45.5a shows the premature phenomenon in the genetic algorithm and fast convergence; Too slow to converge in Fig. 45.5b, c convergence speed is faster than Fig. 45.5b, but the fitness value does not change much; Fig. 45.5d convergence rate is between Fig. 45.5b, c, and the fitness value is lower, which means that there is a better recognition rate.

Figure 45.6 shows the results of the accuracy of the rolling bearing fault identification for the test group. In this figure, The CSBP model has a very high recognition accuracy for faulty bearings, excluding outer ring faults, reaching values of close to 100% accuracy in the classification. Figure 45.7 shows the results of the average accuracy of the five training models for test group, the CSBP model has a relatively high recognition accuracy by 93%.

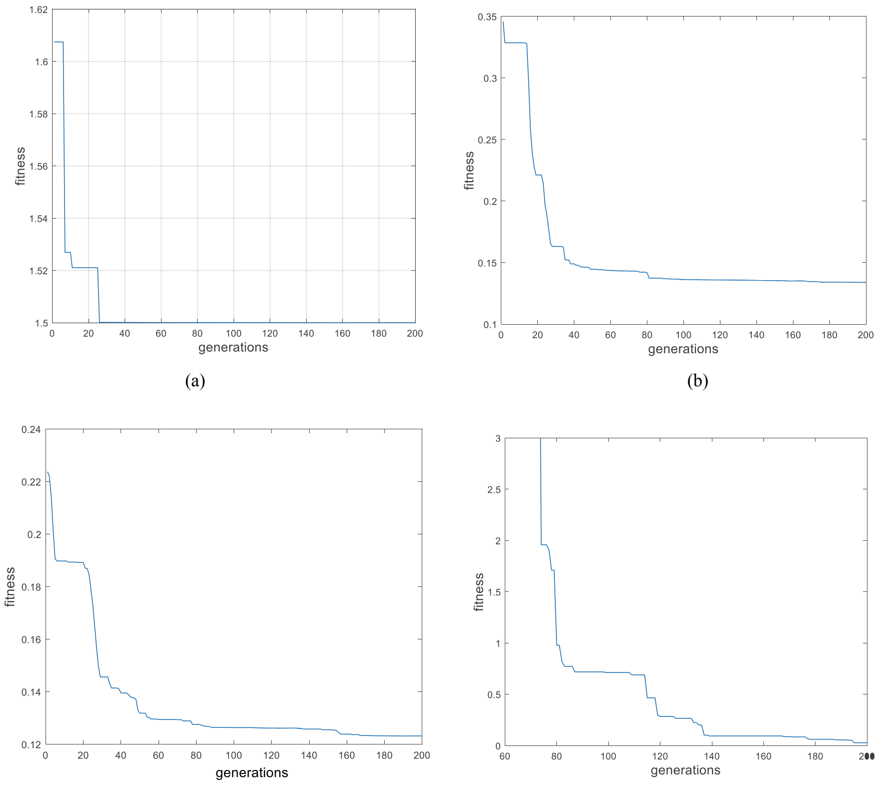

(a)

(b)

(c)

(d)

Fig. 45.5 The fitness evolution curve of four network models (generation = 200)

45.5 Conclusion

This paper has demonstrated that CSBP neural network model as a useful technique to recognize roller bearing fault by outer ring failure, Inner ring failure, Rolling element failure and Cage failure with high classification accuracy for classifying. Based on the statistics studied here, The CSBP neural network model has a very high accuracy and stability, accurate values of close to 93% in the classification. The effectiveness of the newly proposed algorithm is verified by examples of roller bearing fault.

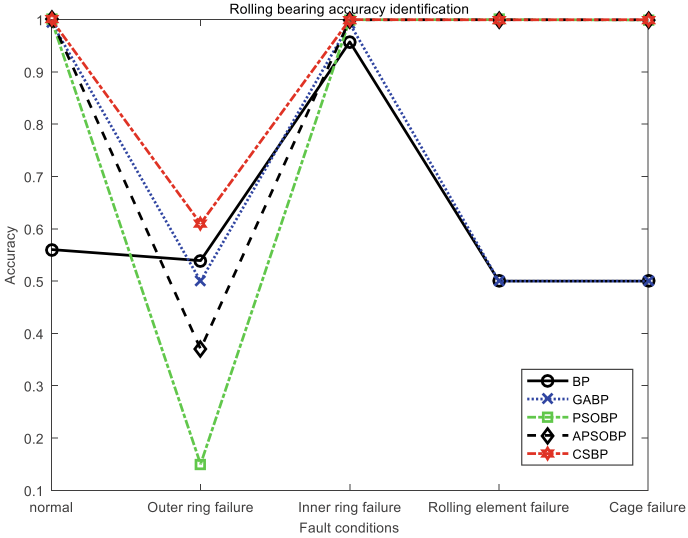

Fig. 45.6 Rolling bearing fault identification accuracy

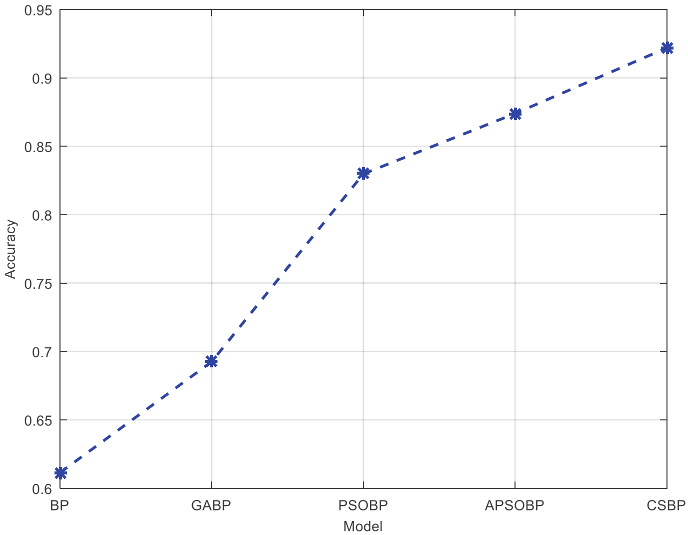

Fig. 45.7 Model average accuracy

References

1. Z. Wang, X. Wu, X. Liu, Damage sensitivity evaluation algorithm for rolling bearing features based on PCCDET. J. Vib. Shock **38**(1), 65–71 (2019)

2. C. Liu, X. Wu, J. Mao et al., Acoustic emission signal processing for rolling bearing running state assessment using compressive sensing. Mech. Syst. Signal Process. **91**, 395–406 (2017)
3. M. Song, H. Song, S. Xiao, A study on fault diagnosis method of rolling bearing based on wavelet packet and improved BP neural network. IOP Conf. Ser.: Mater. Sci. Eng. **274**(1), 1–6 (2017)
4. D. Qing, A BP neural network optimisation method based on dynamical regularization. J. Control Decis. **6**(2), 111–121 (2019)
5. G. Ghosh, P. Mandal, S.C. Mondal, Modeling and optimization of surface roughness in keyway milling using ANN, genetic algorithm, and particle swarm optimization. Int. J. Adv. Manuf. Technol. **100**(5), 1–20 (2017)
6. J. Wang, Q. Xu, Q. Li, Some remarks on the deterministic particle swarm optimization algorithm. Math. Methods Appl. Sci. **41**(5), 1–6 (2017)
7. K. Koteswara Rao, G.S.V.P. Rajuc, Reducing interactive fault proneness in software application using genetic algorithm based optimal directed random testing. Int. J. Comput. Appl. **41**(4), 1–10 (2018)
8. M. Abdel-Basset, A.N. Hessin, L. Abdel-Fatah, A comprehensive study of cuckoo-inspired algorithms. Neural Comput. Appl. **29**(2), 345–361 (2016)
9. X.S. Yang, S. Deb, in *Cuckoo search via Levy Flights.* Proceeding of World Congress on Nature and Biologically Inspired Computing, India (2009), pp. 210–214
10. N. Wang, X. Zhu, Y. Chen, J. Tao, in *Improved cuckoo search algorithm based RBF-NN for modeling reactor-regenerator system.* IECON 2017-43rd Annual Conference of the IEEE Industrial Electronics Society (IEEE, Beijing, 2017), pp. 5447–5452

Chapter 46
Bearing Fault Diagnosis Using Grad-CAM and Acoustic Emission Signals

Jaeyoung Kim and Jong-Myon Kim

Abstract Bearing failure generates burst signals when the rolling elements touch a crack on the outer race or inner race of the bearing. Over a decade, the acoustic emission (AE) has been used for detecting low-speed bearing failures. Since high sampling rate of the AE signal makes it difficult to design and extract good features, deep neural network-based approaches have been proposed in several recent researches. However, the weak point of deep neural network is uninterpretable. Gradient-weighted class activation mapping (Grad-CAM) is used for visual explanation of deep neural networks in computer vision domain. This paper implements and validates a deep neural networks-based bearing fault diagnosis method with understandable visualization using Grad-CAM.

46.1 Introduction

Bearing is a vital component of heavy rotating machines to reduce friction between rotating shaft and the fixed component such as bearing housing. Since the role of bearing is important, it is highly required to detect bearing failure in earlier stage for preventing secondary failure. 45–55% of broken machines are caused by bearing faults [1]. For a decade, many AE-based bearing fault diagnosis techniques have been developed. Acoustic emission (AE) means the generation of transient elastic waves from sudden cyclic fatigue, fraction, impacting, etc. [2]. The advantages of AE-based analysis compared with vibration-based analysis is that AE sensor can measure very low energy signals caused by bearing failures in early stage or slow-speed operation [2]. However, since the sampling rate of AE signal is higher than 1 MHz, it is difficult to analyze the AE signal because of the complexity of large data and computational time for analysis. To overcome this issue, DNN-based bearing fault diagnosis

---

J. Kim · J.-M. Kim (✉)
Department of Electrical, Electronics and Computer Engineering, University of Ulsan, Ulsan 44610, South Korea
e-mail: jongmyon.kim@gmail.com

J. Kim
e-mail: kjy7097@gmail.com

© The Author(s), under exclusive license to Springer Nature Singapore Pte Ltd. 2021

G. Shen et al. (eds.), *Advances in Acoustic Emission Technology*, Springer Proceedings in Physics 259, https://doi.org/10.1007/978-981-15-9837-1_46

methods have been developed [3, 4]. Although the performance of the DNN-based methods achieved high classification accuracy, the result is uninterpretable due to the black box-like approach of DNN. This problem makes DNN unreliable and unvalidated for applications. Gradient-weighted class activation mapping (Grad-CAM) is a promising method to provide visual explanations of the classification result with DNN, which has been validated for object detection and recognition [5]. This paper applies Grad-CAM for bearing fault diagnosis method and validate the performance by visualizing important regions in the envelope spectrum of AE signal.

46.2 Proposed Method

The proposed method consists of the following steps. (Step 1) Envelope spectrums are calculated from pre-acquired AE signals containing healthy and faulty condition. (Step 2) frequency magnitudes in the characteristic frequency range of bearing are extracted as features. (Step 3) DNN is trained using the extracted features. The envelope spectrums of new AE signals are classified into healthy or faulty condition using the trained DNN. (Step 4) A importance weights with frequency are generated including important regions in the envelope spectrum using Grad-CAM for the acquired AE signals.

46.2.1 Step 1: Envelope Spectrum Calculation

Since the burst signals from bearing failures is amplitude-modulated, AE signals are demodulated to extract pure burst signals. In this paper, Hilbert transform-based envelope analysis is used for demodulation of the AE signal [6]. Firstly, Hilbert transform is applied to the AE signal as follows:

$$\widehat{x}(t) = \frac{1}{\pi} \int_{-\infty}^{\infty} \frac{x(\tau)}{t - \tau} d\tau, \tag{46.1}$$

where t is the time, $x(\tau)$ is a sample of input signal at τ, and $\widehat{x}(t)$ is a sample of Hilbert transformed signal at time t.

To obtain the analytical signal, z(t), Hilbert transformed signal, $\widehat{x}(t)$, and input signal, $x(t)$ are combined as complex numbers:

$$z(t) = x(t) + i\widehat{x}(t), \quad i = \sqrt{-1}. \tag{46.2}$$

Then, the envelope signal, $e(t)$ is computed as $|z(t)|$. Finally, envelope spectrum is calculated as the root-square of the fast Fourier transform of $e(t)$.

46.2.2 Step 2: Characteristic Frequency Magnitude Extraction

Bearing failures generate periodic burst signals which are represented as bearing characteristic frequency in the spectrum. The bearing characteristic frequency is categorized to ball pass frequency on outer race, *BPFO*, ball pass frequency on inner race, *BPFI*, and ball spin frequency, *BSF*. Outer race failure, Inner race failure, and Rolling element failure of the bearing cause *BPFO*, *BPFI*, and 2 × *BSF*, respectively. The bearing characteristic frequencies are defined as follows [6]:

$$
\begin{aligned}
BPFO &= \frac{Nb}{2} \times S \times \left[1 - \left(\frac{Bd}{Pd} \times \cos\theta\right)\right], \\
BPFI &= \frac{Nb}{2} \times S \times \left[1 + \left(\frac{Bd}{Pd} \times \cos\theta\right)\right], \\
BSF &= \frac{Pd}{2Bd} \times S \times \left[1 - \left(\frac{Bd}{Pd} \times \cos\theta\right)^2\right],
\end{aligned}
\tag{46.3}
$$

where *Nb* is the number of rolling elements, *S* is the shaft speed, *Bd* is the diameter of the rolling element, *Pd* is the pitch diameter, i.e., the distance between the center of a rolling element and the center of the inner race, and θ is a contact angle of the rolling element with respect to the shaft.

The frequency magnitudes in bearing characteristic frequency band, *FBC*, are extracted as an input vector of *DNN*. *FBC* is defined as follows:

$$FBC(i) = f(i), i = 0, \ldots, F_{max}, \tag{46.4}$$

where f is the values of the envelope spectrum and F_{max} is defined to cover the multiple harmonics of the maximal defect frequency with their sideband frequency S as follows:

$$F_{max} = max(BPFO, BPFI, BSF) \times n + S. \tag{46.5}$$

FBC is finally min-max normalized as follows:

$$
\begin{aligned}
FBC_{norm}(i) = (FBC(i) - min(FBC))/(max(FBC) - min(FBC)) \\
, i = 0, \ldots, F_{max}.
\end{aligned}
\tag{46.6}
$$

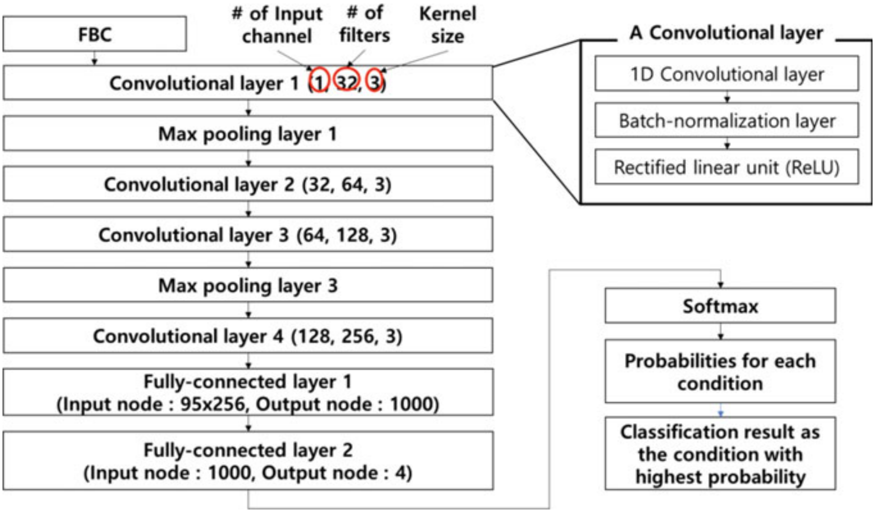
FBC
# of Input channel
# of filters
Kernel size
Convolutional layer 1 (1, 32, 3)
Max pooling layer 1
Convolutional layer 2 (32, 64, 3)
Convolutional layer 3 (64, 128, 3)
Max pooling layer 3
Convolutional layer 4 (128, 256, 3)
Fully-connected layer 1
(Input node : 95x256, Output node : 1000)
Fully-connected layer 2
(Input node : 1000, Output node : 4)
A Convolutional layer
1D Convolutional layer
Batch-normalization layer
Rectified linear unit (ReLU)
Softmax
Probabilities for each condition
Classification result as the condition with highest probability

Fig. 46.1 DNN structure for bearing fault diagnosis

46.2.3 Step 3: Training DNN and Classification

The structure of DNN is represented in Fig. 46.1. The DNN consists of six convolutional layers and two fully-connected layers. Each convolutional layer includes 1-dimensional (1-D) convolutional layer, batch-normalization layer, and rectified linear unit (ReLU), sequentially. All convolutional layers are connected each other using max pooling layer with down-sampling factor as 2. Therefore, the input size of each convolutional layer is half of the input size of previous convolutional layer except first layer. The full-connected layers and softmax role classification as last layer. All layers and softmax are traditional in this paper [7]. For training process, cross-entropy is used as loss function, and Adam optimization is used for backpropagation [8].

46.2.4 Step 4: Importance Weights Calculation

Grad-CAM is used to calculated importance weights, M_c, that represents the importance weight with frequency in the input data, FBC. In order to obtain M_c, a partial derivation, p_k^c, of the score for class c, y_c, is calculated with respect to the kth output of a convolutional layer, A^k. Following equation represents the definition of p_c:

$$p_k^c = \frac{1}{N}\sum_{i=1}^{N}\frac{\partial y_c}{\partial A_i^k}, \tag{46.7}$$

The mean of p_k^c indicates a 'importance' weight of *k*th filter for class, *c*.

46.3 Experimental Setup and Data Acquisition

In order to validate the method, a bearing fault simulator is used for measuring healthy and faulty-state AE signals of the bearing. The established bearing fault simulator is illustrated in Fig. 46.2. In driven-end shaft, 3-phase induction motor is connected to a gearbox by flexible coupling. The gearbox transfers the torque of the induction motor to non-driven-end shaft with gear reduction ratio as 1.52:1. A tachometer is installed to measure the rotating speed of non-driven-end shaft. A cylindrical roller bearing (FAG NJ206-E-TVP2), which is a target bearing of the experiment, is equipped in the bearing housing of non-driven-end shaft. To apply radial and axial load, a fan with adjustable blades is connected to non-driven-end shaft via a belt. The shaft speed is 500 revolutions per minute (RPM) in this paper. An AE sensor is attached on the bearing housing of the target bearing. Figure 46.3 shows a picture of the experimental setup.

The measurement device for obtain AE signals is PCI-2-based system. A general-purpose wideband AE sensor, whose frequency response is between 100 and 1000 kHz, is used for capturing resonance frequency signals containing modulated bearing signals.

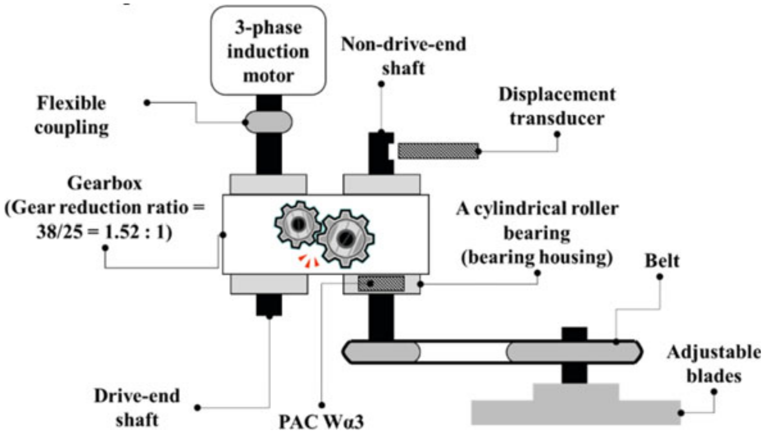
3-phase induction motor
Non-drive-end shaft
Flexible coupling
Displacement transducer
Gearbox (Gear reduction ratio = 38/25 = 1.52 : 1)
A cylindrical roller bearing (bearing housing)
Belt
Adjustable blades
Drive-end shaft
PAC Wα3

Fig. 46.2 The illustration of the bearing fault simulator

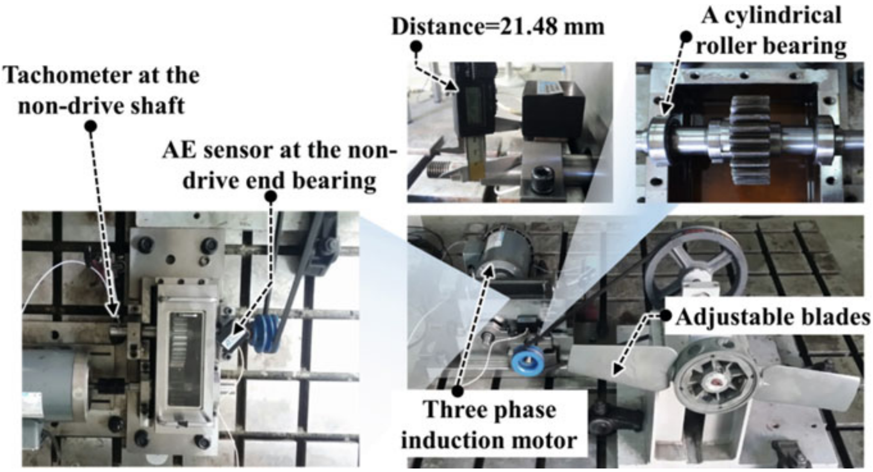
Tachometer at the non-drive shaft
AE sensor at the non-drive end bearing
Distance=21.48 mm
A cylindrical roller bearing
Adjustable blades
Three phase induction motor

Fig. 46.3 The picture of the experimental setup

46.4 Experimental Result and Discussion

To validate the performance of Grad-CAM for bearing fault diagnosis, AE signals from healthy-state and three types of bearing fault are acquired using the testbed The length of a measured AE signal is 1-s with 1 MHz sampling rate, and the number of AE signals for each condition is 600, half of the dataset is selected for training DNN, randomly. Remaining half of the dataset are used for validation. The trained DNN achieved 99% accuracy of classification with the validation dataset as shown in Fig. 46.4.

Figure 46.5 shows the importance weight over frequencies from Grad-CAM for the trained DNN. As shown, DNN learned that the harmonics of defect frequencies are important information to classify the FBC to each condition. In this experiment,

Fig. 46.4 Confusion matrix of classification result

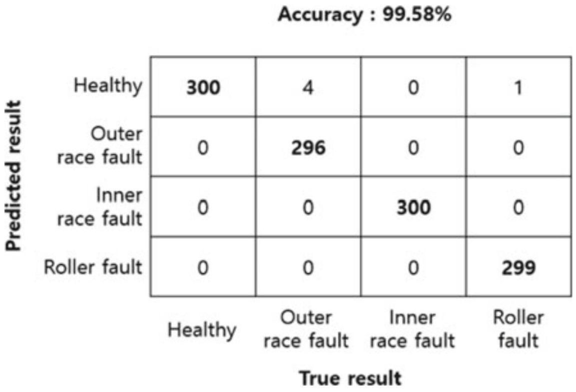
Accuracy : 99.58%

Predicted result \ True result	Healthy	Outer race fault	Inner race fault	Roller fault
Healthy	**300**	4	0	1
Outer race fault	0	**296**	0	0
Inner race fault	0	0	**300**	0
Roller fault	0	0	0	**299**

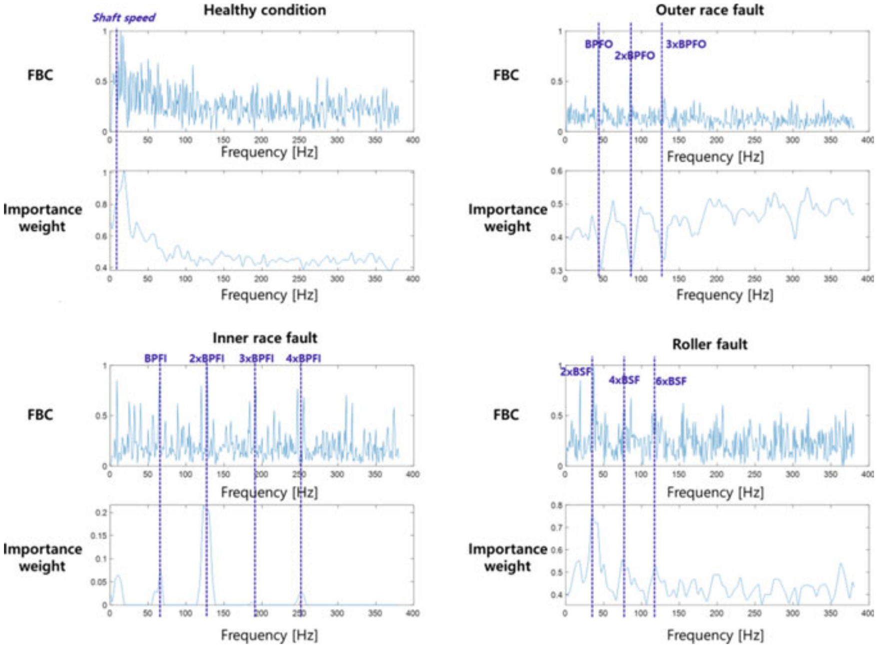

Fig. 46.5 Importance weights from Grad-CAM for DNN

BPFO, BPFI, BSF, and the shaft speed are 44, 42, 65 Hz, and 8.33 Hz, respectively. For healthy condition, DNN learned low frequency band components are important since the low frequency band contains the harmonics of the shaft speed frequency which appear clearly in the healthy condition. Since the defect and shaft speed frequencies are also important in traditional bearing failure method, DNN seems to be reasonably learned even the information is not provided except outer fault case. In the case, the issue is that the 2xBSF and BPFO are too close to classify the input data based on 2 × BSF and BPFO. Therefore, DNN choose the sideband of BPFO as useful information instead of BPFO, itself.

46.5 Conclusion

Although DNN-based fault diagnosis is effective with high classification performance, it is still difficult to understand the reason of classification result. In this paper, we tried to understand trained DNN for bearing fault diagnosis using an effective tool, Grad-CAM, for extracting explainable information from DNN. In the experiment, a simulator is used to imitate bearing failures and measure AE signals for healthy and three different types of bearing failures. Using the AE signals, DNN is trained and achieves 99% average accuracy. Grad-CAM provided the importance weights of DNN, which indicates the degree of importance for each input sample. The result shows the low frequency magnitudes are important to classify the AE signals from healthy-conditioned bearing, and bearing characteristic frequencies are important to classify the AE signals from bearing failures. In the future works, the explainable method for DNN should be researched for various experiment for verification.

Acknowledgements This work was supported by the Korea Institute of Energy Technology Evaluation and Planning (KETEP) and the Ministry of Trade, Industry & Energy (MOTIE) of the Republic of Korea (No. 20181510102160, No. 20192510102510).

References

1. N. Subhasis, T. Hamid, L. Xiaodong, Condition monitoring and fault diagnosis of electrical motors—a review. IEEE Trans. Energy Convers. **20**(4), 719–729 (2005)
2. M, Elforjani, D. Mba, Accelerated natural fault diagnosis in slow speed bearings with acoustic emission. Eng. Fract. Mech. **77**(1), 112–127 (2010)
3. K. Wasmer, F. Saeidi, B. Meylan, T.L. Quan, S.A. Shevchik, When AE (Acoustic Emission) meets AI (Artificial Intelligence) II. EWGAE (2018)
4. M.M. Manjurul Islam, J.-M. Kim, Automated bearing fault diagnosis scheme using 2D representation of wavelet packet transform and deep convolutional neural network. Comput. Ind. **106**(1), 142–153 (2019)
5. R.R. Selvaraju, M. Cogswell, A. Das, R. Vedantam, D. Parikh, D. Batra, Grad-CAM: visual explanations from deep networks via gradient-based localization. ICCV (2017)
6. M. Kang, J. Kim, L.M. Wills, J.-M. Kim, Time-varying and multiresolution envelope analysis and discriminative feature analysis for bearing fault diagnosis. IEEE Trans. Ind. Electron. **62**(12), 7749–7761 (2015)
7. T.N. Sainath, A.R. Mohamed, B. Kingsbury, B. Ramabhadran, Deep convolutional neural networks for LVCSR. ICASSP (2013)
8. Z. Zhang, S. Mert, Generalized cross entropy loss for training deep neural networks with noisy labels. NeurIPS (2018)

Chapter 47
Bearing Fault Transfer Diagnosis Based on Acoustic Emission Signal Under Variable Working Conditions

Jiwang Zhang, Keqin Ding, Hongzhu Wang, and Guang Chen

Abstract In recent years, the intelligent diagnosis of bearing fault under stable condition based on machine learning and vibration signal has made a lot of achievements. However, the performance degradation of these methods is obvious under variable working conditions, which makes the intelligent diagnosis of bearing fault still a challenge. In order to solve this problem, a rolling bearing fault transfer diagnosis method based on acoustic emission signal is proposed in this paper. The AE data under different working conditions are collected and converted to signal map firstly, then the sensitive features are extracted and the labeled knowledge in source domain is transferred to the without labeled target domain by using convolutional neural network and domain adaptation. Finally, the feasibility and superiority of the proposed method was verified by lots of bearing experiments, and the classification accuracy reached 88.40%, which is much higher than the traditional methods.

47.1 Introduction

Rolling bearing is the key component of rotating machinery equipment. It mainly bears the weight and working load of the rotating body and ensures the rotating accuracy of the rotating body [1]. Therefore, it is of great significance to monitor and diagnose its health condition [2–4]. In recent years, a lot of research has been done on bearing fault diagnosis based on machine learning and vibration signal, and many useful results have been achieved [5–8]. However, the performance degradation of these methods under variable working conditions is still a challenge [9]. In order to solve this problem, a rolling bearing fault transfer diagnosis method based on acoustic emission signal is proposed in this paper. The goal is to build a common space to unify the data of different distribution in the source domain and the target domain, and realize the knowledge transfer from labeled data to unlabeled data, which mainly solves two problems: (1) reducing the interference of signal under

---

J. Zhang · K. Ding (✉) · H. Wang · G. Chen
China Special Equipment Inspection and Research Institute, Beijing 100029, China
e-mail: kqding@sina.com

© The Author(s), under exclusive license to Springer Nature Singapore Pte Ltd. 2021

G. Shen et al. (eds.), *Advances in Acoustic Emission Technology*, Springer Proceedings
in Physics 259, https://doi.org/10.1007/978-981-15-9837-1_47

variable working condition, (2) improving the universality of fault intelligent diagnosis methods based on machine learning. The remainder of this paper is organized as follows. In Sect. 47.2, background of domain adaptation and convolutional neural network is briefly introduced. Section 47.3 introduced the proposed method in detail. In Sect. 47.4, experiments are carried out to demonstrate the effectiveness and the superiority of the proposed improved method. Finally, some major conclusions are drawn in Sect. 47.5.

47.2 Background

47.2.1 Domain Adaptation

Domain adaptation is a machine learning method to solve the problem that the accuracy of classification decreases when the source data and the target data come from different feature distributions [10]. In transfer learning, domain adaptation is an effective technology that can transfer knowledge from a large number of source domain data to unlabeled target domain as in Fig. 47.1. Domain adaption completes knowledge transfer without label in the target domain by reducing the difference between the source domain and the target domain. The purpose of domain adaptation is to find a feature space shared by source domain and target domain, and train classifier in this feature space. In the field of fault diagnosis, domain adaptive technology has been initially applied. In order to solve the problem of cross domain feature extraction, the transfer component analysis algorithm is applied in the field of fault in the literature to reduce the difference of feature distribution of fault signals under different working conditions. Domain adaption will be defined as in (47.1):

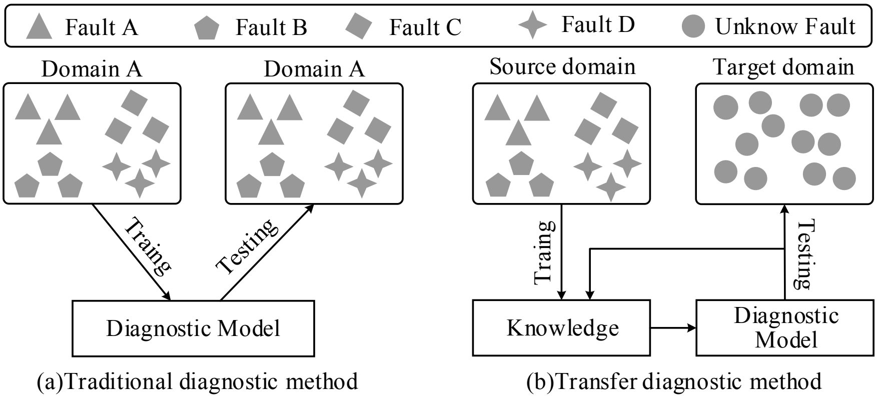

(a)Traditional diagnostic method (b)Transfer diagnostic method

Fig. 47.1 Comparison of fault intelligent diagnosis methods between transfer learning and without transfer learning

$$D^{\mathrm{s}} = \{(x_1^{\mathrm{s}}, y_1^{\mathrm{s}}), \ldots, (x_n^{\mathrm{s}}, y_{n_{\mathrm{s}}}^{\mathrm{s}})\} D^{\mathrm{t}} = \{x_1^{\mathrm{t}}, \ldots, x_{n_{\mathrm{t}}}^{\mathrm{t}}\} \tag{47.1}$$

where D^{s} and D^{t} represent the source and target domains respectively, x^{s} and x^{t} represent the source and target domain data samples respectively, y^{s} represent the source domain data samples label. n_{s} and n_{t} represent the number of source and target domains samples.

It is supposed that the data samples collected from the source and target domains are subject to the marginal probability distribution, which is $\mathrm{P}(x^{\mathrm{s}}) \neq \mathrm{P}(x^{\mathrm{t}})$. Therefore, the aim of domain adaptation is to build an intelligent diagnosis model, which extracts transferable features from the collected data to reduce the cross-domain discrepancy, and then forces the domain-shared classifier to minimize the target domain $\sum_{j=1}^{n_{\mathrm{t}}} \left\| \hat{y}_i^t - y_i^t \right\|$, $\hat{y}_i^t$ and y_i^t represents the real label and forecast label of the ith sample respectively.

Domain adaptation is to minimize the difference between the source domain and the target domain in the shared feature subspace through feature mapping. In order to evaluate this difference, the index maximum mean discrepancy (MMD) is introduced as in (47.2). MMD is a nonparametric distance metric to measure the distribution discrepancy between two datasets [11]. where n_{s} and n_{t} are the numbers of source and target samples respectively.

$$\mathrm{MMD}(X^{\mathrm{s}}, X^{\mathrm{t}}) = \left\| \frac{1}{n_{\mathrm{S}}} \sum_{i=1}^{n_{\mathrm{s}}} h(x_i^{\mathrm{s}}) - \frac{1}{n_{\mathrm{t}}} \sum_{i=1}^{n_{\mathrm{t}}} h(x_i^{\mathrm{t}}) \right\|_2^2 \tag{47.2}$$

where M stand for MMD matrix, M_{ij} represents elements in MMD matrix.

47.2.2 Convolutional Neural Network

Convolutional neural network is a deep learning method that can automatically extract sensitive features from raw data without relying on expert knowledge [12]. Its network structure includes input layer, convolution layer and pool layer, full connection layer and output layer. The input layer usually inputs the original data directly, convolution layer and pooling layer are mainly used to mine sensitive features, the full connection layer is formed by connecting the output of the last pooling layer in turn. The same kernel is used to mine the local feature in convolutional layer. Therefore, the convolution process is described as in (47.3):

$$y^{l(i,j)} = \mathrm{K}_i^l * \mathrm{X}^{l(\mathrm{r}^j)} = \sum_{j'=0}^{W} \mathrm{K}_i^l(j')\mathrm{X}^{l(j+j')} \tag{47.3}$$

where, K_i^l denotes the weights of the ith filter kernel in layer l, $\mathrm{X}^{l(\mathrm{r}^j)}$ represents the jth local region in convolutional layer l.

Usually, a pooling layer is connected behind the convolution layer to reduce the feature dimension and model training time. The common pooling methods include maxi-pooling, average-pooling and weight-pooling. Among them, maxi-pooling is widely used because it can extract the local maximum value and invariant features from input features directly. The max-pooling can be described as in (47.4):

$$p^{l(i,j)} = \max_{(j-1)W+1 \le t \le jW} \left\{ a^{l(i,t)} \right\} \tag{47.4}$$

where $a^{l(i,t)}$ denotes the value of tth neuron in the i-th frame of layer l, $t \in [(j-1)W+1, jW]$, W is the width of the pooling region, and $p^{l(i,j)}$ denotes the corresponding value of the neuron in layer l of the pooling operation.

47.3 Proposed Method

In this paper, we propose a new fault diagnosis method for rolling element bearings under variable working conditions. The core of this method is to use Maximum Mean Discrepancy (MMD) to measure the difference of fault feature distribution under different working conditions, then the features are transferred through domain adaptation. Finally, the fault diagnosis under variable working conditions is realized. The flow chart of the proposed method as shown in Fig. 47.2.

In order to extract more sensitive fault features, 1-D(one-dimensional) AE signals are transformed into 2-D AE gray-scale images firstly. The amplitude of each raw sample will be normalized into the range [−1, 1] and divided into M segments, each segment has N sampling points, i represents the corresponding ith point in each sub-segment signal, j represents the jth sub-segment signal. The detailed conversion process is shown in (47.5).

$$P[i, j] = A[(i-1) * M + j] \tag{47.5}$$

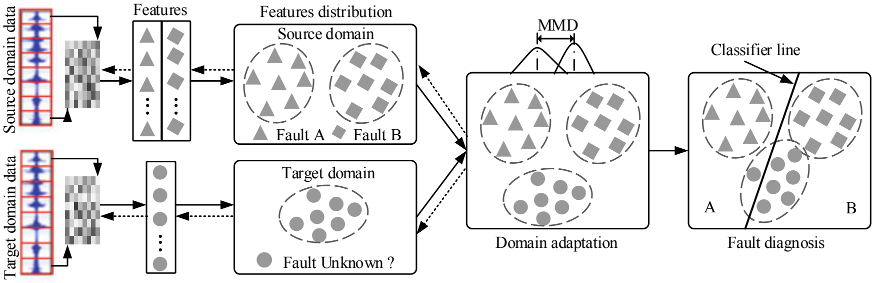
Source domain data
Target domain data
Features
Features distribution
Source domain
Fault A
Fault B
Target domain
Fault Unknown ?
MMD
Domain adaptation
Classifier line
A
B
Fault diagnosis

Fig. 47.2 The flow chart of the proposed method

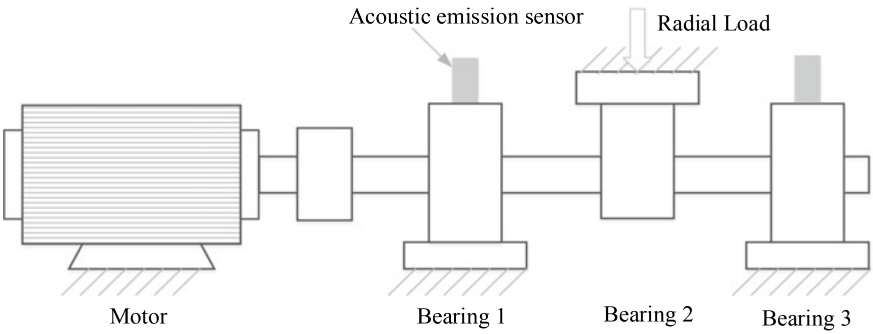

Fig. 47.3 Test rig

Table 47.1 Experimental parameters of bearing failure under variable working conditions

Dataset	Radial load	Fault categories	Number of samples	Samples length	Rotating speed (r/min)
A	0	Outer-race fault	1000	20,736	884
B	200 N	Outer-race fault	1000	20,736	882
C	400 N	Outer-race fault	1000	20,736	879

47.4 Verification

47.4.1 Experimental Set-Up

In order to verify the effectiveness of the proposed method, the bearing fault test were carried out. As shown in Fig. 47.3, the test rig mainly consists of motor, deep groove ball bearing (SKF 61988), acoustic emission sensor (PAC ISPK3IUC). Single point fault with the dimension of 0.1 mm is machined on the outer-race of bearing using electro-discharge machining. The different operating conditions were simulated by applying different radial loads on the shaft. A special coupling agent is used to reduce the attenuation of AE signal. The outputs of the AE sensor are fed into a laptop (ASUS A85V) through a data acquisition box (DAQ, DT9857E). The detailed experimental parameters settings are shown in Table 47.1.

47.4.2 Feature Mining

The original 1-D AE signal is transformed into 2-D gray-scale image using eq. (6), and then the convolution neural network is used to extract the sensitive features and identify the faults. The architecture of the proposed CNN consists of 5 convolutional layers, a fully-connected layers and a Softmax layer. The whole structure

Table 47.2 Diagnostic results with different methods in the bearing cases (%)

Metheds	A → B	B → A	A → C	C → A	B → C	C → B	Average
SAE	43.62	47.58	42.37	44.72	52.18	46.28	46.13
TCA	47.24	44.15	43.46	47.18	49.37	53.04	47.41
CNN	51.28	55.32	45.26	48.17	52.63	47.72	50.06
DCC	61.28	59.47	63.59	57.81	67.42	65.83	62.57
Proposed	87.48	89.26	85.57	88.26	90.27	89.54	88.40

was arranged as follows: "Input-C1(Convolution layer 1)-P1(Pooling layer 1)-C2-P2-C3-P3-C4-P4-C5-P5-Full connected-Softmax". The 2-D AE gray-scale images will be used as input data, the first kernel size of CNN is 6 * 6 and the rest is 3 * 3. The pooling type is max pooling with the size of 2 * 2. The fully-connection layer size is 16 * 1. Finally, four kinds of diagnosis results are output by softmax layer.

47.4.3 Result and Discussions

According to Table 47.1, we create six transfer learning tasks A → B, B → A, A → C, C → A, B → C and C → B. Any one of data sets A, B and C is considered as source domain data, and the other two are considered as target domain data respectively. The diagnosis goal is to identify the fault type of the target domain as much as possible through the data of different domains. To better demonstrate the effectiveness of the proposed fault diagnosis method, the diagnosis results of it are compared with some constructed approaches and related works with or without domain adaptation operation in Table 47.2.

From the comparison of the diagnosis results by using different methods, it can be seen that the traditional diagnosis method has poor diagnosis effect under variable working conditions, and the optimal average diagnosis accuracy is only 62.57%. However, the average diagnosis rate of the proposed method is 88.4%, which is obviously superior to the traditional diagnosis methods.

47.5 Conclusion

Intelligent fault diagnosis of rotating machinery under variable working conditions has always been a research hotspot in this field. When the training data and test data come from different distributions, the classification accuracy of traditional machine learning algorithm is significantly reduced. To solve this problem, a fault transfer diagnosis based on acoustic emission signal is proposed. By sharing the information of label samples in source domain, the problem of insufficient training samples in target domain is solved. The main conclusions are as follows:

1. The difference of data samples distribution under different working conditions is effectively eliminated by domain adaptation, and the labeled knowledge in source domain is transferred to the without labeled target domain. The problem of lack of labeled samples under variable working conditions is well solved.
2. Convolution neural network is used to extract sensitive features directly from acoustic emission signal map, which makes feature extraction independent of professional knowledge. In order to extract better features, one-dimensional acoustic emission waveform is transformed into two-dimensional acoustic emission map, which improves the performance of convolution neural network.
3. Finally, the feasibility and superiority of the proposed method was verified by lots of bearing experiments, and the classification accuracy reached 88.40%, which is much higher than the traditional methods.

Acknowledgements This research was supported by the Science and Technology Plan Projects of State Administration for Market Regulation (2019MK131), China Special Equipment Inspection & Research Institute (2019-Youth-10) and the National Key Research and Development Program of China (2018YFF0214702).

References

1. P. Ma, H. Zhang, W. Fan, C. Wang, A diagnosis framework based on domain adaptation for bearing fault diagnosis across diverse domains. ISA Trans. **359**, 77–92 (2019)
2. K. Yu, T.R. Lin, J. Tan, H. Ma, An adaptive sensitive frequency band selection method for empirical wavelet transform and its application in bearing fault diagnosis. Measurement **134**, 375–384 (2019)
3. S. Lu, Q. He, J. Zhao, Bearing fault diagnosis of a permanent magnet synchronous motor via a fast and online order analysis method in an embedded system. Mech. Syst. Signal Proc. **113**, 36–49 (2018)
4. X. Zhang, Z. Liu, Q. Miao, L. Wang, Bearing fault diagnosis using a whale optimization algorithm-optimized orthogonal matching pursuit with a combined time–frequency atom dictionary. Mech. Syst. Signal Proc. **107**, 29–42 (2018)
5. C. Zhao, Z. Feng, X. Wei, Y. Qin, Sparse classification based on dictionary learning for planet bearing fault identification. Expert Syst. Appl. **108**, 233–245 (2018)
6. T. Berredjem, M. Benidir, Bearing faults diagnosis using fuzzy expert system relying on an improved range overlaps and similarity method. Expert Syst. Appl. **108**, 134–142 (2018)
7. M.S. Hoseinzadeh, S.E. Khadem, M.S. Sadooghi, Quantitative diagnosis for bearing faults by improving ensemble empirical mode decomposition. ISA Trans. **83**, 261–275 (2018)
8. A. Khadersab, S. Shivakumar, Vibration analysis techniques for rotating machinery and its effect on bearing faults. Procedia Manuf. **20**, 247–252 (2018)
9. Y. Yang, W. Yang, D. Jiang, Simulation and experimental analysis of rolling element bearing fault in rotor-bearing-casing system. Eng. Fail. Anal. **92**, 205–221 (2018)
10. X. Li, W. Zhang, Q. Ding, J.-Q. Sun, Multi-layer domain adaptation method for rolling bearing fault diagnosis. Signal Process. **157**, 180–197 (2019)
11. W. Qian, S. Li, P. Yi, K. Zhang, A novel transfer learning method for robust fault diagnosis of rotating machines under variable working conditions. Measurement **138**, 514–525 (2019)
12. W. Zhang, C. Li, G. Peng, Y. Chen, Z. Zhang, A deep convolutional neural network with new training methods for bearing fault diagnosis under noisy environment and different working load. Mech. Syst. Signal Proc. **100**, 439–453 (2018)

Chapter 48
The AE Monitoring in Load Testing in Helicopter Tail Beam with Prefabricated Defects

Zhengjie Shao, Siyi Liu, Wei Wu, Xi Chen, and Guanhua Wu

Abstract Flying rocks thrown by helicopters during take-off and landing could cause damage to composite tail beams, The safety evaluation of the damaged tail beam depends on the results of the fully loaded specimens. Acoustic emission monitoring were be used in the full structural loading test of tail beam, To evaluate the safety of the damaged tail beam during loading and the extensibility of prefabricated defects, The results showed that The energy, amplitude, pulse count and duration of acoustic emission signal all have a good relationship with the loading. Acoustic emission monitoring can be used to evaluate the safety of tail beam structure.

48.1 Introduction

The Helicopter tail beam refers to the single-rotor form of helicopter with tail rotor fuselage after the section of the shape becomes significantly elongated, the end is provided with tail fin, tail rotor and tail sledge. The tail beam adopts honeycomb sandwich structure, during flight and landing loads, may occurring two failure modes, global instability and local instability. In the helicopter taking off and landing, the composite's tail beam may be damaged by raised flying stones. To avoid potential defects or damage to reduce the helicopter flight safety life and strength performance, according to airworthiness requirements, the loading test was carried out in the Civilian helicopters critical parts equipped the shock, scratch, corrosion and other defects, to determine the safety of helicopter tail beam. The AE monitoring were be used to evaluate the safety of tail beam structure, to analyzed and evaluated the expansion of prefabricated defect of tail beam under load in this paper.

Z. Shao · W. Wu · X. Chen · G. Wu (✉)
Key Laboratory of Nondestructive Testing (Nanchang Hangkong University) Ministry of Education, Jiangxi 330063, China
e-mail: Wuguanhua@nchu.edu.cn

S. Liu
Aviation Industry Helicopter Design Institute(602), Jingdezhen 333001, China
e-mail: 562667612@qq.com

© The Author(s), under exclusive license to Springer Nature Singapore Pte Ltd. 2021

G. Shen et al. (eds.), *Advances in Acoustic Emission Technology*, Springer Proceedings in Physics 259, https://doi.org/10.1007/978-981-15-9837-1_48

48.2 Instrument and Test Procedure

The loading testing device showed Fig. 48.1, the device can simulating the load of helicopter tail beam in landing and takeoff, the location of prefabricated defects were be showed in Fig. 48.2.

The acoustic emission instrument designed and manufactured by physical acoustics (PAC), the sensor of choice was an R15 alpha, the center frequency is 15 kHz, the preamplifier is a 2/4/6 preamplifier designed and manufactured by physical acoustics (PAC)., AE preamplifier gain is 40 dB, Sampling rate is set to 2 MHz, PDT 30 μs, HDT 150 μs, HLT 300 μs. The Impact damage size were be measured by ultrasonic phased array instrument make by GE. The Schedule of ultrasonic phased array detection and acoustic emission monitoring and static test, The Impact damage defects were measured by phased array before loading, the two-point horizontal landing state was subjected to 100% static loading test, and the embedded defects and impact damage were detected and the test data were recorded.

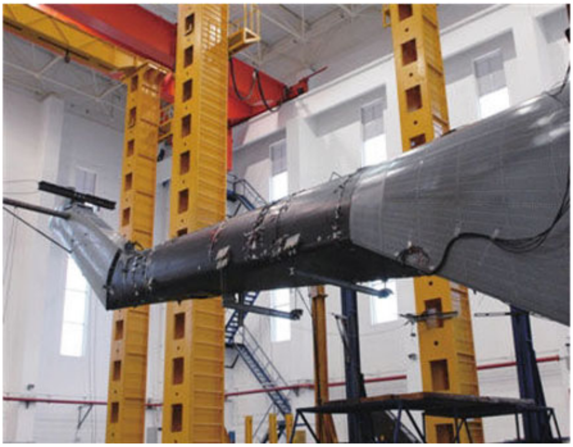

Fig. 48.1 The load testing device of helicopter tail beam

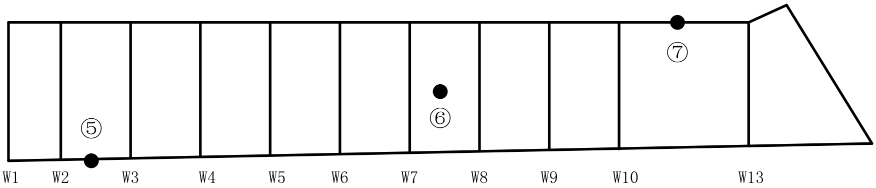

Fig. 48.2 The location of prefabricated defects in helicopter tail beam: ⑤Impact damage by 22.2 J energy; ⑥Impact damage by 5.18 J energy; ⑦Impact damage by 13.5 J energy

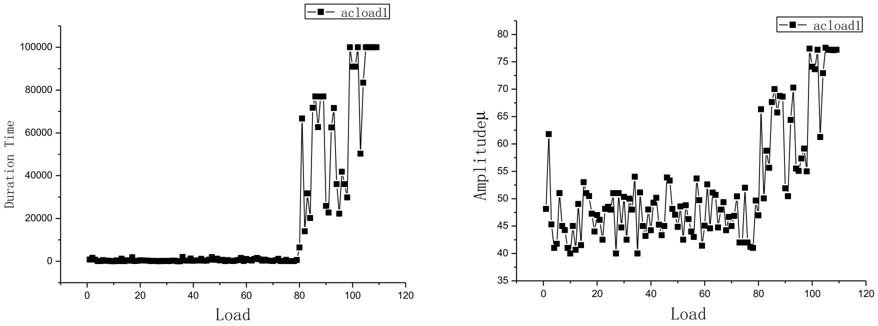

Fig. 48.3 AE duration time amplitude pulse counting and energy in loading testing

48.3 The Test Results

The AE monitoring signals in loading testing showed in Fig. 48.3.

48.4 The Results Analyze

The acoustic emission signals in the loading process were analyzed by clustering analysis, the parameter correlation diagram of acoustic emission signal is established according to the parameter value of acoustic emission signal [1]. Five acoustic emission signal parameters were counted, Including rise time, ring count, energy, duration, amplitude, statistical characteristics of signal parameters during loading [2], the results of the analysis showed in Fig. 48.4. Figure 48.4a showed that the transmitted signal energy is generally low, and the energy value is relatively average. The frequency is in the low frequency range, while the high frequency signal is less, it was the signal generated by fixture friction and fiber friction during loading. Figure 48.4b showed that the ringing count is less, duration is shorter, frequency is in low frequency range, high frequency signal is less, it was the signal generated by composite matrix deforms during loading. Figure 48.4c showed that the average energy of the transmitted signal increases, the ringing count increases, the duration is longer, the frequency is in the low frequency range and contains a small number of high frequency signals, it was the signal generated during crack initiation and propagation and interface debonding of composite matrix during loading. Figure 48.4c showed that the acoustic emission signal energy is large, the average energy is large, the ringing count signal is small, the duration is short, the frequency range is large and contains a large number of high frequency signals, it was a large number of fibers break, which is the signal of happen immediately instability fracture [3].

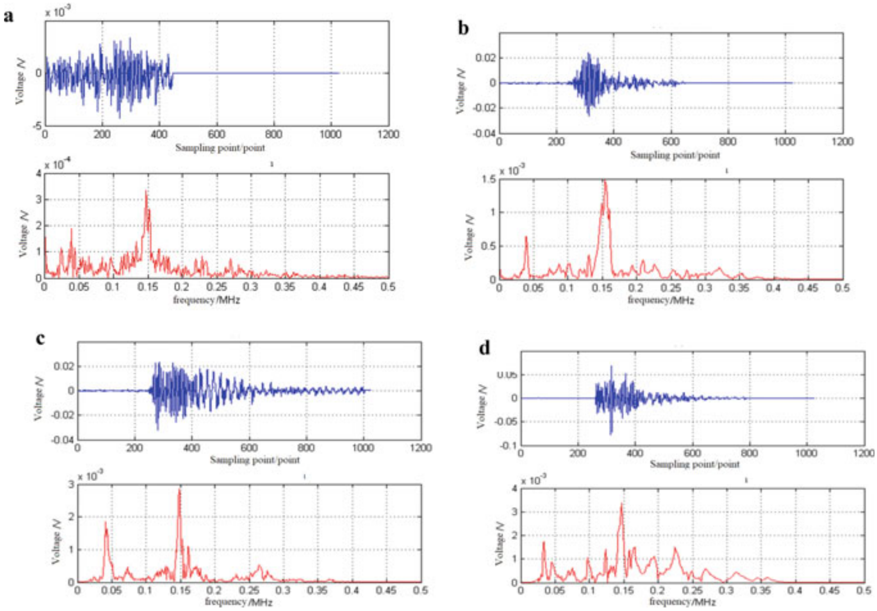

Fig. 48.4 AE signal during helicopter tail beam loading test. **a** Signal in fixture friction and fiber friction. **b** Signal in composite matrix deforms. **c** Crack initiation and propagation and interface debonding. **d** Large number of fibers break and instability fracture

48.5 Conclusion

The acoustic emission signals gained in helicopter tail beam loading testing were be analyzed by clustering analysis,the four types of signals gained, it was corresponding to load of the helicopter tail beam loading testing, We can extracting signal features of acoustic emission to judging the safety of helicopter composite tail beam.

References

1. H. Zhenlong, S.H. Gongtian, W. Guanhua, L. Shifang, W. Zhanwen, Pattern recognition of Aircraft fatigue cracking based on Waveform analysis method and Artificial neural networks of Acoustic Emission signals. Trans. Mater. Report(China) **34**(3), 4–7 (2012)
2. W. Wei, L. Siyi, W. Guanhua, Research on acoustic Emission characteristics of honeycomb sandwich composite in compression damage. Trans. NDT(China) **27**(6), 110–113 (2013)
3. T. Jin, W. Guanhua, W. Wei, " ACCC conductor carbon fiber composite core damage Acoustic Emission signals. Trans. Sci. Technol. Eng. (China) **13**(14), 3978–3982 (2013)

Part VII
Miscellaneous

Chapter 49
A Comparison of Acoustic Emission in Cadaveric Specimens and Artificial Sawbones During Surgical Screw Implants

S. Grigg, B. J. Wright, and R. Pullin

Abstract The overtightening of cancellous surgical screws is a major problem for orthopaedic surgeons, especially inexperienced ones. This problem is made worse still when the patient suffers from osteoporosis, which significantly reduces the density of the bone. Overtightening a screw leads to stripping of the bone and potential complications to surgery leading to increased recovery time and potential expense to the health organisation. Acoustic Emission (AE) has previously been investigated to monitor the insertion of such screws into artificial Sawbones. This paper presents the testing of two sizes of surgical screws into both artificial Sawbones and cadaveric femurs monitored for AE using piezoelectric sensors. The results show that there are some significant differences between the AE given off from the two structures when the energy and frequency of the waveforms are analysed.

49.1 Introduction

Orthopaedic surgeons use screws in most fracture fixation surgeries. There are, broadly speaking, two types of screw for the two types of bone: cortical and cancellous. Cortical bone is the outer layer of dense bone whereas cancellous bone is the inner core, which is typically more porous [1], as shown in Fig. 49.1. To enable cancellous screws to have optimal pull out strength they have an increased thread depth and reduced cross sectional thickness compared to cortical screws [2]. Cancellous bone screws are used for a range of orthopaedic surgeries for fixation into the metaphyseal area of bone such as femoral condyles. Cancellous bone, being less dense than cortical, can be difficult to gain suitable purchase into without risking stripping the bone, especially in osteopenic patients. Stripping a screw causes micro failure of material around the screw leading to screw loosening or complete failure. This can

---

S. Grigg (✉) · R. Pullin
Cardiff School of Engineering, Cardiff University, Cardiff, UK
e-mail: griggs@cardiff.ac.uk

B. J. Wright
Vestre Viken, Ringerike Sykehus, Hønefoss, Norway

© The Author(s), under exclusive license to Springer Nature Singapore Pte Ltd. 2021

G. Shen et al. (eds.), *Advances in Acoustic Emission Technology*, Springer Proceedings in Physics 259, https://doi.org/10.1007/978-981-15-9837-1_49

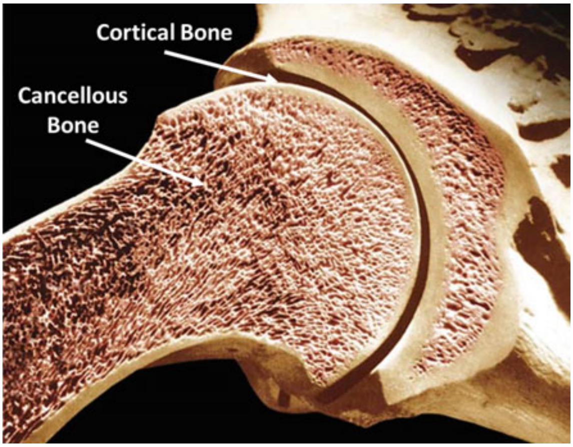

Fig. 49.1 Cut out image of hip joint with cortical and cancellous bone annotated. Adapted from [9]

cause complications including increased fracture healing time, fibrous non-union of the fracture, incorrect positioning of the articular surface or premature failure of the implant particularly in bone with osteoporosis [3]. Overall screw stripping has been shown to lower the pull-out strength of the screw by 80% [4]. Currently surgeons tighten a screw based on experience and feel, this means that it is not always successful. A study of experienced trauma surgeons by Andreassen et al. [5] analysed the insertion of 225 screws, it was found that 86 (38%) of these were stripped. Stoesz et al. [6] had similar findings when assessing 10 surgeons insert a total of 240 screws in artificial bone, with 109 (45.4%) stripping. What is worrying is that 90.8% of the time the surgeon did not realise that it had stripped. These values are anticipated to be much higher in new, inexperienced surgeons, as studies have shown that they have not yet got the right ‘feel’ of the correct torque to apply [7]. This problem is made worst still when surgery is being performed on older, or osteoporotic patients, for which bone mineral density (BMD) is reduced [8].

A device which can tell a surgeon when to stop tightening a screw would be very beneficial. One avenue that has been explored is the use of torque limiting drivers, which have been applied for screws in cortical bone, based on an approximation of the BMD. In cancellous bone, if the BMD (such as through a computerized tomography (CT) scan) is known it is possible to accurately predict the stripping torque [10]. This in practice however is not ideal as a CT scan is costly and time consuming, also as density varies greatly in patients with osteoporosis can be seen in Fig. 49.2, the exact value for BMD in the exact region is very difficult to know. Gilmer and Lang [11] investigated approximating the pullout force, and so required torque of screw insertion, by analysing the drill motor energy. In this work a good relationship ($r^2 = 0.95$) was found between drilling energy and pullout force in artificial cortical bone. This shows good potential; however no testing was conducted within cancellous bone models.

It is clear that alternative technology needs investigation, either to identify the point at which tightening of a screw should be stopped, or to approximate the BMD in

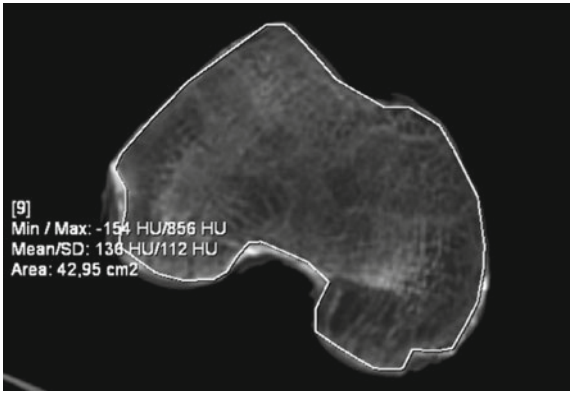

Fig. 49.2 Cross sectional intercondylar axial slice of a left distal femur from a cadaver with osteoporosis. The region of interest has been drawn around excluding the thin cortical wall. Light areas represent high density and dark low

order to predict the required stopping torque. One area of interest for this is the monitoring of Acoustic Emission (AE) during screw insertion. A study was conducted by Pullin et al. [12] where this was done for cancellous screws in artificial bone models, called Sawbones [13]. Sawbones are made from solid rigid polyurethane foam [13] and are the ASTM standard for testing of Orthopaedic Devices and Instruments [14] and they are used to train surgeons how to perform screw insertions correctly. In this work a commercially available AE system was used to monitor the tightening of screws in PCF 15 Sawbones blocks, which represent healthy cancellous bone. This work was a good preliminary study, and identified a change in AE energy acquired at different stages of the tightening process. It was theorized that the monitoring of AE could enable a stopping criterion to be identified, to inform the surgeon when to stop tightening the screw.

This work presents the findings of further testing of orthopaedic screw insertion monitored for AE. For this a bespoke data acquisition environment was created within LabVIEW, an overview of this is given. The LabVIEW equipment was used to monitor not only the insertion of surgical screws in a variety of sawbones densities, but into 12 cadaveric specimens of differing quality. This data is presented as well as some trends discovered from its analysis.

49.2 LabVIEW Development

For this testing a custom LabVIEW environment was developed in order to acquire AE data which was run on a National Instruments PXIe-1071 system. This was used instead of a commercial AE system for two main reasons. Firstly, it enabled a variety of parameters to be recorded from a single device, all time synchronized together. During this testing as well as AE data axial load between the screw and the bone was recorded using a doughnut load cell at 100 Hz, this is beneficial as there is a good relationship between axial load and torque when inserting surgical screws [15]. Shear strain is currently being added to the system; however, it was not in place during the testing presented. The second main reason for using the LabVIEW system is that it enables further processing to be performed live, such as waveform classification and filtering. This live processing and user feedback is vital so that the system can inform the operator to stop tightening the screw, if a stop criteria can be developed.

AE was acquired using a Mistras Pico piezoelectric sensor bonded to the shaft of the screwdriver using superglue. A Mistras 2/4/6 preamplifier with a built in 20 kHz–1200 kHz analogue filter and external power source was used to amplify the signal, with gain set to 40 dB. Data was recorded on a 'hit' basis, i.e. when a threshold is crossed a certain quantity of data is recorded as well as a pre-trigger. For this testing a threshold of 0.1 V (60 dB) was used and 2 ms of data recorded of which 400 μs was pre-trigger. After each hit a timeout period of 3 ms was put in place. The signal was sampled at 2 MHz.

49.3 Test Methods

Two different screws were tested for this work; a Synthes standard AO large fragment set and a small fragment set. The large fragment set consisted of a screw with a 3.2 mm inner core and 6.5 mm outer thread diameter. For this a 3.2 mm hole was drilled and the corresponding AO screwdriver used. A Pico sensor was bonded using superglue to the curved surface near the end of the driver, as shown in Fig. 49.3a. The small fragment set consisted of a 2.5 mm inner core screw with 4 mm outer thread diameter. For this a 2.5 mm hole was drilled and the corresponding AO screwdriver used with Pico sensor bonded to the same location as the large fragment set. The hole was left untapped as the screws were self-tapping. The two screws can be seen in Fig. 49.3b. Tightening of the screws were performed half a turn at a time in all testing.

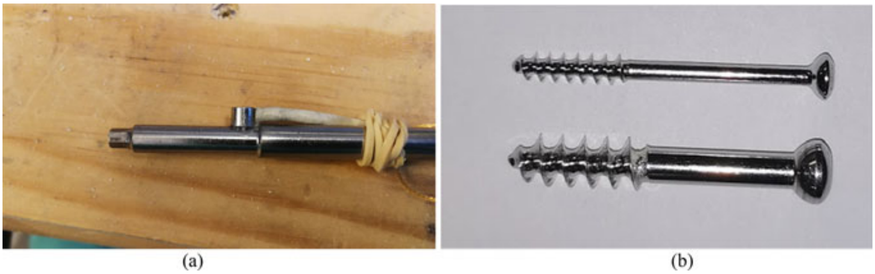

Fig. 49.3 Pico sensor bonded to standard AO large fragment screwdriver (**a**) and both screws (**b**)

49.3.1 Sawbones

Sawbones blocks are available in a large variety of densities ranging from PCF 3 (48 kg/m^3) to PCF 50 (800 kg/m^3) and represent a variety of differing bone types and quality. For this testing PCF 3, 5, 8, 10 and 15 were tested with both screws and 5 tests on each; a total of 50 tests. A direct comparison to bone health is difficult, however these Sawbones represent low-good quality cancellous bone. Holes were drilled using a pillar drill to ensure they were perpendicular to the surface of the structure.

49.3.2 Cadaveric

A total of 12 femurs were used for cadaveric testing, these were from six pairs of femurs harvested from human bodies donated for research at the Division of Anatomy, University of Oslo, Norway. Four of the pairs were from females and two from males between the ages of 68 and 89 years old (mean 82). They had been prepared in 5.6% formalin embalming solution and preserved in 40% ethanol. CT was used prior to screw testing to assess the lateral condyles (knee) which was the region of interest for this testing, an image of one of these scans is shown in Fig. 49.2. These results showed that the cancellous bone quality was low. The CT found the Hounsfield Units (HU) (a measure of radiodensity) within the cancellous region. The relationship between HU and BMD was investigated by Schreiber et al. [16] an approximation of the relationship can be made by interpreting their presented data, this relationship is shown in (49.1).

$$BMD = \frac{25 + HU}{1.25} \tag{49.1}$$

For each specimen at least five tests were conducted; however, in some cases sporadic results meant more were performed. Each insertion was performed by BJ Wright, an experienced orthopaedic surgeon. A photo of the setup is shown in Fig. 49.4. Holes were drilled using a hand drill.

49.4 Results

The results from the CT scans on the femurs produced the metric HU for each of the specimens, these are shown in Table 49.1. These were converted to BMD using (49.1) for further processing.

The data collected by the LabVIEW system was extracted and post processed. An example set of data collected from Sawbones can be seen in Fig. 49.5a where the cumulative AE energy per turn has been plotted alongside the axial load. A cadaveric

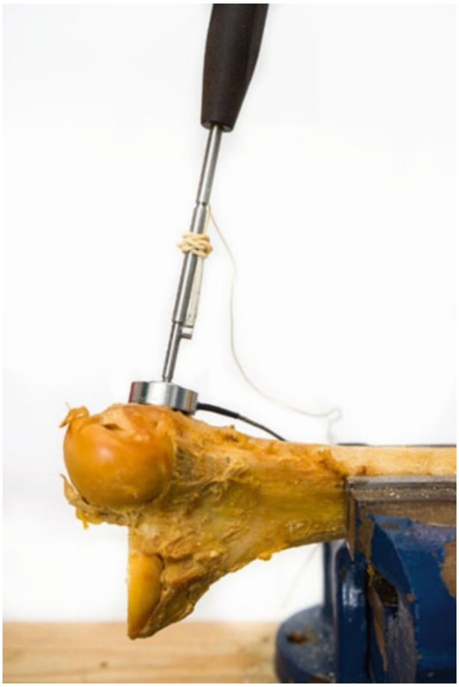

Fig. 49.4 PICO sensor bonded to screwdriver and load cell during cadaveric test

Table 49.1 Hounsfield units for the cadaveric test specimens

Cadaver ID	18	21	22	30	35	37
Right Femur HU	136	183	82	206	62	179
Left Femur HU	208	194	83	218	80	198

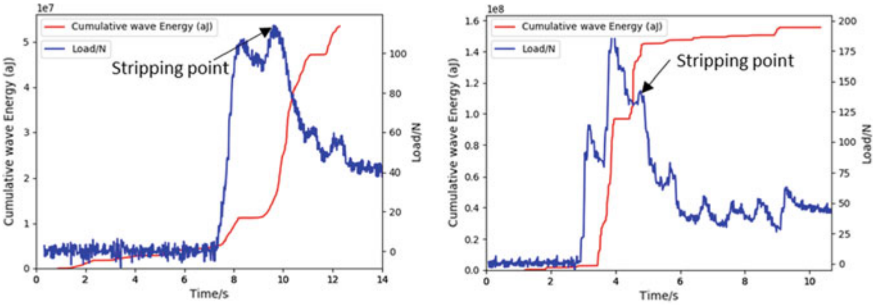

(a)

(b)

Fig. 49.5 Cumulative AE energy versus Time, alongside Load for test using large fragment set on PCF 8 Sawbones (BMD of 128) (**a**) and on right femur 18 (BMD 163) (**b**)

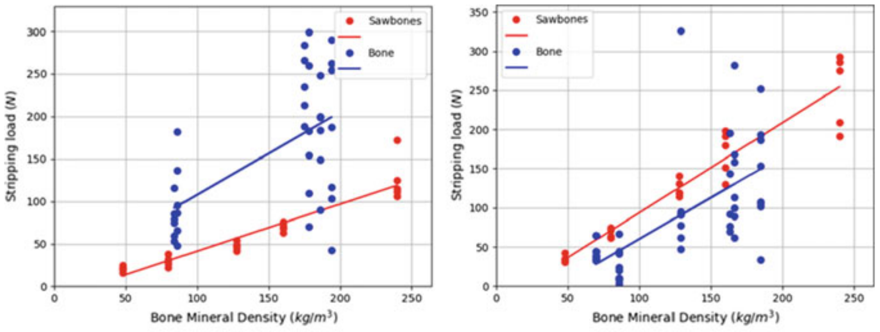

(a) (b)

Fig. 49.6 BMD versus Stripping load for small fragment set testing on Sawbones and left femurs (**a**) and large fragment set testing on Sawbones and right femurs (**b**) with linear regression

test example is shown in Fig. 49.5b. The load (continuous line) can be seen to drop between turns, this is a result of the load being applied by screwdriver no longer being in place. This means that the maximum load is not always the stripping load, as in the case in the example shown in Fig. 49.5b. The stripping load has been identified as the point where load drops whilst AE is still being collected.

The stripping load compared to BMD for both Sawbones testing and cadaveric testing for the small fragment set is shown in Fig. 49.6a where linear regression has been performed. The r^2 for the Sawbones tests is 0.89 and 0.34 for the cadaveric. The same results for the large fragment set are shown in Fig. 49.6b where the r^2 for the Sawbones testing is 0.92 and 0.36 for the cadaveric.

In addition to the stripping time and load the point at which load began was identified, this is important as it allows the AE recorded prior to loading be differentiated from the AE during loading. The cumulative AE energy collected between load being applied and the point of stripping was considered for each test. It can be seen in Fig. 49.7a, b that only a week relationship exists between cumulative AE energy between initiation of load and the point of stripping and BMD. The r^2 values for the large fragment testing were 0.37 for sawbones and 0.18 for cadaveric. For the small fragment testing they were 0.12 for sawbones and 0.23 for cadaveric. The relationship between cumulative AE energy and stripping load was slightly weaker.

The frequency content of received signals was also analysed using a Fast Fourier Transform (FFT) on each recorded waveform. The output of the FFT was then normalized and the average frequency content of each test found, this was then put into 5 kHz bands. The results from this analysis are shown in Fig. 49.8 for each of the different test configurations.

The results shown in Fig. 49.8 show that the testing on Sawbones showed an increased relative level of high frequency content. This was investigated further by extracting the average normalized frequency content between 300 and 500 kHz, this has been plotted against BMD in Fig. 49.9a, b for the small and large fragment testing, where a linear regression model is also shown. No relationship was present

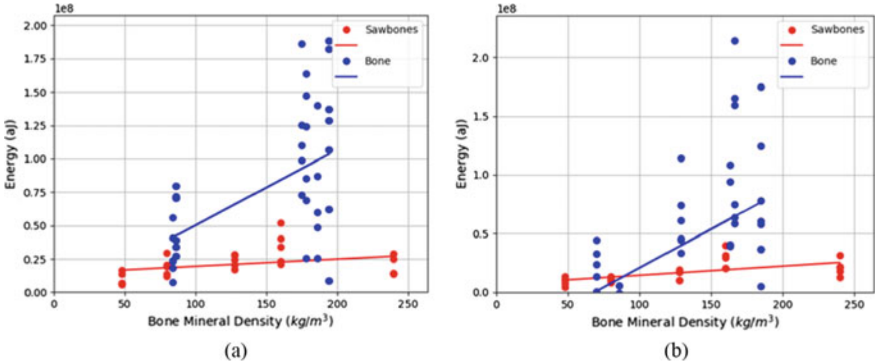

Fig. 49.7 Cumulative AE energy versus BMD for small fragment set testing on Sawbones and left femurs (**a**) and large fragment set testing on Sawbones and right femurs (**b**) with linear regression

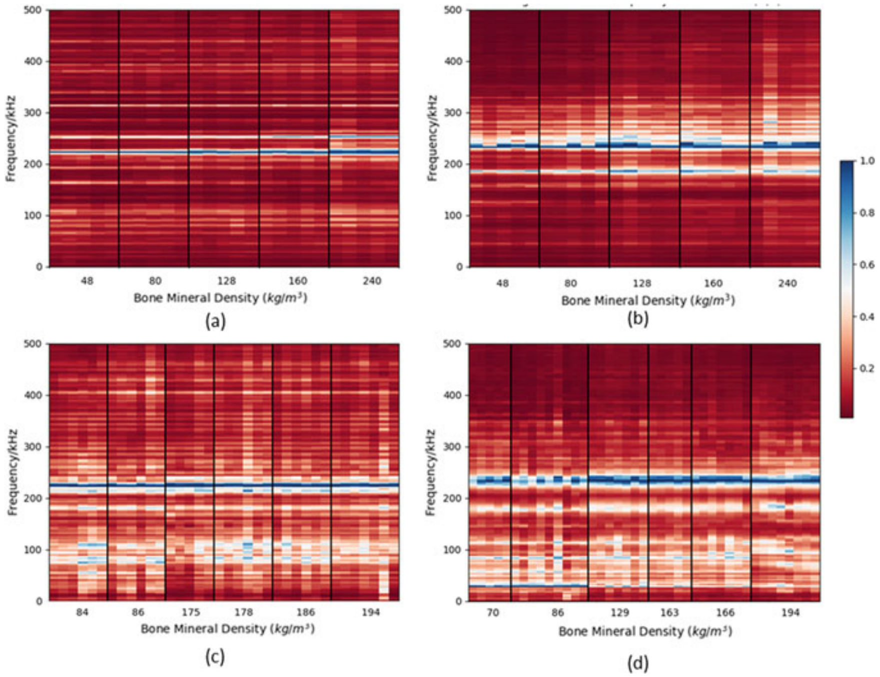

Fig. 49.8 Normalized average frequency of each screwdriver test with small fragment set results for sawbones (**a**) and cadaveric (**c**) and large fragment set results for sawbones (**b**) and cadaveric (**d**)

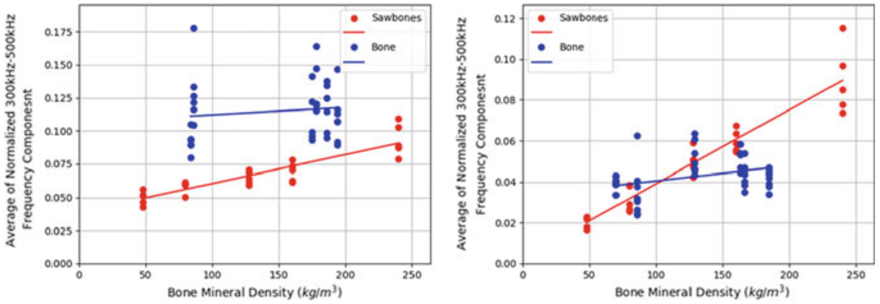

(a) (b)

Fig. 49.9 Sum of 300–500 kHz normalized frequency component versus BMD for small fragment set testing on Sawbones and left femurs (**a**) and large fragment set testing on Sawbones and right femurs (**b**) with linear regression

for the cadaveric testing data, the Sawbones however gave an r^2 of 0.8 for the small fragment set and 0.9 for the large fragment set.

49.5 Discussion

The selection of results presented in the previous section have identified several similarities as well as differences between the AE produced within Sawbones compared to that produced within real bone. The general relationship identified by Pullin et al. [12] was that some AE was generated prior to axial loading and once load was applied it increased significantly, once stripping has occurred and the load dropped the rate of AE energy acquired also dropped. This same relationship was seen in both Sawbones and real bone, an example of which can be seen in Fig. 49.5.

The acquisition of axial load alongside AE using a doughnut load cell was vital in order to identify the point of stripping. It also gave a measure of the strength of the screw in place and an approximation of the maximum torque required to insert it. The Sawbones testing identified a strong relationship between the density of the material and the axial load at point of stripping, as seen in Fig. 49.6, where an r^2 of around 0.9 was seen for both small and large fragment sets. This strong relationship is to be expected as the uniform nature of the Sawbones block and good repeatability of testing ensure each screw insertion is similar. Error was still present however; the main source is assumed to be a result of the force applied by the user when inserting the screw varying. The axial load at stripping in the cadaveric testing gave a much weaker relationship. Although a positive relationship between increase BMD and higher stripping load was seen, the r^2 value for this correlation in both small and large fragment sets was around 0.35, a not particularly meaningful relationship. A large factor for this weak correlation is that BMD is an average of the cross section, not the BMD at a point. In osteoporotic patients this varies heavily depending on location, shown clearly in Fig. 49.2 where some regions are very dense and others very weak. Other factors will also have affected the result. The axial load recorded will have been affected by the force applied by the operator as was the case with the Sawbones testing. The load cell itself is also likely to not have been completely accurate, this is due to factors such as the angle of the hole relative to the surface, the fact that the surface itself is not flat and was covered in a non-uniform thin layer of tissue. These factors all affect the distribution of load over the cell, decreasing its accuracy.

Comparing the linear regression models of Sawbones and cadaveric testing showed a good relationship for the large fragment set was very good. The error could be a result of the aforementioned issues with acquiring load during the cadaveric testing, or the conversion of HU to BMD being inaccurate. The small fragment set testing produced significantly different models between Sawbones and cadaveric testing. The reason for this is not fully clear, however most likely due to variations in the BMD across the bone being more influential on the screws smaller tooth area.

It was proposed by Pullin et al. [12] that cumulative AE energy could be used as a stop criteria to prevent stripping of the screw. For this to be possible AE energy given off would need to be constant no matter the density of the bone. Figure 49.7 shows that this is not the case in Sawbones or cadavers. The linear regression models show an increase in AE energy recorded with increase BMD for all test configurations, however it is always with a low correlation. Although this result is not positive, there is a flaw in the testing that could have caused this; the testing was performed by hand. This means that the rate at which the screw was tightened will have varied. It also meant that tightening had to be stopped every half a turn, in some cases the screw had load applied and stripped within one turn, in others it spanned multiple turns; this will have influenced the AE acquired. One way to combat this would be to test with a constant rate machine driven device. Collecting the torque in the screwdriver would also be beneficial, as it is not dependent on some of the factors mentioned.

The frequency results presented in Fig. 49.8 show that peak frequency is dictated by the set used, a peak of 220 kHz is seen on the small fragment set and 230 kHz when using the large fragment set, be it when inserting screws to Sawbones or cadavers. A lot of differences in frequency component can be seen between cadavers and Sawbones. One obvious difference is the significantly lower low frequency component within the Sawbones compared to the cadavers testing. This additional low frequency is likely the reason for the higher cumulative energy within the cadaveric testing. The Sawbones however have a strange trend in their higher (300–500 kHz) region; as BMD increases as does the average high frequency component, as shown in Fig. 49.9. This strong correlation would enable a prediction of the BMD, and so required torque for optimal tightening, to be made in the initial screw turning process, prior to load being applied. If this could be applied within cadavers it could stop surgeons overtightening and stripping screws. Unfortunately, this relationship is not present within cadavers and it is unclear why, however if a similar relationship could be found it would be very beneficial.

49.6 Conclusion

This paper has presented the results from screw insertion testing into both Sawbones blocks and cadaveric femurs. The general trend of AE seen was similar in both structures however some major differences were also seen. The most major of these being the cumulative energy being greater in the cadaveric testing. When frequency analysis was performed on the AE waveforms it showed that there was several significant differences between the two sets of tests.

The axial load results recorded from the testing showed an increase in axial stripping load with increased BMD, the relationship was strong in Sawbones but weak in cadaveric testing. As well as the variation in BMD across the bone issues there is believed to be some error as a result of the load cell not giving a correct reading. Ways to improve results in future testing would be to use a motor driven constant rate device to turn the screw or to integrate torque measurement into the test setup.

Acknowledgements Thank you to the Medical Research Council (MRC) for funding of the work presented within this paper through their Confidence in Concept (CIC) funding scheme. Additional thanks to the Institute of Mechanical Engineers (IMechE) and the South Wales Institute of Engineers Educational Trust (SWIEET) for funding to travel to the World Conference on Acoustic Emission (WCAE).

References

1. J.R. Chapman, R.M. Harrington, K.M. Lee, P.A. Anderson, A.F. Tencer, D. Kowalski, Factors affecting the pullout strength of cancellous bone screws. J. Biomech. Eng. **118**(3), 391–398 (1996)
2. S.M. Perren, Technical and biomechanical aspects of screws used in bone surgery. Int. J. Orthop. Trauma **2**, 31–48 (1992)
3. T. Drew, P. Allcock, A new method of fixation in osteoporotic bone: a preliminary report. Injury **33**(8), 685–689 (2002)
4. C. Collinge, B. Hartigan, E.P. Lautenschlager, Effects of surgical errors on small fragment screw fixation. J. Orthop. Trauma (2006)
5. G.S. Andreassen, P.R. Høiness, I. Skraamm, O. Granlund, L. Engebretsen, Use of a synthetic bone void filler to augment screws in osteopenic ankle fracture fixation. Arch. Orthop. Trauma Surg (2004)
6. M.J. Stoesz, P.A. Gustafson, B.V. Patel, J.R. Jastifer, J.L. Chess, Surgeon perception of cancellous screw fixation. J. Orthop. Trauma (2014)
7. R.A. McGuire, K.R.J. St, S.G. Agnew, Analysis of the torque applied to bone screws by trauma surgeons. Comparisons based on years of experience and material of implant construction. Am. J. Orthop. (Belle Mead, NJ) **24**(3), 254–256 (1995)
8. B. Li, R.M. Aspden, Material properties of bone from the femoral neck and calcar femorale of patients with osteoporosis or osteoarthritis. Osteoporos. Int. **7**(5), 450–456 (1997)
9. Encyclopædia Britannica Online, "Cancellous Bone [Image] (2019) [Online]. Available: http://media-3.web.britannica.com/eb-media/57/94557-004-CF63D396.jpg. Accessed: 15-Oct-2019
10. K.J. Reynolds, T.M. Cleek, A.A. Mohtar, T.C. Hearn, Predicting cancellous bone failure during screw insertion. J. Biomech. **46**(6), 1207–1210 (2013)

11. B.B. Gilmer, S.D. Lang, Dual motor drill continuously measures drilling energy to calculate bone density and screw pull-out force in real time. JAAOS Glob. Res. Rev. **2**(9), e053 (2018)
12. R. Pullin et al., Feasibility of detecting orthopaedic screw overtightening using acoustic emission. Proc. Inst. Mech. Eng. Part H J. Eng. Med. **231**(3), 213–221 (2017)
13. Sawbones, Sawbones Website [Online]. Available: sawbones.com. Accessed: 16-Oct-2019
14. A. F543-07, Standard Specification and Test Methods for Metallic Medical Bone Screws (2007)
15. K. Johnson, F. Smith, Axial compression generated by cortical and cancellous lag screws in the equine distal phalanx. Vet. J. **166**(2), 159–163 (2003)
16. J.J. Schreiber, P.A. Anderson, H.G. Rosas, A.L. Buchholz, A.G. Au, Hounsfield units for assessing bone mineral density and strength: A tool for osteoporosis management. J. Bone Jt. Surg. Ser. A **93**(11), 1057–1063 (2011)

Chapter 50
Acoustic Emissions of Cathode Carbon Block from Aluminum Electrolytic Cell Under Deformation

Yu Luo, Shengxiang Li, Chao Li, Xiling Liu, and Xibing Li

Abstract In order to understand the propagation mechanism of microcrack developing into destructive penetrating cracks and the evolution process of that in cathode carbon block, the acoustic emission (AE) characteristics of cathode carbon block in the process of failure were studied under uniaxial compression loads. The experiment results show that the failure process of cathode carbon block can be divided into four stages. Based on the characteristic parameters of AE signal and its macroscopic fracture state, the causes and corresponding fracture modes of AE signals in each stage are analyzed. In addition, AE signals in the failure process of cathode carbon block can be divided into four types according to *k*-means clustering analysis. According to the parameter characteristics, waveform characteristics, and time distribution of all types of signals, it can be concluded that class A signals correspond to tensile failure caused by the interaction of macro crack and the friction between aggregate particles in post-peaking stage. Class B signals are considered as the noise generated by the friction between the testing machine and the end face of the cathode carbon block. It is considered that class C signals correspond to the shear slip cracking before the macro cracking as well as the crack propagation and penetrating large-scale shear failure at the peak stress that affects the overall stability of the cathode carbon block. Class D signals are generated by the fracture of the connection between aggregate particles and the compaction of pores between aggregate particles during the early stage of loading. The results provide basic data and experimental basis for the detection of electrolytic cell damage in electrolytic aluminum industry.

Y. Luo · S. Li · X. Liu (✉) · X. Li
School of Resources and Safety Engineering, Central South University, Changsha 410083, China
e-mail: lxlenglish@163.com

C. Li
Aluminum Branch Company, Chongqing Qineng Electrictity and Aluminum Co., LTD,
Chongqing 401420, China

© The Author(s), under exclusive license to Springer Nature Singapore Pte Ltd. 2021

G. Shen et al. (eds.), *Advances in Acoustic Emission Technology*, Springer Proceedings in Physics 259, https://doi.org/10.1007/978-981-15-9837-1_50

50.1 Introduction

In the process of electrolytic aluminum production, the cathode carbon block suffers from the erosion of molten salt at high temperature and the electrochemical action in the process of electrolysis. The original microcrack expand under the action of molten salt erosion and mechanical stress, which will lead to the deformation, uplift and even fracture of the cathode carbon block, all of which will seriously shorten the life of the electrolytic cell [1, 2]. At present, the damage detection of cathode carbon block mainly base on physical indicators such as abnormal cathode voltage drop and temperature. However it is hard to infer the internal crack evolution process and damage degree of cathode carbon block, while acoustic emission (AE) is a promising technique showing great potential for real-time monitoring and condition evaluation of engineering materials and structures [3]. AE is the class of phenomenon whereby transient elastic waves originate from sudden energy release within material caused by crack, dislocation, friction, etc. Moreover, AE parameters are closely related to the crack evolution and fracture mode of materials (tensile fracture, shear fracture and their coupling fracture), such as ringing counts, amplitude, energy, frequency and *RA*-*AF* value, etc. [4–6]. Therefore, AE technology can be used to monitor the elastic wave signals generated by the cathode carbon block under the state of stress, which can obtain the degree of damage and crack growth of the carbon block, so as to provide experimental basis for online monitoring and failure prediction of the cathode carbon block in the service process.

Recently, the AE method has been utilized to monitor the microscopic and macroscopic crack initiation in various materials during deformation by many scholars. Yuyama et al. [4] used AE technology to monitor the fracture process of reinforced concrete columns subjected to simulated seismic lateral loads under different coaxial loads. Shiotani et al. [7] conducted fracture tests of bending and shear loads on rock materials, studied the variation of AE parameters with rock fracture process, and proposed the classification criterion of fracture state based on AE parameters, with good practical application effect. Soulioti et al. [8] showed that AE technology could be used to identify fracture patterns by a four-point bending experiment on steel fiber reinforced concrete beams. Additionally, as shear cracking follows tensile cracking, crack classification using suitable AE descriptors can assist the evaluation of the severity of the damage condition. Aggelis et al. [9] studied the propagation of elastic wave pulses in microstructure materials and used AE parameters to characterize the fracture properties of materials, such as *RA* (rise time/amplitude)-*AF* (average frequency) values. Villalobos [10] applied AE technology to monitor the drying process of bamboo, and pointed out that different avalanche degrees had different characteristics of AE parameters. Ioka et al. [11] studied the behavior of AE for four types of graphite to confirm the sources of AE events caused by tensile and compressive loading. Ekinaga [12] used AE method to monitor the initiation of macroscopic and microscopic cracks under three-point bending and studied the AE signal characteristics generated at each loading stage. Yonga et al. [13] studied the damage mechanisms of carbon fiber reinforced silicon carbide (C/SiC) composites

Table 50.1 The basic physical and mechanical properties of the sample

Sample	Density (g/cm^3)	Porosity (%)	Electrical resistivity (μΩ m)	Wave velocity (m/s)	Ash content (%)	Coefficient of thermal expansion (10^{-6}/K)
Cathode carbon block	1.61	7.89	44	2436	3.49	3.61

under static loading by using the AE technology. The *k*-means clustering method is used to analyze the AE signals and identified the three damage modes. Therefore, the analysis of AE characteristic parameters can well understand the fracture mode and stress state of the material and then evaluate the damage state of the material. However, the cathode carbon block will generate compressive stress under the action of thermal expansion after both ends are fixed in the electrolyzer, and the cathode carbon block will be damaged when the stress exceeds the ultimate strength. But few literatures have studied the AE characteristics of the cathode carbon block under compression. Therefore, in order to further understand the AE characteristics of cathode carbon blocks in the whole failure process, the AE signal characteristic parameters are analyzed, and the signals are classified through *k*-means clustering algorithm based on a variety of AE parameters, then the fracture mechanism of cathode carbon blocks are discussed during loading.

50.2 Experimental Details

50.2.1 Sample Preparation

The cathode carbon block of an aluminum factory was selected and processed into a φ 50 × 100 mm cylinder with a height-diameter ratio of 2:1 according to the size standard of the mechanical experiment. The basic physical and mechanical properties of the cathode carbon block are shown in Table 50.1.

50.2.2 Experimental Set Up

INSTRON 1346 electro-hydraulic servo universal testing machine was employed to carry out the uniaxial compression tests on the cathode carbon block, and the loading speed was 0.6 mm/min through displacement control. A PCI-2 system and two NANO30 sensors with 140 kHz resonant frequency were used for acquiring AE signals, as shown in Fig. 50.1. AE signals detected by the sensor were pre-amplified

Fig. 50.1 Schematics of experiment device

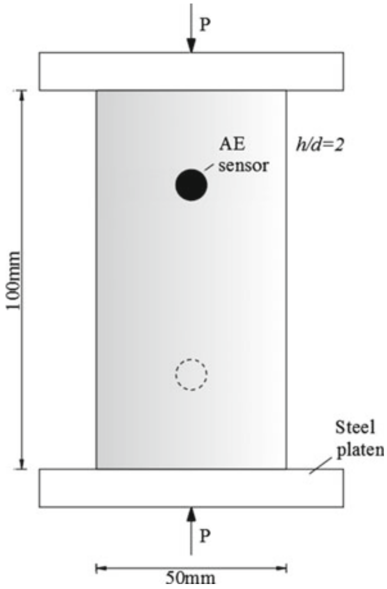

by 40 dB, the detection threshold was 40 dB, the sampling rate and sampling length were set at 10 Msps and 5 K, respectively.

50.3 Results and Discussion

50.3.1 Mechanical Behavior and Acoustic Emission Characteristics

As shown in Fig. 50.2a, the cathode carbon block undergoes four stages under uniaxial compression loads: compaction, elasticity, plasticity and failure. It is shown from the stress-time curve that the stages of compaction and elasticity of carbon block are not obvious, some lower amplitude and energy AE signals are emitted, which resulted from compacting of pores and damage of the connected aggregate particles in cathode carbon block. With the increase of stress, the cathode carbon block enters the stage of plastic deformation, and the internal microcracks gradually propagate and the connections between more aggregate particles are broken, which causes intense AE activities. In particular, plenty of signals with high amplitude and energy are generated in the stress level ranging of 65–97%, and there are almost no AE signals with low amplitude at this stage. After the peak stress, the stress decreases with the increase of time, the cracks expand rapidly, and the macro cracks relate to each other, which is accompanied by a large number of AE events. Different

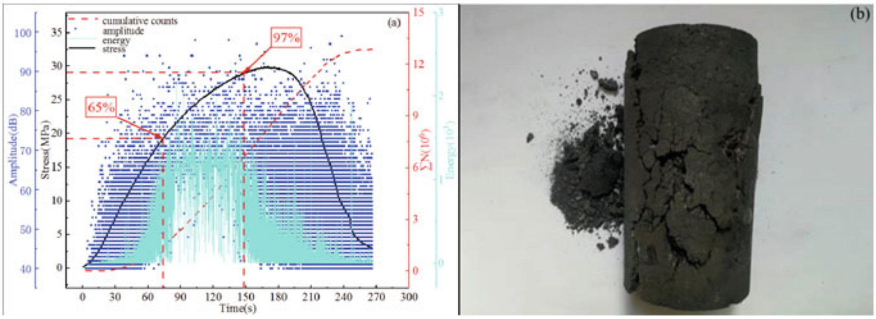

Fig. 50.2 **a** Variation of the stress, AE counts, amplitude and energy with time under uniaxial compression loads. **b** The failure mode of cathode block under uniaxial compression loads

from brittle materials such as rocks, the cathode carbon blocks show strong plasticity instead of obvious stress drop at the post-peaking stage. Figure 50.2b shows the macroscopic failure mode of cathode carbon block under uniaxial compression loads. There are two obvious macro shear cracks on both sides of the upper part which intersect the middle part of the sample. A few aggregate particles are peeled off, and there are many disordered small cracks that showed a "branched" phenomenon in the lower part of the sample. However, it can be seen from the connection trend of the micro-cracks that the internal failure mode of the cathode carbon block is *X*-type conjugate shear failure. During the whole loading process of the samples, the macroscopic cracks were obvious before the peak strength. With the progress of loading, the cracks in the carbon block interacted with each other, and the aggregate particles on the surface dropped off, resulting in the final unstable of the carbon block.

Generally speaking, higher *RA*-value and lower *AF*-value correspond to shear fracture, while lower *RA*-value and higher *AF*-value correspond to tensile fracture. The variation of *AF*-value from high to low indicates that the transition from tensile crack to shear crack, which may also be related to large-scale tensile fracture [14, 15]. As shown in Fig. 50.3a, the *RA*-value increases first and then decreases, while

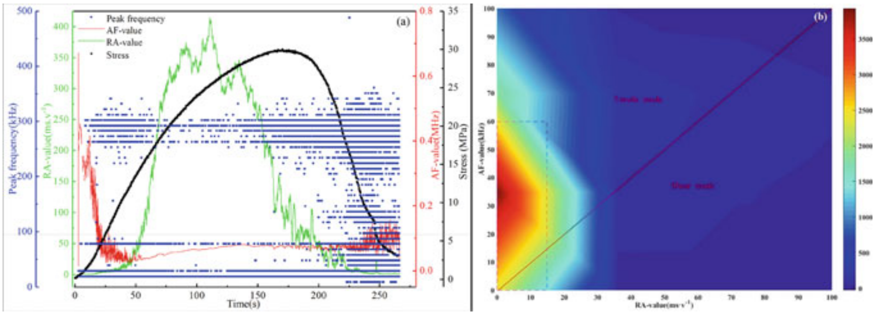

Fig. 50.3 **a** Variation of the *RA*-*AF* value during uniaxial compression in cathode carbon block. **b** Distribution of *RA*-*AF* values during uniaxial compression in cathode carbon block

the *AF*-value is on the contrary. In the initial loading stage, tensile cracks are the main fracture mode of the specimen. With the increase of stress level, there is a transition from tensile to shear fracture, so that large macroscopic shear cracks occur until the late plastic stage. After entering the peak stress, because the carbon block still has a certain bearing capacity, the interaction of macroscopic cracks and the friction between aggregate particles in the block lead to more tensile fractures. As shown in Fig. 50.3b, the distribution characteristics of the cathode carbon block with high *AF*-value and low *RA*-value are relatively significant under uniaxial compression loads, indicating that the fracture mode is mainly tensile fracture.

50.3.2 Cluster Analysis of AE Parameters

50.3.2.1 The *k*-Means Clustering Algorithm

As mentioned above, AE parameters such as rise time, ringing counts, duration, energy, amplitude and peak frequency can all identify the crack evolution process of cathode carbon block during the fracture process to a certain degree. However, it is not clear which parameter of AE signal is sufficiently representative. Therefore, in order to deeply understand the characteristics of fracture signals of cathode carbon blocks in the whole process of failure, *k*-means clustering method is adopted to conduct multivariate analysis of AE signals, so as to identify the crack types of AE signals [16, 17].

Commonly, AE counts and hits reflect the number of cracks and the degree of damage, amplitude and energy are used to describe the strength of the AE signals which is associated with the scale of cracks, peak frequency has close relationship with crack type, duration and rise time can be used for waveform identification [18]. Thus, according to the relationship between AE characteristic parameters and fracture mechanism, the rise time, duration time, ringing counts, amplitude and peak frequency were selected as sample variables. Before clustering, these parameters were normalized to the range of [0,1] to construct the pattern vector so as to eliminate the influence of physical dimension on classification, its principle is to convert data into the interval of [0,1]. For any variable, row *i* and column *j* can be expressed as

$$x'_{ij} = \frac{x_{ij} - x_{j\text{min}}}{x_{j\text{max}} - x_{j\text{min}}} \tag{50.1}$$

where x'_{ij} and x_{ij} are the standardization and original parameters of AE signals,$x_{j\text{max}}$ and $x_{j\text{min}}$ are the maximum and minimum values of column *j*, respectively.

The *k*-means algorithm randomly selects *k* coordinate points from the standardized data as the initial cluster coordinates, calculates the distance from each AE signal point to these cluster centers according to the Euclidean distance formula (refer to 50.2), and classifies them into the class corresponding to the nearest cluster center according to (50.3). Then the cluster center is updated, and the mean value of all objects in the cluster is taken as the new cluster center. Repeat the previous steps until the cluster center does not change. Equations 50.2 and 50.3 are shown as follows [19]:

$$d_{ij}^2(2) = \sum_{k=1}^{N} \left\| x'_{ik} - x'_{jk} \right\|^2 \tag{50.2}$$

$$d_{ij}^2(2) = \sum_{k=1}^{N} \left\| x'_{ik} - x'_{jk} \right\|^2 \to \min \tag{50.3}$$

where $x^{'}_{ik}$ and $x^{'}_{jk}$ is the vector composed of the original and standardized parameters of the AE signals.

In order to ascertain the number of clusters, each k value from 2 to 10 was selected, and clustering was performed. The optimal value of k was determined according to the elbow method [20] and silhouette value method [21]. The elbow method is based on the principle of the sum of squares of errors (SSE), which is the clustering error of all samples. The silhouette-value method is used to measure the degree of clustering and dispersion of clusters, whose value range is [−1,1]. When k corresponds to the inflection points in the SSE-k value curve in the elbow method and the maximum value in the silhouette-value method, it is the optimal clustering number. SSE and silhouette values are defined as [22, 23]:

$$SSE = \sum_{i=1}^{k} \sum_{x \in C_i} (x - \overline{A_i})^2 \tag{50.4}$$

$$S = \frac{1}{n} \sum_{1}^{n} \frac{\min(b_{i_j}) - a_i}{\max\left\{\min(b_{i_j}), a_j\right\}} \tag{50.5}$$

where C_i represents the sample set of cluster i, x represents the sample points in the collection C_i, A_i represents the average value of all samples in cluster i. a_i is the average distance of sample x_i to other sample points in the same cluster, and b_{ij} is the average distance of sample x_i to all sample points in other clusters.

50.3.2.2 Cluster Analysis

According to the above clustering method, the amplitude, peak frequency, counts, rise time and duration of AE signals from the cathode carbon blocks under the uniaxial compression loads were extracted as the characteristic parameters to form a pattern vectors after normalization. Then, clustering analysis was conducted on these vectors to obtain k clusters related to the failure mode. Figure 50.4 shows the silhouette value, the SSE value and the number of classification, k. When the AE signals are classified

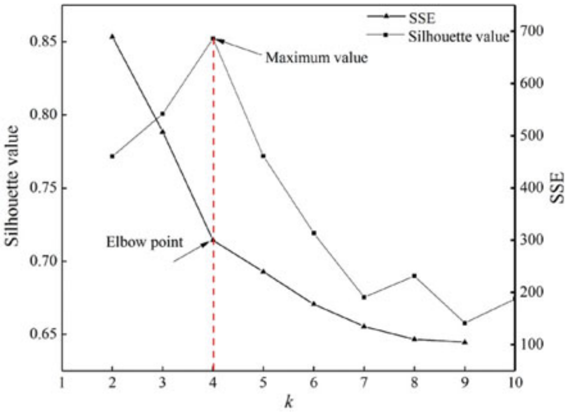

Fig. 50.4 Silhouette and SSE values as a function of the number of clusters, *k*

into four types, the silhouette value has a maximum of 0.8522, corresponding to the elbow point in the curve of SSE-*k*, which confirms the efficiency of the clustering. Figure 50.5 shows the distribution of four clusters of AE signals (labeled A, B, C and D respectively) in each parameter space. It can be seen from Fig. 50.5a that the peak frequency of class C and D signals is distributed at 0–175 kHz and cannot be classified from the peak frequency. However, the amplitude distribution of class C signals is significantly higher than that of class D, where the amplitude of class D signals is between 40 and 52 dB and class C signals is between 51 and 99 dB; The peak frequency of class A signals is distributed at 160–350 kHz, and the amplitude is distributed at 40–99 dB, and the peak frequency is obviously higher than that of class C and D signals. The peak frequency of class B signals is distributed between 0–100 kHz and 230–330 kHz, and the amplitude is distributed between 58 and 99 dB, which can't be separated according to the peak frequency and amplitude. Figure 50.5b shows that the four clusters of AE signals are distributed in the peak frequency and duration space. Among them, class A, C and D signals overlap with each other in the low duration, while class B signals have a relatively long duration and are distributed in 3.5×10^4–10×10^4 μs, which is significantly higher than the other three kinds of signals. Figure 50.5c, d respectively show the distribution of the four clusters of AE signals in the duration, rise time and amplitude space. Class B signals have higher amplitude, duration and rise time, which are significantly different from class A, C and D signals. Therefore, important information can be extracted on whether the parameter is appropriate in discriminating the AE signals. In frequency space, class A, C and D are clearly separated from each other with their distinct frequency bands (see Fig. 50.5a, b),indicating that it is a classifier of the AE signals. However, in the space of duration and rise time, class B signals are obviously different from class A, C and D signals, which can also be used as AE signal classifier (see Fig. 50.5c, d). The value range of characteristic parameters of various AE signals are shown in Table 50.2.

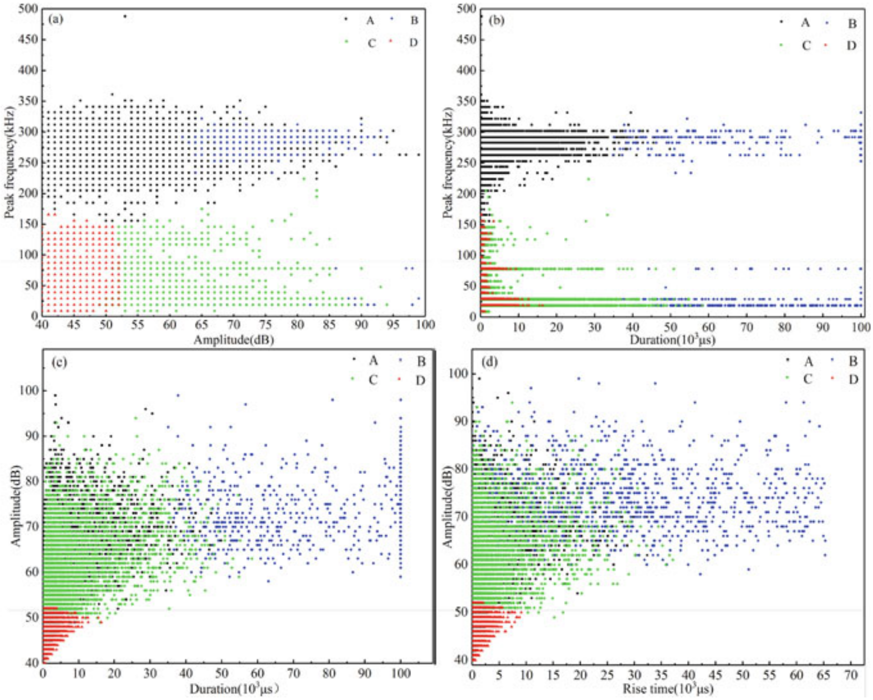

Fig. 50.5 The distribution of four types of AE signals from cathode carbon block under compression in **a** a peak frequency–amplitude space, **b** a peak frequency–duration space, **c** an amplitude–duration space, and **d** an energy–rise time space

50.3.2.3 Fracture Mechanism Analysis of Clustered Signals

The previous results show that the fracture scale of rock is directly proportional to the energy and the amplitude parameters of the AE signal. In the process of rock fracture, the signal of large-scale fracture is characterized by low frequency, high energy and amplitude; the signal of small-scale fractures is characterized by low amplitude, low energy and coexistence of low, medium and high frequency [24]. As shown in Fig. 50.6, according to the energy distribution and the law of cumulative ringing counts of various AE signals in the uniaxial compression process of the cathode carbon block, the whole loading process can also be divided into four stages, which is consistent with the analysis in 3.1 above. Most AE signals of class A, C and D appear in the early phase of loading and post-peaking phase, and have lower energy than those of class B signals; among them, the energy distribution of class D signals is below 250 mV ms, and the corresponding frequency and amplitude are also lower. The energy of class C signals is less than 800 mv ms, and the corresponding frequency is lower and the amplitude is higher. Most of class A signals have lower energy than 800 mV ms, and the corresponding distribution of frequency is higher, and the amplitude distribution is more scattered. Class B signals all appear in the

Table 50.2 Statistical table of characteristic parameters of acoustic emission of various kinds of signals

Cluster	Amplitude (dB)	Frequency (kHz)	Duration (μs)	Rise time (μs)	Ringing counts	Energy (mV ms)	Proportion (%)
A	[40,99]	[156,350]	[0,35814]	[0,17207]	[1,3846]	[0,1831]	32.15
B	[58,99]	[19,78] [234,322]	[34822,100000]	[12,65292]	[1804,11145]	[360,2171]	1.91
C	[51,99]	[9,175]	[77,58383]	[0,37126]	[7,3981]	[1,755]	10.77
D	[40,52]	[9,166]	[0,16283]	[0,9070]	[1,474]	[1,202]	55.17

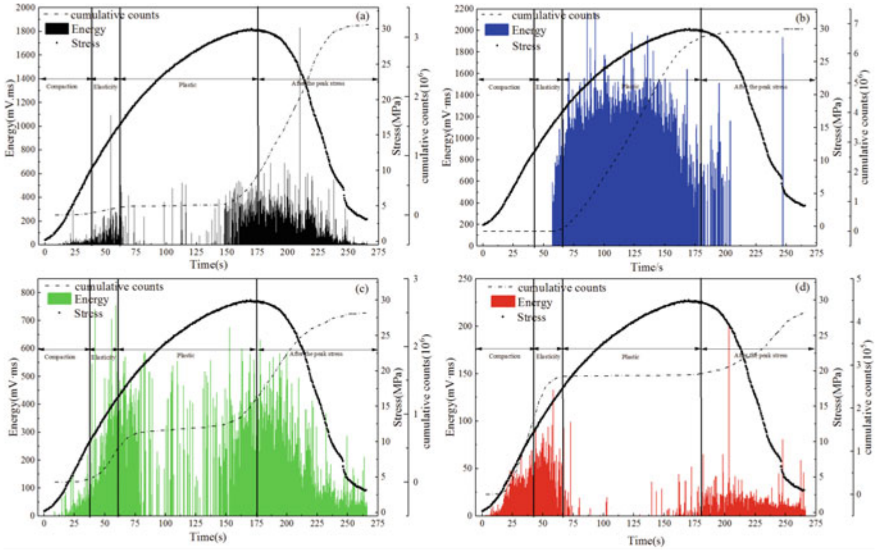

Fig. 50.6 Energy distribution and cumulative counts of four types of signals; **a** Class A signals. **b** Class B signals. **c** Class C signals. **d** Class D signals

plastic stage, the energy of most of the corresponding AE signals is greater than 800 mV ms, the corresponding amplitude is also high, and the frequency is mainly distributed between 19–78 kHz and 234–322 kHz.

It can be seen from Fig. 50.7 that the four types of signals all correspond to two types of cracks, but the distribution trend of high *RA* values and low *AF* values of D, A, C and B signals is gradually significant, indicating that the failure mode of shear cracks corresponding to the four types of signals is gradually increasing. This can be found from the feature parameters value range of various AE signals in Table 50.2 that class A signals are mainly medium and high frequency, and most of the signals are inclined to the *AF* value axis, that is, such signals are mainly generated in the tensile failure mode. Since the cumulative counts of the class A signals increase rapidly in the post-peaking phase, the damage caused by class A signals are mainly distributed in the post-peaking phase. Therefore, it is considered that these signals correspond to tensile failures of the cathode carbon block caused by the interaction of macro crack and the friction between aggregate particles after peak stress. The amplitude, rise time and duration of class D signals are small, and the AE signals are more inclined to the *AF* value axis. In addition, the ringing counts have increased significantly in the early stage, so AE signals mainly distributed in the early stage of loading. These signals may be generated by the sudden fracture between the aggregate particles in the cathode carbon block and the compaction of the pores between the aggregate particles at the early stage of loading. The energy of such signals is far less than that of class A signals, so the degree of rupture is also far less than that of class A signals. The signals of class C show the characteristics of high amplitude, medium

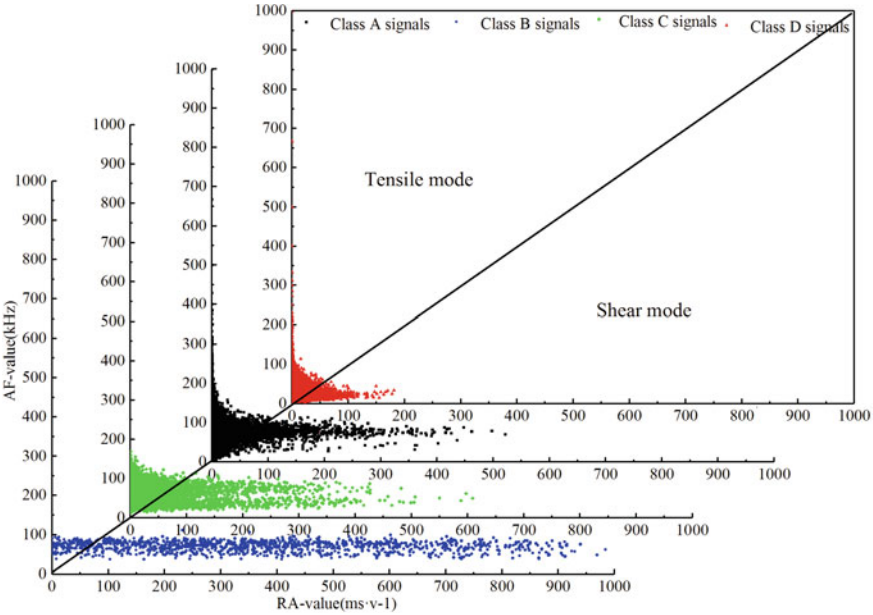

Fig. 50.7 The *RA-AF* value distribution trend of four types of signals during the failure of cathode carbon block

and high energy, and the AE signals are more inclined to the *RA* value axis. This type of signal is mainly distributed in the initial loading stage and peak stress stage, it is considered that such signals correspond to the shear slip cracking before the macro fracture as well as the crack propagation and penetrating large-scale shear failure at the peak stress that affects the overall stability of the cathode carbon block. Class B signals are mainly distributed in the plastic stage, showing the characteristics of high amplitude and high energy. This type of AE signals is mainly inclined to the *RA* value axis, but its average frequency is below 100 kHz, so it is considered as the noise signals generated by the friction between the testing machine and the end face of the cathode carbon block. Figure 50.8 shows the typical waveforms of the four types of AE signals. The rise time, ringing counts, and duration of the class A and D signals are lower, and the waveform attenuation is faster. But the rise time and duration of the class A signals are slightly larger than the signals of class D, so the frequency of class A signals ringing counts is relatively low, both of which are obviously burst type signals. The ringing counts and duration of class C signals are maintained at a high level, and the waveform shows that the signals are continuous type. The average frequency of the class B signal is very low, and its waveform has the characteristic of typical vibration signals.

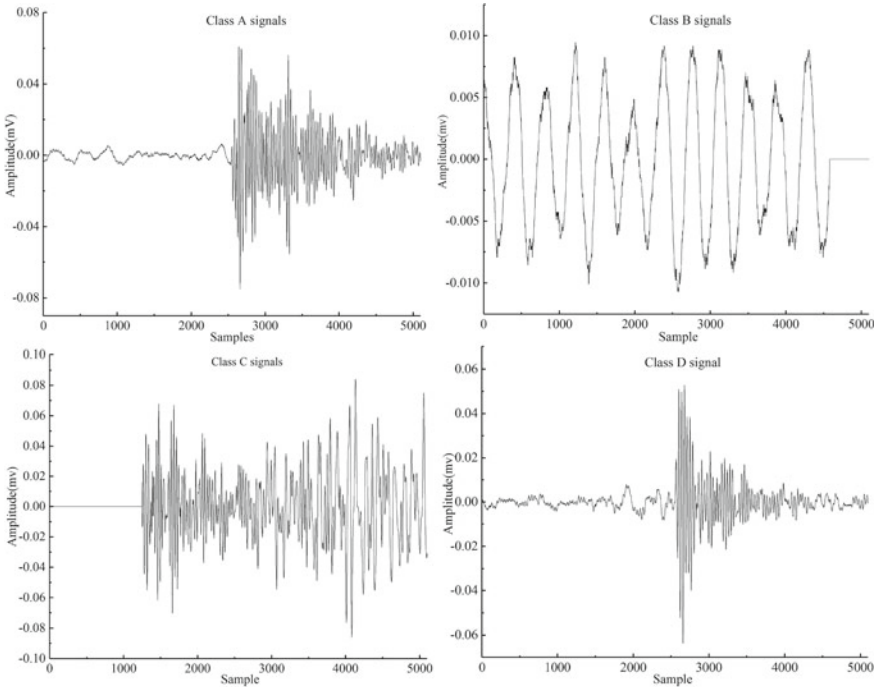

Fig. 50.8 Four types of typical AE signal waveforms during the failure of cathode carbon block

50.4 Conclusion

1. By analyzing the stress-time curve of the cathode carbon block under uniaxial compression loads and the AE characteristic parameters of the entire loading process, it is concluded that the destruction of the cathode carbon block can be divided into four stages. There are fewer AE signals during the compaction and elastic phases. In the plastic phase, the AE activity is the most intense. And after the cathode carbon block enters the peak stress, due to the existence of certain residual stress, more AE signals are also generated; the final failure mode of the specimen is *X*-conjugate shear failure. It is different from brittle materials such as rock in that it has strong plasticity.
2. During the destruction of the cathode carbon block, *RA*-value increases firstly then decreases, while *AF*-value is on the contrary, indicating that there are many tensile cracks in the early stage of loading. As the load continued to increase, the internal cracks evolve from tensile cracks to shear cracks in the cathode carbon block. During the peak stress stage, a few tensile cracks are generated by the internal crack interactions and friction between aggregate particles. It is shown from the distribution of *RA*-*AF* values that the main failure mode of cathode carbon block is a tensile failure.

3. According to *k*-means clustering analysis, AE signals of cathode carbon blocks can be divided into four types under uniaxial compression loads. Combined with the parameter characteristics, waveform characteristics and time distribution of the four types of signals, it is concluded that the class A signals correspond to the sudden tensile failure caused by the interaction of macro crack and the friction between aggregate particles in post-peaking stage. Class B signals are considered as the noise generated by the friction between the testing machine and the end face of the cathode carbon block. Class C signals refer to the shear slip cracking before the macro fracture as well as the crack propagation and penetrating large-scale shear failure at the peak stress that affects the overall stability of the cathode carbon block. Class D signals are considered as the signals generated by the fracture of the connection between aggregate particles and the compaction of pores between aggregate particles during the early stage of loading.

References

1. Q.S. Liu,W.H. Liu, Acoustic emission characteristics and failure modes of cathode carbon blocks under uniaxial compression for aluminum electrolysis. Light Met. **2**, 23–27 (2014) (in Chinese)
2. Q.S. Liu,H.F. Liu, Mechanical properties of carbon cathodes during aluminium electrolysis. Adv. Mater. Res. 399–401:2155–2159 (2012)
3. J. Xu, Z. Fu, Q. Han, G. Lacidogna, A. Carpinteri, Micro-cracking monitoring and fracture evaluation for crumb rubber concrete based on acoustic emission techniques. Struct. Health Monit. **7**. 147592171773053 (2017)
4. S. Yuyama, Z.W. Li, Y. Ito et al., Quantitative analysis of fracture process in RC column foundation by moment tensor analysis of acoustic emission. Constr. Build. Mater. **13**(1–2), 87–97 (1999)
5. D.G. Aggelis, A.C. Mpalaskas, T.E. Matikas, Investigation of different fracture modes in cement-based materials by acoustic emission. Cem. Concr. Res. **48**(2), 1–8 (2013)
6. D.G. Aggelis, T.E. Matikas, Effect of plate wave dispersion on the acoustic emission parameters in metals. Comput. Struct. **98–99**(5):17–22 (2012)
7. T. Shiotani, M. Ohtsu, K. Ikeda, Detection and evaluation of AE waves due to rock deformation. Constr. Build. Mater. **15**(5–6), 235–246 (2001)
8. D. Soulioti, N.M. Barkoula, A. Paipetis et al., Acoustic emission behavior of steel fibre reinforced concrete under bending. Constr. Build. Mater. **23**(12), 3532–3536 (2009)
9. D.G. Aggelis, A.C. Mpalaskas, D. Ntalakas et al., Effect of wave distortion on acoustic emission characterization of cementitious materials. Constr. Build. Mater. **35**, 183–190 (2012)
10. G. Villalobos, Acoustic emission signals resulting from the drying induced fractures of Phyllostachys pubescens bamboo: evidence of scale free phenomena. Wood Sci. Technol. (2016)
11. I. Ioka, S. Yoda, et al., Behavior of acoustic emission caused by microfracture in polycrystalline graphites. Carbon **28**, 879–885 (1990)
12. N. Ekinaga, K. Tamagawa, H. Takahashi, Acoustic emission characteristics and fracture toughness of artificial graphite electrodes. J. Eur. Ceram. Soc. **7**, 49–54 (1991)
13. G. Yonga, X. Denghong et al., Identification of damage mechanisms of carbon fiber reinforced silicon carbide composites under static loading using acoustic emission monitoring. Ceram. Int. **45**, 13847–13858 (2019)

14. A. Carpinteri, M. Corrado, G. Lacidogna, Heterogeneous materials in compression: correlations between absorbed, released and acoustic emission energies. Eng. Fail. Anal. **33**, 236–250 (2013)
15. B. Menendez, C. David, M. Darot, A study of the crack network in thermally and mechanically cracked granite samples using confocal scanning laser microscopy. Phys. Chem. Earth Part A: Solid Earth Geod. **24**(7), 627–632 (1999)
16. L. Yang, Y.C. Zhou, C.S. Lu, Damage evolution and rupture time prediction in thermal barrier coatings subjected to cyclic heating and cooling :an acoustic emission method.Acta Mater. **59**, 6519–6529 (2011)
17. T. Ohira, Y.H. Pao, Quantitative characterization of microcracking in A533B steel by acoustic emission. **20**(6), 1105–1114 (1989)
18. L. Yang, H.S. Kang, Y.C. Zhou et al., Frequency as a key parameter in discriminating the failure types of thermal barrier coatings: Cluster analysis of acoustic emission signals. Surf. Coat. Tech. **264**, 97–104 (2015)
19. A. Likas, N. Vlassis, J. Verbeek, The global k-means clustering algorithm. Pattern Recogn. **366**(2), 451–461 (2003)
20. J.A. Lozano, J.M. Pena, P. Larranaga, An empirical comparison of four initialization methods for the k-means algorithm. Pattern Recog. Lett. **20**, 1027–1040 (1999)
21. P.J. Rousseeuw, Silhouettes: a graphical aid to the interpretation and validation of cluster analysis. J. Comput. Appl. Math. **20**, 53–65 (1987)
22. R. Gutkin, C.J. Green et al., On acoustic emission for failure investigation in CFRP: Pattern recognition and peak frequency analyses. Mech. Syst. Signal Process. **25**, 1393–1407 (2011)
23. S. Momon, N. Godin, et al., Unsupervised and supervised classification of AE data collected during fatigue test on CMC at high temperature. Compos: Part A: Appl. Sci. **43**, 254–260 (2012)
24. Y.B. Zhang, P. Liang, et al., Multi-parameter coupling analysis of acoustic emission signal of granite disaster and experimental study on precursory characteristics of main fracture. J. Rock Mech. Eng. **35**(11), 2248–2258 (2016) (in Chinese)